Synthetic Approaches to Light-Harvesting Materials Containing Earth-Abundant Metals



Trinity College Dublin
Coláiste na Tríonóide, Baile Átha Cliath
The University of Dublin

A thesis submitted to the University of Dublin for the degree of Doctor of Philosophy

Friedrich Wilhelm Steuber, M. Sc.

School of Chemistry
University of Dublin
2020

Declaration

I declare that this thesis has not been submitted as an exercise for a degree at this or any other university and it is entirely my own work.

I agree to deposit this thesis in the University's open access institutional repository or allow the library to do so on my behalf, subject to Irish Copyright Legislation and Trinity College Library conditions of use and acknowledgement.

.....

Friedrich Wilhelm Steuber

Summary

In this thesis, entitled *Synthetic Approaches to Light-Harvesting Materials Containing Earth-Abundant Metals*, a crystal engineering approach is taken to investigate two kinds of materials, namely coordination polymers based on Cu^{I} photosensitive metallo-linkers available from dye-sensitised solar cell research, as well as phosphonate-stabilised titanium-oxo clusters. The resulting materials were characterised using single crystal X-ray diffraction, their photo- and electrochemical properties examined, and structure-property relationships elucidated. Moreover, the inherent synthetic opportunities, but also limitations towards novel materials were investigated.

Chapter 1 provides a summary of available literature, which illustrates the need for light-harvesting materials, the necessity to base those on earth-abundant metals, and the background of the materials discussed in this work.

The first part of this work is concerned with the incorporation of Cu^{I} photosensitisers as metallo-linkers into coordination polymers. In Chapter 2, the synthesis, structural characterisation of five isostructural 2D coordination polymers based on a simple bis(diimine)copper(I) complex is presented. It provides the first investigation of the effect of immobilisation of such Cu^{I} photosensitisers into extended structures with respect to photo- and electrochemical properties.

In Chapter 3, the influence of ligand modifications onto stability of the copper(I) complexes during solvothermal synthesis is elucidated, with respect to extension of the back-bone and steric encumbrance of the metal centre. While no heterometal-containing extended structures could be obtained, valuable information for more refined strategic approaches with respect to future work was obtained.

The second part of this work is focussed on exploring the synthetic robustness of a phosphonate-stabilised titanium-oxo cluster with a $\{Ti_6P_2\}$ skeleton, with respect to the introduction of different functional groups and their influence on *in situ* reactivity of the system, as well as the optical band gap. In Chapter 4, the conditions to functionalise the cluster with various aminobenzoic acids are established and their influence on the clusters optical band gap discussed. Moreover, it is demonstrated that the corresponding Schiff bases are formed *in situ* by the addition of aldehydes. By utilising *o*-aminobenzoic acid, the cluster core is halide-doped and Schiff bases reduced. The

proximity between amine and carboxylic acid as well as the influence of chirality onto the systems was further investigated with alanines.

In Chapter 5, the $\{Ti_6P_2\}$ motif's tendency to form and band gap tunability is further demonstrated with the aid of carboxylic acid azo- and coumarin-dyes, as well as extension of the π-system with respect to previously reported clusters. The anthraquinone-2-carboxylate cluster demonstrates redox non-innocence and viable mechanisms for the *in situ* reduction are elucidated. Moreover, a quantitative relationship between the electronic properties of substituents in terms of Hammett constants and the titanium-oxo cluster's optical band gap is established.

In Chapter 6, a heteroleptic Cu^I photosensitiser is anchored onto the $\{Ti_6P_2\}$ motif as a model compound for photosensitiser-TiO_2 composite materials. This is achieved both by first attaching an ancillary ligand and then the Cu^I centre, as well as by direct cluster formation from the preformed Cu^I complex. Steady-state photophysical and electrochemical features of the heteroleptic Cu^I on the cluster are retained with respect to its ester.

Chapter 7 provides overall conclusions of this work and the details of experimental procedures are presented in Chapter 8.
The bibliography of this thesis is listed in Chapter 9. Additional information is found in the appendix. Crystallographic information files for each structure, FTIR spectra not shown in main body, and EDX spectra are provided on the attached CD.

Acknowledgements

There are a lot of people without whom this work wouldn't have been possible and at this stage I would like to thank them.
First, I would like to thank my supervisor, Prof. Wolfgang Schmitt, for granting me the opportunity to conduct research under his guidance and letting me explore my ideas in the lab. Moreover, I would like to thank the European Research Council for supporting me financially and Science Foundation Ireland for providing research infrastructure.

Dr. Brendan Twamley has my utmost gratitude for all the fun times in the crystal cave, fruitful discussions about crystallography, and appreciating the quality of my crystals. I would like to thank the members of the Schmitt group for broadening my cultural horizon and always being great banter. Without it, the last four years would have been much drier. Specifically, I would like to thank: Éadaoin Whelan for measuring diffuse reflectance spectra on "what are all the yellow samples???", as well as SEM & EDX measurements, but also being there for the Ha Has; Paul Wix for laughing at my German-reference jokes and letting me crash on his couch during my first weeks in Dublin; Dr. Joaquin Soriano-López for all the help with electrochemistry; Dr. Colm Healy, Luana Martins, Éadaoin Whelan, and Mariah O'Doherty for approving all my chemical orders; My project student Lyubomir "Louie... I told you!!!" Burtniak for making bulk characterisable amounts of my CPs. I am grateful for all the hilarious debates we had in the downstairs lab: Thank you Colm, Kevin, Paul, and Dr. sahib Debobroto Sensharma. I thank Swetanshu "Shwaaayyyy" Tandon for conversations about computational chemistry, scientific integrity, and animated shows.

I also thank Dr. John Gough and Prof. Louise Bradley for carrying out the photophysical measurements on my coordination polymers. I thank Dr. John O'Brien and Dr. Manuel Rüther for NMR measurements and the latter also for training me on several instruments. I thank Dr. Martin Feeney and Dr. Gary Hessman for mass spectrometry, Dr. Rónán Crowley for the super fast turn-around on microanalysis, Maura Boland and Frederick Cowzer for help in stores, and Patsy Greene for access to his lab.

The community at Gravity Climbing Centre has my gratitude for helping to retain my sanity and being the most wholesome bunch I have ever encountered.

I would like to thank my parents and their respective partners for the undying support they have given me throughout my life. I know I can always count on you. I am immensely grateful to have friends such as Nils and Felix, who let me crash at their gaff every year during my winter vacation.

Lastly, but also most importantly I would like to thank my girlfriend Elaine, who has been the best partner imaginable, as well as her family (including the late Mr. Momo, Hallie, and Boris; may they rest in purrs) for accepting me into it and making me feel at home.

Contents

Declaration I

Summary II

Acknowledgements IV

Table of Contents VI

Abbreviations X

List of Compounds XIV

1. Introduction 1

1.1. Energy Crisis 1
1.2. Solar Hydrogen Production 2
1.3. Dye-Sensitised Solar Cells 3
1.4. Earth-Abundant Metal Photosensitisers 4
1.4.1. Ru^{II}- *vs.* Cu^{I}-Photosensitisers 5
1.4.2. Synthesis of Diimine Ligands 8
1.4.3. Heteroleptic Cu^{I}-Photosensitisers 9
1.5. Metal-Organic Frameworks & Coordination Polymers 13
1.5.1. Reticular Chemistry 13
1.5.2. Synthesis 16
1.5.3. Potential Applications of Metal-Organic Frameworks 17
1.5.4. Metal–Organic Frameworks for Photocatalysis and Light Harvesting 19
1.6. Titanium-Oxo Clusters 22
1.6.1. Synthetic Approaches for Titanium-Oxo Clusters 23
1.6.2. Structural Diversity of Titanium-Oxo Clusters 24

1.6.3. Applications of Titanium-Oxo Clusters 29
1.7. Objectives 30

2. Coordination Polymers with Cu^{I}-Photosensitisers as Linkers 32
2.1. Introduction 32
2.2. Synthesis 34
2.3. Structural Characterisation of **2(M)** 35
2.4. Photophysical Properties 48
2.5. Electrochemistry 52
2.6. Additional Characterisations 53
2.7. Conclusion 56

3. Diimine Ligands and Bis(diimine)copper(I) Complexes 57
3.1. Bipyridine Derivates 57
3.1.1. Introduction 57
3.1.2. Synthesis 57
3.1.3. Crystal Structure of *N*-acetonylpyridiunium chloride (**4**) 60
3.1.4. Crystal Structures of $[Cu(H_2\mathbf{L1})(H\mathbf{L1})]$ (**3**) and $[Cu(H_2\mathbf{L2})(H\mathbf{L2})]$ (**5**) 63
3.1.5. Crystal Structure of 4,4'-Difuryl-6,6'-diisopropyl-2,2'bipyridine (**6**) 68
3.2. Neocuproines 70
3.2.1. Introduction 70
3.2.2. Synthesis 70
3.2.3. Crystal Structure of 4,7-Dichlorocuproine ($CuprCl_2$, **7**) 72
3.2.4. Crystal Structure and Properties of $[Cu(CuprPy_2)_2]PF_6$ (**8**) . . 75
3.2.5. Crystal Structure of $[Cu(CuprCobal_2)(Cl)_2(OH_2)]$ $[Co(CuprCobal_2)(Cl)_2]$ (**9**) 78
3.3. Conclusion 82

4. Phosphonate Stabilised Titanium-Oxo Clusters from Amino Acids 83
4.1. Introduction 83
4.2. Aminobenzoate Functionalised Titanium-Oxo Clusters 85
4.2.1. Synthesic Approach 85
4.2.2. The $\{Ti_5\}$-Oxo Cluster **10** 86
4.2.3. $\{Ti_6\}$-Oxo Clusters from Aminobenzoic Acids 90

4.2.4. Optical Properties of Aminobenzoate Functionalised Titanium-Oxo Clusters . . . 100
4.3. Schiff Base-Benzoate Functionalised $\{Ti_6\}$-Oxo Clusters . . . 102
4.3.1. Synthesis . . . 102
4.3.2. Ferrocenyl- and Pyridyl-Schiff Bases in the *para*- and *meta*-Position 103
4.3.3. $\{Ti_6\}$-Oxo Cluster with Methylimidazolyl-Schiff Bases . . . 110
4.3.4. $\{Ti_6\}$-Oxo Clusters with Reduced Schiff Base-Benzoates . . . 116
4.3.5. Optical Properties Schiff Base-Benzoate Functionalised $\{Ti_6\}$-Oxo Clusters . . . 120
4.4. Quinoxalinecarboxylate Functionalised $\{Ti_6\}$-Oxo Cluster . . . 122
4.4.1. Synthesis . . . 122
4.4.2. $\{Ti_6\}$-Oxo Clusters with Quinoline-6- and 5-Carboxylic Acid . . 122
4.4.3. Optical Properties of Quinoxalinecarboxylate Functionalised $\{Ti_6\}$-Oxo Cluster . . . 126
4.5. Titanium-Oxo Clusters Derived from Alanines . . . 128
4.5.1. Synthesis . . . 128
4.5.2. Structural Characterisation . . . 129
4.5.3. Optical Properties of **20** . . . 135
4.6. Conclusion . . . 136

5. Phosphonate Stabilised $\{Ti_6\}$-Oxo Clusters with Extended π-Systems 138
5.1. Introduction . . . 138
5.2. Synthesis . . . 139
5.3. $\{Ti_6\}$-Oxo Clusters with Azobenzoates . . . 140
5.3.1. Structural Characterisation . . . 140
5.3.2. Optical Properties of Azo-Functionalised $\{Ti_6\}$-Oxo Clusters . . 144
5.4. $\{Ti_6\}$-Oxo Clusters with Fused Aromatic Rings . . . 145
5.4.1. Structural Characterisation . . . 145
5.4.2. Optical Properties of Pyrene- and Acridine Functionalised $\{Ti_6\}$-Oxo Clusters . . . 154
5.5. $\{Ti_6\}$-Oxo Clusters with Coumarin-3-carboxylates) . . . 155
5.5.1. Structural Characterisation . . . 155
5.5.2. Optical Properties . . . 161
5.6. $\{Ti_6\}$-Oxo Clusters of Anthraquinone-2-carboxylic acid . . . 162
5.6.1. Synthesis . . . 162
5.6.2. Structural Characterisation of the Polymorphs of **25** . . . 165

5.6.3. Optical Properties 174
5.7. Quantified Bandgap Engineering 175
5.8. Conclusions 179

6. Anchoring of a Heteroleptic Cu^{I} Photosensitiser onto a Titanium-Oxo Cluster 180
6.1. Introduction 180
6.2. Synthesis 181
6.3. Crystal Structures 183
6.4. Additional Charactersiations 192
6.5. Photo- and Electrochemical Properties 195
6.6. Conclusions 198

7. Conclusions & Future Work 199

8. Experimental 202
8.1. Materials & Methods 202
8.2. Syntheses 205

9. Bibliography 229

A. Appendix 256

Abbreviations

1D	One-Dimensional
2D	Two-Dimensional
3D	Three-Dimensional
Acr	Acridine
approx.	approximately
ARU	Asymmetric Residual Unit
ATR	Attenuated Total Reflection
$AQCO_2$	Anthraquinone-2-carboxylate
bpy	2,2'-Bipyridine
C343H	Coumarin 343
Cat	Catecholate
CB	Conduction Band
CIGS	Cd-In-Ga-Se
CSD	Cambridge Structural Database
$CuprCl_2$	4,7-Dichlorocuproine
$CuprCobal_2$	4,7-(chloro(4'-pyridinyl)cobaloxime)cuproine
$CuprPy_2$	4,7-Dipyridylcuproine
CV	Cyclovoltammetry
dba	dibenzylideneacetone
DCM	Dichloromethane
DEF	*N,N*-Diethylformamide
DMA	*N,N*-Dimethylacetamide
DmAbz	3,5-Diaminobenzoate
DMF	*N,N*-Dimethylformamide
dmp	2,9-Dimethylphenanthroline, Cuproine
$dmgH_2$	Dimethylglyoxime
DMSO	Dimethyl sulfoxide
dpp	2,9-Diphenylphenanthroline
$dp(OH)_2phen$	4,4'-(1,10-Phenanthroline-2,9-diyl)diphenol
dsbtmp	2,9-di(sec-butyl)-3,4,7,8-tetramethyl-1,10-phenanthroline
DSC	Dye-sensitised Solar Cell
e.g.	*exempli gratia*, for example
EDX	Energy Dispersive X-ray
et al.	*et alii*, and others

ESI	Electrospray Ionisation
Fluo	Fluorene
Fc	Ferrocene, Ferrocenyl
FTIR	Fourier-transform infrared
FTO	Fluorine-doped Tin Oxide
GooF	Goodness of Fit
H_2**L1**	6,6'-dimethyl-2,2'-bipyridine-4,4'-dicarboxylic acid
H_2**L2**	6,6'-dimethyl-2,2'-bipyridyl-4,4'-dibenzoic acid
H_2**L1**	6,6'-diisopropyl-2,2'-bipyridine-4,4'-carboxylic acid
HER	Hydrogen Evolving Reaction
HETPHEN	HETeroleptic PHENanthroline
HKUST	Hong Kong University of Science and Technology
HOMO	Highest Occupied Molecular Orbital
i.e.	*id est*, that is
IC	Internal Conversion
$iPr_2BpyFur_2$	4,4'-Difuryl-6,6'-diisopropyl-2,2-bipyridine
IRF	Instrument Response Function
ISC	Intersystem Crossing
ITO	Indium Tin Oxide
m_{30}phen	4,7,10,13,16,19-Hexaoxa-2(2,9)-phenanthrolina-1,3(1,4)-dibenzena-cyclononadecaphane
mAbz	3-Aminobenzoate
$Me_2BpyFur_2$	4,4'-Di(2-furyl)-6,6'-dimethyl-2,2'-bipyridine
MeBpyBz	6-Methyl-2,2'-Bipyridinyl-4-(4'-Benzoate)
MeIm	1-Methyl-Imidazole, 1-Methyl-Imidazolyl
MIL	Matériaux de l'Institut Lavoisier
MLCT	Metal-to-Ligand Charge Transfer
MOF	Metal-Organic Framework
MRH	Methyl Red
MS	Mass Spectrometry
NaphthAla	*S*-2-(1,8-naphthalimido)propanoate
NMR	Nuclear Magnetic Resonance
NU	Northwestern University
oAbz	2-Aminobenzoate
OER	Oxygen Evolving Reactio

ORTEP	Oak Ridge Thermal Ellipsoid Plot
pAbz	4-Aminobenzoate
pAPhBz	4'-Amino-4-phenylbenzoate
param.	Parameters
PC	Photocatalytic Cell
PCN	Porous Coordination Network
PEC	Photoelectrochemical Cell
PhN_2BzH	4-(Phenylazo)benzoic acid
phen	Phenanthroline
PL	Photoluminescence
POM	Polyoxometallate
POP	Bis(2-(diphenylphosphino)phenyl)ether
PTC	Phosphate-Stabilised Titanium Cluster, Polyoxo-Titanium Clusters
PV-EC	Photovoltaic-Electrochemical Cell
PXRD	Powder X-ray Diffraction
Py	Pyridine, 2-Pyridinyl
Pyr	Pyrene
RCSR	Reticular Chemistry Structural Resource
Refl.	Reflections
rest.	Restraints
SALSAC	Surfaces-As-Ligands, Surfaces-As-Complexes
SBU	Secondary Building Unit
SC	Semiconductor
SCXRD	Single Crystal X-ray Diffraction
SEM	Scanning Electron Microscopy
Sphos	2-Dicyclohexylphosphino-2',6'-dimethoxybiphenyl
TFA	Trifluoroacetic Acid
TGA	Thermal Gravimetric Analysis
TGA	Thermogravimetric Analysis
TOC	Titanium-Oxo Cluster
TRPL	Time-resolved photoluminescence
UiO	Universitetet i Oslo
UV	Ultraviolet
VB	Valence Band
Vis	Visible

viz	*videlicet*, namely
vs	*versus*, against
Xantphos	4,5-Bis(diphenylphosphino)-9,9-dimethylxanthene

List of Compounds

1	$[Cu(H_2\mathbf{L1})_2]PF_6$
2(Mn)	$[Cu(H_{0.53}\mathbf{L1})_2Mn_{0.5}][Mn(OH_2)_4]_{0.53}$
2(Co)	$[Cu(H_{0.62}\mathbf{L1})_2Co_{0.5}][Co(OH_2)_4]_{0.38}$
2(Cu)	$[Cu(H_{0.86}\mathbf{L1})_2Cu_{0.5}][Cu(OH_2)_4]_{0.14}$
2(Zn)	$[Cu(H_{0.75}\mathbf{L1})_2Zn_{0.5}][Zn(OH_2)_4]_{0.25}$
2(Cd)	$[Cu(H_{0.68}\mathbf{L1})_2Cd_{0.5}][Cd(OH_2)_4]_{0.32}$
3	$[Cu(H_2\mathbf{L1})(H\mathbf{L1})]$
4	*N*-Acetonylpyridinium chloride
5	$[Cu(H_2\mathbf{L2}_2)(H\mathbf{L2})]$
6	$iPr_2BpyFur_2$, 4,4'-Difuryl-6,6'-diisopropyl-2,2-bipyridine
7	4,7-Dichloroneocuproine
8	$[Cu(CuprPy_2)_2]PF_6$
9	$[Cu(CuprCobal_2)(Cl)_2(OH_2)][Co(CuprCobal_2)(Cl)_2]$
10	$[Ti_5O_2(OiPr)_6(O_3PPh)_2(pAbz)_4]$
11a	$[Ti_6O_4(OiPr)_{10}(O_3PPh)_2(pAbz)_2]$
11b	$[Ti_6O_4(OiPr)_{10}(O_3PPh)_2(FcCHN{-}4{-}Bz)_2]$
11c	$[Ti_6O_4(OiPr)_{10}(O_3PPh)_2(PyrCHN{-}4{-}Bz)_2]$
11d	$[Ti_6O_4(OiPr)_{10}(O_3PPh)_2(MeImCHN{-}4{-}Bz)_2]$
11e	$[Ti_6O_4(OiPr)_{10}(O_3PPh)_2(BzN_2Ph)_2]$
12a	$[Ti_6O_4(OiPr)_{10}(O_3PPh)_2(pAPhBz)_2]$
12d	$[Ti_6O_4(OiPr)_{10}(O_3PPh)_2(MeImCHN{-}4{-}PhBz)_2]$
13a	$[Ti_6O_4(OiPr)_{10}(O_3PPh)_2(mAbz)_2]$
13b	$[Ti_6O_4(OiPr)_{10}(O_3PPh)_2(FcCHN{-}3{-}Bz)_2]$
13c	$[Ti_6O_4(OiPr)_{10}(O_3PPh)_2(PyrCHN{-}3{-}Bz)_2]$
13d	$[Ti_6O_4(OiPr)_{10}(O_3PPh)_2(MeImCHN{-}3{-}Bz)_2]$
14a	$[Ti_6O_4(OiPr)_{10}(O_3PPh)_2(DmAbz)_2]$
15a	$[Ti_6O_4(OiPr)_{10}(O_3PPh)_2(oAbz)_2]$
15b	$[Ti_6O_4(OiPr)_{10}(O_3PPh)_2(PyrCH_2NH{-}2{-}Bz)_2]$
15c	$[Ti_6O_4(OiPr)_{10}(O_3PPh)_2(MeImCH_2NH{-}2{-}Bz)_2]$
15d	$[Ti_6O_4(OiPr)_{10}(O_3PPh)_2(MR)_2]$
16a	$[Ti_6O_4(OiPr)_8(Cl)_2(O_3PPh)_2(oAbz)_2]$
17	$[Ti_6O_4(OiPr)_{10}(O_3PPh)_2(Me_2Quinox{-}6{-}CO_2)_2]$
18	$[Ti_6O_4(OiPr)_{10}(O_3PPh)_2(Me_2Quinox{-}5{-}CO_2)_2]$

19	$[Ti_{14}O_6(OiPr)_{26}(O_3PPh)_8(\beta-Ala)_2]$
20	$[Ti_6O_4(OiPr)_{10}(O_3PPh)_2(NaphthAla)_2]$
21	$[Ti_6O_4(OiPr)_{10}(O_3PPh)_2(O_2CFluo)_2]$
22	$[Ti_6O_4(OiPr)_{10}(O_3PPh)_2(O_2CPyr)_2]$
23	$[Ti_6O_4(OiPr)_{10}(O_3PPh)_2(O_2CAcr)_2]$
24a	$[Ti_6O_4(OiPr)_{10}(O_3PPh)_2(O_2CCoum)_2]$
24b	$[Ti_6O_4(OiPr)_{10}(O_3PPh)_2(O_2CCoumNEt_2)_2]$
24c	$[Ti_6O_4(OiPr)_{10}(O_3PPh)_2(C343)_2]$
25	$[Ti_6O_4(OiPr)_{10}(O_3PPh)_2(O_2CAQ)_2]$
26a	$[Cu(Xantphos)(MeBpyBzMe)]PF_6$
26b	$[Cu(Xantphos)(MeBpyBzH)]PF_6$
27a	$[Ti_6O_4(OiPr)_{10}(O_3PPh)_2(BzMeBpy)_2]$
27b	$[Ti_6O_4(OiPr)_{10}(O_3PPh)_2\{Cu(Xantphos)(MeBpyBz)\}_2](PF_6)_2$

1. Introduction

1.1. Energy Crisis

The global population is steadily increasing, from an estimated 7.7 billion people in 2019 the medium-variant projection indicates growth to 8.5 billion by 2030, 9.7 billion by 2050, and will reach 10.9 billion by 2100.[1] Coupled with increasing urbanisation and modernisation, society's energy demand is ever growing and heavily reliant on fossil fuels, such as oil, gas and coal.[2] The associated excessive emissions of CO_2 into the atmosphere, which increased from 313 ppm to 412 ppm over the last 60 years,[3] cause entrapment of heat and more extreme weather events due to climate change.[4] While renewable energy sources, *e.g.* hydropower, wind power and solar energy, already account for over a quarter of electricity demand, heating and cooling as well as the transport sectors respectively made up 51% and 32% of global energy consumption in 2016.[5] Within those sectors, only 9.8% and 3.3% of the demand is met by renewable energy sources, respectively.[5] With regards to the transport, in 2015 passenger transport as well as cars and motorbikes were respectively responsible for 63% and 45% of energy usage.[5] While renewable heat sources, such as geothermal, biomass and solar thermal energy, can help decarbonise the industrial sector, hydrogen represents of three options, alongside biofuels and electric vehicles, to decarbonise the transport sector.[5,6] Here, the land-use and air quality impacts of biofuels as well as the long recharging times and limited range of electric vehicles are avoided by hydrogen.[7] Moreover, hydrogen vehicles have virtually zero CO_2, NO_x, and particulate emissions and can thus improve air quality.[8] However, elemental hydrogen is not naturally abundant and thus the greatest obstacle to overcome is the cost-competitive low-carbon hydrogen production at a range of scales.[9] Currently, around 45-65 $Mt\,a^{-1}$ of hydrogen are globally produced as a feedstock the chemical and petrochemical industries, with only 4% produced from water electrolysis and the remainder derived from fossil fuels, by steam reforming of natural gas, partial oxidation of of crude oil products, and coal gasification.[6]

1.2. Solar Hydrogen Production

With an energy supply of 173 000 TW to the total surface of the earth,[10] solar energy provides almost 9600 times the global demand.[11] Currently, photovoltaics serves as one of the most disseminated technologies and is one of the fastest growing industries,[12] but produces electricity which is intrinsically difficult to store.[13] The solar spectrum, as well as an energy diagram for photolytic water splitting, as well as three systems to accomplish this task, *i.e.* photocatalytic (PC), photoelectrochemical (PEC), and photovoltaic-electrochemical (PV-EC) cells, are shown in Figure 1.1. Reactions occurring in photolytic water splitting in Equations (1.1) to (1.4).

$$\text{Absorption of light :} \quad \mathrm{SC} + h\nu(> E_g) \longrightarrow \mathrm{e^-_{CB}} + \mathrm{h^+_{VB}} \tag{1.1}$$

$$\text{Water oxidation (OER) :} \quad 2\,\mathrm{H_2O} + 4\,\mathrm{h^+_{VB}} \longrightarrow \mathrm{O_2} + 4\,\mathrm{H^+} \tag{1.2}$$

$$\text{Proton Reduction (HER) :} \quad 2\,\mathrm{H^+} + 2\mathrm{e^-_{CB}} \longrightarrow \mathrm{H_2} \tag{1.3}$$

$$\text{Overall water splitting :} \quad 2\,\mathrm{H_2O} \longrightarrow 2\,\mathrm{H_2} + \mathrm{O_2} \tag{1.4}$$

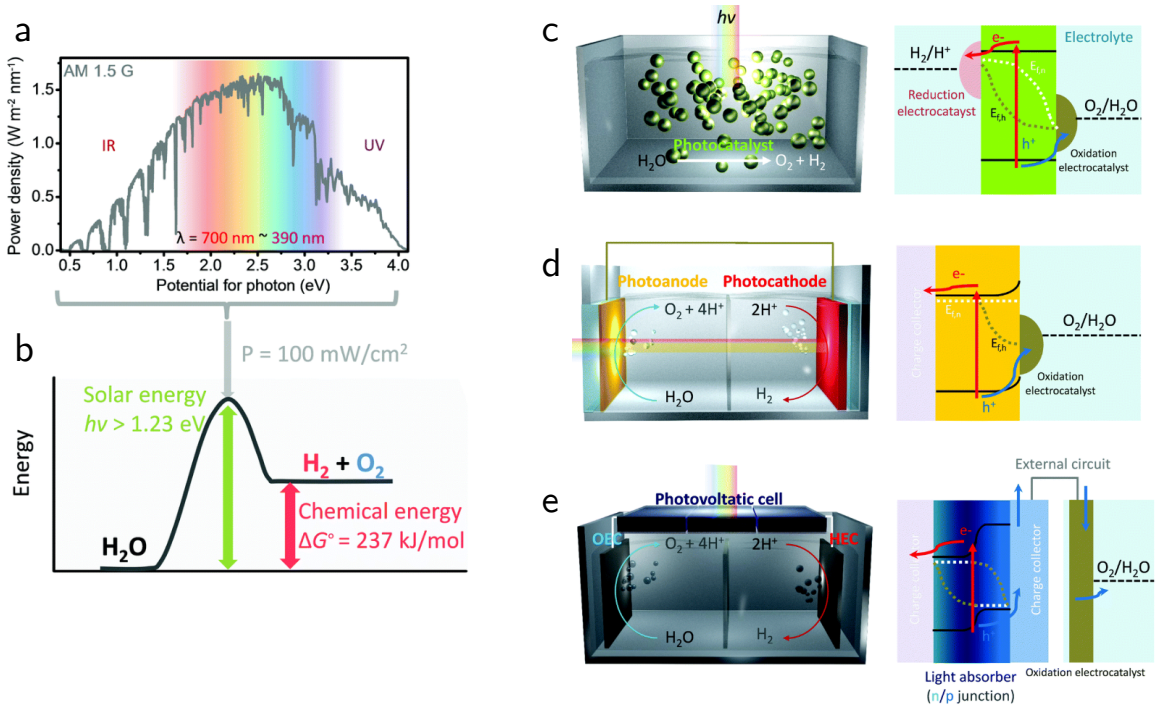


Figure 1.1: (a) Spectrum of AM 1.5 G, *i.e.* 1 sun condition. (b) Photochemical water splitting is an endergonic process. Light-driven water splitting systems and the charge flows upon light absorption in PC (c), PEC (b), and PV-EC (c) systems. Reprinted from Lee *et al.*[13]

An n-type semiconductor (SC) absorbs light with energy exceeding its band gap ($E_g = E_{CB} - E_{VB}$), where CB and VB are conduction and valence band) leading to charge separation. The photogenerated electrons (e^-_{CB}) and holes (h^+_{VB}) then respectively facilitate the oxygen (OER) and hydrogen evolving reactions (HER). In a PC system, the reduction and oxidation catalysts are both dispersed on a SC particle, whereas they are separately placed on photoelectrodes in a PEC cell. In a PV-EC cell, the reaction is driven on electrocatalysts by a current generated in a photovoltaic cell.[13]

With respect to photovoltaics, there are several approaches of device design: First generation solar cells are based on crystalline silicon and are currently the most used solar cells, however the high price of the materials and manufacture are a large drawback.[14–16] The second generation solar cells are base on thin films of amorphous silicon, CdTe, or CIGS (Cd-In-Ga-Se) on a glass or ceramics support material. The cost efficiency is significantly increased due to the low amount of material appliedand high solar power conversion efficiencies.[14–16] Both first and second generation devices are based on a single junction, which are restricted by the Shockley-Queisser limit of 31% power conversion efficiency, in which it is assumed that the absorption of a photon leads to the formation of a single electron-hole pair and that all photon energy above the band gap is lost as heat.[14] Devices overcoming this limit are considered third generation, such as tandem cells, hot carrier cells, multiband cells, and thermophotovoltaics.[14,17] The development of research-cell efficiencies since 1976 is presented in Figure A.1.[18]

1.3. Dye-Sensitised Solar Cells

An emerging type of photovoltaic devices are dye-sensitised solar cells (DSCs), which can be considered in between second and third generation, and are also known as Grätzel-type cell.[19] An n-type DSC is typically composed of sintered nanoparticles of a wide band semiconductor (typically TiO_2 in the form of anatase), which are coated onto a transparent conducting glass (usually fluorine-doped tin oxide, FTO, or indium tin oxide, ITO), and the surface is coated with a dye.[20] A schematic drawing of such a DSC is shown in Figure 1.2.[21] Upon the absorption of visible light, an electron is excited from the highest occupied molecular orbital (HOMO) into the lowest unoccupied molecular orbital (LUMO) of the dye yielding the excited state. The electron transfer (injection) into the conducting band of the SC formally oxidises the dye, whose ground state is regenerated by oxidation of the electrolyte (here iodide/triiodide). The latter is

regenerated by catalytic reduction at a platinised counter-electrode, completing the electric circuit. However, competing back reactions such as decay of the excited state dye back to the ground state, as well as recombination of the the injected electron with the oxidised dye or electrolyte also exist. Understanding the dynamics and interplay between these processes are crucial for the optimisation of DSC performances.[20,21] Conventional Grätzel n-type DSCs feature Ru^{II} complexes as photosensitisers: The

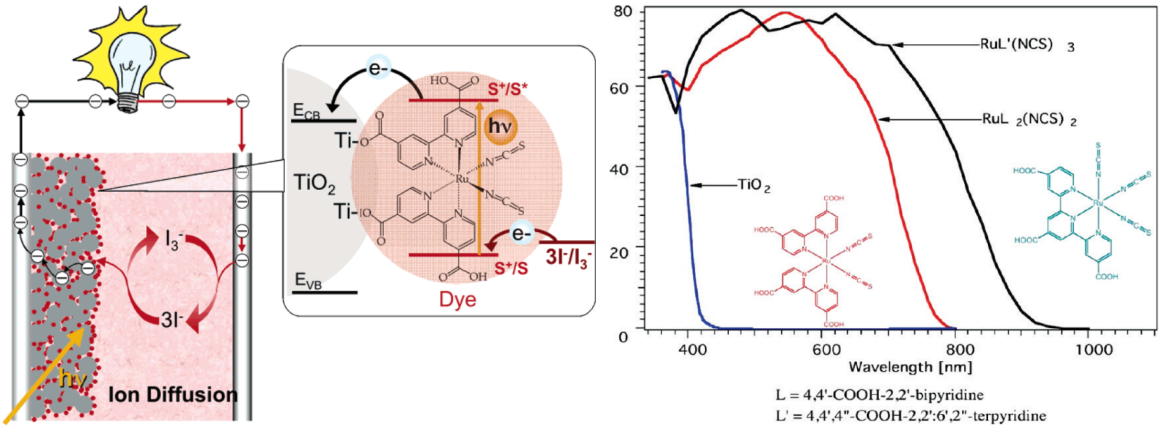


Figure 1.2: Schematic drawing of a DSSC (left) and incident photon to current conversion efficiency as a function of the wavelength for blank nanocrystalline TiO_2 film (blue line) with the ruthenium phtotosensitisers N3 (red line) and the "black dye" N749 (black line). Reprinted from Grätzel.[21,22]

structure of the benchmark dyes N3 and N749 ("black dye") as well as their photon to current conversion are shown also shown in Figure 1.2. While TiO_2 can only induce a current in the ultraviolet (UV) region, with the addition of N3 or N749 the entire visible (vis) region and even beyond can be utilised.[21,22] While DSCs with Ru-dyes present the benchmark, due to its scarcity (0.037 ppb) and high cost (7235 € kg^{-1}) necessitate the development of alternative dyes for commercial viability.[23,24]

1.4. Earth-Abundant Metal Photosensitisers

The abundance of elements in the earth's crust is shown in Figure 1.3. With a crustal abundance of 27 ppm and a three order of magnitude lower cost (5.87 € kg^{-1}), copper has drawn a considerable amount of attention in replacing ruthenium in DSCs over the last decade.[23,25–39]

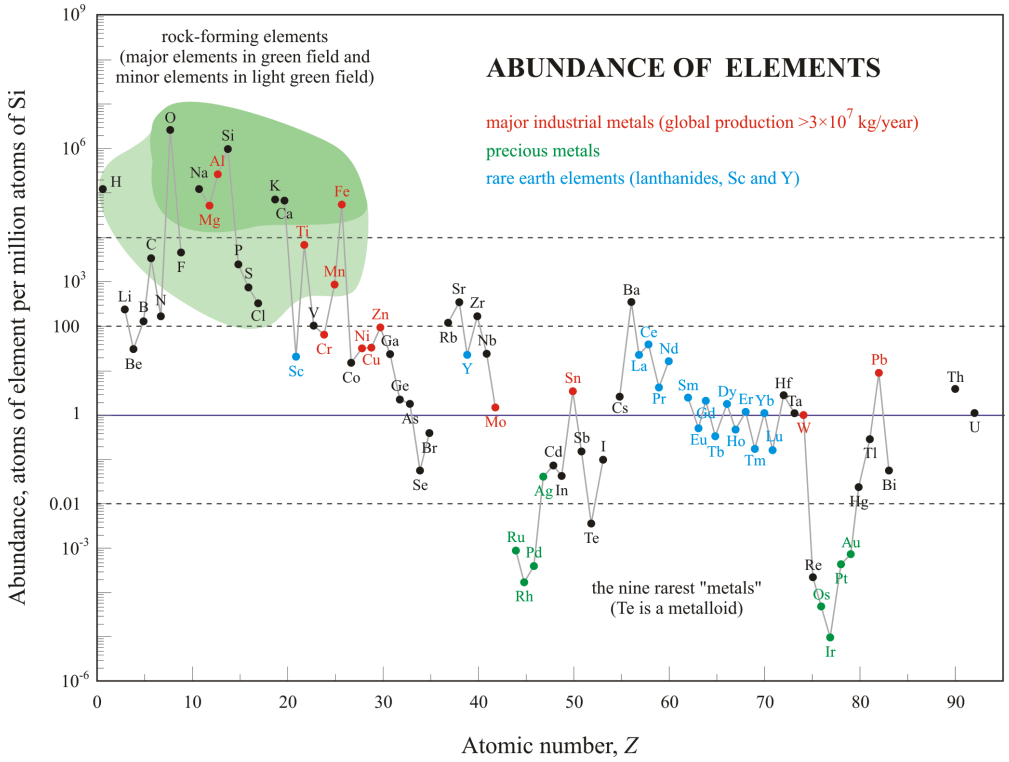


Figure 1.3: Crustal abundance of elements. Courtesy of Generalic.[40]

In the late 1970s, groundbreaking work by McMillin *et al.* established $[Cu(dmp)_2]^+$ (dmp: 2,9-dimethyl-1,10-phenanthroline, neocuproine) as a photosensitiser, resulting in great interest in bis(diimine)copper(I) complexes.[41]

1.4.1. Ru^{II}- *vs.* Cu^{I}-Photosensitisers

Ruthenium(II)-polypyridine complexes have drawn tremendous attention over the past 60 years due to their ease of preparation, reversible electrochemical behaviour, light absorption in the visible spectrum, long lived lectronically excited states, and intense luminescence.[42–45] The archetype of these complexes is tris-2,2'-bipyridylruthenium(II) ($[Ru(bpy)_3]^{2+}$), which features the d^6 metal centre in an octahedral coordination environment. As copper(I) is a d^{10} ion it prefers a tetrahedral environment and is thus only coordinated by two diimine ligands. The photophysical and electrochemical properties of $[Ru(bpy)_3]^{2+}$ and $[Cu(dpp)_2]^+$ (dpp: 2,9-diphenylphenanthroline) are compared in Figure 1.4. The excited state potentials can be estimated from the Rehm-Weller

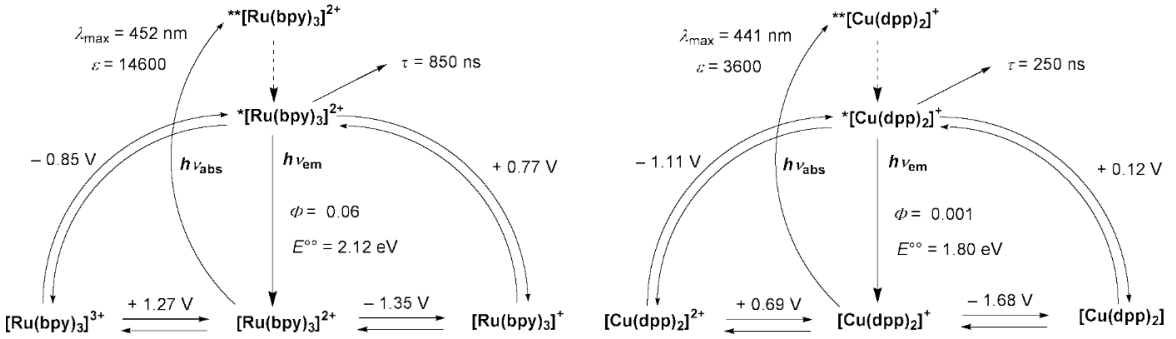


Figure 1.4: Comparison of the photophysical and electrochemical properties of $[Ru(bpy)_3]^{2+}$ and $[Cu(dpp)_2]^{+}$. Potentials are given *vs.* SCE. Reprinted from Armaroli.[42]

expressions, *viz.*

$$E(A^+/{}^*A) = E(A^+/A) - E_{00} \tag{1.5}$$

$$E({}^*A/A^-) = E(A/A^-) + E_{00} \tag{1.6}$$

where $^*A$ denotes the lowest-lying excited state and E_{00} is estimated from the emission spectra.[44] While both complexes are better oxidant and reductant in the excited than in ground state, $^*[Cu(dpp)_2]^+$ is a considerably more powerful reductant than $^*[Ru(bpy)_3]^{2+}$. Moreover, Cu^I is a closed shell d^{10} ion and hence does not suffer from parasitic *d*-*d*-transitions and has less spin-orbit coupling than the heavier d^6 ion Ru^{II}.[46] However, $^*[Cu(dpp)_2]^+$ is disfavoured with respect to $^*[Ru(bpy)_3]^{2+}$ in absorption intensities, photoluminescence quantum yields (Φ) and excited state lifetimes (τ). Yet, these properties can be finely tuned by the correct choice of diimine ligands.

The effects of different substituents in the 2,9-substituents on the copper(I) complexes of 1,10-phenanthroline ligands are shown in Figure 1.5. Intense ligand centred $\pi \rightarrow \pi^*$ transitions are typically found in the UV region of the absorption spectrum. With respect to metal-to-ligand charge transfer (MLCT) transitions, extensive work in the groups of McMillin, Karphishin, and Sauvage have culminated in the following assignment: Band I ($S_0 \rightarrow S_1$) typically appears above 500 nm, band II ($S_0 \rightarrow S_2$) is usually the strongest band and appears around 430-480 nm, whereas band III (390-420 nm) is often hidden in the onset of band II as it dipole forbidden, but can be vibronically induced.[42,47–54] Upon photoexcitation into the MLCT transition, one electron from the central Cu^I ion HOMO is transferred to the π^*-orbital LUMO localised on one of the ligands, formally oxidising the metal centre to d^9 Cu^{II}. This results in a pseudo-Jahn-

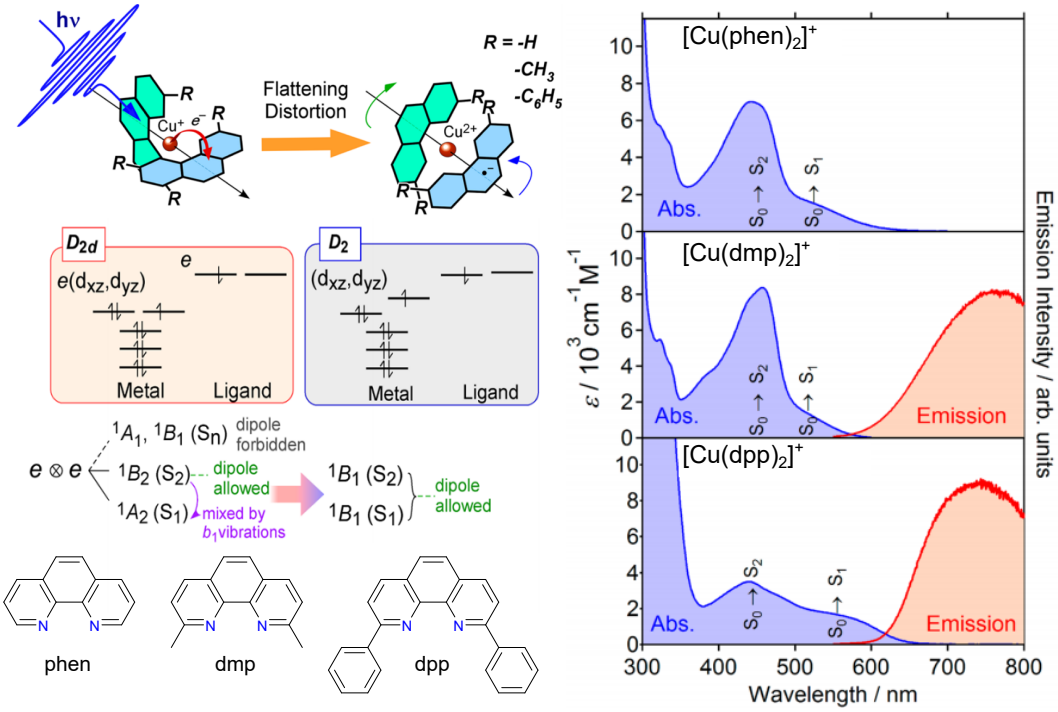


Figure 1.5: Photoinduced structural and electronic changes of three archetype copper(I) complexes featuring 1,10-phenanthroline (phen) ligands (left), as well as their steady state absorptiona nd emission spectra (right). Reprinted from Tahara *et al.*[47]

Teller flattening distortion, which reduces the molecular symmetry from D_{2d} to D_2. The steric effects of the phenyl groups in $[Cu(dpp)_2]^+$ lead to ground state flattening of the complex, which is accompanied by an increase and decrease of band II and band I, respectively. The lack of emission in $[Cu(phen)_2]^+$ can be explained by the large structural changes it undergoes upon excitation, making the d^9 ion vulnerable to nucleophilic attack by solvent and counterions, leading to pentacoordinated excited complexes (exciplexes), which in turn deactivate *via* non-radiative pathways.[42,47] However, methyl groups are already sufficient enough with regard to steric shielding of the metal centre to facilitate luminescence, which for bis(diimine)copper(I) complexes typically occurs in the orange-red region of the visible spectrum. The excited state dynamics of the above mentioned copper(I) complexes were investigated by Tahara *et al.* using femtosecond time-resolved fluorescence, the results of which are shown in Figure 1.6.[47] In essence, excitation of the complex, internal conversion (IC) to the S_1 state and the flattening distortion occur in the sub-picosecond region, which is followed by intersystem crossing (ISC) to the lowest lying triplet state T_1 in the early picosecond region.[47] Thus, ^{3}MLCT largely exceed the population of ^{1}MLCT and is responsible for

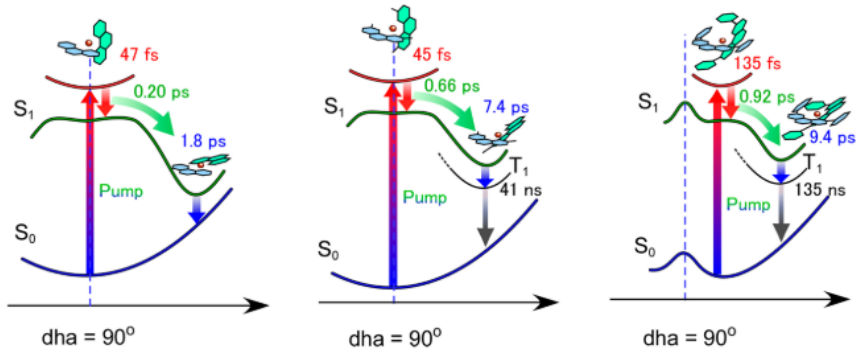


Figure 1.6: Schematic potential curves as a function of the dihedral angel (dha) and ultrafast relaxation processes of $[Cu(phen)_2]^+$, $[Cu(dmp)_2]^+$, and $[Cu(dpp)_2]^+$. Reprinted from Tahara *et al.*[47]

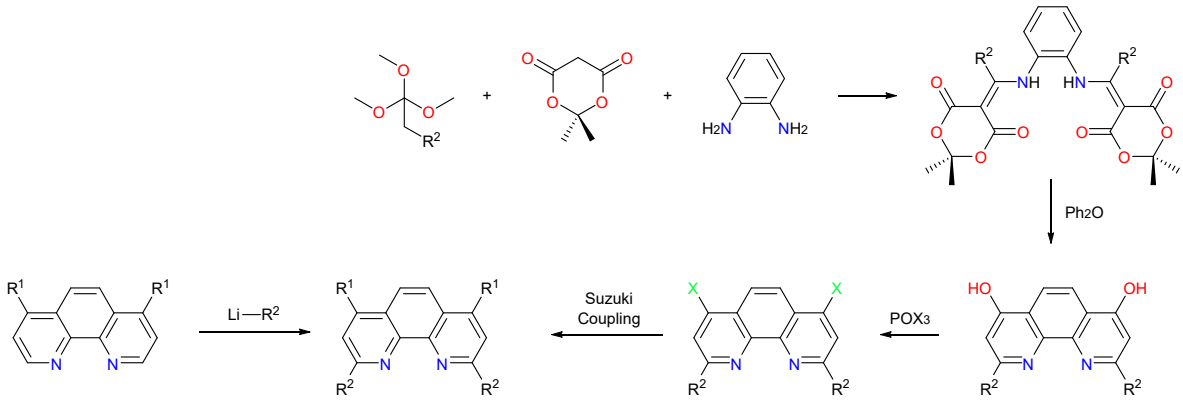
the luminescence and interactions with other molecules.[42]

With respect to tuning of photophysical properties of bis(diimine)copper(I) complexes, alkyl- and aryl-substituents respectively increase absorption and excited state in the *ortho* positions of the imine.[42] In the *para*-position, alkyl-groups barely have any effect whereas aryl-groups greatly increase light absorption bands.[42] Excited state lifetimes are expected to be below 100 ns for methyl groups and 250-500 ns phenyl-groups. Work in the group of Castellano has produced the homoleptic copper(I) complex of 2,9-di(sec-butyl)-3,4,7,8-tetramethyl-1,10-phenanthroline (dsbtmp), which exhibits an excited state lifetime of up to 2.8 µs.[55] A draw back of bigger alkyl-substituents such as the *tert*-butyl group is that the corresponding copper(I) complexes become thermodynamically unstable.[55–57]

Application of bis(diimine)copper(I) complexes has so far been largely focussed on fine tuning for DSCs especially for 2,2'-bipyridine-based ligands, whereas phenanthroline-based ligands have been used as photosensitiser in aqueous proton reduction, and as a photocatalyst in the C−C coupling of benzylic bromides, atom-transfer radical addition (*e.g.* alkenes and allylbromdies, allylation of α-halocarbonyl compounds), intramolecular aminodifluoromethylation of unactivated alkenes *etc.*[58–62]

1.4.2. Synthesis of Diimine Ligands

The two types of diimine ligands are based on 1,10-phenanthroline and 2,2'-bipyridine. With respect to 2,4,7,9-tetrasubstituted 1,10-phenanthroline ligands, there are two main approaches as outlined in Scheme 1.1. Derivates of phenanthroline (R^1=H) or



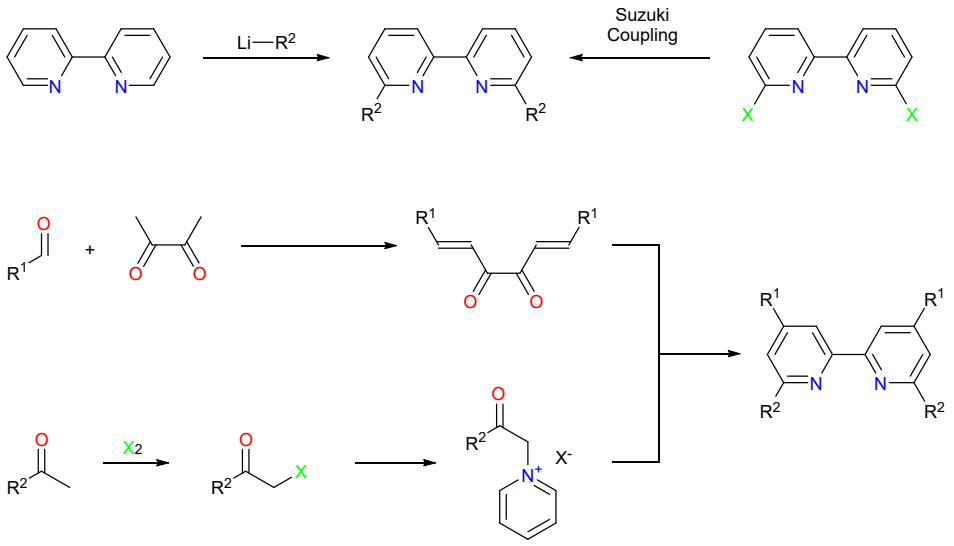
Scheme 1.1: Selected synthetic approaches for 2,4,7,9-tetrasubstituted 1,10-phenanthroline ligands.

bathocuproine (4,7-diphenylphenanthroline, R^1=Ph) can be easily obtained of the commercially available diimine and the appropriate organolithium reagent.[63–66] Alternatively, 2,9-disubstituted-4,7-dihydroxyphenanthroline can be obtained in a two step reaction starting from *orhto*-phenylenediamine, Meldrum's acid (2,2-dimethyl-1,3-dioxane-4,6-dione), and the appropriate trialkyl orhtoester, followed by a pericyclic reaction under elimination of CO_2 and acetone.[67–70] Functionalisation in the 4,7-positions is achieved by halogenation with phosphorous halides and subsequent Suzuki reaction with the boronic acid or ester of the desired functional group.[69] Of course, functionalisation in the 3,8- and 5,6-positions are also possible but will not be discussed here.

Similarly there are several synthetic routes towards substituted 2,2'-bipyridines (Bpy), some of which are outlined in Scheme 1.2. If substitution is merely desired in 6,6'-positions, R^2 can be attached to Bpy using the corresponding organolithium reagent, or a Suzuki coupling with the appropriate boronic acid or ester can be conducted with 6,6'-dihalo-2,2'-bipyridine.[71] The best way to synthesise 4,4'-6,6-tetrasubstituted 2,2'-bipyridines is *via* Kröhnke pyridine synthesis.[72] For this, aldol condensation between the aldehyde of the functionality desired in the 4,4'-position is carried out with diacetyl. If the desired pyridinium salts are not commercially available, they can be generated from the corresponding α-haloketone.

1.4.3. Heteroleptic Cu^I-Photosensitisers

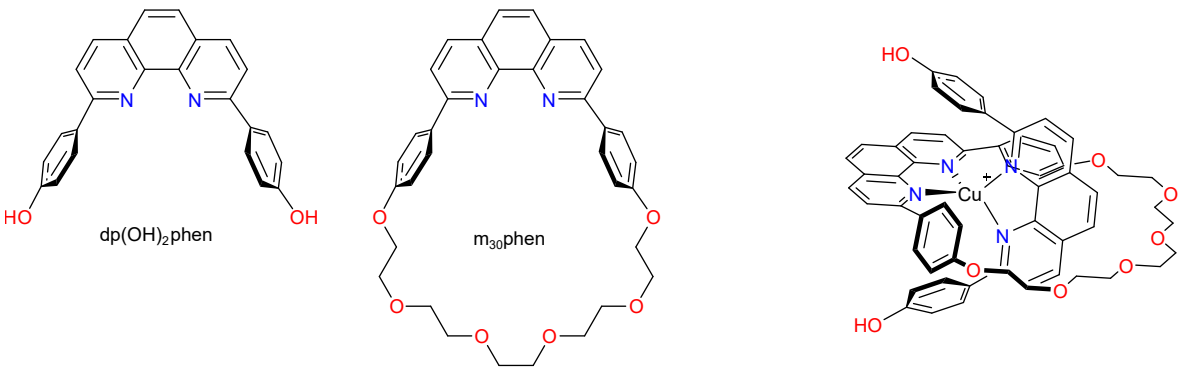
The synthesis of heteroleptic bis(diimine)copper(I) complexes is difficult due to the inherent lability of first-row transition metals and Cu^I in particular. As such ex-



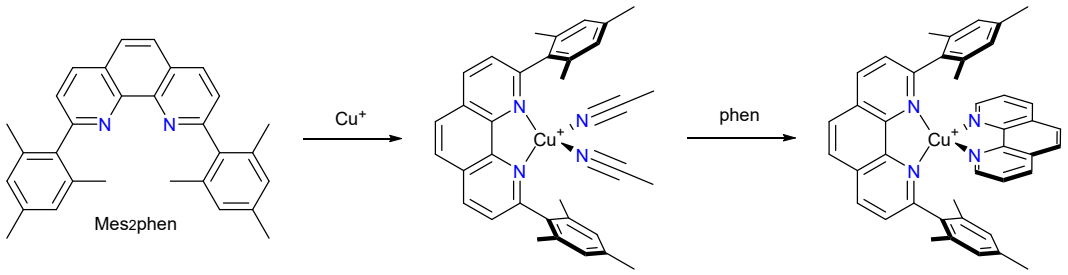
Scheme 1.2: Synthetic routes to 6,6'-disubstituted (top) and 4,4'-6,6-tetrasubstituted 2,2'-bipyridines (bottom).

change reactions occur and lead to statistical mixtures of homo- and heteroleptic complexes.[73] One way to circumvent this issue is through topological constraints, as demonstrated by the groups of Sauvage and Lehn in their pursuit of catenanes.[74–77] As shown in Scheme 1.3, the ligand dp$(OH)_2$phen readily forms homoleptic complexes (which can then be turned into the catenated complex $[Cu(m_{30}phen)_2]^+$), whereas this is not possible for the 30-membered macrocyclic ligand m_{30}phen, due to said topological constraints. However, heteroleptic complexes can easily obtained by first forming $[Cu(m_{30}phen)(MeCN)_2]^+$ followed by addition of a second diimine ligand.[75–78]

Another option is through steric constraints, which is employed in the HETPHEN (HETeroleptic PHENanthroline) concept developed by Schmittel in late 1990s.[73,78] Here, bulky aryl-groups such as mesityl are installed on the in *ortho*-positions of



Scheme 1.3: Heteroleptic bis(diimine)copper(I) complexes *via* topological constraints.[74,78]



Scheme 1.4: Heteroleptic bis(diimine)copper(I) complexes *via* topological constraints (HETPHEN).[78,79]

the nitrogen atoms, which hinder homoleptic bis(diimine)complex formation. An example of this is presented in Scheme 1.4: Sequential addition of the sterically demanding ligand Mes_2phen and phen selectively yields the heteroleptic complex cation $[Cu(Mes_2phen)(phen)]^+$.

Heteroleptic bis(diimine)complexes can also be generated on TiO_2 surfaces, based on the "surfaces-as-ligands, surfaces-as-complexes" (SALSAC) approach developed in the group of Housecroft and Constable.[80,81] As portrayed in Figure 1.7, ancillary ligands are first anchored onto the TiO_2 surface and either dipped into a solution containing a homoleptic complex featuring the desire antenna ligand. This wastes half of the precious organic ligands and alternatively the ancillary ligands, Cu^I, and the antennae ligands are sequentially attached to the surface. This approach however is strictly viable for DSCs and complexes are not isolable.

Furthermore, in recent years a lot of attention has been paid to heteroleptic diimine-

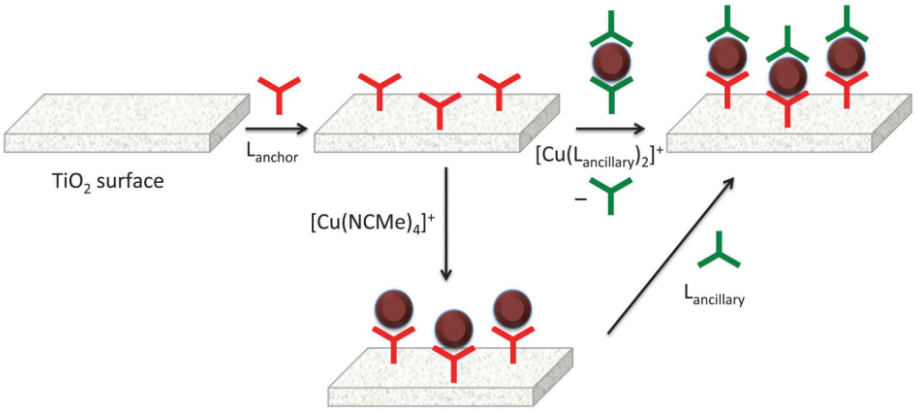


Figure 1.7: Assemble of heterloeptic bis(diimine)copper(I) comples on surfaces (SALSAC). Reprinted from Housecroft and Constable.[20]

diphosphine copper(I) photosensitisers.[82] The first generation of mixed-ligand complexes, $[Cu(dmp)(PPh_3)_2]^+$ and $[Cu(phen)(PPh_3)_2]^+$, were discovered in the group of McMillin.[83] The steric crowding by the phosphine ligands prohibits exciplex quenching, with the complexes showing yellow-green emission, with lifetimes on the range of several hundred nanoseconds.[83] Ether-linkage of the diphosphine moiety and the induced ligand rigidity in bis(2-(diphenylphosphino)phenyl)ether (POP) suppressed ligand disassociation and brought emission lifetimes into the low microsecond region.[84] The chelating diphosphines feature wide bite angles and are thus able to stabilise the tetrahedral and destabilise the square planar coordination environment.[85] These kind of phosphine have long been available from their use in homogeneous catalysis and particular attention has been paid to them as a result of their readily tunable electronic, *e.g.* σ-donor and π-acceptor, as well as steric properties, *e.g.* steric (Tolman) bite angle and accessible surface area.[85–87] As a result, they are often commercially available which has led to a cornucopia of mixed diimine-diphosphine copper(I) complexes (an extensive review was recently given by Dietzek *et al.*).[70,82,88–93] Unlike for bis(diimine) complexes, when a diphosphine, diimine and a copper(I) source are mixed, the heteroleptic complex readily forms. While they also undergo dynamic ligand exchange, this is highly dependant on the solvent, *i.e.* almost none is observed in MeCN, THF, DCM, and acetone, but dissociation is observed in MeOH and homoleptic complexes form almost instantly in chloroform.[90] Of course the steric and electronic properties of the diphosphine ligand also influence the photo- and electrochemical properties.[82] The ability of the diphosphine ligand to accept π-electron density from the centre lead to an energetic decrease of the HOMO.[94] As the LUMO is generally located in the diimine ligand, this increases the HOMO-LUMO gap,*i.e.* blue-shifts the absorption spectrum into the violet region, and only possess half the extinction coefficient.[82,89] Moreover, the oxidation potential of the copper(I) centre are typically quasi-reversible and appears at much higher anodic potentials.[82]

While their comparably low absorption in the visible region renders them moot for DSCs, diimine-diphosphine copper(I) complexes have found broad application as photosensitisers for photocatalytic water and CO_2 reduction, photocatalytic organic reactions, light emitting diodes, as well as oxygen sensing.[63,65,66,70,84,89,90,95–105]

1.5. Metal-Organic Frameworks & Coordination Polymers

A research topic that has seen an explosive growth over the past two decades is the field metal-organic frameworks (MOFs), which are defined as coordination polymers or networks with organic ligands containing potential voids.[106] After the concept of crystal engineering was introduced by Schmidt in 1971, Hoskins and Robson reported the first MOF like structure, *i.e.* the three dimensional cationic framework $[Cu^{I}(C(C_6H_4CN))_4]_n^{n+}$, in 1989 and expanded on this in the early 1990s[107–114] In the subsequent years, progress towards highly porous was made in the groups of Zaworotko, Fujita, and Yaghi, who first introduced the term "metal-organic framework" in 1994 referring to diamondoid networks.[115–121] In 1995, Yaghi *et al.* reported the first selective binding and removal of pyridine guests in MOFs and in the coming years they and Kitagawa demonstrated reversible gas sorption in microporous MOF .[122–125]

1.5.1. Reticular Chemistry

The functions of MOFs are of course based on their underlying structural chemistry, hence the predictability of the assembled frameworks plays a crucial part in the target synthesis. The concept of reticular chemistry (Latin: *reticulum*, "net") is based on the idea that a MOF can be reduced into the geometrical features of its subcomponents and be categorised accordingly.[108,126–129] That is, MOFs are composed of two kinds of building units, which are named in analogy to zeolite topochemsitry:[130,131] The inorganic node (composed of metal ions, clusters, or metal-oxo clusters) determines the relative orientation in which the organic ligands assemble and is referred to as secondary building unit (SBU). The organic linkers severs as connectors and extensions between the inorganic SBUs, but can also SBUs (or even tertiary building units) themselves.[132,133] The idea behind reticular synthesis is that target MOFs whose components possess the same geometrical features will have form the same net (or topology), *i.e.* they are isoreticular. An early example of this is the an isoreticular series of metal-organic frameworks (IRMOF), which are based on MOF-5 (IRMOF-1), is shown in Figure 1.8. Basic zinc carboxylate ($[Zn_4(\mu_4{-}O)(O_2CR)_6]$) is a six connected SBU which is linked to adjacent SBUs by linear dicarboxylates, resulting in a primitive cubic (**pcu**) net. As reticular chemistry gained increasing popularity, with it came the need for a universal

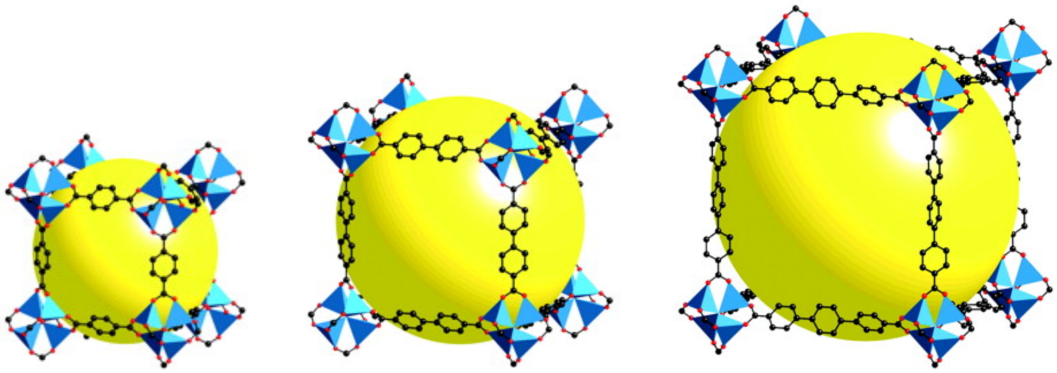


Figure 1.8: Three examples of isoreticular MOFs with an underlying **pcu** net, featuring a basic zinc acetate SBU and a linear dicarboxylate linker: IRMOF-1 (also known as MOF-5, left), IRMOF-10 (middle), and IRMOF-15 (right). The large yellow ball represents the largest van der Waals sphere that fits into the cavities without touching the framework. Adapted from Yaghi *et al.*[134]

system for nomenclature, classification, identification, which was accomplished in a collaborative effort between Blatov, O'Keeffe and Proserpio.[135] Moreover, a database was designed to catalogue default nets called the Reticular Chemistry Structure Resource (RCSR).[129] RCSR symbols are composed of three lower case bold letters with abbreviations either based on materials with that topology (*e.g.* **dia** for diamond or **pto** for platinum oxide) or geometrical shapes (*e.g.* **pcu** for primitive cubic lattice or **sql** for square lattice) and can be extended, *e.g.* **dia-c** for two interpenetrating (catenated) diamond nets.

A series of frequently observed inorganic SBUs and a variety of organic linkers is presented in Figure 1.9. The UiO (Universitetet i Oslo) type frameworks, which is based on a 12-connected $\{Zr_6\}$-oxo node and a linear decarboxylate (terephthalic acid for UiO-66) in a face-centred cubic (**fcu**) arrangement, are of high interest in research owing their high stability and porosity, as well as possible incorporation of various functional building blocks.[137] MIL-100 and MIL-101 (Matériaux de l'Institut Lavoisier) are assembled from a six-connected M_3O SBU with trimesic and terephthalic acid adopting the complex **moo** and **mtn-e** topologies, respectively.[138–140] The isoreticular MIL-47 and MIL-53 are comprised of *trans*-connected rod-SBUs that are linked by terephthalic acid in **sra** nets.[141] Reversible water uptake in the tunnels of MIL-53(Al) causes a large breathing effect and shrinkage of the pores, but does not affect the topology.[142] The combination of four-connected paddle-wheel and the three-connected trimesic acid gives a twisted boracite (**tbo**) net found in HKUST-1 (Hong Kong University of Science and Technology).[143]

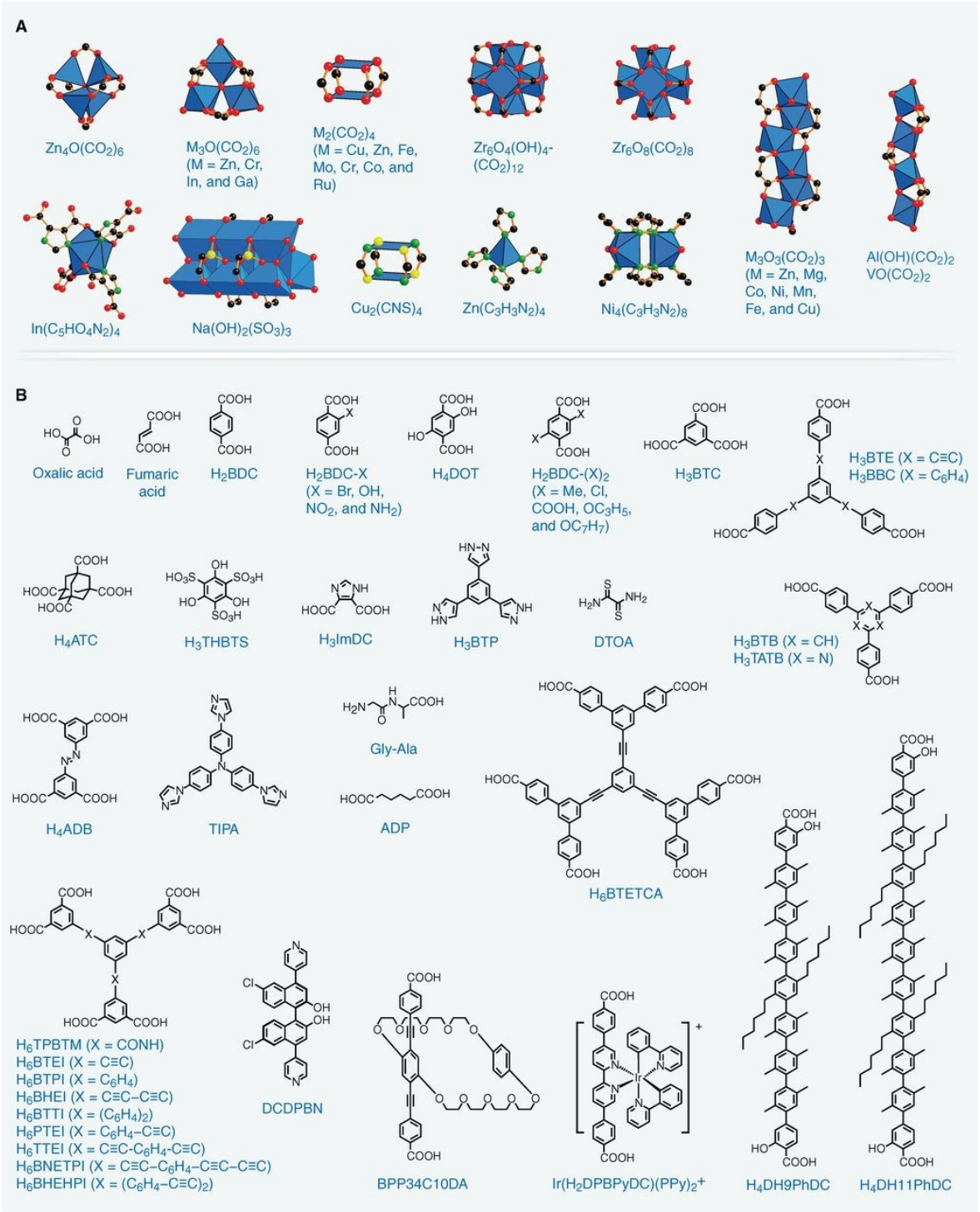


Figure 1.9: Inorganic secondary building units (A) and organic linkers (B). Reprinted from Yaghi *et al.*[136]

1.5.2. Synthesis

In the conventional synthesis of MOFs, temperature is one of the main parameters and its choice is highly dependant on the type of interaction between the inorganic node and the organic linker. Early work by Robson and Hoskins feature single metal ion nodes and 4,4'-bipyridine, whose interaction is comparably weak, and could be grown by slow evaporation of the solvent at room temperature.[108,144] However, as MOFs are strongly bonded coordination polymers, recrystallisation and characterisation in solution are not possible and the growth of single crystals for X-ray structural analysis are vital.[144] MOF synthesis under high temperature is the most widely used approach and can be subdivided into solvothermal and non-solvothermal: In the former, reactions are carried out in closed vessels under autogenous pressure at a temperature over the boiling point fo the solvent, whereas the opposite is the case in the latter.[144,145] Solvothermal conditions provide the means to overcome thermodynamic as well as kinetic barriers in the synthesis of single crystalline MOFs.[144]

Solvents are chosen based on the solubility of the metal salts and organic compounds in them, typically alcohols, water, pyridine, dialkylamides, or a mixture thereof.[144] They aid in the stabilisation large voids and are often highly disordered when no clear host-guest interactions are observed.[144] Furthermore, the choice of solvent can influence the network formation and degree of interpenetration.[146,147] Similar effects were observed for deep eutectic solvents and ionic liquids, where chirality of the can be conveyed onto a MOF with otherwise achiral building blocks.[148–152] Among solvents, dialkyl amides are the most popular, not only due to their solvation properties and high boiling point, but also because of their slow decomposition into dialkylammonium carboxylates, *viz.*

$$\mathrm{R'C(O)NR_2 + H_2O \longrightarrow R'CO_2H + HNR_2 \rightleftharpoons R'CO_2{}^- + H_2NR_2{}^+} \tag{1.7}$$

which slowly increases the pH as the reaction proceeds. Moreover, alkylammonium ions have been shown to template formation of SBUs different from those obtained in pristine solvent.[153,154] Additionally, the carboxylic acid may act as a modulator which facilitates crystal growth over nucleation.[144] A modulator is a capping additive with the same chemical functionality as the framework linker, which alters the coordination equilibrium at the crystal surface during the growth process, hence modulates the materials size and morphology.[155,156] For soft Lewis acids, such as Cu^{II} and Zn^{II}, solvents are usually sufficient to facilitate crystal growth. Hard Lewis acids, such as Al^{III} and

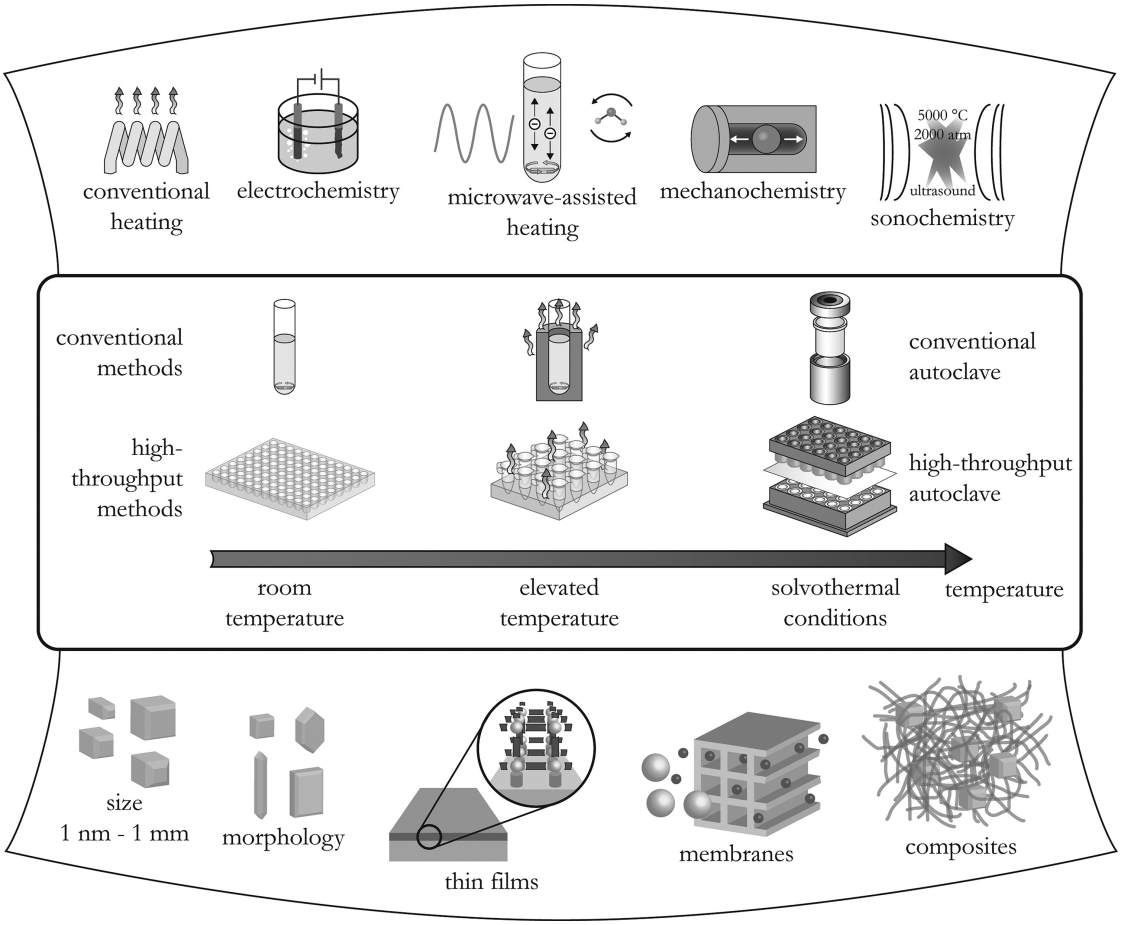


Figure 1.10: Overview of synthetic methods, possible reaction temperatures, and reactions products in MOF synthesis. Reprinted from Stock *et al.*[144]

Zr^{IV}, on the other can greatly benefit from modulation, with Zr:modulator ratios of close to 1:1000.[157]

Figure 1.10 gives an overview of different approaches to MOF synthesis and and the resulting materials.[144] Conventional heating is commonly used to obtain single crystal for structure elucidation, whereas thin films can be grown electrochemically onto electrodes.[158–161] Microwave-assisted, mechano-, or sono-chemical methods are used for scale-up reactions.[162–168]

1.5.3. Potential Applications of Metal-Organic Frameworks

Porous materials are highly important in established processes such as carbon capture, hydrogen storage, chemical purification, catalysis and many more niche areas.[169]

While MOFs have yet to be employed in industrial processes, since there is virtually an infinite number of combinations between metal ions and linkers, research activities are vigorous.[170] With their intrinsic and tunable porosity MOFs the most studied potential applications are the storage of hydrogen, CO_2, methane and other hydrocarbons, as well as separation of the latter.[171–201] Further applications are the detection of gases and volatile organic compounds, as well as teh removal and sequestration of toxic gases.[202–207] Tunability of the void has also enabled crystallographic characterisation of immobilised natural products, biomolecule protection, and enantioselective separation.[208–214]

While there are many more applications, one of the most interesting ones is arguably catalysis, as the can possess the high selectivity of homogeneous catalysts, but also the stability and recyclability of heterogeneous catalysts.[215] MOFs can be seen as an ordered array of microflasks and as such there are four sites in a MOF that may act as the catalytic centre: coordinatively unsaturated sites metal sites, metalloligands (which can be introduced in post-synthetic modification), functional organic sites, or guests immobilised in the frameworks voids.[215,216] For example, a series of MILs such as MIL-101(Cr), MIL-100(Fe), MIL-100(Sc), MIL-53(Al), and MIL-47(V) have been used in a wide variety of Lewis acid catalysed reactions and oxidations reactions occurring at the coordinatively unsaturated site.[142,217–220] Metalloligands commonly featured in MOFs are based on either salen-type, 2,2'-bipyridine, or porphyrin.[215] The latter two are also interesting from photosensitive point of view and will be discussed in more detail in subsection 1.5.4. An application for MOFs featuring salen-type metalloligands, which are based on enantiopure α-diamines and Mn^{III}, is asymmetric epoxidation of olefins.[221] With respect to functional organic sites, some examples are Knoevenagel condensation with an amino derivative of MIL-101(Al), esterification with sulfoxy derivatised MIL-53(Al), or urea promoted Friedel-Crafts reaction in NU-601.[222–224] Regarding heterogeneous catalysis, the immobilisation of metal nanoparticles (*e.g.* Cu, Ru, Au, Pd, Pt) bears particular interest, as the porous structures of MOFs can determine the aggregation and migration of the nanoparticle.[215] This is typically accomplished by impregnation of the MOF with a metal precursor salt, followed by reductive decomposition. Hydrogenation of olefins, Suzuki-Miyaura, Ullmann and Heck coupling reactions, and more have been accomplished with Pd@MIL-101(Cr).[215,225,226]

1.5.4. Metal–Organic Frameworks for Photocatalysis and Light Harvesting

In nature, photosynthesis is facilitated by highly efficient integration of chromophores and charge separation centers into a network.[227,228] On a much more simplistic fashion, MOFs can be designed to accommodate desired functional groups in specified positions, *e.g.* a linker can be replaced with a photosensitive or catalytically active ligand.[215]

Figure 1.11 shows two examples of photochemical hydrogen evolution based on UiO frameworks. Ott *et al.* incorporated a diiron(I) hydrogen evolution catalyst based linker into a UiO-66 type framework, which shows superior performance to just the linker and photosensitiser in solution.[229] A different approach was taken by Lin *et al.*, who used a photosensitive $[Ru(bpy)_3]^{2+}$ derivatised linker in order to form a UiO type framework. The reaction mixture also contained the Wells-Dawson polyoxotungstate $[P_2W_{18}O_{62}]^{6-}$, which was trapped in the pores and acts as a hydrogen evolution catalyst.[230]

Figure 1.12 shows an example of the encapsulation of $[Co_4(PWO_9O_{34})_2(H_2O)_2]^{10-}$, a cobalt containing Weakley sandwich showing remarkable water oxidation, in the inert MOF MIL-100(Fe) reported by Kögerler *et al.*[231,232] Here, immobilisation in the MOF lead to increased oxygen yield and turnover frequencies, as well as recyclability *via* filtration in comparison with the pristine catalyst.

Furthermore, the Grätzel-type DSC developed by Morris *et al.* in which a UiO-67

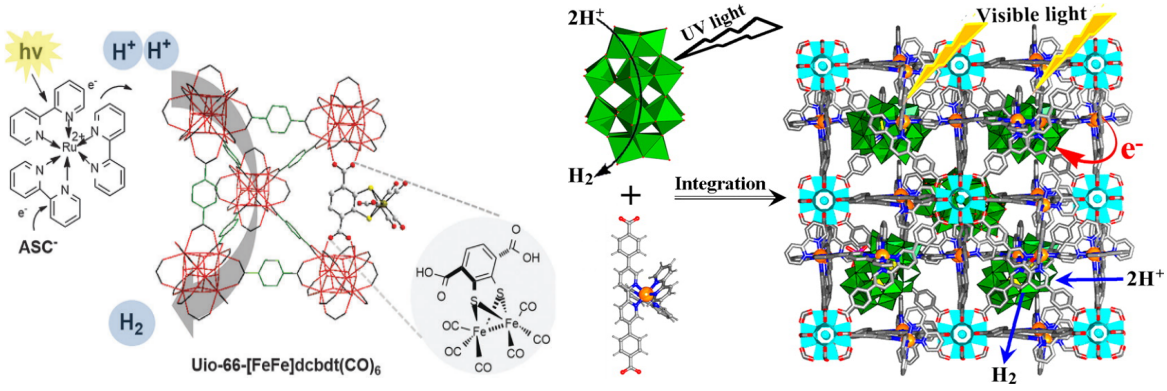


Figure 1.11: Photochemical hydrogen evolution in UiO frameworks: Linker as catalytic centre with photosensitiser in solution (left), reprinted from Su *et al.*.[215] Linker as photosensitiser with catalyst immobilised in the pore (right), reprinted from Lin *et al.*[230]

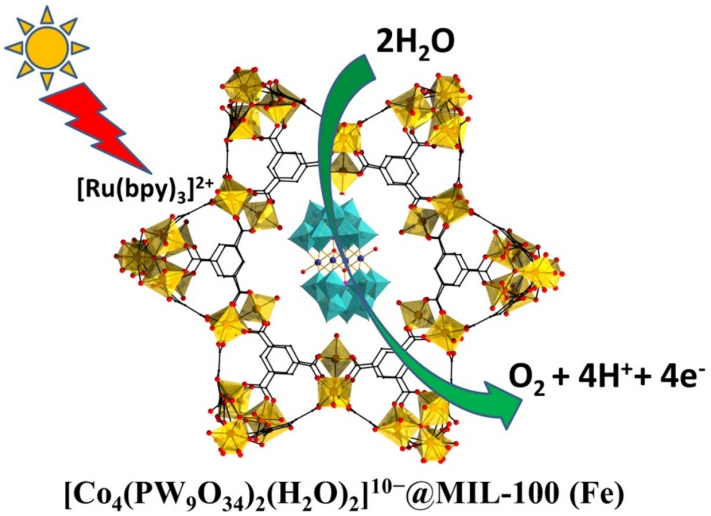


Figure 1.12: Photochemical oxygen evolution with a catalyst in the pore and photosensitiser in solution. Reprinted from Kögerler *et al.*[232]

type framework, sensitised by a ruthenium-based linker, replaced the traditional dye is shown in Figure 1.13. Importantly, the MOF-derived solar cell outperformed the dye-TiO_2 counterpart, paving the way for future developments.

Yet, all of the above examples are utilise precious metal photosensitisers. Akin to the vast interest garnered by TiO_2 and TiO_2-based semi-conductive materials, tremendous effort has been put into the exploration of titanium based MOFs.[234] The first Ti-MOF showing good photochemical response is MIL-125, a MOF comprised of a 12-

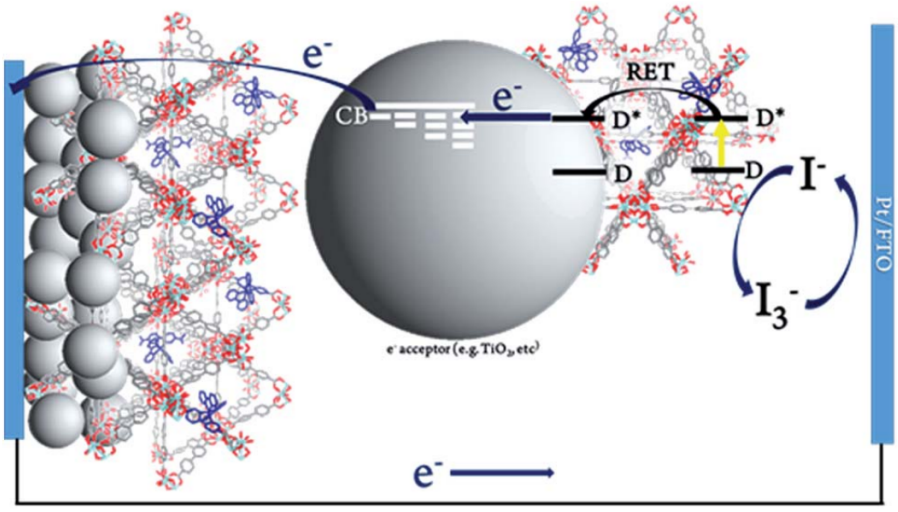


Figure 1.13: Schematic representation of a Ru-MOF sensitised solar cell. Reprinted from Morris *et al.*[233]

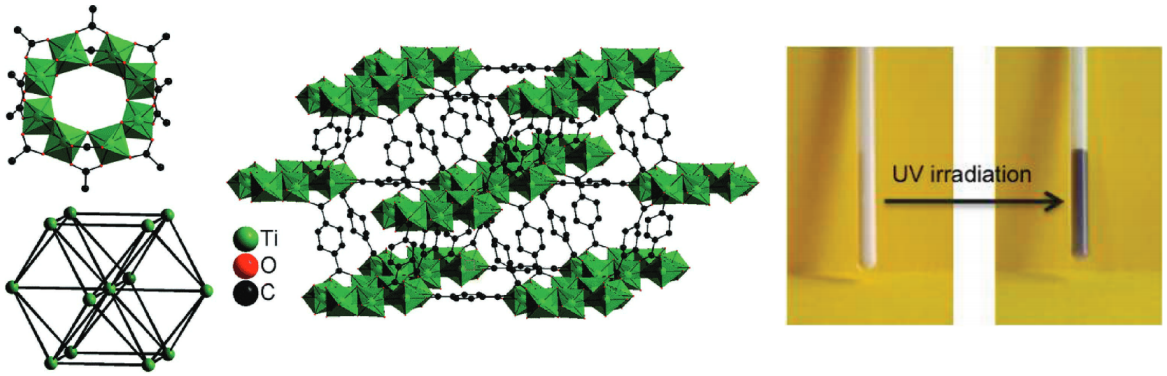


Figure 1.14: The structure of MIL-125: The $Ti_8O_8(OH)_4(CO_2)_{12}$ SBU (top left), **fcu** net (bottom left), packing fo the crystal structure (middle), and photochromic response upon UV irradiation. Reprinted from Serre *et al.*[235,243]

connected octameric SBU (analogous to $[Cr_8(OH)_{12}(OAc)_{12}]$) in an **fcu** net, is shown in Figure 1.14 and possesses an optical band gap of 3.57 eV.[235,236] The generation of Ti^{III} upon irradiation with UV light in benzyl alcohol was confirmed by electron spin resonance (ESR) spectroscopy and quenching with oxygen yielded $O_2^{\cdot -}$.[235] The optical band gap was brought into the visible region using aminoterephthalic acid (2.72 eV) and into the near infrared region with a 90%:10% mixture of amino- and diaminoterephthalic acid (1.23 eV).[237,238] NH_2-MIL-125 has since been used as a visible light photocatalyst for CO_2 reduction to formate, Pt nanoparticle assisted hydrogen production, as well as the aerobic oxidation of amines.[239–241] Moreover, it was recently shown that MIL-125 and NH_2-MIL-125 can be formally charged with sodium ($e^- + Na^+$). Clean and reversible reduction is possible with up to 1 electron per node throughout the entire material, but reduction of every Ti^{IV} to oxidation state +III was also accomplished.[242] Another approach in the synthesis of Ti-based MOFs is the use of preformed titanium-oxo clusters as Ti-source. MOF-901 and MOF-902 are based on the $\{Ti_6\}$-oxo cluster $[Ti_6O_6(OiPr)_6(pAbz)_6]$ (pAbz = 4-aminobenzoate) linked into hexagonal lattices (**hxl**) by Schiff base formation with linear aromatic dialdehydes.[244–246] The same cluster was used into the synthesis of the porphyrinic linker Ti-MOF PCN-22, where the cluster has completely rearranged into $\{Ti_7\}$-oxo node.[247] The most daunting challenge to date, with respect to the exploration of novel Ti-based MOFs, the problems encountered in synthesising materials with sufficient crystallite size for single crystals structure X-ray diffraction analysis.[235,244,245,248] Hence, not only the polymeric Ti-based MOFs, but also the monomers that lie at their heart *i.e.* titanium oxo-clusters, have found a lot of attention over the past two decades.

1.6. Titanium-Oxo Clusters

Not only do clusters bridge the gap between mono- or binuclear molecular compounds and nanoparticles, but may also exhibit special inherent properties, *e.g.* molecular magnets, optical and redox properties.[249–253] In comparison to nanoparticles, clusters possess a series of advantages: In bulk material, each cluster is identical in composition, size and shape on a molecular level, meaning they surmount inhomogeneous characteristics often encountered of nanoparticulate materials. Clusters are essentially big molecules and therefore they readily dissolve in suitable solvents, which makes them available for post-functionalisation, bottom-up assembly of novel functional materials as described above, and recrystallisation.[254,255] Moreover, the acquisition of single crystals encompasses precise structural information from X-ray diffraction techniques, which form the basis for theoretical calculations and offer mechanistic insights.[256]

Polyoxometalates (POMs) are arguably the most widely researched member of the cluster family, in both top-down and bottom-up approaches, and have displayed outstanding performance in a vast area of applications.[257–259] Titanium dioxide (TiO_2) has been widely used as a pigment, in sunscreens, paints *etc.* since its commercial availability in the early 20th century.[260] After groundbreaking work by Fujishima and Honda demonstrated that TiO_2 covered electrodes could be utilised in photocatalytic water splitting in 1972, research interest in TiO_2-based materials skyrocketed.[260–262] This is not only due to its promising photo-related properties, but also because titanium is the ninth most abundant element in the earths crust (4136 ppm) and comparably cheap (52.16 € kg^{-1}).[23,263] Due to the structural kinship of titanium-oxo clusters with POMs (*e.g.* $[Ti_6O_8(OH_2)_{20}]^{8+}$ is related to Lindqvist hexatungstate $[W_6O_{19}]^{2-}$, $[Ti_7O_4(OEt)_{20}]$ is isostructural to heptamolybdate $[Mo_7O_{24}]^{6-}$) were originally termed polyoxotitanate nanoclusters (although they are typically charge neutral or cationic), which was followed by titanium-oxo clusters.[254–256,264–267] More recently, Zhang *et al.* introduced the abbreviation PTC for both polyoxo-titanium cluster and phosphonate-stabilised titanium cluster.[255] As this however leaves ambiguity, this work will adhere to titanium-oxo cluster (TOC).

1.6.1. Synthetic Approaches for Titanium-Oxo Clusters

As implied in the name, POMs are typically polyanionic metal-oxo clusters featuring group 6B (*i.e.* Mo and W) or group 5B (V, Nb, and Ta) metals in their highest or second highest oxidation state, whereas aluminium(III)-oxo clusters are typically polycationic, and both are readily synthesised in aqueous solution.[255,268] However, titanium ions are notorious for their sensitivity towards water and their hydrolysis leads to the spontaneous precipitation of TiO_2, which has stifled the crystallisation of TOCs in the past. Initial syntheses with titanium(IV) alkoxides ($Ti(OR)_4$) and even some of the analytics were carried out under Schlenk, *i.e.* dry and oxygen free, conditions.[249,269–274] Solvo- and hydrothermal synthesis have experienced increasing popularity not only in the field of MOFs, but also POMs, and TOCs.[254,275–277] The high temperature and pressure facilitate accelerated reactions (from weeks or even months to days) and better solubility of reagents, thus enabling expansion of the reaction mixture to more components and functionalities. Moreover, excess carboxylic acid make the TOCs more resilient with respect to moisture, allowing for the use of technical grade rather than dry solvents.[249,275] Here, teflon-lined Parr bombs bear the advantage of being more resilient to higher temperatures and pressures, but thick Pyrex tubes enable *in situ* observation of the crystallisation process.[275,278,279] Dai *et al.* introduced a combined approach, were the starting material is placed in a Pyrex tube, degassed with an inert gas, sealed and the reaction carried out under autogenous pressure.[280,281] The use of $Ti(OR)_4$ in aqueous solution has been largely restricted to the sol-gel synthesis of TiO_2 nanomaterials and few examples of TOCs made in water exist from the last century.[282,283] Yet, the uncontrolled precipitation of TiO_2 can be prevented if the reaction is carried out at low pH, *e.g.* through the use if $TiCl_4$ or $TiOSO_4$, and the addition of different salts provides synthetic control in the preparation of discrete TOCs.[284–287] In addition, after ionothermal synthesis, *i.e.* reaction in ionic liquids or deep eutectic solvents, had been popularised for zeolites and MOFs, it has also recently found use for in the exploration of new TOCs.[148,288,289] Finally, as mentioned in the previous section TOCs can serve as precursors for MOFs or other TOCs by either ligand exchange (usually of the OR species or neutral N-donor ligands), oligomerisation (*e.g.* dimerisation of $[Ti_{17}O_{24}(OiPr)_{16}(pAbz)_4]$ to $[Ti_{34}O_{50}(OiPr)_{30}(pAbz)_6]$, pAbz = 4-aminobenzoate), or complete rearrangement of the cluster (*e.g.* $[Ti(Cat)_4(DMA)_2]$ to $[Ti_{10}O_{12}(Cat)_8(Py)_8]$, DMA = dimethylacetamide, Cat = catecholate, Py = pyridine).[278,283,290–292]

1.6.2. Structural Diversity of Titanium-Oxo Clusters

Unlike group 5B and 6B metals in POMs, titanium only very rarely forms terminal M=O double bonds which passivate the surface of those metal-oxo clusters.[293] Moreover, titanium may assume coordination numbers between four and eight, with six of course being the most common one. In order to understand the structures of TOCs, it helps to start at the most common bulk TiO_2 phases rutile, anatase (see Figure 1.15), which are all composed of six-coordinated titanium atoms and μ_3-oxo bridges.[256] Rutile is the thermodynamically most stable phase of TiO_2, features Ti coordinated in distorted octahedra which form edge connected chains along the tetragonal axis. Adjacent chains are shifted by $\frac{a+b}{2}$, rotated 90° and are vertex connected.[294] The octahedra in the photocatalytically active anatase are more distorted than in rutile and are not vertex- but edge-connected fourfold. The Ti_3O subunit taken from rutile is commonly observed in TOCs.[254]

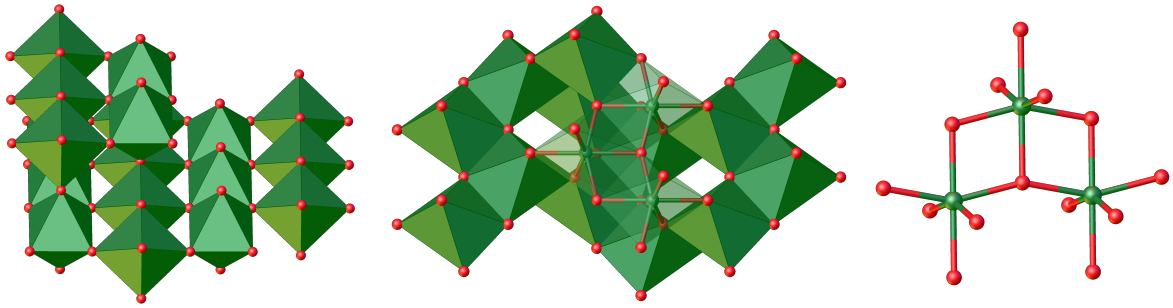


Figure 1.15: Polyhdreal representations of the TiO_2 phases rutile (left) and anatase (centre), highlighting a Ti_3O motif (right) commonly observed in TOCs. Adopted from Swope *et al.* and Dickson *et al.*[294,295]

By now, 573 TOCs (nuclearity ≥3) had been deposited in the Cambridge Structural Database (CSD, Version 5.41, November 2019 update). In the following, examples of TOCs will be given based on the their bridging ligands. It should be noted, that the hydrolised cluster is highly dependant on the Ti(OR) source due to templating effects, *e.g.* Ti(OEt) as dimers and trimers in benzene and as tetramers in the solid state while $Ti(OiPr)_4$ is monomeric.[254,296] Titanium-oxoalkoxide clusters can be generalised with sum formula $[Ti_nO_m(OR)_{4n-2m}]$, some of which are presented in Figure 1.16. The smallest hydrolised cluster available from Ti(OiPr) is $[Ti_3O(OMe)(OiPr)_9]$, which is a trinuclear M_3O_{13} unit of edge sharing octahedra (often encountered in group 6B POMs) capped by an additional μ_3-OR ligand, replacing three terminal alkoxides.[283]

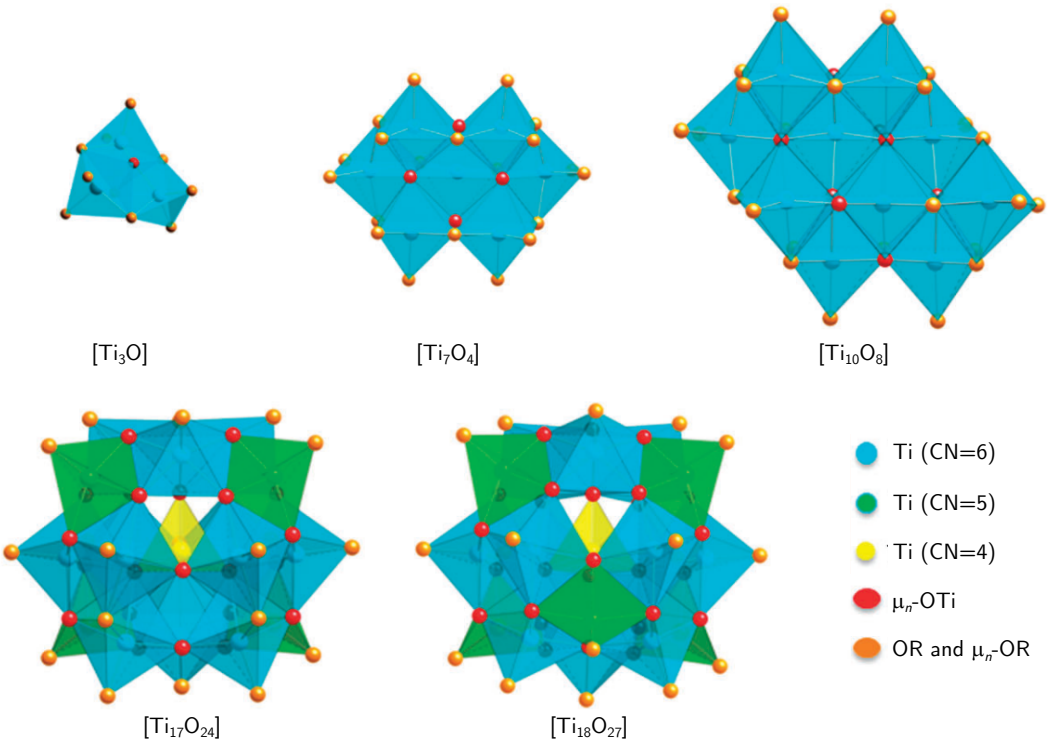


Figure 1.16: Polyhedral representation of titanium-oxoalkoxides $[Ti_nO_m(OR)_{4n-2m}]$.Adopted from Rozes and Sanchez.[254]

The cluster $[Ti_7O_4(OEt)_{20}]$ displays a compact structure of octahedral titanium atoms connected by μ_2-oxo, μ_3-oxo and μ_4-oxo ligands, with its cluster core being isostructural to $[Mo_7O_{24}]^{6-}$.[254,297] $[Ti_{10}O_8(OEt)_{24}]$ is derived from $[Ti_7O_4(OEt)_{20}]$, that is the $\{Ti_{10}O_8\}$ cluster core can be described as a centrosymemtric molecule resulting from the interpnetration of two $\{Ti_7O_4\}$ clusters.[254,297] The larger clusters $[Ti_{17}O_{24}(OiPr)_{20}]$ and $[Ti_{18}O_{28}(OtBu)_{20}]$ are based on the Keggin structure, *i.e.* a central TiO_4 tetrahedron is encapsulated by four trimeric edge-sharing octahedral units, that are vertex connected to each other.[254,290,298,299] Respectively three and four of the square faces between trimers are then capped by five-coordinated titanium atoms.

Carboxylate supported titanium-oxo alkoxo clusters are currently the fastest growing type of TOC for the following reason:[255] they are multidentate oxo-ligands that provide an *in situ* water source through the esterification with the eliminated alkoxide. Moreover, a cornucopia of carboxylic acids is commercially available, which has resulted in fast high nuclearity development and isostructural expansion for the purpose of band gap engineering.[275,300] Figure 1.17 shows a few examples of carboxylate stabilised low nuclearity TOCs. $Ti_3O(OR)_8(O_2CR')$ features two six- and one five-coordinated

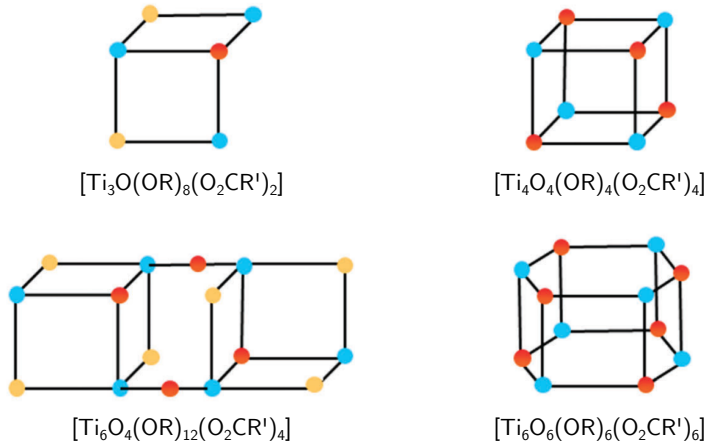


Figure 1.17: Schematic representation of the polyhedral arrangement of small carboxylate supported titanium-oxo-alkoxo clusters. Colour code: blue, Ti; red, μ_n-OTi; yellow, μ_2-OR. Adopted from Rozes and Sanchez.[254]

titanium atoms assembly around a μ_3-oxo bridge, but exhibit an asymmetrical distribution of ligands depending on the organic groups.[254,301] The hexanuclear cluster type $[Ti_6O_4(OR)_{12}(O_2CR')_4]$ can be seen as a vertex connected (*via* two μ_2-oxo bridges) dimer of the previous one, but displays a higher degree of condensation.[254] The tetra- and hexanuclear cluster types $[Ti_4O_4(OR)_4(O_2CR')_4]$ and $[Ti_6O_6(OR)_6(O_2CR')_6]$ are respectively arranged in a cube and a hexagonal prism with titanium atoms and μ_3-oxo bridges occupying the vertices. Ti atoms are additionally bridged by carboxylates on the equatorial square face, and capped by terminal alkoxides in the axial positions.[254,301]

The TOCs that currently have the highest nuclearity are presented in Figure 1.18. $[Ti_{42}O_{60}(OiPr)_{42}(OH)_{12})]^{6-}$ (TOF-1) displays icosahedral symmetry, only features five- and seven- but not six-coordinated titanium atoms, and was obtained using but does

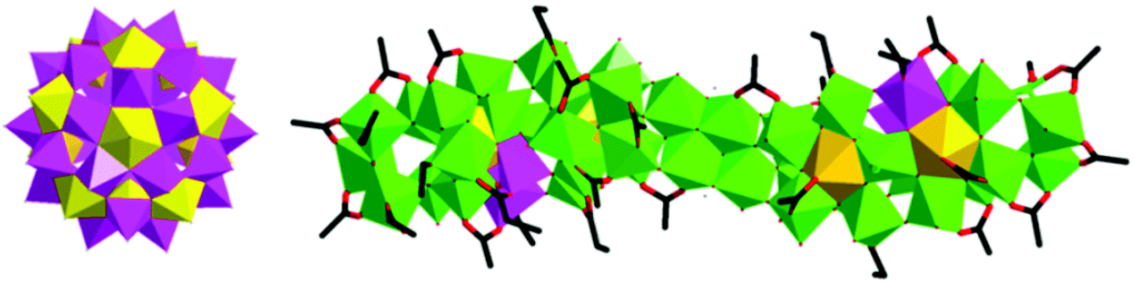


Figure 1.18: Polyhedral representations of the high nuclearity TOCs TOF-1 (left) and COM-3 (right). Colour code: purple, TiO_5; green, TiO_6; yellow, TiO_7. Adopted from Zhang *et al.*[255]

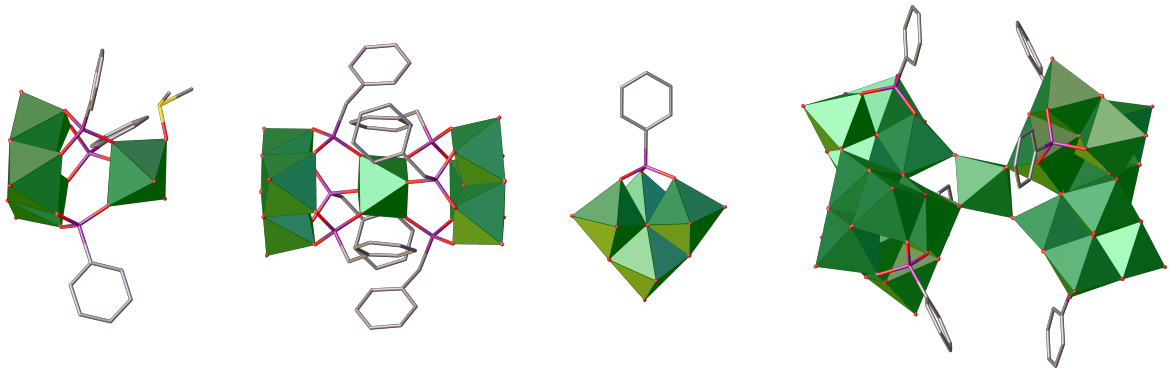


Figure 1.19: Polyhedral representations of the phosphonate-stabilised TOCs $[Ti_4O(OiPr)_8(DMSO)(O_3PPh)]$, $[Ti_7O_2(OiPr)_{12}(O_3PBz)_6]$, $[Ti_4O(OEt)_{12}(O_3PPh)]$, and $[Ti_{25}O_{26}(OEt)_{36}(O_3PPh)_6]$ (left to right, Bz = benzyl).[274,303,305]

not feature formic acid.[279] $[Ti_{52}O_{72}(OH)_2(PA)_{34}(OiPr)_{28}]$ (COM-3, PA = propionate) one the other hand is only centrosymmetric and is obtained using propionic acid.[302]

Furthermore, phosphinic and phosphonic acids have also been utilised in the synthesis of TOCs.[255] Due to the kinship of their ligand properties, isostructural clusters may be obtained from carboxylic and phosphinic acids. For example, $[Ti_4O_4(OiPr)_4(O_2PPh_2)_4]$ is isostructural with $[Ti_4O_4(OiPr)_4(O_2CPh)_4]$, was reported 20 years ago but it was only recently discovered that it could be doubly photoreduced *via* a current doubling mechanism and forms a high spin cluster with ferromagnetically coupled electrons delocalised over the core.[303,304] Examples of phosphonate-stabilised TOCs are given in Figure 1.19. The $\{Ti_4P_3\}$-oxo cluster features a TiO_3 subunit that is capped by three bridging phosphonates on one side, which are capped by a fourth titanium atom. Charge neutrality requires coordination by one neutral molecule, here dimethyl sulfoxide (DMSO).[303] The $\{Ti_7P_6\}$-oxo cluster can be seen as two $\{Ti_4P_3\}$-oxo clusters fused at the apical titanium atom.[274] Coppens *et al.* reported an edge-connected tetranuclear TOC, which is centred around a μ_4-oxo bridge and capped by a single phosphonate. Two of these $\{Ti_4P\}$-oxo clusters can further trimerise and assemble around a central titanium atom through vertex connections, resulting in a $\{Ti_{25}P_6\}$-oxo cluster T_h symmetry around the central atom.[305]

The class of TOCs has been gaining the most attention in the recent years since their initial discovery by Schubert *et al.* in 2014, feature both carboxylate and phosphonate ligands.[306] The $\{Ti_5P_3\}$-oxo cluster features the same trigonal base as $\{Ti_4P_3\}$, but is capped by an edge-connected dimer bridged by a carboxylate. The $\{Ti_5P_2\}$-

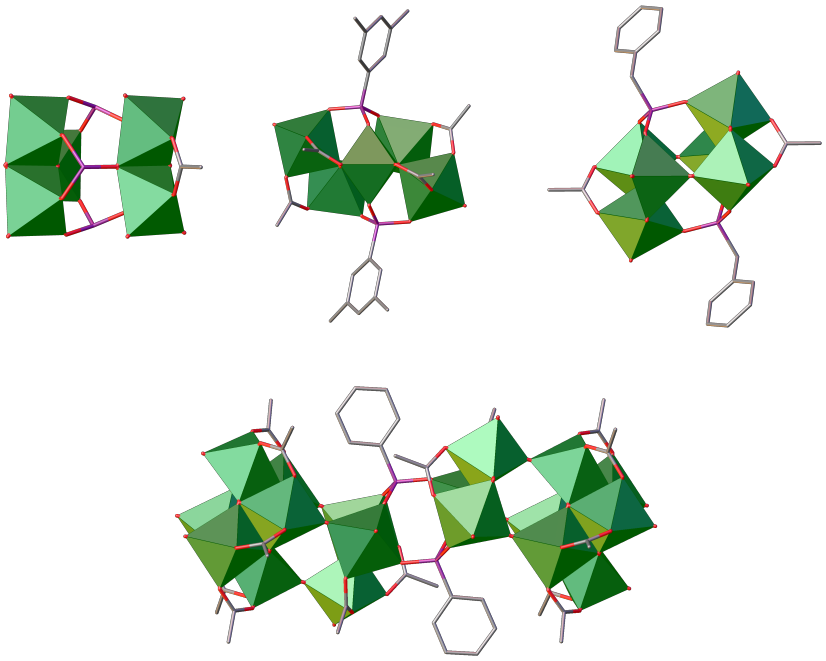


Figure 1.20: Polyhedral representations of mixed phosphonate-carboxylate TOCs $[Ti_5O(OiPr)_{11}(O_3PC_3H_6Br)(O_2CMe)_4]$, $[Ti_5O_3(OiPr)_6(O_3PPh)_2(OC_2Me)_4]$, $[Ti_6O_2(OiPr)_{10}(O_3PBz)_2(O_2CMe)_2]$ (top, left to right), and $H_2[Ti_{18}O_{20}(OiPr)_{14}(O_3PPh)_2(PA)]$ (bottom, PTC-51).[306,307]

oxo cluster possesses C_2 symmetry and is composed of two edge-connected dimers, which are vertex-connected to each other and a fifth titanium atom through a μ_2- and μ_3-oxo bridge, respectively. The centrosymmetric $\{Ti_6\}$-oxo cluster is a vertex- and phosphate-connected dimer from edge-connected Ti_3O subunits that are comprised of two octahedral and one five-coordinated titanium atoms.[306] The $\{Ti_{18}\}$-oxo cluster PTC-51 reported by Zhang *et al.* is based on two $[Ti_6O_6(OR)_6(O_2CR')_6]$, where the alkoxides on one hexagonal face have been substituted by a carboxylate stabilised Ti_3O, fused together by two phosphonates resulting in C_2 symmetry.[307]

Modifications in the following are mentioned for completeness, but are not subject of this work. Other emerging types of TOCs are based on N-donor ligands, such as pyridine or phen, and also mixed N,O-donor ligands such as oximes or amino-polyols.[255,289,291,292,308–310] Furthermore, inorganic bridged TOCs from aqueous solution based on synthesis from acidic media and sulfate stabilisation.[284,287,311,312] In addition, TOCs and POMs have been fused successfully with lacunary Keggin and Wells-Dawson polyoxotungstates assembled around a titanium-oxo centres.[313–316] Other mixed metal TOCs, especially featuring lanthanides, have also gained tremendous attention of the

past years and have been summarised in an extensive review by Zhang *et al.*[317]

1.6.3. Applications of Titanium-Oxo Clusters

Due to the wide band gap of anatase (3.20 eV), its photoactivity is limited to roughly 5% of the solar flux, which severly impacts its applicability in the real world. Akin to DSCs, TOCs can be modified with organic groups in order to form a crystalline dye-sensitised photoactive system.[255] In this regard, a global effort has been made in terms of band gap engineering and tuning of the photoresponse, which are highly dependant on both the titanium-oxo cluster core but also the attached ligand. Investigations by Coppens *et al.* on provided fundamental insights into the photoexcited interfacial electron transfer in p-type sensitised $\{Ti_{17}\}$-oxo clusters. They revealed a highly wavelength dependant charge injection, *i.e.* an anodic response (electron injection) in the UV region whereas a cathodic response (hole injection) was observed in the visible region[266,318]

Titanium-oxo clusters find a range of applications due to their tailorable photoactivity.[255] For example, Dai *et al.* have shown that dye-sensitised TOCs on show a superior attachment and photoresponse on TiO_2 than just the dye.[319,320] Moreover, the good solubility of a lot of TOCs in various organic solvent facilitates the fabrication of photoresponsive thin-film devices by simply depositing TOC solutions on flourine-doped tin oxide (FTO) or indium tin oxide (ITO) working electrodes.[255,286,321–323] Furthermore, TOCs find application in photocatalysis, specifically the degradation of aqueous pollutants such as methyl orange and methylene blue, hydrogen evolution, water oxidation.[300,324–328] In addition, they have shown potential applications in fluorescent labelling, integrated electrochromic supercapacitors, and CO_2 adsorption.[246,329–333]

1.7. Objectives

The fundamental objective of the work presented in this thesis was to develop light-harvesting materials based on earth-abundant metals. For this purpose, a crystal engineering approach was taken in the design of two types of materials:

1. Coordination polymers or MOFs featuring metallo-linkers based on copper(I) photosensitisers used in DSCs,
2. Titanium-oxo clusters stabilised by both phosphonates and carboxylates, of particular interest are:
    - inclusion of a large variety of functional groups derived from commercially available carboxylic acids,
    - exploration of *in situ* reactions with those functional groups,
    - systematic band gap engineering based on said functionalities.

As the target materials are obtained in the solid state, a particular focus of this work is structure elucidation from single crystal X-ray diffraction and the analysis structure-property relationships.

The first part of the work is focussed on the synthesis of diimine ligands, the corresponding copper(I) complexes, and their immobilisation in coordination polymers or MOFs. In Chapter 2, the simplest ligand known in Cu^{I}-dye DSCs, that is 6,6'-methyl-2,2'-bipyridine-4,4'-dicarboxylic acid, was used for the formation of one homo- and four heterometallic coordination polymers. The effects of immobilisation on the photo- and electrochemical properties of Cu^{I} metallo-linker based materials are investigated for the first time.

This applied concept is expanded on in Chapter 3, in which the influence of ligand extension (for porosity) and steric encumbrance of the metal centre (for prolonged photoluminescence lifetimes) are evaluated with regards to stability of the copper(I) complex. Moreover, the use of a pyridyl-substituted phenanthroline ligand for coordination polymers was explored.

The second part of this thesis is concerned with TOCs, specifically with the $\{Ti_6P_2\}$ motif as it features two five-coordinated titanium atoms, *i.e.* a vacant coordination sites, hence possesses a great aptitude for substitution. In Chapter 4, the regio-specific

influence of aminobenzoic acids on cluster and *in situ* Schiff base formation, as well as the introduction of chirality near the cluster core and their influence on the TOCs' optical band gaps are discussed.

Investigations described in Chapter 5 feature the use of organic dye molecules and fused aromatic rings as substituents, as well as the potential reduction of the cluster featuring anthraquinone-2-carboxylate.

In Chapter 6, different routes of attaching a heteroleptic diimine-diphophine copper(I) complex onto the $\{Ti_6P_2\}$ motif and it's effect on the photo- and electrochemical properties are presented.

2. Coordination Polymers with Cu^{I}-Photosensitisers as Linkers

2.1. Introduction

Ancillary ligands used to attach complex-dyes to TiO_2 in DSCs typically feature carboxylic or phosphonic acid groups.[20,27] This terminal functionality makes them potential ligands for coordination polymers and MOFs.[133] Moreover, the coordination of several ditopic linkers to a metal centre results in a node of higher connectivity, *e.g.* the coordination of three 2,2'-bipyridine-4,4'-dicarboxylic acid linkers to Ru^{II} result in a photosenstive metallo-linker with octahedral symmetry.[334] While an abundance of MOFs featuring Ru, Os, or Ir photosensitive metallo-linker exist, MOFs with bis(diimine)copper(I) metallo-linkers are still scarce.[133,230,233,335,336] The first example is collaborative effort between the groups of Slawin, Stoddart, Sauvage, and Yaghi and was reported in 2012, details of which are shown in Figure 2.1.[337] A heteroleptic [2]pseudorotaxane bis(diimine)copper(I) metallo-linker was assembled making use of the topological constraints imposed by m_{30}phen and subsequently used to form MOF-1040, a triply interpenetrated **pcu** net featuring a basic zinc acetate SBU. Moreover, oxidation and demetalation of the copper(I) centre did not result in the loss of crystallinity of the framework but instead respectively yielded MOF-1041 and MOF-1042, which features a [2]rotaxane.[337] In 2008 Constable, Housecroft, Grätzel *et al.* presented the first employed homoleptic copper(I) complexes of 4,4'- and 5,5'-dicarboxylate functionalised 6,6'-dimethyl-2,2'-bipyridine ligands as dyes in DSCs.[27,28] One of these copper(I) complexes, $[[Cu(dmdcbpy)_2]^+$ (dmdcbpy = 6,6'dimethyl-2,2'-bipyridine-5,5'-dicarboxylic acid), was then used by Kato *et al.* in 2014 to form a porous coordination polymer (La_2Cu), which represents the only other example of a bis(diimine)copper(I) photosensitiser in a coordination polymer or MOF.[28,338] As shown in Figure 2.2, La_2Cu

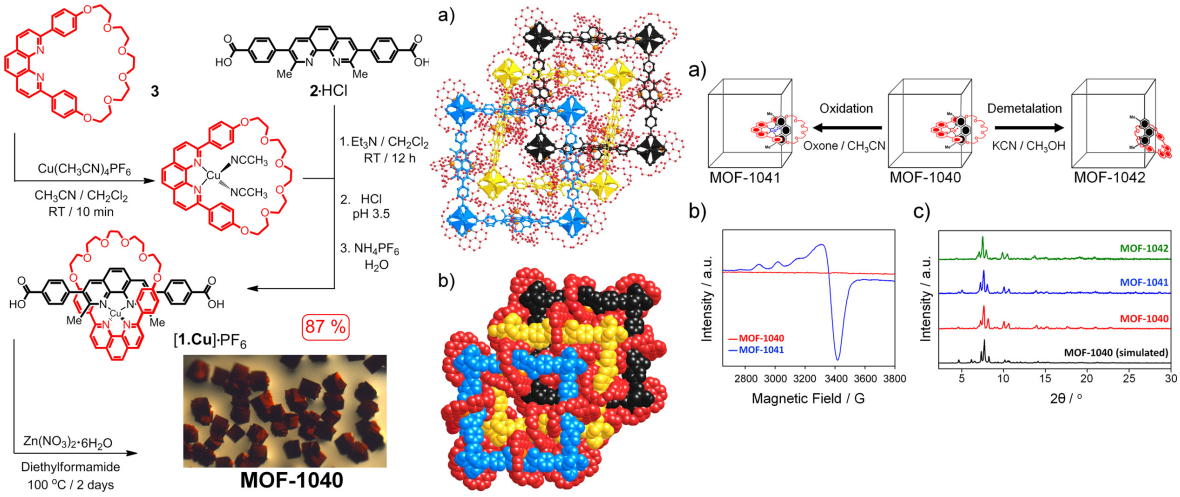


Figure 2.1: Left: Assembly of metallo-linker and synthesis of MOF-1040. Centre: Ball-and-stick (a) and space-filling (b) representation of the triply interpenetrated (nets in black, yellow and blue, m_{30}phen in red) MOF-1040. Right: Oxidation, observed with ESR spctroscopy (b), and demetalation of MOF-1040 do not affect crystallinity (c). Reprinted from Yaghi *et al.*[337]

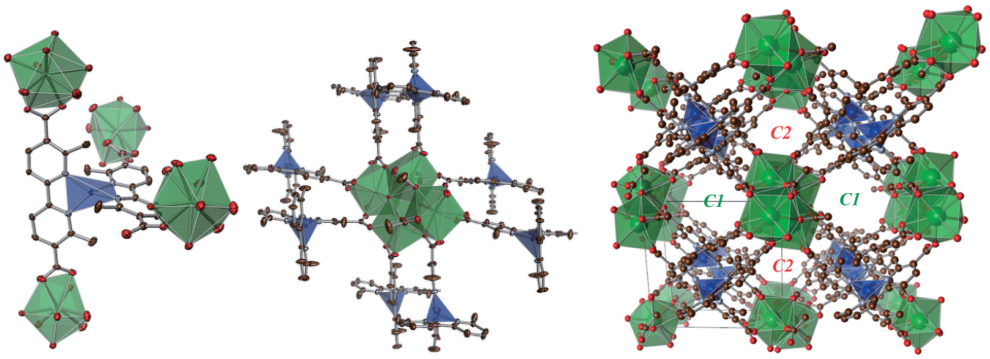


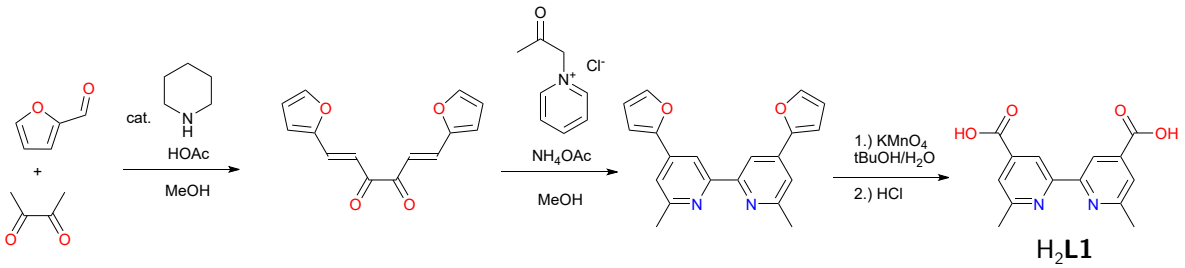
Figure 2.2: The metallolinker $[Cu(dmdcbpy)_2]^+$ (left) and the tetranuclear La^{III} SBU (centre) in a porous 3D coordination network (La_2Cu, right). Reprinted from Kato *et al.*[338]

is composed of a four-connected metallo-linker and an eight-connected tetranuclear La-SBU, which result in a fluorite (**flu**) net, and can undergo reversible guest ad- and desorption.[338] Yet, none of the compounds were investigated for their photo- and electrochemical properties. The aim of this chapter is the synthesis of coordination polymers using bis(6,6'-dimethyl-2,2'-bipyridine-4,4'-dicarboxylic acid)copper(I) as photosensitive metallo-linker, their structural characterisation as well as the investigation of the photo- and electrochemical properties, and their evaluation as photocatalysts or photocathode materials.

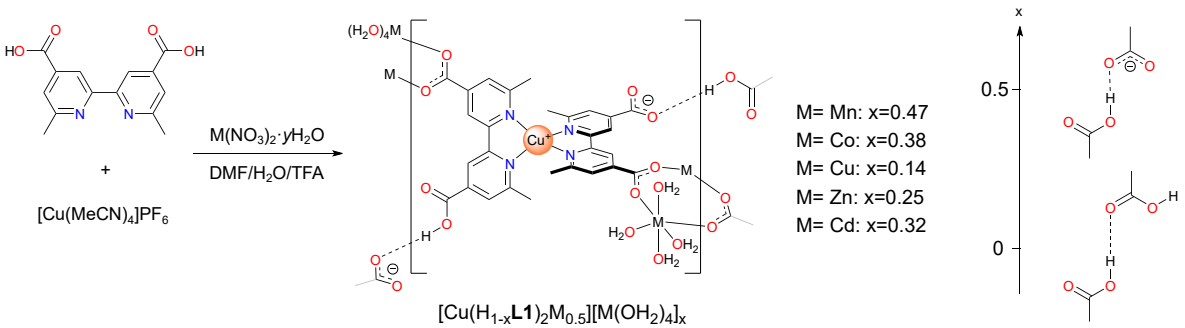
2.2. Synthesis

The synthesis of 6,6'-dimethyl-2,2'-bipyridine-4,4'-dicarboxylic acid (H_2**L1**) is presented in Scheme 2.1, and was accomplished in three steps following procedures reported by Mukalla, as well as Constable and Housecroft.[28,339] First, an aldol condensation of furfural and diacetyl catalysed by piperidinium acetate gave (1*E*,5*E*)-1,6-di(2-furyl)hexa-1,5-diene-3,4-dione. Subsequent Kröhnke pyridine synthesis utilising *N*-acetonyl-pyridinium chloride gave 4,4'-di(2-furyl)-6,6'-dimethyl-2,2'-bipyridine ($Me_2BpyFur_2$). Finally, the furyl moieties were oxidised with potassium permanganate ($KMnO_4$) and following acidification H_2**L1** was obtained.

The successful synthesis of coordination polymers from $[Cu(H_2\mathbf{L1})_2]PF_6$ (**1**) with divalent metal nitrates is outlined in Scheme 2.2. **1** was generated *in situ* from H_2**L1** and $[Cu(MeCN)_4]PF_6$ in DMF and was added to a solution containing the metal nitrate and trifluoroacetic acid (TFA) in DMF and water. The mixture was heated to 80 °C,



Scheme 2.1: Synthesis of the ligand 6,6'-dimethyl-2,2'-bipyridine-4,4'-dicarboxylic acid (H_2**L1**).



Scheme 2.2: Synthesis of the coordination polymers $[Cu(H_{1-x}\mathbf{L1})_2M_{0.5}][M(OH_2)_4]_x$ (**2(M)**) featuring the divalent metals Mn, Co, Cu, Zn, and Cd. To achieve charge balance when $[M(OH_2)_4]_x$ is absent the non-coordinating carboxylates have to be partially protonated, leading to different hydrogen bond formations as shown on the right.

yielding the desired coordination polymer $[Cu(H_{1-x}\mathbf{L1})_2M_{0.5}][M(OH_2)_4]_x$ (**2(M)**, M= Mn, Co, Cu, Zn, or Cd) overnight as deep dark red crystals, featuring the divalent metal M^{II} at full occupancy linking four Cu^{I} complexes, as well as a partially occupied and disordered as tetraquametal(II) moiety ($[M(OH_2)_4]_x$). Here the occupancy can lie between zero and 0.5, where the upper limit is constrained by overlapping with a symmetry equivalent moiety. In the absence of $[M(OH_2)_4]_x$, charge balance is acquired by partial protonation of a hydrogen bonding carboxylate.

Optimisation of the crystallisation reactions revealed the following: water is a necessary co-solvent and no product formation is observed in pure DMF, with an ideal H_2O:DMF ratio of 1:2. The addition of TFA as modulator is not indispensable, but vastly improves crystal size and yield. Reaction times exceeding 24 h may result in the co-crystallisation of dimethylammonium M^{II}-formates, however the yield of **2(Co)** vastly increases if the mixture is heated for 2 d.[340] Changes in **1**:$M(NO_3)_2$ ratio merely affect yields and crystal size as well as side product formation but not the partial occupancy x of $[M(OH_2)_4]_x$, *e.g.* a ratio of 1:20 yields tiny crystals and a large amount of dimethylammonium M^{II}-formates whereas a ratio of 2:1 severely decreases yield. The optimal **1**:$M(NO_3)_2$ ratio was found to be 1:4. Solvents more sterically demanding than DMF such as dimethylacetamide (DMA) or diethylformamide (DEF) do not give the desired product either, but can result in the crystallisation of a partially deprotonated copper complex (see subsection 3.1.4). The highest temperature tested was 100 °C, which leads to decomposition of the Cu^{I} complex, which is observed by decoloration.

2.3. Structural Characterisation of 2(M)

Crystal data and refinement results for the coordination polymers **2(M)** are presented in Table 2.1. With the exception of disorder of the $[M(OH_2)_4]_x$ moiety, **2(M)** are isostructural. The crystals have a strong tendency to crystallise as twins or multiplets, however for **2(Mn)**, **2(Cu)** and **2(Zn)** single crystals or twins with one dominant domain and few composite reflections could be obtained. **2(Co)** and **2(Cd)** were refined as non-merohedral twins with a volume fraction of the second domain of 40%. They crystallise as dark red plates and were solved and refined in the monoclinic space group $C2/c$, with $[Cu(H_{1-x}\mathbf{L1})_2M_{0.5}][M(OH_2)_4]_x$ as the asymmetric units, which are depicted in Figure 2.3 (ORTEP = Oak Ridge Thermal Ellipsoid Plot).[341]

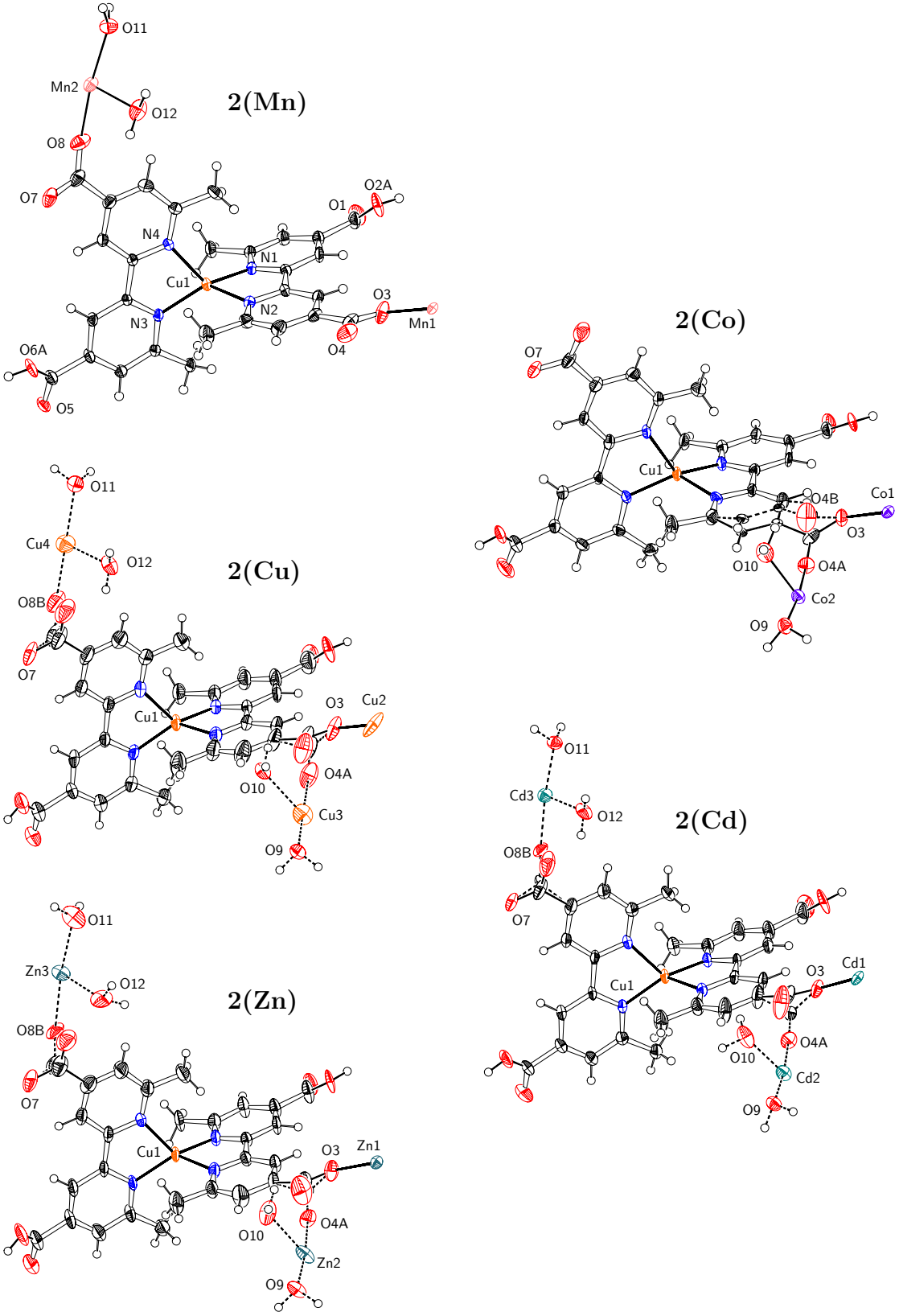


Figure 2.3: ORTEPs of the asymmetric units in the coordination polymers **2(M)**.

Table 2.1: Crystal data and refinement results of coordination polymers **2(M)**.

Identification code	**2(Mn)** · 0.78DMF · 0.5 H_2O	**2(Co)** · 0.75DMF · H_2O	**2(Cu)**
Empirical formula	$C_{30.35}H_{33.06}CuMn_{0.96}N_{4.79}O_{12.07}$	$C_{30.25}H_{31.29}Co_{0.88}CuN_{4.75}O_{11.26}$	$C_{28}H_{22.2}Cu_{1.64}N_4O_{8.6}$
Formula weight	774.5	757.06	656.74
Temperature/K	100	100	100
Crystal description	red plate	red plate	red plate
Crystal size/mm^3	0.363 × 0.117 × 0.036	0.13 × 0.12 × 0.03	0.18 × 0.14 × 0.04
Crystal system	monoclinic	monoclinic	monoclinic
Space group	$C2/c$	$C2/c$	$C2/c$
a/Å	28.0304(13)	27.908(3)	27.3901(16)
b/Å	11.3577(6)	11.4067(10)	11.4893(7)
c/Å	25.3189(18)	25.371(3)	25.7372(15)
α/°	90	90	90
β/°	122.9350(10)	123.430(3)	122.1390(10)
γ/°	90	90	90
V/$Å^{-3}$	6765.1(7)	6740.5(12)	6858.2(7)
Z, Z'	8, 1	8, 1	8, 1
ρ_{calc}/g cm^{-3}	1.521	1.487	1.272
μ/mm^{-1}	1.058	1.130	1.074
$F(000)$	3187	3094	2677
Refl. total/unique	68066/8482	25797/6781	37634/7033
R_{int}, R_σ	0.1297, 0.0631	0.0672, 0.0695	0.0811, 0.0727
Data/restr./param.	8482/87/486	6781/145/510	7033/190/486
GooF	1.035	1.021	1.013
R_1 $[I \geq 2\sigma(I)]$, all	0.0608, 0.1062	0.0565, 0.0888	0.0605, 0.1191
wR_2 $[I \geq 2\sigma(I)]$, all	0.1449, 0.1670	0.1414, 0.1563	0.1601, 0.1910
$\Delta\rho_{max}/\Delta\rho_{min}$/e $Å^{-3}$	1.60/-0.54	0.79/-0.81	0.93/-0.64

Identification code	**2(Zn)**	**2(Cd)** · 0.5DMF · 0.5H_2O
Empirical formula	$C_{28}H_{23.12}CuN_4O_9Zn_{0.75}$	$C_{29.5}H_{27.1}Cd_{0.82}CuN_{4.5}O_{10.3}$
Formula weight	672.17	765.73
Temperature/K	100	110
Crystal description	red plate	red plate
Crystal size/mm^3	0.20 × 0.19 × 0.05	0.22 × 0.21 × 0.05
Crystal system	monoclinic	monoclinic
Space group	$C2/c$	$C2/c$
a/Å	27.8455(7)	28.2933(16)
b/Å	11.4728(3)	11.3935(6)
c/Å	25.3414(7)	25.8190(15)
α/°	90	90
β/°	123.3130(10)	123.2500(10)
γ/°	90	90
V/$Å^{-3}$	6765.4(3)	6960.4(7)
Z, Z'	8, 1	8, 1
ρ_{calc}/g cm^{-3}	1.32	1.461
μ/mm^{-1}	1.216	1.176
$F(000)$	2741	3093
Refl. total/unique	61044/8363	116185/7192
R_{int}, R_σ	0.0679, 0.0444	0.0560, 0.0182
Data/restr./param.	8363/12/486	7192/270/566
GooF	1.073	1.025
R_1 $[I \geq 2\sigma(I)]$, all	0.0627, 0.0886	0.0494, 0.1453
wR_2 $[I \geq 2\sigma(I)]$, all	0.1591, 0.1694	0.0574, 0.1551
$\Delta\rho_{max}/\Delta\rho_{min}$/e $Å^{-3}$	0.72/-0.52	0.98/-0.63

Table 2.2: Naming and occupancy of tetraquametals at different sites in **2(M)**.

2(M)	Site 1		Site 2	
$M^{II}{}_{oct}$	Name	Occupancy [%]	Name	Occupancy [%]
Mn	-	-	Mn2	93
Co	Co2	76	-	-
Cu	Cu3	15	Cu4	14
Zn	Zn2	26	Zn3	24
Cd	Cd2	49	Cd3	16

All atoms of $[Cu(H_{1\text{-}x}\mathbf{L1})_2]$ lie on general positions, however the divalent metals lie on a twofold axis (Wyckoff position 4*e*). Moreover, there are two potential site for the $[M(OH_2)_4]_x$ to attach, which are however chemically equivalent. In the following metals attached to O4(A) will be referred to as site 1 and metals attached to O8(B) as site 2, occupancies of which are listed in Table 2.2 and were refined freely (except for Cu3 in **2(Cu)**). Interestingly, in **2(Mn)** and **2(Co)** only one site is occupied, in **2(Cu)** and **2(Zn)** they are approximately equally occupied, whereas one site is occupied three times as much as the other in **2(Cd)**. An inspection of the Irving-Williams series and ionic radii of M^{II}, respectively, display no clear correlation with the occupancy of $[M(OH_2)_4]$.[342,343]

A selection of distances and angles in **2(M)** as well as continuous shape measures (CShM) of the four-coordinated divalent metals ($M^{II}{}_{tetr}$) is given in Table 2.3. Cu1 is coordinated fourfold by the bipyridyl moieties of two $H_{1\text{-}x}\mathbf{L1}$ ligands in a distorted tetrahedron and is present in oxidation state +I. Each ligand features two distinct Cu1—N distances that are identical between ligands and across all five compounds. Similarly the N—Cu1—N bite angles are approximately 82.5°, with coplanar pyridine rings in the ligands. The dihedral angle between Bpy moities on Cu1 φ deviates from orthogonality from 0.4° for **2(Zn)** to 2.1° for **2(Cu)**. This is significantly less than the almost 9° observed in **3**, which should be locked by the framework's rigidity.

The coordination polydedra of the divalent metals in **2(M)** are shown in Figure 2.4. The divalent metal $M^{II}{}_{tetr}$ is coordinated fourfold by carboxylate oyxgen atoms O3 and O7 and their symmetry equivalents through twofold rotation. The bond distances are approximately 1.96 Å for Co1, Cu2, and Zn1 and within standard deviations of each other. For Mn1 the Mn—O bond to the bridging carboxylate O7 is slightly longer than to O3, which is part of a monodentate carboxylate. Akin to Co, Cu, and Zn, the Cd1—O distances are identical at approx. 2.16 Å. O3—M—O3* and O7—M—O7* (where * denotes a twofold rotation) are approximately equal within each compound

Table 2.3: Distances (Å) and angles (°) in **2(M)** and coninuous shape measures (CShM) of the divalent tetracoordinate metals.

Bond	Distance	**2(Mn)**	**2(Co)**	**2(Cu)**	**2(Zn)**	**2(Cd)**
Cu^{I}—N	Cu1—N1	1.990(3)	1.992(5)	1.997(4)	2.000(3)	1.991(4)
	Cu1—N2	2.036(3)	2.035(6)	2.051(4)	2.047(3)	2.043(6)
	Cu1—N3	1.988(3)	1.993(5)	1.995(4)	1.998(3)	1.992(4)
	Cu1—N4	2.032(3)	2.032(6)	2.051(4)	2.042(3)	2.044(6)
M^{II}_{tetr}—O_2C	M—O3	1.996(3)	1.960(4)	1.951(4)	1.962(3)	2.162(4)
	M—O7^a	2.018(3)	1.955(4)	1.951(3)	1.960(3)	2.150(4)
M^{II}_{oct}—O_2C	M—O4A	-	2.082(6)	2.264(17)	2.132(12)	2.234(9)
	M—O8(B)	2.122(4)	-	2.259(16)	2.119(12)	-
M^{II}_{oct}—OH_2	M—O9	-	2.114(6)	2.348(13)	2.105(12)	2.300(7)
	M—O10	-	2.065(6)	2.371(12)	2.072(16)	2.251(10)
	M—O11	2.147(4)	-	2.350(13)	2.092(12)	-
	M—O12	2.193(4)	-	2.368(13)	2.086(15)	-
Angle		**2(Mn)**	**2(Co)**	**2(Cu)**	**2(Zn)**	**2(Cd)**
N1···Cu1···N2		82.55(14)	82.06(19)	82.17(15)	82.31(13)	82.71(19)
N3···Cu1···N4		82.79(13)	82.83(19)	82.47(15)	82.47(13)	82.87(19)
φ(Cu1)		92.02(16)	88.3(2)	87.89(18)	89.58(16)	88.4(3)
O3—M^{II}_{tetr}—O3^b		128.6(2)	125.1(3)	144.7(3)	126.3(2)	133.0(3)
O3—M^{II}_{tetr}—O7^c		103.04(14)	103.88(16)	96.33(15)	102.99(13)	98.67(14)
O3—M^{II}_{tetr}—O7^d		99.58(15)	100.81(16)	94.19(15)	100.88(13)	98.92(14)
O7^d—M^{II}_{tetr}—O7^c		126.3(2)	124.7(3)	144.8(3)	125.5(2)	134.9(3)
O4—M^{II}_{oct}—O4^a		-	88.2(3)	75.2(8)	87.3(7)	86.4(5)
O8^d—M^{II}_{oct}—O8^c		89.2(2)	-	74.5(8)	87.1(7)	86.5(16)
CShM(M^{II}_{tetr})		Mn1	Co1	Cu2	Zn1	Cd1
Square plane		19.653	21.422	9.208	20.649	15.295
Tetrahedron		2.459	1.818	9.159	2.066	4.499
See-saw		5.448	5.847	5.843	5.688	5.035
Vacant trigonal bipyramid		5.831	5.257	12.213	5.491	7.764

Symmetry key: $^a -\frac{1}{2}+x, \frac{1}{2}+y, z$; $^b 1-x, y, \frac{3}{2}-z$; $^c \frac{3}{2}-x, \frac{1}{2}+y, \frac{3}{2}-z$; $^d -\frac{1}{2}+x, \frac{1}{2}+y, z$.

and span as low as 126° in **2(Zn)** and as wide as 144° in **2(Cu)**, which is a significant distortion from the ideal 109° in a tetrahedron. To determine the actual coordination environment continuous shape measurements were used (note that these are normalised and can be compared across compounds):[344] Mn1, Co1, Zn1, and Cd1 are closest to being coordinated in a tetrahdral environment, whereas the coordination geometry of Cu2 is closest to a see-saw. Moreover, the distortion of the coordination environment follows the trend Co1<Zn1<Mn1<Cd1<Cu2.

The partially occupied metals M^{II}_{oct} are *cis*-coordinated by two monodentate carboxylates (either O4 or O8 and their symmetry equivalents through twofold rotation) as well

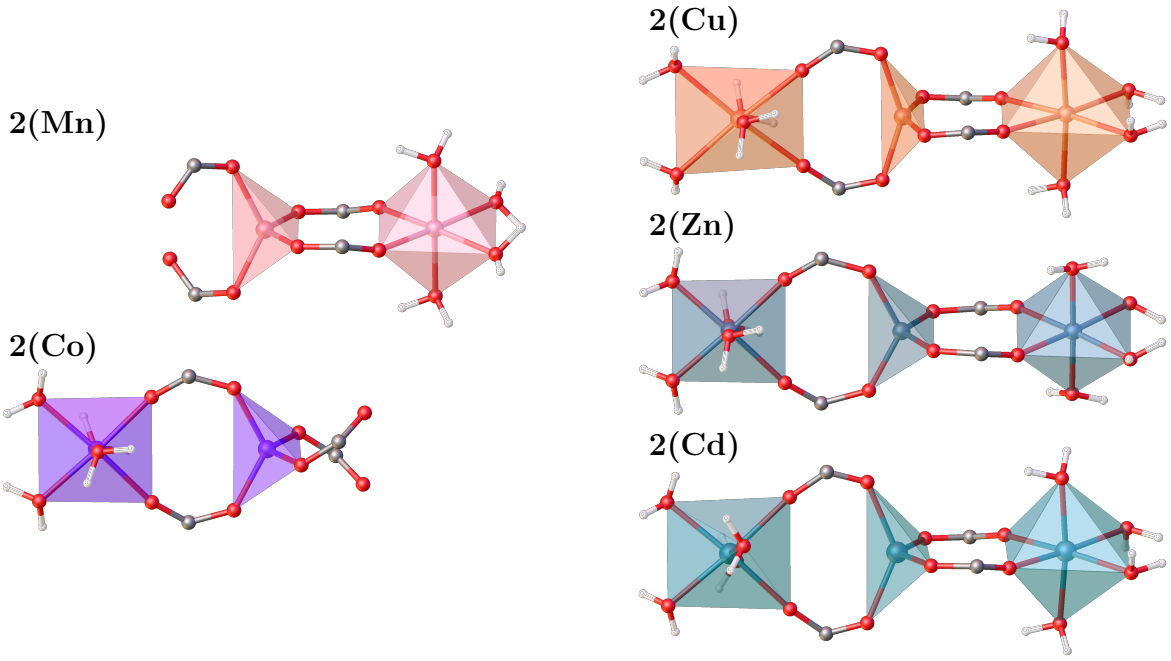


Figure 2.4: Coordination polyhedra of the divalent metals in the coordination polymers **2(M)**. Note that only up to one tetraaquametal(II) site is occupied per SBU.

as four water molecules, namely O9 and O10 for site 1 or O11 and O12 for site 2 and their symmetry equivalents through twofold rotation. This results in an octahedral coordination environment, which is significantly distorted in in **2(Cu)**. This distortion is reflected in the carboxylate-metal-carboxylate angles, which are close to the ideal 90° for the Mn, Co, Zn, and Cd, but deviate by 15° for Cu.

The packing of **2(M)** is fairly dense, but features solvent pockets filled with approx. 0.75 molecules of DMF and 0.5-1 molecule of water per Cu^{I} complex. These are however severely disordered and had to be removed in the refinement of **2(Cu)** and **2(Zn)** using the BYPASS routine.[345] The packing is governed by the SBUs' and copper(I) complexes connectivity as well as hydrogen bonding, and also features π-π-stacking. Packing of two adjacent SBUs along *b* is shown in Figure 2.5 for **2(Mn)**, **2(Co)**, and **2(Zn)** (identical for **2(Cu)** and **2(Cd)**). It is apparent that the SBUs cannot exceed dinuclearity, as this would superimpose two tetraquametal(II) moeities (see **2(Zn)**). In conjuction with Table 2.2 the nuclearities are as follows: 93% dinuclear and 7% mononuclear for **2(Mn)**, 76% dinuclear and 24% mononuclear for **2(Co)**, 15% dinuclear and 85% mononuclear for **2(Cu)**, 25% dinuclear and 75% mononuclear for **2(Zn)**, and 33% dinuclear and 67% mononuclear for **2(Cd)**. However, this and whether site 1 or 2 are occupied does not affect the SBUs' connectivity in topological terms,

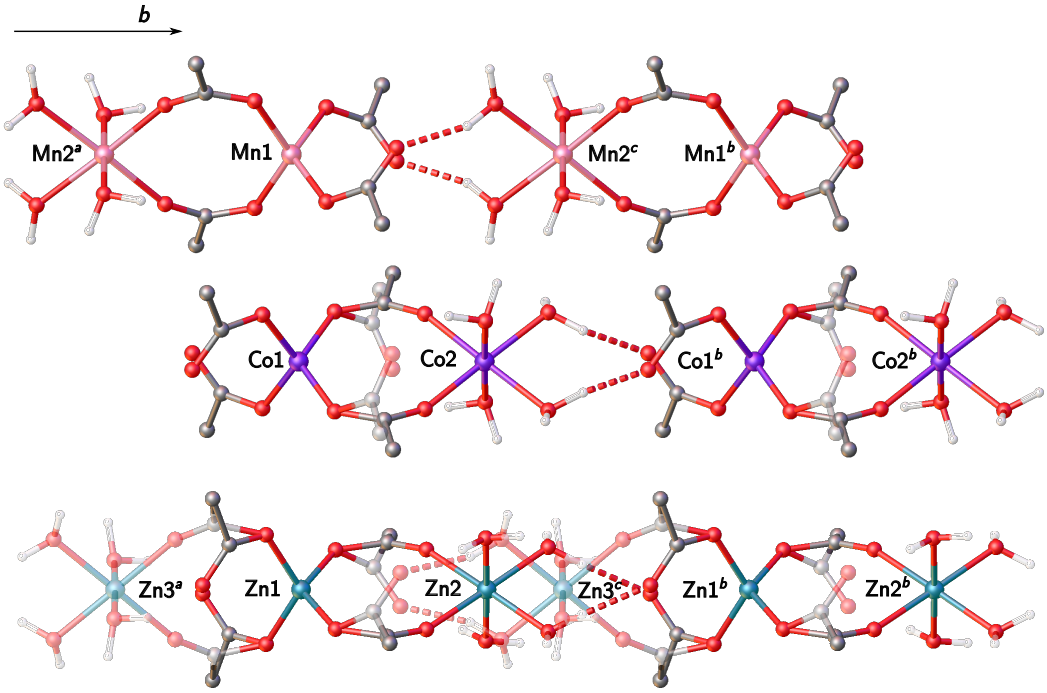


Figure 2.5: Packing of SBUs along b in **2(Mn)**, **2(Co)**, and **2(Zn)** (identical for **2(Cu)** and **2(Cd)**). One part of the disorder is shown translucent for clarity, however note that they have similar occupancy in **2(Zn)**, **2(Cu(** and **2(Cd)**. Due to packing constraints the maximum nuclearity of the SBUs is two. Symmetry key: $^{a} -\frac{1}{2}+x, \frac{1}{2}+y, z$; $^{b} -1+x, 1+y, \frac{3}{2}-z$, $^{c} -\frac{3}{2}-x, -\frac{1}{2}+y, \frac{3}{2}-z$.

i.e. the SBU is always a four connected node. Hence, packing and topology will be described in the following using **2(Mn)** as an example for all five. The $[Cu^{I}(Me_2Bpy)_2]$ moieties are connected to two SBUs and thus only form a strut, but not a node. This results in a 4-connected uninodal two dimensional net forming a corrugated square lattices parallel to C, with topological symbol **sql**. A monolayer of **2(Mn)** and its topological reduction are shown in Figure 2.6. The mesh wire-like corrugation of the layers becomes apparent viewing along b, as depicted in Figure 2.7. Here, if a vector was drawn from Mn1 to Mn2 it would differ in sign between orange and blue layers.

However, these layers are connected by hydrogen bonding *via* the partially deprotonated carboxylic acids and their symmetrie exquivalents through inversion (values given in Table 2.4). That is, H2A is delocalised around Wyckoff position 4*d* and hops between O2A and O2B, whereas H6A is delocalised around Wyckoff position 4*a* and hops between O6A and O6B. With donor$\cdots$acceptor ($D\cdots A$) distances below 2.5 Å and D—H$\cdots A$ often close to 170° to 180° these classify as moderate to strong hydro-

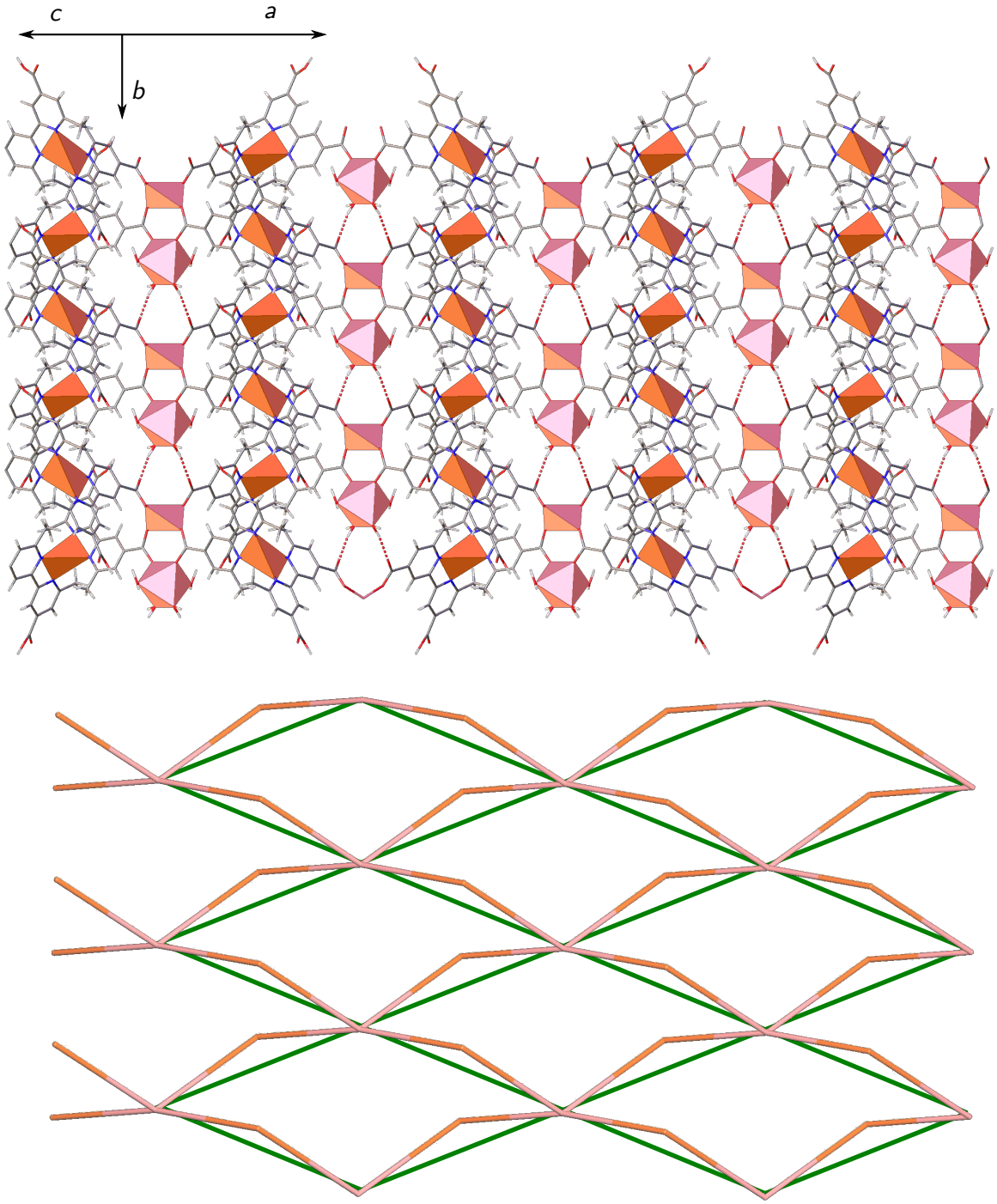


Figure 2.6: View onto a single layer of **2(Mn)** (top) and its topological reduction (bottom). Note that Cu^{I} nodes (orange) are two-connected and thus further reduced into a strut, resulting in a square lattice net (**sql**, green) with Mn-SBU as a four-connected node (pink).

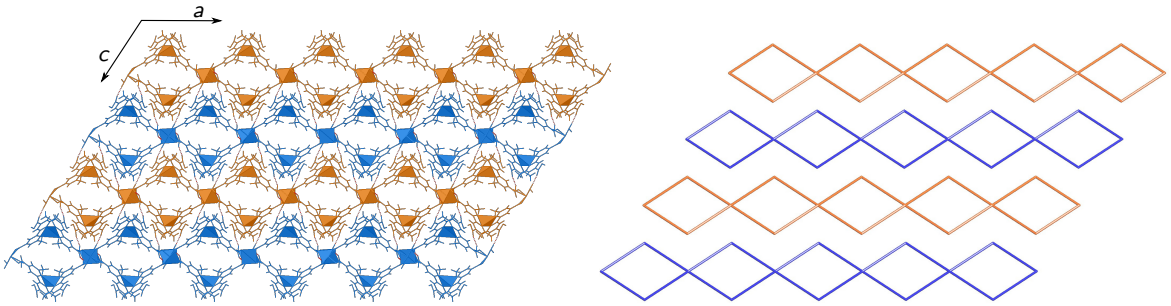


Figure 2.7: View along layers of **2(Mn)** (left) and its partial topological reduction (right) viewed along *b*.

Table 2.4: Carboxylic acid/carboxylate hydrogen bonds in **2(M)**.

2(M)	Donor—H···Acceptor	*D*—H [Å]	H···*A* [Å]	*D*···*A* [Å]	*D*—H···*A* [°]
2(Mn)	O2A—H2A···O2B	0.84	1.62	2.440(8)	165
	O6A—H6A···O6B	0.84	1.61	2.425(6)	163
2(Co)	O2A—H2A···O2B	0.84	1.57	2.408(10)	178
	O6A—H6A···O6B	0.84	1.60	2.441(12)	176
2(Cu)	O2A—H2A···O2B	0.84	1.65	2.4688(2)	165
	O6A—H6A···O6B	0.84	1.66	2.4543(1)	158
2(Zn)	O2A—H2A···O2B	0.84	1.61	2.4339(1)	166
	O6A—H6A···O8	0.84	1.60	2.4364(1)	174
2(Cd)	O2A—H2A···O2B	0.84	1.57	2.4055(1)	175
	O6A—H6A···O6B	0.84	1.73	2.4883(1)	149

gen bonds.[346] These hydrogen bonds connect $[Cu^{I}(Me_2Bpy)_2]$ moieties along $[3\bar{1}0]$ and $[\bar{3}10]$, expanding them into four-connected nodes. Thus, the net is now a 4,4-connected binodal 3D net, portrayed in Figure 2.8, with point symbol $\{6^2.8^4\}\,\{6^4.8^2\}_2$. Moreover, every hydrogen atom in the tetraquametal(II) moiety engages in hydrogen bonding with co-crystallised solvents (O15, O16) but more importantly adjacent carboxylates. Tables for all additional hydrogen bond are listed in the appendix (see Tables A.1 to A.5). As depicted in Figure 2.5, O11 hydrogen bonds to monodentate carboxylates (O4) of adjacent SBU translated in *b* via H11A. The same water molecule forms a hydrogen bond *via* H11B with a partially deprotonated carboxylate (O5) adjacent through the *c*-glide plane. Furthermore, O12 engages in a hydrogen bond with the partially deprotonated carboxylate involving O1, also related through the *c* glide plane. In total, this results in a 6,10-connected net with point symbol $\{3^3.4^7.5^3.6^2\}_2\{3^6.4^{14}.5^{17}.6^8\}$, which is also depicted in Figure 2.8.

Furthermore, layers are connected by the aforementioned π-π-interactions. Namely,

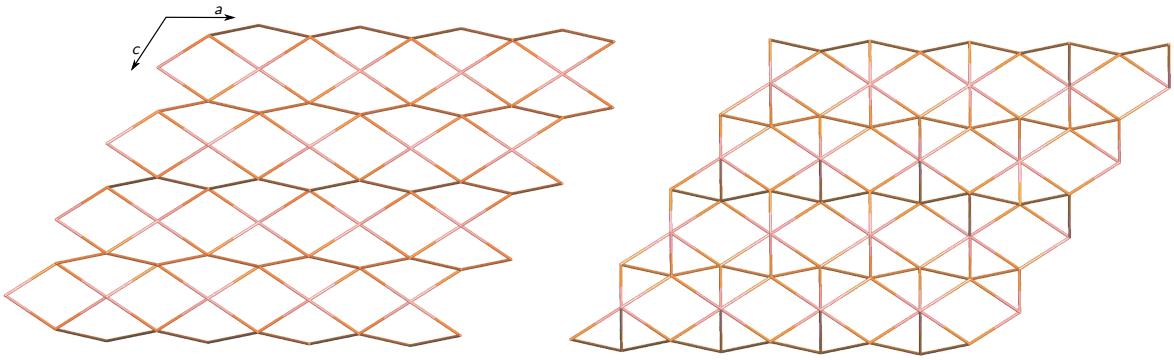


Figure 2.8: Connection of **sql** nets into a 4,4-connected 3D net by hydrogen bonds between partially deprotonated carboxylic acids (left) and a 6,10-connected 3D net by all hydrogen bonds, viewed along *b*. Cu^{I}- and Mn^{II}-nodes are respectively coloured orange and pink.

both bipyridyl moieties engage in parallel displaced π-π-stacking with their symmetry equivalents through inversion, forming a one dimensional chain along [$\bar{1}$10]. Interplane distances and shifts are listed in Table 2.5 and respectively range from 3.42 Å to 3.53 Å and 1.12 Å to 1.48 Å, and are well within expected values for pyridine-metal complexes.[347] Following the trend of single site or disordered site occupation **2(Mn)** and **2(Co)** show distinct values for each plane, whereas they are virtually identical within **2(Cu)** and **2(Zn)**. The unevenly disordered site occupation **2(Cd)** is also reflected in these distances. Moreover, ligands with monodentate carboxylates seem to enjoy more translational freedom, as their interplanar distances are up 0.1 Å longer than for their respective bidentate analogues.

Table 2.5: Plane distances and shifts for π-π-stacking in **2(M)**. Planes interact with their symmetry equivalents through inversion.

2(M)	Ligand	$d_{\pi-\pi}$ [Å]	Shift [Å]
2(Mn)	N1N2	3.529(3)	1.362(5)
	N3N4	3.439(5)	1.417(5)
2(Co)	N1N2	3.416(5)	1.374(7)
	N3N4	3.517(4)	1.352(7)
2(Cu)	N1N2	3.516(5)	1.119(8)
	N3N4	3.512(3)	1.123(6)
2(Zn)	N1N2	3.508(5)	1.260(7)
	N3N4	3.510(3)	1.265(5)
2(Cd)	N1N2	3.450(7)	1.479(9)
	N3N4	3.499(4)	1.376(8)

The powder X-ray diffraction patterns of **2(M)** are presented in Figure 2.9. While **2(Mn)** and **2(Cu)** seem to contain minor impurities, **2(Co)**, **2(Zn)**, and **2(Cd)** are phase pure, but display preferential orientation. Hence, the background uncorrected powders were fit using Le Bail methods, as shown in Figure 2.10.[348] Indeed, **2(M)** are phase pure with the exception of **2(Cu)**, whose PXRD pattern displays significant peaks at 11.5° and 14.5° 2θ that are not accounted for by its single crystal structure model. As crystals of **2(Cu)** are comparatively brittle and the SBU is energetically unfavourable, these peaks like stem from decomposed or collapsed **2(Cu)**, induced by mechanical grinding in air.

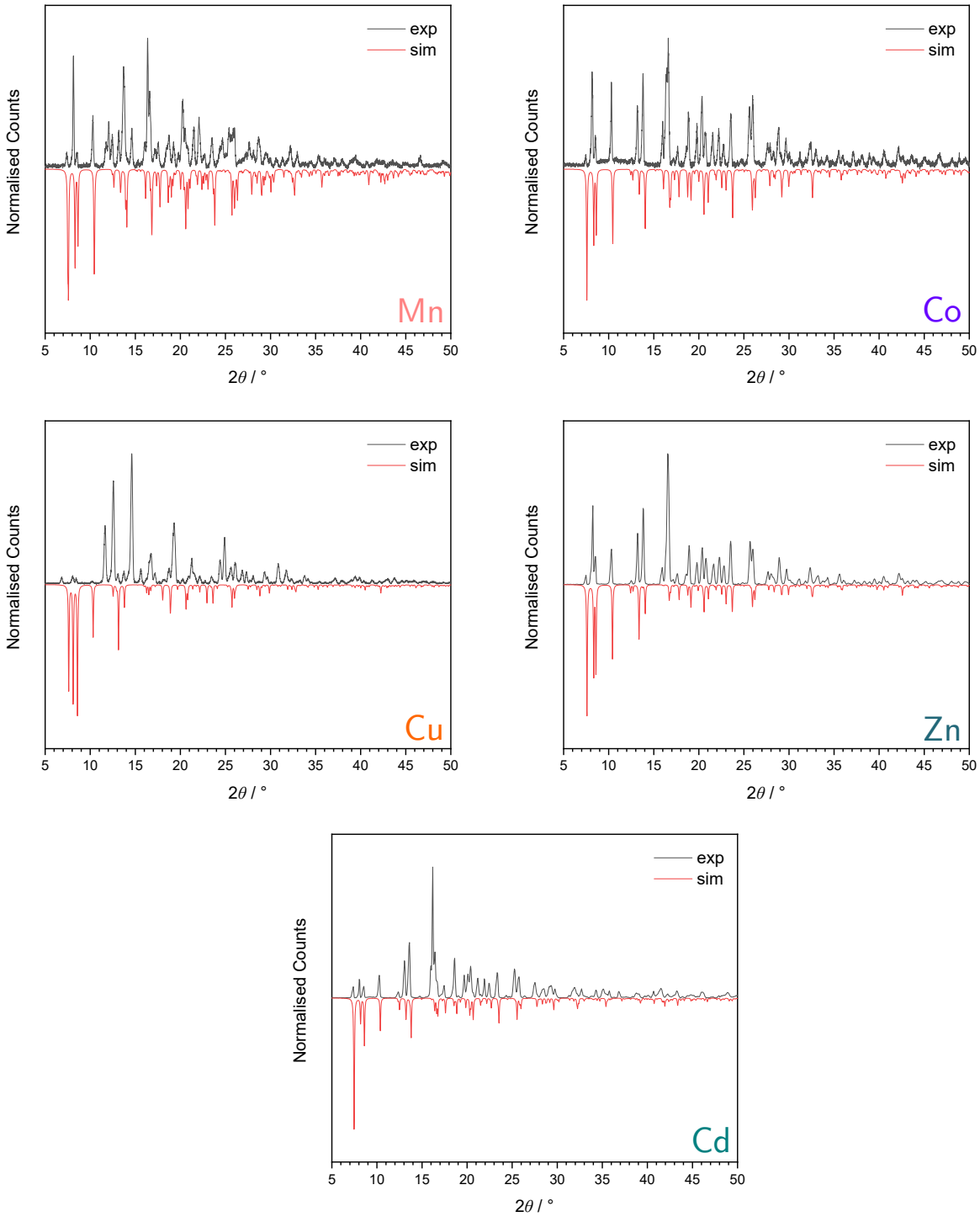


Figure 2.9: Experimental (black) and simulated (red) powder X-ray diffraction patterns of **2(M)**.

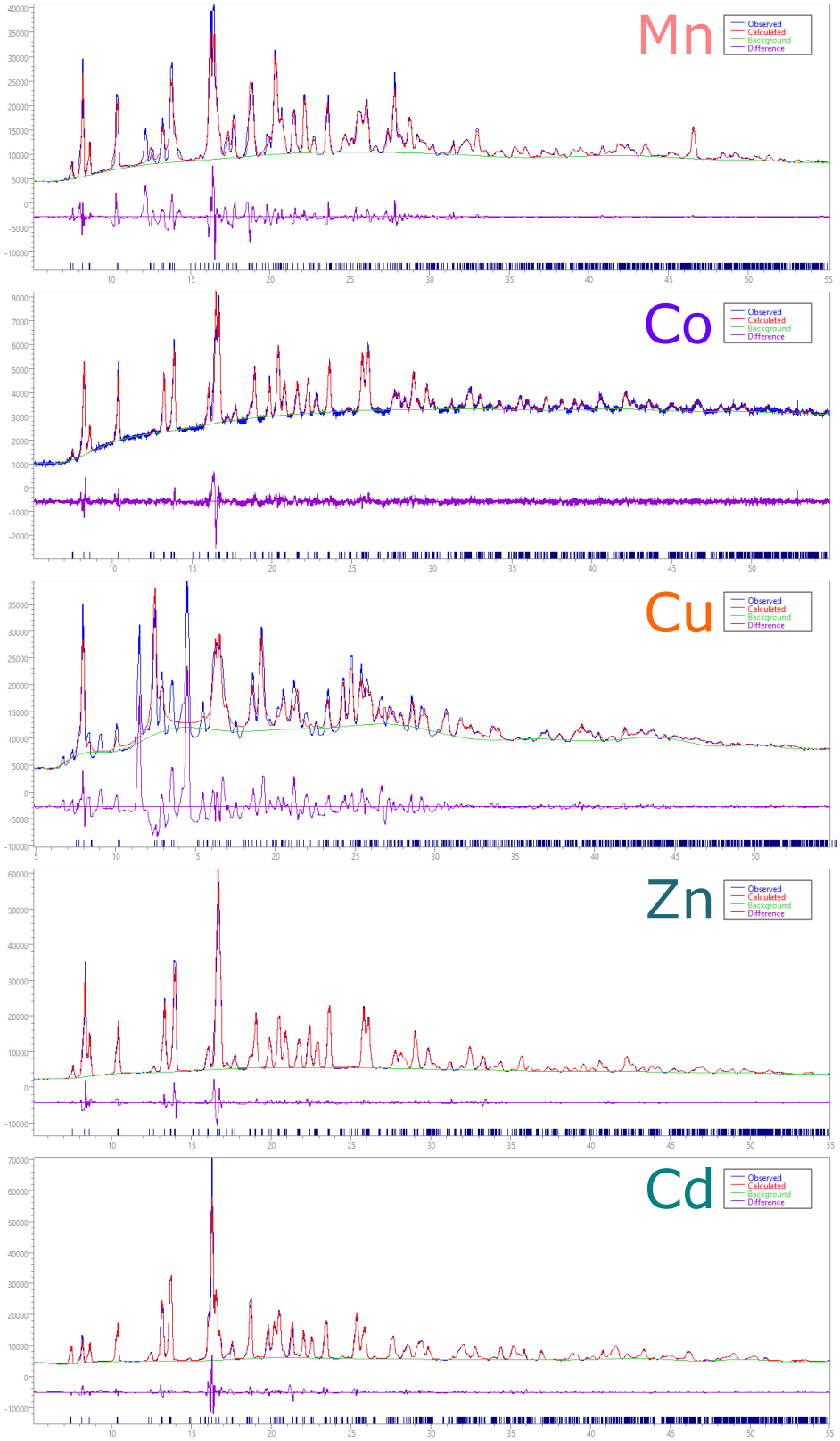


Figure 2.10: Le Bail fits of PXRD patterns of **2(M)**. Observed and calculated data are respectively shown in blue and red, their difference in violet, as well as the background in green. Navy ticks indicate positions of reflections predicted from the unit cell.

2.4. Photophysical Properties

$[Cu(H_2\mathbf{L1})_2]^+$ is well established as a photosensitiser for DSCs, where it is adsorbed on TiO_2.[28] To find out whether it retains its photosensitive properties upon immobilisation in the coordination polymers **2(M)**, solid state photophysical studies were carried out on $[Cu(H_2\mathbf{L1})_2]PF_6$ and crystals of **2(M)**, optical photographs of which are shown in Figure 2.11.

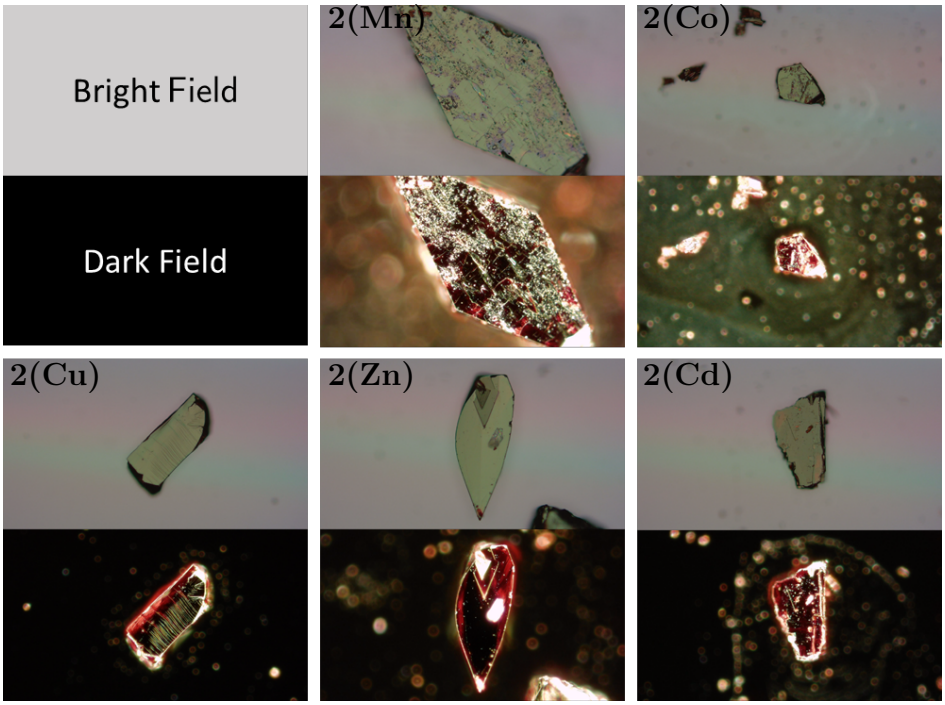


Figure 2.11: Bright and dark field optical photographs of crystals of **2(M)** used for photophysical characterisation.

The absorption and emission spectra of $[Cu(H_2\mathbf{L1})_2]PF_6$ and **2(M)** are plotted in Figure 2.12. Solid $[Cu(H_2\mathbf{L1})_2]PF_6$ exhibits broad absorption across the visible spectrum and the MLCT band displays a bathochromic shift of 23 nm to 505 nm, when compared to $[Cu(H_2\mathbf{L1})_2]Cl$ in MeOH.[28] Interestingly, upon inclusion of $[Cu(H_2\mathbf{L1})_2]^+$ into the coordination polymers **2(M)**, only minor differences are observed within the series. The MLCT transitions are identical with that of $[Cu(H_2\mathbf{L1})_2]Cl$ in MeOH at 483 nm ($S_0 \rightarrow S_2$). A second peak at 558 nm with a shoulder showing strong absorption up to 630 nm and tapering off at 700 nm, likely stems from the $S_0 \rightarrow S_1$ transition and shows increased absorption due to reduction of symmetry.

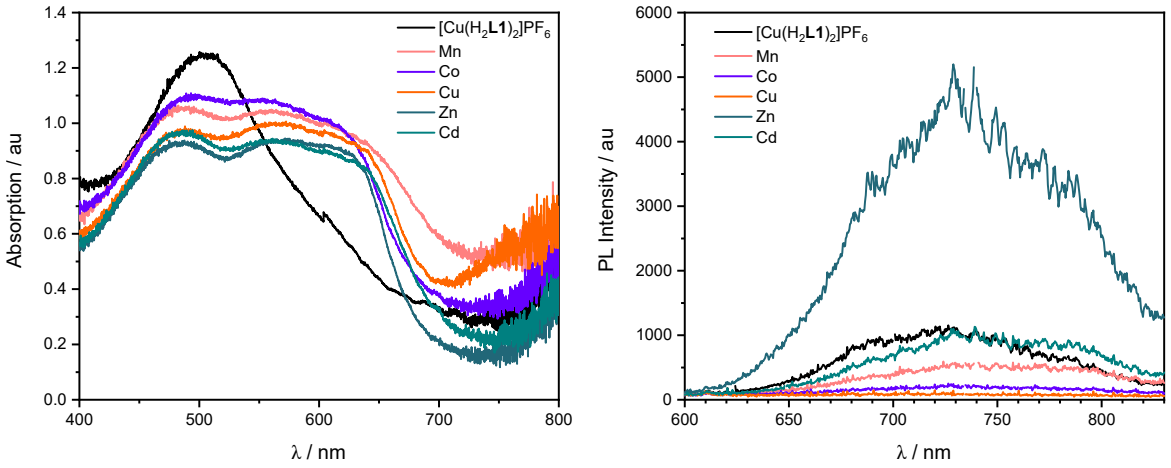


Figure 2.12: Absorption (left) and steady state emission spectra (right) of $[Cu(H_2\mathbf{L1})_2]PF_6$ and the coordination polymers **2(M)**. Samples were excited at $\lambda_{exc} = 405\,nm$ with a power of $0.2\,\mu W$.

When excited at 405 nm, solid $[Cu(H_2\mathbf{L1})_2]PF_6$ exhibits a broad emission spectrum across over 200 nm in the red region, peaking at 728 nm (1.70 eV). With the exception of **2(Cu)**, all of **2(M)** exhibit similar photoluminescence. The significantly higher intensity of **2(Zn)** likely stems from far greater crystal size. A comparison between normalised emission spectra of $[Cu(H_2\mathbf{L1})_2]PF_6$ and the remaining four coordination polymers **2(M)** is depicted in Figure 2.13. The spectra of **2(Co)** and **2(Zn)** are virtually identical with that of $[Cu(H_2\mathbf{L1})_2]PF_6$, whereas **2(Mn)** and **2(Cd)** exhibit an additional shoulder at roughly 780 nm.

Time-resolved photoluminescence decays of $[Cu(H_2\mathbf{L1})_2]PF_6$ and **2(M)** are plotted in Figure 2.14. The fast initial decays of the ^{1}MLCT state occurs on the picosecond time scale, thus overlaps with the instrument response function (IRF). Residual photoluminescence is associated with the ^{3}MLCT state, lifetimes of which are listed in Table 2.6. Note, that for the latter fit ranges were chosen so that there is no interference with the IRF and normalised counts exceed 10^{-4}, due to the diminished signal to noise ratio at lower values. The luminescence decay did not occur in a mono-exponential fashion as photoluminescent molecules can exhibit multiple lifetimes in the solid state.[52,349] Here a bi-exponential fit was sufficient and average lifetime $\langle\tau\rangle$ was calculated according to Equation 2.1, where α_i and τ_i are the pre-exponential and lifetime of the ith component.

$$\langle\tau\rangle = \frac{\sum \alpha_i \tau_i^2}{\sum \alpha_i \tau_i} \tag{2.1}$$

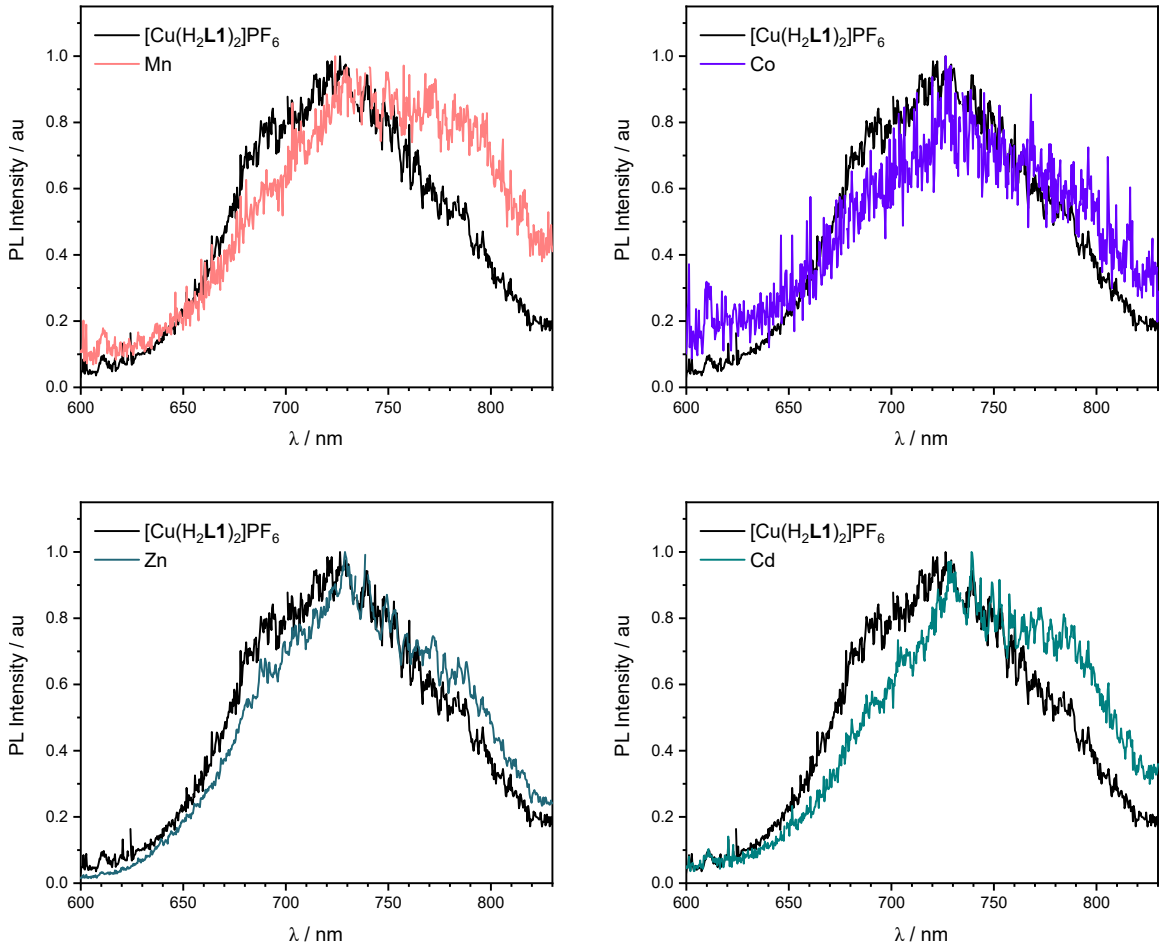


Figure 2.13: Comparison of normalised emission spectra of $[Cu(H_2\mathbf{L1})_2]PF_6$ and **2(M)**. **2(Cu)** was not included as the intensity was too low.

Table 2.6: Pre-exponential factors and lifetimes extracted of $[Cu(H_2\mathbf{L1})_2]PF_6$ and **2(M)**.

	α_1	τ_1 [ns]	α_2	τ_2 [ns]	$\langle\tau\rangle$ [ns]
$[Cu(H_2\mathbf{L1})_2]PF_6$	0.0066(2)	3.7(3)	0.0270(15)	27.5(5)	26.8
2(Mn)	0.0210(4)	3.38(9)	0.0440(4)	12.19(9)	11.2
2(Co)	0.0437(7)	1.118(17)	0.0057(2)	5.69(17)	3.0
2(Zn)	0.0117(4)	4.4(2)	0.0906(4)	22.64(15)	22.2
2(Cd)	0.0184(4)	3.60(8)	0.0327(4)	11.14(9)	10.0

Over 96.5% of the excited state $[Cu(H_2\mathbf{L1})_2]PF_6$ decay in a within 1 ns after irradiation, with the residual triplet state exhibiting an average lifetime of 26.8 ns. As mentioned before, **2(Cu)** is essentially non-emissive and is entirely quenched inunder 5 ns, hence no lifetimes were extracted. Similarly, **2(Co)** is barely fluorescent but shows an average lifetime of 3.0 ns. While both Cu^{II} and Co^{II} have unpaired electrons, the stronger quenching is attributed to a more facile reduction to the monovalent cation in **2(Cu)**.

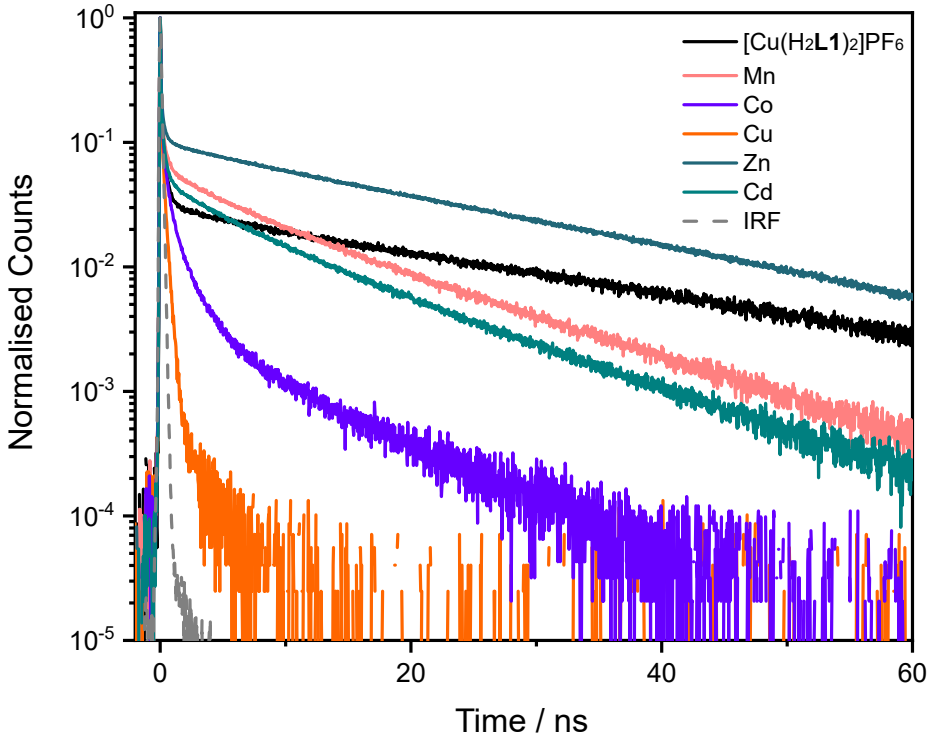


Figure 2.14: Photoluminescence decay of $[Cu(H_2\mathbf{L1})_2]PF_6$ and **2(M)**. Extracted lifetimes are listed in Table 2.6. Samples were excited at $\lambda_{exc} = 405\,nm$ with a power of 0.2 µW. The instrument response function (IRF) is shown as a grey dashed line.

The luminescence behaviour of **2(Mn)** and **2(Cd)** is quite similar, with 95.5% and 94.0% of quenching having occurred within the first nanosecond, and residual luminescence decay occurring with average lifetimes of 11.2 ns and 10.0 ns, respectively. Here, charge transfer does not occur as Cd^{II} possesses a closed shell (d^{10}) and the Mn^{II} ions are coordinated by carboxylates and water molecules, which do not exhibit the required backbonding to stabilise Mn^{I}. Interestingly, the initial decay in **2(Zn)** is not as strong as in $[Cu(H_2\mathbf{L1})_2]PF_6$ and indicates that the transition from the singlet into the triplet state is favoured in **2(M)**. This can be rationalised by the frameworks' rigidity hindering significant structural distortion in the excited state. Indeed, after 1 ns only 90.2% of excited states have decayed in **2(Zn)**, leaving twice the excited state population compared to $[Cu(H_2\mathbf{L1})_2]PF_6$, which then decay with an average lifetime of 22.2 ns. However, it is not clear why the luminescence decay in **2(Cd)** behaves similarly to **2(Mn)** instead of the isoelectronic **2(Zn)**. Yet, the rigidity imposed onto the metallolinker upon immobilisation in the framework seems to benefit the intersystem crossing from the rapidly decaying singlet into the longer lived triplet state.

2.5. Electrochemistry

To assess the influence of immobilisation of $[Cu(H_2\mathbf{L1})_2]PF_6$ on the electrochemical properties of **2(M)**, cyclovoltammetry was conducted, the results of which are presented in Figure 2.15 and corresponding values are listed in Table 2.7.

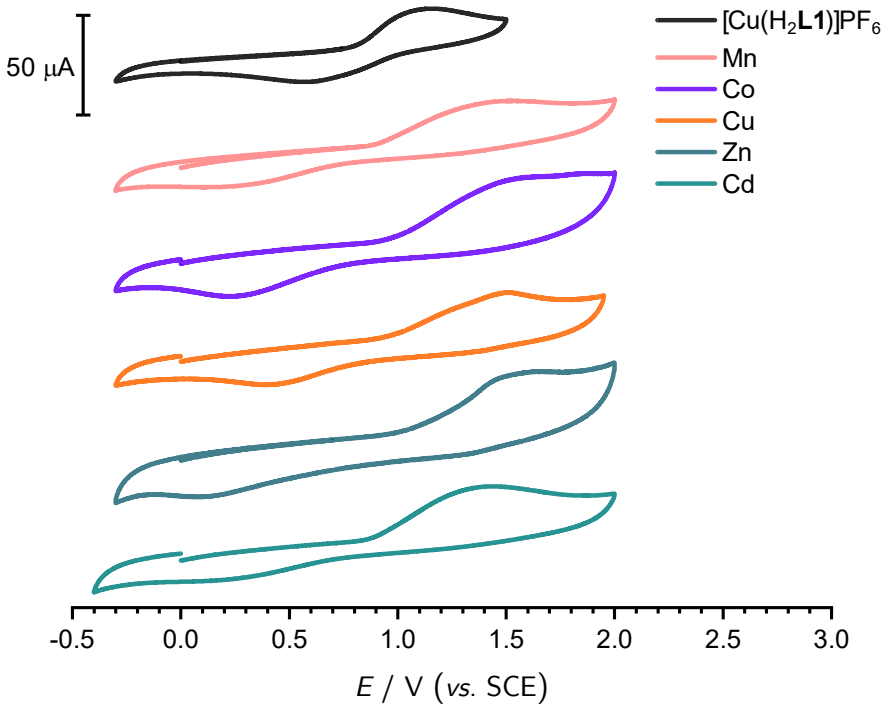


Figure 2.15: Cyclic voltammograms of $[Cu(H_2\mathbf{L1})_2]PF_6$ and **2(M)**. Samples were drop cast onto a glassy carbon electrode and fixated with Nafion ink. A 0.1 M nBu_4PF_6 solution was used as electrolyte. Scan rates were 250 mV s^{-1} (500 mV s^{-1} for **2(Zn)**).

Table 2.7: Electrochemical data (*vs.* $Fc^{0/+}$) extracted from the cyclic voltammograms of $[Cu(H_2\mathbf{L1})_2]PF_6$ and **2(M)**.

	$[Cu(H_2\mathbf{L1})_2]PF_6$	**2(Mn)**	**2(Co)**	**2(Cu)**	**2(Zn)**	**2(Cd)**
E_{ox} / V	0.45	0.42	0.51	0.56	0.53	0.42
$E_{pa} - E_{pc}$ / mV	50	108	108	111	132	105
E^*_{red} / V	−1.25	−1.28	−1.19	−1.14	−1.17	−1.28

The $Cu^{I/II}$ oxidation is observed at 0.45 V *vs.* ferrocene and is quasi-reversible, which is both in accordance with reported data in MeOH solution.[28] Upon immobilisation in the coordination polymers **2(M)**, the oxidation becomes electrochemically irreversible due to electron transfer limitations between the material and the electrode. If the

divalent metal is Mn or Cd, the oxidation potential is reduced to 0.42 V *vs.* $Fc^{0/+}$, whereas for Co, Cu, and Zn it increases by 0.06 V to 0.11 V. The excite state reduction potential E^{*}_{red} can be deduced by the subtraction of the excited state luminescence energy E_{00} from the ground state electrochemical potential according the Rehm-Weller expression, *viz.*

$$E^{*}_{red} = E_{red} - E_{00} \tag{2.2}$$

Assuming unitary charge transfer $E_{00} = 1.70\,V$, which gives excited state reduction potentials between $-1.28\,V$ and $-1.14\,V$ for **2(M)**. In this regard, they are comparable to $[Ru(bpy)_3]^{2+}$.

2.6. Additional Characterisations

Scanning electron microscopy (SEM) images and energy dispersive X-ray (EDX) mapping of **2(Co)** and **2(Cd)** are shown in Figure 2.16. Quantitative EDX measurements confirm the incorporation of the respective M^{II} species and reveal M:Cu ratios in **2(M)** of 1:1 (0.96:1) for Mn, 0.82:1 (0.88:1) for Co, 0.71:1 (0.75:1) for Zn, and 0.78 (0.82:1) for Cd.

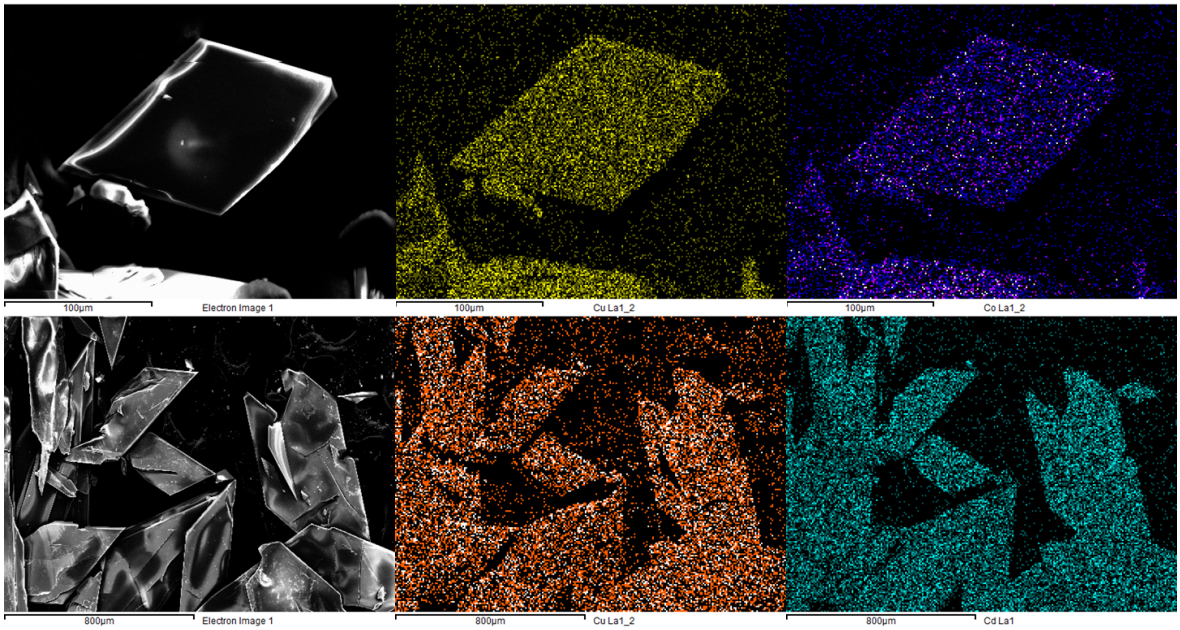


Figure 2.16: SEM image and EDX maps of **2(Co)** (top) and **2(Cd)** (bottom).

Thermal gravimetric analysis of **2(M)** is shown in Figure 2.17. Initial weight loss

between 30 °C to 120 °C is associated with loss of water molecules. Further weight loss between 175 °C to 240 °C stems from the loss of DMF molecules. Interestingly this only starts occurring at 210 °C for **2(Cu)**. Finally, decomposition of the organic ligand initiates between 270 °C for **2(Cu)** and 310 °C for **2(Zn)**.

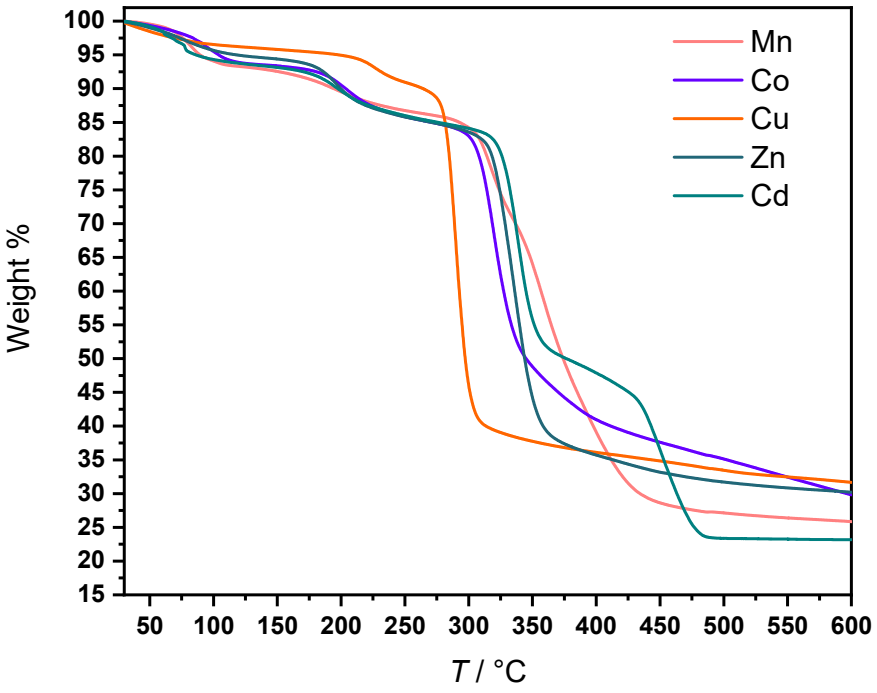


Figure 2.17: Thermal gravimetric analysis of **2(M)** under nitrogen.

The Fourier-transform infrared (FTIR) spectra of **2(M)** (see Figure 2.18) are virtually identical, although minor differences are observed for **2(Cu)**. The vibrational band observed at 3462 cm^{-1} as a peak in **2(Cu)** and a shoulder in the rest is associated with ν(O−H) of water molecules. The broad band between 3350 cm^{-1} and 2500 cm^{-1} stems from C−H stretching vibrations, ν(O−H) of the carboxylic acids, as well as co-crystallised DMF molecules. ν(C=O) of the latter two are respectively observed at 1720 cm^{-1} and 1650 cm^{-1}. The coordination carboxylates lead to asymmetric stretching vibrations at around 1604 cm^{-1} and 1547 cm^{-1}, as well as symmetric stretching vibrations at 1402 cm^{-1} and 1365 cm^{-1}. Application of the criteria reported by Deacon and Phillips, the differences (Δ) between the averaged asymmetric and symmetric vibration are Δ = 171 cm^{-1} (Cu), Δ = 192 cm^{-1} (Mn, Co, Cd), and Δ = 204 cm^{-1} (Zn).[350] All of these are typical for bridging bidentate carboxylates.

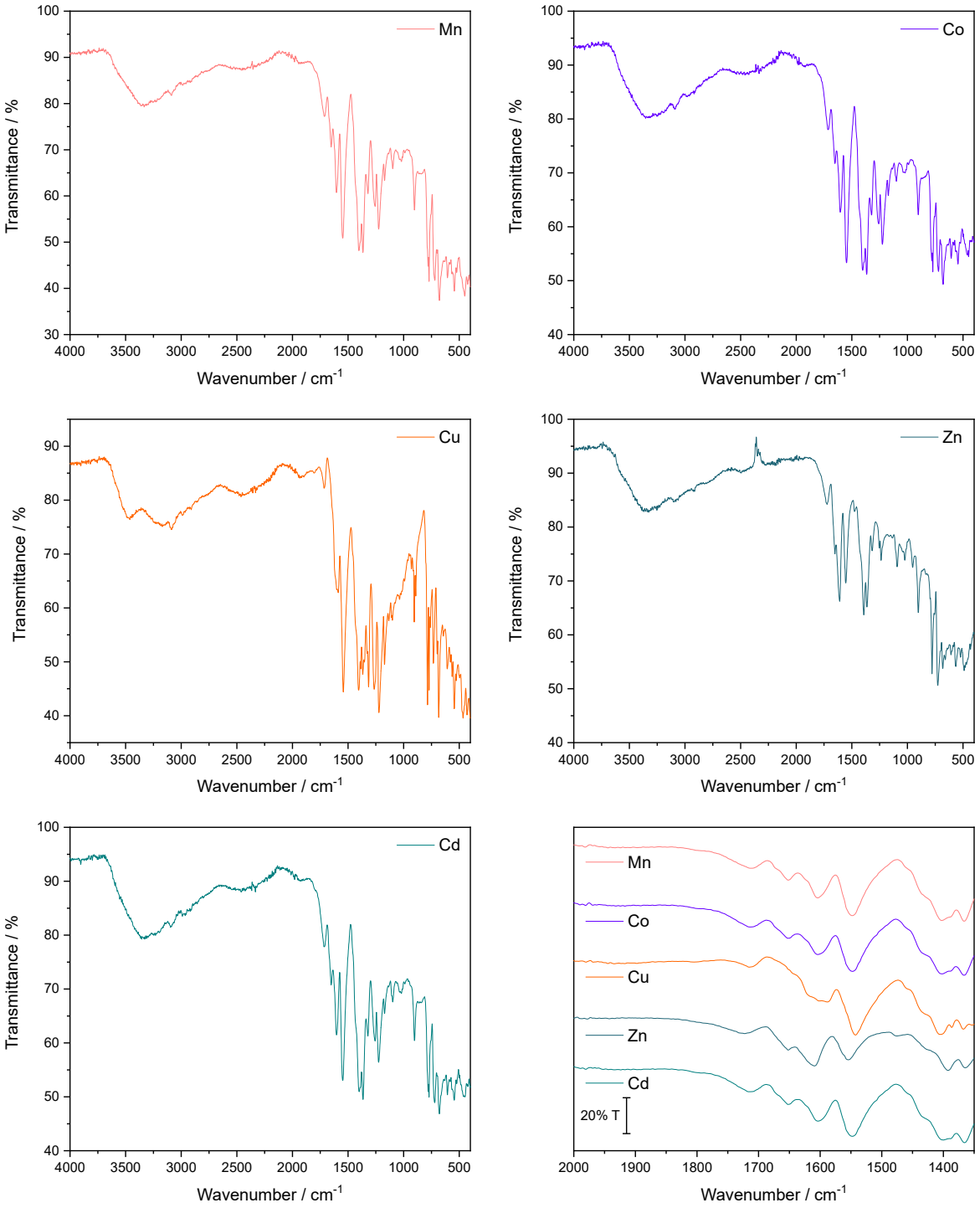


Figure 2.18: Fourier transformed infrared spectra of **2(M)** and comparison of the carbonyl bands.

2.7. Conclusion

Mixed mono-/dinuclear SBUs are connected into a 2D net which is extended into the third dimension through hydrogen bonds and π-π interactions. The photo- and electrochemical properties of this kind of material was investigated for the first time, revealing extended visible light absorption, and more efficient intersystem crossing as a result the frameworks' rigidity, when compared to the parent photosensitiser. Depending on the node metal, photoluminescence lifetimes of **2(M)** can reach up to 22 ns (Zn) or be quenched efficiently *via* photoexcited charge transfer (Cu). With excited state reduction potentials between -1.28 V (Mn, Cd) and -1.14 V (Cu) *vs.* $Fc^{0/+}$, **2(M)** present viable, earth-abundant alternatives to polypyridyl-ruthenium MOFs.

Future work will be the investigation of their applicability as photocatalysts for proton reduction and photocathodes, respectively.

3. Diimine Ligands and Bis(diimine)copper(I) Complexes

3.1. Bipyridine Derivates

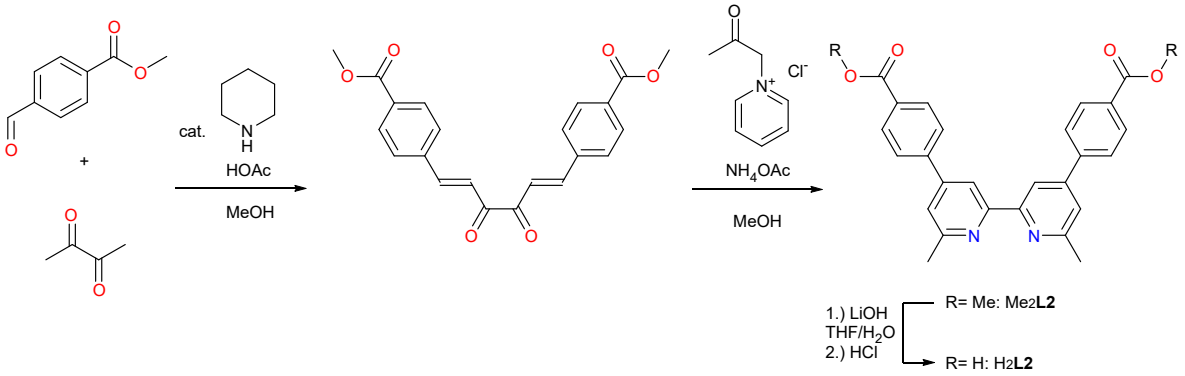
3.1.1. Introduction

In the previous chapter, $[Cu(H_2\mathbf{L1})_2]^+$ was used as a photosensitive metallo-linker in coordination polymers, which however only exhibited small voids but no pores. A common solution in reticular chemistry to address this problem is the extension of linkers by acetylen- or *p*-phenylene spacers.[351] Extension of the π-system might also be beneficial as Roberto *et al.* reported significantly superior performance of DSCs, when 6,6'-dimethyl-2,2'-bipyridyl-4,4'-dibenzoic acid was used in place of $H_2\mathbf{L1}$.[38] Moreover, the increase of steric bulk around the metal centre, especially with branched alkanes, significantly increases the luminescence lifetimes.[55,58,352] The aim of the first part of this chapter are the respective extension of $H_2\mathbf{L1}$ in the 4,4'-positions and increase of steric bulk in the 6,6'-positions, as well to synthesise coordination polymers with the metallo-linkers.

Additionally, during futile attempts to form titanium organic frameworks with using **1** as a metallo-linker, single crystals of the complex $[Cu(H_2\mathbf{L1})(H\mathbf{L1})]$ (**3**) were obtained and its structure will be described.

3.1.2. Synthesis

The extension of $H_2\mathbf{L1}$ was accomplished by insertion of phenylene moieties in the 4,4'-positions. The synthesis was accomplished by adopting a procedures developed in the

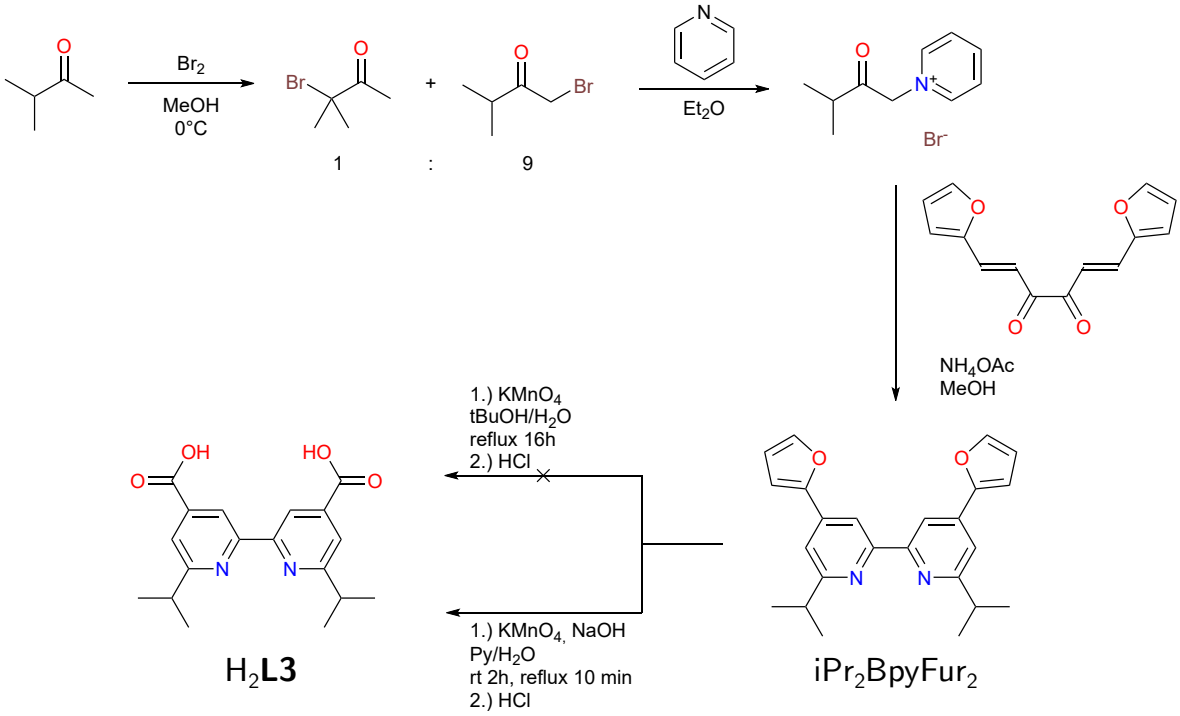


Scheme 3.1: Synthesis of 6,6'-dimethyl-2,2'-bipyridyl-4,4'-dibenzoic acid (H_2**L2**).

groups of Housecroft and Roberto, respectively, is outlined in Scheme 3.1.[38,353] That is, a piperidine catalysed aldol condensation of diacetyl with methyl 4-formylbenzoate gave dimethyl 4,4'-((1*E*, 5*E*)-3,4-dioxohexa-1,5-diene-1,6-diyl)dibenzoate, which was followed by a Kröhnke pyridine synthesis with *N*-acetonylpyrdiniym chloride to yield dimethyl 6,6'-dimethyl-2,2'-bipyridyl-4,4'-dibenzoate (Me_2**L2**). The reported purification of Me_2**L2**, *i.e.* quadruple flash column chromatography, is rather cumbersome and requires copious amounts of chlorinated solvents to acquire few hundred milligrams of product. However, it was found that overnight Soxhlet extraction with chloroform yields sufficient purity. Finally, 6,6'-dimethyl-2,2'-bipyridyl-4,4'-dibenzoic acid (H_2**L2**) was obtained by deesterification and subsequent acidification of Me_2**L2**. *N*-Acetonylpyridinium chloride (**4**) was used from commercial suppliers but was also synthesised by mixing of pyridine and chloroacetone. Surprisingly, while *N*-acetonylpyrdinium halides are commonly used their crystal structures had not been reported so far. Attempts to synthesis coordination polymers or MOFs featuring copper(I) complexes of H_2**L2** were unsuccessful, however one of the attempts yielded crystals of the partially deprotonated complex [Cu(H_2**L2**)(H**L2**)] (**5**).

To increase of steric bulk in the 6,6'-positions with respect to H_2**L1** functionalisation is is sumamrised in Scheme 3.2. Here, isopropyl- rather than *tert*-butyl-groups were chosen as the bigger steric repulsion in the latter is so big that it leads to thermodynamically labile copper(I) complexes.[56] This necessitated the use of *N*-(3-methyl-2-oxobutyl)pyridinium bromide, which was prepared in two steps from 3-methyl-2-butanone. First, following Gaudry and Marquet's procedure the bromination gave a 1:9 mixture of 3-bromo-3-methyl-2-butanone and the target compound 1-bromo-3-methyl-2-butanone. However, product purification was not necessary for the next step, as formation of the pyridinium salt occurred selectively with the primary bromide. Next,

4,4'-difuryl-6,6'-diisopropyl-2,2-bipyridine ($iPr_2BpyFur_2$, **6**) was obtained in a Kröhnke pyridine synthesis analogous to $Me_2BpyFur_2$. The increased steric bulk is reflected in the solubility, enabling recrystallisation of **6** in Et_2O at room temperature. Oxidation of the furyl groups to carboxylic acid following the same procedure as for H_2**L1**, *i.e.* overnight reflux with $KMnO_4$ in *t*BuOH and water, resulted in partial oxidation of the isopropyl groups. Selective oxidation of the former was accomplished under milder conditions following a procedure reported by Zyryanov *et al.*, which largely occurs at room temperature and *t*BuOH is substituted by pyridine and aided by the use of sodium hydroxide. Subsequent acidification gave 6,6'-diisopropyl-2,2'-bipyridine-4,4'-carboxylic acid (H_2**L3**). Crystallisations akin to the ones in the previous chapter were attempted but only yielded amorphous material. Moreover, after heating for several hours a loss of the red colour associated with bis(diimine)copper(I) complex was observed, instead a light blue tint was observed. Hence, the steric bulk imposed by the isopropyl groups in the 6,6'-positions in H_2**L3** make its corresponding Cu^I complex thermally labile, which leads to disassociation of the complex followed by oxidation of Cu^I during attempted coordination polymer synthesis.



Scheme 3.2: Synthesis of 6,6'-diisopropyl-2,2'-bipyridine-4,4'-carboxylic acid (H_2**L3**) starting from 3-methyl-2-butanone *via* 4,4'-difuryl-6,6'-diisopropyl-2,2-bipyridine ($iPr_2BpyFur_2$).

3.1.3. Crystal Structure of *N*-acetonylpyridiunium chloride (4)

Single crystals of suitable size for SCXRD analysis of *N*-acetonylpyridiunium chloride (**4**) were obtained from a $CDCl_3$ solution from previous NMR spectroscopy experiments. Surprisingly, the structure had not been reported before. Crystal data and refinement results are listed in Table 3.1 and the thermal ellipsoid of the asymmetric unit is plotted in Figure 3.1. **4** crystallises neat as colourless rods and was solved and refined in the monoclinic space group $P2_1/c$ with one molecule in the asymmetric unit. All bond distances are within expectations, with d(N1−C3) = 1.464(6) Å, d(O1 =C2) = 1.198(6) Å and a twist between the acetonyl- and pyridinium-moieties of 78.951(6) Å. As the pyridinium ring is cationic it does not engages in π-π-stacking. However, inspection of the molecule's Hirshfeld surface (Figure 3.2, left) reveals a multitude of close contacts. The carbonyl group engages in to-and-fro dipole-dipole interactions with its symmetry equivalents through inversion with $d_{O\cdots C}$ = 3.1053(3) Å

Table 3.1: Crystal data and refinement results for **4**.

Identification code	**4**
Empirical formula	$C_8H_{10}ClNO$
Formula weight	171.62
Temperature/K	100
Crystal description	colourless rod
Crystal size/mm^3	0.22 × 0.09 × 0.06
Crystal system	monoclinic
Space group	$P2_1/c$
a/Å	8.0001(7)
b/Å	11.8955(10)
c/Å	9.0519(8)
α/°	90
β/°	91.391(3)
γ/°	90
V/Å^{-3}	861.17(13)
Z, Z'	4, 1
ρ_{calc}/g cm^{-3}	1.324
μ/mm^{-1}	3.457
F(000)	360
Refl. total/unique	23352/1573
R_{int}, R_σ	0.0577, 0.0213
Data/restr./param.	1573/0/101
GooF	1.016
R_1 [$I \geq 2\sigma(I)$], all	0.0662, 0.0676
wR_2 [$I \geq 2\sigma(I)$], all	0.1899, 0.1904
$\Delta\rho_{max}/\Delta\rho_{min}$/e Å^{-3}	1.32/-0.41

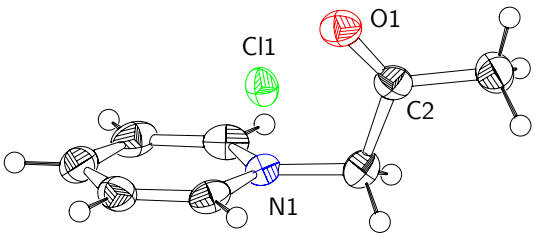


Figure 3.1: ORTEP of **4** drawn at 50% probability.

($r_{\mathrm{vdW}}(\mathrm{C}) = 1.70\,\text{Å}$, $r_{\mathrm{vdW}}(\mathrm{O}) = 1.52\,\text{Å}$) and also forms a close contact ($d(\mathrm{O1}\cdots\mathrm{C8}^{\,b}) = 3.0258(2)\,\text{Å}$, $r_{\mathrm{vdW}}(\mathrm{Cl}) = 1.75\,\text{Å}$), ${}^{b}x, \frac{1}{2}-y, \frac{1}{2}+z$) with the pyridinium ring of a molecule adjacent through the *c*-glide plane. The chloride anion Cl1 engages in a total of five non-classical C—H$\cdots$Cl hydrogen bonds with five different acetonylpyridinium cations *via* aliphatic (twice C3) and aromatic (C4, C5, C7) C—H donors, the distances and angles of which are listed in Table 3.2. The packing resulting from these interactions is displayed in Figure 3.3.

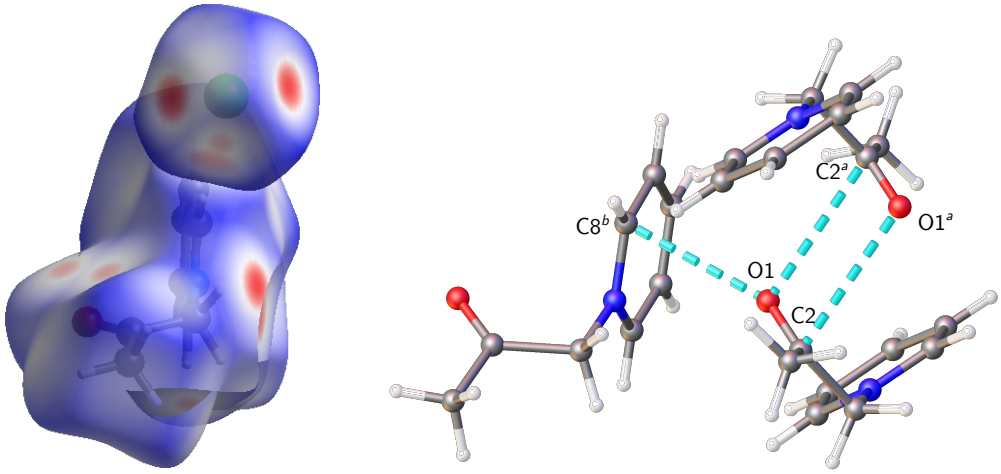


Figure 3.2: Hirshfeld surface molecules **4** (left) and highlight of the C$\cdots$O close contacts (right). Symmetry key: ${}^{a}1-x, 1-y, 1-z$; ${}^{b}x, \frac{1}{2}-y, \frac{1}{2}+z$.

Table 3.2: Non-classical hydrogen bonds in **4**.

Donor—H$\cdots$Acceptor	*D*—H [Å]	H$\cdots$*A* [Å]	*D*$\cdots$*A* [Å]	*D*—H$\cdots$*A* [°]
C3–H3A$\cdots$Cl1^{a}	0.99	2.63	3.501(5)	147
C3—H3B$\cdots$Cl1^{b}	0.99	2.62	3.396(6)	136
C4—H4$\cdots$Cl1	0.95	2.59	3.390(5)	142
C5—H5$\cdots$Cl1^{c}	0.95	2.8	3.616(6)	144
C7 —H7$\cdots$Cl1^{d}	0.95	2.75	3.530(5)	140

Symmetry key: ${}^{a}1-x, 1-y, -z$; ${}^{b}1-x, -\frac{1}{2}+y, \frac{1}{2}-z$; ${}^{c}-x, 1-y, -z$; ${}^{d}x, \frac{1}{2}-y, \frac{1}{2}+z$.

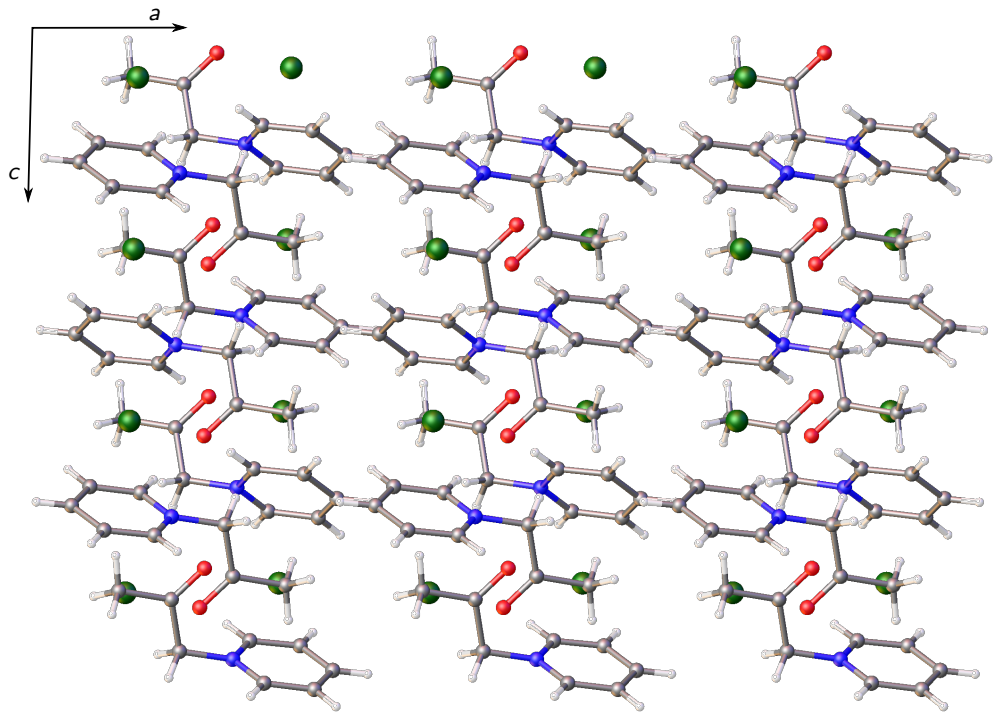


Figure 3.3: The packing of **4** viewed along [010].

3.1.4. Crystal Structures of [Cu(H_2L1)(HL1)] (3) and [Cu(H_2L2)(HL2)] (5)

The crystal data and refinement results for the mono-deprotonated copper(I) complexes [Cu(H_2**L1**)(H**L1**)] (**3**) and [Cu(H_2**L2**)(H**L2**)] (**5**) are listed in Table 3.3 and the thermal ellipsoids of their asymmetric units are shown in Figure 3.4. **3** co-crystallises with a well resolved molecule of DMA and one molecule of DMF (which had to be removed using BYPASS) as red needles, whereas **5** co-crystallises with two molecules of DMF and one molecule of water as red blocks. Both were solved and refined in the triclinic space group $P\bar{1}$ with on molecule in the asymmetric unit and two molecules per unit cell.

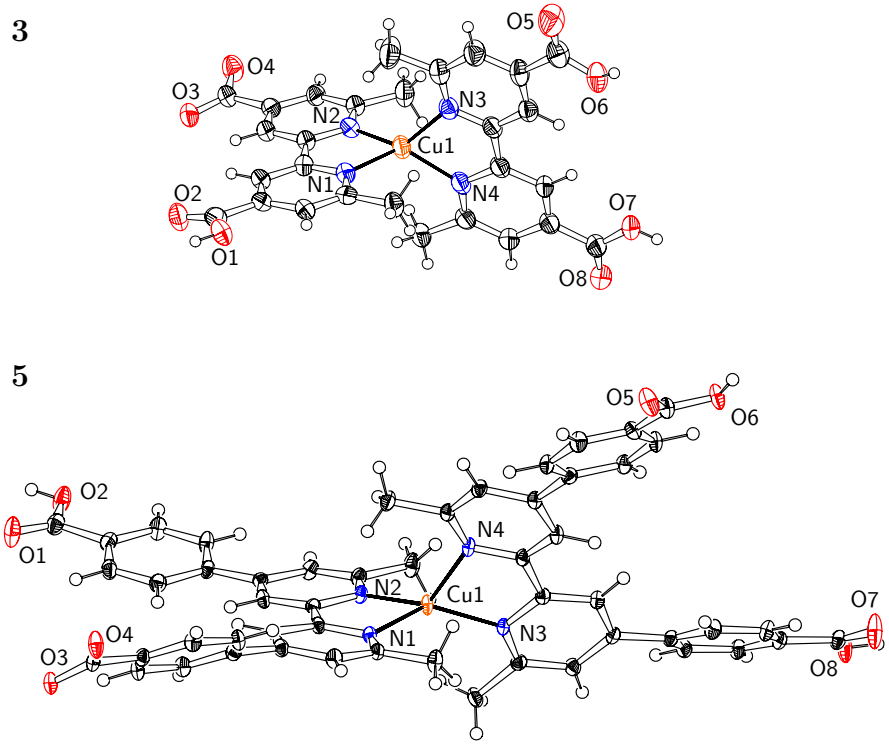


Figure 3.4: ORTEPs of the asymmetric units in partially deprotonated Cu^I complexes **3** and **5**, shown at 50% probablity. Co-crystallised solvents were omitted for clarity.

Moreover, both feature Cu in oxidation state +I coordinated in a distorted tetrahedral coordination environment by four nitrogen atoms of two dimethylbipyridine ligands. Charge neutrality is achieved by deprotonation of one of the four carboxylic acids and could be clearly located in one position based on C—O distances ($d_{C=O} = 1.26$ Å *vs.* $d_{C=O} = 1.21$ Å and $d_{C-OH} = 1.31$ Å). Distances and angles found in **3** and **5** are listed

Table 3.3: Crystal data and refinement results for **3** and **5**.

Identification code	**3** $\cdot$ DMA $\cdot$ DMF	**5** $\cdot$ 2 DMF $\cdot$ H_2O
Empirical formula	$C_{32}H_{32}CuN_5O_9$	$C_{58}H_{55}CuN_6O_{11}$
Formula weight	694.16	1075.62
Temperature/K	100	100
Crystal description	red needle	red block
Crystal size/mm^3	0.13 × 0.03 × 0.02	0.14 × 0.12 × 0.11
Crystal system	triclinic	triclinic
Space group	$P\bar{1}$	$P\bar{1}$
a/Å	8.6672(5)	12.8543(14)
b/Å	13.3778(6)	15.3125(17)
c/Å	15.5605(7)	15.4360(17)
α/°	75.847(3)	67.470(3)
β/°	74.147(4)	86.712(3)
γ/°	78.332(4)	67.804(3)
V/Å^{-3}	1665.07(15)	2584.8(5)
Z, Z'	2, 1	2, 1
ρ_{calc}/g cm^{-3}	1.385	1.382
μ/mm^{-1}	1.438	0.492
$F(000)$	720	1124
Refl. total/unique	13162/4882	21368/10719
R_{int}, R_σ	0.0624,0.0764	0.0637, 0.0811
Data/restr./param.	4882/0/434	10719/0/693
GooF	1.028	1.019
R_1 [$I \geq 2\sigma(I)$], all	0.0576, 0.0785	0.0476, 0.0840
wR_2 [$I \geq 2\sigma(I)$], all	0.1476, 0.1616	0.1000, 0.1096
$\Delta\rho_{max}/\Delta\rho_{min}$/e Å^{-3}	0.42/-0.41	0.40/-0.40

in Table 3.4. Cu—N bond distances are within expectations from similar complexes and are from 2.017(3) Å to 2.032(3) Å, and 2.0092(18) Å to 2.0522(19) Å with bite angles of 82.2° and 81.4° for **3** and **5**, respectively. Although both feature methyl-groups for steric hindrance, the dihedral angle φ respectively deviates from orthogonality by ca. 8.7° and 15.5° for **3** and **5**. Furthermore, a larger twist between pyridyl moieties within a ligand (Py$\cdots$Py) is observed in the phenylene-extended **5** and in the doubly protonated ligands when compared to the deprotonated ligand in both. Interestingly, the phenylene moieties in **5** are approximately twisted by expected 33°, but the one exception is a benzoic acid rather than the benzoate is twisted by 10°.

The packing of **3** is goverened by hydrogen bonding, distances and angle of which are given in Table 3.5. Here, the carboxylic acid of H**L1** forms a hydrogen bond with the co-crystallised DMA, whereas both carboxylic acids of H_2**L1** form hydrogen bonds with one oxygen atom each of H**L1** carboxylates adjacent through translations. Thus, each complex of **3** is connected to four adjacent complexes *via* hydrogen bonding which is

Table 3.4: Distances (Å) and angles (°) in **3** and **5**.

	Distance	**3**	**5**
Cu—N	Cu1—N1	2.028(3)	2.0445(19)
	Cu1—N2	2.017(3)	2.0171(18)
	Cu1—N3	2.032(3)	2.0092(18)
	Cu1—N4	2.025(3)	2.0522(19)
	Angle	**3**	**5**
N—Cu—N	N1···Cu1···N2	82.20(13)	81.34(7)
	N3···Cu1···N4	82.33(13)	81.47(7)
	N1···Cu1···N3	115.76(13)	134.57(8)
	N1···Cu1···N4	126.44(13)	105.40(7)
	N2···Cu1···N3	131.51(13)	129.95(7)
	N2···Cu1···N4	124.47(13)	128.04(8)
Bpy—Cu—Bpy	φ	98.66	74.45
Py···Py	HL	1.95(13)	7.70(9)
	H_2L	6.71(15)	19.18(9)
Py···Bz	Py1···Bz1	-	32.96(10)
	Py2···Bz2	-	10.17(9)
	Py3···Bz3	-	33.26(10)
	Py4···Bz4	-	31.15(10)

Bz*i* is attached to Py*i*, which involves N*i*.

Table 3.5: Hydrogen bonds in **3**.

Donor—H···Acceptor	*D*—H [Å]	H···*A* [Å]	*D*···*A* [Å]	*D*—H···*A* [°]
O1—H1···O9	0.84	1.69	2.503(4)	162
O6—H6···O4^a	0.84	1.66	2.460(4)	158
O7—H7···O3^b	0.84	1.76	2.570(4)	162

Symmetry key: $^a x, y, 1+z$; $^b -1+x, y, 1+z$.

results in a 2D square lattice (**sql**) network parallel to B. Interestingly, these layers are related through inversion and intercalated by layers of DMA as depicted in Figure 3.5.

The packing in **5** is more complex and features both hydrogen bonding and π-π-stacking. In terms of the hydrogen bonding (distances and angles in Table 3.6), the benzoate moiety accepts hydrogen bond from all benzoic acids of adjacent complexes, twice to O3 and once to O4, with an additional bridge to O7 *via* the co-crystallised water molecule (O11). Hence, each complex of **5** is connected to five adjacent complexes resulting in 2D network with point symbol $\{4^8.6^2\}$ extending along $[10\bar{1}]$ and $[0\bar{1}2]$ forming planes with base vector (121). These nets have an underlying **sql** net, however the fifth connection links two nets together. Furthermore, entanglement of

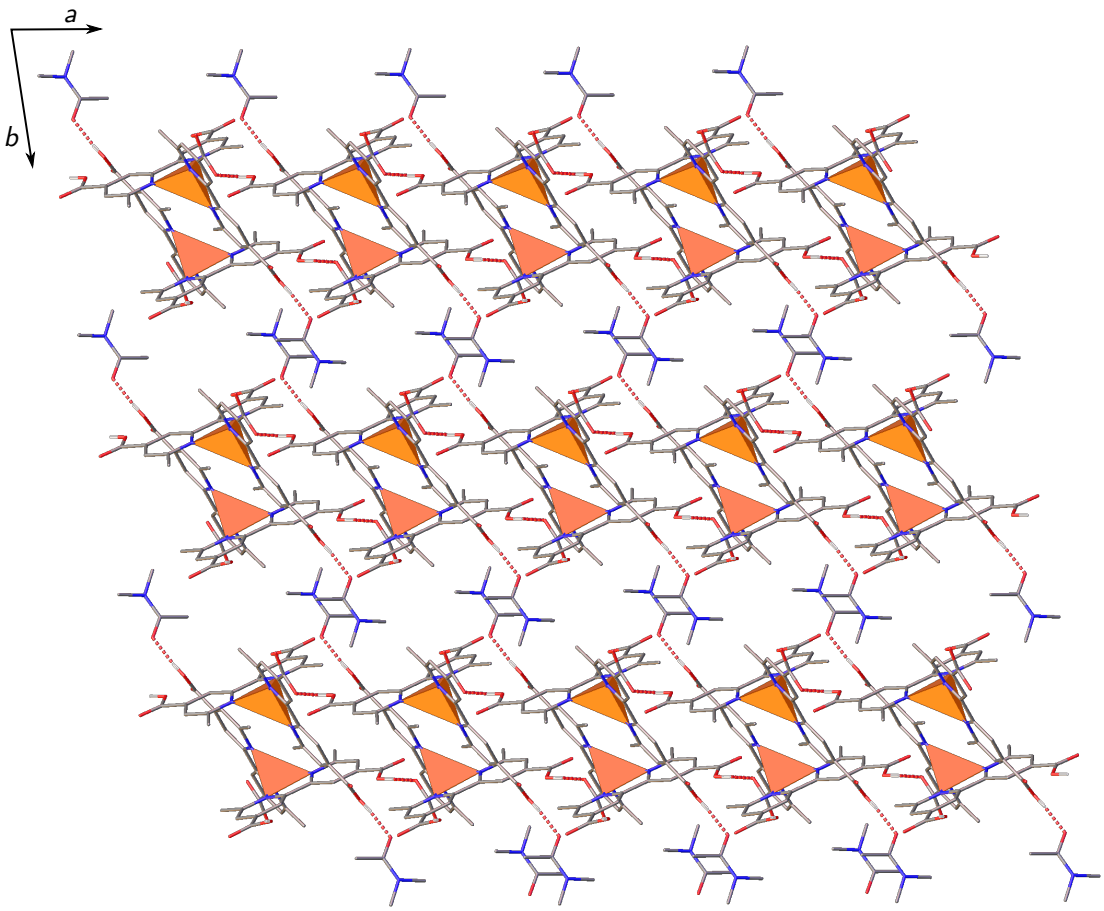


Figure 3.5: The packing of **3** viewed along [00$\bar{1}$]. Non-hydrogen bonding hydrogen atoms were omitted for clarity.

Table 3.6: Hydrogen bonds in **5**.

Donor—H$\cdots$Acceptor	D—H [Å]	H$\cdots A$ [Å]	$D\cdots A$ [Å]	D—H$\cdots A$ [°]
O2—H2$\cdots$O3^{a}	0.84	1.79	2.620(3)	168
O6—H6$\cdots$O3^{b}	0.84	1.85	2.663(2)	164
O8—H8$\cdots$O4^{c}	0.84	1.77	2.591(3)	165
O11—H11A$\cdots$O4^{d}	0.87	2.00	2.806(3)	153
O11—H11B$\cdots$O7^{e}	0.87	2.04	2.864(3)	159

Symmetry key: $^{a}\,-x, 1-y, 1-z$; $^{b}1+x, y, -1+z$; $^{c}2+x, -1+y, z$; $^{d}1+x, -1+y, z$; $^{e}\,-1+x, y, z$.

these nets leads to parallel polycatenation of the networks into a three dimensional network (2 D + 2 D $\rightarrow$ 3 D) as shown in Figure 3.6.[354] Additionally, parallel displaced π-π-stacking is observed between Bz1 and Bz4 with $d_{\pi-\pi}$ = 3.450(3) Å (shifted by 1.603(5) Å and tilted by 7.49(11)°), as well as Py1 and Bz2 with $d_{\pi-\pi}$ = 3.462(2) Å (shifted by 1.385(4) Å and tilted by 13.08(9)°).

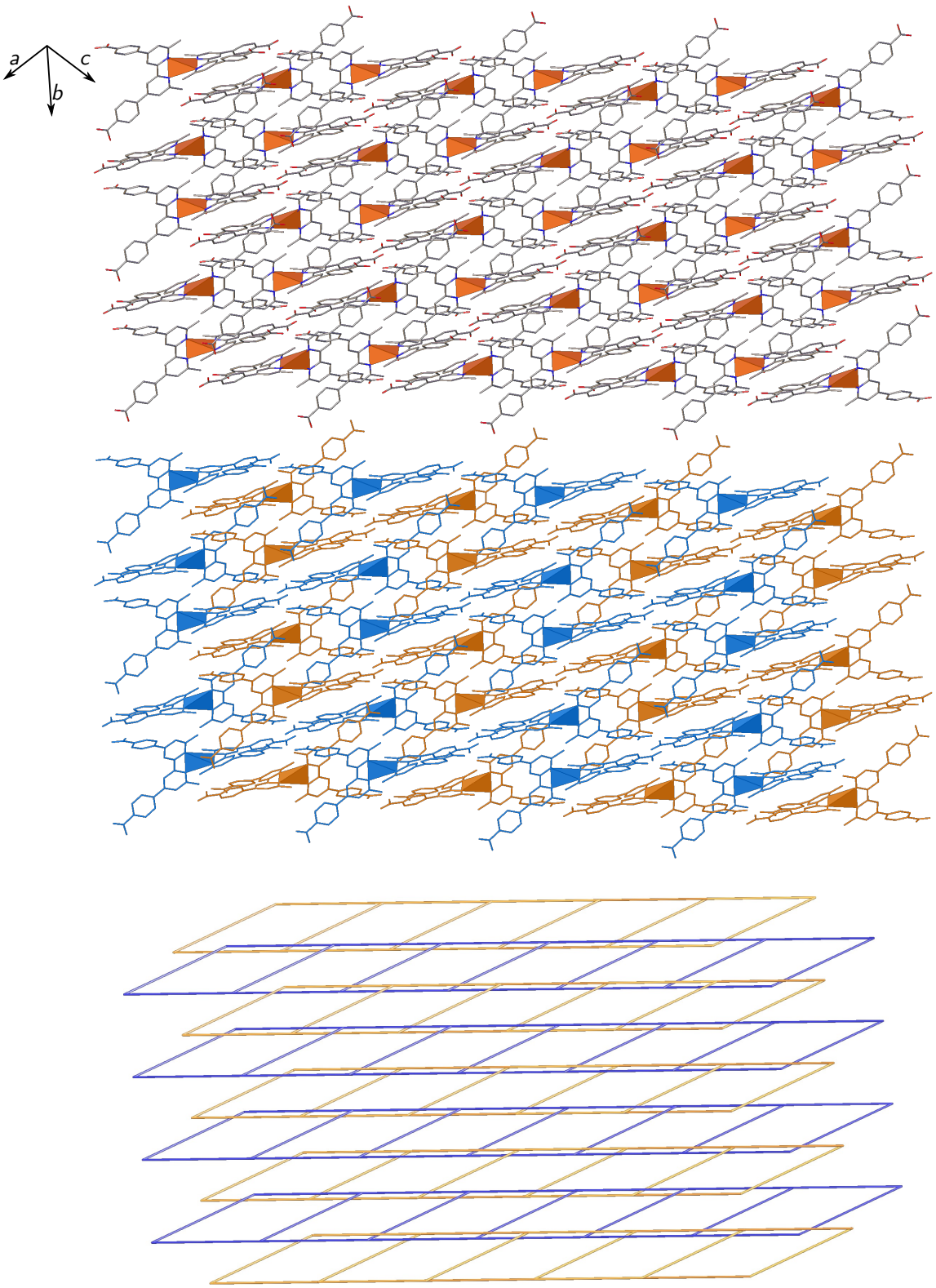


Figure 3.6: The packing (top) , colour coded by net (middle) and catenated nets (bottom) of **5** viewed along [1$\bar{1}$1].

3.1.5. Crystal Structure of 4,4'-Difuryl-6,6'-diisopropyl-2,2'bipyridine (6)

Single crystals of **6** were obtained from slow evaporation of a Et_2O solution of the compound. Crystal data and refinement results are listed in Table 3.7. **6** was solved and refined in the orthorhombic space group *Pbcn* with half a molecule in the asymmetric unit, thermal ellipsoids of which are plotted in Figure 3.7, and four molecules per unit cell. All atoms lie on general positions, however the central bipyridine bond is located on an inversion centre (Wyckoff position 4*b*), hence due to lone pair-lone interactions the nitrogen atoms N1 and N1* (* $= -x, 1-y, z$) **6** are *anti*. Moreover, the furyl moiety is disordered with a rotation of ca. 180° and is rotated 14° with respect to the pyridine ring. The isopropyl group is rotated so that it points away from N1.

Table 3.7: Crystal data and refinement results for **6**.

Identification code	**6**
Empirical formula	$C_{24}H_{24}N_2O_2$
Formula weight	372.45
Temperature/K	100
Crystal description	colourless plate
Crystal size/mm^3	0.28 × 0.19 × 0.06
Crystal system	orthorhombic
Space group	*Pbcn*
a/Å	13.8277(5)
b/Å	9.0140(3)
c/Å	15.6329(6)
α/°	90
β/°	90
γ/°	90
V/Å^{-3}	1948.53(12)
Z, Z'	4, 0.5
ρ_{calc}/g cm^{-3}	1.27
μ/mm^{-1}	0.081
$F(000)$	792
Refl. total/unique	24979/2008
R_{int}, R_σ	0.0715, 0.0276]
Data/restr./param.	2008/163/175
GooF	1.083
R_1 [$I \geq 2\sigma(I)$], all	0.0416, 0.0614
wR_2 [$I \geq 2\sigma(I)$], all	0.0917, 0.1027
$\Delta\rho_{max}/\Delta\rho_{min}$/e Å^{-3}	0.20/-0.23

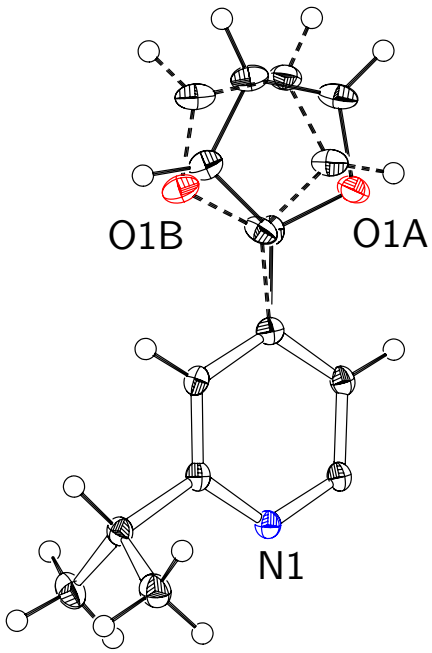


Figure 3.7: ORTEP of the asymmetric unit **6** drawn at 50% probability.

Figure 3.8 depicts the packing of **6**. The parallel displaced π-π-stacking between pyrid-

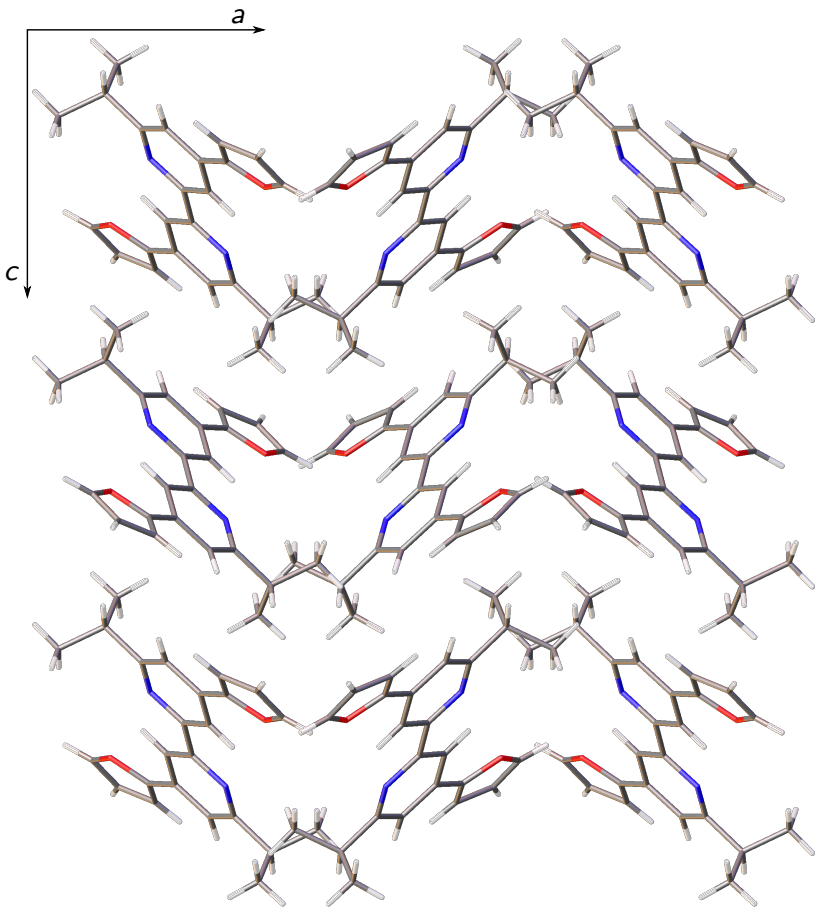


Figure 3.8: The packing of **6** viewed along [010]. Disorder was omitted for clarity.

ine rings found in its dimethyl analogue are absent due to steric constraints imposed by the isopropyl groups.

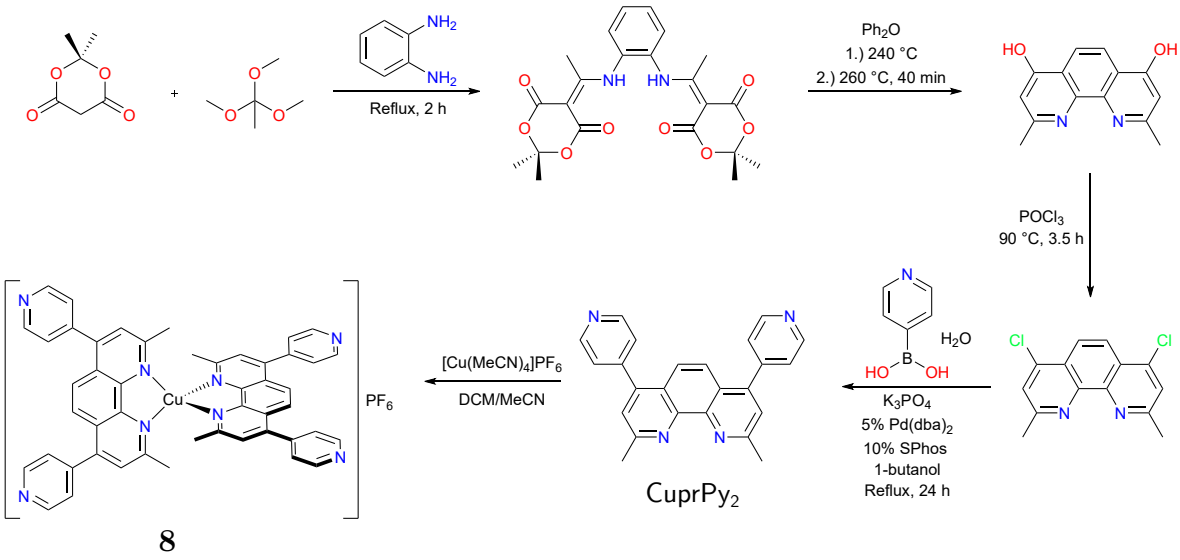
3.2. Neocuproines

3.2.1. Introduction

The second part of this chapter features phenanthroline based ligands. Castellano *et al.* have reported an example of solar hydrogen photocatalysis in which $[Cu(dsbtmp)_2]^+$ serves photosensitiser and chloro(4-pyridyl)cobaloxime ($[Co(Cl)(dmgH)_2(Py)]$ as hydrogen evolution catalyst. Direct attachment of the catalyst to a photosensitiser might enable faster charge transfer after photoexcitation. Moreover, $[Co(dmgH)_2]$ is known to form 1D coordination polymers with 4,4'-bipyridine and thus a $[Co(dmgH)_2(py)_2]$ moiety could be seen as a linear strut from a topological point of view.[355,356] The copper(I) complex of a phenanthroline based ligand with 4'-pyridyl-groups in the 4,7-positions, *i.e.* 2,9-dimethyl-4,7-(4'-dipyridyl)phenanthroline (4,7-dipyridylneocuproine, $CuprPy_2$), could then be used as a tetrahedral node. The combination of catalytic linear strut and photosensitive tetrahedral node could then give a photocatalytic diamond network (**dia**). Hence, the aim is to synthesise $CuprPy_2$, investigate its copper(I) complex, form coordination polymers with it and test these for solar hydrogen photocatalysis.

3.2.2. Synthesis

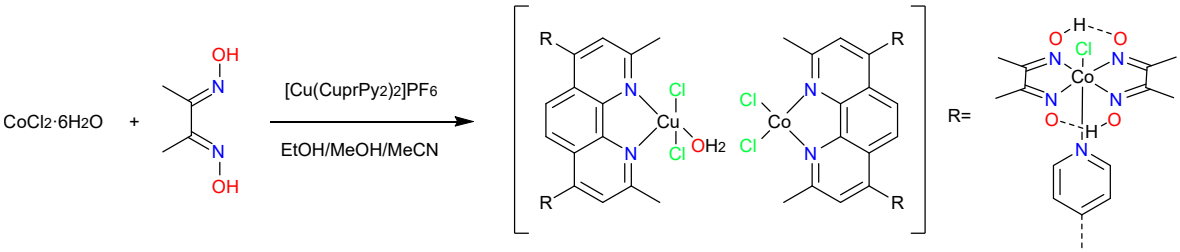
The synthesis of $[Cu(CuprPy_2)_2]PF_6$ was accomplished in five step reaction, which is outlined in Scheme 3.3, following a procedures reported by Harwoord *et al.* as well as Ulven *et al.*.[68,69] Meldrum's acid and trimethyl orthoacetate undergo an aldol condensation under the exclusion of methanol, which is followed by the addition *o*-phenylenediamine yielding 5,5'-((1,2-phenylenebis(azanediyl))bis(ethan-1-yl-1-ylidene))bis(2,2-dimethyl-1,3- dioxane-4,6-dione). Subsequent thermal cyclisation-decarboxylation in refluxing diphenylether gave 4,7-dihydroxy-neocuproine, however the reported solubility in D_2O with NaOD in an attempt to acquire NMR spectra was not observed. Nevertheless, treatment of 4,7-dihydroxy-neocuproine with oxyphosphorous-trichloride ($POCl_3$) gave 4,7-dichlorocproine ($CuprCl_2$, **7**). It was found that 20 eq. rather than the reported 75 eq. of $POCl_3$ are not only sufficient for the reaction, but also make workup safer and easier. Suzuki-Miyaura coupling of **7** with 4-pyridylboronic acid hydrate was accomplished following Buchwald's procedure, to yield $CuprPy_2$.[357] Here, potassium phosphate as used as base and the active catalyst $[Pd(SPhos)_2]$ is generated *in situ* using $Pd(dba)_2$(dba = dibenzylideneacetone). The copper(I) complex



Scheme 3.3: Synthesic route from *o*-phenylenediamine to the 4-pyridyl substituted neocuproine ligand $CuprPy_2$ and its complexation to $[Cu(CuprPy_2)_2]PF_6$.

$[Cu(CuprPy_2)_2]PF_6$ (**8**) was obtained by mixing a solution of the ligand in dichloromethane (DCM) with a solution of tetrakisacetonitrile copper(I) hexafluorophosphate ($[Cu(MeCN)_4]PF_6$).

Subsequent attempts to attach cobalt bis(dimethylglyoximate) units to the pyridyl moeties of **8** was met with moderate success. As shown in Scheme 3.4, the reaction of cobalt(II) chloride with dimethylglyoxime ($dmgH_2$) in ethanol (EtOH) followed by layering with an acetonitrile solution of **8** did result in the formation of chloro(4-pyridyl)cobaloxime ($[Co(Cl)(dmgH)_2(Py)]$) moieties in the 4- and 7-positions of $CuprPy_2$, which will be referred to as $CuprCobal_2$. However, the copper(I) centre was oxidised an is coordianted by two chlorides as well as a water molecule, whereas the detached $CuprCobal_2$ ligand is coordinated to cobalt(II) dichloride.



Scheme 3.4: Synthesis of $[Cu(CuprCobal_2)(Cl)_2(OH_2)][Co(CuprCobal_2)(Cl)_2]$ (**9**).

3.2.3. Crystal Structure of 4,7-Dichlorocuproine ($CuprCl_2$, 7)

4,7-Dichlorocuproine (**7**) was obtained as the bisdeuterochloroformate from an NMR spectroscopy sample in $CDCl_3$. It was solved and refined in the triclinic space group $P\bar{1}$ with one molecule in the asymmetric unit and two per unit cell. Crystal data and refinement results are listed in Table 3.8 and the thermal ellipsoids of the asymmetric unit are plotted in Figure 3.9. The molecule displays non-crystallographic C_{2v} symmetry and shows no peculiarities in bond lengths, with Cl—C distances of 1.73 Å. Both co-crystallised $CDCl_3$ molecules engage in bifurcated hydrogen bonds with the nitrogen atoms of **7**. Distances and angles of these hydrogen bonds, listed in Table 3.9, indicate that these classify as weak hydrogen bonds. Moreover, Hirshfeld surface analysis (Figure 3.10, left) reveals that **7** engages in short contacts with adjacent *d*-chloroform molecules: First, through the δ^+ polarised C3 with Cl1 ($d_{C\cdots Cl}$ = 3.386(4) Å) and second, a short repulsive contact between Cl8 and Cl4 ($d_{Cl\cdots Cl}$ = 3.4277(12) Å) which

Table 3.8: Crystal data and refinement results for **7**.

Identification code	$\mathbf{7}\cdot 2\,CDCl_3$
Empirical formula	$C_{16}H_{10}Cl_8D_2N_2$
Formula weight	517.89
Temperature/K	100
Crystal description	colourless block
Crystal size/mm^3	0.19 × 0.15 × 0.13
Crystal system	triclinic
Space group	$P\bar{1}$
a/Å	8.8489(9)
b/Å	9.2962(10)
c/Å	13.1875(14)
α/°	88.282(2)
β/°	75.548(2)
γ/°	78.205(2)
V/Å^{-3}	1028.06(19)
Z, Z'	2, 1
ρ_{calc}/g cm^{-3}	1.673
μ/mm^{-1}	1.100
$F(000)$	516
Refl. total/unique	17386/4517
R_{int}, R_σ	0.0361, 0.0332
Data/restr./param.	4517/0/237
GooF	1.127
R_1 [$I \geq 2\sigma(I)$], all	0.0432, 0.0539
wR_2 [$I \geq 2\sigma(I)$], all	0.1049, 0.1111
$\Delta\rho_{max}/\Delta\rho_{min}$/e Å^{-3}	0.56/-0.59

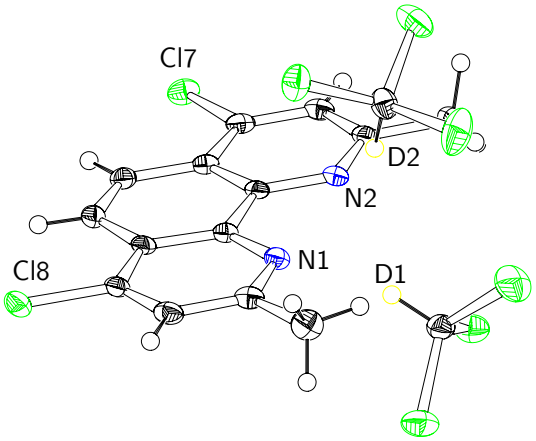


Figure 3.9: ORTEP of $\mathbf{7}\cdot 2\,CDCl_3$ drawn at 50% probability.

Table 3.9: Hydrogen bonds in **7**.

Donor—H···Acceptor	D—H [Å]	H···A [Å]	D···A [Å]	D—H···A [°]
C1—D1···N1	1.00	2.38	3.277(5)	149
C1—D1···N2	1.00	2.41	3.242(4)	140
C2—D2···N1	1.00	2.53	3.354(5)	139
C2—D2···N2	1.00	2.56	3.395(5)	141

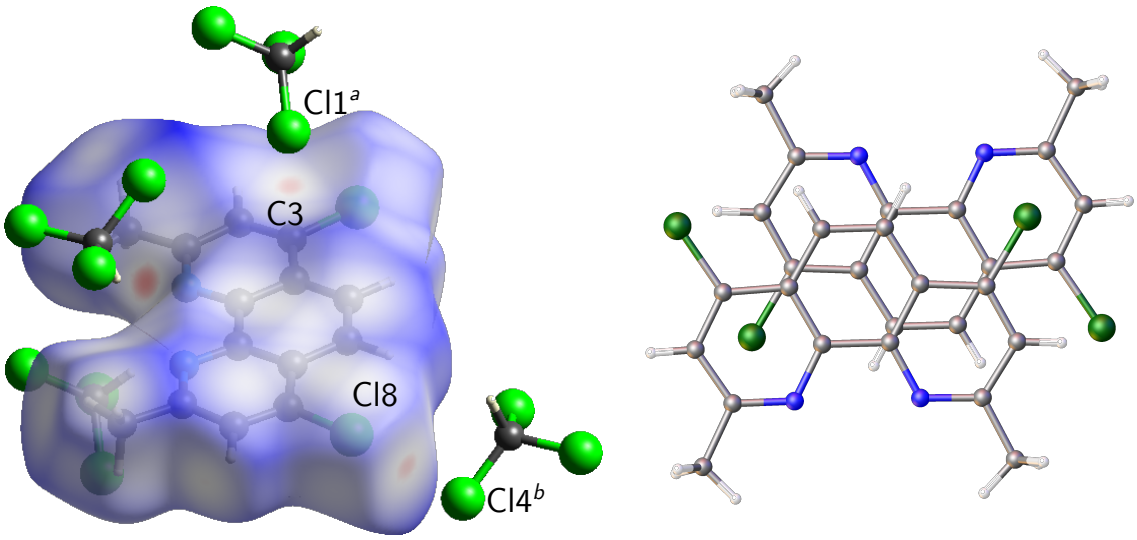


Figure 3.10: Hirshfeld surface, highlighting close contacts with adjacent *d*-chloroform molecules (left) and top view of the π-π-stacking (right) of **7**. Symmetry key: $^a -1+x, y, z$; $^b 1-x, -y, 1-z$.

is slightly shorter than the sum of the van der Waals radii ($r_{\mathrm{Cl}} = 1.75$ Å). In addition, it engages in parallel displaced π-π-stacking with a symmetry equivalent through inversion (Figure 3.10, right) with $d_{\pi-\pi} = 3.390(3)$ Å and a shift of 1.652(3) Å. The packing of **7** is shown in Figure 3.11 and features alternating layers of **7** and *d*-chloroform parallel to C.

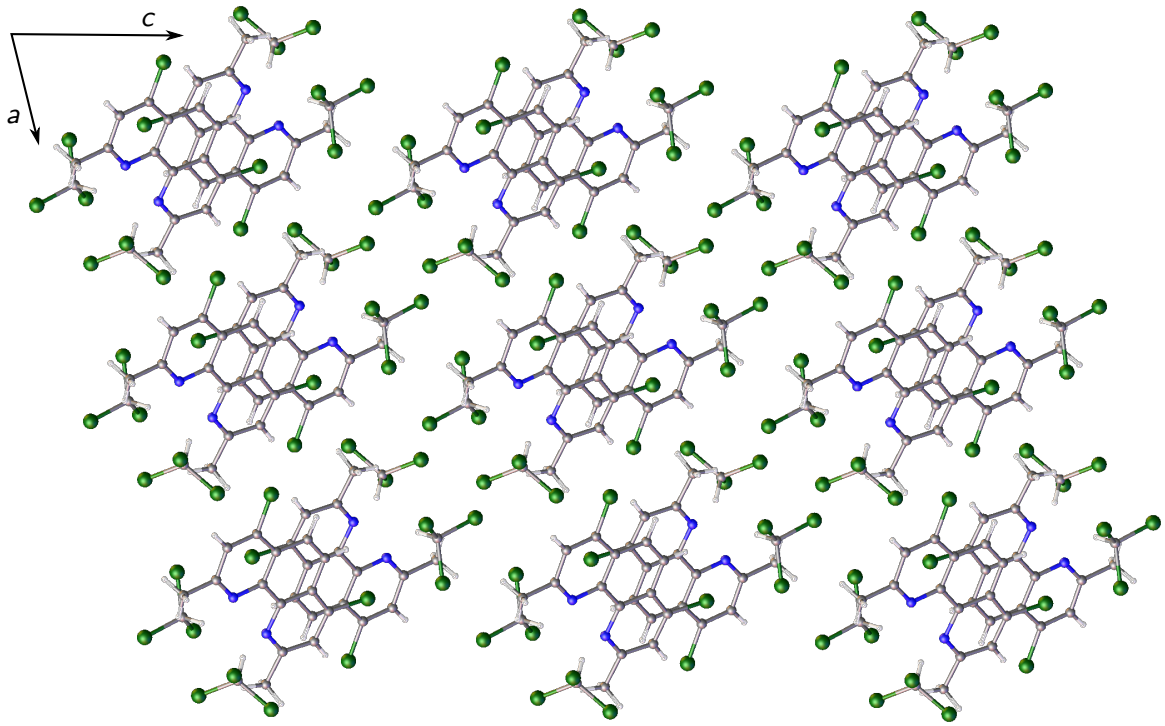


Figure 3.11: The packing of **7** viewed along [0$\bar{1}$0].

3.2.4. Crystal Structure and Properties of $[Cu(CuprPy_2)_2]PF_6$ (8)

Single crystals of $[Cu(CuprPy_2)_2]PF_6$ (**8**) were obtained from diffusion of Et_2O into an acetonitrile solution of the complex. Crystal data and refinement results are given in Table 3.10. It co-crystallises with two molecules of MeCN and one molecule of Et_2O as red blocks, was solved and refined in the orthorhombic space group *Pbca*, with one complex in the asymmetric unit as depicted in Figure 3.12 and all atoms on general positions.

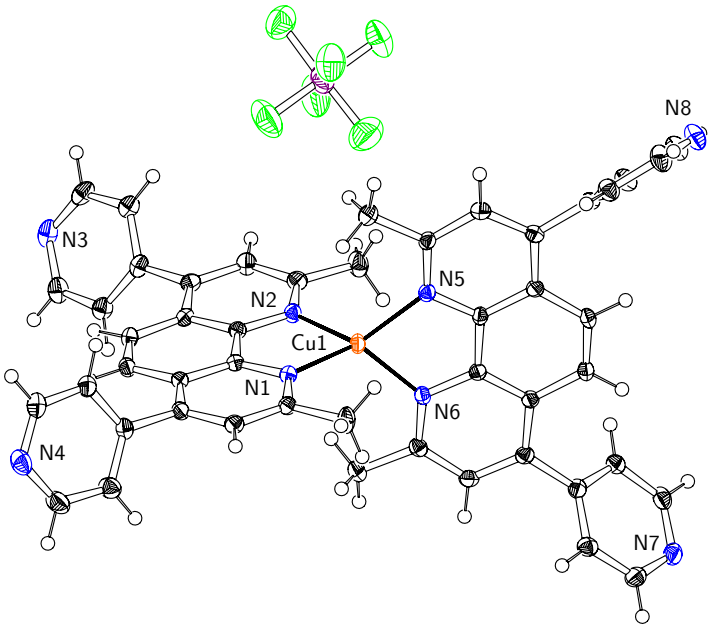


Figure 3.12: ORTEP of the asymmetric unit in **8** plotted at 50% probability. Solvents were omitt for clarity.

A selection of distances and angles found in **8** is listed in Table 3.11. Cu1 is present in oxidation state +I and is coordinated by the neocuproine moieties of two $CuprPy_2$ ligands in a distorted tetrahedron, with three Cu—N distances of 2.01 Å and one of 2.02 Å. The ligands bite at 82.5 Å and display a dihedral angle φ of 91.7° around Cu1. These values are in accordance with those obtained from the bis(bathocuproin)copper(I) cation.[358,359] Torsion angles between pyridyl moieties lie between 57° and 68°, and are rotated in the same and opposite direction on ligands involving N1 and N5, respectively.

The packing of **8** features a series of π-π-interactions (all parallel displaced stacking), with each ligand engaging through the central phenyl rings Ph1 and Ph2 as well as

Table 3.10: Crystal data and refinement results for **8**.

Identification code	$\mathbf{8} \cdot 2\,\mathrm{MeCN} \cdot \mathrm{Et_2O}$
Empirical formula	$C_{56}H_{52}CuF_6N_{10}OP$
Formula weight	1089.58
Temperature/K	100
Crystal description	red block
Crystal size/mm^3	0.205 × 0.194 × 0.159
Crystal system	orthorhombic
Space group	*Pbca*
a/Å	14.6999(5)
b/Å	25.2735(9)
c/Å	28.3272(10)
α/°	90
β/°	90
γ/°	90
V/Å^{-3}	10524.1(6)
Z, Z'	8, 1
ρ_{calc}/g cm^{-3}	1.375
μ/mm^{-1}	0.517
$F(000)$	4512
Refl. total/unique	102241/11657
$R_{\mathrm{int}}, R_\sigma$	0.0726, 0.0355]
Data/restr./param.	11657/0/684
GooF	1.060
R_1 $[I \geq 2\sigma(I)]$, all	0.0425, 0.0711
wR_2 $[I \geq 2\sigma(I)]$, all	0.0998, 0.1165
$\Delta\rho_{\mathrm{max}}/\Delta\rho_{\mathrm{min}}$/e Å^{-3}	0.56/-0.50

Table 3.11: Distances (Å) and angles (°) in **8**.

Distance	
Cu1—N1	2.0102(17)
Cu1—N2	2.0132(18)
Cu1—N5	2.0101(17)
Cu1—N6	2.0209(18)
Angle	
N1···Cu1···N2	82.53(7)
N1···Cu1···N6	124.09(7)
N1···Cu1···N5	131.32(7)
N2···Cu1···N5	121.94(7)
N5···Cu1···N6	82.51(7)
N2···Cu1···N6	119.57(7)
φ	91.71(8)
Py1···Py4	67.72(8)
Py2···Py3	57.33(8)
Py5···Py8	62.89(8)
Py6···Py7	58.08(8)

Pyi involves Ni.

Py3 and Py7 (where Ph1 is attached to N1 and N2 and Pyi involves Ni). Py3 and Ph1 respectively engage in stacking with Ph2 and Py7 of a complex related through the 2_1-screw acis along b with centroid-centroid distances of 3.7400(12) Å (shifted by 1.342(3) Å and tilted by 11.66(7)°) and 3.9047(12) Å (shifted by 1.837(3) Å and tilted by 7.23(7)°). Additionally, Py3 stacks with Py7 related through the c-glide plane with a centroid-centroid distance of 3.8053(13) Å (shifted by 1.610(4) Å and tilted by 2.43(8)°). This π-π-stacking tetrad as well as the packing of **8** are shown in Figure 3.13.

Figure 3.14 shows the absorption and emission spectrum, as a well as a cyclic voltammogram of **8**. A ligand centered $\pi \rightarrow \pi^*$ transition is observed at 284 nm, whereas the broad absorption from *ca.* 370 nm to 650 nm is attributed to MLCT transitions. The bands at roughly 400 nm and 484 nm are respectively assigned to anti-symmetric and symmetric transitions of the D_{2d}-symmetric molecule, whereas the shoulder from 520 nm to 650 nm is attributed to the dipole forbidden $S_0 \rightarrow S_1$ which can be vibronic-

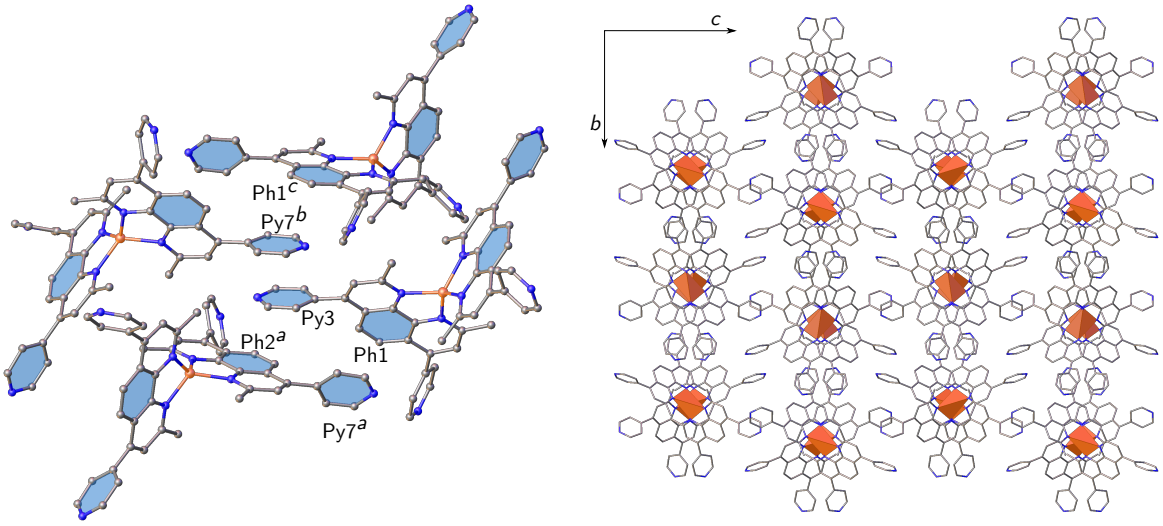


Figure 3.13: The π-π-stacking tetrad (left) and packing of **8** viewed along [100] (right).

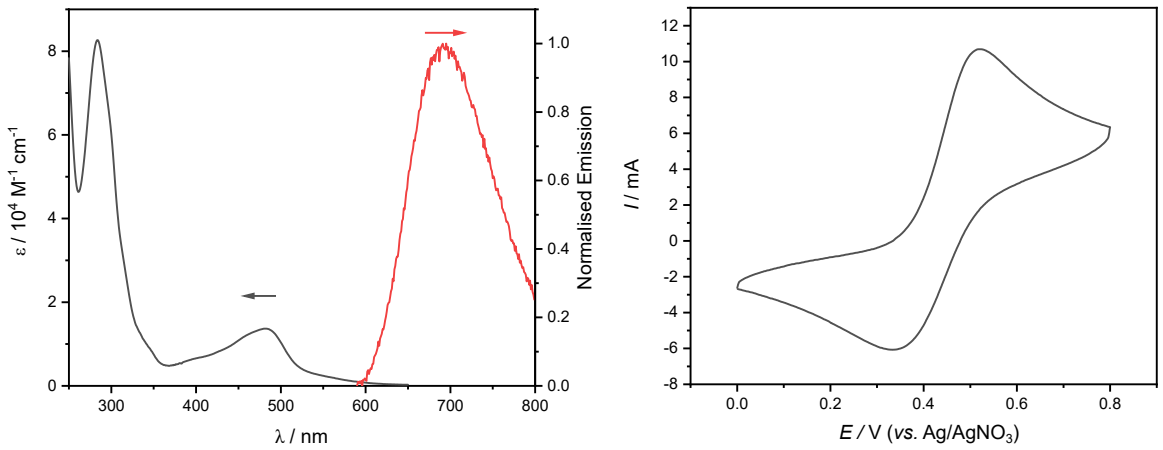


Figure 3.14: Absoprtion and emission spectrum (left, DCM) and cyclic voltammogram (right, MeCN, 0.1 M $nBuPF_6$, 100 mV s^{-1}) of **8**.

ally induced.[360,361] When excited at 484 nm, **8** shows broad emission in the orange-red region with a maximum at 695 nm (E_{00} = 1.78 V assuming unitary charge). **8** undergoes quasi-reversible oxidation with a potential of $E^{ox}_{½}$ = 0.28 V *vs.* $Fc^{0/+}$ (0.68 *vs.* SCE), hence typical sacrificial electron donors such as triethylamine (0.69 *vs.* SCE) or dimethylaniline (0.81 *vs.* SCE) or 4-dimethylaminotoluene (0.71 *vs.* SCE) aren't good candidates as sacrifical electron donors, whereas ascorbic acid (0.46 *vs.* SCE) is.[362] The excited state reduction potential of $^*[Cu(CuprPy_2)]^+$ is -1.50 V *vs.* $Fc^{0/+}$, thus the first reduction of $[Co(dmgH)_2(Py)(Cl)]$ (-1.07 V) should be quick whereas the second reduction (−1.52 V), in which the Co^I species is generated, is expected to occurs very slowly as the potentials are within experimental error.[58] This was also the case for

$[Cu(dsbtmp)_2]PF_6$, nevertheless it was successfully used as a photosensitiser in solar hydrogen photocatalysis with $[Co(dmgH)_2(Py)(Cl)]$.[58]

3.2.5. Crystal Structure of $[Cu(CuprCobal_2)(Cl)_2(OH_2)]$ $[Co(CuprCobal_2)(Cl)_2]$ (9)

The complex $[Cu(CuprCobal_2)(Cl)_2(OH_2)][Co(CuprCobal_2)(Cl)_2]$ (**9**) co-crystallises with 4.5 molecules of acetonitrile as well as one molecule of MeOH. Crystal data and refinement results are listed in Table 3.12. It was solved and refined as a non-merohedral twin,with a volume fraction of 13% for the second domain, in the monoclinic space group $P2_1/c$.

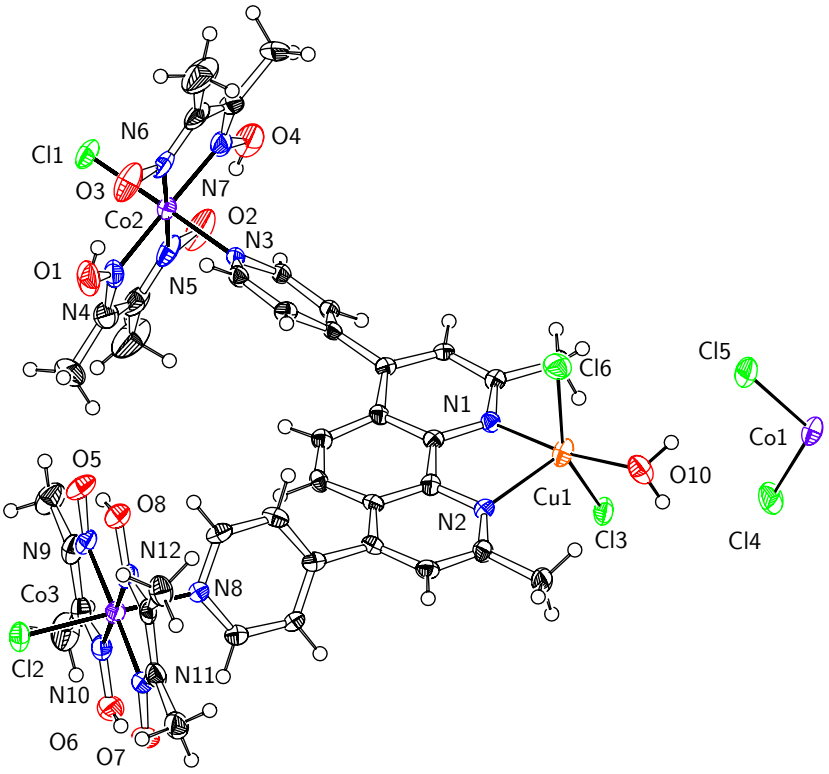


Figure 3.15: ORTEP of the asymmetric unit of **9** drawn at 50% probability. Solvents omitted for clarity.

The asymmetric unit (thermal ellipsoids plotted in Figure 3.15) features one bis(4'-pyridinyl-chlorocobaloxime)neocuproine which is coordinated to either aqua-dichloro-copper(II) and dichlorocobalt(II), each with an occupancy of 50%. Due to packing constraints the latter two come as a pair, as shown in Figure 3.16, but are positionally

Table 3.12: Crystal data and refinement results for **9**.

Identification code	**9** · 4.5 MeCN · MeOH
Empirical formula	$C_{90}H_{111.5}Cl_8Co_5CuN_{28.5}O_{18}$
Formula weight	1261.18
Temperature/K	100
Crystal description	green plate
Crystal size/mm^3	0.22 × 0.15 × 0.06
Crystal system	monoclinic
Space group	$P2_1/c$
a/Å	20.4213(11)
b/Å	13.6463(7)
c/Å	20.7682(11)
α/°	90
β/°	110.0209(15)
γ/°	90
V/Å^{-3}	5437.8(5)
Z, Z'	4
ρ_{calc}/g cm^{-3}	1.540
μ/mm^{-1}	1.210
$F(000)$	2590.0
Refl. total/unique	75092/10749
R_{int}, R_σ	0.0723, 0.0610
Data/restr./param.	10749/45/747
GooF	1.177
R_1 $[I \geq 2\sigma(I)]$, all	0,0643, 0.1017
wR_2 $[I \geq 2\sigma(I)]$, all	0.1395, 0.1546
$\Delta\rho_{max}/\Delta\rho_{min}$/e Å^{-3}	0.83/-0.65

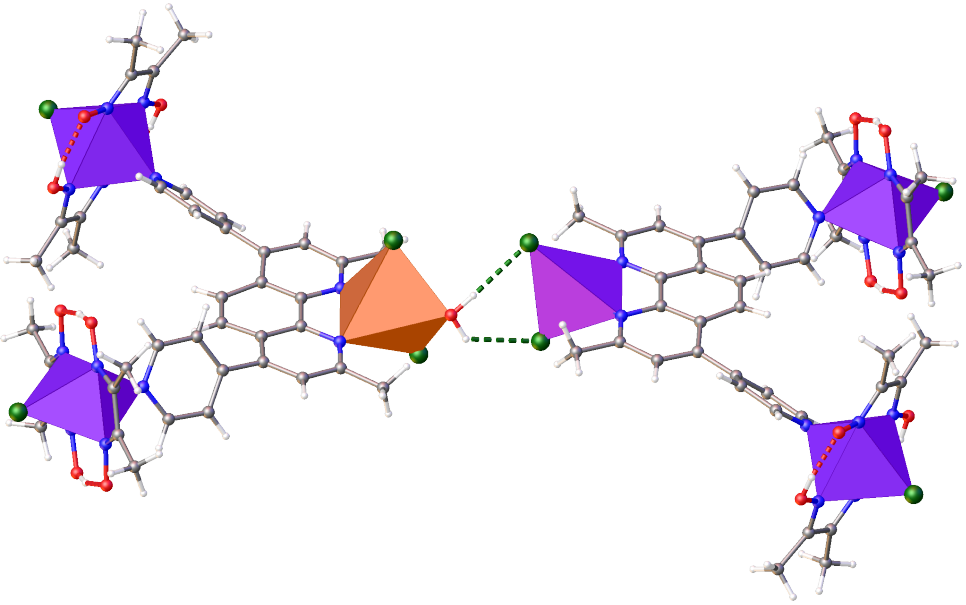


Figure 3.16: The dimer $[Cu(CuprCobal_2)(Cl)_2(OH_2)][Co(CuprCobal_2)(Cl)_2]$ (**9**).

Table 3.13: Distances in **9**.

Bond		Distance		
M—N	Cu1—N1	2.046(16)	Co1—N11	1.984(19)
	Cu1—N2	2.263(15)	Co1—N21	2.040(18)
M—Cl	Cu1—Cl3	2.295(17)	Co1—Cl4	2.209(13)
	Cu1—Cl6	2.316(14)	Co1—Cl5	2.20(2)
M—OH_2	Cu1—O10	2.003(17)		
Co—Cl	Co2—Cl1	2.2350(17)	Co3—Cl2	2.2320(17)
Co—N_{Py}	Co2—N3	1.949(5)	Co3—N8	1.948(5)
Co—N_{Hdmg}	Co2—N4	1.889(5)	Co3—N9	1.898(5)
	Co2—N5	1.891(6)	Co3—N10	1.883(5)
	Co2—N6	1.899(6)	Co3—N11	1.887(5)
	Co2—N7	1.892(5)	Co3—N12	1.885(5)

disordered through inversion. A selection of distances is given Table 3.13. Cu1 is present in oxidation state +II and is chelated by one $CuprCobal_2$ ligand, and further coordinated two chlorides , and a water molecule in a square pyramidal fashion, with N2 as the apex. Co1 has oxidation state +II and is chelated by one $CuprCobal_2$ ligand and two chlorides in a distorted tetrahedron. Metal nitrogen distances to the neocuproine moiety differ by 0.22 Å for Cu1 and are equidistant (*i.e.* within 3σ) for Co1. The $CuprCobal_2$ ligand features bite angles of 77.3(5)° and 84.1(7)° accompanied by Cl—M—Cl angles of 154.5(7)° and 114.7(7)° for Cu1 and Co1, respectively.

The two pyridinyl-chlorocobaloxime moieties feature Co2 and Co3 in oxidation state +III, which coordinated in an octahedral fashion with two dimethylglyoximate (Hdmg) ligands' nitrogen atoms occupying the equatorial positions, as well as the chloride and pyridinyl moiety in axial positions. Distances and angles are identical for Co2 and Co3 with Hdmg bite angels of ca. 81° and are in accordance with literature values.[363]

The packing of **9**, shown in Figure 3.17 features hydrogen bond and π-π-interactions. Distances and angles of the former are listed in Table 3.14, and feature the water$\cdots$chloride hydrogen bonds responsible for dimerisation, as well as the four Hdmg hydrogen bonds found in the chlorocobaloxime moieties. Furthermore, parallel displaced π-π-stacking between the neocuproine moiety and its symmetry equivalent through inversion is observed with $d_{\pi-\pi} = 3.472(4)$ Å and a shift of 1.101(5) Å.

Table 3.14: Hydrogen bonds in **9**.

Bond	Donor—H···Acceptor	*D*—H [Å]	H···*A* [Å]	*D*···*A* [Å]	*D*—H···*A* [°]
$Cu(OH_2)\cdots(Cl)_2Co$	O10—H10A···Cl4	0.89	2.54	3.150(10)	126
	O10—H10B···Cl5	0.91	2.49	3.371(10)	163
Hdmg	O1—H1···O3	0.84	1.67	2.484(8)	164
	O4—H4···O2	0.84	1.66	2.473(8)	163
	O6—H6···O7	0.84	1.67	2.478(7)	161
	O8—H8···O5	0.84	1.65	2.460(6)	163

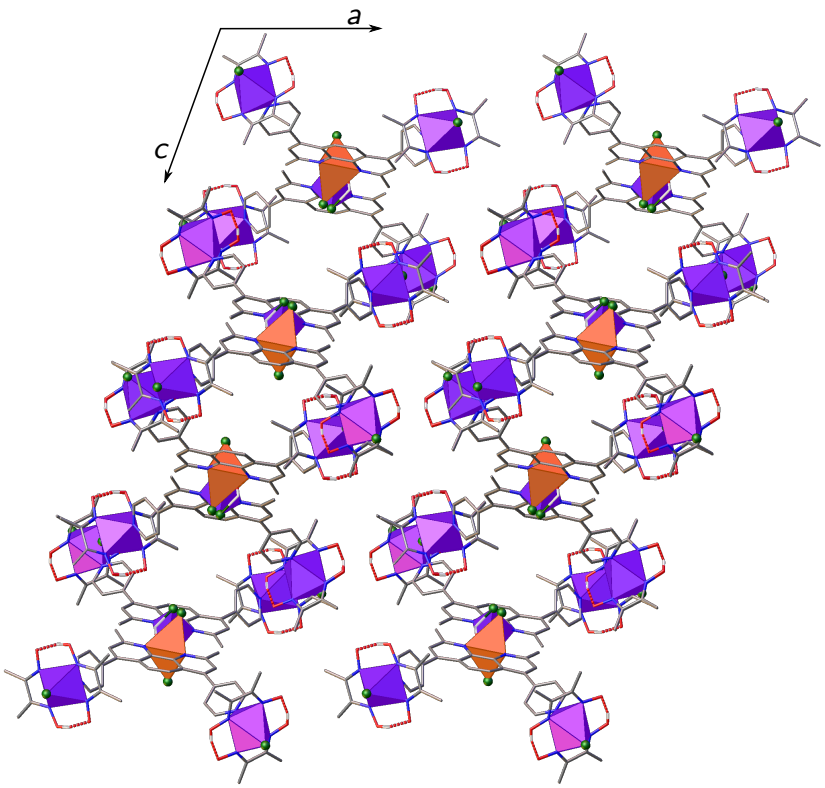


Figure 3.17: The packing of **9** viewd along [010]. Disorder between the $[Cu(Cl)_2(OH_2)]$ and $[Co(Cl)_2]$ as well as solvents were omitted for clarity.

3.3. Conclusion

After the successful incorporation of a Cu^{I} photosensitiser in coordination polymers, this chapter was focussed on the use of further diimine ligands for analogous coordination polymers.

Modification based on H_2**L1**, by either extension of the backbone (H_2**L2**) or steric expansion near the metal centre (H_2**L3**), lead to a further destabilisation of the already labile Cu^{I} complex. While no coordination polymers were obtained, the single crystal structures of **3** and **5** provided an insight into charge neutral analogues of **1**.

Furthermore, the Cu^{I} complex of $CuprPy_2$ was explored as photosensitive metallolinker for photocatalytically active coordination polymers. With oxidation and excited state reduction potentials of 0.28 V and −1.50 V *vs.* $Fc^{0/+}$, **8** is a more potent photoreductant than **1**. However, attempts to from coordination polymers a chlorocobaloxime node resulted in the oxidation of the copper centre and dissociation of the complex (**9**). In conclusion, while the previous chapter provides groundlaying work of utilising Cu^{I} dyes as metallolinkers, the work in this chapter gives in insight into the issues associated with their inherent lability.

4. Phosphonate Stabilised Titanium-Oxo Clusters from Amino Acids

4.1. Introduction

While a large numbers of TOCs had been reported by 2016, studies on systematic band gap engineering of clusters were still scarce. The groups of Coppens and Wright concentrated on the influence of ligand binding modes, and doping of metal and halide ions.[278,364–368] Yet, only one of these studies was performed on an isostructural set of clusters.[369] In 2014, Schubert *et al.* reported that the $\{Ti_6P_2\}$ motif was robust with respect to the introduction of various substituents at the phosphonate.[306] This was expanded upon by Zhang *et al.*, who conducted a band gap engineering study by ligand substitution at the carboxylate site as presented in Figure 4.1.[300] Moreover, work by Schubert *et al.* was carried out under Schlenk conditions using

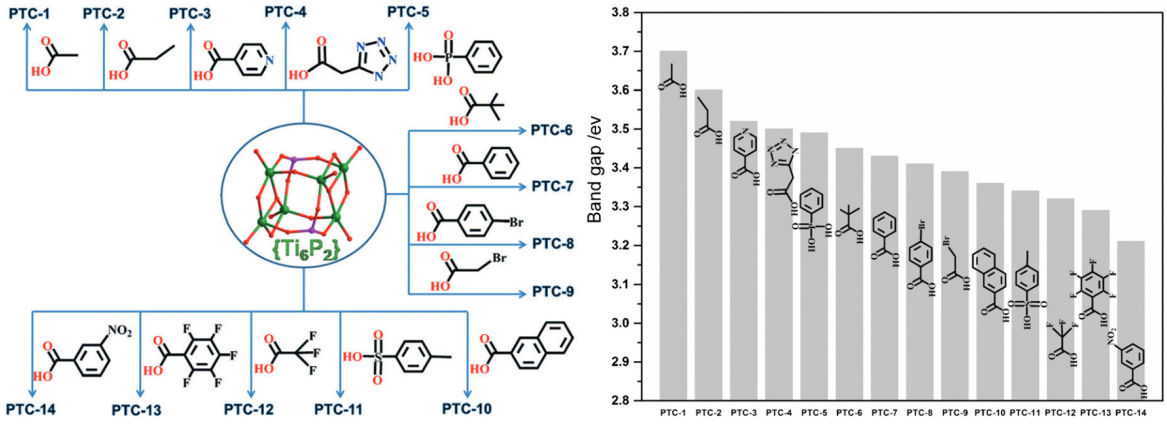


Figure 4.1: Illustration of the assembly of PTC-1-14 based on the $\{Ti_6P_2\}$ motif (left) and their optical band gaps. Adopted from Zhang *et al.*[300]

bis(trimethylsilyl) phosphonates at room temperature with crystallisation times taking up to several months.[306] Zhang *et al.* improved the synthetic approach threefold: Schlenk conditions were replaced by solvothermal synthesis, utilising a phosphonic acid, and reaction times of only three days.[300] Yet, the resulting band gaps all lie in the UV region (3.70-3.21 eV). Additionally, they carried out hydrogen evolution photocatalysis with these TOCs, however no direct correlation between catalytic activity and the optical band gaps were observed.

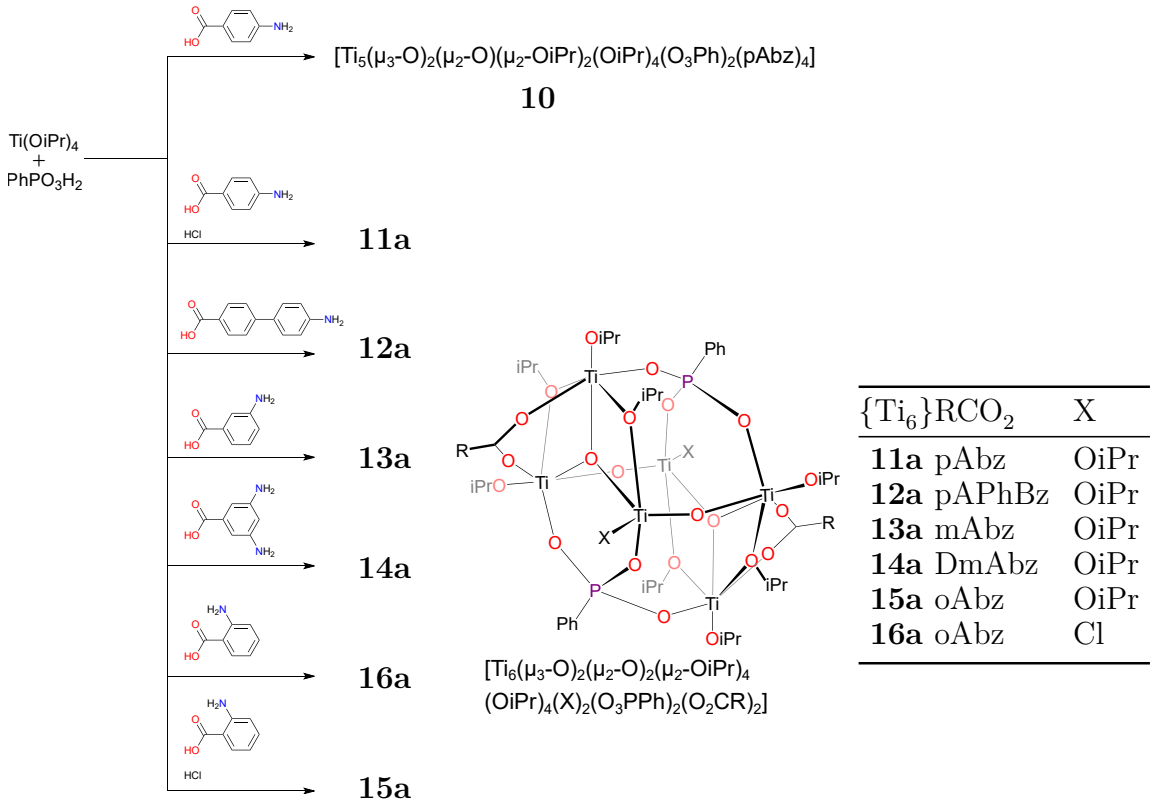
Since then, the $\{Ti_6P_2\}$ motif has received a lot of attention: the cluster type forms in the presence of cyano-, ferrocenyl-, thiophenyl-, tetrathiafulvalene-, and very recently also alkyl- and arylamine-functionalised carboxylic acids.[322,370–372] However, in the presence of catechols a structural analogue of the phenylphosphonate capped PTC-5 forms, which doubly augmented by titanium(IV) catecholate diisopropoxide .[373]

The aim in this chapter was the crystal and band gap engineering based on the $\{Ti_6P_2\}$ motif. Specifically, the introduction of free amines and *in situ* formation of new ligands were of great interest.

4.2. Aminobenzoate Functionalised Titanium-Oxo Clusters

4.2.1. Synthesic Approach

The syntheses of TOCs with aminobenzoic acids and the general constitution of $\{Ti_6\}$ with molecular formula $[Ti_6(O)_4(OiPr)_8(X)_2(O_3PPh)_2(O_2CR)_2]$ (where X is typically OiPr) encountered is presented in Scheme 4.1. The reaction of titanium(IV) isopropoxide ($Ti(OiPr)_4$) with and phenylphosphonic acid ($PhPO_3H_2$) and aminobenzoic acids (AbzH) with ratio 9:2:2.66 was conducted in isopropanol (iPrOH) at 80 °C under autogenous pressure. Surprisingly, this reaction with *p*-aminobenzoic acid (pAbzH) gave the $\{Ti_5\}$-oxo cluster $[Ti_5(\mu_3{-}O)_2(\mu_2{-}O)(\mu_2{-}OiPr)_2(OiPr)_4(O_3PPh)_2(pAbz)_4]$ (**10**). The reason for this might be, as Zhang *et al.* hypothesised, that the $\{Ti_6\}$-oxo cluster only forms under acidic conditions, which is why they use a small excess of the carboxylic acid. However, ratios of 9:2:5 or 9:2:2 both led to only **10**. Unfortunately, **10**



$\{Ti_6\}RCO_2$	X
11a pAbz	OiPr
12a pAPhBz	OiPr
13a mAbz	OiPr
14a DmAbz	OiPr
15a oAbz	OiPr
16a oAbz	Cl

Scheme 4.1: Synthesis of $\{Ti_5\}$-oxo cluster **10** and the $\{Ti_6\}$-oxo clusters **11a**, **12a**, **13a**, **14a**, **15a** and **16a** with aminobenzoic acids and their structural motif.

as well its analogues from *meta*- and *ortho*-aminobenzoic acid (mAbzH, oAbzH) were recently reported by Zheng *et al.*, who used Ti:$PhPO_3H_2$:AbzH ratios of 7.68:2:1.[374]

The desired $\{Ti_6\}$-oxo cluster $[Ti_6(O)_4(OiPr)_{10}(O_3PPh)_2(pAbz)_2]$ (**11a**)was finally obtained through the addition of aqueous HCl the reaction mixture (Ti:$PhPO_3H_2$:pAbzH: HCl ratio of 9:2:2.66:3). The analogous $\{Ti_6\}$-oxo clusters **12a**, **13a**, **14a** and **15a** featuring 4'-amino-4-phenylbenzoate (pAPhBz), mAbz, 3,5-diaminobenzoic acid (DmAbz), and oAbzH respectively were synthesised following Zhang's procedure. In fact, the addition of HCl hindered the crystallisation of **12a**, **13a** and **14a**, whereas its addition to the reaction mixture with oAbzH led to the formation of **16a** in which the terminal isopropoxide coordinated to the five-coordinated titanium atoms is replaced by a chloride ion.

4.2.2. The $\{Ti_5\}$-Oxo Cluster 10

The pentanuclear TOC **10** was obtained as orange block shaped single crystals. Crystal data and refinement results are listed in Table 4.1.

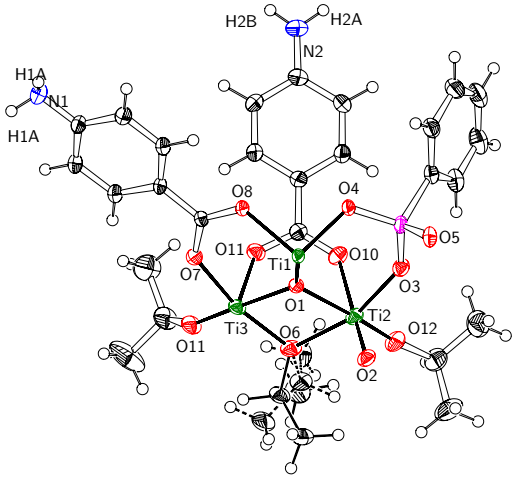


Figure 4.2: ORTEP of the asymmetric unit of **10** drawn at 50% probablity.

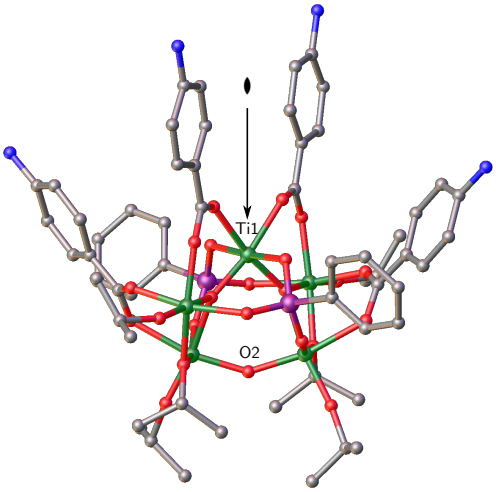


Figure 4.3: Molecular structure of **10** with twofold axis (⧫) along Ti1···O2. Hydrogen atoms and disorder were omitted for clarity.

10 was solved and refined in the monoclinic space group $C2/c$ with four molecules per unit cell and half a molecule in the asymmetric unit (see Figure 4.2). A selection of bond

Table 4.1: Crystal data and refinement results for **10**.

Identification code	**10**
Empirical formula	$C_{58}H_{76}N_4O_{23}P_2Ti_5$
Formula weight	1498.66
Temperature/K	100(2)
Crystal description	orange block
Crystal size/mm^3	$0.281 \times 0.25 \times 0.24$
Crystal system	monoclinic
Space group	$C2/c$
a/Å	21.490(12)
b/Å	15.425(9)
c/Å	20.746(13)
α/°	90
β/°	96.180(13)
γ/°	90
V/Å^{-3}	6837(7)
Z, Z'	4, 0.5
ρ_{calc}/g cm^{-3}	1.456
μ/mm^{-1}	0.682
$F(000)$	3104
Refl. total/unique	75693/11447
R_{int}, R_σ	0.0537, 0.0379
Data/restr./param.	11447/6/453
GooF	1.035
R_1 $[I \geq 2\sigma(I)]$, all	0.0514, 0.0845
wR_2 $[I \geq 2\sigma(I)]$, all	0.1125, 0.1310
$\Delta\rho_{max}/\Delta\rho_{min}$/e Å^{-3}	0.81/-0.68

Table 4.2: Bond distances in **10** in Å.

Bond		Distance
Ti—μ_3-O	Ti1—O1	1.8193(18)
	Ti2—O1	2.096(2)
	Ti3—O1	2.0334(19)
Ti—μ_2-O	Ti2—O2	1.8126(13)
Ti—μ_2-OiPr	Ti2—O6	2.051(2)
	Ti3—O6	1.964(2)
Ti—OiPr	Ti2—O12	1.770(2)
	Ti3—O11	1.762(2)
Ti—O_2CR	Ti1—O8	2.0713(19)
	Ti3—O7	2.020(2)
	Ti2—O10	2.131(2)
	Ti3—O9	1.974(2)
RCO_2	O7—C4	1.276(3)
	O8—C4	1.271(3)
	O9—C11	1.288(3)
	O10—C11	1.260(3)
Ti—O_3PPh	Ti1—O4	2.0023(19)
	Ti2—O3	1.980(2)
	Ti3—O5^a	1.963(2)
P—O	P1—O3	1.516(2)
	P1—O4	1.5371(18)
	P1—O5	1.543(2)
N—C_{Ar}	N1—C8	1.385(3)
	N2—C15	1.363(4)

Symmetry key: $^a 1-x, y, \frac{1}{2}-z$.

distances in **10** are listed in Table 4.2. The cluster exhibits C_2-symmetry, with Ti1 and O2 lying on a twofold axis (Wyckoff position 4*e*) with all other atoms on general position (see Figure 4.3). The {Ti_5}-cluster can be described as two vertex-sharing (Ti1) Ti_3O units in which all titanium atoms are octahedrally coordinated and in oxidation state +IV. These Ti_3O unites are tilted by 54.01(4)°, further connected by a μ_2-O bridge (O2) with a Ti2—O2—Ti2^a ($^a 1-x, y, \frac{1}{2}-z$) angle of 145.72(15)°, as well as two symmetry equivalent phenylphosphonates. Moreover, **10** can be described as a Janus like cluster Ti3, P1 and their symmetry equivalents in an equatorial position, with the *p*-aminobenzoates and isopropoxides point upwards and downwards, respectively (see Figure 4.3). The μ_3-O atom O1 exhibits one short bond of 1.81 Å to Ti1, comparable to the bond between the μ_2-O atom O2 and Ti2, as well as two longer bonds to Ti2

and Ti3 of 2.0 Å, similar to their respective bonds bridging isopropoxide featuring O6. The phenylphosphonate is fully mesomerised (see P—O distances) and engages in a μ_3–$\eta^1\eta^1\eta^1$ binding mode with an Ti—O distance of *ca.* 1.98 Å. Both *p*-aminobenzoates engage in μ_2–$\eta^1\eta^1$-binding modes and are fully mesomerised (see C—O), with Ti—pAbz distances averaging to 2.05 Å. The C_{Ar}—NH_2 distances aver to 1.37 Å, which is expected for anilines due their partial double bond character, which is also reflected in the almost coplanarity of the amine group involving N2 with its phenyl ring. Note that due to the high quality of the data set, amine hydrogen atoms could be included from the Fourier density map and were subsequently restrained to idealised distances.

Packing in **10**, which is displayed in Figure 4.4, is governed by intermolecular hydrogen bonding (Table 4.3) and π–π-stacking. The amine N1 engages in a single hydrogen bond to an phosphonate (through *C*-centering) which results in a 2D hydrogen bonds network parallel to the *C*-face. N2 hydrogen bonds with both hydrogen atoms to the aminobenzoate and phenylphosphonate of an adjacent cluster through an inversion centre, leading to a back-and-forth ladder type 1D chain along the *c*-axis. In total, a **10** forms a 3D primitive cubic (**pcu**) hydrogen bond network. Furthermore, the phenylphosphonate engages in a parallel displaced π-π-stacking with its symmetry equivalent through an inversio centre with a $d(\pi\cdots\pi) = 3.248(5)$ Å and a plane to plane shift of 3.985(5) Å. This π–π-stacking leads to a 1D chain along $[10\bar{1}]$. The powder X-ray diffraction pattern of **10**, depicted in Figure 4.5 confirms phase purity of the cluster.

Table 4.3: Hydrogen bonds in **10**.

Donor—H$\cdots$Acceptor	*D*—H [Å]	H$\cdots$*A* [Å]	*D*$\cdots$*A* [Å]	*D*—H$\cdots$*A* [°]
N1—H1A$\cdots$O5^a	0.89	2.31	3.176(4)	165
N2—H2A$\cdots$O8^b	0.87	2.27	2.981(4)	139
N2—H2B$\cdots$O4^b	0.88	2.35	3.103(4)	144

Symmetry key: $^a -\frac{1}{2}+x, \frac{1}{2}+y, z$; $^b 1-x, 1-y, -z$.

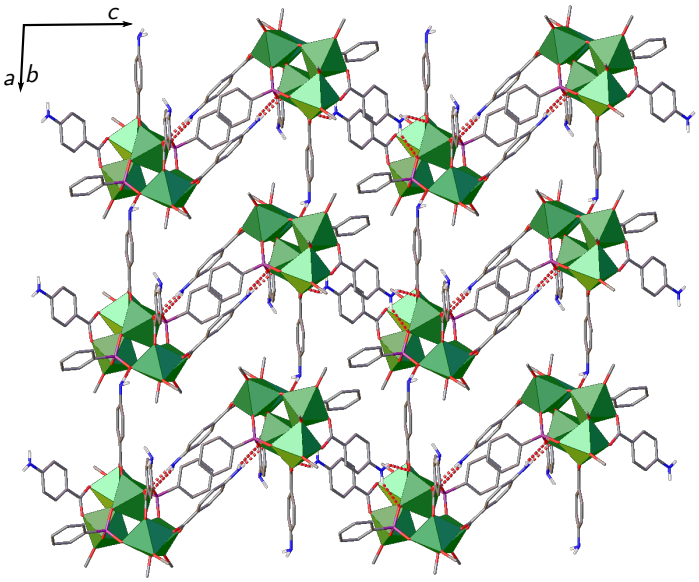


Figure 4.4: Packing of the **pcu**-type hydrogen bond network formed by **10** viewed along [1$\bar{1}$0]. Methyl groups and non-hydrogen-bonding hydrogen atoms were omitted for clarity.

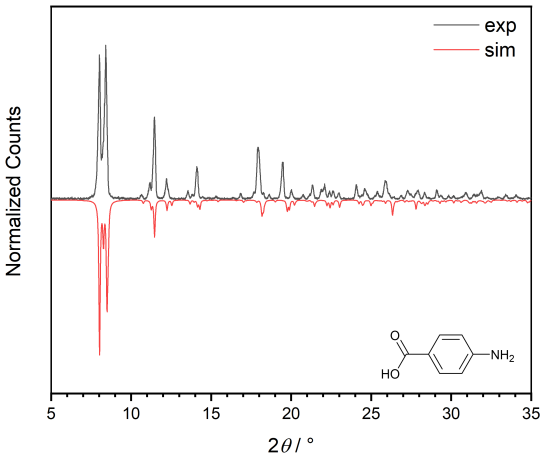


Figure 4.5: Powder X-ray diffraction patterns of **11a**.

4.2.3. $\{Ti_6\}$-Oxo Clusters from Aminobenzoic Acids

The $\{Ti_6\}$-oxo clusters **11a**, **12a**, **13a**, **14a**, **15a** and **16a** are isostructural to those reported by Schubert and Zhang.[300,306] Figure 4.6 displays the naming scheme adhered to for this type of cluster throughout this work (unless mentioned otherwise), as well as the general structure of these clusters.

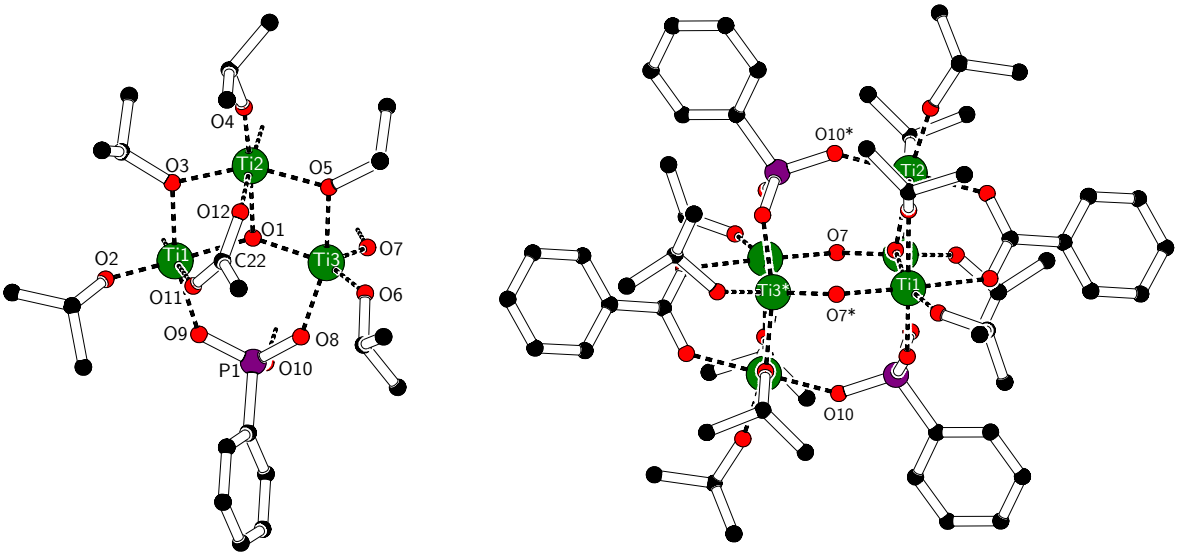


Figure 4.6: Naming scheme adhered to for $\{Ti_6\}$-oxo clusters unless otherwise mentioned (left) and full cluster highlighting connectivity through symmetry (right). Inversion symmetry is denoted by asterisks. In case of pseudo-inversion symmetry Ti1*-Ti3* are labeled Ti4-6.

The clusters can be described as two bridged Ti_3O units, connected by two μ_2-O atoms and two phenylphosphonates in a $\mu_3-\eta^1\eta^1\eta^1$ binding mode, and related through inversion symmetry at the centre of the cluster. The μ_3-O atom O1 is connected to three crystallographcially distinct titanium atoms, the octahedrally coordinated Ti1 and Ti2, as well as Ti3 which is coordinated in a square pyramid with O7 in the apical position. The isopropoxides featuring O2, O4, and O6 (or Cl6 for **16a**) are terminally coordinated to Ti1, Ti2 , and Ti3, respectively, while the ones featuring O3 and O5 are bridging Ti1 and Ti2, as well as Ti2 and Ti3 respectively. The μ_2-O atom O7 is connected to Ti3 and Ti1*, and the $PhPO_3$ oxygen atoms O8, O9, and O10 respectively coordinate to Ti3, Ti2*, and Ti1. Finally, Ti1 and Ti2 are coordinated to O11 and O12, respectively, which belong to a bridging carboxylate.

Crystal data and refinement results for **11a**, **12a**, **13a**, **14a**, **15a** and **16a** are listed in Table 4.4 and the thermal ellipsoids of their asymmetric units (half a molecule in each case) are plotted in Figure 4.7. A selection of bond lengths is given in Table 4.5 and a list hydrogen bonds in Table 4.6. It should be noted, that H atoms engaging in hydrogen bonding could be included from the Fourier density map due to the high quality of diffraction data and were then refined with idealised distances.

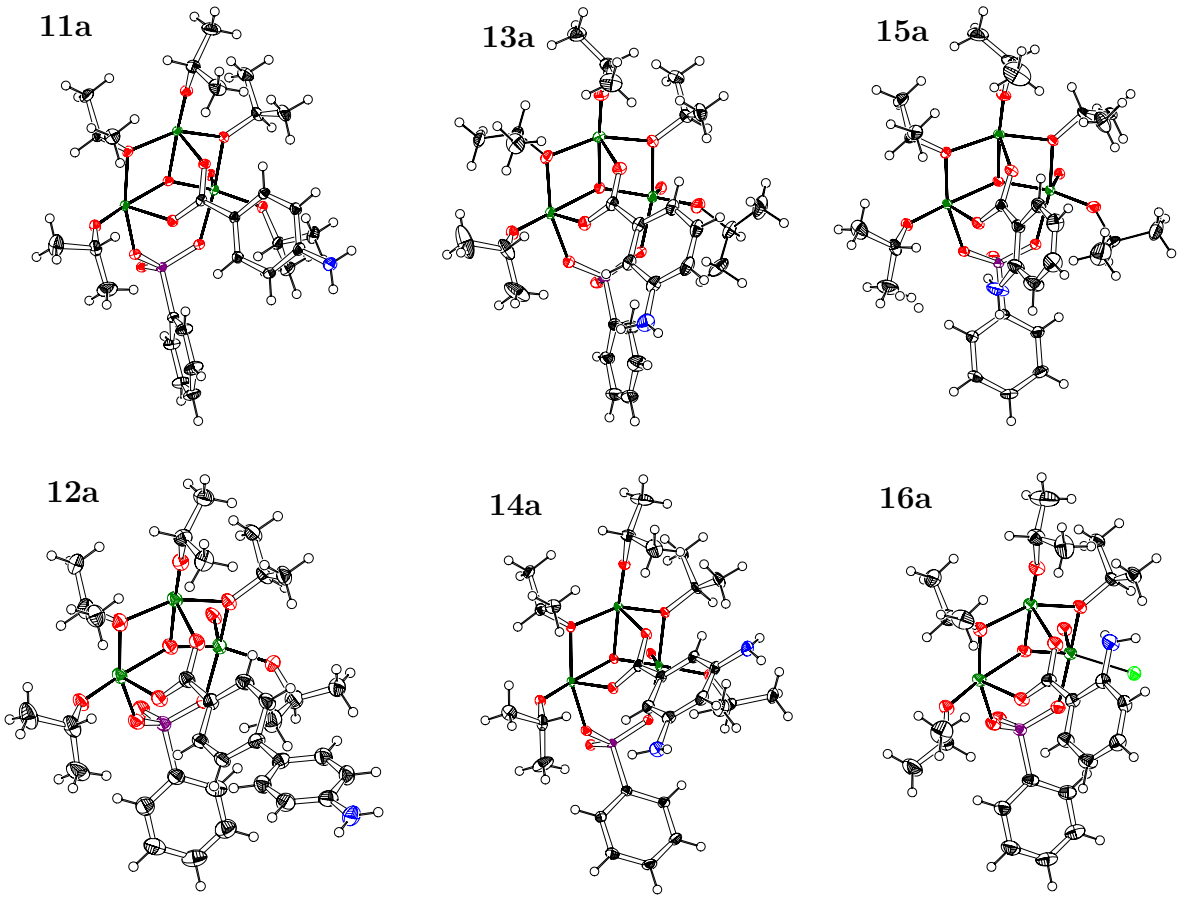


Figure 4.7: ORTEPs of the asymmetric units in the $\{Ti_6\}$-oxo clusters **11a-16a** with various aminobenzoates, drawn at 50% probablity.

The central oxygen atom of the Ti_3O unit O1 forms two longer bonds to the six-coordinated Ti1 and Ti2 of approx. 1.99 Å. The shorter Ti3—O1 bonds ranges from 1.886(4) Å to 1.9156(12) Å in **11a**, **12a**, **13a**, **14a** and **15a**, and is shorter in **16a** at 1.847(18) Å. Similarly, the difference in bond lengths of Ti1 and Ti3 to μ_2−O atom O7 is 0.09 Å in **11a**, **12a**, **13a**, **14a** and **15a** and 0.19 Å in **16a**. Ti—O distances with bridging isopropoxides are generally shorter to the apical Ti2 (1.9617(12) Å to 1.9984(18) Å) than to the equatorial Ti1 and Ti3 (1.9906(18) Å to 2.0348(14) Å). Ter-

Table 4.4: Crystal data and refinement results of **11a**, **12a**, **13a**, **14a**, **15a** and **16a**.

Identification code	**11a**	**12a**	**13a**
Empirical formula	$C_{56}H_{92}N_2O_{24}P_2Ti_6$	$C_{68}H_{100}N_2O_{24}P_2Ti_6$	$C_{56}H_{92}N_2O_{24}P_2Ti_6$
Formula weight	1526.65	1678.83	1526.65
Temperature/K	100.15	100	100.15
Crystal description	yellow rod	yellow rod	colourless block
Crystal size/mm^3	$0.206 \times 0.143 \times 0.134$	$0.316 \times 0.113 \times 0.085$	$0.265 \times 0.257 \times 0.247$
Crystal system	monoclinic	monoclinic	orthorhombic
Space group	$P2_1/n$	$C2/c$	$Pbca$
a/Å	12.4034(6)	28.517(7)	18.9595(7)
b/Å	13.8757(6)	12.996(3)	19.3313(7)
c/Å	21.4666(10)	23.350(5)	19.5934(8)
$\alpha/°$	90	90	90
$\beta/°$	94.972(2)	115.625(4)	90
$\gamma/°$	90	90	90
Volume/Å^3	3680.6(3)	7802(3)	7181.2(5)
Z, Z'	2, 0.5	4, 0.5	4, 0.5
ρ_{calc} g cm^{-3}	1.378	1.429	1.412
μ/mm^{-1}	0.734	0.699	0.752
$F(000)$	1592	3504	3184
Refl. total/unique	153480/12810	11290/7711	138778/8984
R_{int}, R_σ	0.0675, 0.0330	0.0741, 0.1249	0.0529, 0.0170
Data/restr./param.	12810/2/422	7711/2/470	8984/73/477
GooF	1.061	0.982	1.01
R_1 $[I \geq 2\sigma(I)]$, all	0.0367, 0.0626	0.0668. 0.1497	0.0348, 0.0474
wR_2 $[I \geq 2\sigma(I)]$, all	0.0762, 0.0872	0.1588, 0.2073	0.0803, 0.0898
$\Delta\rho_{max}/\Delta\rho_{min}$/e Å^{-3}	0.52/-0.58	0.72/-0.52	0.56/-0.42
Identification code	**14a** · 2 iPrOH	**15a** · 0.85 iPrOH	**16a**
Empirical formula	$C_{62}H_{110}N_4O_{26}P_2Ti_6$	$C_{58.6}H_{100.1}N_2O_{24.9}P_2Ti_6$	$C_{50}H_{78}Cl_2N_2O_{22}P_2Ti_6$
Formula weight	1676.87	1578.41	1479.38
Temperature/K	100.15	100	99.95
Crystal description	red block	colourless block	yellow block
Crystal size/mm^3	$0.251 \times 0.179 \times 0.15$	$0.39 \times 0.301 \times 0.281$	$0.306 \times 0.263 \times 0.126$
Crystal system	monoclinic	monoclinic	triclinic
Space group	$C2/c$	$C2/c$	$P\bar{1}$
a/Å	24.3290(8)	27.217(14)	11.2055(7)
b/Å	17.6284(5)	16.188(12)	12.7962(8)
c/Å	22.7448(8)	17.771(9)	12.9189(7)
$\alpha/°$	90	90	69.750(2)
$\beta/°$	127.0720(10)	104.929(13)	76.342(2)
$\gamma/°$	90	90	74.223(2)
Volume/Å^3	7783.2(4)	7565(8)	1651.63(17)
Z, Z'	4, 0.5	4, 0.5	1, 0.5
ρ_{calc} g cm^{-3}	1.431	1.386	1.487
μ/mm^{-1}	0.703	0.717	0.891
$F(000)$	3520	3301	764
Refl. total/unique	60786/9347	44236/9344	23528/7708
R_{int}, R_σ	0.0370, 0.0217	0.0264, 0.0218	0.0406, 0.0467
Data/restr./param.	9347/5/471	9344/93/491	7708/0/398
GooF	1.051	1.061	1.043
R_1 $[I \geq 2\sigma(I)]$, all	0.0319, 0.0412	0.0326, 0.0394	0.0421, 0.0651
wR_2 $[I \geq 2\sigma(I)]$, all	0.0824, 0.0880	0.0857, 0.0922	0.1015, 0.1133
$\Delta\rho_{max}/\Delta\rho_{min}$/e Å^{-3}	0.73/-0.56	1.23/-0.43	0.60/-0.57

Table 4.5: Bond lengths (Å) and angles (°) in **11a**, **12a**, **13a**, **14a**, **15a** and **16a**.

Bond	Distance	**11a**	**12a**	**13a**	**14a**	**15a**	**16a**
Ti—μ_3-O	Ti1—O1	1.9817(11)	1.978(4)	1.9975(12)	1.9860(12)	1.9902(15)	1.9999(18)
	Ti2—O1	2.0116(10)	2.001(4)	1.9753(13)	2.0021(12)	1.9963(16)	2.0279(18)
	Ti3—O1	1.8909(10)	1.886(4)	1.9156(12)	1.8957(12)	1.9072(14)	1.8470(18)
Ti—μ_2-O	Ti1—O7^a	1.8794(10)	1.868(4)	1.8746(13)	1.8652(12)	1.8626(15)	1.9165(18)
	Ti3—O7	1.7890(11)	1.759(4)	1.7683(13)	1.7619(12)	1.7730(14)	1.7298(18)
Ti—μ_2-OiPr	Ti1—O3	2.0136(11)	2.029(4)	2.0348(14)	2.0161(12)	2.0203(18)	1.9906(19)
	Ti2—O3	1.9950(11)	1.976(4)	1.9714(14)	1.9740(12)	1.9808(15)	1.9984(18)
	Ti2—O5	1.9836(11)	1.975(4)	1.9665(13)	1.9617(12)	1.9774(15)	1.9687(18)
	Ti3—O5	2.0211(11)	2.010(4)	2.0259(13)	2.0165(12)	2.0334(17)	2.0205(18)
Ti—OiPr	Ti1—O2	1.7984(11)	1.784(4)	1.7991(13)	1.8067(12)	1.7971(14)	1.7773(19)
	Ti2—O4	1.7660(11)	1.769(4)	1.7661(14)	1.7627(12)	1.7676(15)	1.7526(19)
	Ti3—O6	1.8198(10)	1.824(4)	1.7909(14)	1.8221(12)	1.7988(14)	-
Ti—X	Ti3—Cl6A	-	-	-	-	-	2.3201(11)
	Ti3—Cl6B	-	-	-	-	-	2.20(2)
Ti—O_2CR	Ti1—O11	2.1677(11)	2.149(4)	2.0854(13)	2.1042(12)	2.1343(16)	2.1005(18)
	Ti2—O12	2.0102(11)	2.034(4)	2.0963(13)	2.0730(12)	2.0631(15)	2.0404(18)
RCO_2	O10	1.2636(18)	1.261(7)	1.261(2)	1.261(2)	1.269(2)	1.268(3)
	O11	1.2792(18)	1.275(6)	1.265(2)	1.269(2)	1.275(2)	1.270(3)
Ti—O_3PPh	Ti1—O9	1.9681(11)	1.963(4)	1.9527(13)	1.9647(12)	1.9705(18)	1.9530(19)
	Ti2—O10^a	1.9392(11)	1.939(4)	1.9499(13)	1.9490(12)	1.9449(15)	1.9171(18)
	Ti3—O8	1.9554(11)	1.965(4)	1.9549(13)	1.9637(12)	1.9832(16)	1.9494(19)
P—O	P1—O8	1.5250(11)	1.526(4)	1.5272(14)	1.5274(12)	1.5323(13)	1.5257(19)
	P1—O9	1.5243(11)	1.526(4)	1.5265(14)	1.5275(13)	1.5321(13)	1.527(2)
	P1—O10	1.5227(11)	1.515(4)	1.5241(14)	1.5213(12)	1.5263(15)	1.5219(18)
N—C_{Ar}	N1	1.370(2)	1.371(7)	1.383(3)	1.385(2)	1.363(3)	1.352(4)
	N2	-	-	-	1.410(3)	-	-
Angle		**11a**	**12a**	**13a**	**14a**	**15a**	**16a**
$Ti_2O_2\cdots O_2C$		11.95(18)	0.4(9)	13.6(2)	0.00(5)	2.7(2)	1.1(3)
$O_2C\cdots C_6$		8.30(6)	8.3(3)	5.48(7)	12.52(52)	13.02(8)	0.92(11)

Symmetry key: $^a -x, -y, -z$ for **11a** and **14a**; $\frac{1}{2}-x, \frac{1}{2}-y, 1-z$ for **12a**; $-x, -y, 1-z$ for **11a** ;$\frac{1}{2}-x, \frac{3}{2}-y, 1-z$ for **15a**; $1-x, 1-z, 1-z$ for **16a**.

minal isopropoxide bonds to titanium atoms are even shorter, ranging from 1.7526(19) Å to 1.824(4) Å with the Ti2—O4 bond always being the shortest. In **16a**, Ti3 is bound to a disordered chloride ion (Cl6A/B) with Ti—Cl distances of 2.3201(11) Å (95.2%) and 2.20(2) Å (4.8%). Titanium-carboxylate distances range from 2.0102(11) Å to 2.149(4) Å and bonds are usually shorter to Ti2 than to Ti1. Moreover, as is evident from C—O bond distances the charge on the carboxylates is fully delocalised. The phenylphosphonates are fully delocalised as can be seen from P—O distances (*ca.*

Table 4.6: Hydrogen bonds in **11a**, **12a**, **13a**, **14a**, **15a** and **16a**.

Compound	Donor—H···Acceptor	*D*—H [Å]	H···*A* [Å]	*D*···*A* [Å]	*D*—H···*A* [°]
11a	N1—H1B···O7^{a}	0.88	2.13	2.969(2)	160
12a	N1—H1A···O7^{b}	0.88	2.48	3.077(7)	126
	N1—H1A···O2^{c}	0.88	2.45	3.269(8)	155
13a	N1—H1B···O7^{d}	0.88	2.12	2.977(2)	164
14a	N1—H1A···O2^{e}	0.88	2.40	3.139(2)	142
	N1—H1B···O7^{f}	0.88	2.47	3.063(2)	125
	N2—H2A···O13^{g}	0.90	2.14	3.024(3)	165
	O13—H13···N2	0.84	2.06	2.897(4)	171
15a	N1—H1A···O11	0.89	2.00	2.658(3)	130
16a	N1—H1A···Cl1A^{h}	0.88	2.54	3.323(3)	148
	N1—H1B···O11	0.88	2.00	2.633(3)	127

Symmetry key: $^{a}-\frac{1}{2}-x,\frac{1}{2}+y,-\frac{1}{2}-z$; $^{b}1-x,1+y,\frac{3}{2}-z$; $^{c}\frac{1}{2}+x,\frac{3}{2}-y,\frac{1}{2}+z$; $^{d}x,-\frac{1}{2}-y,\frac{1}{2}+z$; $^{e}\frac{1}{2}+x,\frac{1}{2}-y,\frac{1}{2}+z$; $^{f}\frac{1}{2}-x,\frac{1}{2}+y,\frac{1}{2}-z$; $^{g}-x,1-y,-z$; $^{h}1-x,1-y,-z$.

1.525 Å) and exhibits slightly longer bonds to the equatorial Ti1 and Ti3 (1.9527(13) Å to 1.9832(16) Å) than to the apical Ti2 (1.9171(18) Å to 1.499(13) Å). As expected, C—N bond lengths are shorter for *o*- and *p*- (1.352(4) Å to 1.371(7) Å) than for *m*-substituted (1.383(3) Å to 1.410(3) Å) aminobenzoates due partial double bond character in the former.

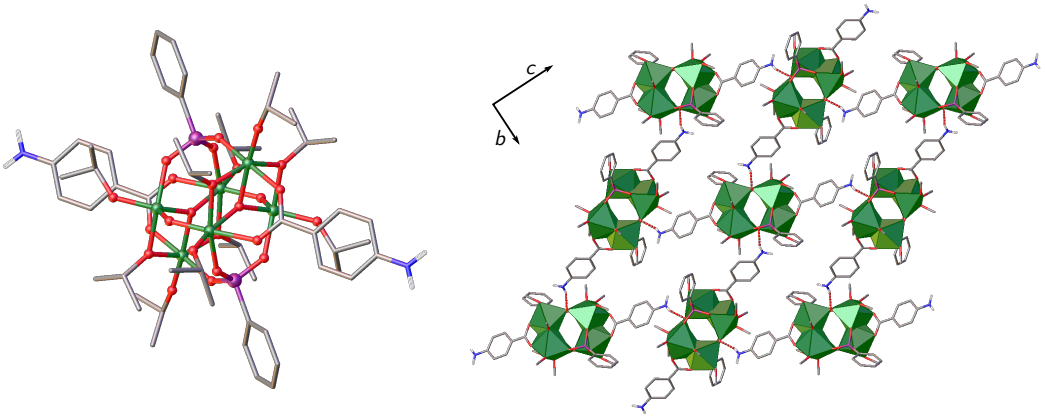


Figure 4.8: The {Ti_6}-oxo cluster **11a** (left) from pAbzH and its packing along [100] (right).

The {Ti_6}-oxo cluster **11a** featuring pAbz crystallises as yellow rods, was solved and refined in the monoclinic space group $P2_1/n$. Figure 4.8 displays the cluster **11a** and its packing, which is governed by hydrogen bonding. The amine group hydrogen bonds to the μ_2−O atom of a cluster adjacent *via* a 2_1-screw axis. Hence, each cluster doubly donating and accepting hydrogen bonds, resulting in a 2D net with topological

symbol **sql** parallel to the *A*-face. Phase purity of **11a** was asserted with powder X-ray diffraction (see Figure 4.10).

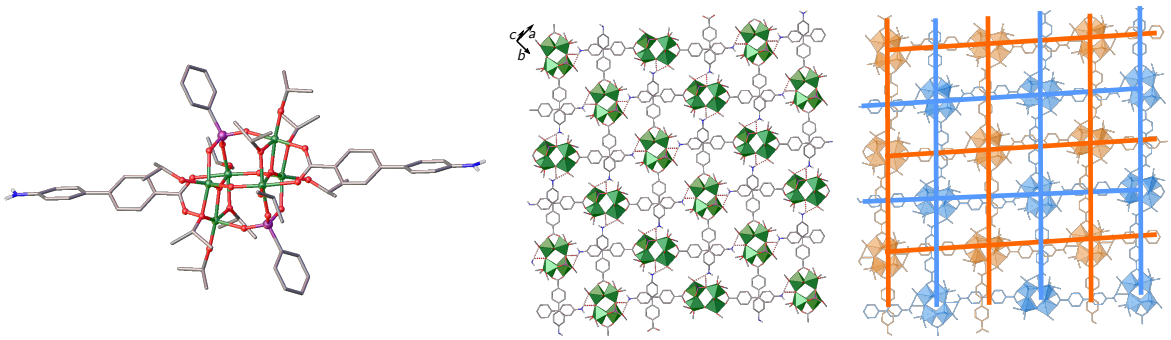


Figure 4.9: The $\{Ti_6\}$-oxo cluster **12a** (left) from pAPhBzH and its packing (middle) and interwoven **sql** nets (right).

The $\{Ti_6\}$-oxo cluster **12a**, made from pAPhBzH, crystallises as yellow rods and was solved in the monoclinic space group $C2/c$. The molecular structure and packing of **12a** are shown in Figure 4.9. Here, the packing is also governed by hydrogen bonds, with the amine group hydrogen bonding *via* H1A to O7 and O2 of a single cluster adjacent through a 2_1-screw axis and *c*-glide plane. Thus, each cluster severs as a four connected node in a 2D hydrogen bond network with topological symbol **sql** parallel to $(10\bar{1})$. Moreover, a second **sql**-net, generated by *C*-centering, is interwoven with the first one (see Figure 4.9, right). Powder X-ray diffraction reveals that the sample of **12a** is not phase pure, but that **12a** is the major phase (see Figure 4.10).

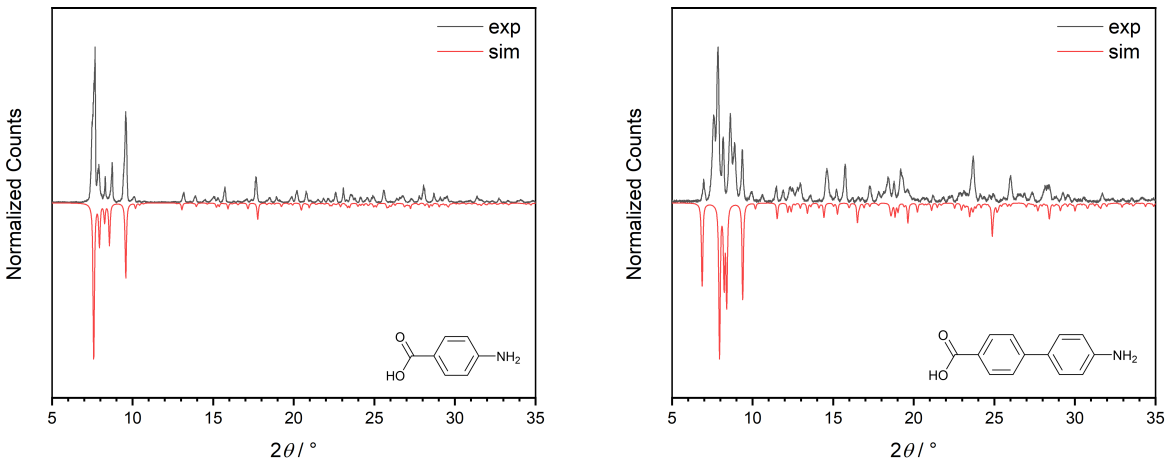


Figure 4.10: Powder X-ray diffraction patterns of **11a** (left) and **12a** (right), with their corresponding carboxylic acids inset.

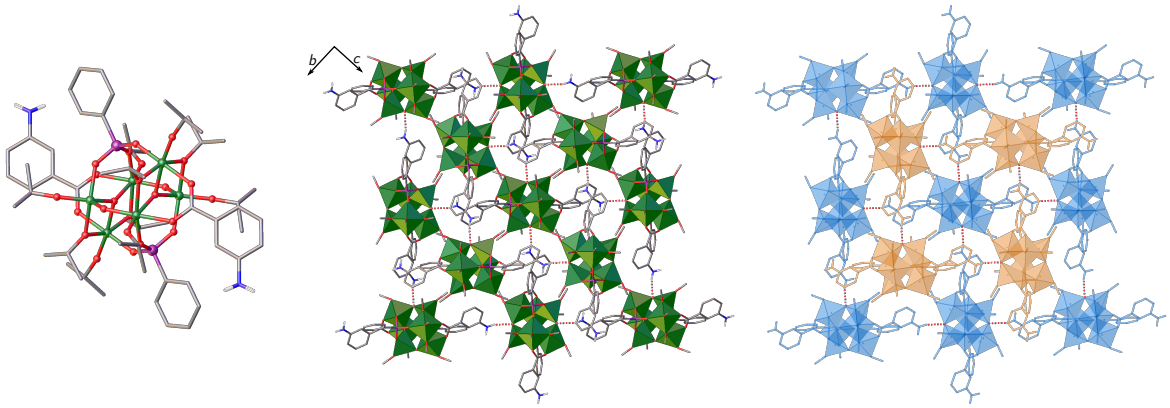


Figure 4.11: The $\{Ti_6\}$-oxo cluster **13a** (left) from mAbzH, its packing along view along [100] (middle) and illustration of AB layers (right).

The $\{Ti_6\}$-oxo cluster **13a** featuring mAbz crystallises as colourless blocks and was solved and refined in the orthorhombic space group *Pbca*. The cluster and its hydrogen bonding governed packing are portrayed in Figure 4.11. Here, the amine group hydrogen bonds to O7 of an adjacent cluster related through a *c*-glide plane. Again, the cluster serves as a four-connected node resulting in a **sql** net with ABAB parallel to the *A*-face. Phase purity of **13a** was confirmed with powder X-ray diffraction (see Figure 4.13).

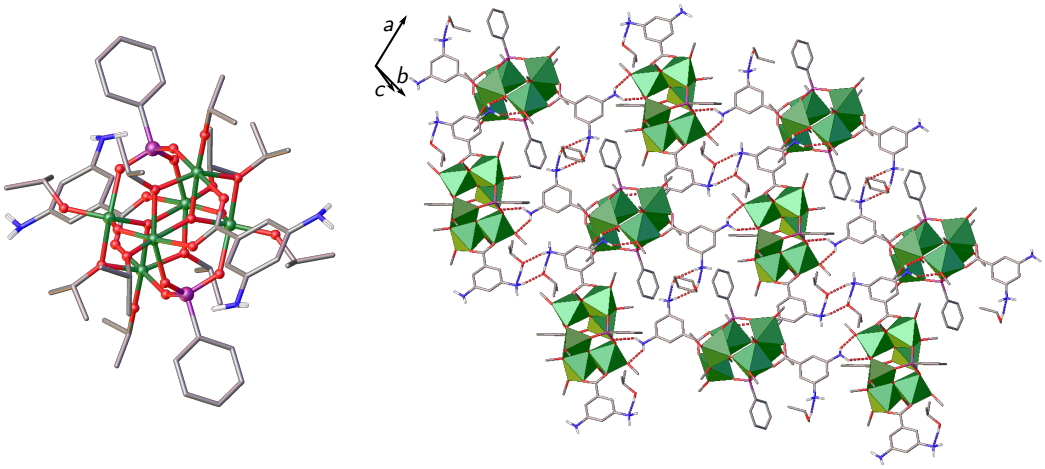


Figure 4.12: The $\{Ti_6\}$-oxo cluster **14a** (left) from DmAbzH and its packing (right).

The $\{Ti_6\}$-oxo cluster synthesised from DmAbzH under air (**14a**) co-crystallises with two molecules of isopropanol as red blocks and was solved and refined in the monoclinc space group $C2/c$. Figure 4.12 shows the cluster and packing through an intricate hydrogen bond network. The amine with N1 hydrogen bonds with both H atoms to

O2 and O7 of a neighbouring cluster related by a *c*-glide plane and a $2-1$ screw axis, respectively. The amine of N2 hydrogen bonds to its symmetry equivalent through an inversion centre with the help of two co-crystallised isopropanol molecules. Thus, every cluster serves as a six-coordinated node in a 2D hexagonal lattice (**hxl**) hydrogen bond network orthogonal to $(10\bar{1})$ with ABAB stacking. The powder X-ray diffraction pattern reveals that **14a** is phase pure (see Figure 4.13). **14a** was recently reported by Dai *et al.* as yellow crystals with cell parameters differing from the ones found in this work. Moreover, they use different reagent ratios and conduct their synthesis under nitrogen at 100 °C. As their crystal data was not available at the time of publication, the synthesis of **14a** was repeated under nitrogen, indeed resulting in yellow crystals. Single crystal X-ray structure analysis of these however revealed that they are identical in structure with the red crystals obtained in air. Analysis of the crystallographic data, once it became available, brought to light that they had misindexed the cell, resulting in a wrong model. While this explains the difference in unit cells, the reason for differences in colour when synthesised in air or nitrogen still remains obscure.

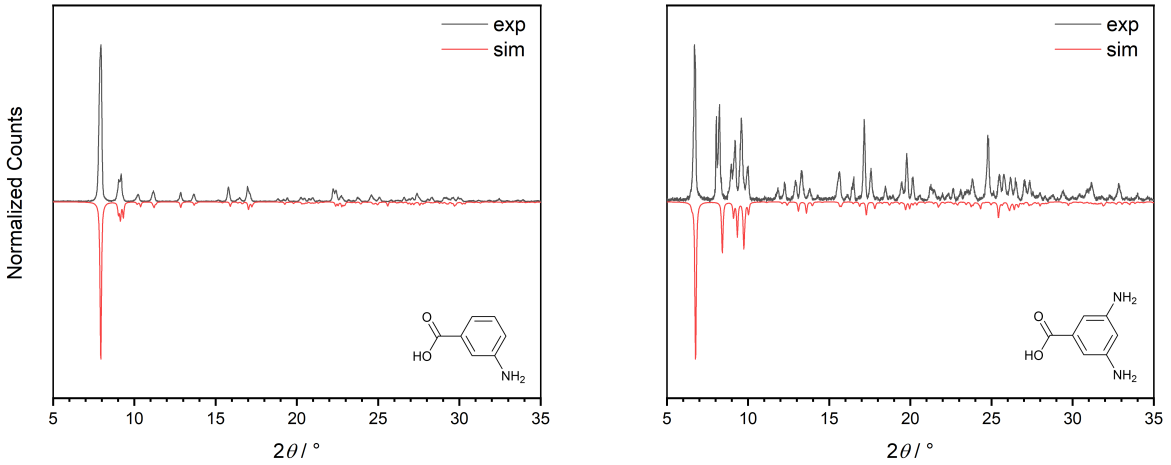


Figure 4.13: Powder X-ray diffraction patterns of **13a** (left) and **14a** (right), with their corresponding carboxylic acids inset.

The $\{Ti_6\}$-oxo cluster **15a**, featuring oAbz, co-crystallises with 0.85 molecules of iPrOH as colourless blocks and was solved and refined in the monoclinic space group $C2/c$. Here, the amine N1 undergoes intramolecular hydrogen bonding *via* H1A with O11, the carboxylate oxygen atom bound to Ti1. Moreover, the co-crystallised iPrOH molecule (disordered due to location on a twofold axis) engages in O—H$\cdots\pi$ interaction to the oAbz with $d(\mathrm{O}\cdots\pi) = 3.2356(13)$ Å. The cluster and its packing are displayed in Figure 4.14. Note, that the largest Q-peak is located at the other *ortho*-site of the

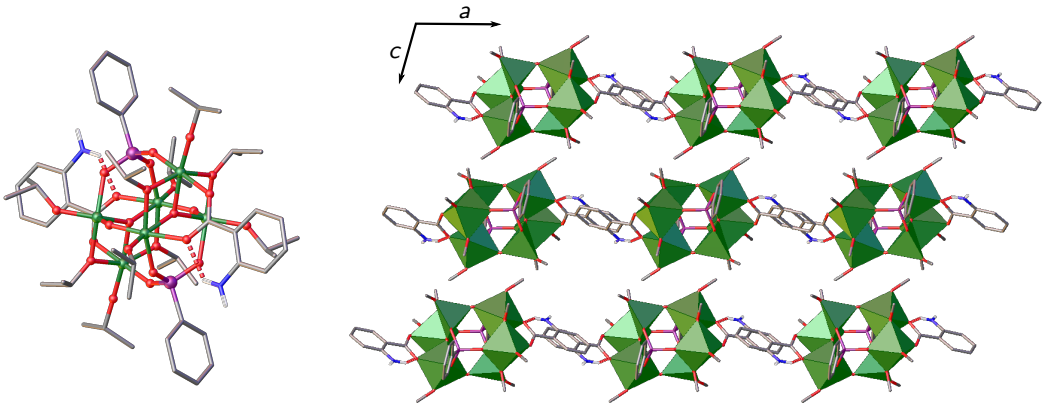


Figure 4.14: The $\{Ti_6\}$-oxo cluster **15a** (left) from oAbzH and its packing (right) viewed along [010].

benzoate. Refinement of the disorder resulted in less than 5% occupancy and a worse fitting model, and was thus omitted. **15a** was obtained phase pure, as confirmed by powder X-ray diffraction (see Figure 4.16).

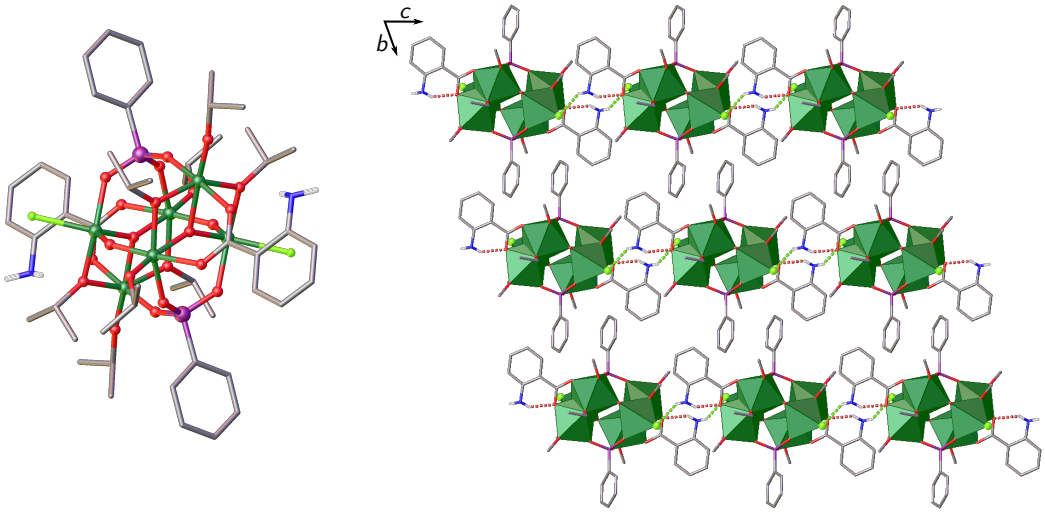


Figure 4.15: The halide doped $\{Ti_6\}$-oxo cluster **16a** (left) from oAbzH and its packing (right) viewed along [100].

Substitution of the terminal isopropoxide on Ti3 in **15a** yields the $\{Ti_6\}$-oxo cluster **16a**, which crystallises as deep yellow blocks. It was solved and refined in the triclinic space group $P\bar{1}$. As in **15a**, the amine group undergoes intramolecular hydrogen bonding with a carboxylate, however this time with O12 which is bound to Ti2. Moreover, it forms an intramolecular hydrogen bond with the disordered chloride ions Cl6A/Cl6B (95.8:4.2%) attached to Ti3 of a cluster adjacent through inversion symmetry. This

results in a back-and-forth 1D hydrogen bond ladder along c. Moreover, parallel displaced $\pi-\pi$ stacking of the phenylphosphonates, related by inversion symmetry, with $d(\pi\cdots\pi) = 3.288(3)$ Å and a plane shift of 1.666(6) Å is observed. These $\pi-\pi$ interactions link clusters along b, totaling in a **sql**-net parallel to A. The experimental powder X-ray diffraction pattern measure at room temperature (see Figure 4.16) shows discrepancies with the pattern simulated from the structure measured at 100 K. However, a well fitting pattern could be simulated using the fractional coordinates of the low temperature data set in combination with a cell indexed from the experimental RT data. The results of a Le Bail refinement of **16a** with the RT cell, depicted in Figure 4.17, are in good agreement with the experimental diffraction pattern.

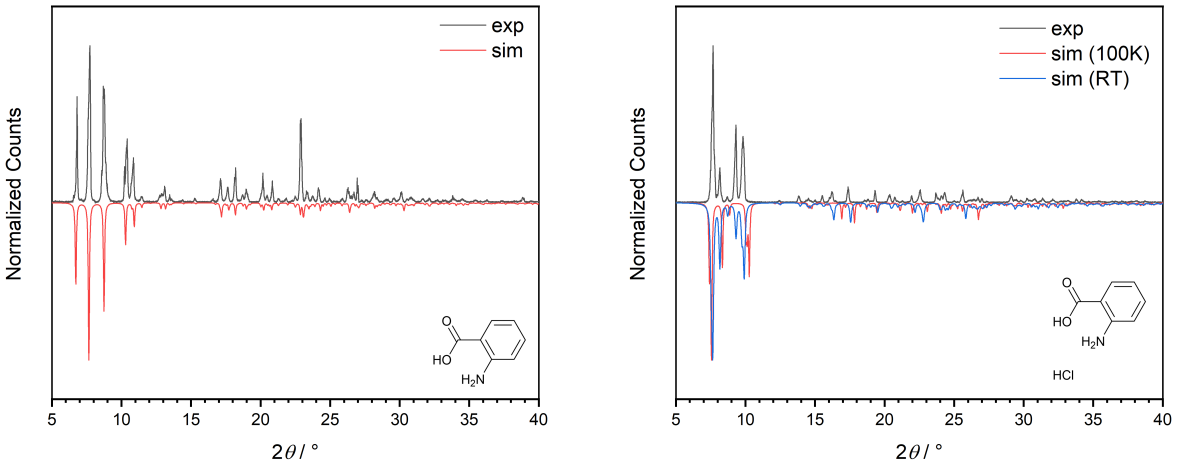


Figure 4.16: Powder X-ray diffraction patterns of **15a** (left) and **16a** (right), with their corresponding acids inset.

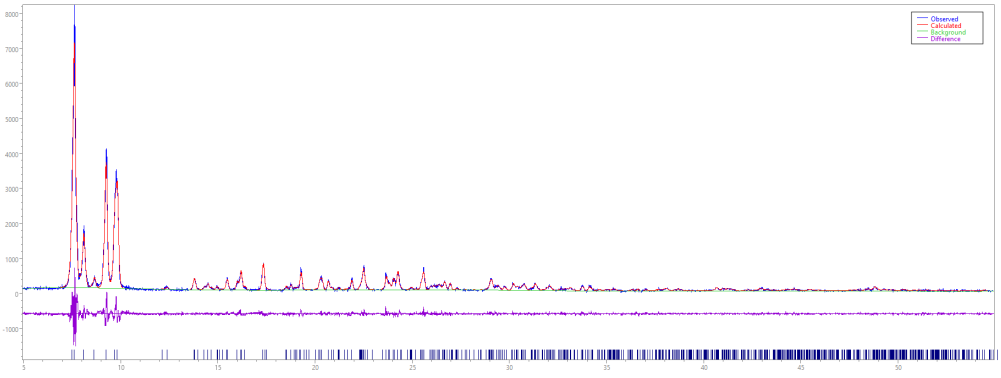


Figure 4.17: Le Bail fit of **16a**. Observed and calculated patterns in blue and red resepctively, background in green, and difference in purple. Blue ticks indicate predicted reflections based on the cell.

4.2.4. Optical Properties of Aminobenzoate Functionalised Titanium-Oxo Clusters

The optical band gaps of the titanium-oxo clusters can be obtained from the diffuse reflectance spectra (DRS) of the compounds. The DRS were then transformed using the Kubelk-Munk (also referred to as remission) function, *viz.*

$$F(R) = \frac{(1-R)^2}{2R} \tag{4.1}$$

where R is the diffuse reflectance. The band gap can then be extracted by direct extrapolation of the absorption edge onto the energy axis. The Kubelka-Munk functions of titanium-oxo clusters discussed in section 4.2 and direct extrapolation for their band gaps are plotted in Figure 4.18.

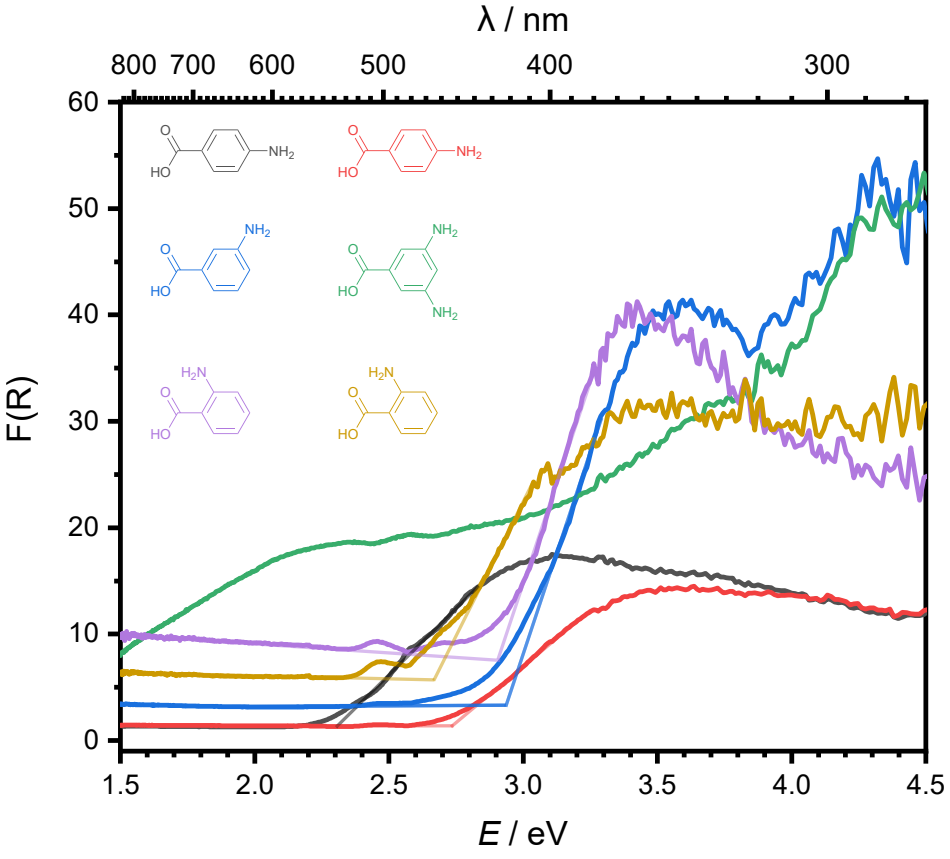


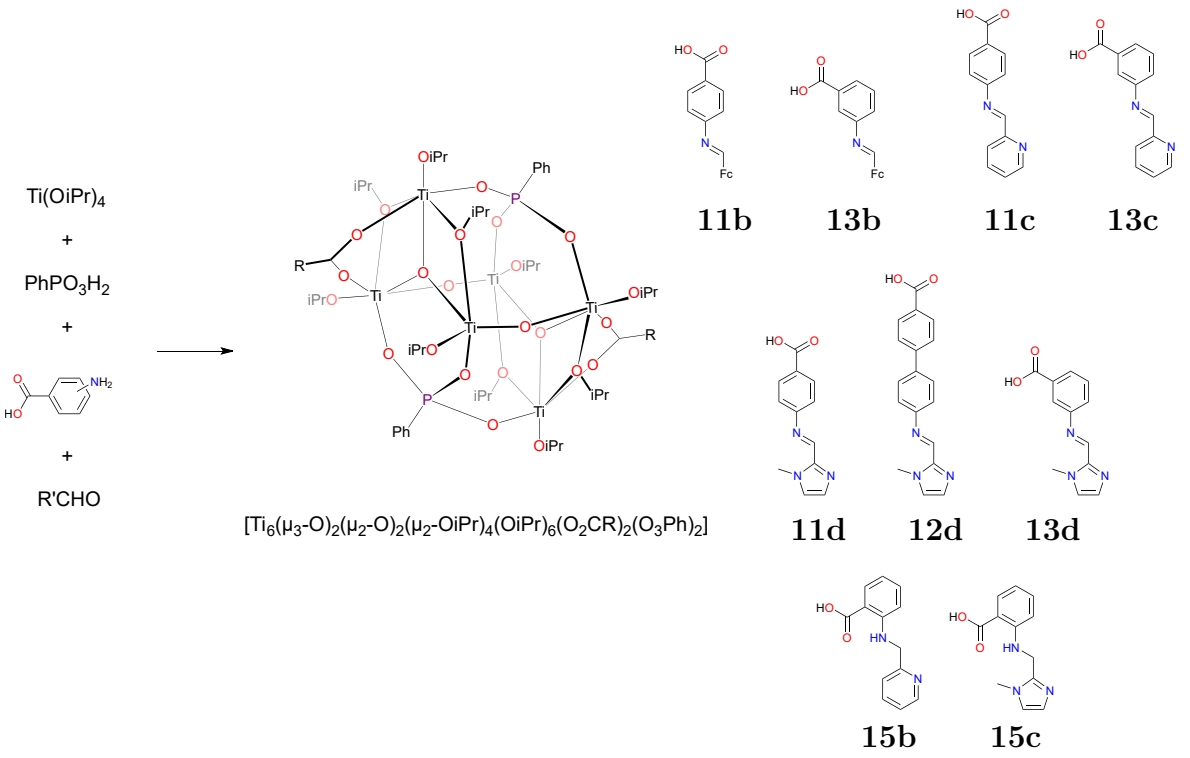
Figure 4.18: Kubelka-Munk function from the DRS of the $\{Ti_5\}$-oxo cluster **10** (black, 2.31 eV), and the $\{Ti_6\}$-oxo clusters **11a** (red, 2.76 eV), **13a** (blue, 2.94 eV), **14a** (green), **15a** (violet, 2.91 eV), **16a** (ochre, 2.67 eV). Band gaps were determined by direct extrapolation. Bumps at *ca.* 2.5 eV are measurement artefacts.

Although Zheng *et al.* had reported the structure of the $\{Ti_5\}$-oxo cluster **10** and had used it in conjunction with $BiVO_4$ for photocurrent measurements and water splitting, they neither reported its diffuse reflectance spectrum nor band gap which was determined to be 2.31 eV.[374] The Kubelka-Munk function of the $\{Ti_6\}$-oxo cluster **11a** is in agreement with the one reported by Dai *et al.* (who assigned the band gap from solution at 3.22 eV) and has a band gap of 2.76 eV.[281] This value is slightly higher than that of its analogue from 4-(dimethylamino)-benzoic acid at 2.6 eV, as the methylated carboxylate ligand is more electron donating.[370] Substitution of the amine in the *meta*- instead of *para*-position leads to an increase of the band gap by 0.18 eV to 2.94 eV in **13a**, as the amine's +M effect is stronger in the latter. Interestingly, even though the +M effect of an amine in the *ortho*-position should be similar to that in the *para*-position, the band gap of **15a** at 2.91 eV is much closer to **13a** rather than **11a**. Moreover, substitution of the terminal isopropoxide by a chloride ion on Ti3 lowers the band gap to 2.67 eV in **16a**. According to reports by Wright *et al.*, this band gap reduciton is due to the higher contribution of the halide valence orbitals to the valence band, with Cl(-p) orbitals lying at a higher energy than the O(-p) orbitals.[368] Interestingly, the 3,5-diamino-substituted cluster **14a** absorbs so strongly, not only across the entire visible spectrum but also beyond the instrument capabilities, that the optical band gap could not be determined accurately but lies below 1.5 eV.

4.3. Schiff Base-Benzoate Functionalised $\{Ti_6\}$-Oxo Clusters

4.3.1. Synthesis

After the successful synthesis of $\{Ti_6\}$-oxo clusters with aminobenzoic acids, the next step was to further explore tandem cluster-formation and Schiff base condensation. Thus, it was investigated whether the addition of carbonyl-containing aromatic compounds (2.66-3 eq.) to the reaction mixtures in subsection 4.2.3 would lead to an *in situ* formation of their corresponding imines (or Schiff bases) and what effect this would have the photo- and electrochemical properties. The $\{Ti_6\}$-oxo clusters obtained by this approach are shown in Scheme 4.2.



Scheme 4.2: Synthesis of $\{Ti_6\}$-oxo clusters formed from aminobenzoic acids pAbzH (**11**), pAPhBzH (**12**), mAbz (**13**), and oAbz (**15**) and the aldehydes (R′CHO) FcCHO (**b**), PyCHO (**c**), and MeImCHO (**d**) .

While the addition of ketones (acetophenone, 2-acetylpyridine, and fluorene) merely resulted in their parent aminobenzoate-clusters (**a**), the reaction with aldehydes (R′CHO)

ferrocenyl- (FcCHO, **b**), 2'pyridyl- (PyCHO, **c**), and 1-methyl-imidazole-2-carboxaldehyde (MeImCHO, **d**) was fruitful. For pAbzH, pAPhBzH, and mAbzH the reactions proceeded to yield clusters of the corresponding Schiff bases, regardless of which aldehyde was used, and even suppressed the formation of side products observed for pAbzH and pAPhBzH. Interestingly, for oAbzH two distinct observations were made based on the added aldehyde: If R′ is electron donating (Fc, 4-(dimethylamino)phenyl), only results in the parent amine cluster **15a**. However, if R′ is electron withdrawing, (Py, MeIm), $\{Ti_6\}$-oxo clusters form in which the corresponding Schiff base has been reduced to a secondary amine in a Meerwein-Ponndorf-Verley type reaction. A similar observation was made by Katsuki *et al.* for the insertion of $Ti(OiPr)_4$ into a salen-type ligand.[375]

Moreover, synthesis of supramolecular cages using diimine-functionalised (**c**,**d**) and Co(II) salts was attempted, but ultimately failed. The bespoke ability of these $\{Ti_6\}$-oxo clusters to crystallise under mild solvothermal conditions is accompanied by their incredibly low solubility. One-pot one- or two-step reactions merely resulted in amorphous material.

4.3.2. Ferrocenyl- and Pyridyl-Schiff Bases in the *para*- and *meta*-Position

Crystals data and refinement results for **11b**, **11c**, **13b** and **13c**, the ferrocenyl- (**b**) and 2'-pyridyl-Schiff bases (**c**) of **11a** and **13a**, are listed in Table 4.7 and thermal ellipsoid plots of their asymmetric units is presented in Figure 4.19 andFigure 4.20. Bond distances for **11b**, **11c**, **13b** and **13c** are given in Table 4.8.

The $\{Ti_6\}$-cluster **11b** co-crystallises with one molecule of iPrOH as orange blocks. **11b** was solved and refined in the triclinic space group $P\bar{1}$ with half a molecule in the asymmetric unit and one molecule per unit cell. A full cluster and the packing of **11b** are displayed in Figure 4.21. The only significant change in bond distances is observed in the C—N bond, which elongated to a single bond upon imine formation. The cluster is charge neutral with Fe1 in oxidation state +II and Fe—C distances from 2.023(4) Å to 2.042(4) Å and Fe$\cdots$Cp distances that are within each others standard deviation (1.638(2) Å and 1.643(3) Å). Moreover, the Cp rings are eclipsed (twist *ca.* 12.5°) and quasi-parallel ($\measuredangle$(Cp$\cdots$Fe1$\cdots$Cp) = 178.16(11)°). The packing of **11b** is neither governed by $\pi-\pi$-interactions nor hydrogen bonding (althoug present) and ferrocene

Table 4.7: Crystal data and refinement results of **11b**, **11c**, **13b** and **13c**.

Identification code	**11b** · 2 iPrOH	**13b**
Empirical formula	$C_{84}H_{124}Fe_2N_2O_{26}P_2Ti_6$	$C_{78}H_{108}Fe_2N_2O_{24}P_2Ti_6$
Formula weight	2038.88	1918.7
Temperature/K	100	100
Crystal description	orange block	orange rod
Crystal size/mm^3	$0.318 \times 0.183 \times 0.156$	$0.379 \times 0.13 \times 0.089$
Crystal system	triclinic	triclinic
Space group	$P\bar{1}$ (2)	$P\bar{1}$ (2)
a/Å	12.8969(17)	12.1035(14)
b/Å	14.303(3)	13.9913(14)
c/Å	14.829(2)	14.6085(18)
α/°	74.092(4)	72.174(4)
β/°	64.685(6)	80.951(3)
γ/°	80.770(5)	68.259(3)
V/Å^{-3}	2375.0(6)	2184.9(4)
Z, Z'	1, 0.5	1, 0.5
ρ_{calc}/g cm^{-3}	1.426	1.458
μ/mm^{-1}	0.879	0.949
$F(000)$	1064	996
Refl. total/unique	53077/10613	53982/11389
R_{int}, R_σ	0.0500, 0.0346	0.0874, 0.0617
Data/restr./param.	10613/272/761	11389/0/524
GooF	1.034	1.009
R_1 $[I \geq 2\sigma(I)]$, all	0.0499 0.0783	0.0459, 0.0862
wR_2 $[I \geq 2\sigma(I)]$, all	0.1301, 0.1489	0.0992, 0.1167
$\Delta\rho_{max}/\Delta\rho_{min}$/e Å^{-3}	1.05/-0.70	0.67/-1.01
Identification code	**11c**	**13c**
Empirical formula	$C_{68}H_{98}N_4O_{24}P_2Ti_6$	$C_{68}H_{98}N_4O_{24}P_2Ti_6$
Formula weight	1704.84	1704.84
Temperature/K	100	100
Crystal description	yellow fragment	colourless fragment
Crystal size/mm^3	$0.51 \times 0.312 \times 0.237$	$0.28 \times 0.232 \times 0.214$
Crystal system	triclinic	monoclinic
Space group	$P\bar{1}$ (2)	$P2_1/n$ (14)
a/Å	13.1190(17)	12.886(3)
b/Å	13.2967(14)	21.272(5)
c/Å	14.0483(18)	14.307(3)
α/°	114.496(4)	90
β/°	96.721(4)	94.314(7)
γ/°	112.357(4)	90
V/Å^{-3}	1949.4(4)	3910.6(15)
Z, Z'	1, 0.5	2, 0.5
ρ_{calc}/g cm^{-3}	1.452	1.448
μ/mm^{-1}	0.702	0.7
$F(000)$	888	1776
Refl. total/unique	43535/8670	70139/8679
R_{int}, R_σ	0.0281, 0.0205	0.0616, 0.0281
Data/restr./param.	8670/0/479	8679/3/497
GooF	1.029	1.068
R_1 $[I \geq 2\sigma(I)]$, all	0.0304, 0.0359	0.0469, 0.0625
wR_2 $[I \geq 2\sigma(I)]$, all	0.0780, 0.0815	0.1157, 0.1287
$\Delta\rho_{max}/\Delta\rho_{min}$/e Å^{-3}	0.94/-0.42	0.89/-0.54

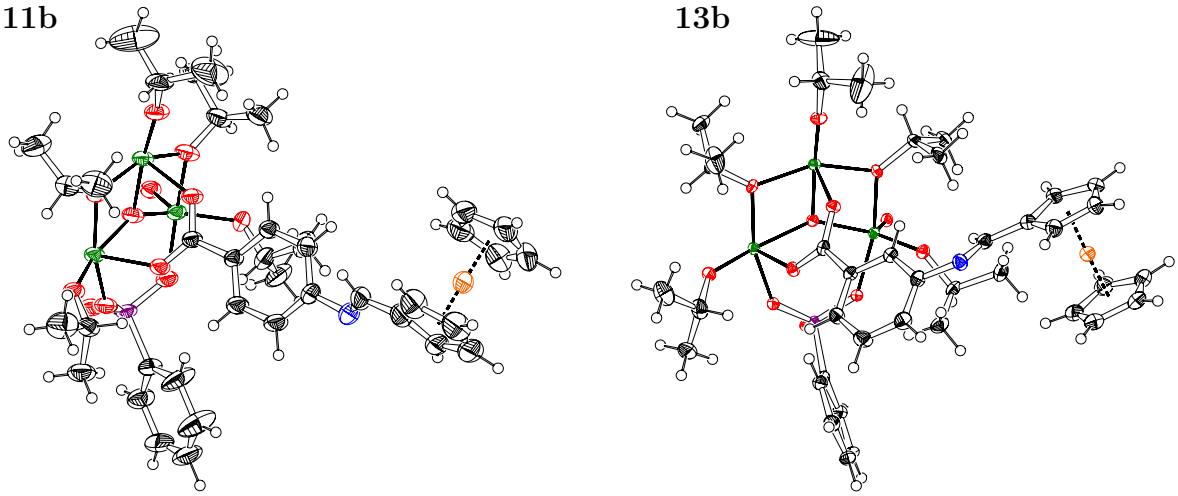


Figure 4.19: ORTEPs of the asymmetric units in the $\{Ti_6\}$-oxo clusters **11b** and **13b** with ferrocenyl-iminobenzoates, drawn at 50% probablity. Disorder and co-crystallised solvent molecules were omitted for clarity.

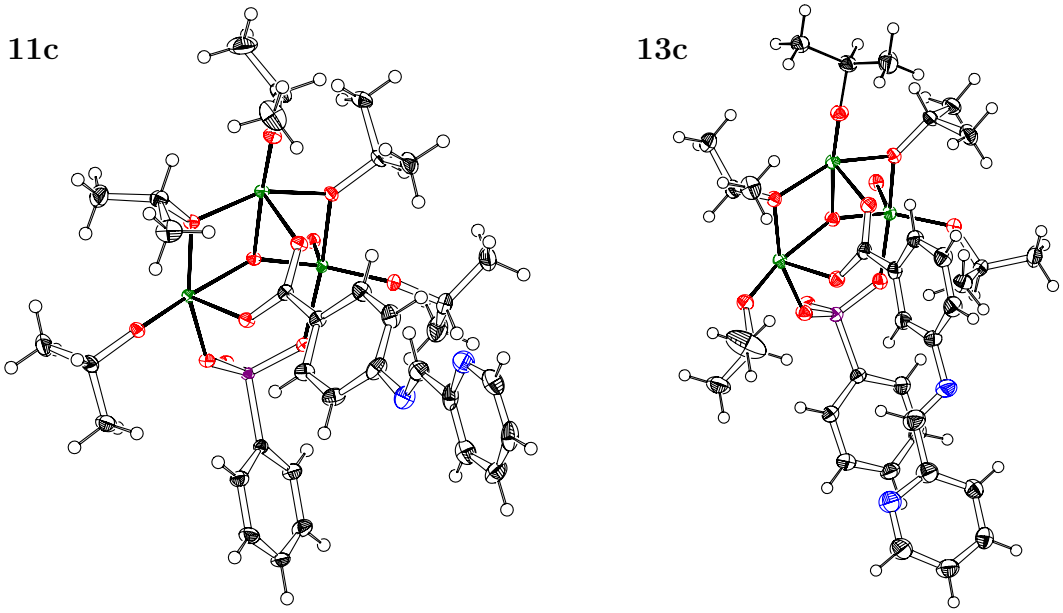


Figure 4.20: ORTEPs of the asymmetric units in the $\{Ti_6\}$-oxo clusters **11c** and **13c** with pyridyl-iminobenzoates, drawn at 50% probablity. Disorder and co-crystallised solvent molecules were omitted for clarity.

centres are closest by $d(\mathrm{Fe}\cdots\mathrm{Fe}) = 7.1051(13)$ Å. The co-crystallised isopropanol is disordered over two orientations (47:53) and either hydrogen bonds to O7 of an adjacent cluster (O13A) or the imine nitrogen N1 (O13B).

The structural analogue of **11b** from mAbzH, **13b**, crystallises as orange rods and was solved and refined in the triclinic space group $P\bar{1}$. A complete molecule and

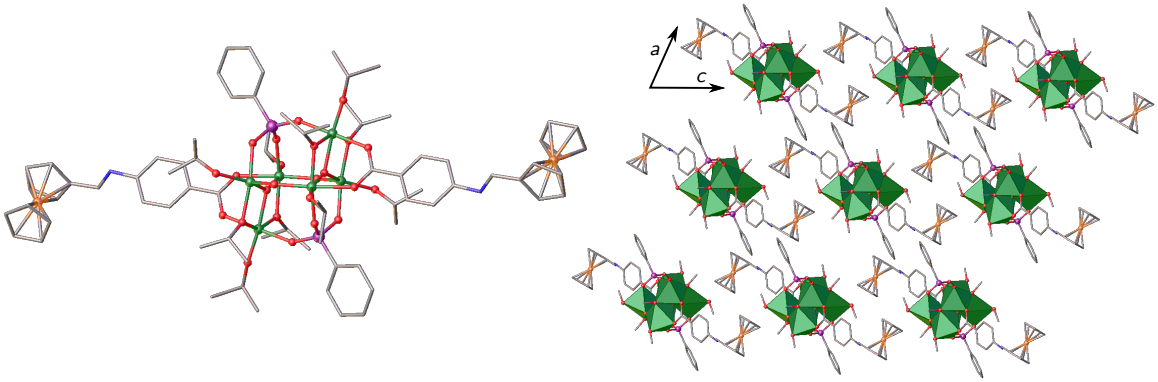


Figure 4.21: The $\{Ti_6\}$-oxo cluster **11b** (left) and its packing (right) viewed along [010].

the packing are displayed in Figure 4.22. Akin to **11b**, the only notable difference in bond lengths compared to its free amine analogue (**13a**) is observed in the well defined C_{Ar}−N single and N=CHFc double bonds. Moreover, the imine group is found on the other *meta*-position of the benzoate in comparison to the amine in **13a**. Additionally, Fe—C distances range from 2.031(3) Å to 2.052(4) Å (d(Fe1 ··· Cp) = 1.6449(19) Å and 1.651(2) Å) with eclipsed (twist *ca.* 7.6°) quasi-parallel Cp rings ((∡(Cp ··· Fe1 ··· Cp) = 178.56(7)°)). In the packing pf **13b** neither π-π-stacking nor hydrogen bonding are present and the closest inter-ferrocene distance is d(Fe ··· Fe) = 7.8913(14) Å.

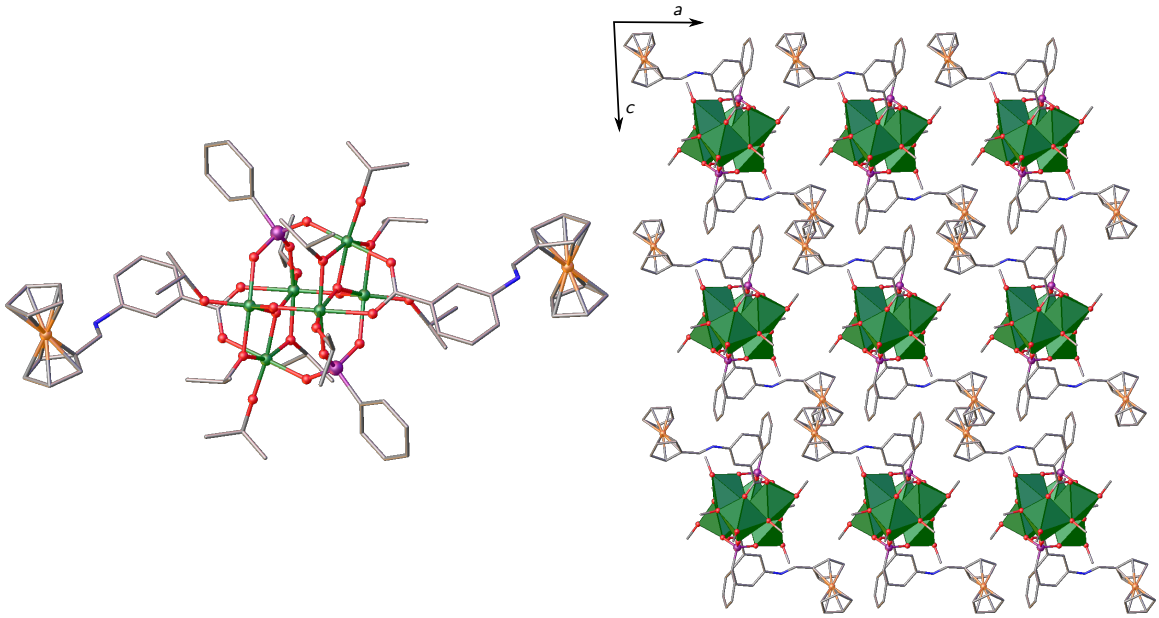


Figure 4.22: The $\{Ti_6\}$-oxo cluster **13b** (left) and its packing (right) viewed along $[0\bar{1}0]$.

Table 4.8: Bond lengths (Å) and angles (°) in **11b**, **11c**, **13b** and **13c**.

Bond	Distance	**11b**	**13b**	**11c**	**13c**
Ti—μ_3-O	Ti1—O1	2.000(2)	2.0065(18)	1.9986(11)	1.9886(18)
	Ti2—O1	1.988(2)	1.9726(18)	1.9662(11)	1.9983(18)
	Ti3—O1	1.893(2)	1.9168(18)	1.9204(11)	1.8914(18)
Ti—μ_2-O	Ti1—O7^a	1.867(2)	1.8685(19)	1.8943(11)	1.8598(18)
	Ti3—O7	1.767(2)	1.7636(19)	1.7418(11)	1.7772(18)
Ti—μ_2-OiPr	Ti1—O3	2.018(2)	2.0176(19)	2.0204(11)	2.0096(19)
	Ti2—O3	1.981(2)	1.9773(19)	1.9853(12)	1.9836(18)
	Ti2—O5	1.960(3)	1.9669(19)	1.9552(12)	1.9725(18)
	Ti3—O5	2.026(2)	2.0364(18)	2.0427(12)	2.0253(19)
Ti—OiPr	Ti1—O2	1.799(2)	1.7836(19)	1.7765(11)	1.7994(19)
	Ti2—O4	1.770(2)	1.7634(19)	1.7664(12)	1.7646(19)
	Ti3—O6	1.711(12) 1.845(5)	1.8181(19)	1.8197(12)	1.8113(18)
Ti—O_2CR	Ti1—O11	2.128(2)	2.1321(19)	2.1070(11)	2.1806(19)
	Ti2—O12	2.068(2)	2.0823(19)	2.0890(12)	2.0344(19)
RCO_2	C22—O10	1.259(3)	1.260(3)	1.267(2)	1.253(3)
	C22—O11	1.271(3)	1.274(3)	1.264(2)	1.278(3)
Ti—O_3PPh	Ti1—O9	1.953(2)	1.9571(19)	1.9697(12)	1.9551(19)
	Ti2—O10^a	1.943(2)	1.9765(19)	1.9391(11)	1.9434(19)
	Ti3—O8	1.967(2)	1.9433(18)	1.9737(12)	1.9665(19)
P—O	P1—O8	1.527(2)	1.5267(19)	1.5320(12)	1.5182(19)
	P1—O9	1.514(3)	1.5229(19)	1.5269(12)	1.5258(19)
	P1—O10	1.516(2)	1.528(2)	1.5223(11)	1.5247(19)
N—C	N1—C_{Ar}	1.414(4)	1.423(4)	1.424(2)	1.412(4)
	N1—CHR′	1.262(5)	1.283(4)	1.256(3)	1.241(4)
Angle		**11b**	**13b**	**11c**	**13c**
$Ti_2O_2\cdots O_2C$		0.7(3)	8.1(4)	2.3(2)	5.0(3)
$O_2C\cdots C_6$		5.06(11)	14.4(13)	1.37(7)	17.57(9)
$C_6\cdots NCR'$		64.08(17)	30.67(15)	40.31(9)	68.28(10)

Symmetry key: $^a 1-x, 1-y, 1-z$ for **11b**, **11c** and **13c**; $1-x, 2-y, 1-z$ for **13b**.

Table 4.9: Hydrogen bonds in **11b**.

Donor—H$\cdots$Acceptor	D—H [Å]	H$\cdots A$ [Å]	$D\cdots A$ [Å]	D—H$\cdots A$ [°]
O13A—H13G$\cdots$O7^a	0.84	2.15	2.941(10)	157
O13B—H13H$\cdots$N1	0.84	2.08	2.905(8)	169

Symmetry key: $^a 1-x, 1-y, 2-z$.

11c crystallises as yellow blocks and was solved and refined in the triclinic space group $P\bar{1}$ with one molecule per unit cell and half of a molecule in the asymmetric unit. A

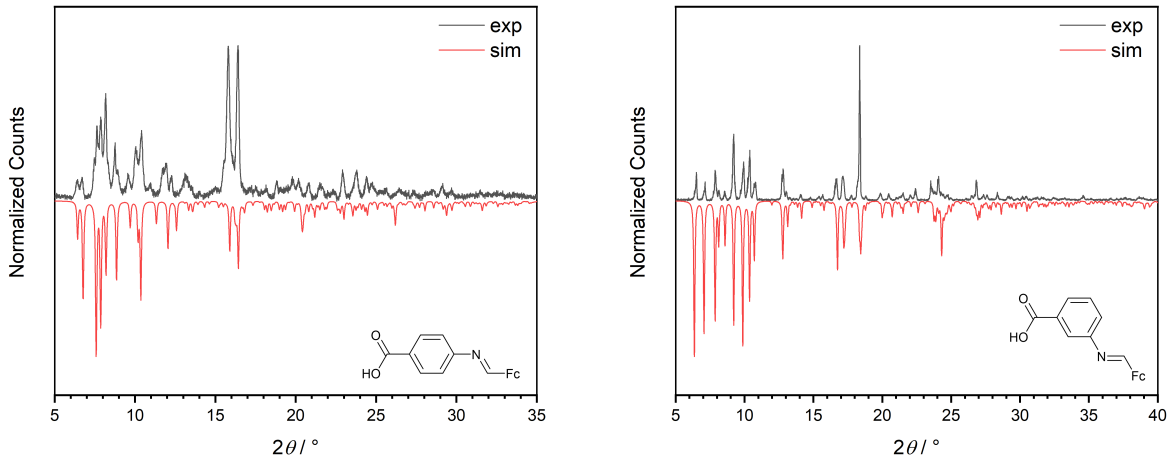


Figure 4.23: Powder X-ray diffraction patterns of **11b** (left) and **13b** (right), with their corresponding carboxylic acids inset.

full cluster and the packing of **11c** is shown in Figure 4.24. While no drastic change in bond distances is observed, with the exception of imine N—C bonds, the carboxylate is essentially orthogonal to the Ti_3O unit and coplanar to the phenyl moiety. The PyCHN moiety is twisted by 40.31(9)° with respect to the phenyl moiety and parallel to O1—Ti2. The imine and pyridyl nitrogen atoms adopt an open *anti*-conformation due to lone pair-lone pair repulsion. As neither hydrogen bonding nor π-π-stacking are observed, there are no special features in the packing of **11c**.

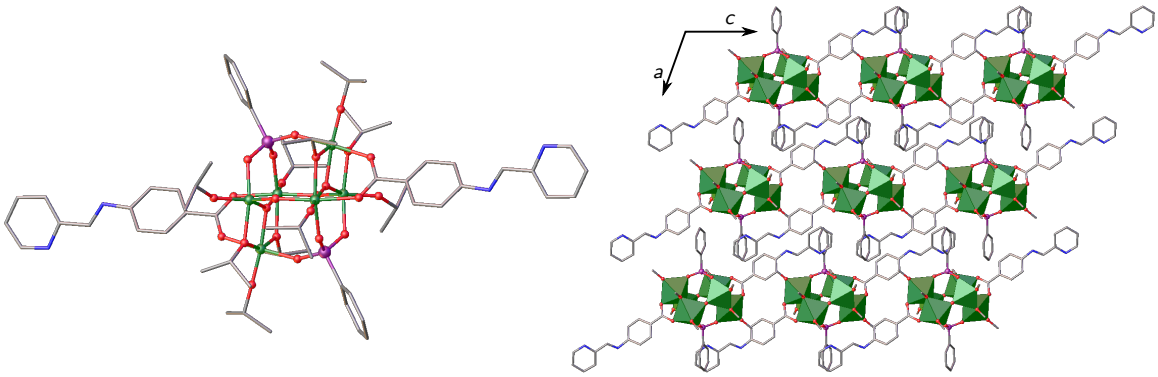


Figure 4.24: The $\{Ti_6\}$-oxo cluster **11c** (left) and its packing (right) viewed along [010].

The 2'-pyridyl-Schiff base analogue of **13a**, **13c**, crystallises as colourless blocks and was solved and refined in the monoclinic space group $P2_1/n$ with two molecules per unit cell and half of a molecule in the asymmetric unit. Akin to **11c**, the N—C bonds show the greatest bond distance disparity , with the exception of Ti—O_2C distances which

differ by 0.15 Å instead of 0.01 Å, when compared to **13a**. The higher symmetry in **13c** can be explained by T-shaped π-π-stacking by a phenylphosphonate and pyridyl-moiety onto the benzoate. Short contact distances are listed in Table 4.10 and CH $\cdots$ C distances are 0.1 Å shorter than the sum of the van der Waals radii of H and C (1.2 and 1.7 Å, respectively). These CH-π-interactions accumulate to a 2D **sql**-net parallel to the *B*-face.

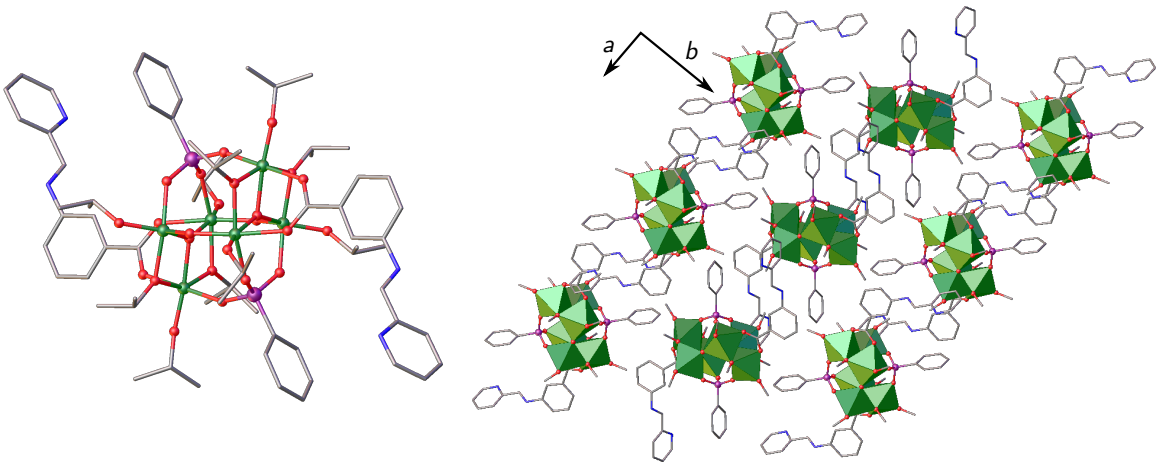


Figure 4.25: The $\{Ti_6\}$-oxo cluster **13c** (left) and its packing (right) viewed along [001].

Table 4.10: Short contacts in **13c**.

Donor—H$\cdots$Acceptor	*D*—H [Å]	H$\cdots$*A* [Å]	*D*$\cdots$*A* [Å]	*D*—H$\cdots$*A* [°]
C20^a—H20$^a\cdots$C27	0.95	2.795(3)	3.700(4)	159.76(18)
C34^b—H34$^b\cdots$C27	0.95	2.812(3)	3.706(4)	157.2(2)

Symmetry key: $^a 2-x, 1-y, 1-z$; $^a 2-x, 1-y, -z$.

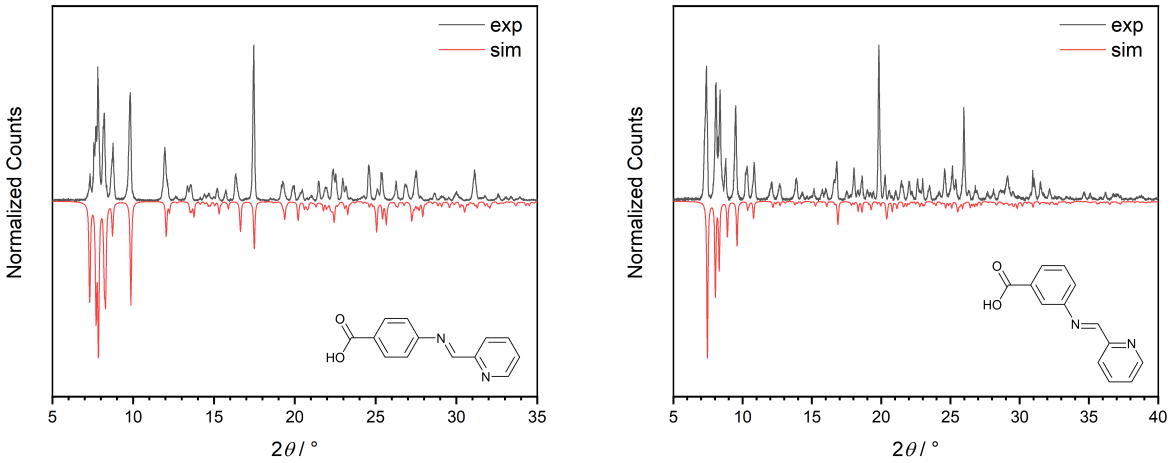


Figure 4.26: Powder X-ray diffraction patterns of **11b** (left) and **13b** (right), with their corresponding carboxylic acids inset.

4.3.3. $\{Ti_6\}$-Oxo Cluster with Methylimidazolyl-Schiff Bases

The crystals data and refinement results of **11d**, **12d** and **13d**, $\{Ti_6\}$-oxo clusters from *in situ* generated Schiff bases of MeImCHO and the respective carboxylic acids pAbzH, pAPhBzH, mAbzH, is listed in Table 4.11. Thermal ellipsoids of **11d** and **12d**, and **13d** are shown in Figure 4.27 and 4.28, respectively. Selected bond distances and angles are given in Table 4.12.

Both **11d** and **12d** crytallise as yellow blocks and were solved and refined in the triclinic space group $P\bar{1}$, with half of a molecule in the asymemtric unit and one molecule per unit cell. Full molecules and packing diagrams are portrayed in Figure 4.29 for **11d** and Figure 4.30 for **12d**. While **11d** co-crystallises with approximately one molecule of iPrOH per unit cell, it is so disordered at 200 K that it was removed using the BYPASS routine.[345] No remarkable changes in bond distances are observed upon Schiff base condensation with MeImCHO, with respect to **11d** and **12d**. The MeImCHN group is in plane with the Ti2—O1 bond in **11d** , it is almost aligned with the Ti1—O1 bond in **12d**. In both, the heteroaromatic nitrogen atom N3 is *anti* to the imine nitrogen atom N1 due to lone pair-lone pair repulsion. Due to absence of hydrogen bonding and π-π-stacking in both, there a no notable features in their packing.

The $\{Ti_6\}$-oxo cluster **13d**, derived from mAbz and MeImCHO, was isolated as colourless blocks and was solved and refined in the triclinic space group $P\bar{1}$. Surprisingly, it crystallises with one molecule in the asymmetric unit and two molecules per unit

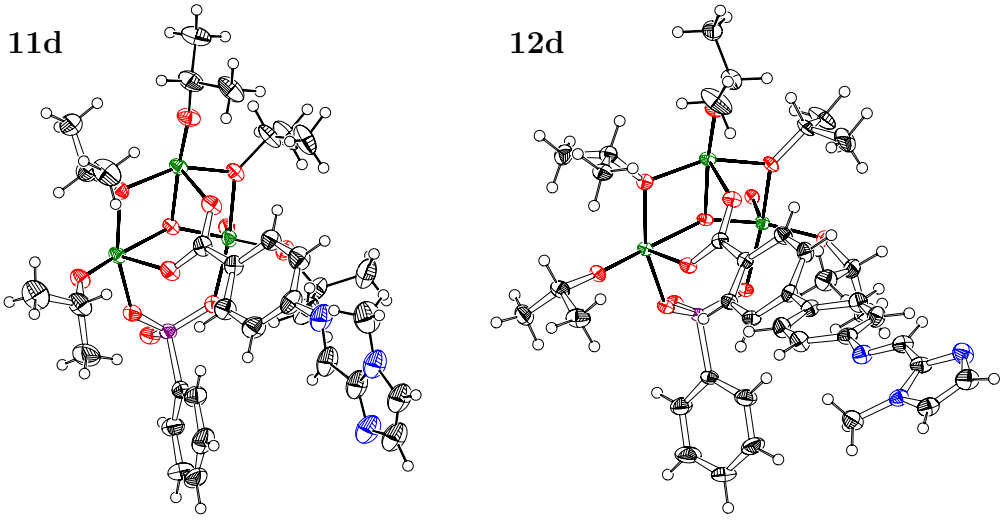


Figure 4.27: ORTEPs of the asymmetric units in the $\{Ti_6\}$-oxo clusters **11d** and **12d** with methylimidazole-iminobenzoic acid at 50% probablity. Disorder and co-crystallised solvents were omitted for clarity.

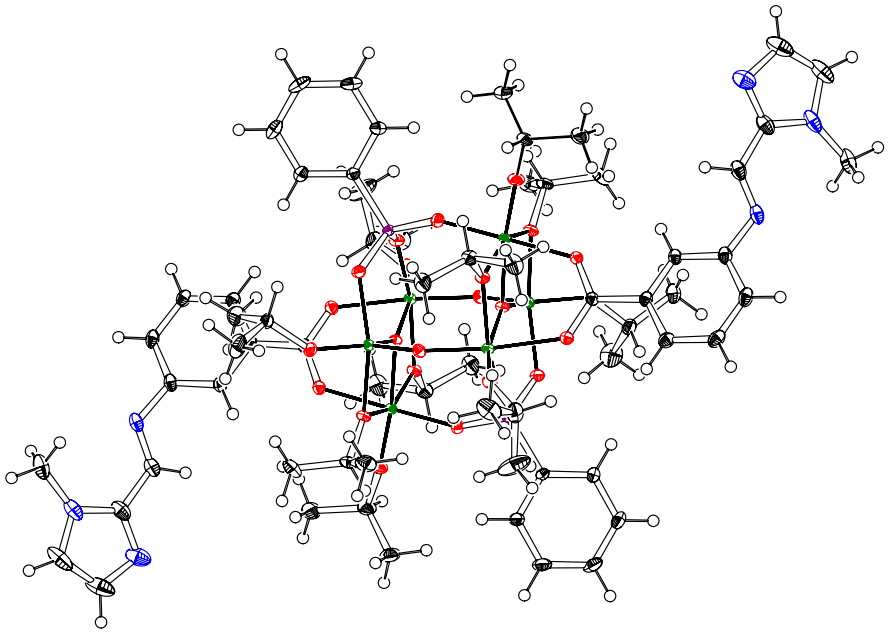


Figure 4.28: ORTEP of the asymmetric unit in the $\{Ti_6\}$-oxo cluster **13d** with methylimidazolyl-3-iminobenzoate, drawn at 50% probability. Disorder was omitted for clarity.

cell, meaning a loss of symmetry has occurred. Yet, the cluster still displays pseudo-centrosymmetry. A full cluster and the packing of **13d** are shown in Figure 4.31. Examination of the bond distances and angles does not give any indication on the symmetry loss, and do not differ remarkably from the parent aminobenzoate cluster **13a**. Interestingly, akin **13b** the MeImCHN group in **13d** is found in the other *meta*-position as

Table 4.11: Crystal data and refinement results of **11d**, **12d** and **13d**.

Identification code	**11d** · *x*iPrOH	**12d**	**13d**
Empirical formula	$C_{66}H_{100}N_6O_{24}P_2Ti_6$	$C_{78}H_{108}N_6O_{24}P_2Ti_6$	$C_{66}H_{100}N_6O_{24}P_2Ti_6$
Formula weight	1710.85	1863.04	1710.85
Temperature/K	200	100	100
Crystal description	yellow block	yellow fragment	colourless block
Crystal size/mm^3	0.301 × 0.246 × 0.142	0.231 × 0.123 × 0.039	0.361 × 0.279 × 0.259
Crystal system	triclinic	triclinic	triclinic
Space group	$P\bar{1}$ (2)	$P\bar{1}$ (2)	$P\bar{1}$ (2)
a/Å	12.2559(6)	12.617(8)	11.7322(5)
b/Å	13.4830(7)	13.429(10)	12.1602(5)
c/Å	14.7508(8)	14.190(8)	28.4786(11)
α/°	79.878(2)	112.26(3)	85.5150(10)
β/°	68.849(2)	94.33(2)	82.1340(10)
γ/°	88.946(2)	100.09(2)	89.4320(10)
V/Å^{-3}	2235.2(2)	2164(2)	4012.4(3)
Z, Z'	1, 0.5	1, 0.5	2, 1
ρ_{calc}/g cm^{-3}	1.271	1.43	1.416
μ/mm^{-1}	0.613	0.64	0.683
$F(000)$	892	972	1784
Refl. total/unique	39851/9966	28984/8912	140219/26895
R_{int}, R_σ	0.0657, 0.0584	0.0866, 0.0962	0.0348, 0.0257
Data/restr./param.	9966/429/634	8912/18/552	26895/0/979
GooF	1.015	1.007	1.025
R_1 $[I \geq 2\sigma(I)]$, all	0.0432, 0.0778	0.0519, 0.1097	0.0347, 0.0500
wR_2 $[I \geq 2\sigma(I)]$, all	0.0994, 0.1131	0.0983, 0.1178	0.0838, 0.0919
$\Delta\rho_{max}/\Delta\rho_{min}$/e Å^{-3}	0.40/-0.41	0.40/-0.43	0.77/-0.63

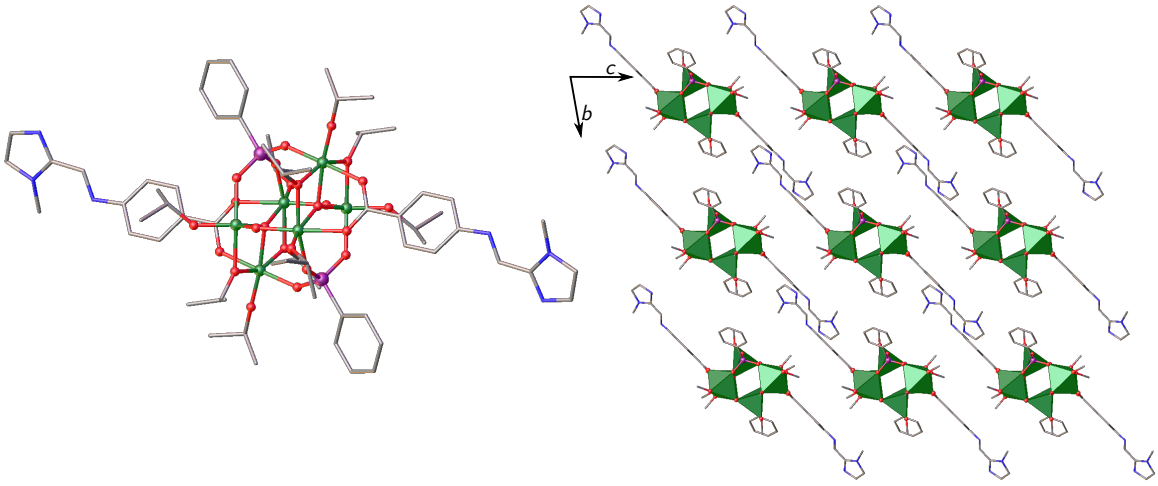


Figure 4.29: The {Ti_6}-oxo cluster **11d** (left) and its packing (right) viewed along [100].

the amine in **13a**. The packing in **13d** is governed by parallel displaced π-π-stacking between the benzoate moeties and their symmetry equivalents through inversion. While

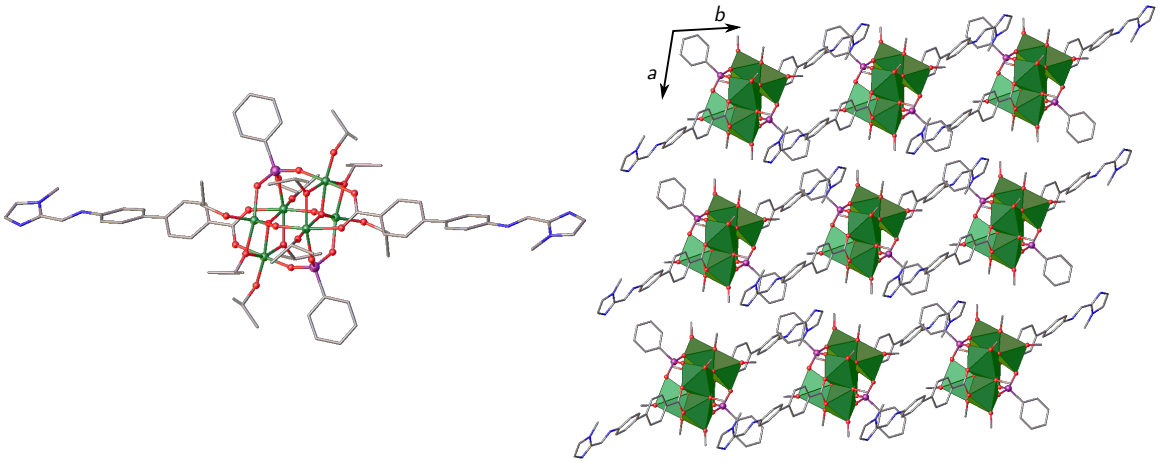


Figure 4.30: The $\{Ti_6\}$-oxo cluster **12d** (left) and its packing (right) viewed along [001].

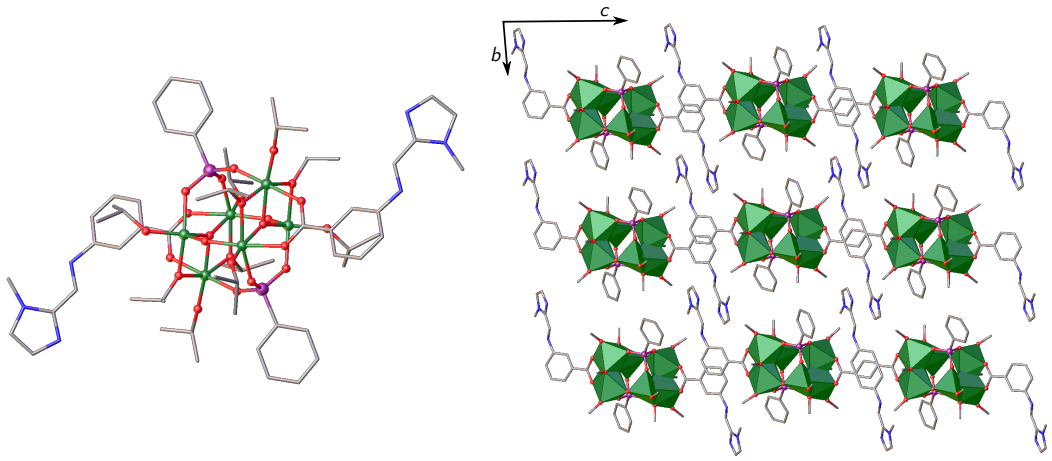


Figure 4.31: The $\{Ti_6\}$-oxo cluster **13d** (left) and its packing (right) viewed along [100].

the plane to plane distances are quite similar (d(C23−28$\cdots$C23*−28*) = 3.3066(16) Å and d(C56−61$\cdots$C56*−61*) = 3.2085(19) Å the plane to plane shifts differ by 1.15 Å (1.653(2) Å involving C23-28, 2.712(2) Å involving C56-61). This might be due to steric hindrance in the overall packing. Phase purity of $\{Ti_6\}$-oxo clusters featuring methylimidazolyl-iminobenzates was confirmed by powder X-ray diffraction, the patterns of which are plotted in Figure 4.32.

Table 4.12: Bond lengths in **11d**, **12d** and **13d** in Å.

Bond	Distance	**11d**	**12d**	**13d**			
Ti—μ_3-O	Ti1—O1	1.9921(16)	1.986(3)	Ti1—O1	1.9930(9)	Ti4—O13	1.9915(9)
	Ti2—O1	1.9725(16)	1.960(3)	Ti2—O1	1.9705(9)	Ti5—O13	1.9660(9)
	Ti3—O1	1.9058(17)	1.897(3)	Ti3—O1	1.9040(9)	Ti6—O13	1.9140(9)
Ti—μ_2-O	Ti1—O7^a	1.8548(16)	1.865(2)	Ti2—O22	1.8629(10)	Ti4—O7	1.8639(9)
	Ti3—O7	1.7638(17)	1.736(2)	Ti3—O7	1.7598(9)	Ti6—O19	1.7533(9)
Ti—μ_2-OiPr	Ti1—O3	2.0106(17)	2.038(3)	Ti1—O3	2.0268(9)	Ti4—O15	2.0313(9)
	Ti2—O3	1.9761(17)	1.949(3)	Ti2—O3	1.9637(9)	Ti5—O15	1.9678(10)
	Ti2—O5	1.9553(18)	1.954(3)	Ti2—O5	1.9613(10)	Ti5—O17	1.9609(10)
	Ti3—O5	2.0382(17)	2.024(3)	Ti3—O5	2.0315(9)	Ti6—O17	2.0279(9)
Ti—OiPr	Ti1—O2	1.7862(17)	1.759(3)	Ti1—O2	1.7761(9)	Ti4—O14	1.7875(9)
	Ti2—O4	1.7535(17)	1.770(3)	Ti2—O4	1.7691(10)	Ti5—O16	1.7705(10)
	Ti3—O6	1.774(8) 1.855(15)	1.804(3)	Ti3—O6	1.8099(10)	Ti6—O18	1.8110(10)
Ti—O_2CR	Ti1—O11	2.1400(17)	2.120(2)	Ti1—O11	2.1465(10)	Ti4—O23	2.1376(10)
	Ti2—O12	2.0751(17)	2.052(3)	Ti2—O12	2.0650(10)	Ti5—O24	2.0819(10)
RCO_2	C22—O11	1.250(3)	1.265(4)	C22—O11	1.2581(16)	C55—O23	1.2586(16)
	C22—O12	1.271(3)	1.267(4)	C22—O12	1.2719(15)	C55—O24	1.2677(16)
Ti—O_3PPh	Ti1—O9	1.9459(17)	1.964(3)	Ti1—O9	1.9644(9)	Ti4—O21	1.9559(10)
	Ti2—O10^a	1.9525(17)	1.934(3)	Ti2—O22	1.9388(10)	Ti5—O10	1.9378(10)
	Ti3—O8	1.9646(17)	1.975(3)	Ti3—O8	1.9755(9)	Ti6—O20	1.9758(9)
P—O	P1—O8	1.5167(18)	1.517(2)	P1—O8	1.5241(10)	P2—O20	1.5268(10)
	P1—O9	1.5231(19)	1.528(3)	P1—O9	1.5294(10)	P2—O21	1.5292(10)
	P1—O10	1.5196(18)	1.512(2)	P1—O10	1.5224(10)	P2—O22	1.5218(10)
N—C	N1—C_{Ar}	1.415(3)	1.418(5)	N1—C_{Ar}	1.4199(19)	N4—C_{Ar}	1.4165(18)
	N2—CHR′	1.276(15) 1.28(3)	1.266(5)	N1—CHR	1.279(2)	N4—CHR	1.275(2)

Angles	**11d**	**12d**	**13d**	
$Ti_2O_2\cdots O_2C$	0.5(3)	0.8(4)	3.33(15)	0.64(3)
$O_2C\cdots C_6$	2.13(8)	8.46(9)	4.82(5)	3.18(5)
$C_6\cdots NCR'$	40.2(2) 37.7(4)	18.90(12)	41.66(6)	41.45(6)

Symmetry operations: $^a 1-x, 1-y, 1-z$ for **11d**; $2-x, 1-y, -z$ for **12d**.

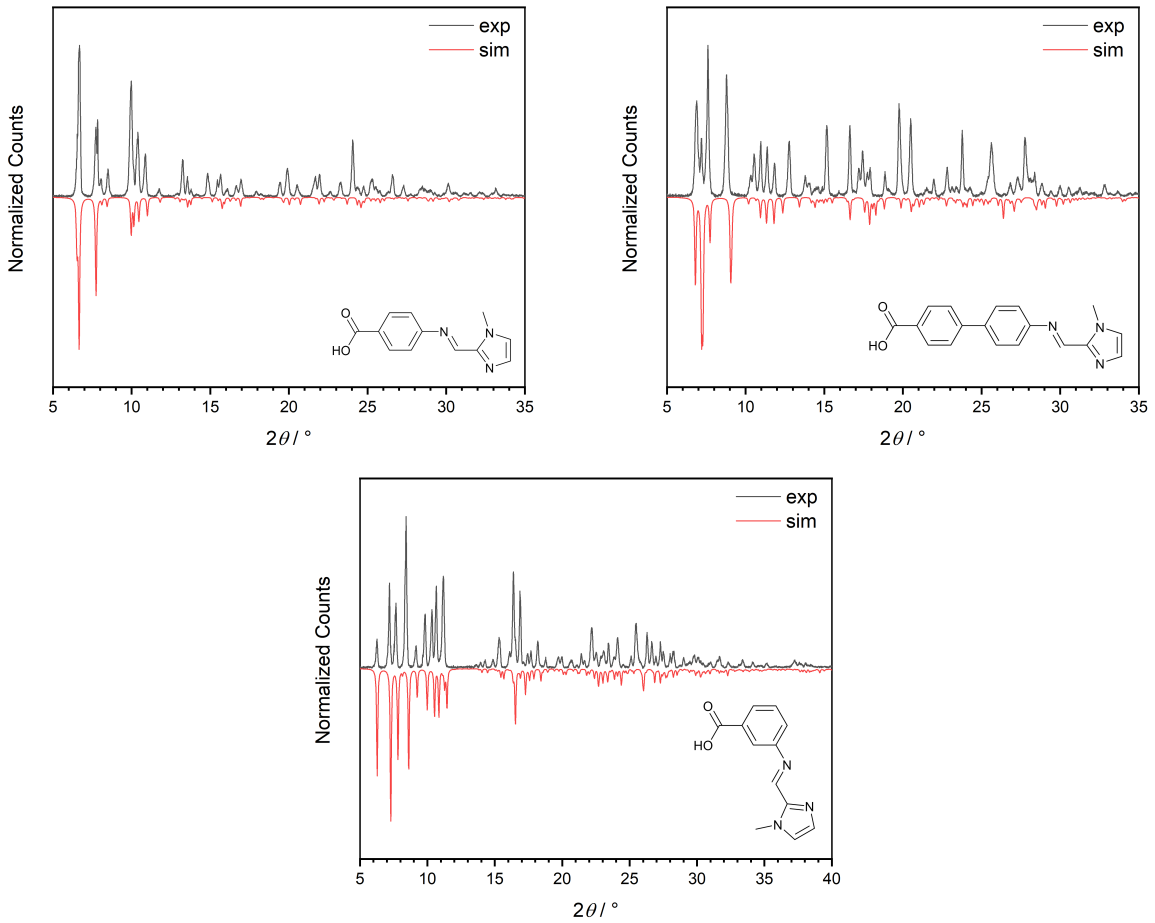


Figure 4.32: Powder X-ray diffraction patterns of **11d** (top left), **12d** (top right) and **13d** (bottom), with their corresponding carboxylic acids inset.

4.3.4. $\{Ti_6\}$-Oxo Clusters with Reduced Schiff Base-Benzoates

Crystal data and refinement results for the $\{Ti_6\}$-oxo clusters **15b** and **15c**, respectively featuring 2'-pyridyl- and 1'-methyl-imidazolyl-2-iminobenzoate, are listed in Table 4.11. Their thermal ellipsoids are plotted in Figure 4.33 and selected distances and angles are listed in Table 4.14.

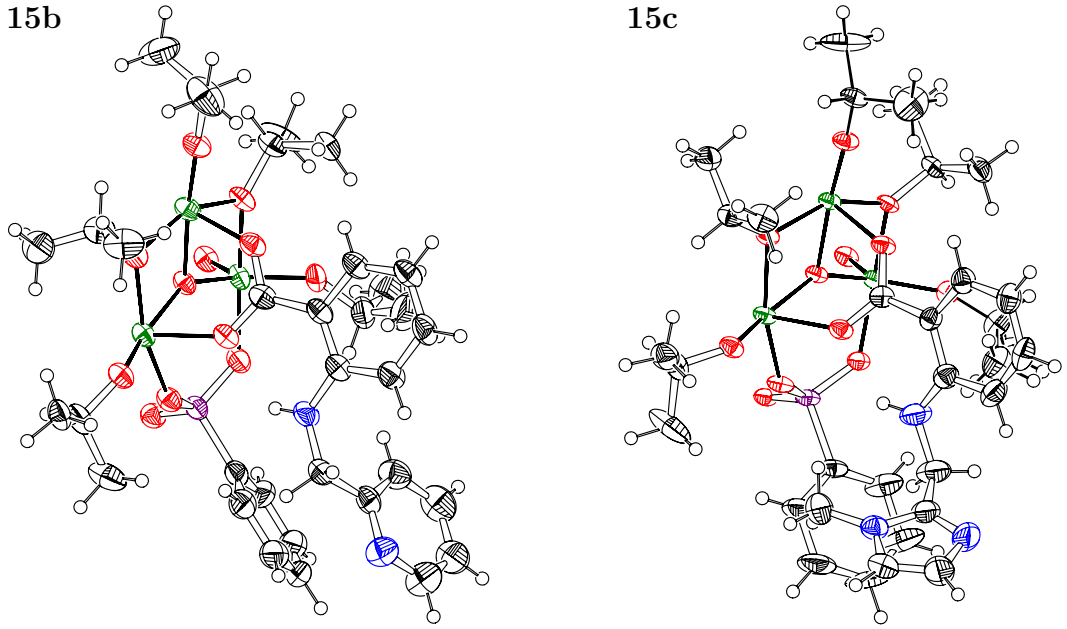


Figure 4.33: ORTEPs of the asymmetric units in the $\{Ti_6\}$-oxo clusters **15b** and **15c** with aminobenzoic acids at 50% probablity. Disorder and co-crystallised solvents were omitted for clarity.

Both **15b** and **15c** crystallise as pale yellow blocks with half of a molecule in the asymmetric unit, and were respectively solved and refined in the triclinic space group $P\bar{1}$ and the monoclinic space group $C2/c$ with one and four molecules per unit cell. **15b** crystallises neat, whereas **15c** co-crystallises with with one molecule of iPrOH. **15b** and **15c** are isostructural to each other and their parent amine **15a**, with the amine on the same *ortho*-position and thus N1 hydrogen bonding to O11 *via* H11 (see Table 4.15) and without any remarkable change in bond distances. Interestingly, the R′-group lie on opposite sides of the benzoate, with their lone pair nitrogen atoms *anti* in **15b** (N2) and partially eclipsed in **15c**. Packing is governed by π-π-interactions in both compounds: In **15b**, two benzoate moieties related through an inversion centre engage in parallel shifted π-π-stacking ($d(\mathrm{Bz}\cdots\mathrm{Bz}^{*}) = 3.474(6)$ Å with a shift of 2.264(8) Å). In **15c**, the methylimidazole engages in dipole-dipole interactions ($d(\mathrm{N2}\cdots\mathrm{C31}^{*}) = 3.563(6)$ Å)

Table 4.13: Crystal data and refinement results of **15b** and **15c**.

Identification code	**15b**	**15c** · iPrOH
Empirical formula	$C_{68}H_{102}N_4O_{24}P_2Ti_6$	$C_{69}H_{112}N_6O_{25}P_2Ti_6$
Formula weight	1708.87	1774.98
Temperature/K	100	100
Crystal description	yellow fragment	yellow fragment
Crystal size/mm^3	0.253 × 0.219 × 0.175	0.328 × 0.222 × 0.148
Crystal system	triclinic	monoclinic
Space group	$P\bar{1}$ (2)	$C2/c$ (15)
a/Å	12.2453(12)	24.538(2)
b/Å	12.3799(12)	17.2039(14)
c/Å	14.4806(14)	21.946(3)
α/°	66.710(3)	90
β/°	88.581(4)	117.043(2)
γ/°	89.577(4)	90
V/Å^{-3}	2015.7(3)	8251.4(14)
Z, Z'	1, 0.5	4, 0.5
ρ_{calc}/g cm^{-3}	1.408	1.429
μ/mm^{-1}	0.679	0.668
$F(000)$	892	3720
Refl. total/unique	23522/7375	44123/9151
R_{int}, R_σ	0.0946, 0.0973	0.0872, 0.0644
Data/restr./param.	7375/4/499	9151/42/572
GooF	1.005	1.022
R_1 [$I \geq 2\sigma(I)$], all	0.0548, 0.1179	0.0502, 0.0987
wR_2 [$I \geq 2\sigma(I)$], all	0.1257, 0.1535	0.1164, 0.1415
$\Delta\rho_{max}/\Delta\rho_{min}$/e Å^{-3}	0.56/-0.43	0.50/-0.40

with its symmetry equivalent related through C-centring and inversion, as well as T-shaped π-π-stacking the benzoate ($d(\text{H1} \cdots \text{Bz}^*) = 2.505(2)$ Å).

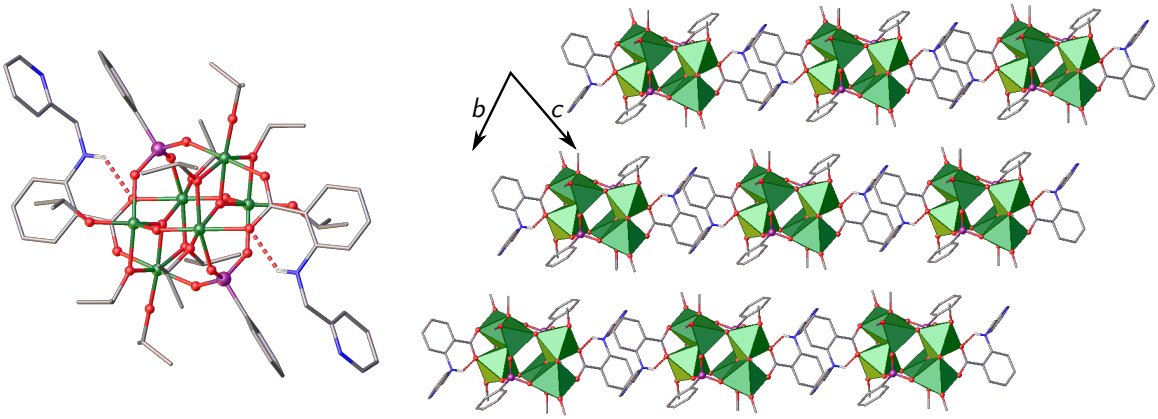


Figure 4.34: The {Ti_6}-oxo cluster **15b** (left) and its packing (right) viewed along [100].

The powder X-ray diffraction patters of **15b** and **15c** are plotted in Figure 4.36 and

Table 4.14: Bond lengths in **15b** and **15c** in Å.

Bond	Distance	**15b**	**15c**
Ti—μ_3-O	Ti1—O1	2.021(3)	2.000(2)
	Ti2—O1	1.983(3)	1.986(2)
	Ti3—O1	1.879(3)	1.893(2)
Ti—μ_2-O	Ti1—O7^a	1.836(3)	1.844(2)
	Ti3—O7	1.775(3)	1.766(2)
Ti—μ_2-OiPr	Ti1—O3	2.023(3)	2.013(2)
	Ti2—O3	1.975(3)	1.976(2)
	Ti2—O5	1.952(3)	1.953(2)
	Ti3—O5	2.020(3)	2.018(2)
Ti—OiPr	Ti1—O2	1.790(3)	1.792(2)
	Ti2—O4	1.759(3)	1.758(2)
	Ti3—O6	1.793(3)	1.790(2)
Ti—O_2CR	Ti1—O11	2.114(3)	2.104(2)
	Ti2—O12	2.041(3)	2.057(2)
RCO_2	C22—O11	1.271(5)	1.266(4)
	C22—O12	1.268(5)	1.265(4)
Ti—O_3PPh	Ti1—O9	1.973(3)	1.958(2)
	Ti2—O10^a	1.944(3)	1.942(2)
	Ti3—O8	1.953(3)	1.973(2)
P—O	P1—O8	1.525(3)	1.514(2)
	P1—O9	1.525(3)	1.518(2)
	P1—O10	1.525(3)	1.524(2)
N—C	N1—C_{Ar}	1.370(5)	1.363(5)
	N1—CH_2R'	1.445(6)	1.452(5)
Angles		**15b**	**15c**
$Ti_2O_2\cdots O_2C$		2.48(9)	4.8(3)
$O_2C\cdots C_6$		7.26(18)	26.93(11)
$C_6\cdots R'$		84.0(2)	65.32(18)

Symmetry key: $^a 1-x, 1-y, 1-z$ for **15b**; $\frac{3}{2}-x, \frac{1}{2}-y, 1-z$ for **15c**.

Table 4.15: Hydrogen bonds in **15b** and **15c**.

Compound	Donor—H$\cdots$Acceptor	*D*—H [Å]	H$\cdots$*A* [Å]	*D*$\cdots$*A* [Å]	*D*—H$\cdots$*A* [°]
15b	N1—H1$\cdots$O11	0.88	2.04	2.670(5)	128
15c	N1—H1$\cdots$O11	0.88	2.02	2.687(5)	132
	O13—H13$\cdots$N3	0.84	2.18	3.019(7)	174

confirm the phase purity of both clusters.

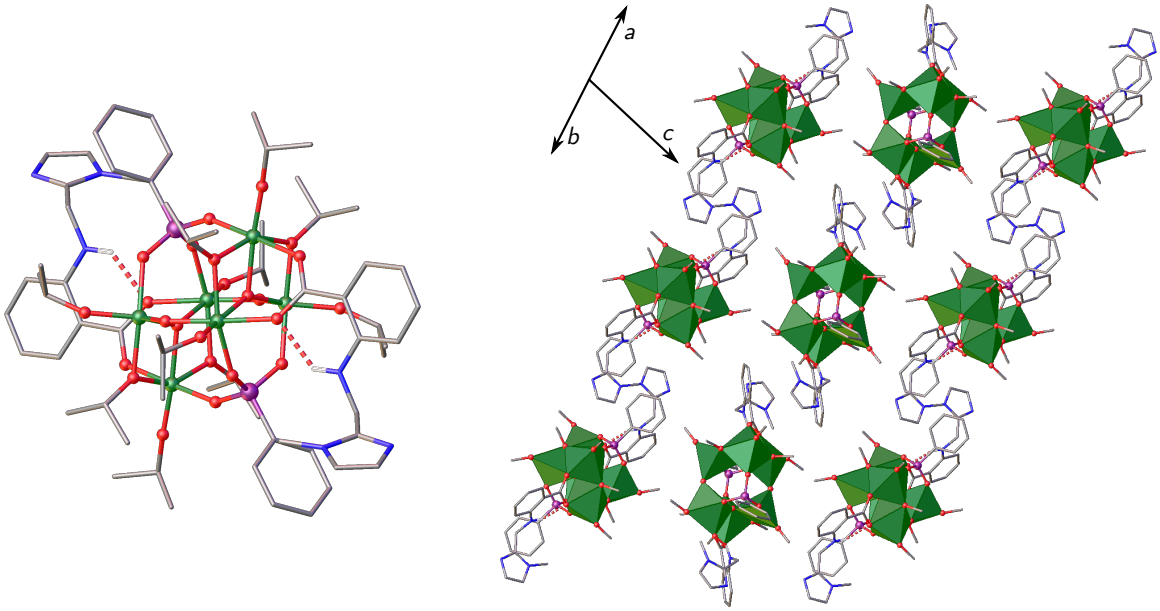


Figure 4.35: The $\{Ti_6\}$-oxo cluster **15c** (left) and its packing (right) viewed along [110].

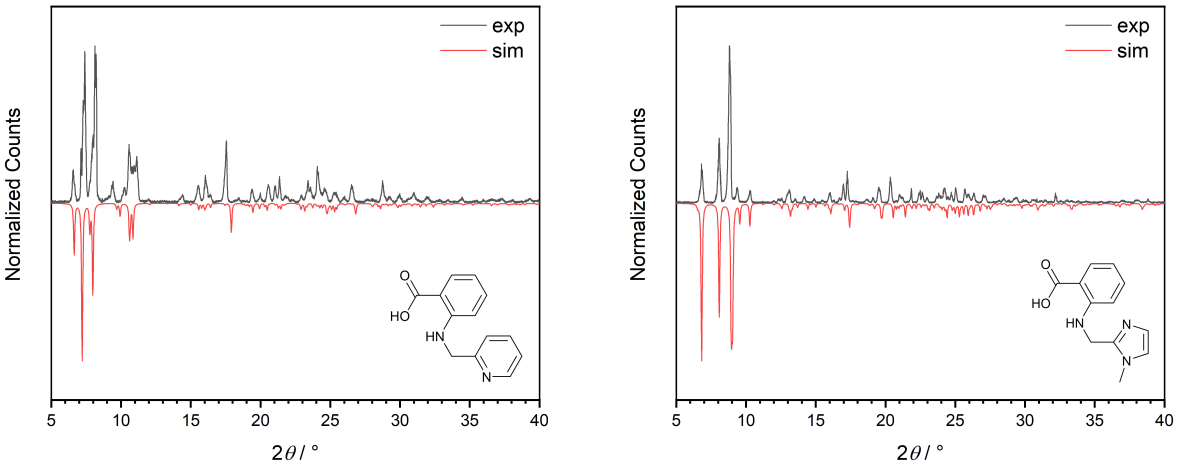


Figure 4.36: Powder X-ray diffraction patterns of **15b** (left) and **15c** (left), with their corresponding carboxylic acids inset.

4.3.5. Optical Properties Schiff Base-Benzoate Functionalised $\{Ti_6\}$-Oxo Clusters

The Kubelka-Munck function obtained from diffuse reflectance spectra of $\{Ti_6\}$-oxo clusters featuring Schiff base derivatives of **11a**, as well as the Schiff base obtained from **13a** and FcCHO are plotted in Figure 4.37. As other derivatives of **13a** are colourless, their band gaps are assumed to be in the near UV region and were not measured.

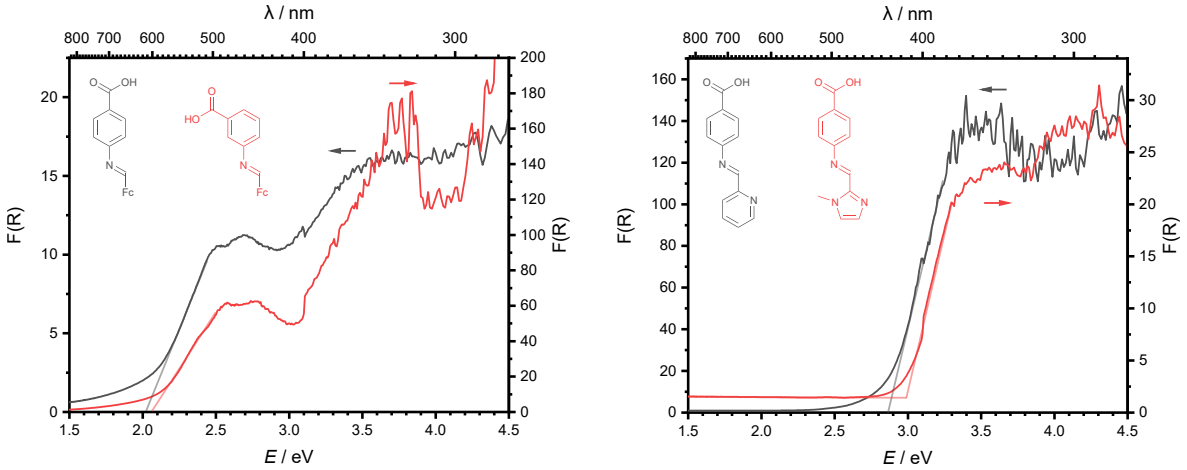


Figure 4.37: Kubelka-Munk function from the diffuse reflectance spectra of the $\{Ti_6\}$-oxo clusters **11b** (left, black, 2.02 eV), **13b** (left, red, 2.06 eV), **11c** (right, black, 2.86 eV), **11d** (right, red, 2.99 eV). Band gaps were determined by direct extrapolation.

The band gaps in **11b** and **13b** are virtually identical at 2.02 eV and 2.06 eV, respectively, and are slightly lower than that of the analogous $\{Ti_6\}$-oxo cluster featuring ferrocene carboxylic acid (2.2 eV) reported by Fan *et al.*[322] The absorption band from 400 nm to 600 nm arise from Laporte-forbidden d-d transitions.[376] However, due to the substitution of one cyclopentadienyl (Cp) ring the ferrocene moiety loses its centrosymmetry, thus the d-d transitions become allowed.[322] Moreover, π-conjugation between the Cp ring *via* the iminobenzoate should allow charge transfer from the Fc group to the titanium-oxo cluster core. Condensation of the amine in **11a** to Schiff bases with electron withdrawing groups such as Py and MeIm has the opposite effect, as the band gaps respectively increase 0.10 eV and 0.23 eV.

On the other hand, the band gaps of **15b** and **15c** are respectively decreased by 0.31 eV and 0.14 eV, as shown in Figure 4.38, when compared to their parent amine cluster **15a**.

The reduction, rather than an increase, is attributed to the formation of a primary amine instead of an imine, hence the TiO cluster core is not conjugated to the electron withdrawing group.

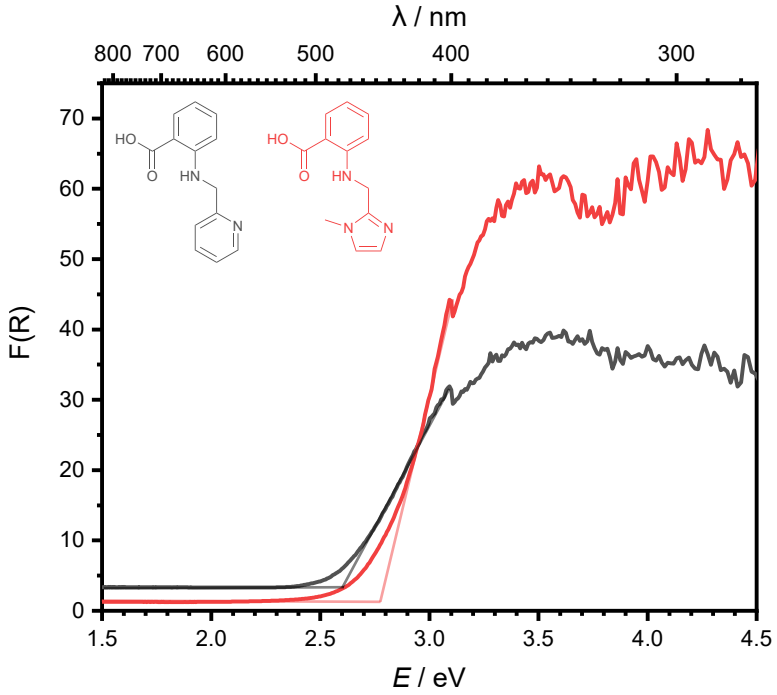
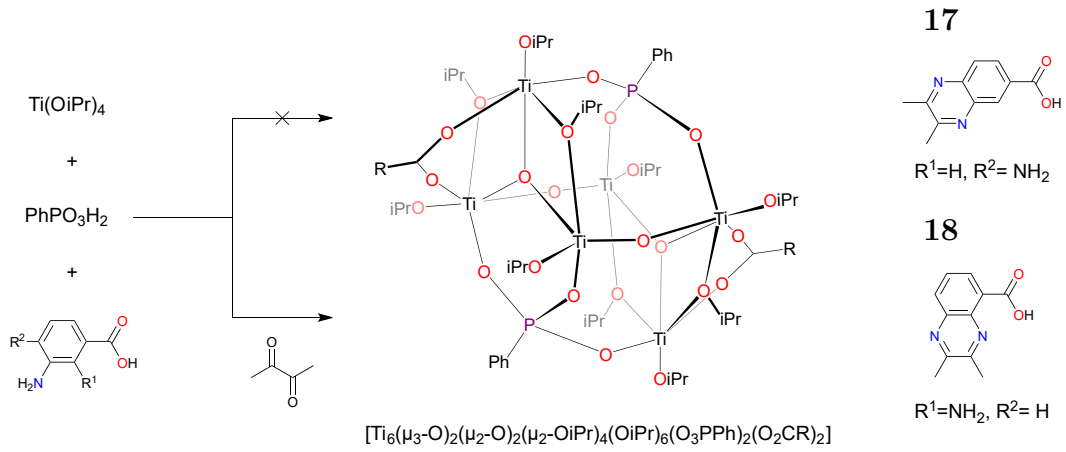


Figure 4.38: Kubelka-Munk function from the diffuse reflectance spectra of the $\{Ti_6\}$-oxo clusters **15b** (black, 2.60 eV), **15c** (red, 2.77 eV). Band gaps were determined by direct extrapolation.

4.4. Quinoxalinecarboxylate Functionalised $\{Ti_6\}$-Oxo Cluster

4.4.1. Synthesis

The well behaved crystallisation of **14a** and wide absorption window sparked the investigation of further commercially available diaminobenzoic acids, namely 2,3- and 3,4-diaminobenzoic acid. Yet, no attempt succeeded in the crystallisation of their corresponding $\{Ti_6\}$-oxo clusters. This might be due their ability to chelate and easily oxidise (akin to catechols). However, as portrayed in Scheme 4.3 the addition of diacetyl to the reaction mixture prior to $Ti(OiPr)_4$ resulted in an *in situ* formation of the $\{Ti_6\}$-oxo clusters of 2,3-dimethylquinoxaline-6-carboxylic acid (**17**) and 2,3-dimethylquinoxaline-5-carboxylic acid (**18**), respectively.



Scheme 4.3: Synthesis of $\{Ti_6\}$-clusters featuring quinoxalinecarboxylic acids generated *in situ* from their corresponding diaminobenzoic acids.

4.4.2. $\{Ti_6\}$-Oxo Clusters with Quinoline-6- and 5-Carboxylic Acid

Crystal data and refinement results for **17** and **18** are listed in Table 4.16. They respectively crystallise as yellow blocks and brown plates, and were both solved and refined in the triclinic space group $P\bar{1}$ with half of a molecule in the asymmetric unit and one molecule per unit cell. The thermal ellipsoids of their asymmetric units are

plotted in Figure 4.39. Bond distances and angles, presented in Table 4.17, reveals no remarkable features in the $\{Ti_6\}$-oxo cluster cores.

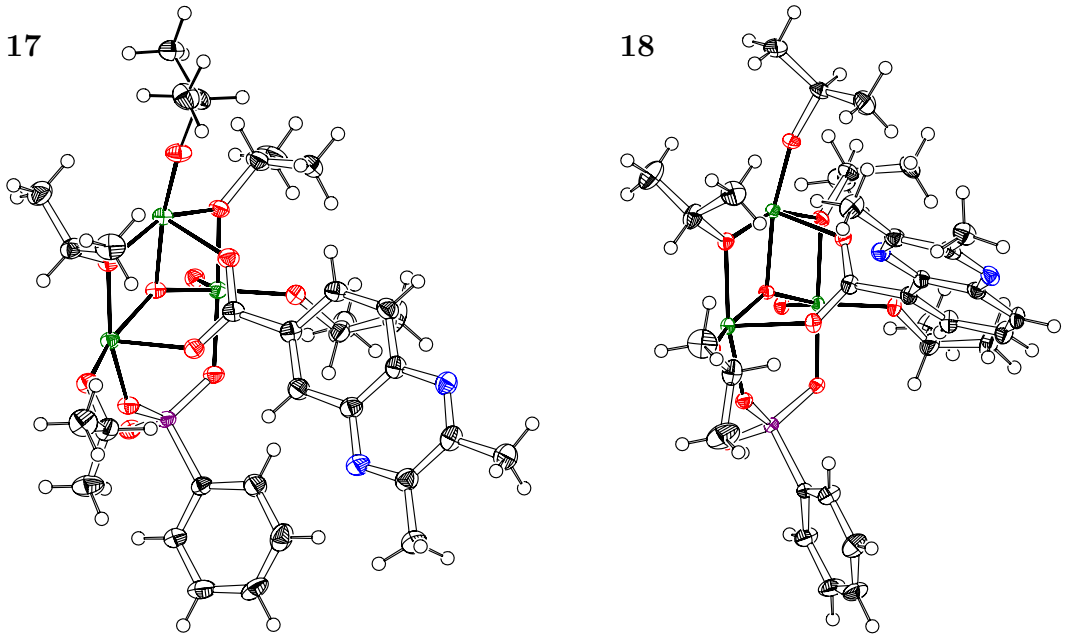


Figure 4.39: ORTEPs of the asymmetric units in the $\{Ti_6\}$-oxo clusters **17** and **18** with 2,3-dimethylquinoxaline carboxylates at 50% probablity.

In both **17** and **18**, N—C distances are *ca.* 0.06 Å longer to the benzoate moiety than to C29 and C30, with respective C29—C30 bond distances of 1.428(4) Å and 1.450(3) Å. Moreover, C—C bonds in the benzoates range from 1.358(4) Å to 1.408(3) Å in **17** and from 1.373(4) Å to 1.418(3) Å in **18** indicate weak delocalisation in the quinoxaline moieties. The quinoxaline moiety in **17** is coplanar with the carboxylate, whereas they are orthogonal in **18** leaving the quinoxaline moiety aligned with O3—C5. This is likely due to lone pair-lone pair repulsion of N1 with the carboxylate oxygen atoms, as well as steric repulsion by the methyl groups.

A full cluster and the packing of **17** is shown Figure 4.40. Here, back-and-forth π-π-stacking between the quinoxaline's pyrazine ring and the phenylphosphonate of a cluster adjacent through inversion symmetry with $d_{\pi-\pi}$ = 3.563(4) Å, a shift of 1.453(7) Å and tilted by 9.37(13)°, results in a ladder type 1D polymer along [011].

Figure 4.41 shows a complete cluster and the packing of **18**. The latter is governed by π-π-stacking between the quinoxaline's pyrazine ring and its symmetry equivalent through an inversion centre with a distance and shift of 3.435(3) Å and 1.092(5) Å, respectively.

Table 4.16: Crystal data and refinement results of **17** and **18**.

Identification code	**17**	**18**
Empirical formula	$C_{64}H_{98}N_4O_{24}P_2Ti_6$	$C_{64}H_{98}N_4O_{24}P_2Ti_6$
Formula weight	1656.8	1656.8
Temperature/K	100	100
Crystal description	yellow block	brown plate
Crystal size/mm^3	$0.59 \times 0.269 \times 0.235$	$0.314 \times 0.165 \times 0.088$
Crystal system	triclinic	triclinic
Space group	$P\bar{1}$	$P\bar{1}$
a/Å	12.177(2)	12.614(8)
b/Å	13.678(3)	12.970(8)
c/Å	13.745(3)	14.405(9)
α/°	117.86(3)	65.28(2)
β/°	105.70(3)	68.80(2)
γ/°	93.41(3)	79.18(3)
V/Å^{-3}	1901.4(8)	1994(2)
Z, Z'	1, 0.5	1, 05
ρ_{calc}/g cm^{-3}	1.447	1.38
μ/mm^{-1}	0.717	0.684
$F(000)$	864	864
Refl. total/unique	25564/8532	35458/8841
R_{int}, R_σ	0.0433, 0.0455	0.0501, 0.0421
Data/restr./param.	8532/73/493	8841/0/463
GooF	1.034	1.015
R_1 $[I \geq 2\sigma(I)]$, all	0.0469, 0.0686	0.0366, 0.0581
wR_2 $[I \geq 2\sigma(I)]$, all	0.1101 , 0.1258	0.0808, 0.0899
$\Delta\rho_{max}/\Delta\rho_{min}$/e Å^{-3}	0.69/-0.63	0.96/-0.35

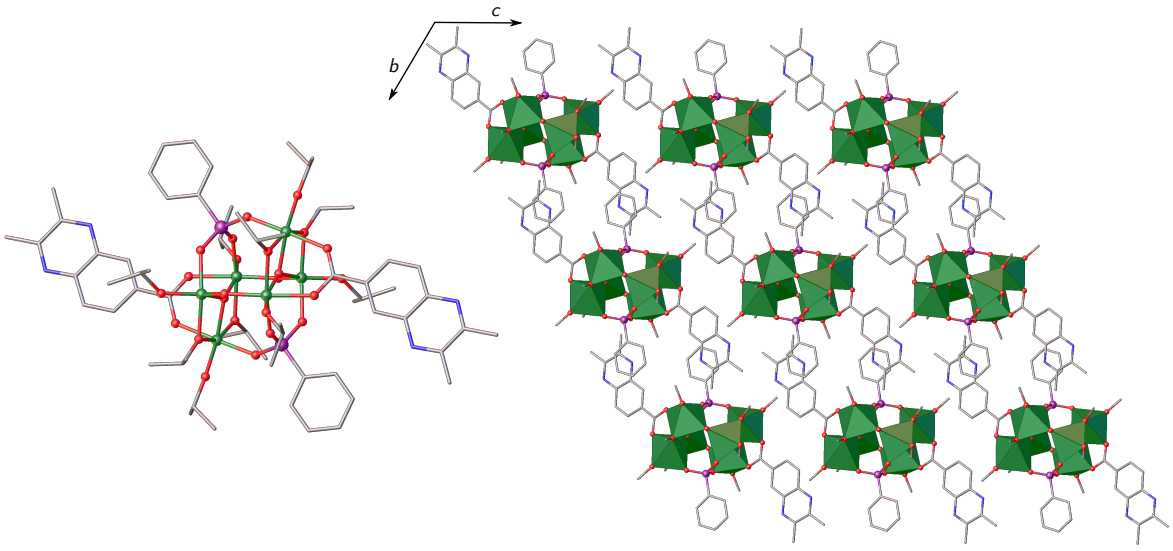


Figure 4.40: The $\{Ti_6\}$-oxo cluster **17** (left) and its packing (right) viewed along [100].

Table 4.17: Bond distances (Å) and angles (°) in **17** and **18**.

Bond	Distance	**17**	**18**
Ti—μ_3-O	Ti1—O1	2.006(2)	1.9987(18)
	Ti2—O1	1.9545(19)	1.9698(18)
	Ti3—O1	1.900(2)	1.9222(17)
Ti—μ_2-O	Ti1—O7^a	1.849(2)	1.8831(19)
	Ti3—O7	1.746(2)	1.7508(18)
Ti—μ_2-OiPr	Ti1—O3	1.991(2)	2.0173(18)
	Ti2—O3	1.975(2)	1.9842(19)
	Ti2—O5	1.966(2)	1.9691(18)
	Ti3—O5	2.014(2)	2.0277(19)
Ti—OiPr	Ti1—O2	1.777(2)	1.7842(19)
	Ti2—O4	1.753(2)	1.7676(18)
	Ti3—O6	1.803(2)	1.8219(19)
Ti—O_2CR	Ti1—O11	2.108(2)	2.136(2)
	Ti2—O12	2.060(2)	2.087(2)
RCO_2	O11—C22	1.253(3)	1.261(3)
	O12—C22	1.255(3)	1.261(3)
Ti—O_3PPh	Ti1—O9	1.928(2)	1.9549(19)
	Ti2—O10^a	1.944(2)	1.9483(19)
	Ti3—O8	1.946(2)	1.9787(18)
P—O	P1—O8	1.515(2)	1.5339(17)
	P1—O9	1.516(2)	1.5276(17)
	P1—O10	1.514(2)	1.5293(18)
C=N	N1—C_{Ar}	1.358(4)	1.376(3)
	N2—C_{Ar}	1.361(4)	1.374(3)
	N1—C29	1.298(4)	1.312(3)
	N2—C30	1.300(4)	1.312(3)

Angle	**17**	**18**
$Ti_2O_2 \cdots O_2C$	7.9(4)	4.6(3)
$O_2C \cdots C_6$	0.77(14)	88.97(1)

Symmetry key: ^{a} $1-x, 1-y, 1-z$.

Phase purity of **17** and **18** was asserted by powder X-ray diffraction, as shown in Figure 4.42.

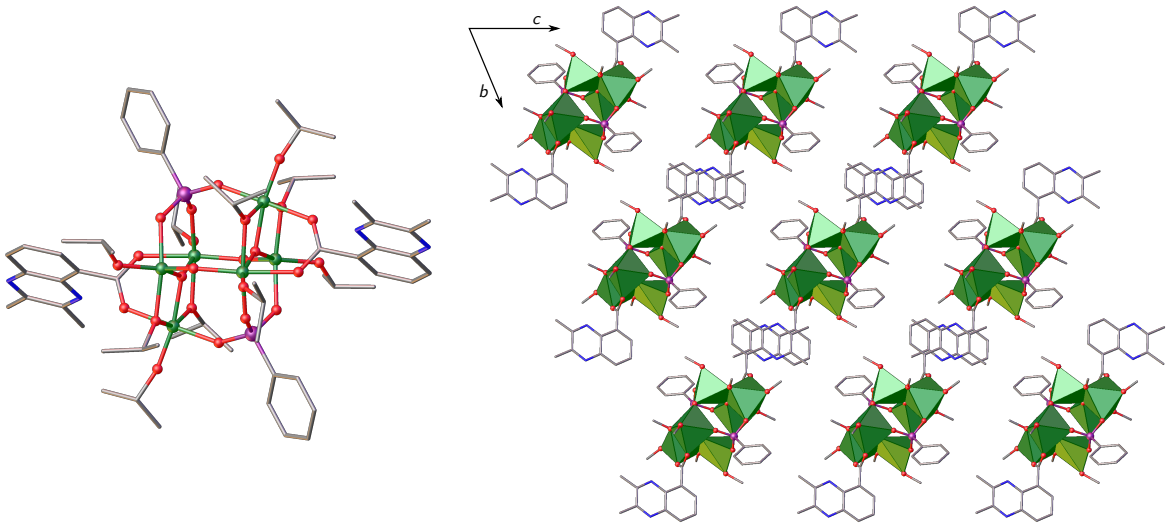


Figure 4.41: The $\{Ti_6\}$-oxo cluster **17** (left) and its packing (right) viewed along [100].

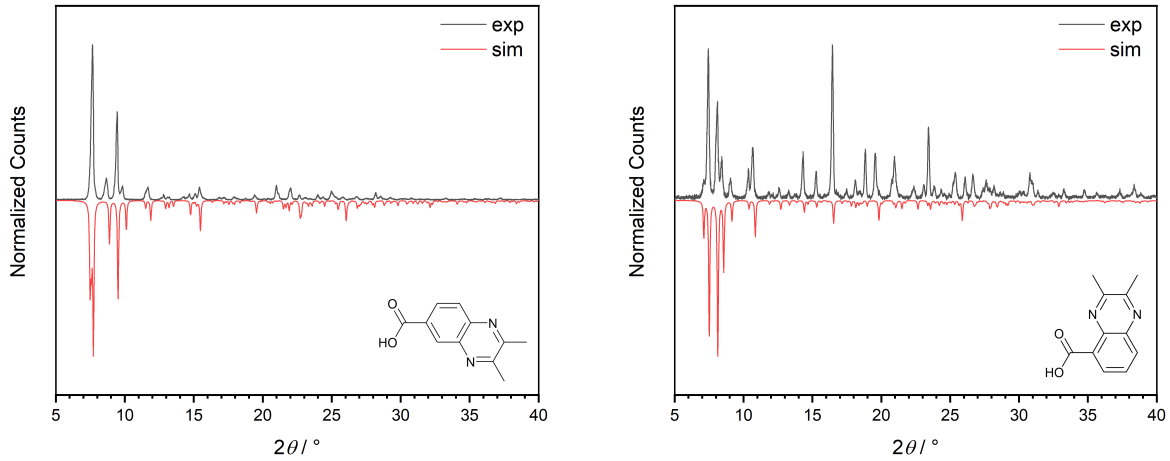


Figure 4.42: Powder X-ray diffraction patterns of **17** (left) and **18** (right), with their corresponding carboxylic acids inset.

4.4.3. Optical Properties of Quinoxalinecarboxylate Functionalised $\{Ti_6\}$-Oxo Cluster

The Kubelka-Munk function of **17** and **18** are plotted in Figure 4.43. While the π-system is extended the electron withdrawing nature of the pyrazine ring leads to band gaps in the near-UV region of 3.29 eV and 3.13 eV. The yellowish beige colour of **17** is attributed to weak absorption from 390 eV to 500 eV, whereas the strong absorption across the visible region observed for **18** are likely due to amorphous impurities of unreacted 2,3-diaminobenzoic acid.

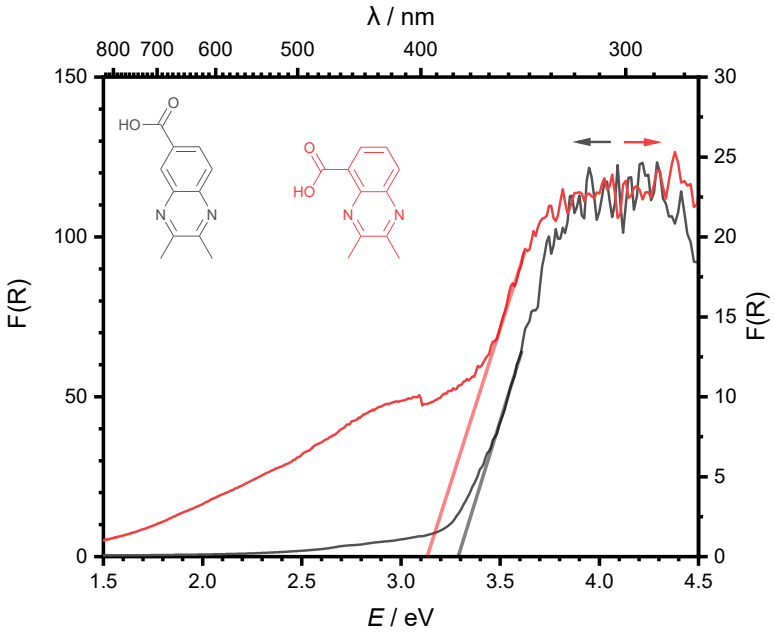
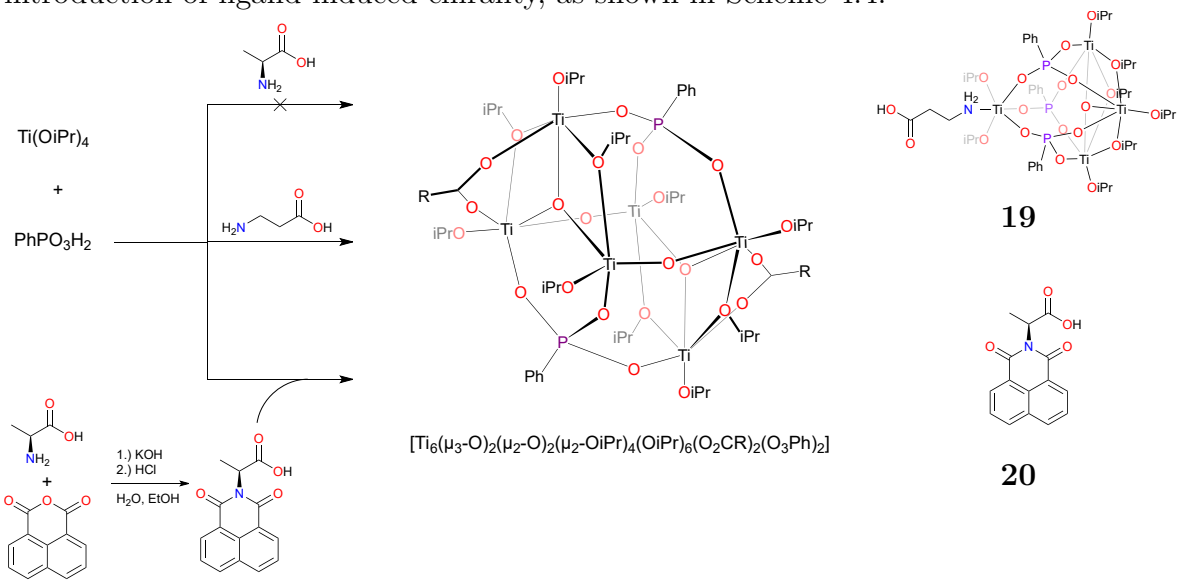


Figure 4.43: Kubelka-Munk function from the diffuse reflectance spectra of the $\{Ti_6\}$-oxo clusters **17** (black, 3.29 eV), **18** (red, 3.13 eV). Band gaps were determined by direct extrapolation.

4.5. Titanium-Oxo Clusters Derived from Alanines

4.5.1. Synthesis

The next step in the exploration of titanium-oxo clusters with amino acids was the introduction of ligand induced chirality, as shown in Scheme 4.4.



Scheme 4.4: Synthesis of the $\{Ti_6\}\{Ti_4\}_2$-oxo cluster **19** from β-alanine and the $\{Ti_6\}$-oxo cluster **20** featuring *S*-2-(1,8-naphthalimido)propanoic acid (NaphthAlaH), derived from L-alanine and naphthoic anhydride.

Here, L-alanine was chosen as a model acid as the small size of its substituents should not affect the formation of the cluster. Yet, crystallisation attempts with the free acid and the corresponding hydrochloride remained futile. It was concluded that two factors could majorly impare the cluster formation: First, proximity of the amine to the carboxylic acid, and/or second, the introduction of a chiral centre. To rule out the first, the achiral amino acid β-alanine was used which resulted in the formation of the $\{Ti_6\}$-oxo cluster **19** featuring the same core as the above compounds. Surprisingly, the amines are capped by a charge neutral $\{Ti_4\}$-oxo cluster with formula $[Ti_4(\mu_3{-}O)(\mu_2{-}OiPr)_3(OiPr)_7(O_3PPh)_3]$, a cluster first described by Mutin *et al.*.[303] This behaviour is akin to an analogous cluster described by Zhang *et al.*, made from 2-aminoisonicotinic acid, in which the $\{Ti_4\}$-oxo cluster is attached *via* the pyridine rather than the amine moiety.[377] Then, to rule out proximity of a stereocentre the free amine of L-alanine was protected as a naphthalimide. The ligand *S*-2-(1,8-naphthalimido)propanoic acid (NaphthAlaH) was prepared using the procedure of

Reger *et al.*, in which the amino acid is refluxed in an ethanolic solution containing naphthalic anhydride and potassium hydroxide, followed by acidic workup. This procedure is favourable over reactions in refluxing DMF and DMSO, as the configuration of the stereocentre is retained, as well as simple product isolation and high yields. NaphtAlaH was then used in the successful synthesis of its corresponding $\{Ti_6\}$-oxo cluster **20** under full retention of the ligand's chirality.

4.5.2. Structural Characterisation

Crystallographic data and refinement results of **19** and **20** are listed in Table 4.18. Thermal ellipsoids of their respective asymmetric units are plotted in Figure 4.44.

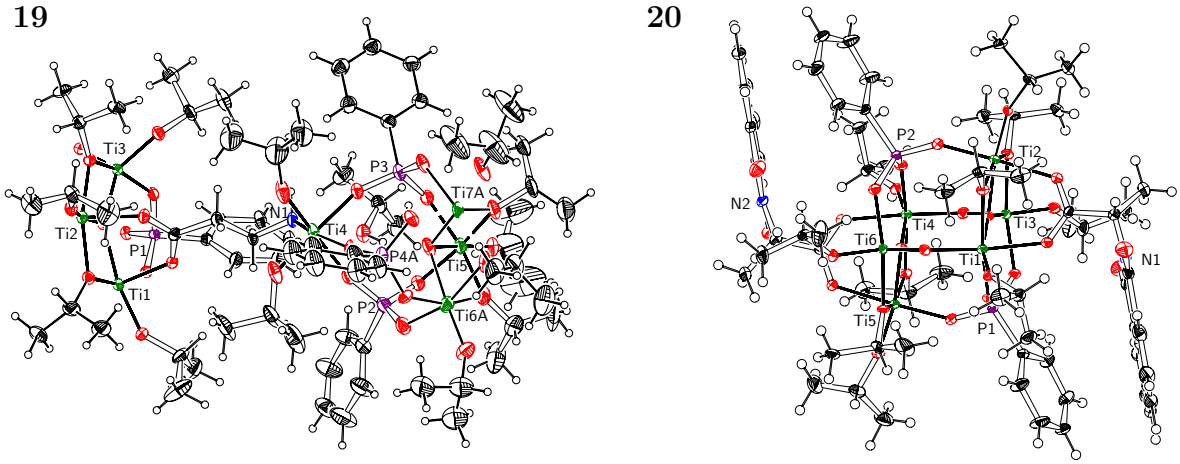


Figure 4.44: ORTEPs of the asymmetric units in the $\{Ti_6\}\{Ti_4\}_2$-oxo cluster **19** and the $\{Ti_6\}$-oxo cluster **20** at 50% probablity.

The titanium-oxo cluster **19** crystallises as the diisopropanolate as colourless needles, was solved and refined in the triclinic space group $P\bar{1}$ with half a molecule in the asymmetric unit and one molecule per unit cell. A full molecule and the packing of **19** are shown in Figure 4.45, and bond distances which are separated by cluster type are listed in Table 4.19. Bond distances in the $\{Ti_6\}$-oxo cluster are within expectations from known analogues. The $\{Ti_4\}$-oxo cluster can be described as a trigonal pyramid with Ti4 as its apex and a Ti_3O unit (Ti5-Ti7, O13) as the basal plane. The former is capped by two terminal isopropoxides as well as β-alanines amine nitrogen atom N1. The latter is respectively edge- and vertex-capped by a total of six bridging and terminal isopropoxides. The basal plane is connected to the vertex by a triad of phenylphosphonates engaging in μ_3–$\eta^1\eta^1\eta^1$ binding mode, each face-capping the

Table 4.18: Crystal data and refinement results of **19** and **20**.

Identification code	**19** · 2 iPrOH	**20**
Empirical formula	$C_{138}H_{249}N_2O_{62}P_8Ti_{14}$	$C_{72}H_{100}N_2O_{28}P_2Ti_6$
Formula weight	3846.74	1790.87
Temperature/K	100	100
Crystal description	colourless needle	colourless plate
Crystal size/mm^3	$0.202 \times 0.105 \times 0.058$	$0.361 \times 0.289 \times 0.106$
Crystal system	triclinic	triclinic
Space group	$P\bar{1}$	$P1$
a/Å	11.8643(4)	11.596(6)
b/Å	12.8947(5)	12.509(5)
c/Å	34.4722(12)	15.377(9)
α/°	91.2636(15)	101.543(16)
β/°	98.6106(13)	105.13(2)
γ/°	116.6216(12)	92.455(11)
V/Å^{-3}	4637.8(3)	2099.1(18)
Z, Z'	1, 0.5	1, 1
ρ_{calc}/g cm^{-3}	1.377	1.417
μ/mm^{-1}	0.714	0.658
$F(000)$	2015	932
Refl. total/unique	63724/19928	98681/24413
R_{int}, R_σ	0.0926, 0.1074	0.0434, 0.0408
Data/restr./param.	19928/731/1324	24413/107/1052
GooF	1.013	1.008
R_1 $[I \geq 2\sigma(I)]$, all	0.0671, 0.1414	0.0364, 0.0545
wR_2 $[I \geq 2\sigma(I)]$, all	0.1565, 0.1947	0.0751, 0.0826
$\Delta\rho_{max}/\Delta\rho_{min}$/e Å^{-3}	0.95/-0.89	0.53/-0.38
Flack parameter	-	-0.007(8)

trigonal pyramid. In total, each titanium atom in the $\{Ti_4\}$-oxo cluster is connected sixfold in a disorted octahedron. It should be noted that the coordination environment around and including Ti6 and Ti7 is disordered with half occupancy for each part, so that part of the cluster is shifted by *ca.* 0.5 Å and the terminal isopropoxides attached to the basal plane are badly resolved (here distances should be taken with a pinch of salt).

The μ_3-bridging oxygen atom O13 engages in three distinctively different bonds, separated by 0.1 Å each, with either Ti6 or Ti7 engaging in the longest and shortest bond. As packing is not affected by this, it is likely the reason for the disorder. Furthermore, when compared the $\{Ti_6\}$-oxo cluster the Ti_3O unit in the $\{Ti_4\}$-oxo cluster is contracted with respect to Ti $\cdots$ Ti distances, resulting in the O13 and the bridging isopropoxides bending out of plane. That is, $d(\text{Ti1}-3 \cdots \text{O1}) = 0.248(3)$ Å compared to $d(\text{Ti5}-7 \cdots \text{O13}) = 0.869(6)/0.711(5)$ Å. While four phenylphosphonates are present in **19**, no π-π-interactions are observed in its packing. However, the co-crystallised iso-

Table 4.19: Bond distances in the $\{Ti_6\}$- and $\{Ti_4\}$-oxo clusters of **19**.

Bond	$\{Ti_6\}$		$\{Ti_4\}$	
Ti—μ_3-O	Ti1—O1	1.999(3)	Ti5—O13	1.955(4)
	Ti2—O1	1.970(3)	Ti6—O13	2.049(7)/1.868(7)
	Ti3—O1	1.905(3)	Ti7—O13	1.852(10)/2.076(9)
Ti—μ_2-O	Ti1—O7^a	1.862(3)		
	Ti3—O7	1.758(3)		
Ti—μ_2-OiPr	Ti1—O3	2.026(3)	Ti5—O25	2.018(4)
	Ti2—O3	1.969(3)	Ti5—O29	2.002(4)
	Ti2—O5	1.957(3)	Ti6—O25	1.793(7)/2.189(6)
	Ti3—O5	2.017(3)	Ti6—O27	2.05(2)/2.002(19)
			Ti7—O27	1.98(2)/2.08(2)
			Ti7—O29	1.907(11)/2.160(10)
Ti—OiPr	Ti1—O2	1.782(3)	Ti5—O30	1.764(4)
	Ti2—O4	1.762(3)	Ti6—O26	1.75(2)/1.810(19)
	Ti3—O6	1.825(3)	Ti7—O28	1.879(10/1.696(10)
Ti—O_2CR	Ti1—O11	2.132(3)		
	Ti2—O12	2.071(3)		
RCO_2	O11—C22	1.255(5)		
	O12—C22	1.270(6)		
Ti—O_3PPh	Ti1—O9	1.970(3)	Ti4—O14	2.026(4)
	Ti2—O10^a	1.961(3)	Ti4—O17	2.051(3)
	Ti3—O8	1.946(3)	Ti4—O20	2.006(18)/1.903(19)
			Ti5—O16	1.990(4)
			Ti5—O19	1.974(4)
			Ti6—O15	1.887(7)/2.067(7)
			Ti6—O22	1.964(16)/1.933(16)
			Ti7—O18	2.105(9)/1.816(9)
			Ti7—O21	2.03(3)/1.94(3)
P—O	P1—O8	1.524(3)	P2—O14	1.497(4)
	P1—O9	1.521(3)	P2—O15	1.540(4)
	P1—O10	1.525(3)	P2—O16	1.547(4)
			P3—O17	1.497(3)
			P3—O18	1.538(4)
			P3—O19	1.539(4)
			P4—O20	1.516(19)/1.52(2)
			P4—O21	1.51(3)/1.57(3)
			P4—O22	1.548(10)/1.549(10)
Ti—N			Ti4—N1	2.199(4)

Symmetry key: ^{a} $1-x, 1-y, 1-z$.

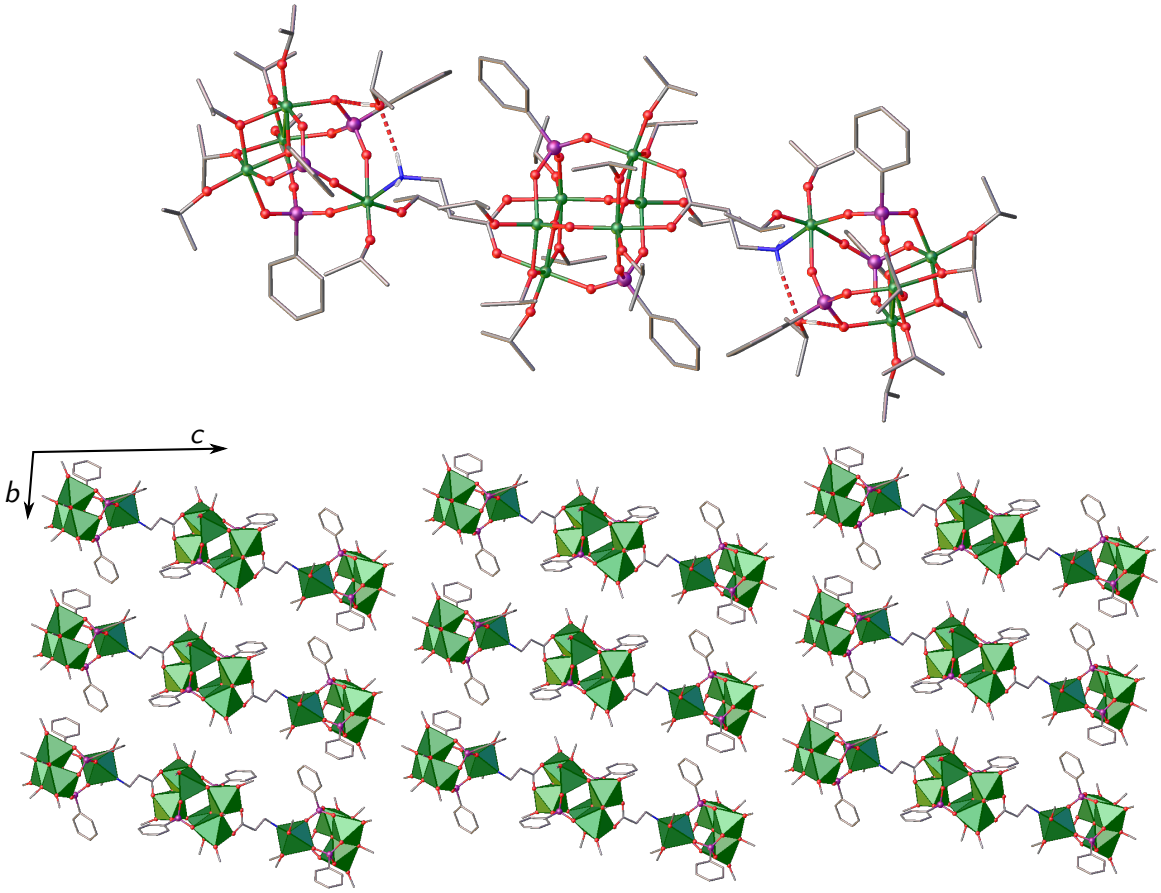


Figure 4.45: The $\{Ti_6\}\{Ti_4\}_2$-oxo cluster **19** (top) and its packing (bottom) viewed along [100].

Table 4.20: Hydrogen bonds in **19**.

Donor—H···Acceptor	*D*—H [Å]	H···*A* [Å]	*D*···*A* [Å]	*D*—H···*A* [°]
N1—H1B···O31	0.91	2.07	2.965(6)	168
O31—H31···O16	0.84	2.17	2.966(5)	158
O31—H31···O19	0.84	2.54	3.138(5)	129

propanol acts as both an acceptor in a moderate hydrogen bond from β-alanine's N1, as well as donor in a bifurcated hydrogen bond to phenylphosponates on the $\{Ti_4\}$-oxo cluster with O16 (moderate) and O19 (weak) as acceptors (see Table 4.20).

The $\{Ti_6\}$-oxo cluster **20**, featuring the chiral carboxylate NaphthAla, crystallises as colourless plates and was solved and refined in the chrial triclinic space group $P1$ with one molecule in the asymmetric unit and unit cell. A full cluster of **20** and its packing are shown in Figure 4.46. While the molecule exhibits overall chirality the cluster core

remains pseudo-centrosymmetrical, which is reflected in the bond distances listed in Table 4.21. The biggest discrepancy between the two Ti_3O units is seen in the titanium carboxylate bonds, namely those attached to Ti1 and Ti2, differ by 0.02 Å, whereas those attached to Ti4 and Ti5 are within standard deviation.

The naphthalimides are located and oriented in pseudo-centrosymmetric positions and orientations with torsion angles of θ(O11—C22—C23—N1)= 21.3(5)° and θ(O25—C59—C60—N2)= 20.5(5)°. However, as both ligands possess the same chirality, the C—H bonds at the stereocentre are pointing away from and into the Ti_3O unit, respectively for the ligands involving N1 and N2. The packing of **20** is governed by parallel displaced π-π-interactions, leading to a 1D chain along [111], between symmetry independent naphthalimides with $d_{\pi-\pi}$ = 3.436(3)/3.394(3) Å, a shift of 1.458(4) Å at an angle of 1.70(6)°, making the planes essentially parallel.

Figure 4.47 shows a comparison between stacking of the naphthalimides in **20** and NaphthAlaH.[378] Stacking naphthalimides in the latter are displaced by 3.49 Å, shifted by 1.20 Å and tilted by 0.4°.

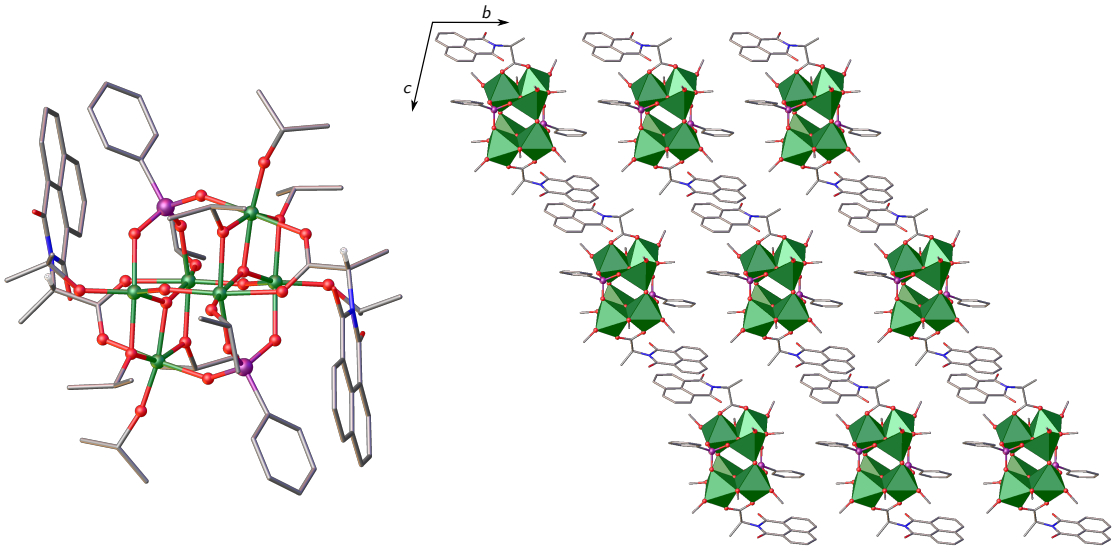


Figure 4.46: The $\{Ti_6\}$-oxo cluster **20** (top) and its packing (bottom) viewed along [$\bar{1}$00].

Table 4.21: Bond distances in the {Ti_6}–oxo clusters of **20**.

Bond		Distance		
Ti—μ_3-O	Ti1—O1	2.003(3)	Ti4—O15	2.003(3)
	Ti2—O1	1.968(3)	Ti5—O15	1.978(3)
	Ti3—O1	1.919(3)	Ti6—O15	1.901(3)
Ti—μ_2-O	Ti1—O21	1.874(3)	Ti4—O7	1.859(4)
	Ti3—O7	1.770(4)	Ti6—O21	1.766(3)
Ti—μ_2-OiPr	Ti1—O3	2.045(3)	Ti4—O17	2.030(3)
	Ti2—O3	1.974(3)	Ti5—O17	1.970(3)
	Ti2—O5	1.959(3)	Ti5—O19	1.954(3)
	Ti3—O5	2.042(4)	Ti6—O19	2.030(3)
Ti—OiPr	Ti1—O2	1.797(3)	Ti4—O16	1.792(3)
	Ti2—O4A	1.793(8)	Ti5—O18	1.769(4)
	Ti2—O4B	1.739(14)		
	Ti3—O6	1.797(4)	Ti6—O20	1.814(4)
Ti—O_2CR	Ti1—O11	2.117(4)	Ti4—O25	2.121(4)
	Ti2—O12	2.139(4)	Ti5—O26	2.128(3)
RCO_2	O11—C22	1.257(6)	O25—C59	1.268(6)
	O12—C22	1.260(6)	O26—C59	1.264(6)
Ti—O_3PPh	Ti1—O9	1.967(3)	Ti4—O23	1.976(3)
	Ti2—O24	1.946(3)	Ti5—O10	1.937(3)
	Ti3—O8	1.968(3)	Ti6—O22	1.972(3)
P—O	P1—O8	1.534(4)	P2—O22	1.530(4)
	P1—O9	1.536(3)	P2—O23	1.526(3)
	P1—O10	1.541(4)	P2—O24	1.531(4)

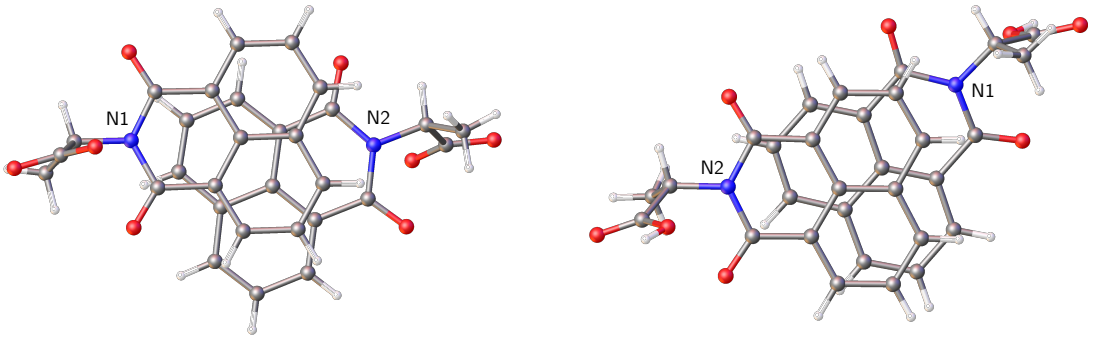


Figure 4.47: Comparison between the π-π-stacking in **20** (left) and NaphthAlaH (right).

4.5.3. Optical Properties of 20

The Kubelka-Munk function of and solid state emission spectrum of **20** are shown in Figure 4.48. It displays a band gap of 3.19 eV, as well as a strong absorption band with a maximum at 264 nm which is associated with a $\pi \rightarrow \pi^*$ transition in the naphthalimide. When excited at 365 nm, **20** fluoresces yellowish green with a maximum at 674 nm, which is a redshift of 125 nm to the blue fluorescing NaphthAlaH.

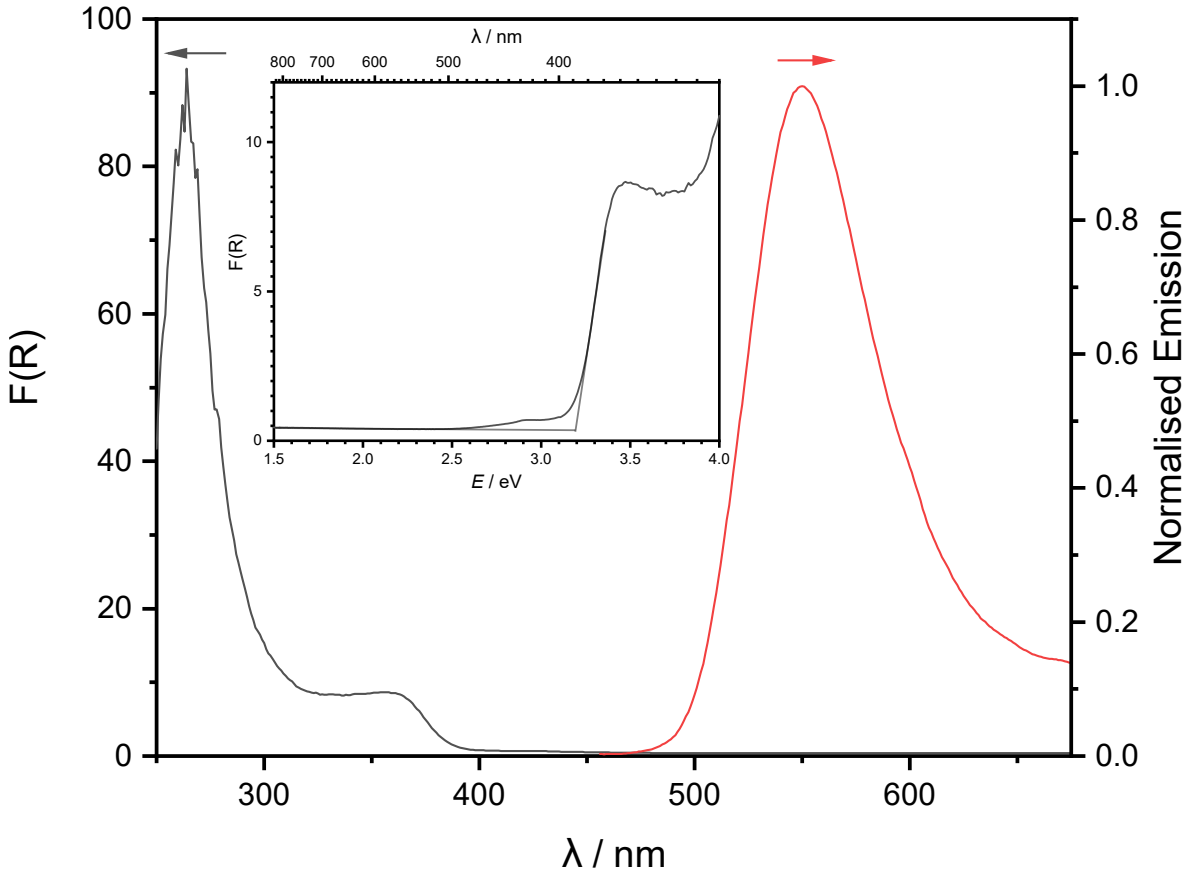


Figure 4.48: Kubelka-Munk function (black) from the diffuse reflectance spectrum and solid state emission spectrum (red, $\lambda_{exc} = 365$ nm) of the $\{Ti_6\}$-oxo cluster **20**. The inset highlights the band gap (3.19 eV), determined by direct extrapolation. The intense absorption band with $\lambda_{max} = 264$ nm is associated with a $\pi \rightarrow \pi^*$ transition in the naphthalimide.

4.6. Conclusion

A series of phosphate stabilised TOCs based on the $\{Ti_6P_2\}$ motif featuring amino acids and their respective Schiff bases were synthesised, structurally analysed, and functional as well as positional effects of the substituent on the optical band gap of the clusters discussed. As the clusters self assemble in a mixture of at least four components and side products cannot be separated conveniently, the exploration of chemical reaction space and understanding synthetic limitations provide a necessary handle in designing reactions to obtain pure target materials.

While *meta*- and *ortho*-aminosubstituted benzoatic acids produce pure products (**13a**-**15a**), the addition of aq. HCl provides a handle that facilitates formation of the *para*-aminosubstituted $\{Ti_6\}$-oxo cluster **11** over the $\{Ti_5\}$-oxo cluster **10**, or can lead to chloride doping of the cluster core (**16a**). Introduction of these electron-rich substituents leads to reduction of the TOCs optical band gap, more severely so when the mesomeric effect dominates the inductive effect (*meta*>*ortho*>*para*). Depending on whether it was formed under nitrogen or in air, **14a** may be obtained with a band gap in the violet or infrared regions, while analytically otherwise identical, highlighting the importance of serendipity when in TOC synthesis.

The addition of aldehydes to the reaction mixture provided further insights into the importance of serendipity in these reactions as well as substituent influence onto the optical band gap: while *meta*- and *para*-substitution resulted in the formation of corresponding Schiff bases, *ortho*-substitution has either no effect or leads to a Meerwein-Ponndorf-Verley type reduction to the corresponding methylamine for electron-donating or -withdrawing aldehydes, respectively. Akin to previous observations, band gap reductions are more pronounced when substituents are electron-rich and in conjugation-enabling positions.

While the no TOCs could be obtained for *ortho*-diaminosubstitution, the addition of diacetyl led to quinoxaline functionalised TOCs, featuring wider band gaps than those observed for free amines due to the quinoxalines' electron-withdrawing nature.

Finally, chirality could be introduced near the cluster core and the proximity of a free aliphatic amine determined to be a limiting factor in the synthesis of $\{Ti_6P_2\}$ clusters.

The aminobenzoate substituted $\{Ti_6\}$-oxo clusters **11a**, **14a**, **15a** and **16a** show great promise for proton reduction catalysis using visible instead of UV light. Moreover, **15a** and **16a** features amines in the vicinity of the titanium-oxo cluster core which could promote CO_2 reduction akin NH_2-MIL-125(Ti). Lastly, the introduction of chirality near the cluster core should be investigated further and might find application in enatioselective Lewis acid catalysis.

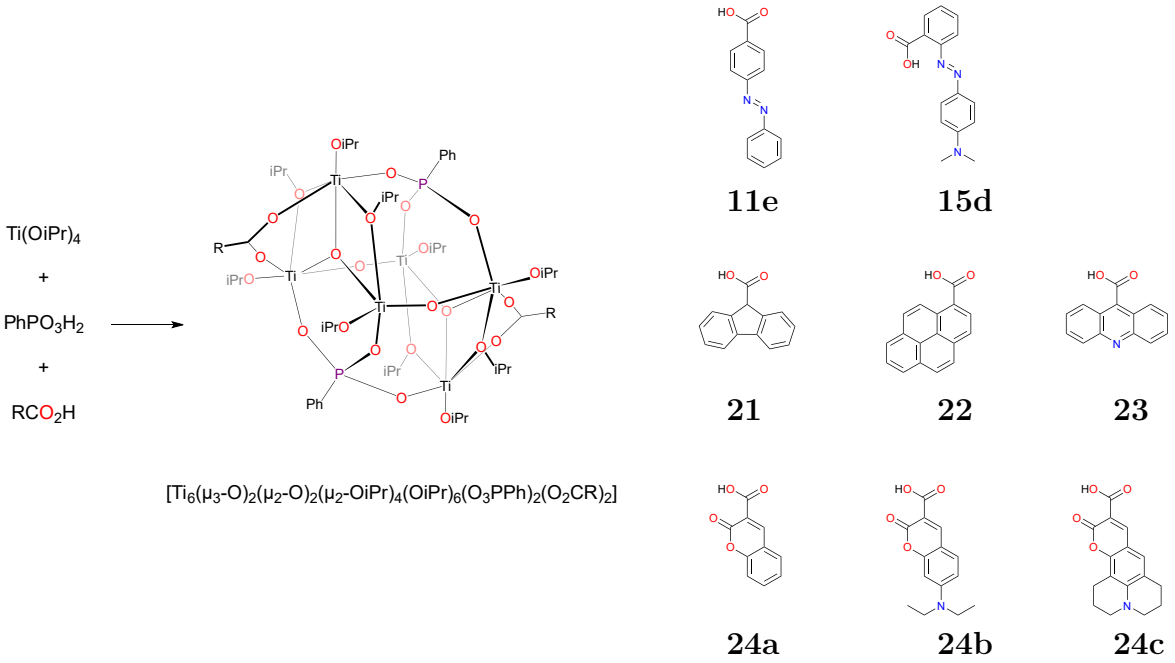
5. Phosphonate Stabilised $\{Ti_6\}$-Oxo Clusters with Extended π-Systems

5.1. Introduction

The results presented in the previous chapter have corroborated the robustness of the $\{Ti_6P_2\}$ motif and is expanded on in this chapter. The objective was to conduct further band gap engineering by making use of organic dye molecules and fused-aromatic ring systems. Moreover, further investigations of Meerwein-Ponndorf-Verley (MPV) type reaction were undertaken. Finally, an attempt to quantify the band gaps of TOCs featuring the $\{Ti_6P_2\}$ motif reported in this work and the literature based on electronic ligand properties through Hammett constants is made.

5.2. Synthesis

The synthesis of {Ti_6}-oxo clusters with extended π-systems is shown in Scheme 5.1.



Scheme 5.1: Synthesis of {Ti_6}-clusters featuring azo groups (**11e** and **15d**), larger fused-aromats (**21**, **22** and **23**) and coumarin carboxylates (**24a**–**c**) with their corresponding carboxylic acids.

Here, the azo-dyes 4-(phenylazo)benzoic acid (PhN_2BzH) and Methyl Red (MRH) were chosen for strong absorption in the visible spectrum and their kinship to Schiff base-benzoates used in the previous chapter. fused-aromatic rings such as fluorene-9-, pyrene-1- and acridine-9-carboxylic acid were chosen to conduct further band gap engineering and test the influence of low solubility (pyrene) and steric limitations (acridine). However, neither of the latter seemed to hinder the crystallisation of the {Ti_6}-system. Moreover, π-π-stacking of the larger aromatic rings might be beneficial for charge transfer throughout the material. Furthermore, the system was exposed to coumarin carboxylic acids to see whether they would also attach with a bridging carboxylate or chelating malonate binding mode, akin to {Ti_{17}}-oxo cluster featuring coumarin 343 (C343) reported by Coppens *et al.*[266]

5.3. {Ti_6}-Oxo Clusters with Azobenzoates

5.3.1. Structural Characterisation

Crystal data and refinement results for the {Ti_6}-oxo clusters **11e** and **15d** from the azobenzoic acids PhN_2BzH and MRH is listed in Table 5.1 and the thermal ellipsoids of their asymmetric units are plotted in Figure 5.1. A selection of distances and angles is given in Table 5.2.

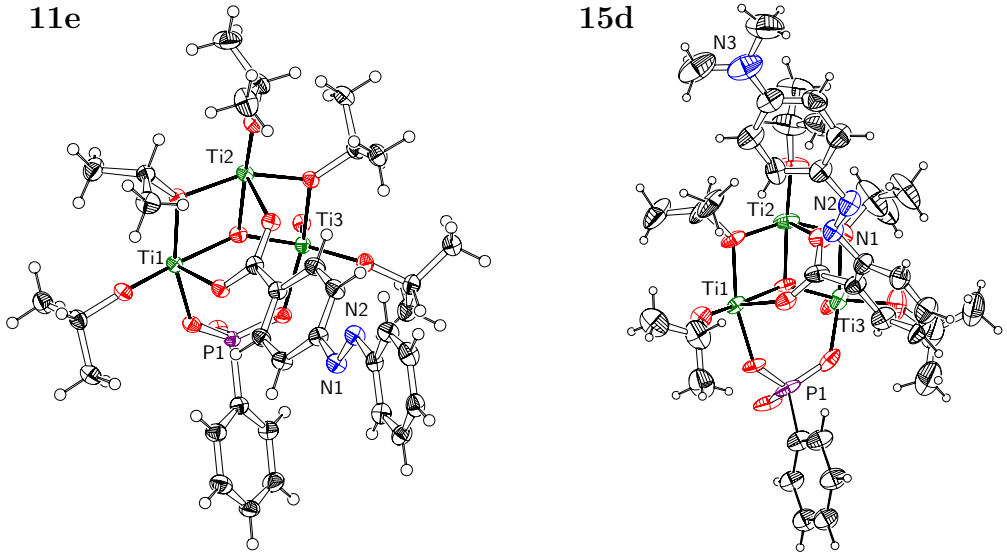


Figure 5.1: ORTEPs of the asymmetric units in the {Ti_6}-oxo clusters **11e** and **15d** with azo-dye benzoic acids, respectively at 50% and 30% probablity. Disorder was omitted for clarity.

11e was isolated as red plates and was solved and refined in the triclinic space group $P\bar{1}$. A complete cluster and the packing of **11e** are portrayed in Figure 5.2. Moreover, **11e** is not only isostructural and isoelectronic to **11c**, but also isomorphous. Thus, hydrogen bonding and π-stacking are absent as well and the packing displays no special features. Additionally, even their bond lengths are almost within 5σ.

The {Ti_6}-oxo cluster **15d**, obtained from Methyl Red, crystallises as red needles that tend to intergrow, twin, and generally diffract poorly, leading to a low-quality data set. **15d** was solved and refined in the monoclinic space group $P2_1/n$ with half of a molecule in the asymmetric unit and two molecules per unit cell. A full cluster and a packing diagram are shown in Figure 5.3. While **15d** can be seen as a derivative of **15a**, unlike in **15b**, the N=X double bound is not reduced during the cluster formation, leading

Table 5.1: Crystal data and refinement results of **11e** and **15d**.

Identification code	**11e**	**15d**
Empirical formula	$C_{68}H_{98}N_4O_{24}P_2Ti_6$	$C_{72}H_{108}N_6O_{24}P_2Ti_6$
Formula weight	1704.84	1790.98
Temperature/K	100	100
Crystal description	orange plate	red fragment
Crystal size/mm^3	0.481 × 0.196 × 0.066	0.171 × 0.180 × 0.05
Crystal system	triclinic	monoclinic
Space group	$P\bar{1}$	$P2_1/n$
a/Å	13.1446(10)	17.024(2)
b/Å	13.3536(10)	14.5808(19)
c/Å	13.9746(11)	19.425(3)
α/°	114.555(2)	90
β/°	96.306(2)	114.741(4)
γ/°	113.224(2)	90
V/Å^{-3}	1937.3(3)	4379.1(10)
Z, Z'	1, 0.5	2, 0.5
ρ_{calc}/g cm^{-3}	1.461	1.358
μ/mm^{-1}	0.706	0.629
$F(000)$	888	1872
Refl. total/unique	8372/38465	8063/35876
R_{int}, R_σ	0.0738, 0.0538	0.0948, 0.1032
Data/restr./param.	8372/0/479	8063/155/539
GooF	1.026	1.041
R_1 $[I \geq 2\sigma(I)]$, all	0.0487, 0.0862	0.1448, 0.2468
wR_2 $[I \geq 2\sigma(I)]$, all	0.1074, 0.1292	0.2740, 0.3303
$\Delta\rho_{max}/\Delta\rho_{min}$/e Å^{-3}	0.84/-0.49	0.89/-0.68

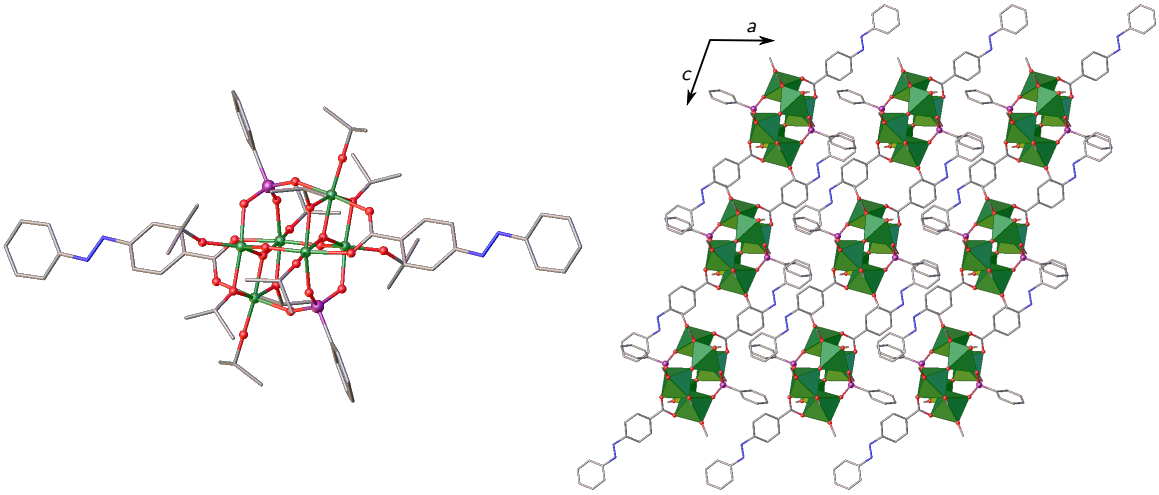


Figure 5.2: The {Ti_6}-oxo cluster **11e** (left) and its packing (right) viewed along [010].

to a lack of flexibility in the former compared to the latter. The steric encumbrance between the (dimethylamino-4-phenyl)azo group and isopropoxides forces the whole

Table 5.2: Bond lengths in **11f** and **15d** in Å.

Bond	Distance	**11e**	**15d**
Ti—μ_3-O	Ti1—O1	1.998(2)	1.979(9)
	Ti2—O1	1.961(2)	1.956(7)
	Ti3—O1	1.913(2)	1.910(9)
Ti—μ_2-O	Ti1—O7^a	1.892(2)	1.876(9)
	Ti3—O7	1.737(2)	1.732(8)
Ti—μ_2-OiPr	Ti1—O3	2.010(2)	2.001(8)
	Ti2—O3	1.984(2)	1.969(11)
	Ti2—O5	1.943(2)	1.950(11)
	Ti3—O5	2.037(2)	2.027(10)
Ti—OiPr	Ti1—O2	1.776(2)	1.774(9)
	Ti2—O4	1.761(2)	1.755(9)
	Ti3—O6	1.810(2)	1.802(11)
Ti—O_2CR	Ti1—O11	2.105(2)	2.126(9)
	Ti2—O12	2.093(2)	2.089(9)
RCO_2	O11—C22	1.265(4)	1.260(17)
	O12—C22	1.267(4)	1.272(15)
Ti—O_3PPh	Ti1—O9	1.965(2)	1.945(8)
	Ti2—O10^a	1.935(2)	1.952(9)
	Ti3—O8	1.974(2)	1.936(11)
P—O	P1—O8	1.525(2)	1.547(11)
	P1—O9	1.522(2)	1.528(9)
	P1—O10	1.522(2)	1.509(9)
N=N	N1—N2	1.253(4)	1.267(16)
N—C	N1—C_{Bz}	1.435(4)	1.419(18)
	N2—C_{Ph}	1.434(4)	1.407(19)
Angles		**11e**	**15d**
$Ti_2O_2 \cdots O_2C$		3.2(5)	12.9(19)
$O_2C \cdots C_6$		0.74(3)	73.6(5)
$C_6 \cdots N_2R$		33.35(15)	36.9(6)

Symmetry key: ^{a} $1-x, 1-y, -z$ (for **11e**); $1-x, 1-y, 1-z$ (for **15d**).

group to turn almost perpendicular to Ti1$\cdots$Ti2 (76.1(7)°). Neither hydrogen bonding nor π-πstacking are observed in the packing of **15d**.

The powder X-ray diffraction patterns of **11e** and **15d**, shown in Figure 5.4, confirm phase purity of both clusters.

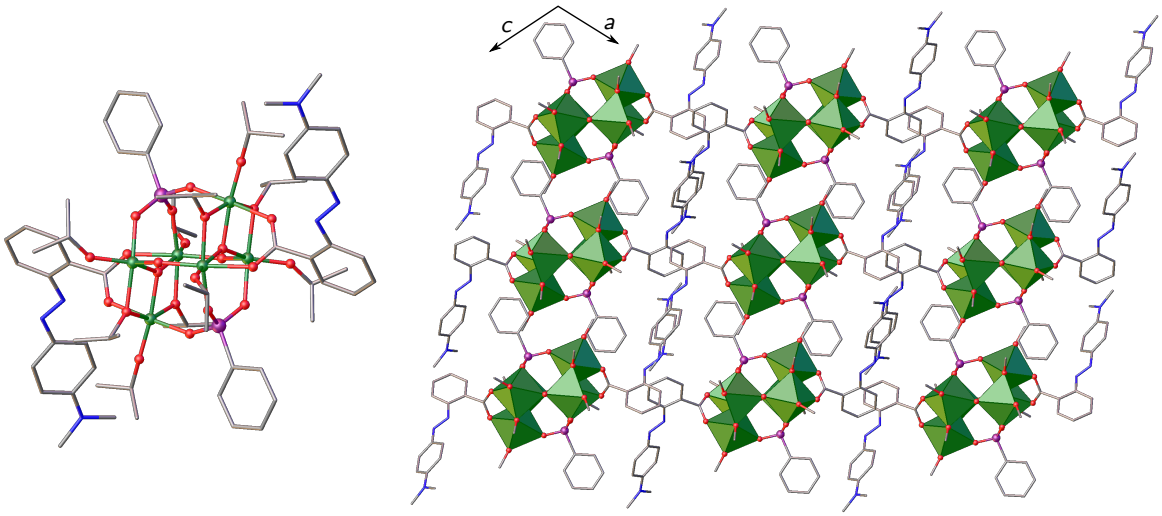


Figure 5.3: The {Ti_6}-oxo cluster **15d** (left) and its packing (right) viewed along [010].

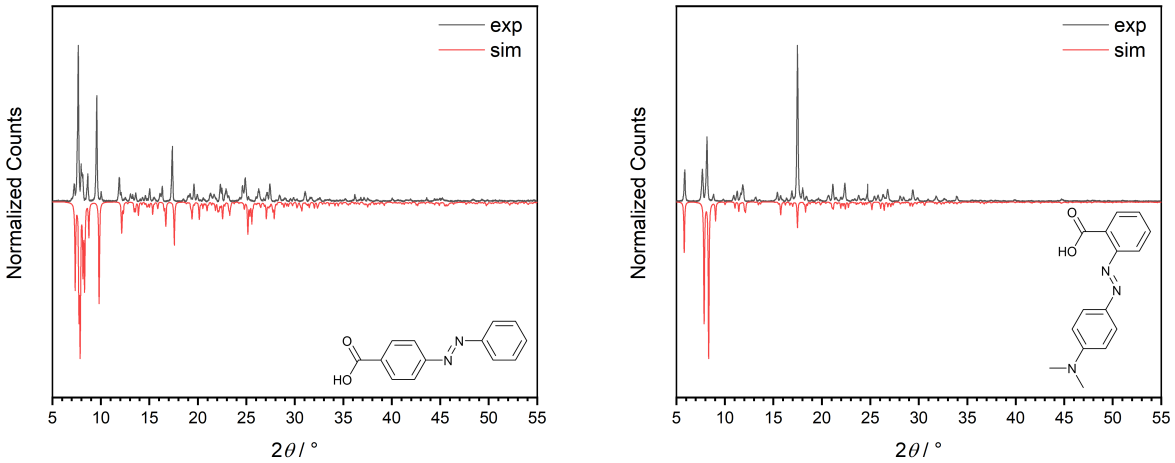


Figure 5.4: Powder X-ray diffraction patterns of **11e** (left) and **15d** (right), with their corresponding carboxylic acids inset.

5.3.2. Optical Properties of Azo-Functionalised $\{Ti_6\}$-Oxo Clusters

The Kubelk-Munck function derived from diffuse reflectance spectra of the azobenzoate substituted $\{Ti_6\}$-oxo cluster **11e** and **15d** are plotted in Figure 5.5. For **11e** two distinct optical transitions, the O(p)→Ti(d) band gap at 3.10 eV as well as a second band with a maximum at 459 nm, associated with ligand entered n→ π transition of the phenylazobenzoate, are observed. However, for **15d** the absorption of light is consistent up to 500 nm and exhibits a band gap of 2.00 eV. The lower band gap of **15d** compared to **11e** is attributed to the electron donating nature of the dimethylamino group and the resulting push-pull properties of the molecule. Further studies of azobenzoate functionalised $\{Ti_6\}$-oxo cluster should incorporate *para*-Methyl Red to investigate whether the more consistent absorption of **15d** stems from spacial proximity or the push-pull effect.

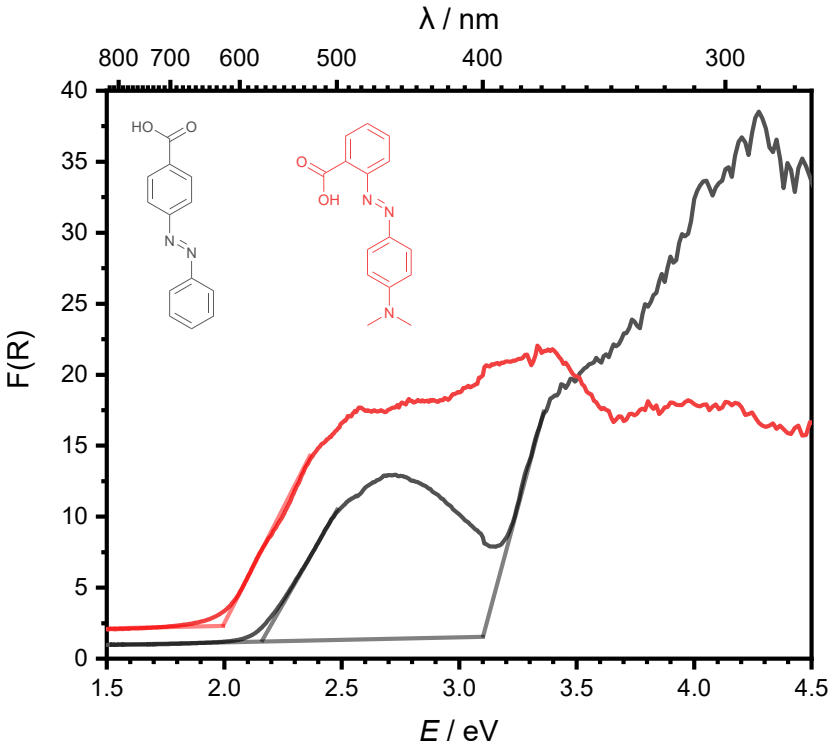


Figure 5.5: Kubelka-Munk function from the diffuse reflectance spectra of the azobenzoate substituted $\{Ti_6\}$-oxo clusters **11e** (black, 3.10 eV, 2.16 eV), **15d** (red, 2.00 eV). Bandgaps were determined by direct extrapolation.

5.4. {Ti_6}-Oxo Clusters with Fused Aromatic Rings

5.4.1. Structural Characterisation

Crystal data and refinement results of the {Ti_6}-oxo clusters **21**, **22** and **23**, respectively featuring fluorene-9-, pyrene-1-, and acridine-9-carboxylate, are listed in Table 5.3. Thermal ellipsoid plots of the asymmetric units in **21** and **22** are shown in Figure 5.6, and a selection of bond distances and angles are given in Table 5.4. All three crystallise neat and were solved and refined in the triclinic space group $P\bar{1}$.

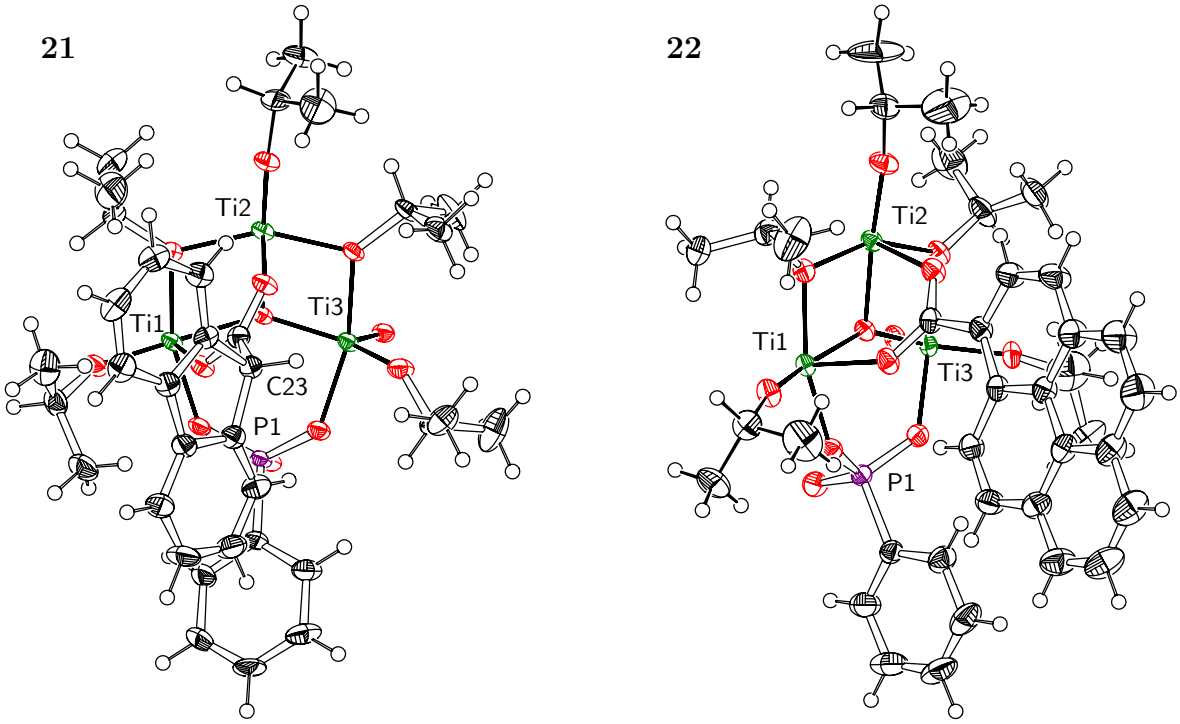


Figure 5.6: ORTEPs of the asymmetric units in the {Ti_6}-oxo clusters **21** and **22**, featuring carboxylates of extended π-systems, plotted at 50% probablity. Disorder was omitted for clarity.

21 was isolated as colourless plate and has half of a molecule in the asymmetric unit and one per unit cell. All bond distances lie within expectation. The fluorenyl moiety is twisted towards the isopropoxide coordinated to Ti1, with its plane normal almost perpendicular to O2—C2 (96.2(2)°) and C23—H23 and Ti1—O1 quasi-aligned (159.15(19)°). The packing of **21** exhibits weak T-shaped π-π-stacking from the phenylphosphonate onto the fluorenyl moiety of an adjacent cluster, with distances of 2.67 Å and 3.04 Å from H18 to the plane and closest carbon atom, respectively. As

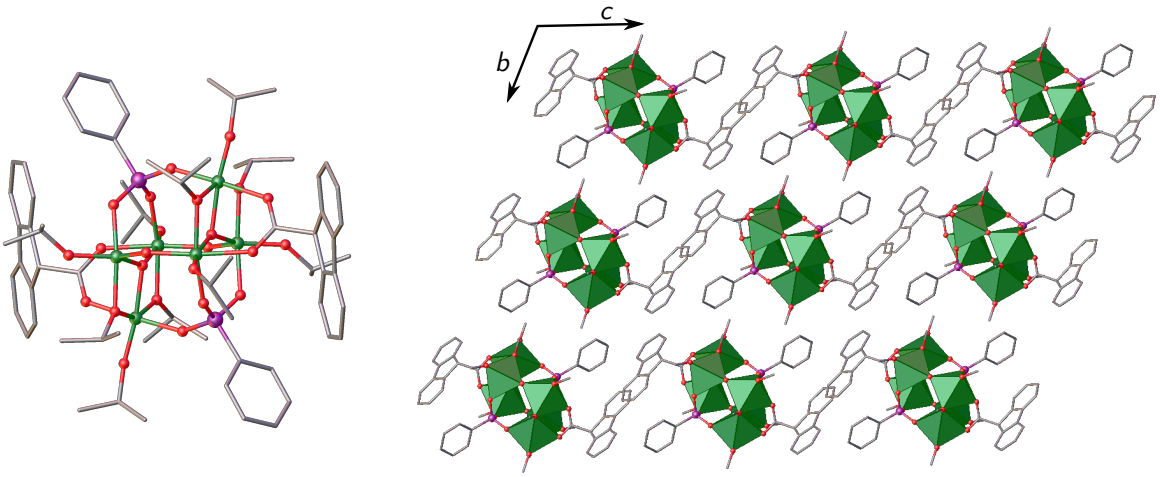


Figure 5.7: The {Ti_6}-oxo cluster **21** (left) and its packing (right) viewed along [100].

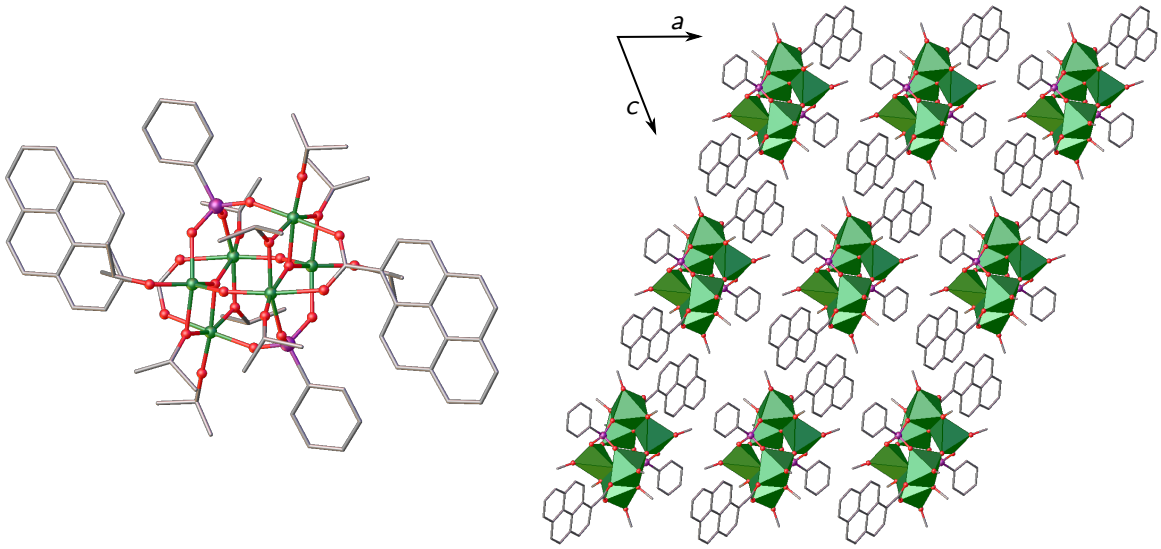


Figure 5.8: The {Ti_6}-oxo cluster **22** (left) and its packing (right) viewed along [010].

this occurs back and forth between clusters related through inversion symmetry, the result is a π-stacked 1D chain along the *c*-axis.

The {Ti_6}-oxo cluster **22** was isolated as yellow crystals. All bond distances are within the expected range and the pyrene moiety is twisted from the carboxylate in a way that it is almost parallel to Ti2—O1. The packing in **22** is governed by parallel displaced π-π-stacking involving the pyrene moiety: on one side of the ligand, with its symmetry equivalent through inversion ($d_{\pi-\pi}$ = 3.598(2) Å, shifted by 3.021(2) Å) so that the rings involving C25 and C38 overlap. And on the other side, the ring involving C33 interacts with the phenylphosphonate of an adjacent cluster with $d_{\pi-\pi}$ = 3.495(3) Å,

Table 5.3: Crystal data and refinement results of **21**, **22** and **23**.

Identification code	**21**	**22**	**23**
Empirical formula	$C_{70}H_{98}O_{24}P_2Ti_6$	$C_{76}H_{98}O_{24}P_2Ti_6$	$C_{70}H_{96}N_2O_{24}P_2Ti_6$
Formula weight	1672.82	1744.88	1698.82
Temperature/K	100	100	100
Crystal description	colourless plate	yellow fragment	yellow fragment
Crystal size/mm^3	$0.256 \times 0.099 \times 0.056$	$0.256 \times 0.191 \times 0.178$	$0.205 \times 0.183 \times 0.129$
Crystal system	triclinic	triclinic	triclinic
Space group	$P\bar{1}$	$P\bar{1}$	$P\bar{1}$
a/Å	12.090(4)	12.0329(5)	14.243(10)
b/Å	12.385(4)	13.0644(5)	25.533(18)
c/Å	15.460(5)	14.8187(5)	34.92(2)
α/°	107.934(8)	83.5870(10)	82.586(10)
β/°	98.987(11)	67.3040(10)	80.605(19)
γ/°	110.183(8)	74.4840(10)	78.063(10)
V/Å^{-3}	1975.9(11)	2070.73(14)	12197(15)
Z, Z'	1, 0.5	1, 0.5	6, 3
ρ_{calc}/g cm^{-3}	1.406	1.399	1.388
μ/mm^{-1}	0.69	0.661	0.672
$F(000)$	872	908	5304
Refl. total/unique	8113/34177	9624/48105	58243/268772
R_{int}, R_σ	0.0980, 0.0772	0.0374, 0.0261	0.0785, 0.0819
Data/restr./param.	8113/73/500	9624/34/557	58243/1102/3244
GooF	1.016	1.018	1.002
R_1 $[I \geq 2\sigma(I)]$, all	0.0473, 0.0972	0.0341, 0.0476	0.0588, 0.1401
wR_2 $[I \geq 2\sigma(I)]$, all	0.0942, 0.1122	0.0869, 0.0947	0.1180, 0.1458
$\Delta\rho_{max}/\Delta\rho_{min}$/e Å^{-3}	0.42/-0.39	0.95/-0.49	1.44/-0.83

shifted by 1.444(5) Å and tilted by 9.94(11)°. In total, this four plane π-π-stack results in a 2D network with symbol **sql** with plane normal (110).

Table 5.4: Bond lengths in **21** and **22** in Å.

Bond	Distance	**21**	**22**
Ti—μ_3-O	Ti1—O1	1.989(2)	2.0009(12)
	Ti2—O1	1.985(2)	1.9625(13)
	Ti3—O1	1.894(2)	1.9030(12)
Ti—μ_2-O	Ti1—O7^a	1.868(2)	1.8568(13)
	Ti3—O7	1.764(2)	1.7540(13)
Ti—μ_2-OiPr	Ti1—O3	2.017(2)	2.0312(13)
	Ti2—O3	1.978(2)	1.9798(13)
	Ti2—O5	1.966(2)	1.9517(13)
	Ti3—O5	2.025(2)	2.0355(13)
Ti—OiPr	Ti1—O2	1.773(2)	1.7696(13)
	Ti2—O5	1.966(2)	1.9517(13)
	Ti3—O6	1.808(2)	1.7933(14)
Ti—O_2CR	Ti1—O11	2.119(2)	2.1186(13)
	Ti2—O12	2.082(2)	2.0794(13)
RCO_2	O11—C22	1.258(4)	1.254(2)
	O12—C22	1.257(4)	1.272(2)
Ti—O_3PPh	Ti1—O9	1.969(2)	1.9677(13)
	Ti2—O10^a	1.942(2)	1.9377(13)
	Ti3—O8	1.974(2)	1.9632(13)
P—O	P1—O8	1.519(2)	1.5231(13)
	P1—O9	1.522(2)	1.5256(14)
	P1—O10	1.521(2)	1.5197(13)
Angles		**21**	**22**
$Ti_2O_2\cdots O_2C$		3.1(4)	0.4(3)
$O_2C\cdots Ar$		123.82(18)	25.66(10)

Symmetry key: $^a 2-x, 1-y, 1-z$ (for **21**), $1-x, 1-y, 1-z$ (for **22**).

The {Ti_6}-oxo cluster from acridine carboxylic acid, **23**, crystallises as yellow blocks with six molecules per unit cell. The asymmetric unit of three molecules can be divided into four asymmetric residue units (ARUs), with ARU 1 (Ti1-3, acridine involving N1) and ARU 2 (Ti4-6, acridine involving N2) containing half of a cluster, and ARU 3 (Ti6-12, acridines involving N3A/B and N4) and ARU 4 (Ti13-18, acridines involving N3A/B and N4) containing a full pseudo-inversion symmetric cluster each. This means, that a loss of symmetry has occurred, relative to the aforementioned clusters. The thermal ellipsoids of the asymmetric unit are plotted in Figure 5.9 and full clusters of each ARU are shown in Figure 5.10. The only notable difference between the ARUs in the latter is rotation of the phenyl phosphonate.

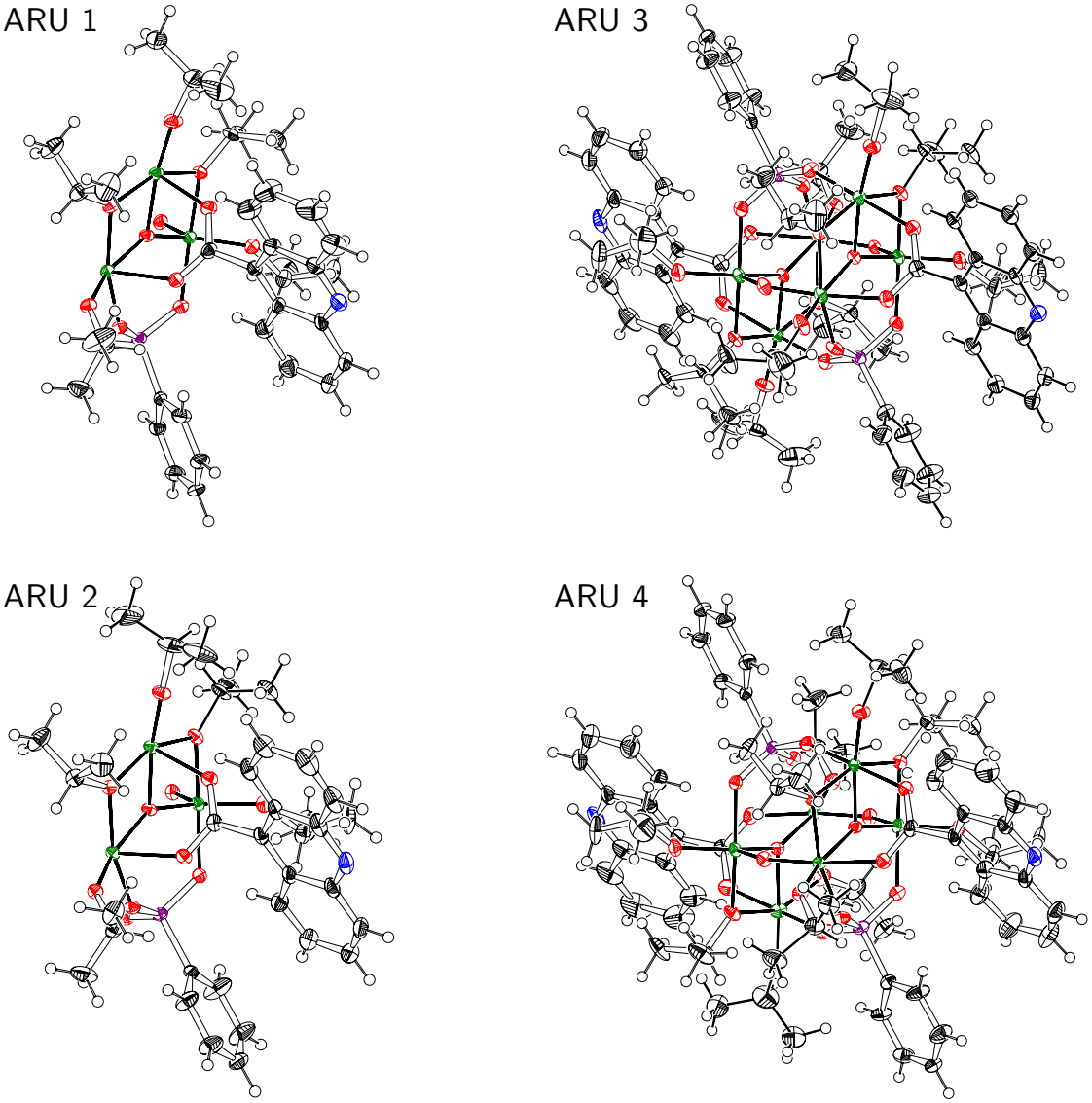


Figure 5.9: ORTEPs of the four asymmetric residue units (ARUs) found in **23** drawn at 50% probability. Disorder was ommited for clarity.

An inspection of the bond distances (see Table 5.5) in **23** reveals only minor deviations from each other among different ARUs, and pseudo-inversion symmetric distances within a cluster deviate at most by 3σ. The acridine moeties are twisted by approx. 54° to 63° to the carboxylate, so that their planes are essentially orthogonal to Ti1—O1 (and equivalents for other residues).

The packing of **23**, shown in Figure 5.11, is governed by π-π-stacking between acridine moieties. An elucidation of of these interactions is given in Figure 5.12.

It should be noted that stacking, unlike in most other {Ti_6}-oxo cluster in this work,

Table 5.5: Bond distances and angles in **23** in Å.

Bond		ARU 1/2		ARU 3/4		
Ti—μ_3-O	Ti1—O1	1.990(3)	Ti7—O25	2.021(3)	Ti10—O37	1.994(3)
	Ti2—O1	1.9625(13)	Ti8—O25	1.985(3)	Ti11—O37	1.985(3)
	Ti3—O1	1.921(3)	Ti9—O25	1.900(3)	Ti12—O37	1.913(3)
Ti—μ_2-O	Ti1—O7^a	1.861(3)	Ti7—O43	1.856(3)	Ti10—O31	1.862(3)
	Ti3—O7	1.772(2)	Ti9—O31	1.770(2)	Ti12—O43	1.781(3)
Ti—μ_2-OiPr	Ti1—O3	2.019(3)	Ti7—O27	2.033(3)	Ti10—O39	2.023(3)
	Ti2—O3	1.986(3)	Ti8—O27	1.982(3)	Ti11—O39	1.990(3)
	Ti2—O5	1.971(3)	Ti8—O29	1.972(3)	Ti11—O41	1.976(3)
	Ti3—O5	2.028(3)	Ti9—O29	2.029(3)	Ti12—O41	2.024(3)
Ti—OiPr	Ti1—O2	1.804(3)	Ti7—O26	1.789(3)	Ti10—O38	1.794(3)
	Ti2—O4	1.773(3)	Ti8—O28	1.769(3)	Ti11—O40	1.764(3)
	Ti3—O6	1.806(3)	Ti9—O30	1.809(3)	Ti12—O42	1.805(3)
Ti—O_2CR	Ti1—O11	2.176(3)	Ti7—O35	2.144(3)	Ti10—O47	2.175(3)
	Ti2—O12	2.088(3)	Ti8—O36	2.091(3)	Ti11—O48	2.098(3)
RCO_2	O11—C22	1.253(4)	O35—C92	1.260(4)	O47—C127	1.266(4)
	O12—C22	1.270(4)	O36—C92	1.272(4)	O48—C127	1.272(4)
Ti—O_3PPh	Ti1—O9	1.966(3)	Ti7—O33	1.966(3)	Ti10—O45	1.973(3)
	Ti2—O10^a	1.951(3)	Ti8—O46	1.948(2)	Ti11—O34	1.956(3)
	Ti3—O8	1.988(3)	Ti9—O32	1.981(3)	Ti12—O44	1.973(3)
P—O	P1—O8	1.529(3)	P3—O32	1.529(3)	P4—O44	1.532(3)
	P1—O9	1.529(3)	P3—O33	1.531(3)	P4—O45	1.529(3)
	P1—O10	1.524(2)	P3—O34	1.525(3)	P4—O46	1.529(3)
Ti—μ_3-O	Ti4—O13	1.996(3)	Ti13—O49	1.983(3)	Ti16—O61	1.983(3)
	Ti5—O13	1.984(3)	Ti14—O49	1.976(3)	Ti17—O61	1.976(3)
	Ti6—O13	1.911(3)	Ti15—O49	1.918(3)	Ti18—O61	1.922(3)
Ti—μ_2-O	Ti4—O19^b	1.860(2)	Ti13—O67	1.863(3)	Ti16—O55	1.863(3)
	Ti6—O19	1.775(2)	Ti15—O55	1.772(2)	Ti18—O67	1.767(2)
Ti—μ_2-OiPr	Ti4—O15	2.027(3)	Ti13—O51	2.020(3)	Ti16—O63	2.016(3)
	Ti5—O15	1.984(3)	Ti14—O51	1.996(3)	Ti17—O63	1.993(3)
	Ti5—O17	1.970(3)	Ti14—O53	1.963(3)	Ti17—O65	1.970(3)
	Ti6—O17	2.029(3)	Ti15—O53	2.031(3)	Ti18—O65	2.029(3)
Ti—OiPr	Ti4—O14	1.790(3)	Ti13—O50	1.795(3)	Ti16—O62	1.802(3)
	Ti5—O16	1.766(3)	Ti14—O52	1.774(3)	Ti17—O64A Ti17—O64B	1.767(6) 1.839(19)
	Ti6—O18	1.804(3)	Ti15—O54	1.802(3)	Ti18—O66	1.803(3)
Ti—O_2CR	Ti4—O23	2.178(3)	Ti13—O59	2.182(3)	Ti16—O71	2.181(3)
	Ti5—O24	2.085(2)	Ti14—O60	2.097(3)	Ti17—O72	2.090(3)
RCO_2	O23—C57	1.259(4)	O59—C162	1.259(4)	O71—C197	1.261(4)
	O24—C57	1.271(4)	O60—C162	1.265(4)	O72—C197	1.264(4)
Ti—O_3PPh	Ti4—O21	1.969(3)	Ti13—O57	1.972(3)	Ti16—O69	1.969(3)
	Ti5—O22^b	1.953(2)	Ti14—O70	1.946(2)	Ti17—O58	1.938(3)
	Ti6—O20	1.979(3)	Ti15—O56	1.983(3)	Ti18—O68	1.990(3)
P—O	P2—O20	1.532(3)	P5—O56	1.531(3)	P6—O68	1.534(3)
	P2—O21	1.533(3)	P5—O57	1.531(3)	P6—O69	1.529(3)
	P2—O22	1.526(2)	P5—O58	1.525(3)	P6—O70	1.526(2)

Angles	ARU 1	ARU 2	ARU 3		ARU 4	
$Ti_2O_2\cdots O_2C$	4.831(4)	0.33(6)	1.9(4)	1.1(4)	4.4(4)	6.8(4)
$O_2C\cdots Ar$	59.593(14)	54.23(4)	54.86(11)	55.95(10)	62.99(9)	61.04(9)

Symmetry key: $^a -x, 1-y, 1-z$; $^b 2-x, -y, 1-z$

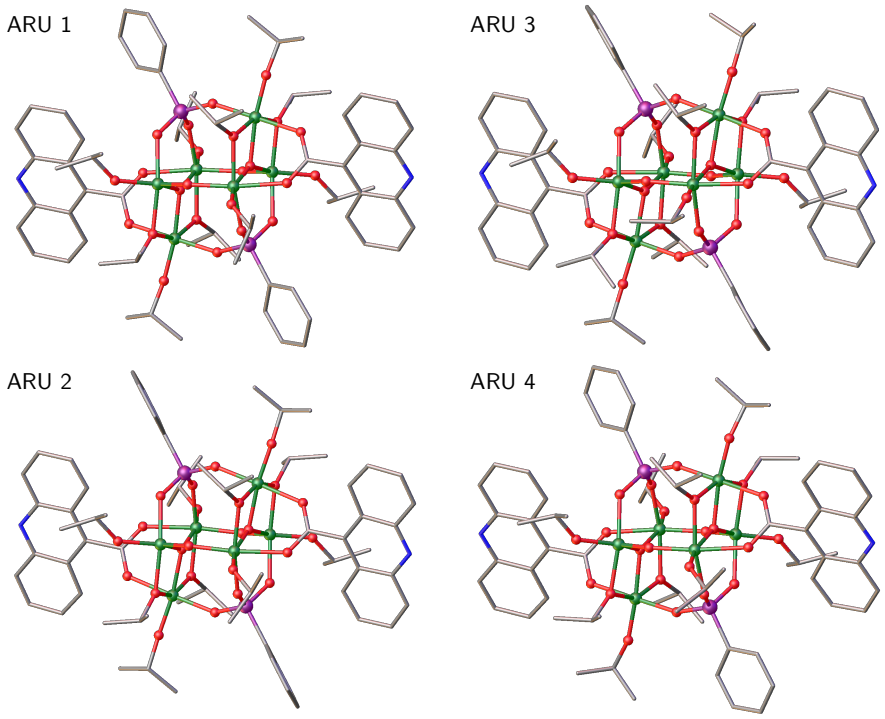


Figure 5.10: The {Ti_6}-oxo clusters of the four asymmetric residue units (ARUs) in **23**.

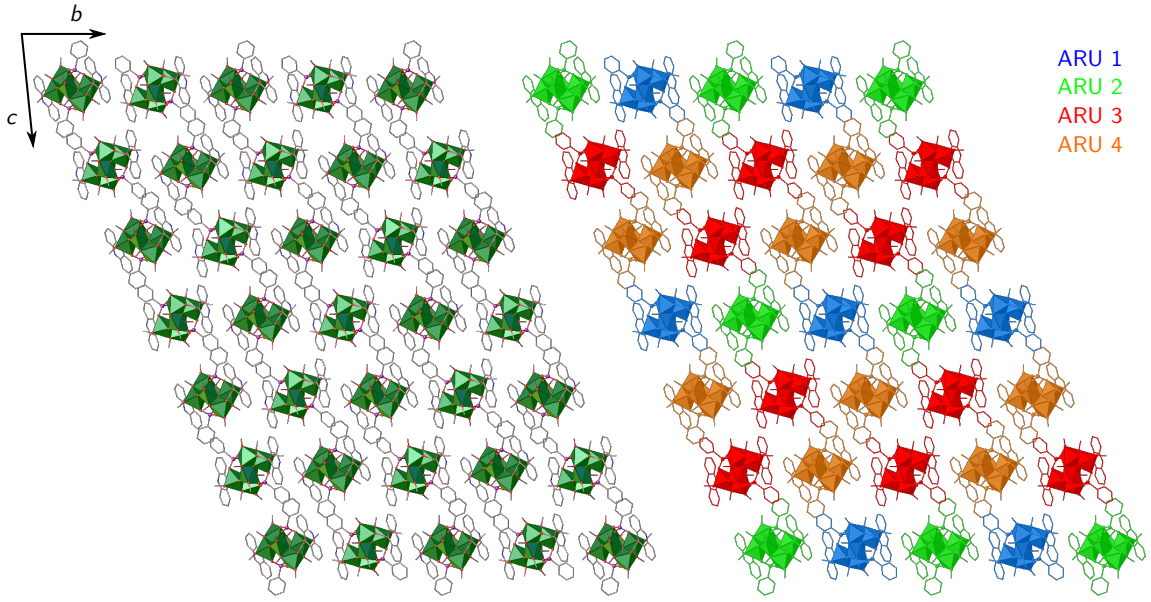


Figure 5.11: The packing of **23** (left) viewed along [$\bar{1}$00] and with colour-coded asymmetric residue units (right) to highlight π-πstacking between ARU 1 and 2, as well as ARU 3 and 4, respectively.

only occurs between symmetry independent clusters. That is ARUs 1 and 2, as well as ARUs 3 and 4, respectively, form 1D chains along [$\bar{2}$10]. Moreover, stacking oc-

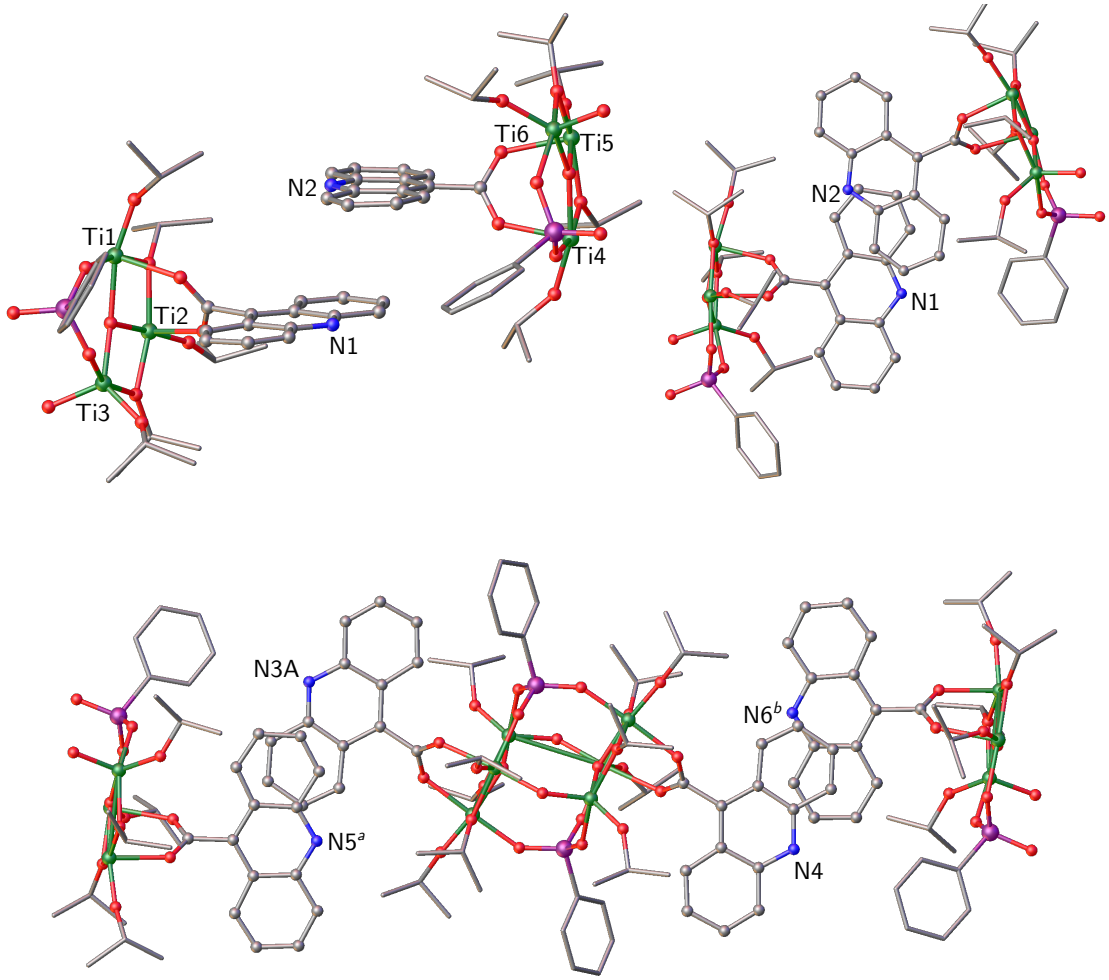


Figure 5.12: Elucidation of the π-π-stacking in **23** between ARUs 1 and 2 (top), as well as ARUs 3 and 4 (bottom). Interacting Ti_3-subunits are pseudo-rotation symmetric. Symmetry key: $^{a} -1+x, y, z$, $^{b} 1+x, 1+y, z$.

curs between Ti_3-subunits that are pseudo-rotation symmetric, rather than (pseudo-)inversion symmetric. That is the acridine involving N1 interacts with an acridine involving N2, rather than N1* or N2* (where * denotes inversion). Similarly, the ligands involving odd and even numbered containing nitrogen atoms in ARUs 3 and 4 respectively engage in π-π-stacking. The stacking interactions are quite different with decreasing overlap from ligands involving N1···N2, through N4···N6, to N3A···N5. In the same order, centroid-centroid distances are 5.428(3) Å, 5.670(4) Å, and 6.037(4) Å.

The powder X-ray diffraction patterns of **21**, **22** and **23**, shown in Figure 5.13, confirm that all three were obtained phase pure.

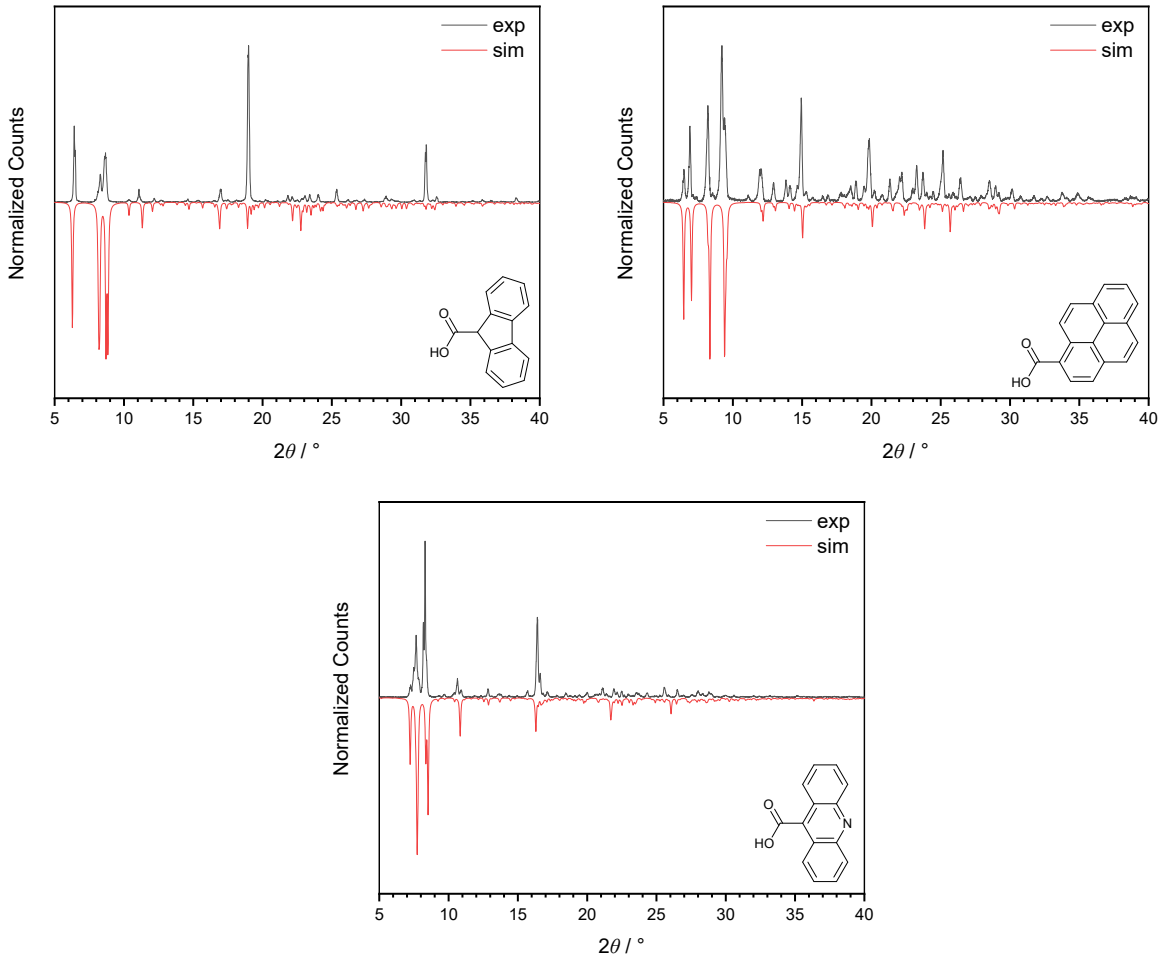


Figure 5.13: Powder X-ray diffraction patterns of **21** (top left), **22** (top right), and **23** (bottom), with their corresponding carboxylic acids inset.

5.4.2. Optical Properties of Pyrene- and Acridine Functionalised $\{Ti_6\}$-Oxo Clusters

The Kubelka-Munk functions, derived from DRS, of the pyrene-1- and acridine-9-carboxylate substituted $\{Ti_6\}$-oxo clusters **22** and **23** are presented in Figure 5.14. The DRS of **21** was not obtained, however due to its lack of colour the optical band gap is assumed to be in the UV-region. This can be rationalised by lack of π-conjugation between the fused ring and the carboxylate. From a ligand point of view, **22** is comparable to its naphthalene-carboxylate analogue PTC-10, which exhibits a band gap of 3.36 eV, and the expansion of the aromatic system leads to a reduction of 0.57 eV.[300] Similarly, **23** can be compared to the PTC-3, which features isonicotinate and a band gap of 3.52 eV. Here, the expansion of aromatic system causes a reduction of the band gap by 0.58 eV to 2.94 eV.

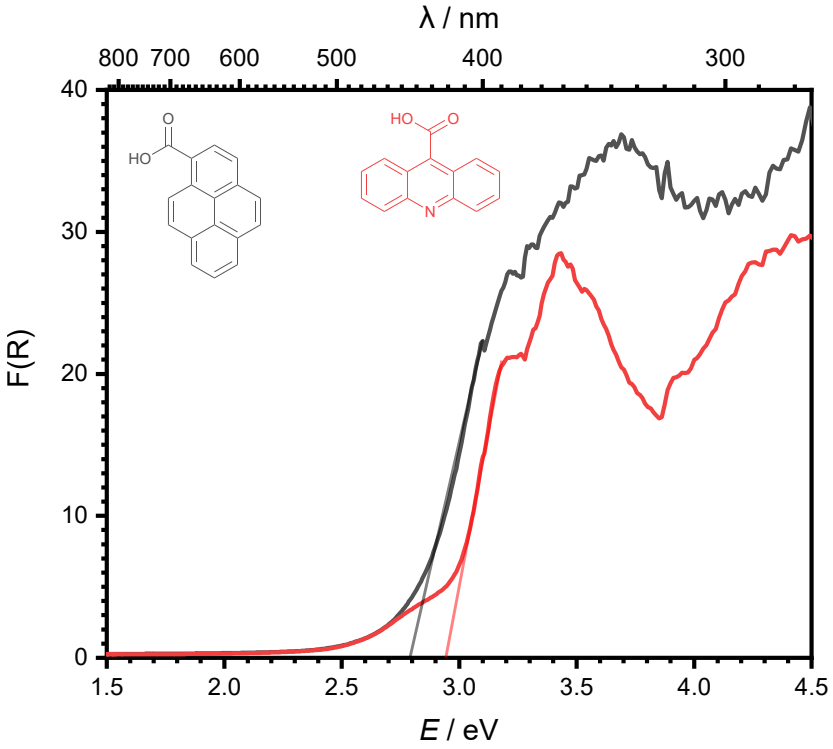


Figure 5.14: Kubelka-Munk function from the diffuse reflectance spectra of the $\{Ti_6\}$-oxo clusters **22** (black, 2.79 eV), **23** (red, 2.94 eV). Bandgaps were determined by direct extrapolation.

5.5. $\{Ti_6\}$-Oxo Clusters with Coumarin-3-carboxylates)

5.5.1. Structural Characterisation

Table 5.6 lists the crystal data and refinement results for the $\{Ti_6\}$-oxo clusters **24**, respectively made from coumarin-3-carboxylic acid (**a**), 7-(diethylamino)coumarin-3-carboxylic acid (**b**) and coumarin 343 (C343H, **c**). The thermal ellispoids of their asymmetric unit are plotted in Figure 5.15, with selected distances and angles presented in Table 5.7.

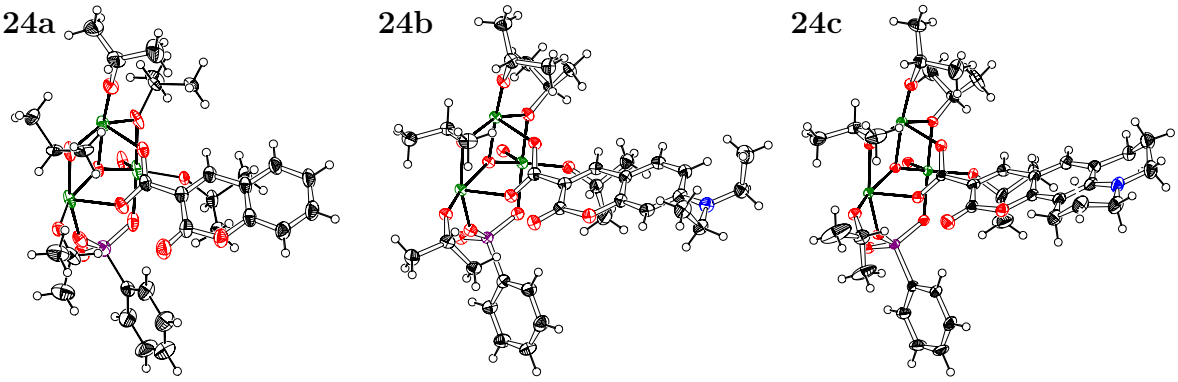


Figure 5.15: ORTEPs of the asymmetric units in the $\{Ti_6\}$-oxo clusters **24a**–**c**, featuring coumarin-3-carboxylates, plotted at 50% probablity.

All three were solved and refined in the triclinic space group $P\bar{1}$ with one molecule per unit cell and half of a cluster in the asymmetric unit. While **24a** crystallises as colourless blocks, **24b** and **24c** crystallise as yellow plates. Moreover, the latter are almost isostructural*.

Table 5.7 reveals little to no difference in bond distances among **24a**–**c**, however the carboxylate is more orthorgonal onto the Ti_3 plane and less aligned with the coumarin moiety from **a**–**c**. Full clusters and packing diagrams of **24a**–**c** are shown in Figures 5.16 to 5.18.

The packing in all three is governed by parallel dispalced π-π-stacking: In **24a** one part of a disordered (54%) phenyl phosphonate stacks with its symmetry equivalent

*The cells of **24b** and **24c** are given in standard setting, but can easily be transformed into each other with:

$$(a', b', c') = \begin{pmatrix} -1 & 0 & 0 \\ 0 & 0 & -1 \\ 0 & -1 & 0 \end{pmatrix} (a, b, c)$$

Table 5.6: Crystal data and refinement results of **24a**–**c**.

Identification code	**24a**	**24b**	**24c**
Empirical formula	$C_{62}H_{90}O_{28}P_2Ti_6$	$C_{70}H_{108}N_2O_{28}P_2Ti_6$	$C_{74}H_{108}N_2O_{28}P_2Ti_6$
Formula weight	1632.67	1774.92	1822.96
Temperature/K	100	100	100
Crystal description	colourless fragment	yellow plate	yellow plate
Crystal size/mm^3	$0.38 \times 0.26 \times 0.18$	$0.502 \times 0.308 \times 0.128$	$0.38 \times 0.23 \times 0.13$
Crystal system	triclinic	triclinic	triclinic
Space group	$P\bar{1}$	$P\bar{1}$	$P\bar{1}$
a/Å	11.5100(5)	11.6150(8)	12.104(13)
b/Å	12.7588(6)	14.5051(9)	14.45(3)
c/Å	13.9902(6)	14.7550(10)	14.477(16)
α/°	83.221(2)	70.156(2)	72.16(6)
β/°	89.7970(10)	70.175(2)	65.658(18)
γ/°	65.1390(10)	66.538(2)	69.63(4)
V/Å^{-3}	1848.67(14)	2084.1(2)	2123(5)
Z, Z'	1, 0.5	1 , 0.5	1, 0.5
ρ_{calc}/g cm^{-3}	1.467	1.414	1.426
μ/mm^{-1}	0.739	0.662	0.652
$F(000)$	848	928	952
Refl. total/unique	8601/41168	8644/33357	10963/41015
R_{int}, R_σ	0.0512, 0.0377	0.0743, 0.0673	0.0594, 0.0600
Data/restr./param.	8601/223/618	8644/0/499	10963/0/515
GooF	1.053	1.05	1.019
R_1 $[I \geq 2\sigma(I)]$, all	0.0457, 0.0788	0.0502, 0.0852	0.0515, 0.0858
wR_2 $[I \geq 2\sigma(I)]$, all	0.1031, 0.1257	0.1169, 0.1339	0.1032, 0.1172
$\Delta\rho_{max}/\Delta\rho_{min}$/e Å^{-3}	0.60/-0.77	0.74/-0.70	0.94/-0.54

stack *via* C20A and C21A with $d_{\pi-\pi} = 3.677(5)$ Å and are shifted by 2.562(9) Å so that overlap with their symmetry equivalents. The other part of the disorder has the phenyl exhibits a plane to plane distance of 4.527(7) Å and thus is void of interactions.

In **24b** and **24c** π-π-stacking is observed between the dye moeities and their symmetry equivalents through inversion, as shown in Figure 5.19. Both share that the stacking results in the alkyl moieties attached to N1 bend away from the stacking, with $d_{\pi-\pi} = 3.409(5)$ Å and 3.596(6) Å with shifts of 2.523(5) Å and 1.634(10) Å for **24b** and **24c**, respectively. In **24b** N1 lies on top of the center symmetry equivalents ring ($d(\text{N1} \cdots \text{Cg}^*) = 3.412(3)$ Å), whereas in **24c** N1 lies atop C26 (3.792(7) Å), with C29 aligned with the symmetry equivalent's ring centre ($d(\text{C29} \cdots \text{Cg}^*) = 3.412(3)$ Å).

The powder X-ray diffraction patterns of **21**, **22** and **23**, shown in Figure 5.20, confirm that all three were obtained phase pure.

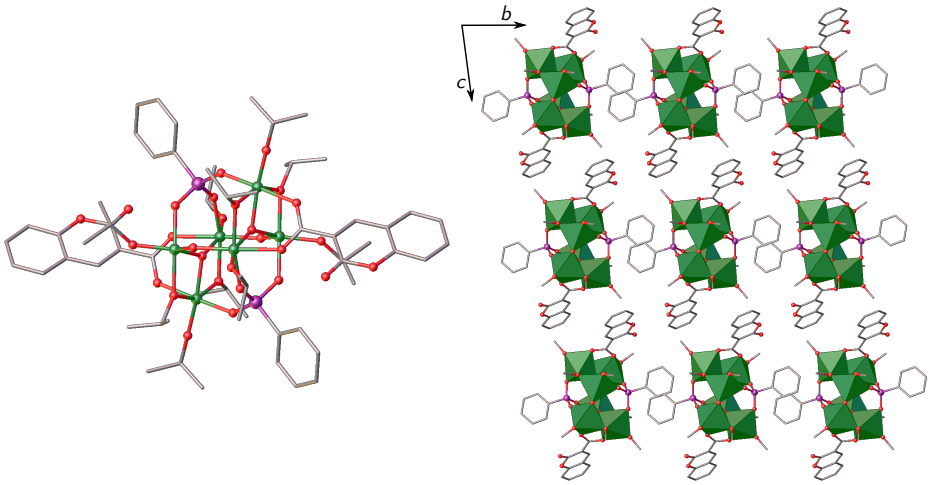


Figure 5.16: The {Ti_6}-oxo cluster **24a** (left) and its packing (right) viewed along [100].

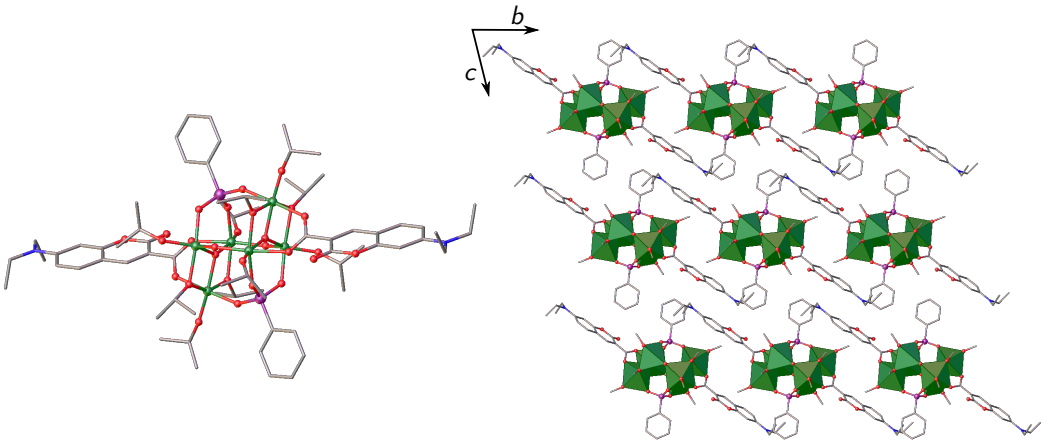


Figure 5.17: The {Ti_6}-oxo cluster **24b** (left) and its packing (right) viewed along [$\bar{1}$00].

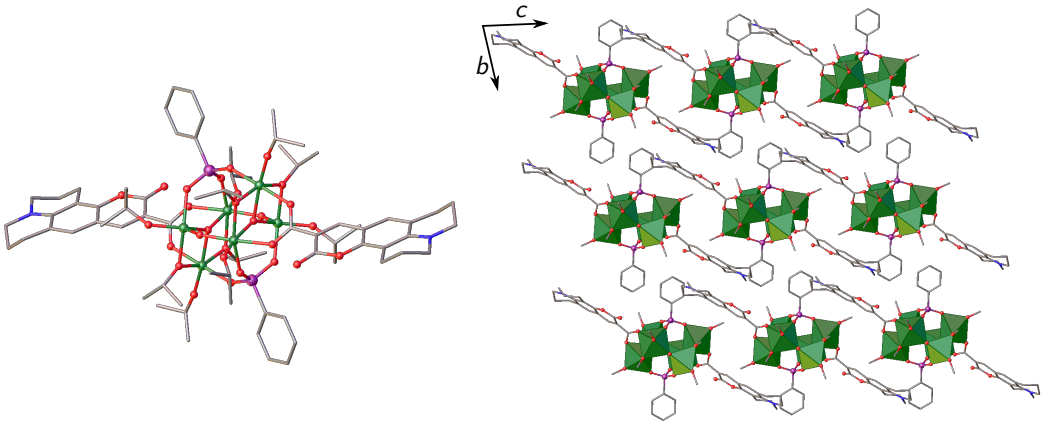


Figure 5.18: The {Ti_6}-oxo cluster **24c** (left) and its packing (right) viewed along [100].

Table 5.7: Bond lengths in **24a**–**c** in Å.

Bond	Distance	**24a**	**24b**	**24c**
Ti—μ_3-O	Ti1—O1	1.9921(19)	2.006(2)	2.005(3)
	Ti2—O1	1.9735(19)	1.973(2)	1.982(3)
	Ti3—O1	1.9059(18)	1.886(2)	1.905(3)
Ti—μ_2-O	Ti1—O7^a	1.864(2)	1.875(2)	1.877(3)
	Ti3—O7	1.764(2)	1.752(2)	1.762(2)
Ti—μ_2-OiPr	Ti1—O3	2.011(2)	2.012(2)	2.030(3)
	Ti2—O3	1.993(2)	1.981(2)	1.984(3)
	Ti2—O5	1.952(2)	1.949(2)	1.957(3)
	Ti3—O5	2.042(2)	2.044(2)	2.043(3)
Ti—OiPr	Ti1—O2	1.75(2) 1.809(10)	1.760(2)	1.775(3)
	Ti2—O4	1.765(2)	1.768(2)	1.775(3)
	Ti3—O6A	1.771(14)	1.813(2)	1.811(3)
	Ti3—O6B	1.846(11)		
Ti—O_2CR	Ti1—O11	2.163(2)	2.151(2)	2.135(3)
	Ti2—O12	2.079(2)	2.087(2)	2.095(3)
RCO_2	O11—C22	1.251(3)	1.250(4)	1.267(3)
	O12—C22	1.268(3)	1.269(4)	1.272(3)
Ti—O_3PPh	Ti1—O9	1.943(2)	1.954(2)	1.971(3)
	Ti2—O10^a	1.940(2)	1.938(2)	1.958(3)
	Ti3—O8	1.953(2)	1.972(2)	1.971(3)
P—O	P1—O8	1.518(2)	1.521(2)	1.527(2)
	P1—O9	1.523(2)	1.522(2)	1.523(2)
	P1—O10	1.527(2)	1.521(2)	1.526(2)
N—C	N1—C29	-	1.365(4)	1.378(4)
	N1—C32	-	1.468(5)	1.467(4)
	N1—C34	-	1.461(5)	1.457(5)

Angles	**24a**	**24b**	**24c**
$Ti_2O_2 \cdots O_2C$	7.7(4)	6.1(4)	1.3(4)
$O_2C \cdots Ar$	21.19(10)	29.96(11)	34.10(11)

Symmetry key: $^a 1-x, 1-y, 1-z$ for **24a**; $2-x, -y, 1-z$ for **24b**; $1-x, 1-y, 2-z$ for **24c**.

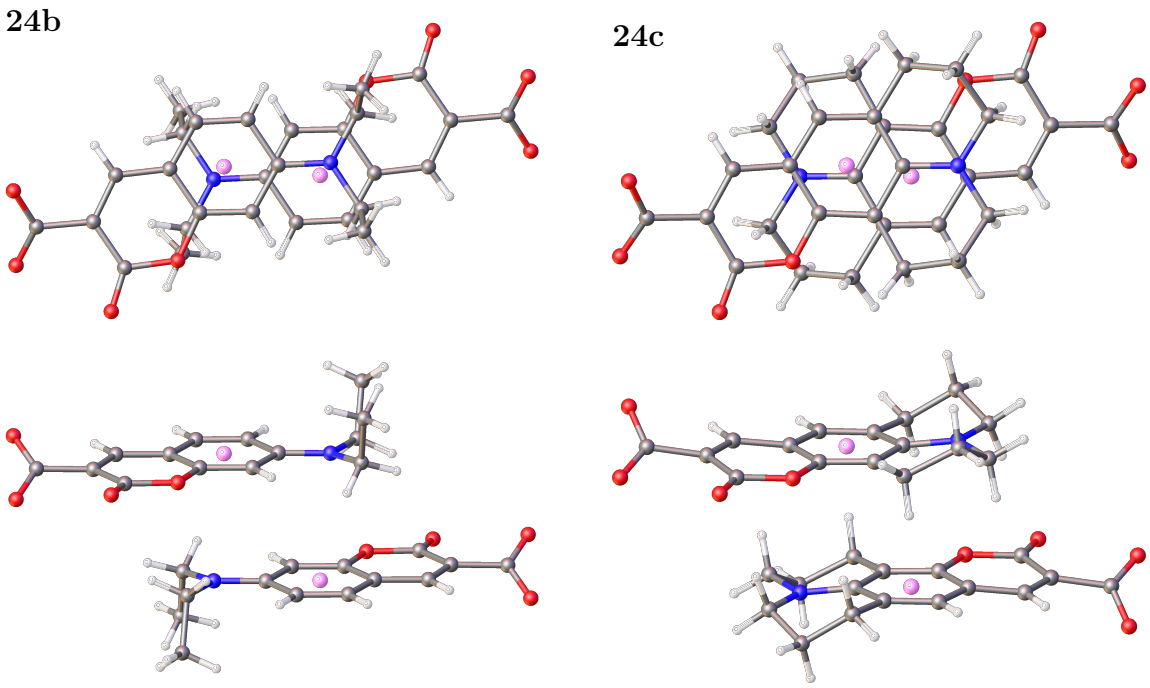


Figure 5.19: Comparison of π-π-stacking in **24b** and **24c** viewed onto (top) and between (bottom) the planes. Centroids are shown in pink.

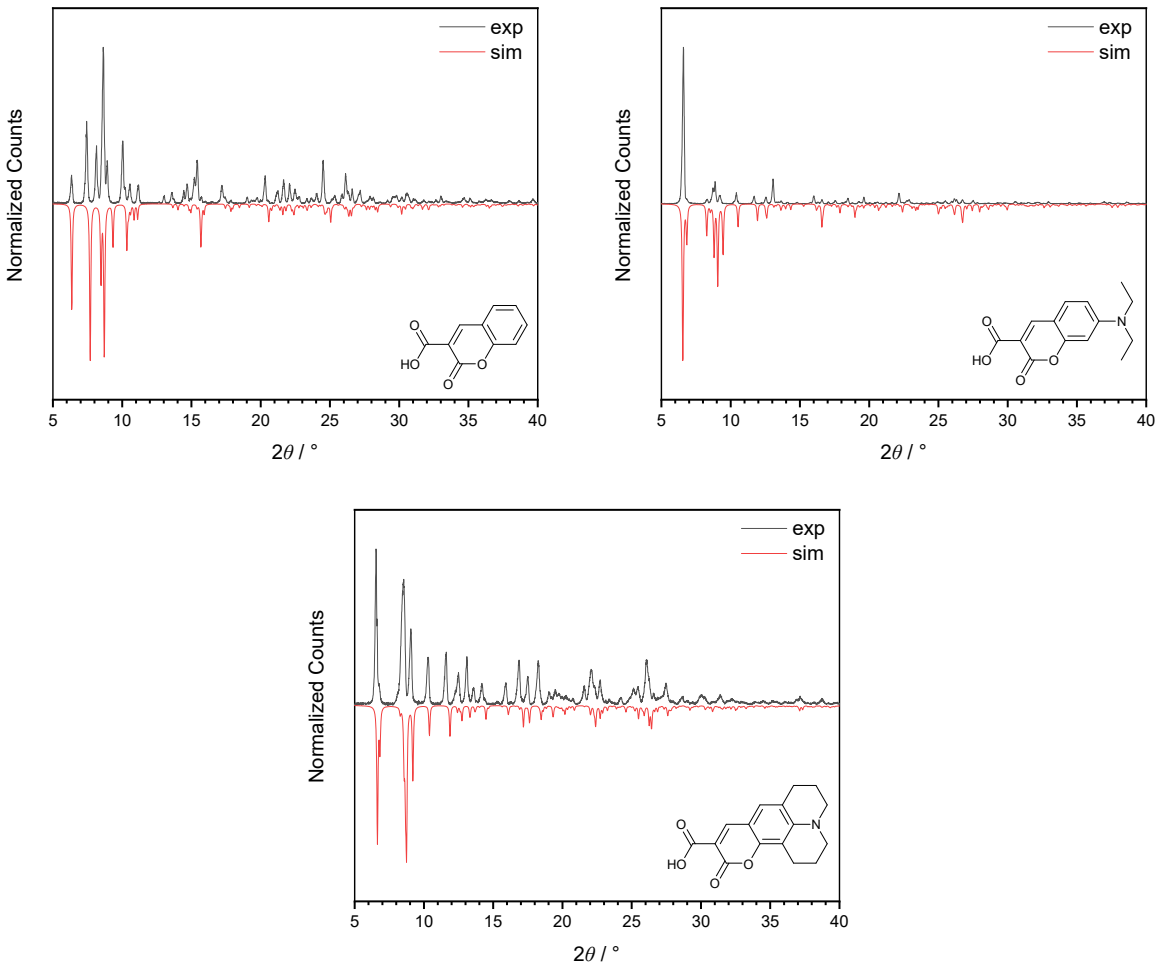


Figure 5.20: Powder X-ray diffraction patterns of **24a** (top left), **24b** (top right), and **24c** (bottom), with their corresponding carboxylic acids inset.

5.5.2. Optical Properties

The Kubelka-Munk functions of the coumarin substituted {Ti_6}-oxo clusters **24a**–**c** are shown in Figure 5.21. The band gap of the unsubstituted coumarin carboxyalate cluster **24a** is 3.26 eV and the introduction of the electron donating diethylamino group in 7-position (**24b**) results in a reduction of 0.78 eV to 2.48 eV, which is in the greenish blue region. This is within experimental error of the band gap of 2.50 eV observed for the C343 substituted {Ti_6}-oxo cluster **24c**.

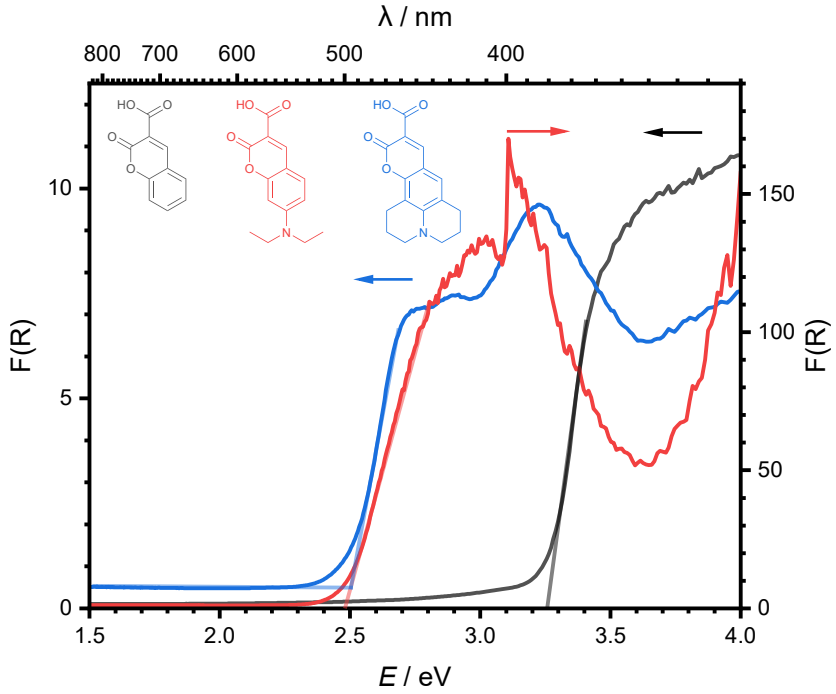
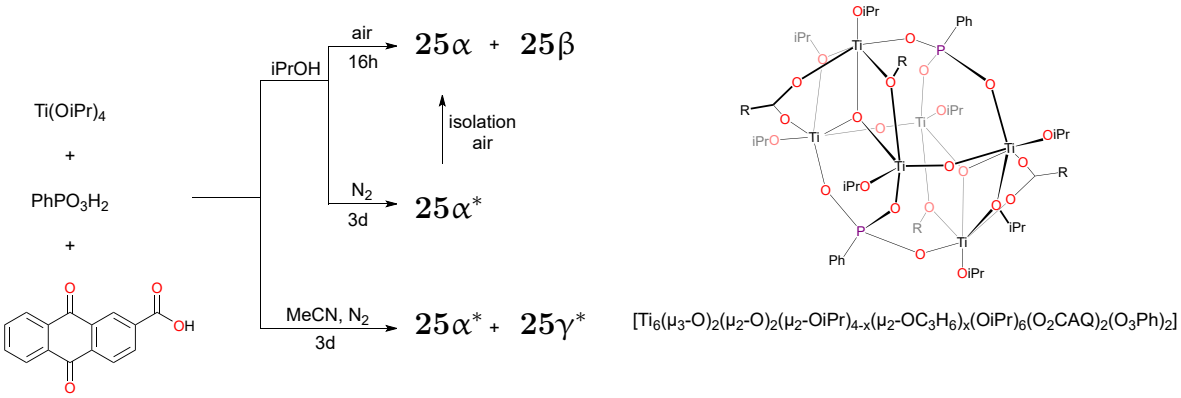


Figure 5.21: Kubelka-Munk function from the diffuse reflectance spectra of the coumarin carboxylate substituted {Ti_6}-oxo clusters **24a** (black, 3.26 eV), **24b** (red, 2.48 eV), and **24c** (red, 2.50 eV). Bandgaps were determined by direct extrapolation. The intense drop at *approx.* 400 nm for **24b** is a measurement artifact.

5.6. {Ti_6}-Oxo Clusters of Anthraquinone-2-carboxylic acid

5.6.1. Synthesis

During the synthesis of the {Ti_6}-oxo cluster **25** from anthraquinone-2-carboxylic acid ($AQCO_2H$) several polymorphs were encountered, as shown in Scheme 5.2.



Scheme 5.2: Synthesis of various polymorphs of {Ti_6}-oxo cluster **25** from anthraquinone-2-carboxylic acid ($AQCO_2H$). A bridging isopropoxide has been partially oxidised to 2-propenolate in **25α** (x=11.5%) and **25α*** (x=13.7%).

Initial mixing of the starting materials in iPrOH gave a beige suspension, which upon heating to 80 °C under autogenous pressure (20 mL crimp vial, 50-75% headspace) gave a light beige solution. The light yellow crystals which had formed overnight were isolated by hot filtration and initial analysis by SCXRD gave the structure **25α**. After the isolated crystals had been left on a glass slide over night a portion had turned magenta, which single crystal X-ray structure analysis revealed to be the polymorph **25β**. Interestingly, if the reaction mixture is left at 80 °C for more than 1 d it starts turning deep violet from the bottom up, an indication of the presence of Ti(III). If said vial is then shaken to reintroduce air into the reaction mixture, decolouration back to light beige is observed, which indicates quenching of Ti(III) back to Ti(IV) by oxygen. Thus, the reaction was repeated with nitrogen bubbled for 30 min after the organics were suspended in iPrOH and another 15 min after $Ti(OiPr)_4$ was added. During the second period a colour change of the suspension from light beige to light violet was observed, which turns into a deep dark violet solution upon heating. After 3 d a dark violet single crystal of **25α*** was analysed, the structural data of which

is virtually identical with **25α** (hence the asterisk is used to denote the potential existence of Ti^{III}). Optical photographs of the measured single crystals of **25α** and **25α*** , as well as bulk sample from the initial reaction yielding **25α** and **25β** are shown in Figure 5.22. Moreover, if the latter reaction is conducted in acetonitrile it yields mostly of amorphous material and few dark violet single crystals of both **25α*** and a third polymorph **25γ*** , which is closely related to **25β**. Upon exposure to air crystals of **25*** turn grey from outside to inside within minutes, and during storage at ambient conditions proceed to turn yellow.

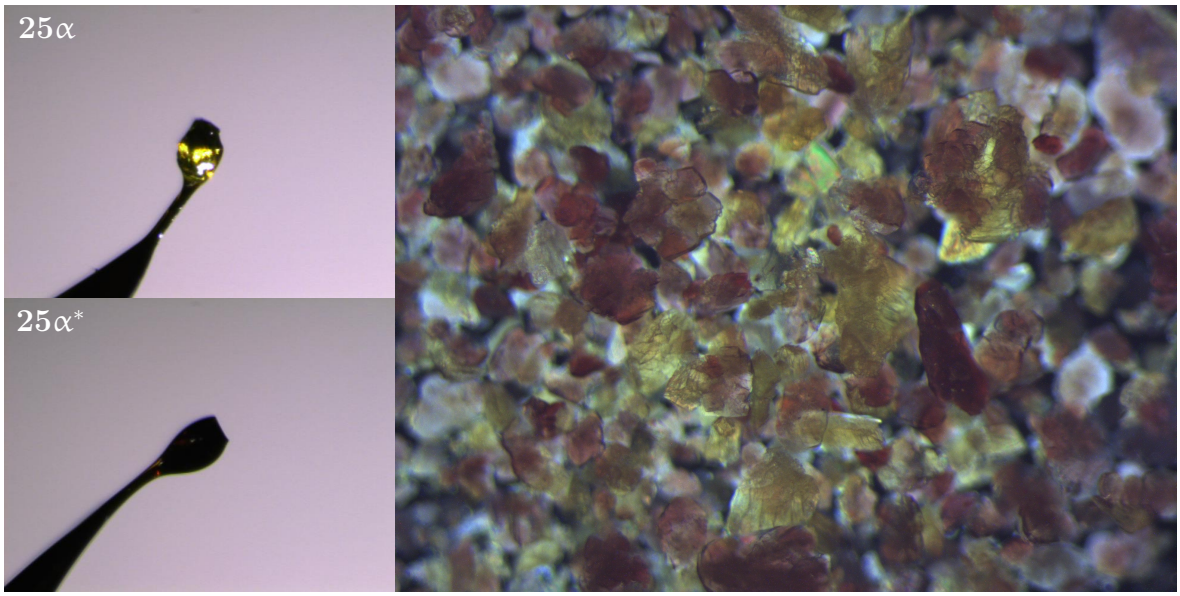
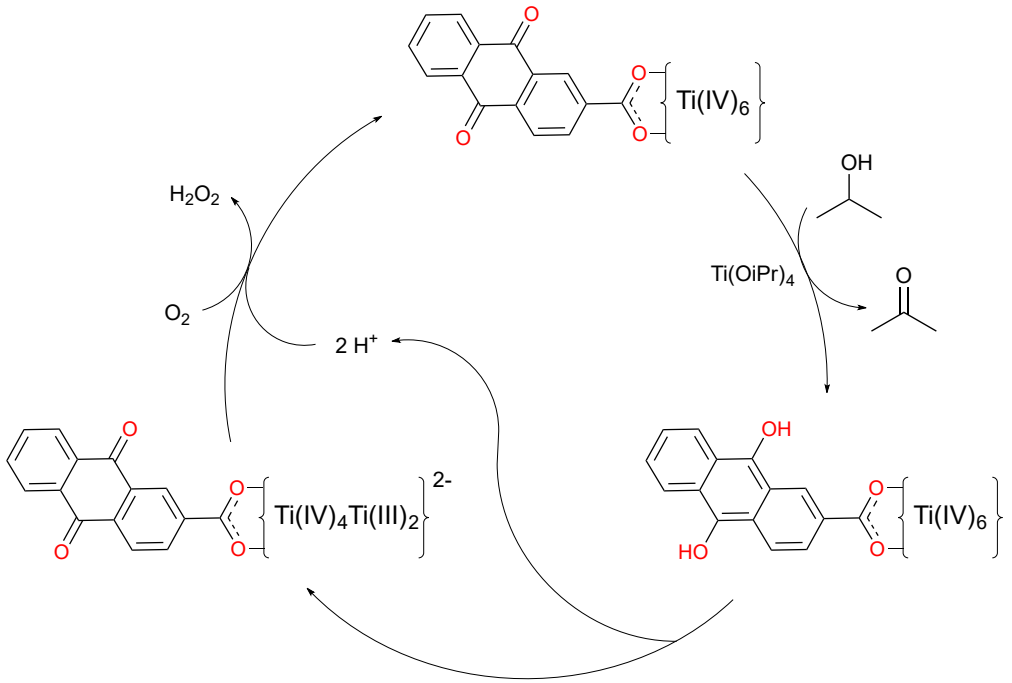


Figure 5.22: Optical photographs of single crystals of **25α** and **25α*** (left), and mixture of **25α** (yellow) and **25β** (red) isolated after reacting for 16 h and left at ambient conditions for several weeks.

Note that in **25α** and **25α*** a bridging isopropoxide has been partially (11.5% and 13.7%) oxidised twice to a 2-propenolate, the deprotonated enol form acetone. Hence it is likely the electron donor in the potential reduction of the $\{Ti_6\}$-oxo cluster **25α** and **25α*** . An alternative reduction pathway would be *via* a Meerwein-Ponndorf-Verley type reaction as depicted in Scheme 5.3.[379,380] In fact, Coffey and Boyd have demonstrated that anthraquinone can be reduced with Al(OiPr)3 in a Meerwein-Poondorf-Verley type reaction.[379] Here, $Ti(OiPr)_4$ facilitates a hydride transfer from an isopropoxide to the anthraquinone moiety of the cluster, yielding acetone and anthrahydroquinone. The latter is protonated by the reaction medium iPrOH, which also regenerates $Ti(OiPr)_4$. Then, the anthrahydroquinone undergoes oxidation back to anthraquinone and coupled with double deprotonation and injects electrons into



Scheme 5.3: Potential reaction pathway for mixed valence {Ti_6}-oxo clusters **25*** featuring anthraquinone-2-carboxylate: The anthraquinone moiety undergoes a Meerwein-Ponndorf-Verley type reduction to anthrahydroquinone, followed by double deprotonation and electron transfer to the {Ti_6}-oxo cluster. The mixed valence cluster is then quenched by molecular oxygen under the formation of hydrogen peroxide.

the {Ti_6}-oxo cluster, which then becomes mixed valent Ti(IV)/Ti(III). If oxygen is present in the headspace of the reactor it quenches the mixed valent {Ti_6}-oxo cluster forming hydrogen peroxide, which in turn would oxidise iPrOH. When isolated **25α** is suspended in iPrOH and heated to 80 °C under nitrogen a slow colour change of the crystals to violet is observed over several days. If this reaction is repeated in with 4 eq. $Ti(OiPr)_4$ (note that cluster formation occurs with an excess of $Ti(OiPr)_4$) full conversion is achieved overnight and accompanied by a violet solution. Hence, both pathways are possible but the $Ti(OiPr)_4$ promoted reaction seems kinetically favoured. Moreover, the colour change can be induced through irradiation with UV light (λ_{max} = 365 nm) over several hours.

5.6.2. Structural Characterisation of the Polymorphs of 25

The crystal data and refinement results of the polymorphs of **25** are given in Table 5.8 and bond distances are listed in Table 5.9. All polymorphs of **25** crystallise neat and were solved and refined in the triclinic space group $P\bar{1}$.

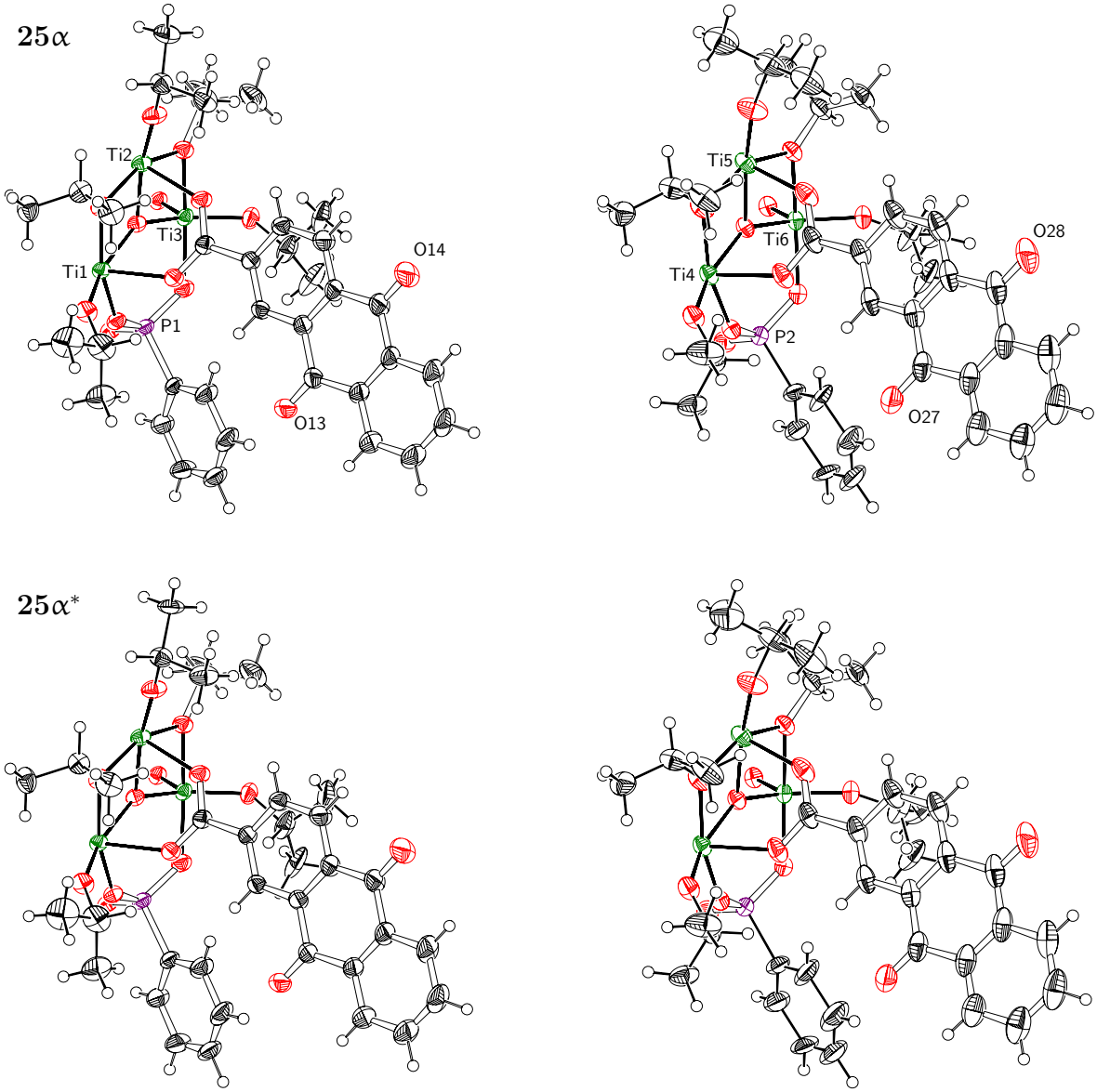


Figure 5.23: ORTEPs of the asymmetric units in the {Ti_6}-oxo clusters **25α** and **25α***, plotted at 50% probablity. The naming scheme is identical in both.

25α and **25α*** crystallise with two half clusters in the asymmetric unit, as portrayed in Figure 5.23, and two clusters per unit unit cell. It should be noted that the partially oxidised isopropoxide or rather 2-propenolate is solely associated with O19, which

Table 5.8: Crystal data and refinement results of the polymorphs of **25**.

Identification code	**25**α	**25**α*
Empirical formula	$C_{72}H_{93.77}O_{28}P_2Ti_6$	$C_{72}H_{93.72}O_{28}P_2Ti_6$
Formula weight	1756.57	1756.53
Temperature/K	100	100
Crystal description	yellow block	violet block
Crystal size/mm^3	$0.28 \times 0.219 \times 0.164$	$0.286 \times 0.277 \times 0.184$
Crystal system	triclinic	triclinic
Space group	$P\bar{1}$	$P\bar{1}$
a/Å	11.7858(5)	11.7976(5)
b/Å	16.3893(7)	16.3955(6)
c/Å	21.1637(8)	21.1771(9)
α/°	88.4147(15)	88.4290(10)
β/°	84.2794(14)	84.2660(10)
γ/°	89.6264(15)	89.7380(10)
V/Å^{-3}	4066.1(3)	4074.2(3)
Z, Z'	2, 1	2, 1
ρ_{calc}/g cm^{-3}	1.427	1.432
μ/mm^{-1}	0.674	0.676
$F(000)$	1824	1823
Refl. total/unique	62806/20405	70679/23147
R_{int}, R_σ	0.0418, 0.0481	0.0344, 0.0388
Data/restr./param.	20405/603/1274	23147/383/1271
GooF	1.013	1.038
R_1 [$I \geq 2\sigma(I)$], all	0.0502, 0.0838	0.0489, 0.0748
wR_2 [$I \geq 2\sigma(I)$], all	0.1150, 0.1333	0.1203, 0.1363
$\Delta\rho_{max}/\Delta\rho_{min}$/e Å^{-3}	0.95/-0.84	1.03/-0.89
Identification code	**25**β	**25**γ*
Empirical formula	$C_{72}H_{94}O_{28}P_2Ti_6$	$C_{72}H_{94}O_{28}P_2Ti_6$
Formula weight	1756.81	1756.81
Temperature/K	100	100
Crystal description	magenta block	violet rod
Crystal size/mm^3	$0.12 \times 0.1 \times 0.08$	$0.483 \times 0.265 \times 0.162$
Crystal system	triclinic	triclinic
Space group	$P\bar{1}$	$P\bar{1}$
a/Å	13.0047(11)	11.3608(8)
b/Å	13.3810(11)	14.2204(10)
c/Å	14.2606(11)	14.3139(10)
α/°	97.013(3)	75.213(2)
β/°	106.500(3)	69.425(2)
γ/°	118.650(3)	69.258(2)
V/Å^{-3}	1987.3(3)	2001.9(2)
Z, Z'	1, 0.5	1, 0.5
ρ_{calc}/g cm^{-3}	1.468	1.457
μ/mm^{-1}	0.693	0.688
$F(000)$	912	912
Refl. total/unique	30100/7378	25755/8702
R_{int}, R_σ	0.1437, 0.1205	0.0422, 0.0483
Data/restr./param.	7378/0/497	8702/146/557
GooF	1.009	1.043
R_1 [$I \geq 2\sigma(I)$], all	0.0567, 0.1328	0.0486, 0.0764
wR_2 [$I \geq 2\sigma(I)$], all	0.1132, 0.1411	0.1185, 0.1343
$\Delta\rho_{max}/\Delta\rho_{min}$/e Å^{-3}	0.63/-0.47	0.58/-0.47

Table 5.9: Distances in the polymorphs of **25**.

Bond	Distance	**25α**	**25α***	Distance	**25β**
Ti—μ_3-O	Ti1—O1	2.0065(19)	2.0079(15)	Ti1—O1	1.999(3)
	Ti2—O1	1.9674(19)	1.9665(16)	Ti2—O1	1.983(3)
	Ti3—O1	1.8986(19)	1.9002(16)	Ti3—O1	1.890(3)
Ti—μ_2-O	Ti1—O7^a	1.8612(19)	1.8611(16)	Ti1—O7^a	1.851(3)
	Ti3—O7	1.7569(18)	1.7599(15)	Ti3—O7	1.767(3)
Ti—μ_2-OiPr	Ti1—O3	2.010(2)	2.0117(17)	Ti1—O3	2.023(3)
	Ti2—O3	1.968(2)	1.9714(17)	Ti2—O3	1.986(3)
	Ti2—O5	1.939(2)	1.9430(17)	Ti2—O5	1.966(3)
	Ti3—O5	2.047(2)	2.0449(17)	Ti3—O5	2.008(3)
Ti—OiPr	Ti1—O2	1.7804(19)	1.7800(16)	Ti1—O2	1.800(3)
	Ti2—O4	1.764(2)	1.7636(17)	Ti2—O4	1.762(3)
	Ti3—O6	1.800(2)	1.8008(17)	Ti3—O6	1.803(3)
Ti—O_2CR	Ti1—O11	2.1480(19)	2.1468(16)	Ti1—O11	2.141(3)
	Ti2—O12	2.117(2)	2.1162(17)	Ti2—O12	2.060(3)
RCO_2	O11—C22	1.257(3)	1.257(3)	O11—C22	1.261(6)
	O12—C22	1.265(3)	1.267(3)	O12—C22	1.261(6)
Ti—O_3PPh	Ti1—O9	1.948(2)	1.9481(17)	Ti1—O9	1.963(3)
	Ti2—O10^a	1.941(2)	1.9439(16)	Ti2—O10^a	1.941(3)
	Ti3—O8	1.973(2)	1.9746(16)	Ti3—O8	1.976(3)
P—O	P1—O8	1.519(2)	1.5221(18)	P1—O8	1.529(3)
	P1—O9	1.530(2)	1.5195(17)	P1—O9	1.523(3)
	P1—O10	1.525(2)	1.5285(17)	P1—O10	1.520(3)
Bond	Distance	**25α**	**25α***	Distance	**25γ***
Ti—μ_3-O	Ti4—O15	1.989(2)	1.9894(16)	Ti1—O1	1.994(2)
	Ti5—O15	1.9787(19)	1.9784(16)	Ti2—O1	1.978(2)
	Ti6—O15	1.9063(19)	1.9075(17)	Ti3—O1	1.902(2)
Ti—μ_2-O	Ti4—O21^b	1.8415(19)	1.8428(17)	Ti1—O7^c	1.868(2)
	Ti6—O21	1.7650(19)	1.7674(17)	Ti3—O7	1.756(2)
Ti—μ_2-OiPr	Ti4—O17	2.019(2)	2.0198(18)	Ti1—O3	2.015(2)
	Ti5—O17	1.977(2)	1.9793(19)	Ti2—O3	1.977(2)
	Ti5—O19	1.948(2)	1.9500(18)	Ti2—O5	1.958(2)
	Ti6—O19	2.027(2)	2.0264(17)	Ti3—O5	2.024(2)
Ti—OiPr	Ti4—O16	1.787(2)	1.7924(18)	Ti1—O2	1.769(2)
	Ti5—O18	1.766(2)	1.7679(19)	Ti2—O4	1.763(2)
	Ti6—O20	1.788(2)	1.7922(18)	Ti3—O6	1.812(2)
Ti—O_2CR	Ti4—O25	2.162(2)	2.1641(18)	Ti1—O11	2.171(2)
	Ti5—O26	2.093(2)	2.094(2)	Ti2—O12	2.078(2)
RCO_2	O25—C58	1.259(4)	1.260(3)	O11—C22	1.258(4)
	O26—C58	1.256(4)	1.258(3)	O12—C22	1.272(4)
Ti—O_3PPh	Ti4—O23	1.966(2)	1.9639(18)	Ti1—O9	1.964(2)
	Ti5—O24^b	1.946(2)	1.9485(19)	Ti2—O10^c	1.943(2)
	Ti6—O22	1.956(2)	1.9551(17)	Ti3—O8	1.968(2)
P—O	P2—O22	1.516(2)	1.5209(18)	P1—O8	1.519(2)
	P2—O23	1.259(4)	1.5197(19)	P1—O9	1.525(2)
	P2—O24	1.256(4)	1.5221(19)	P1—O10	1.521(2)

Symmetry key: $^a 1-x, 1-y, 1-z$ (for **25α** and **25β**), $2-x, 2-y, -z$ (for **25α***); $^b -x, -y, -z$ (for **25α**) $3-x, 1-y, 1-z$ (for **25α***); $^c 1-x, 1-y, 2-z$.

Table 5.10: Fold and twist angles of $AQCO_2$ in polymorphs of **25**.

Angle	**25**α		**25**α*		**25**β	**25**γ*
	Ti1-3	Ti4-6	Ti1-3	Ti4-6		
$Ti_2O_2\cdots O_2C$	3.4(3)	0.4(4)	3.5(3)	0.4(3)	5.5(7)	3.0(4)
$O_2C\cdots Ar$	11.76(10)	1.57(11)	11.64(9)	1.64(9)	174.04(19)	159.23(12)

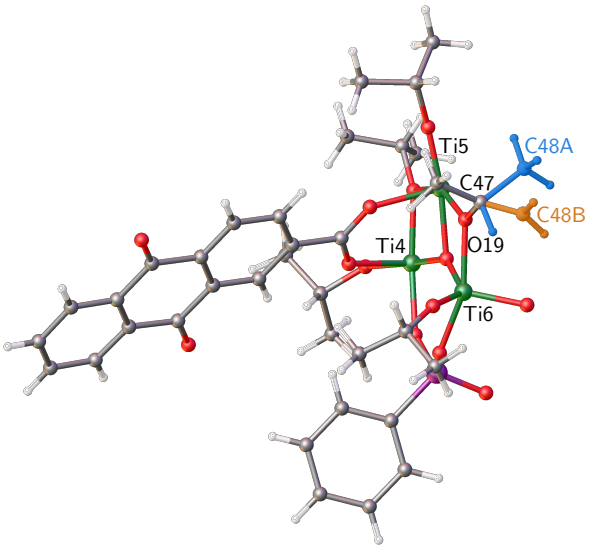


Figure 5.24: Disorder between isopropoxide (blue) and 2-propenolate (orange) in **25**α and **25**α*.

bridges the octahedrally coordinated Ti5 and five-coordinated Ti6, whose coordination geometry is a square pyramid. As portrayed in Figure 5.24, the 2-propenolate is clearly planar and freely refines to d(C47 =C48 B) = 1.26(3) Å (1.27(2) Å) for **25**α (**25**α*), which significantly shorter than the expected 1.31 Å but is within standard deviation. Bond distances in **25**α and **25**α* are within expectations and comparison between the two shows crystallographically significant but chemically irrelevant differences. Moreover, C=O and C—C distances of 1.22 Å and 1.45 Å are typical for C=O double and C—C single bonds in the anthraquinone moieties, hence if electrons had been injected into the clusters of **25**α* they are completely delocalised. The antraquinone is rotated so that O14 (028) aligns with Ti2 (Ti5) and O12 (O26). Fold angles of the carboxylate onto the cluster core ($Ti_2O_2\cdots O_2C$) and twist angles between and the adjacent phenyl ring ($O_2C\cdots Ar$) listed in Table 5.10 reveal that $AQCO_2$ in the clusters involving Ti4-6 is planar, whereas it is rotated approx. 10° more in the cluster involving Ti1-3.

Full clusters and the packing of **25**α and **25**α* are shown in Figure 5.25. The packing is

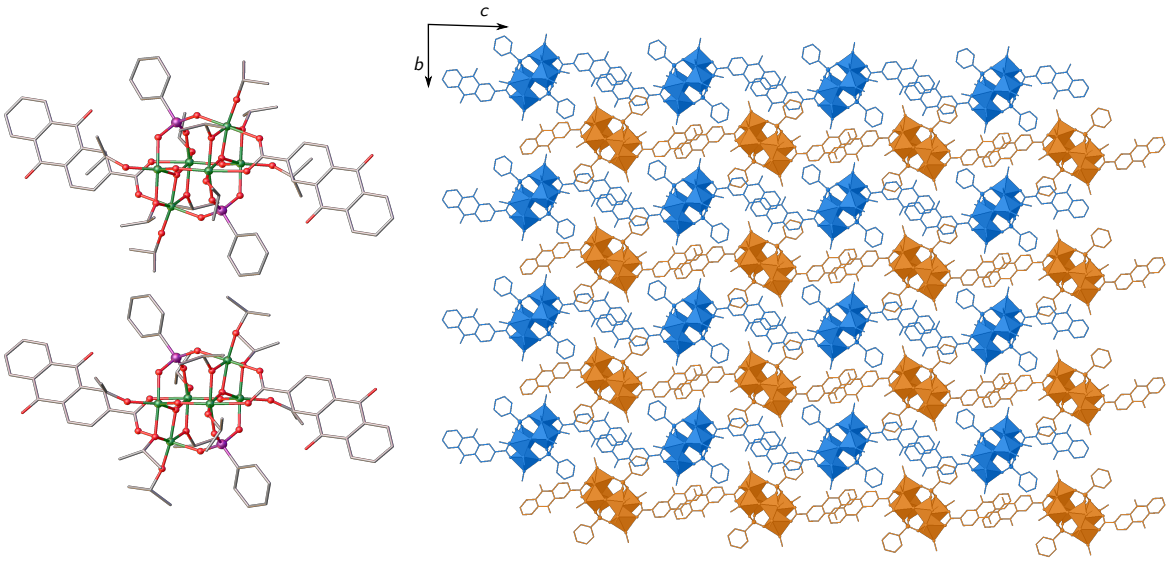


Figure 5.25: The {Ti_6}-oxo clusters in **25α** (left; clusters involving Ti1-3 top and Ti4-6 bottom) and its packing viewed along [100] (right; clusters involving Ti1-3 blue and Ti4-6 orange). Both are virtually identical for **25α***.

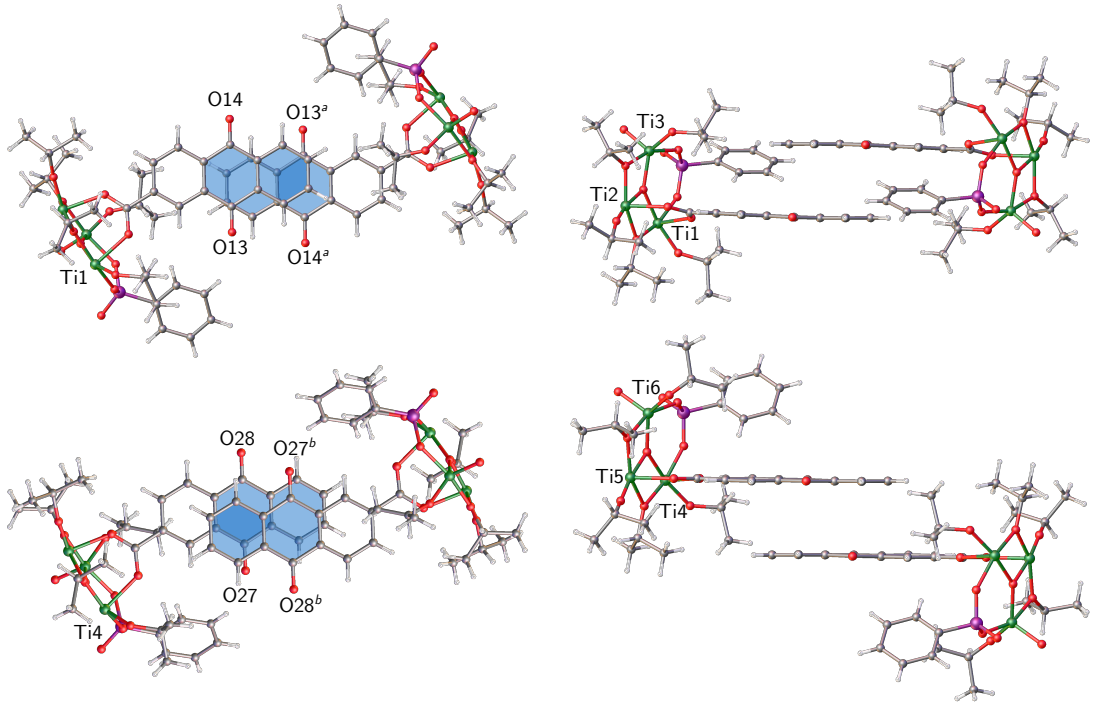


Figure 5.26: Top and side view of the π-π-interactions between {Ti_6}-oxo clusters in **25α** (and **25α***). Note that π-π-stacking occurs on opposite sites of the anthraquinone moieties for clusters involving Ti1-3 and Ti4-6, respectively. Symmetry key: $^a 1-x, 1-y, 2-z$, $^b -x, -y, 1-z$.

governed by parallel displaced π-π-stacking between the quinone and terminal phenyl group of $AQCO_2^-$ and its symmetry equivalent through inversion, but not with each other, resulting in 1D chains along *c*. Figure 5.26 shows an excerpt of the packing, elucidating the π-π-interactions. $AQCO_2$ ligands attached to Ti1 and Ti2 stack with $d_{\pi-\pi} = 3.465(2)$ Å and are shifted by 3.402(2) Å. Interestingly, stacking occurs one the other side of the ligand for 2-anthraquinonecarboxylates attached to Ti4 and Ti5, with $d_{\pi-\pi} = 3.388(3)$ Å and are shifted by 2.324(3) Å. Stacking in **25α*** is identical and within 1σ.

The polymorphs **25β** and **25γ*** crystallise with half of a cluster in the asymmetric unit, as depicted in Figure 5.27, and one molecule per unit cell. Again, bond distances

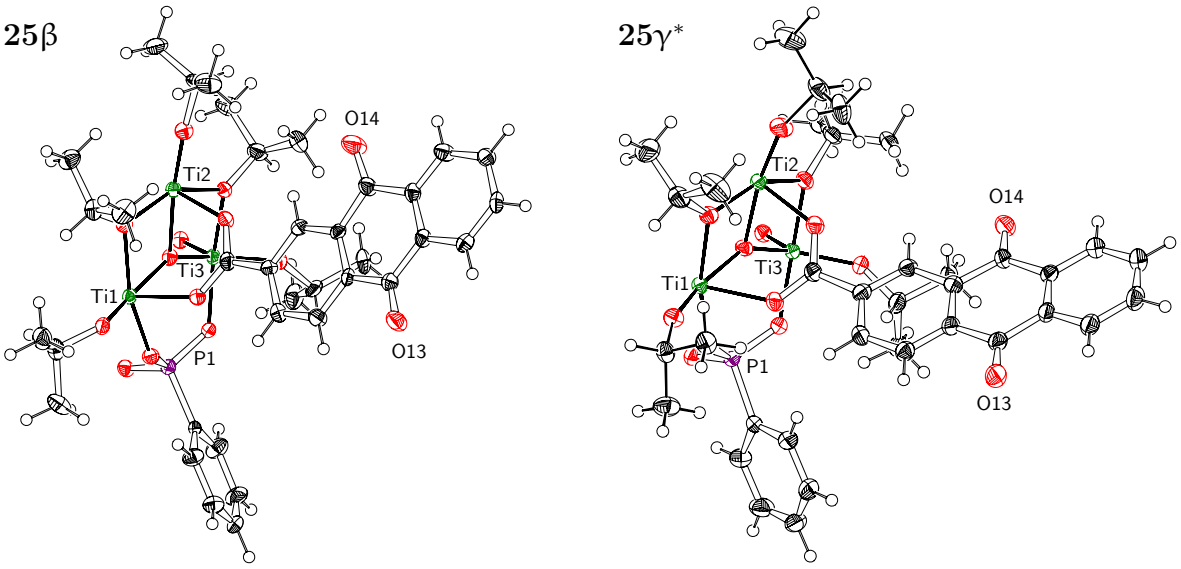


Figure 5.27: ORTEPs of the asymmetric units in the {Ti_6}-oxo clusters **25β** and **25γ***, plotted at 50% probablity. Disorder was omitted for clarity.

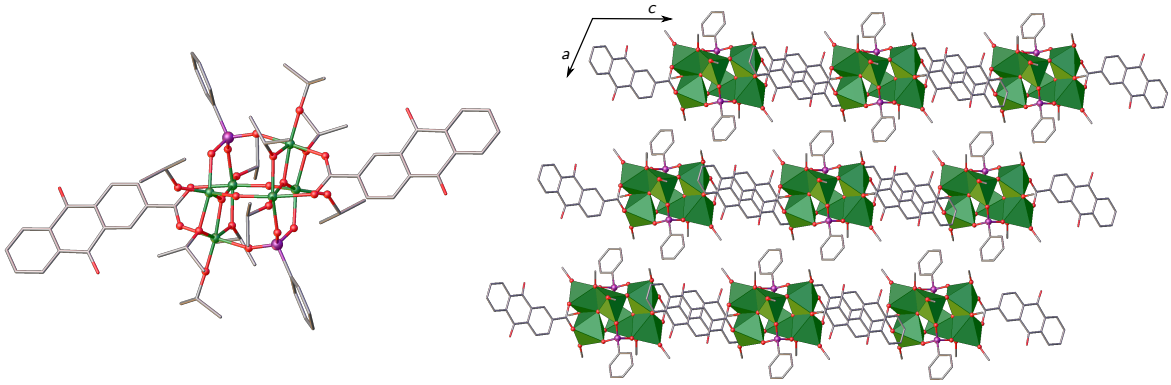


Figure 5.28: The {Ti_6}-oxo cluster **25β** (left) and its packing viewed along [0$\bar{1}$0] (right).

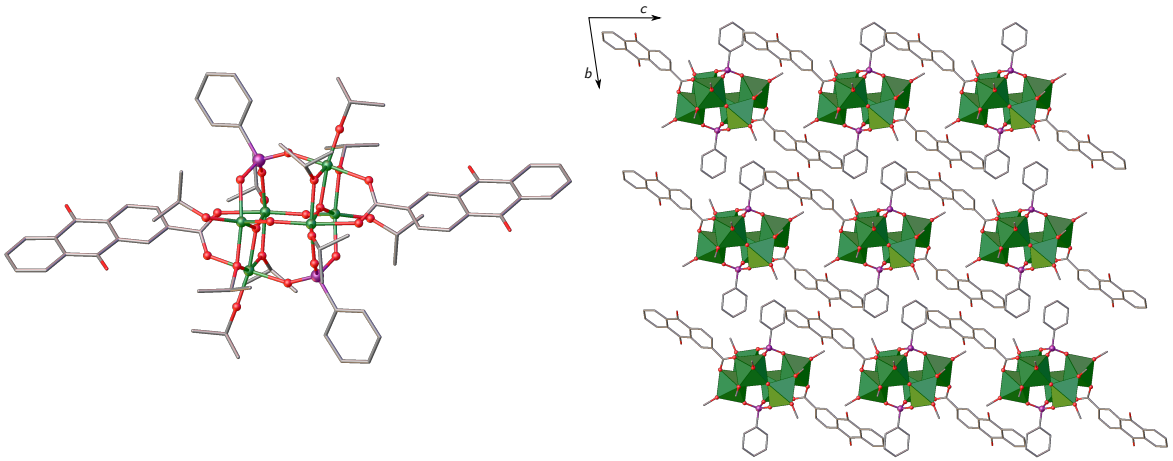


Figure 5.29: The {Ti_6}-oxo cluster **25γ*** (left) and its packing viewed along [100] (right).

are within expectations and no noteworthy deviations from each other or **25α** and **25α*** were observed. However, the ligands are flipped by roughly 180° with respect to **25α**, so that O13 roughly aligns with Ti1 and O11. In **25β** the anthraquinone moiety deviates by 6° from planarity with the carboxylate, in **25γ*** by 21°.

Figure 5.28 shows a full cluster and the packing in **25β**, in which π-π-stacking between 2-anthraquinoncarboxylates and their symmetry equivalents leads to a 1D chain along [011]. A full cluster and the packing of **25γ*** are presented in Figure 5.29. Here, the π-π-stacking results in a 1D chain along [$\bar{1}$11]. An excerpt of the packing of both, elucidating their parallel displaced π-π-stacking, is given in Figure 5.30. In both, interactions occur with the same side as in the clusters in Ti1-3 in **25α**, however the overlap here is greater as all three rings participate in the π-π-stacking. The $AQCO_2$ ligands in **25β** stack with $d_{\pi-\pi}$ = 3.420(3) Å and a shift of 1.490(4) Å. The parallel displacement in **25γ*** places the clusters ca 2.5 Å further apart, with $d_{\pi-\pi}$ = 3.422(3) Å and a shift of 1.831(3) Å. The large overlap of the aromatic systems in **25β** might be the reason for the difference in colour it and **25α** seen in Figure 5.22.

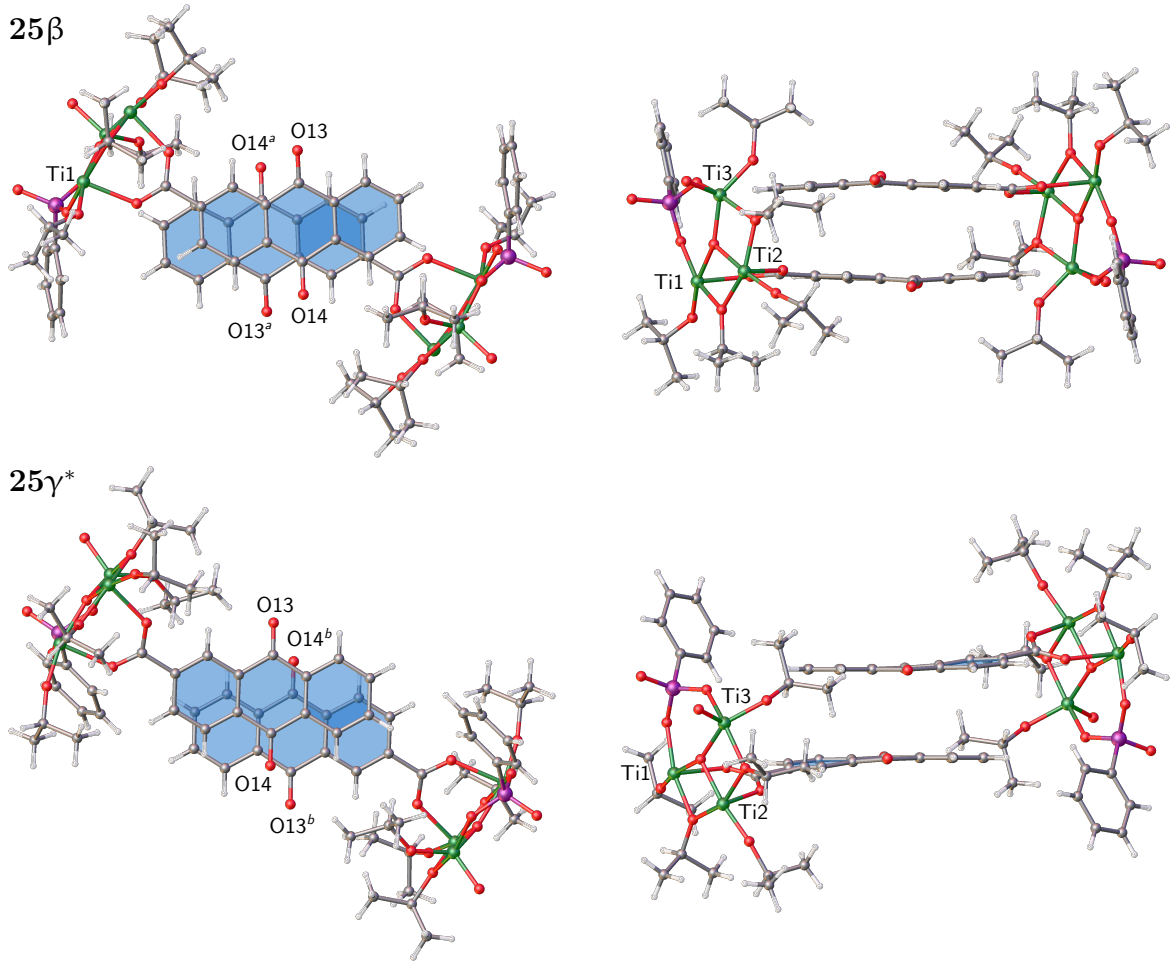


Figure 5.30: Top and side view of the π-π-interactions between {Ti_6}-oxo clusters in **25β** and **25γ***. Note the different shifts in the top view and bends of the anthraquinone moieties in the side views. Symmetry key: $^a1-x,1-y,-z$, $^b2-x,-y,1-z$.

Powder X-ray diffraction was carried out to determine phase compositions of **25**, as shown in Figure 5.31. As all polymorphs crystallise in the triclinic space group $P\bar{1}$, the patterns show an abundance of overlapping reflections, especially above 10° 2θ. However, a peak comprised of the [110] and [1$\bar{1}$0] reflections in **25α** observed at 9.25°, as well as a peak comprised the [010] [1$\bar{1}$0] reflections in **25β** observed at 7.85° show no overlap with the pattern of the other polymorph, respectively. If the reaction is carried out under air in a crimp vial and stopped after one day, a mixture of **25α** and **25β** are obtained, whereas reaction open to air in a round bottom flask or carried out under nitrogen in a crimp vial give phase pure **25α** (*via* **25α*** for the latter). In MeCN, the reaction mostly yields unidentified amorphous material accompanied by few single crystals of **25α*** and **25γ***.

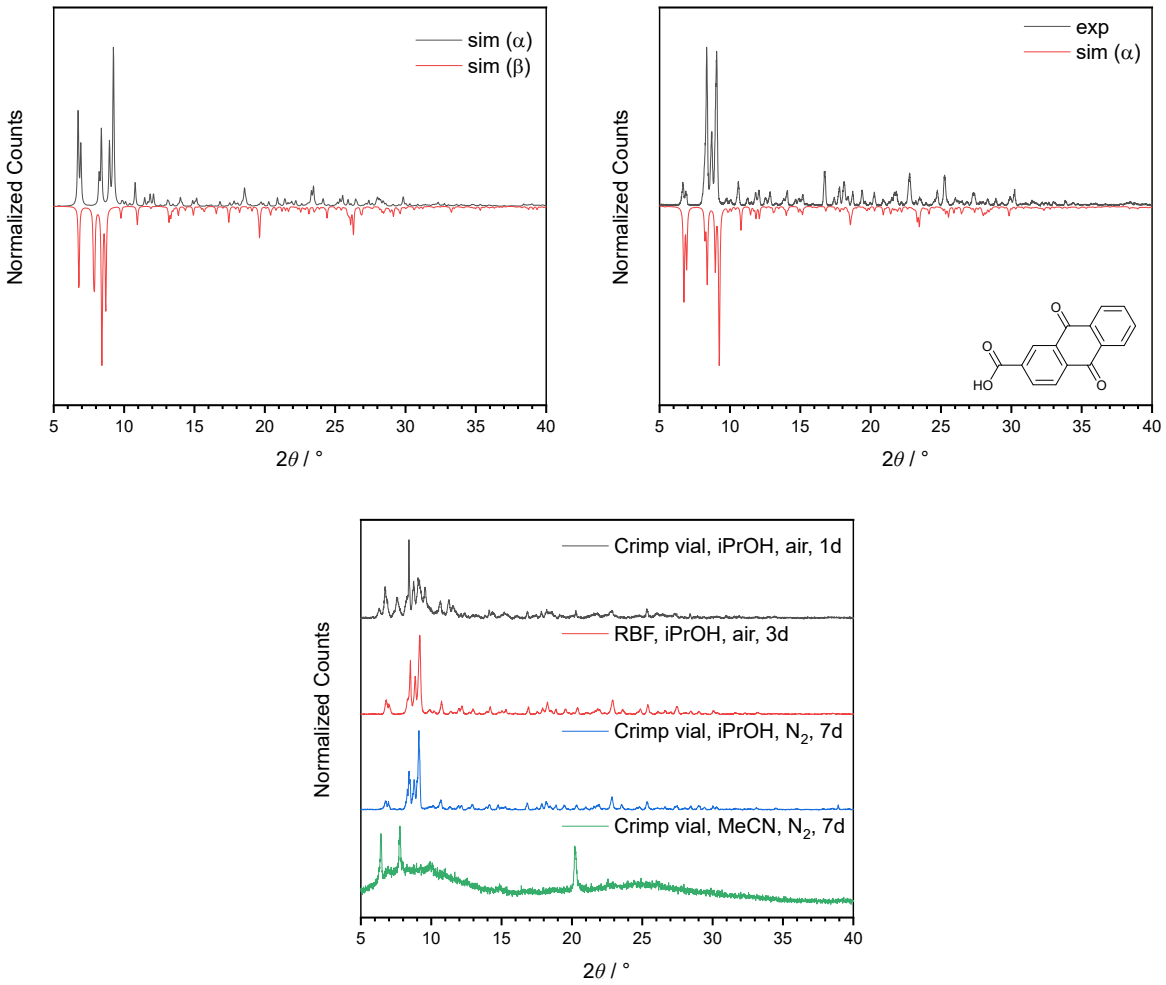


Figure 5.31: Comparisons powder X-ray patterns of polymorphs of **25**: Simulated patterns of polymorphs α and β (top left); experimental pattern of **25**α after reaction under nitrogen for 7 d (top right); influence of different synthetic conditions on the phase purity of **25**.

5.6.3. Optical Properties

The Kubelka-Munk function from the DRS of **25** is presented in Figure 5.32. The sample was obtained by autoclave reaction in iPrOH under nitrogen for 7 d, yielding purple crystals which turned grey upon isolation under ambient conditions, and was identified to be phase pure **25**α. During storage under ambient conditions the sample turned yellow and then slightly orange, which is reflected in the observation of the Kubelka-Munk function of the DRS. Moreover, two band gaps are present one in the near-UV region at 3.22 eV and on in the blue region at 2.70 eV with additional abosprtion up approximately 2.0 eV. The reasons for colour changes remain unknown, however some titanium-oxo clusters are known to undergo photochromism.[235,324,381]

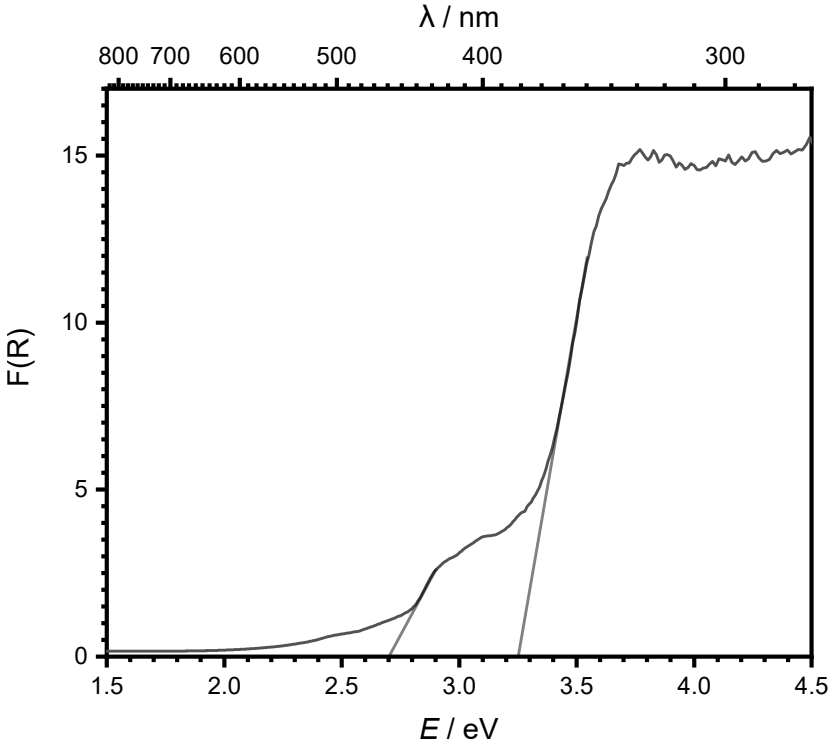


Figure 5.32: Kubelka-Munk function from the diffuse reflectance spectrum of the {Ti_6}-oxo clusters **25** (black, 3.22 eV, 2.70 eV). The bandgaps were determined by direct extrapolation.

5.7. Quantified Bandgap Engineering

This and the previous chapter, combined with the literature culminate in a plethora of TOCs featuring the $\{Ti_6P_2\}$ motif, with band gaps available for 52 clusters.[281,300,370,371,382] The discussion so far was limited to qualitative statements, however the prediction of band gaps based on known ligand properties is of course desirable for targeted band gap engineering. While this has not been attempted for TOCs so far, the use of Hammett constants is a fundamental concept of physical organic chemistry. It is based on the idea, there is a free-energy relationship between rates of reactions or their equilibrium constants of two reactions only differing in substituent, *viz.*

$$\log\left(\frac{K}{K_0}\right) = \rho\sigma \tag{5.1}$$

and may be rearranged to

$$\log K = \log K_0 + \rho\sigma \tag{5.2}$$

where K and K_0 are the rates of reaction or equilibrium constants of substituted and unsubstituted reactants; σ is a substituent constant, dependant upon only the substituent; ρ is a reaction constant and is a measure for electrical perturbation induced by the substituents, dependant upon reaction, medium and temperature.[383] It should be noted that ρ was defined as unity for the ionization of benzoic acid in water at 25 °C.[383] With regard to σ values, for aliphatic compounds only the inductive effect needs to be considered and in such cases σ^* is used. For aromatic compounds on the other hand, resonance effects need to be taken into account and Hammett values are separated into σ_{para} and σ_{meta}. In case of multiple substituents, σ values can simply be added up, *i.e.* $\sum\sigma$. The influence of *ortho*-substituents varies considerably with reaction and is also influenced by proximity effects, such as field effects (operating strongly at short distances), steric effects (hindrance of coplanarity), as well as hydrogen bonding, which contribute on top of the inductive and resonance effect. While Hammett constants have been reported for cornucopia of functionalities, they can be estimated through combination of related functionalities or approximations, when this is not the case.[384,385] Here, it is important to keep in mind that the inductive effect attenuates quickly over space in saturated hydrocarbons, hence transmission factors can be assigned to bridging groups, *e.g.* 0.41 for $-CH_2-$ (as well as $-O-$, $-NH-$, $-S-$, $-SO_2-$ *etc.*) 0.51 for $-CH{=}CH-$, and 0.31 for *para*-phenylene.[384] This however only applies for aliphatic but not to fully conjugated systems. Similarly to Equation 5.2 a

Hammett equation for can be constructed for the influence of substituent effects onto the associated TOC's band gap, *viz.*

$$E_g = E_{g,0} + \rho \sum \sigma \tag{5.3}$$

where both $E_{g,0}$ and ρ are dependant on the TOC motif but also the nature of the attached carboxylic acid, *e.g.* aliphatic, benzoic, or cynnamic acids. A Hammett plot for {Ti_6P_2} clusters featuring aliphatic carboxylates are presented in Figure 5.33. While the addition of one to three methyl groups ($+I$ effect, negative Hammett constants) to acetic acid decreases the band gap, so does the addition of electron-withdrawing groups ($-I$ effect, positive Hammett constants), with no clear correlation between Hammett constants and band gap.

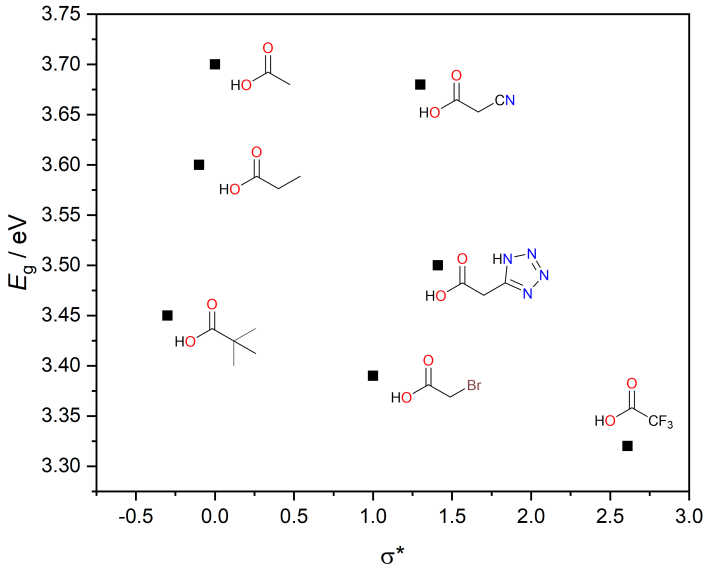


Figure 5.33: Hammett plot of band gaps of TOCs featuring the {Ti_6P_2} motif and aliphatic acids *vs.* Hammett constants of the latter.

Similar treatment was then conducted for TOCs obtained from aromatic acids. Heterocyclic components of six-membered rings in *e.g.* nicotinic acids can be treated as a substituents in that positions and Hammett values are available.[384] The five-membered thiophene ring was approximated as a six-membered ring with an −SR substituent.[384] For 2-naphthoic acid and 9-acridinecarboxylic acid, approximations for unsubsituted annelated rings were made.[384] Moreover, an approach developed by Dewar and Grisdale for polyaromatic systems was taken for quinoxalinecarboxylic acids (but are omitted in the fit).[384,386,387] TOCs featuring *ortho*-substituted carboxylic acids were

omitted in the analysis due to the aforementioned complications, which results in lack of available Hammett values. Moreover, no satisfactory approach to estimate Hammett values for imines (or extended conjugated systems) was found in the literature and are thus also omitted in this analysis. The σ_{para} values of -0.55 and -0.54 for −NCH−Ph and −NCH−4−Ph−OMe indicate that the value is largely dependent on the presence of the imine itself and not that of its substitution.[384,385] This is however in disagreement with strongly varying band gaps observed for **11c** (2.86 eV) and **11d** (2.99 eV), as well as analogues obtained from aminobenzoic acids and 4-diethylamino- and 4-diphenylaminobenzaldehyde with reported band gaps ranging from 2.58 eV to 2.71 eV.[281] The Hammett plot for TOCs featuring aromatic acids is portrayed in Figure 5.34, showing an overall clear correlation ($R^2 = 0.79$) between the Hammett constants of a given substituent with the TOC's optical band gap, giving the overall Hammett equation:

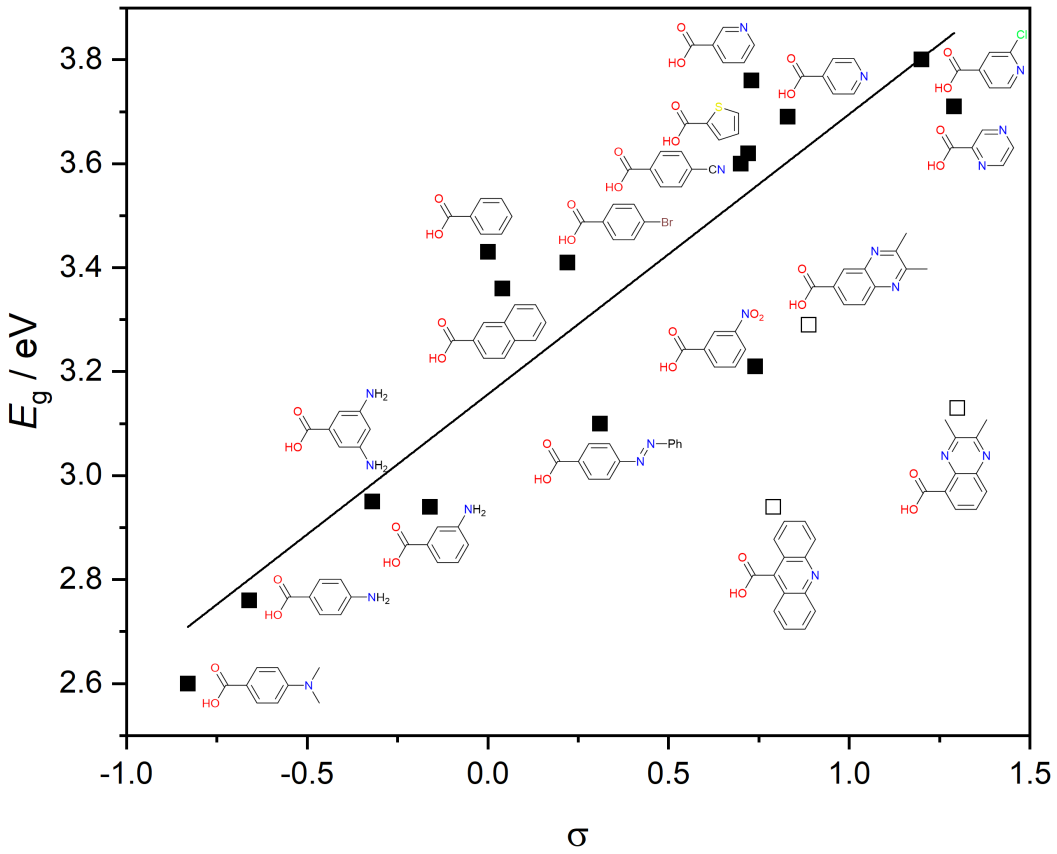


Figure 5.34: Hammett plot of band gaps of TOCs featuring the {Ti_6P_2} motif and aromatic acids *vs.* Hammett constants of the latter. Hollow data points were omitted in the fit.

$$E_g/\text{eV} = 3.16(5) + 0.54(7) \sum \sigma \tag{5.4}$$

As expected, the reaction constant ρ is positive, meaning that electron-donating and -withdrawing substituents respectively decrease and increase the clusters band gap. Curiously, $E_{g,0}$ deviates considerably (0.27 eV) from the band gap of the unsubstituted PTC-7, for which σ is defined as 0.[300] The strong deviation from the trend observed for the TOCs obtained from 9-acridine carboxylic acid and 5-quinolinecarboxylic acid, could be related to strong effects from *ortho*-substitution and deviations from coplanarity.[384] While the origins for strong deviations from the trend remain unclear, in these cases π-π-interactions can be excluded as they are present in none of the fitted structures.[281,300,370,371,382] Hence, Hammett constants are a useful tool for band gap engineering of TOCs, however the model is too simplistic for an accurate prediction.

5.8. Conclusions

This chapter has seen the expansion of the $\{Ti_6P_2\}$ motif with nine carboxylates featuring extended π-systems. For azo-benzene derivatives, the addition of a an electron-donating group seems to induce a push-pull effect, leading to orbital mixing and thus one overall band gap rather than two distinct O(p)→Ti(d) and n→π^* excitation bands. Moreover, it was shown that the expansion of aromatic systems to larger benzannulated systems (**22** and **23**) leads to a reduction of the optical band gap. Utilising push-pull dynamics of 7-aminocoumarin carboxylates leads to band gaps as low 2.48 eV. In addition, anthraquinone-functionalisation of the cluster (**25**) seems to induce a process in which the ligand undergoes an MPV reduction, followed by autoxidation and electron-injection into the cluster core. Interestingly this process can be induced thermally or by irradiation with near-UV light.

Lastly, an attempt to quantify the influence electronic effects of ligand substitution onto the band gap of the associated TOC. While this proofed futile for aliphatic carboxylic acids, a linear free-energy relationship could be established for simple aromatic carboxylic acids revealing a positive correlation between Hammett value and optical band gap. Hammett constants present a useful tool for future design of TOCs regarding ligand choice, however the numerous problems associated with estimating values for extended conjugated systems or *ortho*-substituted carboxylates greatly stifles their use in practical application. Clearly, other factors such as sterics (influence the Taft parameter) play a part, but given the error in estimating band gaps this was not pursued.

6. Anchoring of a Heteroleptic Cu^{I} Photosensitiser onto a Titanium-Oxo Cluster

6.1. Introduction

Heteroleptic diimine-diphosphine copper(I) complexes are becoming an ever more popular class of earht-abundant metal photosensitisers in order to replace a precious metal-containing $[Ru(bpy)_3]^{2+}$ complexes.[82] Especially 4,5-bis(diphenylphosphino)-9,9-dimethylxanthene (Xantphos) are attractive here, as it is not only commercially available but also comparably cheap and its Cu^{I} complexes are strong photoreductants with long lived excited states.[82] The formation of composite materials between photosensitisers with nanoporous TiO_2 is not only of great interest in the field of DSCs, but also find application in photocatalysis.[388–390] Beller *et al.* have reported that a diimine-diphosphine copper(I) photosensitiser-TiO_2 composite materials outperform just the photosensitiser with respect to photocatalytic hydrogen production in the presence of an iron reduction catalyst.[391] The precise attachment of such a photosensitiser onto a TOC might serve as a model compound for mechanistic studies.

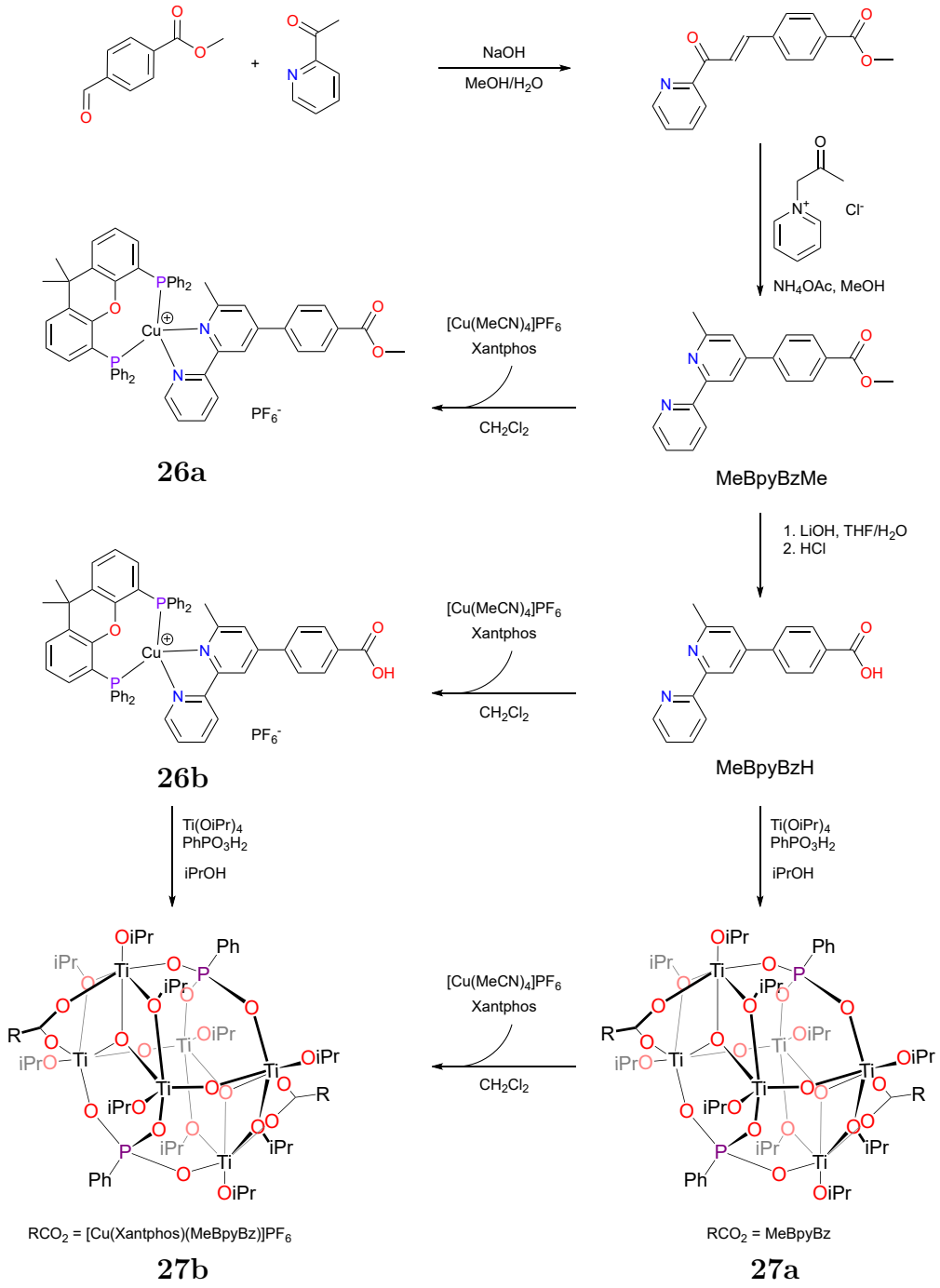
The objective of the work described in this chapter was to anchor diimine-diphosphine copper(I) photosensitiser onto the $\{Ti_6P_2\}$ motif. The LUMO of these heteroleptic complexes is typically found on the diimine ligand, which will thus be modified to function as the ancillary ligand bridging the titanium-oxo cluster core and copper(I) centre.

6.2. Synthesis

The synthetic route of a bipyridyl-functionalised $\{Ti_6\}$-oxo cluster and its modification with a heteroleptic Cu^{I} photosensitiser is presented in Scheme 6.1.

The aldol condensation of 2-acetylpyridine and methyl 4-formylbenzoate gave methyl 4-carboxy-2'-azachalcone, which was followed by a Kröhnke pyridine synthesis with 1-acetonylpyridinium chloride to obtain the ligand methyl-4-(4"-carboxyphenyl)-6-methyl-2,2'-bipyridine (MeBpyBzMe), and finally ester hydrolysis gave in 4-(4"-carboxyphenyl)-6-methyl-2,2'-bipyridine (MeBpyBzH).

The diphosphine-diimine copper(I) complexes $[Cu(Xantphos)(MeBpyBzMe)]PF_6$ (**26a**) and $[Cu(Xantphos)(MeBpyBzH)]PF_6$ (**26b**) were synthesised by adopting a procedure by Beller *et al.* That is, $[Cu(MeCN)_4]PF_6$ with Xantphos were brought to reflux in DCM overnight, followed by the addition of solid bipyridyl ligand, further reflux and subsequent isolation. The $\{Ti_6\}$-oxo cluster $[Ti_6O_4(OiPr)_{10}(O_3PPh)(MeBpyBz)]$ (**27a**) was obtained by modifying Zhang's procedure.[300] The reaction of $[Cu(MeCN)_4]PF_6$ with Xantphos followed by the addition of **27a** yielded the doubly $[Cu(Xantphos)]PF_6$ functionalised $\{Ti_6\}$-oxo cluster $[Ti_6O_4(OiPr)_{10}(O_3PPh)_2\{Cu(Xantphos)(MeBpyBz)\}_2](PF_6)_2$ (**27b**). While this method only afforded **27b** as amorphous powder, single crystals were obtained by an analogous synthesis of **27a** using **26b** as carboxylic acid.



Scheme 6.1: Synthetic routes to the heteroleptic Cu^{I} photosensitiser modfied $\{Ti_6\}$-oxo cluster **27b** *via* $[Cu(Xantphos)(MeBpyBzH)]PF_6$ or bipyridine modified $\{Ti_6\}$-oxo cluster **27a**, from MeBpyBzH and synthesis of the latter.

6.3. Crystal Structures

Crystal data and refinement results for the Cu^{I} complexes **26a** and **26b** as well as the $\{Ti_6\}$-oxo clusters **27a** and **27b** are listed in Table 6.1. Selections of distances and angles for the coordination of Cu^{I} in **26a**, **26b** and **27b**, as well as the $\{Ti_6\}$-oxo cluster in **27a** and **27b** are given in Table 6.2 and Table 6.3, respectively. Continuous shape measurements for the coordination environment the Cu^{I} centres are listed in Table 6.4.

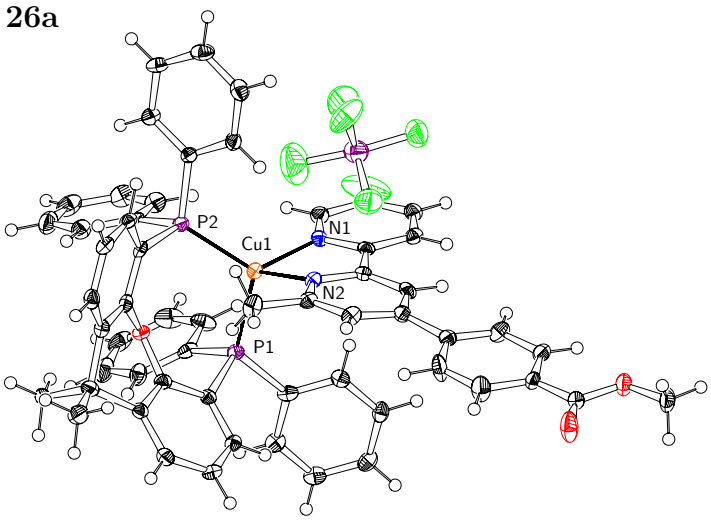


Figure 6.1: ORTEP of the asymmetric unit in $[Cu(Xantphos)(MeBpyBzMe)]PF_6$ (**26a**), at 50% probablity.

Crystals of $[Cu(Xantphos)(MeBpyBzMe)]PF_6$ (**26a**) were grown by diffusion of iPrOH into a MeCN solution of the complex. **26a** crystallises as yellow blocks, was solved and refined in the triclinic space group $P\bar{1}$ with one molecule in the asymmetric unit (thermal ellipsoid plotted in Figure 6.1) and two molecules per unit cell. In the complex cation, Cu1 is chelated by Xantphos and MeBpyBzMe, resulting in a distorted tetrahedral (T-4) coordination environment. Alternatively, the coordination geometry can be described as a vacant trigonal bipyramid (vTBPY), with N1, N2 and P2 forming the trigonal base, and P2 as apex. While continuous shape measurements reveal T-4 to be geometrically more accurate, the description as vTBPY facilitates as an aid in structure discussion. The Cu—N bond distances of 2.057(4) Å and 2.080(4) Å, as well as the Cu—P bond distances of 2.2925(17) Å and 2.2458(18) Å are close the reported values for $[Cu(Xantphos)(Mebpy)]^{+}$. The pyridine rings are twisted by 6.0° and bites Cu1 at 79.27(14)°, with a Xantphos bite angle of 111.71(6)°

Table 6.1: Crystal data and refinement results of **26a**, **26b**, **27a** and **27b**.

Identification code	**26a**	**26b** · 0.52 CH_2Cl_2 · 1.96 Et_2O
Empirical formula	$C_{58}H_{48}CuF_6N_2O_3P_3$	$C_{65.38}H_{66.19}Cl_{1.04}CuF_6N_2O_{4.96}P_3$
Formula weight	1091.43	1266.76
Temperature/K	100	100
Crystal description	yellow block	yellow block
Crystal size/mm^3	0.228 × 0.098 × 0.064	0.267 × 0.211 × 0.189
Crystal system	triclinic	triclinic
Space group	$P\bar{1}$	$P\bar{1}$
a/Å	11.589(6)	14.8774(5)
b/Å	13.644(8)	15.4331(6)
c/Å	16.284(9)	28.7708(10)
α/°	88.48(3)	96.4560(10)
β/°	84.898(19)	103.2610(10)
γ/°	75.06(3)	102.2490(10)
V/$Å^{-3}$	2478(2)	6192.6(4)
Z, Z'	2, 1	4, 2
ρ_{calc}/g cm^{-3}	1.463	1.359
μ/mm^{-1}	0.61	0.544
$F(000)$	1124	2632
Refl. total/unique	37970/9162	109783/27699
R_{int}, R_σ	0.1354, 0.1136	0.0579, 0.0533
Data/restr./param.	9162/0/662	27699/235/1620
GooF	1.009	1.024
R_1 $[I \geq 2\sigma(I)]$, all	0.0587, 0.1263	0.0555, 0.0926
wR_2 $[I \geq 2\sigma(I)]$, all	0.1206, 0.1478	0.1415, 0.1640
$\Delta\rho_{max}/\Delta\rho_{min}$/e $Å^{-3}$	0.60/-0.69	1.56/-1.00
Identification code	**27a**	**27b** · 4 iPrOH
Empirical formula	$C_{78}H_{106}N_4O_{24}P_2Ti_6$	$C_{167.9}H_{201.7}Cu_2F_{12}N_4O_{30}P_8Ti_6$
Formula weight	1833	3646.06
Temperature/K	100	100
Crystal description	colourless plate	yellow plate
Crystal size/mm^3	0.07 × 0.22 × 0.50	0.128 × 0.288 × 0.331
Crystal system	triclinic	triclinic
Space group	$P\bar{1}$	$P\bar{1}$
a/Å	11.860(3)	12.292(9)
b/Å	13.924(3)	14.448(10)
c/Å	15.187(4)	28.93(2)
α/°	68.949(6)	79.863(8)
β/°	67.332(6)	78.428(13)
γ/°	86.606(7)	77.243(7)
V/$Å^{-3}$	2150.6(9)	4862(6)
Z, Z'	1, 0.5	1, 0.5
ρ_{calc}/g cm^{-3}	1.415	1.245
μ/mm^{-1}	0.642	0.587
$F(000)$	956	1895
Refl. total/unique	43703/11111	246846/27409
R_{int}, R_σ	0.0672, 0.0588	0.0511, 0.0295
Data/restr./param.	11111/15/555	27409/1040/1447
GooF	1.029	1.062
R_1 $[I \geq 2\sigma(I)]$, all	0.0478, 0.9868	0.0532, 0.0769
wR_2 $[I \geq 2\sigma(I)]$, all	0.1085, 0.1255	0.1483, 0.1679
$\Delta\rho_{max}/\Delta\rho_{min}$/e $Å^{-3}$	0.62/-0.61	1.04/-0.99

Table 6.2: Bond distances (Å) and angles (°) of the Cu^{I} moieties in **26a**, **26b** and **27b**.

26a	
Cu1—N1	2.057(4)
Cu1—N2	2.080(4)
Cu1—P1	2.2925(17)
Cu1—P2	2.2458(18)
N1—Cu1—N2	79.27(14)
P1—Cu1—P2	111.71(6)
φ(Cu1)	90.45(12)
26b	
Cu1—N1	2.090(3)
Cu1—N2	2.069(2)
Cu1—P1	2.2445(8)
Cu1—P2	2.2843(9)
N1—Cu1—N2	79.95(10)
P1—Cu1—P2	115.50(3)
φ(Cu1)	94.449(2)
Cu2—N3	2.055(3)
Cu2—N4	2.077(2)
Cu2—P3	2.2237(9)
Cu2—P4	2.2872(9)
N3—Cu—N4	80.07(10)
P3—Cu2—P4	119.69(3)
φ(Cu2)	88.6590(16)
27b	
Cu1—N1	2.090(2)
Cu1—N2	2.062(2)
Cu1—P2	2.2457(18)
Cu1—P3	2.2499(15)
N1—Cu1—N2	80.34(9)
P2—Cu1—P3	115.30(3)
φ(Cu1)	94.63(6)

Table 6.3: Bond distances (Å) and angles (°) in **27a** and **27b** in Å.

Bond	Distance	**27a**	**27b**
Ti—μ_3-O	Ti1—O1	1.9967(19)	2.014(2)
	Ti2—O1	1.9755(18)	1.9870(18)
	Ti3—O1	1.9134(18)	1.9046(19)
Ti—μ_2-O	Ti1—O7^a	1.8513(18)	1.8698(19)
	Ti3—O7	1.7615(18)	1.772(2)
Ti—μ_2-OiPr	Ti1—O3	2.0291(18)	2.0258(18)
	Ti2—O3	1.9719(19)	1.988(2)
	Ti2—O5	1.9659(19)	1.953(2)
	Ti3—O5	2.0254(18)	2.0470(19)
Ti—OiPr	Ti1—O2	1.7977(18)	1.804(2)
	Ti2—O4	1.7654(18)	1.7715(19)
	Ti3—O6	1.796(2)	1.809(2)
Ti—O_2CR	Ti1—O11	2.1176(18)	2.136(2)
	Ti2—O12	2.0986(18)	2.0950(19)
RCO_2	O11—C22	1.264(3)	1.263(3)
	O12—C22	1.268(3)	1.270(3)
Ti—O_3PPh	Ti1—O9	1.9585(18)	1.9505(18)
	Ti2—O10^a	1.9458(18)	1.9622(19)
	Ti3—O8	1.9673(19)	1.963(2)
P—O	P1—O8	1.523(2)	1.527(2)
	P1—O9	1.524(2)	1.5270(19)
	P1—O10	1.5231(19)	1.526(2)
Angle		**27a**	**27b**
$Ti_2O_2 \cdots O_2C$		0.8(3)	2.5(3)
$O_2C \cdots Ph$		3.13(8)	4.79(9)
Ph ⋯ Py1		28.26(9)	133.61(8)
Py1 ⋯ Py2		174.66(11)	17.79(8)

Planes: Ti_2O_2 (Ti1-2, O11-12), Ph (C23-28), Py1 (N1, C30-34), Py2 (N2, C35-39).
Symmetry key:$^a -x, 1-y, 1-z$ (for **27a**); $1-x, -y, 1-z$ (for **27b**).

Table 6.4: Continuous shape measures of Cu^{I} coordination environments.

Compound	T-4	vTBPP
[Cu(Xantphos)(MeBpy)]PF_6 [91]	2.845	3.152
26a	3.203	3.993
26b (Cu1)	3.070	3.509
26b (Cu2)	3.276	3.632
27b	2.879	3.440

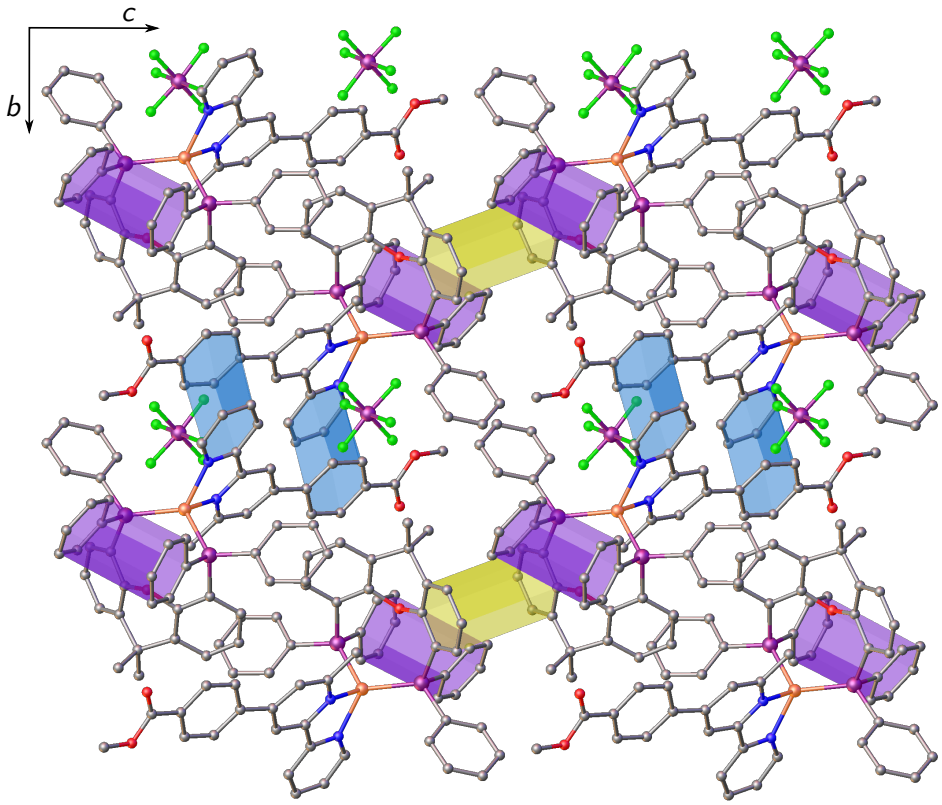


Figure 6.2: Packing of **26a** viewed along [100]. Colour code for face-to-face π-π-interactions: Violet, intraligand between Xantphos phenyl rings; yellow, intramolecular xanthene rings; blue, intermolecular between MeBpyBzMe pyridine and phenyl rings. Hydrogen atoms were omitted for clarity.

and with the chelating planes being orthogonal to each other (dihedral angle φ). The phenyl ring is twisted by 7.60(19)° with respect to the methylpyridine. In line with $[Cu(Xantphos)(Mebpy)]^{+}$, the xanthene moiety adopts a boat-conformation, with the bowl accommodating the methyl group of MeBpyBzMe. Here, a short CH-arene interaction is observed with $d(CH_{Me} \cdots \text{arene}) = 2.71$ Å. Figure 6.2 depicts the packing of **26a**, with highlighted intra- and intermolecular face-to-face π-π-interactions: First, intraligand stacking between two phenyl rings belonging to Xantphos, with a distance of 3.753(4) Å, a shift of 0.804(1) Å and twisted by 16.73(19)°. Second, intermolecular stacking between one of the xanthene moiety's phenyl rings and its symmetry equivalent through inversion, with $d_{\pi-\pi} = 3.359(6)$ Å and a shift of 1.866(8) Å. And lastly, to and fro stacking between the terminal pyridine and phenylene moeties of two MeBpyBzMe ligands related through inversion.

The corresponding free acid of **26a**, $[Cu(Xantphos)(MeBpyBzH)]PF_6$ (**26b**), was crys-

26b

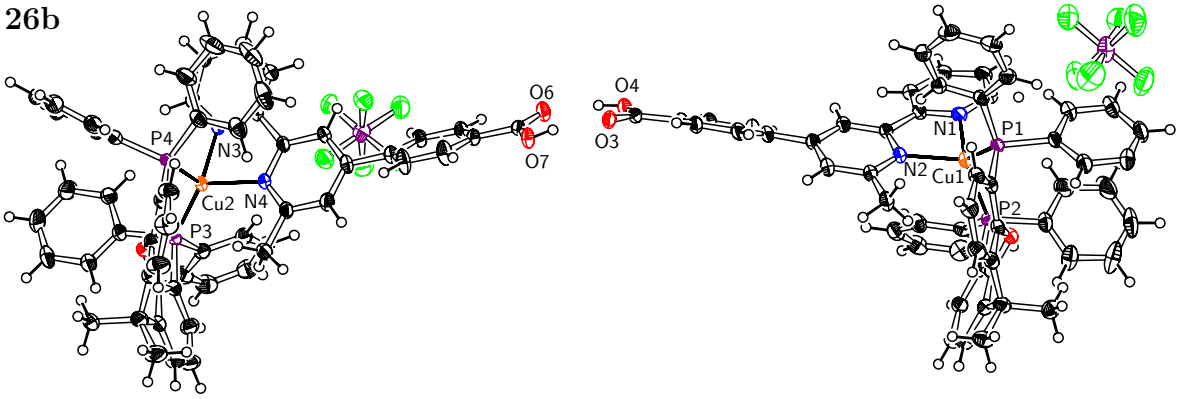


Figure 6.3: ORTEP of the asymmetric unit in the dimer forming [Cu(Xantphos)(MeBpyBzH)]PF_6 (**26b**), at 50% probablity. Co-crystallised solvent molecules were omitted for clarity.

Table 6.5: Hydrogen bonds in **26b**.

Donor—H$\cdots$Acceptor	D—H [Å]	H$\cdots A$ [Å]	$D\cdots A$ [Å]	D—H$\cdots A$ [°]
O4—H4$\cdots$O6	0.84	1.77	2.598(3)	166
O7—H7A$\cdots$O3	0.84	1.83	2.666(3)	172

tallised by diffusion of Et_2O into a CH_2Cl_2 solution of the complex. It co-crystallises with approximately half a molecule of CH_2Cl_2 and two molecules of Et_2O per complex as yellow blocks. It was solved and refined in the triclinic space group $P\bar{1}$ with a dimer of **26b** in the asymmetric unit (thermal ellipsoid plotted in Figure 6.3) and four molecules per unit cell. While two complexes in the asymmetric unit are related through pseudo-C_2 symmetry, significant differences are observed in the coordination environments of Cu1 and Cu2. Both can be described as distorted tetrahedral or vacant trigonal bipyramid, with N1, N2 and P1 (N3, N4 and P3) forming the trigonal base and P2 (P4) as the apex for Cu1 (Cu2). While the N—Cu—N bite angles are virtually identical, the P—Cu—P bite angle is four degrees bigger for Cu2. While the chelating planes around Cu2 are virtually orthogonal, they deviate by 4.4° in for Cu1. The terminal pyridyl and beanzoic acid moieties are respectively twisted by 11.48(11)° (2.32(10)°) and 33.30(11)° (132.55(12)°) in the complex cation involving Cu1 (Cu2). The short $CH_{Me}\cdots$arene contacts are elongated to 3.01 Å (Cu1) and 2.76 Å (Cu2). The packing in **26b**, as shown in Figure 6.4, is influenced by hydrogen bonding (see Table 6.5) and π-π-stacking. Two symmetrically independent complex cations dimerise *via* to and fro hydrogen bonding of their carboxylic acid moieties, which classify as hydrogen bonds of moderate strength with donor-acceptor distances of approx.2.6 Å and donor-H-acceptor angles close to 180°.[346] Intraligand π-π-stacking found in [Cu(Xantphos)(MeBpy)]PF_6

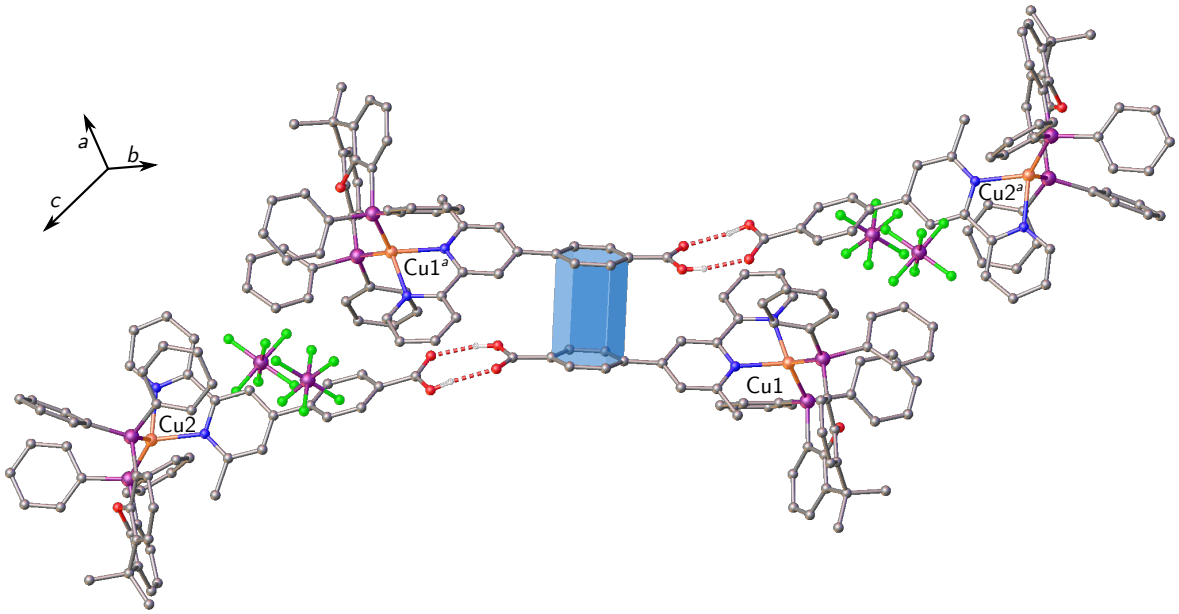


Figure 6.4: The packing of **26b** reveals dimerisation *via* hydrogen bonding and π-π-interactions of the MeBpyBzH moiety bound to Cu1 and it's inversion equivalent Cu1^{a}. Solvents and non-hydrogen bonding hydrogen atoms were omitted for clarity. Symmetry key: $^{a}: 1-x, 1-y, 1-z$.

and **26a** is not observed in **26b**, as the phenyl groups in the complex cation involving Cu1 are 4.058(4) Å apart, shifted by 1.407(8) Å and rotated by 24.30(14)°, wheres in the complex cation of Cu2 they are rotated by 75.58(15)°.[91] Yet, parallel displaced π-π-stacking is observed between MeBpyBzH phenyl ring of the complex cation involving Cu1 and its symmetry equivalent through inversion, with $d_{\pi-\pi} = 3.809(3)$ Å and a shift of 1.096(6) Å.

The {Ti_6}-oxo-cluster **27a** crystallises as colourless plates. The structure was solved and refined in the triclinic space group $P\bar{1}$ with half a molecule in the asymmetric unit (thermal ellipsoid plotted in Figure 6.5) and one molecule per unit cell. A full cluster and the packing of **27a** are shown in Figure 6.6. The carboxylate is perpendicular to the Ti_3-face and co-planar with the phenyl moiety. Moreover, Py1 is in plane with Ti1—O1 and the MeBpy moiety rotated so that Py2 is on the side of Ti1. Moreover, the pyridyl rings are *anti* to each other due to lone pair-lone pair repulsion of N1 and N2. The packing of **27a** is governed by π-π-interactions involving the trisubsituted pyridine ring Py1. First, it engages in parallel displaced π-π-stacking with its symmetry equivalent through inversion translated along a with $d_{\pi-\pi} = 3.448(3)$ Å and a shift of 1.185(5) Å. Second, it engages in T-shaped π-π-stacking with the phenyl phosphonate of a cluster

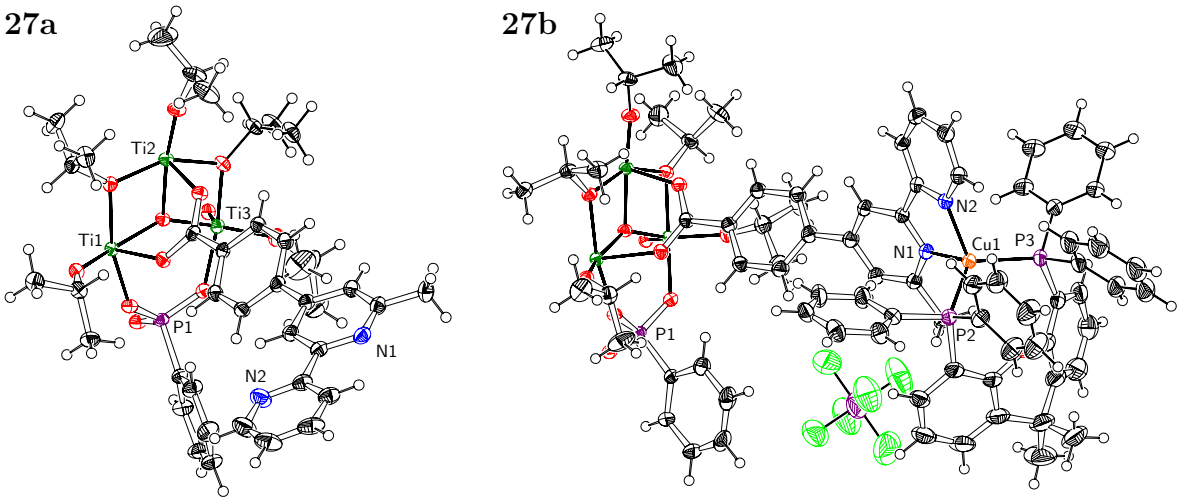


Figure 6.5: ORTEPs of the asymmetric units in the bipyridine functionalised $\{Ti_6\}$-oxo clusters **27a** and it's bis-([Cu(Xantphos)]PF_6) complex **27b**, at 50% probablity. Disorder was omitted for clarity.

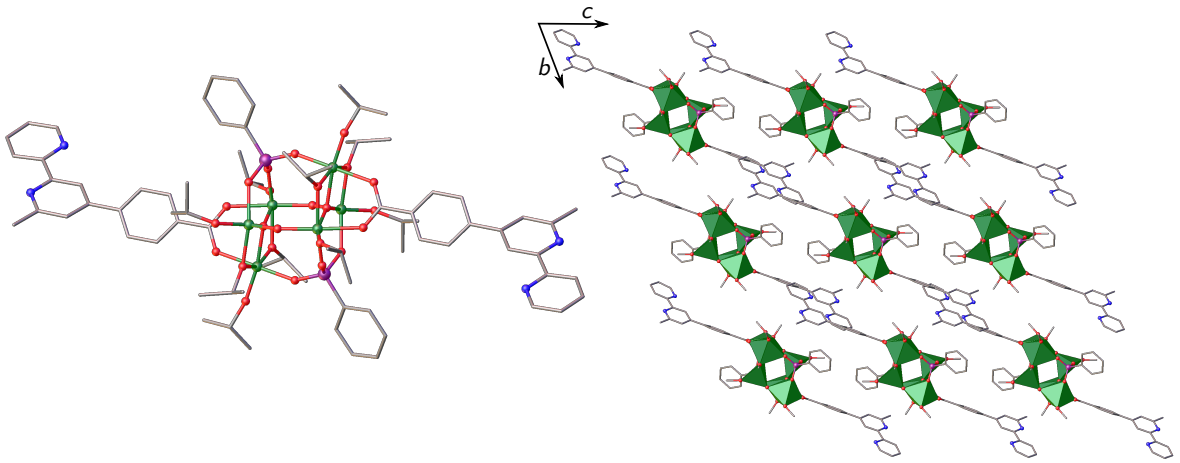


Figure 6.6: The $\{Ti_6\}$ cluster **27a** (left) and its packing (right) viewed along [100].

adjacent through inversion and translation along b , with $d_{H\cdots C} = 2.819(3)$ Å and $\angle_{C-H\cdots C} = 170.8(3)°$.

The [Cu(Xantphos)]PF_6 modified $\{Ti_6\}$-oxo cluster **27b** co-crystallises with 4 molecules of iPrOH per cluster, with half of a molecule in the asymmetric unit (thermal ellipsoids plotted in Figure 6.5) and one molecule per unit cell. A full cluster and the packing of **27b** are shown in Figure 6.7. It is noteworthy, that the shape **27b** can be approxamited as a cylinder with a length and diameter of 45 Å and 17 Å, respectively. Bond distances in the $\{Ti_6\}$-oxo cluster are within expectations and approx.5σ of **27b**, with an elongation of 0.02 Å in the Ti1—O11 bond being the most significant difference.

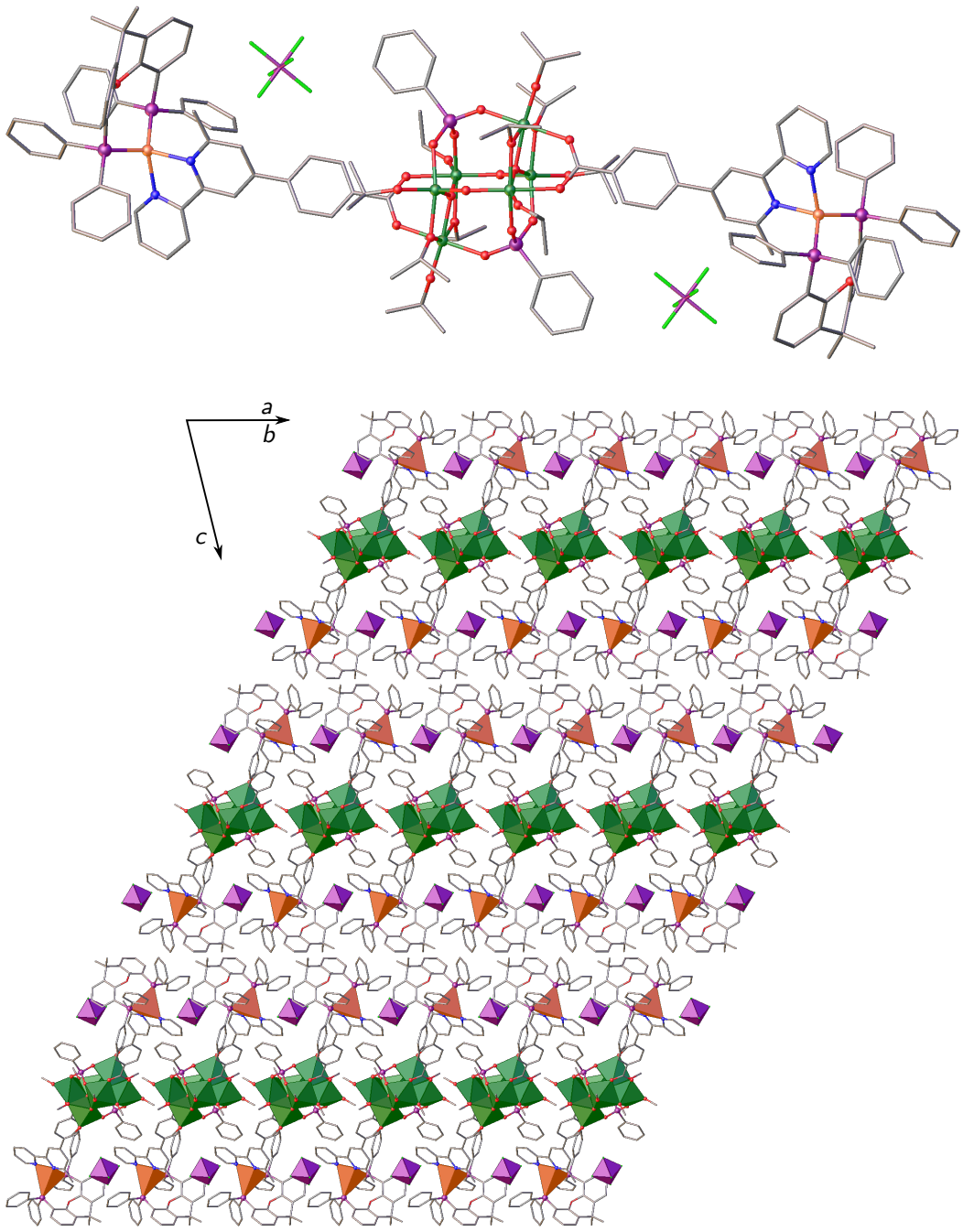


Figure 6.7: The $\{Ti_6\}$ cluster **27b** (top) and its packing (bottom) viewed along $[\bar{1}10]$.

The coordination environment of Cu1 is a distorted tetrahedron, however the alternative description as a vacant trigonal bipyramid is not valid anymore as bonds to P2 and P3 are equidistant at 2.25 Å. Interestingly, the remaining values are virtually identical with the coordination environment of Cu1 in **26b**. The angle between the benzoate and MeBpy moieties is in good agreement with the observations from **26b**, with the

latter being rotated approx.90° with respect to **27a** so that it aligns with Ti2—O1. The aforementioned change of Cu—P distances is accompanied by the formation of an additional $CH_{Me}\cdots$arene interaction between MeBpy and the xanthene bowl with $CH_{Me}\cdots$arene distances of 2.73 Å and 2.66 Å. Furthermore, a phenyl group attached to P2 engages in T-shaped π-π-stacking with Py1 with $d(CH\cdots\pi) = 2.68$ Å. In the packing of **27b**, the phenylphosphonate engages in parallel displaced and T-shaped π-π-stacking, respectively with Py2 ($d_{\pi-\pi} = 3.376(3)$ Å, shifted by 1.767(4) Å and tilted by 12.74(9)°) and the previously mentioned phenyl ring attached to P2 of an adjacent molecule ($d(CH\cdots\pi) = 2.73$ Å).

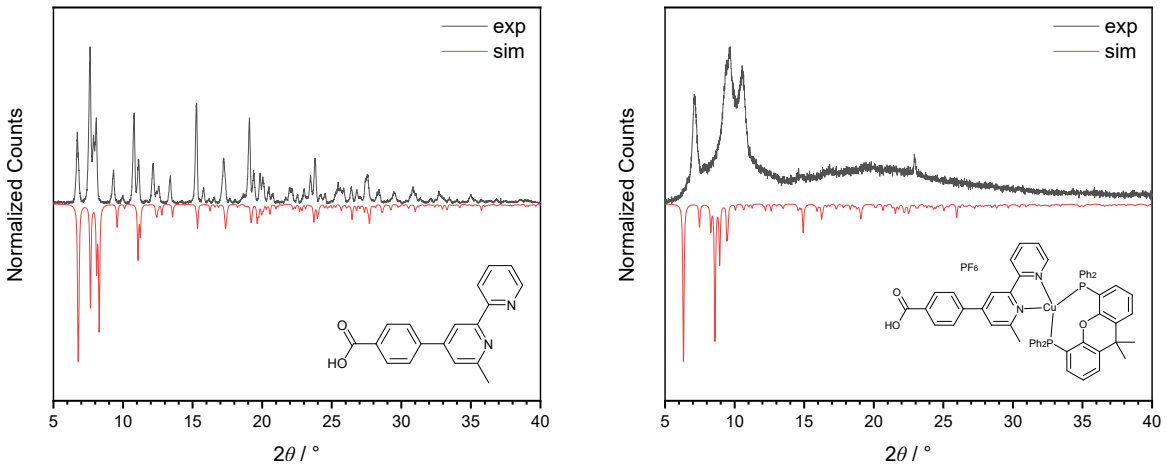


Figure 6.8: Powder X-ray diffraction patterns of **27a** (left) and **27b** (right), with their corresponding carboxylic acids inset.

The powder X-ray diffraction patterns of the free bipyiridyl and Cu^{I}-complexed $\{Ti_6\}$-oxo clusters **27a** and **27b** are shown Figure 6.8. **27a** crystallises phase pure, whereas **27b** does not seem to be stable upon isolation.

6.4. Additional Characterisations

In order to assess whether both synthetic approaches lead to the same product, the samples were analysed by FTIR and NMR spectroscopy. The Fourier transformed infrared spectra of **27b** obtained from **27a** and **26b**, respectively, as well as their spectra are shown in Figure 6.9. While some minor differences between the amorphous and crystalline sample of **27b** are observed, the spectra are largely identical.

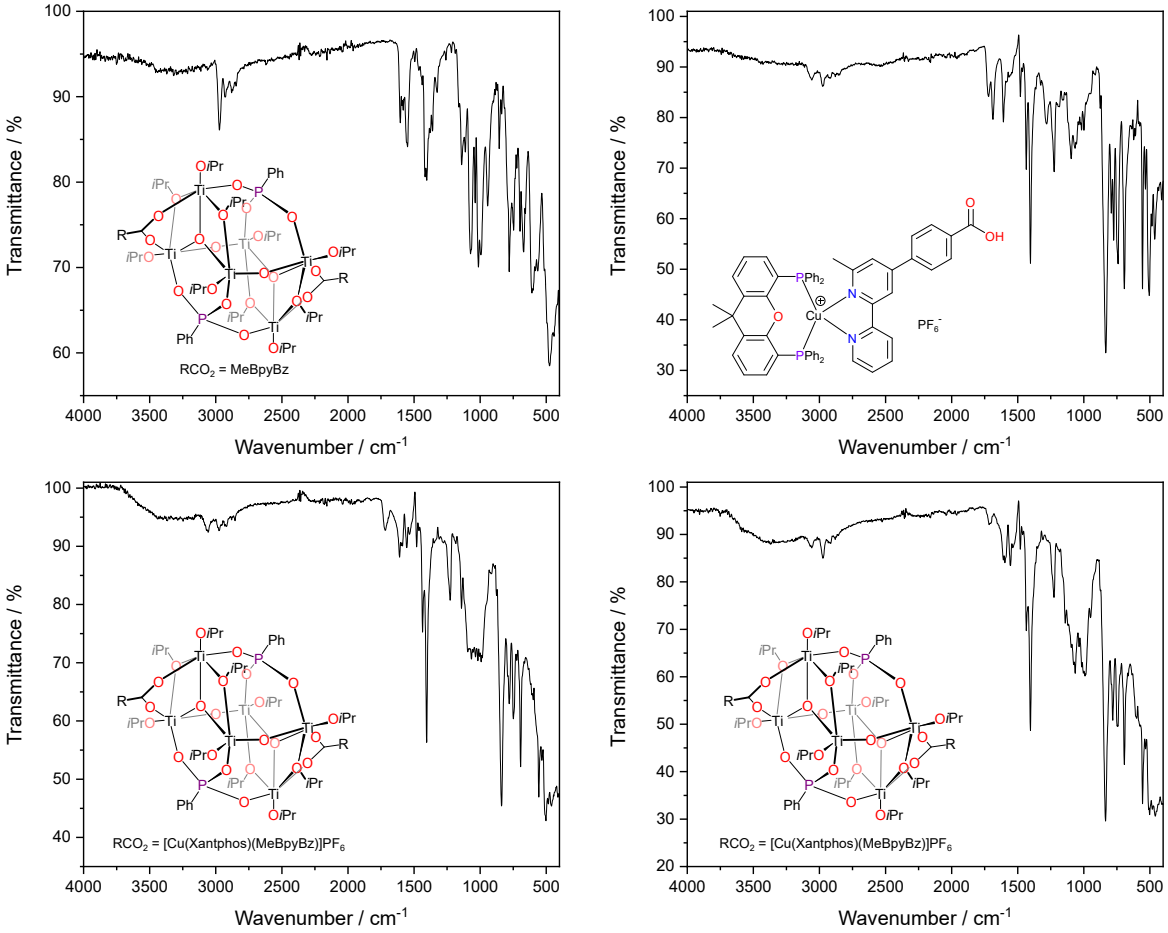


Figure 6.9: FTIR spectra of **27b** (bottom) obtained from **27a** (left) and **26b** (right), as well as the spectra of the respective starting materials (top).

The ^{1}H NMR spectrum of **26b**, as well as selective 1D TOCSYs of the aromatic region are shown in Figure 6.10. While there is a lot of spectral overlap Figure 6.11 shows a comparison of the aromatic region in the ^{1}H NMR spectra at 400 MHz of **26b** with **27b** obtained *via* $\{Ti_6\}$-oxo cluster **27a** or from **26b** with $PhPO_3H_2$ and $Ti(OiPr)_4$. The NMR spectra of the latter two are virtually identical and the exceptional line

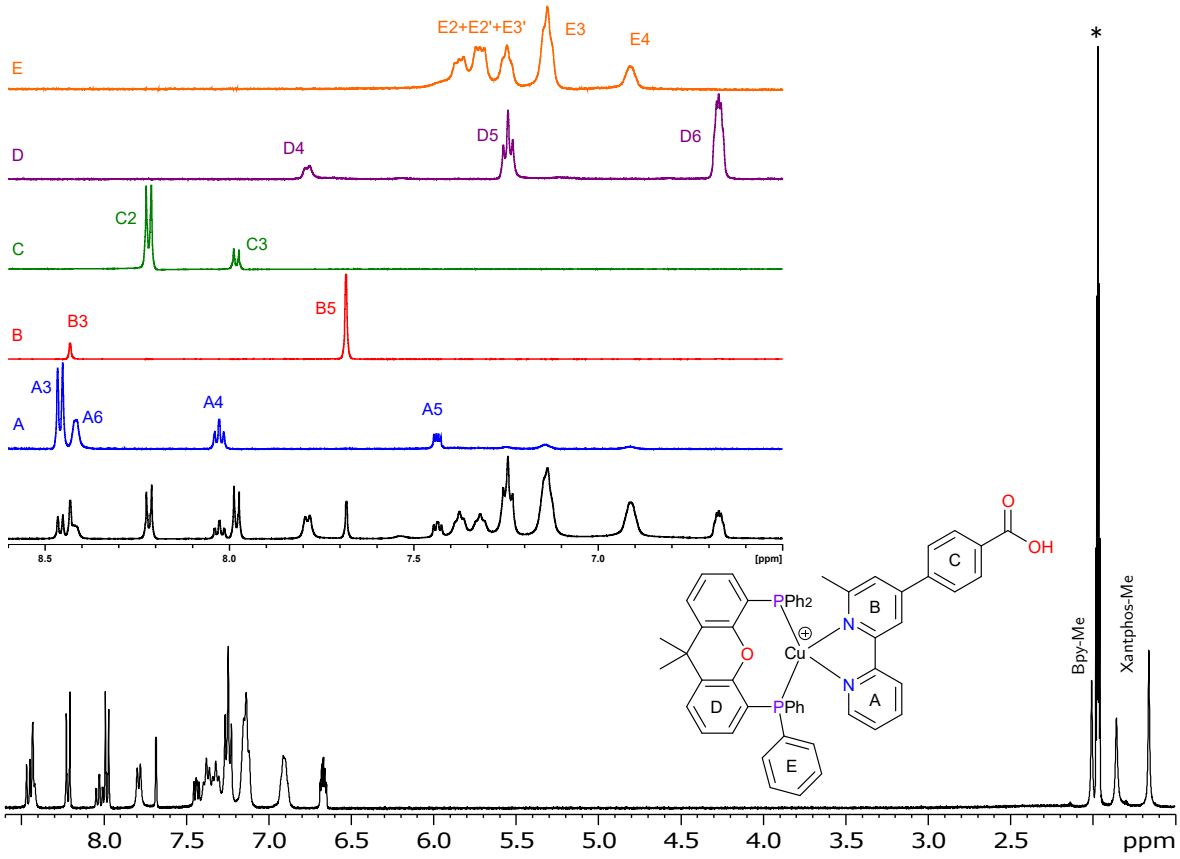


Figure 6.10: ^{1}H NMR spectrum, selective 1D TOCSYs of the aromatic region and signal assignment of **26b** in d_3-MeCN.

broadening compared to **26b** is associated with the slow tumbling if this supramolecular assembly, which in turn leads to faster relaxation of the transverse magnetisation, *i.e.* short T_2.[392]

A scanning electron microscopy (SEM) image as well as elemental mapping from energy dispersive X-ray (EDX) spectroscopy of a crystal of **27b** are shown in Figure 6.12. The EDX map shows a homogenous dispersion throughout the crystal, the however found ratio of Ti:Cu:P of 2.4:1:2.1 deviates from the expected ratio 3:1:4.

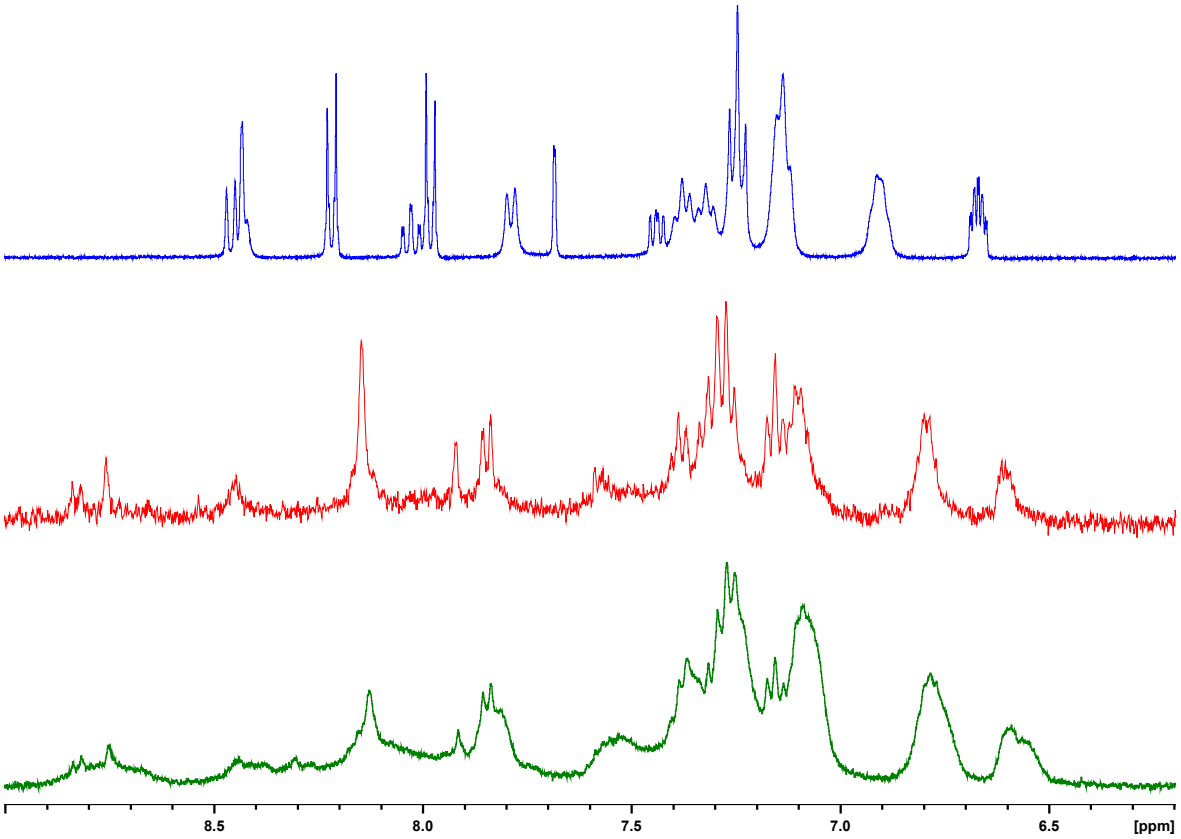


Figure 6.11: Aromatic region of the ^{1}H NMR spectra (400 MHz) of **26b** (blue, d_3-MeCN) and **27b** (d_6-DMSO) obtained by the addition of **27a** to *in situ* formed $[Cu(xantphos)(MeCN)_2]PF_6$ (red), and formed from the reaction of **26b** with $PhPO_3H_2$ and $Ti(OiPr)_4$ (green).

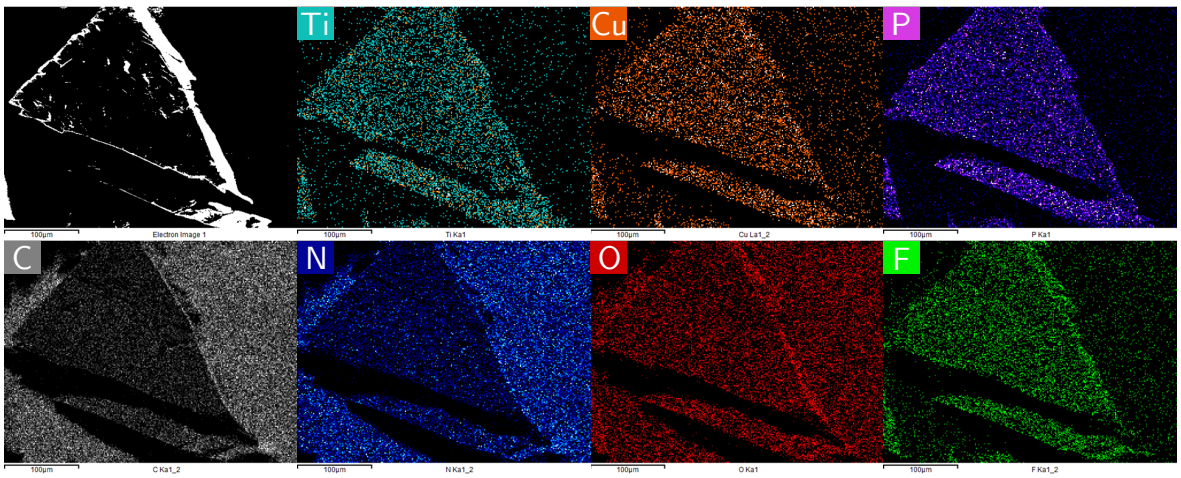


Figure 6.12: SEM image and EDX mapping of a crystal of **27b**.

6.5. Photo- and Electrochemical Properties

The Kubelka-Munk function of the $\{Ti_6\}$-oxo clusters **27a** and **27b** is shown in Figure 6.13. The electron-withdrawing MeBpy group leads an optical band gap in the near-UV region of 3.65 eV, which is 0.13 eV higher than that of the isonicotinate analogue PTC-3. Upon double complexation with Cu(Xantphos)PF_6, the band gap decreases by 0.09 eV and a second one appears at 2.59 eV, which is associated with the metal-to-ligand charge transfer from Cu^{I} into the MeBpy moiety. The absorption and emission

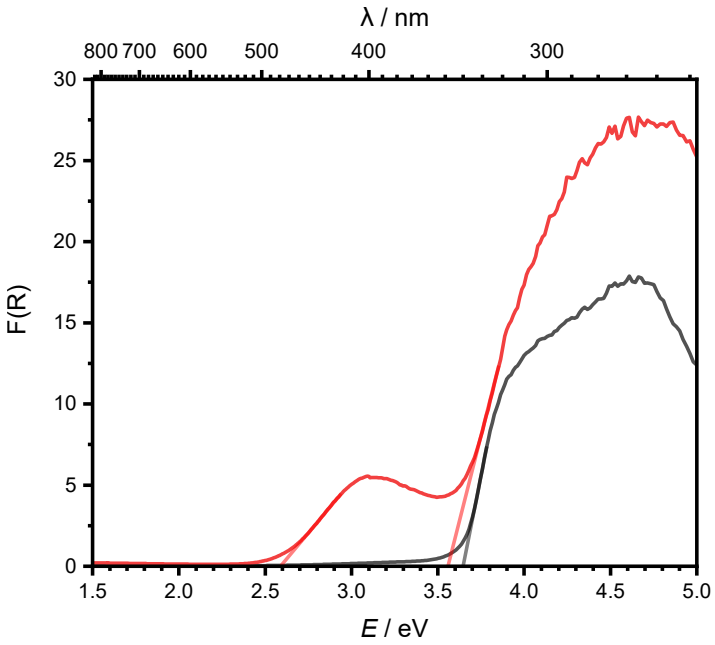


Figure 6.13: Kubelka-Munk function of the diffuse reflectance spectra of **27a** (black, 3.65 eV) and **27b** (red, 3.56 eV, 2.59 eV). Bandgaps were determined by direct extrapolation (transparent).

spectra in DCM as well as solid state emission spectra of **26a**, **26b**, and **27b** are presented in Figure 6.14. Strong absorption below 330 nm is associated with ligand centred $n\rightarrow\pi^*$ and $\pi\rightarrow\pi^*$ transitions, as well as the ligand-to-cluster charge transfer (LCCT) from the benzoate moeity into the TiO cluster for **27b**. The MLCT is observed between 391 nm and 398 nm and is red-shifted with respect to [Cu(Xantphos)(MeBpy)]PF_6 due to the extended π-system.[91] When excited at their respective absorption maxima, broad featureless emission is observed at 655 nm for **26a** and 650 nm for **26b** and **27b** dissolved in DCM. The corresponding powder samples exhibit a blue-shift to 601 nm to 608 nm, which is commonly observed and are associated with increased matrix rigidity, related to the geometric distortion after MLCT excitation from the tetrahedral-like

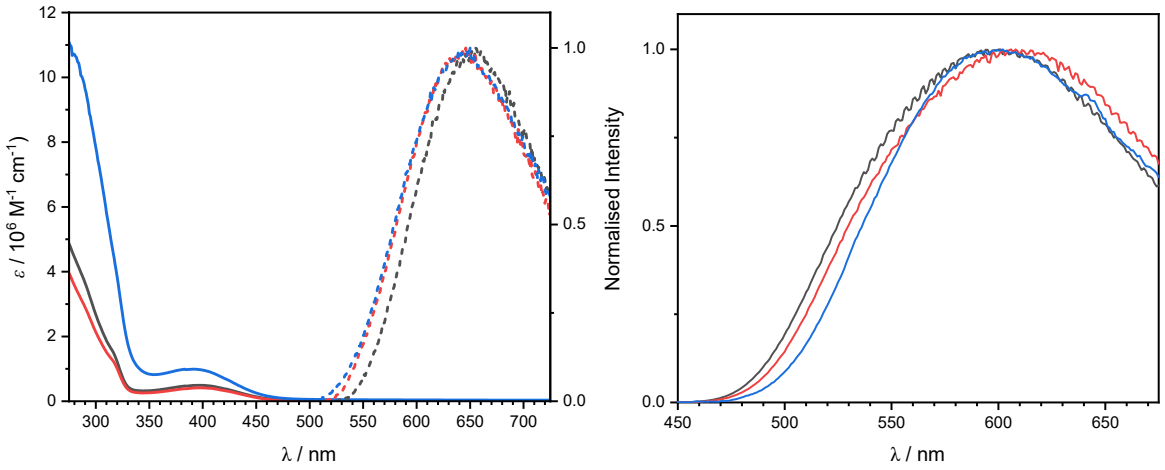


Figure 6.14: Absorption (solid) and emission (dashed) spectra in DCM (left) and solid state emission spectra (right) of **26a** (black), **26b** (red), and **27b** (blue).

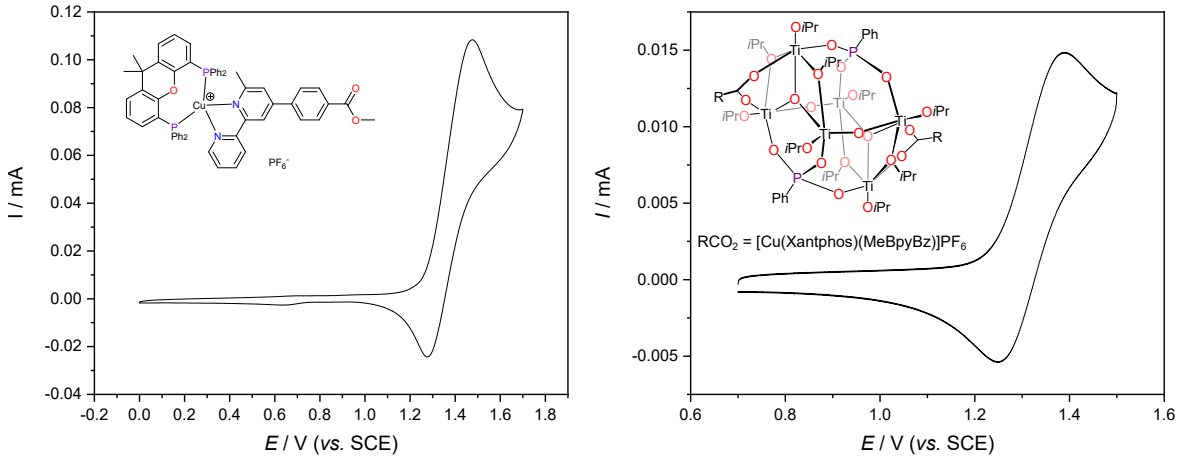


Figure 6.15: Cyclic voltammograms of **26a** (left, 10 mM) and **27b** (right, 1 mM). Experiments were carried using 0.1 M nBu_4PF_6 in DCM as electrolyte, at a scan rate of 100 mV s^{-1}.

ground state (d^{10}) to the flattened excited state (d^9).[42,84,91,393,394] With respect to [Cu(Xantphos)(MeBpy)]PF_6 excited state lifetimes are expected to be on the sub-10 µs scale, necessitating pulsed diode lasers or LEDs.[91] Unfortunately, a light source able to excite the MLCT was not available at the time and neither lifetime measurements nor photoluminescence quantum yields could be determined.

The cyclic voltammogram of **26a** and **27b** are shown in Figure 6.15. The $Cu^{I/II}$ oxidation in both is quasi-reversible and occurs at 0.90 V and 0.84 V *vs.* ferrocene. In the complex carboxylic acid **26b**, the $Cu^{I/II}$ oxidation (see Figure A.2) is not only electrochemically but also chemically irreversible with $E_{pa} = 0.97$ V *vs.* ferrocene. This might

Table 6.6: Photo- and electrochemical properties of **26a**, **26b**, **27b**, and the reference compound $[Cu(Xantphos)(MeBpy)]PF_6$. $E^{ox}_{½}$ is given *vs.* $Fc^{0/+}$.

Compound	λ_{abs} [nm] DCM	λ_{em} [nm] DCM	λ_{em} [nm] solid	$E^{ox}_{½}$ [V]	$E_{pa} - E_{pc}$ [mV]
$[Cu(Xantphos)(MeBpy)]PF_6$ [91]	379	611	547	0.85^{qr}	100
26a	396	655	601	0.90^{qr}	190
26b	398	650	608	0.83^{ir}	-
27b	391	650	602	0.84^{qr}	144

qr: quasi-reversible, ir: irreversible

occur due to oxidative decarboxylation to reduce the oxidised copper centre. Values associated with the photo- and electrochemical properties of the copper complexes discussed in this chapter is given in Table 6.6. With an excited state reduction potential of $-1.08\,V$, **27b** is a potent photo-reductant.

6.6. Conclusions

In this chapter, a heteroleptic diphosphine-diimine copper(I) complex was anchored onto a $\{Ti_6\}$-oxo cluster. This was accomplished following two routes: by complexation of the bipyridyl-functionalised TOC with Xanthphoscopper(I), as well as cluster synthesis from the complex carboxylic acid, with the latter providing single crystals of the otherwise identical material. Upon attachment to the TOC, the photo- and electrochemical properties of the parent copper(I) complex are retained, making **27b** a strong photoreductants and its oxidised species strong oxidants. Yet further photo- and electrochemical studies are needed to investigate electron-transfer processes between the photosensitiser and the TiO cluster core. Furthermore, **27b** is the first example of a charged $\{Ti_6P_2\}$ cluster, making it remarkably soluble in common polar organic solvents. In conclusion, the Cu^{I}-photosensitised TOC **27b** presents as an earth-abundant candidate for homogeneous photocatalysis.

7. Conclusions & Future Work

In summary, crystal engineering has been utilised to synthesise light-harvesting materials based on earth-abundant metals. Specifically, five coordination polymers featuring a homoleptic Cu^{I} photosensitisers as metallo-linkers, as well as 32 titanium-oxo clusters, one of which features a heteroleptic Cu^{I} photosensitiser, were obtained and their structures reported.

The first part of the work is concerned with the use of Cu^{I} photosensitisers utilised in DSCs as metallo-linkers in coordination polymers or MOFs. $[Cu(H_2\mathbf{L1})_2]^+$ was successfully incorporated into the five isostructural 2D coordination polymers **2(M)** with mixed mono- and dinuclear SBUs, featuring divalent metals of Mn, Co, Cu, Zn, and Cd. Packing in **2(M)** is dense and governed by the connectivity between metallolinker and SBU, as well as strong hydrogen bonding and π-π-stacking. Moreover, this is the first study investigating the effects of immobilisation onto a bis(diimine)copper(I) in a coordination polymer with respect to its photo- and electrochemical properties. **2(M)** absorb light across almost the entire visible spectrum and the rigidity imposed by the framework seems to assist intersystem crossing from the rapidly decaying singlet into the longer lived triplet states. However, lifetimes are highly dependant on the node metal, *i.e.* **2(Zn)** possesses an average lifetime of 22 ns whereas **2(Cu)** is non-emissive due to electron transfer processes. Additionally, the electrochemical properties of the parent Cu^{I} complex are retained in **2(M)**, hence they are potent photoreductants comparable with $[Ru^{II}(bpy)_3]$ and could find application as photocatalysts or photocathodes.

The ligand was then modified in two ways: extension at the carboxylate site ($H_2\mathbf{L2}$) in order to increase absorption properties and expand the material into a porous network, as well as the increase of steric bulk around the metal centre ($H_2\mathbf{L3}$) to prolong luminescence lifetimes. Moreover, the neocuproine-based ligand $CuprPy_2$ was synthesised for the purpose of Cu^{I}-photosensitised coordination polymers from cobaloxime. While

none of the target materials where obtained from any of these ligands, the experiments provided important insights into the reactivity and specifically the lability of Cu^{I} metallolinkers: reactions involving hard Lewis acids (Ti^{IV} and Zr^{IV}), temperatures exceeding 100 °C, and halide poisoning lead to the decomposition of the Cu^{I} complex. Moreover, extension of the backbone leads to distortion of the metal centre and increased steric crowding around it result in even lower stability.
In future work using bis(diimine)copper(I) metallolinkers, the metal centre will be stabilised *via* topological or steric constraints. If MOFs with strong Lewis acidic metal are desired, a step-wise approach should be taken: synthesis of the MOF with an ancillary ligand, followed by its complexation with Cu^{I}, and subsequent introduction of an antenna ligand.

The second part of this work was concerned with the combined crystal and band gap engineering of TOCs. A particular goal was to find out how robust the formation of the $\{Ti_6P_2\}$ motif is with regard to functional groups at the carboxylate site and what their influence is on the optical band gap. Initial investigations using aminobenzoic acids and amino acids revealed that the target motif only does not form when derivates of *o*-phenylenediamine or α-amino acids are used. Moreover, Schiff base-functionalised TOCs were obtained by the addition of aldehydes. The importance of serendipity in the exploration of reaction space is highlighted by TOC synthesis involving 2-aminobenzoic acid: addition of aq. HCl resulted in chloride doping of the cluster core, and Schiff bases of electron-withdrawing aldehydes underwent a Meerwein-Ponndorf-Verley type reduction to the corresponding amines. Furthermore, depending on whether 3,5-diaminobenzoic acid derived cluster **14a** was synthesised in the absence or presence of air, its band gap would lie in the blue or infra red region, the cause of which is still unclear. While cluster of free α-amino acids could not be obtained, naphthalimide protection of the amine allowed for the introduction of chirality in close proximity to the cluster core. Further functionalisation was accomplished with azo-dyes and coumarin-dyes, which offer multiple binding modes. Interestingly, anthraquinone-functionalisation appears to lead to redox non-innocent behaviour, resulting in *in situ* alcohol oxidation and electron injection into the cluster core. Future work should include investigations make use of ESR spectroscopy and EIS, as well as photocurrent tests and photocatalysis. Further modifications of the $\{Ti_6P_2\}$ motif should include established dyes as well as redox non-innocent ligands and quinones.

With respect to band gap engineering a clear trend was found, showing positive correlation between the the optical band gap a functionalised TOC and the Hammett constant of the substituent. Hence, a TOC's optical band gap can be decreased by introduction of electron-donating groups in *ortho*- and *para*-positions, and may be further enhanced by push-pull dynamics. Moreover, band gap reductions can be achieved by increasing the size of conjugated system. Hammett constant are a useful tool in choosing functional groups, but are ultimately not practical as their estimation for ligands involving *ortho*-substitution or extended conjugated systems is problematic.

Finally, anchorage of a diimine-diphosphine copper(I) photosensitiser to the $\{Ti_6P_2\}$ motif was accomplished, by either complexation of the TOC or cluster formation from the complex carboxylic acid. Photo- and electrochemical studies revealed the strong photoreducing properties of the Cu^I complex to be retained upon anchorage to the $\{Ti_6\}$-oxo cluster, making it a viable candidate for photocatalysis and a model compound for composite materials comprised of nano-crystalline TiO_2 and complex photosensitisers.
Future work will involve further investigations into electron-transfer processes in this kind of material. Moreover, orthogonal functionalisation of the TOC as well as the use of diimine antenna ligands shows great promise for light earth-abundant light harvesting materials.

In conclusion, synthetic approaches for light-harvesting materials containing earth-abundant metals, *i.e.*Cu^I-photosensitised coordination polymers and phosphate-stabilised TOCs, were demonstrated and limiting factors explored. Where appropriate, photo- and electrochemical properties were determined and structure-property relationships discussed. This is one of very few studies concerned with Cu^I metallolinkers in extended structures and the first investigation of the derived materials' photo- and electrochemical properties. The $\{Ti_6P_2\}$ motif was confirmed to be incredibly robust regarding the introduction of functional groups as well as *in situ* reactions, and provides a unique platform for band gap engineering. It was found that electron-donating groups can tremendously lower the optical band gap, which could be finely controlled using organic dye carboxylates. Some of the presented compounds were revealed to have fascinating photochemical properties and show promising potential for application in photosensitive devices.

8. Experimental

8.1. Materials & Methods

All chemicals and solvents were from Sigma-Aldrich, Fluorochem, VWR, Alfa Aesar, Acros Organics, Santa Cruz Biotechnology, or local chemical suppliers. All chemicals were used without further purification.

Nuclear Magnetic Resonance (NMR) Spectroscopy: Samples were dissolved in deuterated solvents and NMR spectra recorded at 293 K on a Bruker 400 AV AVANCE III or Bruker 600 AVANCE II by Dr. John O'Brien or Dr. Manuel Rüther. Chemical shifts are reported in ppm, with the deuterated solvents serving as internal reference. Standard abbreviations for spectra are used: s, singlet; d, doublet; t, triplet; q, quartet; sept, septet; m, multiplet; br, broad singlet; J, coupling constant.

Mass Spectrometry (MS): Samples were dissolved in HPLC grade solvents and passed through a Teflon syringe filter (pore size 200 µm) to remove residual solids. Experiments were carried out on Waters Maldi/ESI-QTOF or Micromass LCT Premier mass spectrometers by Dr. Martin Feeney and Dr. Gary Hessman.

Fourier-Transform Infrared (FTIR) Spectroscopy: FTIR spectra were recorded on a Perkin Elmer Spectrum 100 FTIR spectrometer with a universal Attenuated Total Reflectance (ATR) sampling accessory

Microanalysis: CHN microanalysis was carried out on a Exeter Analytical CE 440 instrument by Dr. Rónán Crowley in the Microanalysis Lab of the School of Chemistry and Chemical Biology in University College Dublin.

Electrochemistry: Cyclovoltammetry was carried out on a Bio-logic Science Instrument VSP Potentiostat, using a three electrode set-up consisting of a glassy carbon working electrode, a Pt-wire as counter electrode, and a reference electrode. Ferrocene was used as an external standard. Experiments were conducted under nitrogen using tetrabutylammonium hexafluorophosphate in Extra Dry solvents from Acros Organics as electrolyte.

Scanning Electron Microscopy (SEM) and Energy Dispersive X-ray (EDX) spectroscopy: SEM was accomplished using a Zeiss ULTRA plus scanning electron microscope using both InLens and SE2 detectors at a 1 kV acceleration voltage. EDX spectra were recorded under the same microscope using a 20 mm^2 Oxford Inca EDX detector and a 15-20 kV acceleration voltage. Both were recorded by Éadaoin Whelan.

Thermogravimetric Analysis (TGA): TGA was carried out PerkinElmer Pyriss 1 TGA under a nitrogen gas flow (20 mL/min) using a ceramic crucible sample holder at a heating rate of 10 $K\,min^{-1}$.

UV-Vis Spectroscopy: UV-Vis spectra in solution were acquired on a Perkin Elmer Lambda 35 in a 10 mm quartz cuvette using HPLC grade solvents. For solid state absorption spectra of $[Cu(H_2\mathbf{L1})_2]PF_6$ and **2(M)**, samples suspended in MeOH and drop-cast onto a quartz slide. Measurements of the se spectra were carried out by Dr. John Gough, using a custom built Olympus microscope and a Jobin Yvon Triax 190 with an integration time of 0.1 s and averaged over 20 iterations of the same area.

Photoluminescence (PL): The above mentioned samples of $[Cu(H_2\mathbf{L1})_2]PF_6$ and **2(M)** were used for solid state emission spectra and lifetime measurements, which were also carried out by Dr. John Gough. Time-resolved photoluminescence (TRPL) measurements were performed using a PicoQuant Microtime 200 time-resolved confocal microscope system using an excitation of 90 ps pulses at a wavelength of 405 nm with a repetition rate of 10 MHz and an integration time of 4 ms per pixel. The laser spot size was approx. 430 nm. The sample was excited through a 40× objective (NA = 0.65) and the PL was collected through the same objective. The excitation power used for the PL measurements was 0.2 µW. All scans were performed over 5 µm × 5 µm square areas. The steady state PL measurements were performed over the same areas as the

TRPL measurements with a higher excitation power of 4 µW.
Other photoluminescence measurements were acquired either on a Horiba Jobin Yvon Fluorolog or Fluoromax-4. Samples were either dissolved in Extra Dry Solvents from Acros Organics, placed in a 10 mm quartz cuvette and degassed with nitrogen, or placed between two quartz slides for solid state emission.

Diffuse Reflectance Spectroscopy (DRS): DRS were collected at room temperature on a Perkin Elmer Lambda 650 spectrometer using a 150 mm integrating sphere accessory using $BaSO_4$ as a standard (100% reflectance). Powdered samples were placed between two quartz slides and spectra corrected for the background of a single quartz slide. Measurements were carried out by Éadaoin Whelan.

Single Crystal X-ray Diffraction (SCXRD): Crystals of suitable size were mounted on a MiTiGen micromount. Intensity data were collected either on a Bruker APEX DUO equipped with a Mo-Kα source ($\lambda = 0.710\,73$ Å, sealed tube, graphite monochromator), a Cu-Kα ($\lambda = 1.541\,78$ Å, Incoatec IµS, multilayer optics), a Bruker SMART APEX II CCD detector and a Oxford Cryosystems Cobra LT unit, or a Bruker D8 Quest ECO equipped with a Mo-Kα source ($\lambda = 0.710\,73$ Å, sealed tube, graphite monochromator), a PHOTON 50 CMOS detector and a Oxford Cryostream LT unit. **4** and **3** were the only compounds measured using Cu-Kα radiation. In the case of twinning, unit cells and transformation matrices were determined using CELL_NOW.[395] Intensity data was processed with SAINT+ and corrected for absorption by multi-scan methods using SADABS or TWINABS.[396–398] Structure solution was accomplished using intrinsic phasing as implemented in SHELXT and refinement on F^2 with full-matrix least squares procedures was carried out with SHELXL-2013 in Olex2.[399–401] All non-hydrogen atoms were refined with anisotropic displacement parameters and hydrogen atoms where included on idealised positions (unless mentioned otherwise) as riding with U_{iso}(H) being 1.2 or 1.5 times U_{iso}(non−H). If co-crystallised solvent molecules or anions showed disorder, they were included and refined as rigid groups. Where disorder of co-crystallised solvent molecules was too severe to improve the model, they were removed using the SQUEEZE or BYPASS routine.[345,402] Most TOCs show disorder with respect to the orientation of isopropyl groups. When this was the case, the dependant parts were refined with occupancies adding up to unity, C−C distances restrained to 1.51(1) Å with a 1,3-distance of 2.53(1) Å, C−O distances were restrained to be equal

with an effective standard deviation of 0.1 Å, and carbon atoms restrained to have similar displacement parameters (SIMU).

Powder X-ray Diffraction (PXRD): X-ray powder patterns were measured on a Bruker D2 Phaser equipped with a Cu-Kα sealed tube source (λ = 1.541 78 Å) and a Lynxeye detector at room temperature. Samples were mounted on a silicon single crystal zero-background holder. Cell indexing using DICVOL-09 and pattern fitting using Le Bail methods were accomplished in EXPO2014.[348,403,404]

8.2. Syntheses

(1*E*,5*E*)-1,6-Di(2-furyl)hexa-1,5-diene-3,4-dione: Synthesis was accomplished following the procedure reported by Constable and Housecroft.[28] To a solution of 2,3-butadione (16.31 mL, 185.85 mmol) and furfural (61.6 mL, 743.41 mmol) in MeOH (25mL), glacial acetic acid (2.13 mL, 37.17 mmol) and piperidine (3.67 mL, 37.11 mmol) were added. The mixture was allowed to reflux for 6 h. Once cooled to room temperature, MeOH was removed under reduced pressure and the mixture was placed at 4°C overnight. The mixture was washed with cold MeOH giving an orange solid (19.34 g, 80 mmol, 43%).
^{1}H NMR (400 MHz, $CDCl_3$, ring B = furan): δ/ppm 7.62 (d, ^{3}J = 15.9 Hz, 2H, $H^{CHC=O}$), 7.59 (d, ^{3}J = 0.8 Hz, 2H, H^{B5}), 7.33 (d, ^{3}J =15.9 Hz, 2H, H^{FurCHC}), 6.82 (d, ^{3}J =3.4 Hz, 2H, H^{B3}), 6.55 (dd, ^{3}J =1.7 Hz, 2H, H^{B4}).
^{13}C NMR (100 MHz, $CDCl_3$): δ/ppm 188.6($C^{C=O}$), 151.5(C_2^B), 146.0(C^{B5}), 133.0($C^{\mathbf{C}HC=O}$), 117.7(C^{B3}), 117.3 ($C^{Fur\mathbf{C}H=C}$), 113.0 (C^{B4}).
APCI-MS: m/z 242.0575 $[M]^-$.

4,4'-di(2-furyl)-6,6'-Dimethyl-2,2'-bipyridine ($Me_2BpyFur_2$): Synthesis was accomplished following the procedure reported by Constable and Housecroft.[28] (1*E*,5*E*)-1,6-Di(2-furyl)hexa-1,5-diene-3,4-dione (5g, 20.64 mmol), ammonium acetate (NH_4OAc, 10g, 129.73 mmol) and 1-acetonylpyridinium chloride (7.09g, 41.28 mmol) were heated to reflux (85°C) in MeOH (200 mL) overnight. The mixture was cooled to room temperature and the white precipitate was washed with cold MeOH (2 x 80 mL) to give a white solid (3.32g, 10.5 mmol, 51%). ^{1}H NMR (400 MHz, $CDCl_3$, ring A = pyridine,

ring B = furan) δ/ppm 8.47 (s, 2H, H^{A3}), 7.58 (d, ^3J =1.2 Hz, 2H, H^{B5}), 7.47 (d, ^4J =0.8 Hz, 2H, H^{A5}), 7.01 (d, ^3J =3.2 Hz, 2H, H^{B3}), 6.56 (dd, ^3J =3.5 1.7 Hz, 2H, H^{B4}), 2.71 (s, 6H, H^{Me}).
^{13}C NMR (100 MHz, $CDCl_3$): δ/ppm 158.5 (C^{A6}), 156.3 (C^{A2}), 152.0 (C^{B2}), 143.5 (C^{B5}), 138.6 (C^{A4}), 117.2 (C^{A5}), 112.9 (C^{B4}), 112.0 (C^{B4}), 108.7 (C^{B3}), 24.7 (C^{Me}).
ESI-MS: m/z 317.1296 $[M + H]^+$.
IR ($\tilde{\nu}$/cm^{-1}): 3117(w), 2924(w), 1732(w), 1605(s), 1550(s), 1486(m), 1412(s), 1361(m), 1305(w), 1259(w), 1219(s), 1162(m), 1123(w), 1086(w), 1017(s), 986(w), 830(m), 867(s), 815(s), 745(s), 699(s).

6,6'-Dimethyl-2,2'-bipyridine-4,4'-dicarboxylic acid (H_2L1): Synthesis of H_2**L1** was accomplished following the procedure reported by Constable and Housecroft.[28] $KMnO_4$ (21.57 g, 136.49 mmol) was added to a warm mixture of $Me_2BpyFur_2$ (3.32 g, 10.49 mmol), H_2O (132 mL) and *t*BuOH (630 mL). The mixture was heated to reflux (115 °C) overnight to give a brown slurry and was then filtered through celite. The colourless filtrate was concentrated to 125 mL, adjusted to a pH of 2 with HCl (2M) and the precipitate filtered to give a white solid (1.39g, 5.11 mmol, 49%).
^{1}H NMR (400 MHz, d_6-DMSO, ring A = pyridine): δ/ppm 13.72 (s, 2H, H^{COOH}), 8.64 (d, ^4J =0.6 Hz, 2H, C^{A3}), 7.77 (d, ^4J =1.0 Hz, 2H, C^{A5}), 2.68 (s, 6H, H^{Me}).
^{13}C NMR (400 MHz, d_6-DMSO, ring A = pyridine): δ/ppm 166.8 (C^{COOH}), 159.7 (C^{A6}), 155.5 (C^{A2}), 140.2 (C^{A4}), 123.3 (C^{A5}), 117.3 (C^{A3}), 24.7 (C^{Me}).
ESI-MS: m/z 273.0861 $[M + H]^+$.
IR ($\tilde{\nu}$/cm^{-1}): 3093(w), 2849(w), 2685(w), 2624(w), 2555(w), 1833(w), 1696(s), 1568(s), 1427(s), 1395(m), 1305(s), 1257(m), 1226(s), 1145(w), 1099(w), 909(m), 883(m), 842(w), 768(s), 718(w), 679(s).

[Cu($H_{1-x}L_1$)$_2$M$_{0.5}$][M(OH_2)$_{4x}$] (2(M)): $[Cu(MeCN)_4]PF_6$ (37.27 mg, 0.1 mmol) was added to H_2**L1** (54.45 mg, 0.2 mmol) in DMF (20 mL) resulting in a crimson solution. To an aqueous $M(NO_3)_2 \cdot xH_2O$ solution (0.4 mmol, 20 mL) was sequentially added trifluoroacetic acid (TFA, 0.8mL) and DMF (20mL). Both solutions were combined and divided into three 20 mL crimp vials with a butyl rubber seals and the reaction mixture was heated to 80 °C in a pre-heated oven for 16 h (43 h for **2(Co)**). The reaction mixture was cooled to room temperature, and the deep dark red crystals were filtered, washed with DMF (10 mL), H_2O (10 mL), MeOH (10 mL) and dried at air.
2(Mn): $Mn(NO_3)_2 \cdot 4\,H_2O$ (100 mg). Yield: 24 mg (34%).

IR ($\tilde{\nu}$/cm^{-1}): 3358(w), 3090(w), 2919(w), 1728(w), 1651(m), 1607(s), 1554(s), 1390(s), 1317(m), 1235(m), 1171(w), 1096(w), 1019(w), 902(m), 829(w), 779(s), 723(s), 678(s), 607(s).
Anal. Calcd. (Found) for $C_{30.4}H_{33.1}CuMnN_{4.8}O_{12.1}$: C 47.08 (46.67), H 4.30 (3.98), N 8.21 (8.53).
2(Co): $Co(NO_3)_2 \cdot 6\,H_2O$ (116 mg). Yield: 34 mg (49%).
IR ($\tilde{\nu}$/cm^{-1}): 3360(w), 2919(w), 1724(w), 1654(m), 1608(s), 1553(s), 1391(s), 1364(s), 1316(m), 1236(m), 1095(w), 1020(w), 901(m), 829(w), 779(s), 725(s), 682(s), 607(s).
Anal. Calcd. (Found) for $C_{30.3}H_{31.3}Co_{0.9}CuN_{4.8}O_{11.3}$: C 47.99 (45.19), H 4.17 (3.91), N 8.79 (8.66).
2(Cu): $Cu(NO_3)_2 \cdot 3\,H_2O$ (96 mg). Yield: 40 mg (60%).
IR ($\tilde{\nu}$/cm^{-1}): 3372(w), 3081(w), 2919(w), 1720(w), 1657(m), 1610(s), 1554(s), 1391(s), 1365(s), 1316(m), 1235(m), 1172(w), 1094(w), 1020(w), 901(m), 830(w), 779(s), 729(s), 683(s), 604(s).
Anal. Calcd. (Found) for $C_{29.8}H_{32.4}Cu_{1.6}N_{4.6}O_{12.2}$: C 47.60 (45.93), H 4.34 (3.47), N 8.57 (8.02).
2(Zn): $Zn(NO_3)_2 \cdot 6\,H_2O$ (119 mg). Yield: 57 mg (85%).
IR ($\tilde{\nu}$/cm^{-1}): 3361(w), 3098(w), 1723(w), 1611(s), 1554(s), 1392(s), 1365(s), 1317(m), 1236(m), 1173(w), 1096(w), 1021(w), 901(m), 829(w), 779(s), 727(s), 683(s), 607(s).
Anal. Calcd. (Found) for $C_{31}H_{34.1}CuN_5O_{12}Zn_{0.8}$: C 47.46 (47.30), H 4.38 (4.22), N 8.93 (9.22).
2(Cd): $Cd(NO_3)_2 \cdot 4\,H_2O$ (124 mg). Yield: 56 mg (76%).
IR ($\tilde{\nu}$/cm^{-1}): 3341(w), 3082(w), 2918(w), 1722(w), 1654(m), 1605(s), 1555(s), 1391(s), 1366(s), 1317(m), 1235(m), 1094(w), 1018(w), 902(m), 829(w), 779(s), 726(s), 682(s), 659(s), 603(s).
Anal. Calcd. (Found) for $C_{29.5}H_{30.1}Cd_{0.83}CuN_{4.5}O_{11.3}$: C (44.78), H (3.88), N (8.44).

***N*-Acetonylpyridinium chloride (4):** 1-Chloroacetone (3.99 mL, 50 mmol) and pyridine (4.30 mL, 50 mmol) were mixed neat resulting in a yellow solution. After 5 min colourless precipitate started to form and the reaction was allowed to stir over night. The resulting solid was broken up with a spatula, suspended in Et_2O (50mL), filtered and dried in air yielding **4** as a colourless solid (6.79 g, 40 mmol, 79%). The ^{1}H NMR spectrum is in accordance with commercially available material.
^{1}H NMR (400 MHz, $CDCl_3$: δ/ppm 9.38 (d, ^3J =6.0 Hz, 1H, H^{Py2}), 8.48 (t, ^3J =7.7 Hz, 1H, H^{Py4}), 8.05 (d, ^3J =6.9 Hz, 1H, H^{Py3}), 6.75 (s, 2H, H^{CH2}), 2.53 (s, 3H, H^{CH3}).

(1*E*,5*E*)-1,6-Bis[p-(methoxycarbonyl)phenyl]hexa-1,5-diene-3,4-dione:
The compound was prepared by an upscaled version of Renouard's procedure.[405] A mixture of piperidine (3.11 mL, 31.5 mmol), acetic acid (1.80 mL, 31.5 mmol), methyl 4-formylbenzoate(11.49 g, 70 mmol), and diacetyl (3.04 mL, 35 mmol) in MeOH (120 mL) were heated to reflux 6 h. After cooling to room temperature the precipitate was filtered off, washed with MeOH(150mL) and dried at air. The compound was obtained as a yellow powder (2.55g, 6.75 mmol, 19%). The ^{1}H NMR is in good agreement with the one reported in the literature.
^{1}H NMR (400 MHz, $CDCl_3$, ring B= phenyl):δ/ppm 8.12 (d, ^3J =8.3 Hz, 4H, H^{B2}), 7.92 (d, ^3J =16.2 Hz, 2H, H^{CHCO}), 7.75 (d, ^3J =8.3 Hz, 4H, H^{B3}), 7.61 (d, ^3J =16.2 Hz, 2H, H^{CHC}), 3.97 (s, 6H, H^{Me}).

Dimethyl 4,4´-(6,6´-dimethyl-2,2´-bipyridine-4,4'-diyl)dibenzoate (Me_2L2):
The synthesis of Me_2L_2 was accomplished following a reported procedure.[353] (1*E*,5*E*)-1,6-Bis[p-(methoxycarbonyl)phenyl]hexa-1,5-diene-3,4-dione (500 mg, 1.32 mmol), *N*-aceton- ylpyridinium chloride (463 mg, 2.70 mmol) and NH_4OAc (1.00 g, 13.0 mmol) were heated to reflux in ethanol for 18 h. After cooling to room temperature, the precipitate was filtered off, washed with EtOH (5×25mL), and dried in air resulting in a beige powder. Due to the horrendously low solubility of the compound, purification by four subsequent flash column chromatographies was avoided and instead Soxhlet extraction with chloroform (150 mL) was conducted over night. After the extract was cooled to room temperature, the precipitate was filtered off and Me_2L_2 was obtained as a white solid (250 mg, 0.55 mmol,42%). The ^{1}H NMR is in good agreement with the one reported in the literature.
^{1}H NMR (400 MHz, $CDCl_3$, ring A= pyridine, ring B= phenyl):δ/ppm 8.12 (s, 2H, H^{A3}), 8.20 (d, ^3J =8.4 Hz, 4H, H^{B2}), 7.85 (d, ^3J =8.3 Hz, 4H, H^{B3}), 7.46 (s, 2H, H^{A5}), 3.99 (s, 6H, H^{CO2Me}), 2.76 (s, 6H, H^{Me}).
IR ($\tilde{\nu}$/cm^{-1}): 2548(m), 1682(s), 1594(s), 1577(s), 1548(m), 1423(m), 1385(m), 1322(s), 1294(m), 1188(m), 855(m), 808(s), 775(m), 736(s), 699(m), 552(s), 532(s), 492(w), 457(m), 441(m).

4,4´-(6,6´-Dimethyl-2,2´-bipyridine-4,4'-diyl)dibenzoic acid (H_2L_2): Following a reported procedure, Me_2L_2 (414 mg, 0.915 mmol) was deesterified with $LiOH \cdot H_2O$ (3.84 mg, 9.15 mmol) in a mixture of THF (20 mL) and water (15 mL) by heating the

mixture to reflux over night. After cooling room temperature, the solution was acidified with HCl (2M) and the resulting precipitate filtered of, washed with water and then dried under reduced pressure, yielding a white solid (378 mg, 0.891 mmol, 97%). The ^{1}H NMR is in good agreement with the one reported in the literature.
^{1}H NMR (400 MHz, d_6-DMSO, ring A= pyridine, ring B= phenyl):δ/ppm 13.16 (br, 2H, CO_2H), 8.57 (s, 2H, H^{A3}), 8.12 (d, ^3J =8.4 Hz, 4H, H^{B2}), 8.00 (d, ^3J =8.4 Hz, 4H, H^{B3}), 7.79 (s, 2H, H^{A5}), 2.70 (s, 6H, H^{Me}). Anal. Calcd. (Found) for $C_{26}H_{20}N_2O_2O$: C 73.57 (60.59), H 4.75 (4.21), N 6.60 (4.89).
IR ($\tilde{\nu}$/cm^{-1}): 2813(m), 1683(s), 1593(s), 1577(s), 1547(m), 1422(m), 1385(m), 1322(s), 1294(m), 1213(m), 1187(m), 854(s), 808(m), 775(s), 735(m), 699(s), 551(s), 532(w), 492(m), 440(m).

[Cu(H$_2$L1)(HL1)] (3): A solution of *in situ* generated $[Cu(H_2\mathbf{L1})_2]PF_6$ in DMA (25 µmol, 0.5mL, 1 eq) was mixed with a solution containing oxo-titanium(IV) acetylacetonate ($TiO(acac)_2$) in DMF (25 µmol, 0.5mL, 1 eq) and TFA (50 µL) in a mass spectrometry vial (1.5 mL). The mixture was heated to 85 °C for 3 d resulting in fluffy colourless precipitate and orange single crystals of **3**. As the product was not a isolated a yield was not determined.

[Cu(H$_2$L2$_2$)(HL2)] (5): A solution of*in situ* generated of $[Cu(H_2L_2)_2]PF_6$ in DMF (25 µmol, 0.5 mL) was mixed with a solution of $Zn(NO_3)_2 \cdot 6\,H_2O$ (25 µmol, 1 mL) in DMF/water (1:1) and TFA (2020 µL) in a mass spectrometry vial (1.5 mL). The mixture was heated to 85 °C for 3 d resulting in fluffly light blue precipitate and a pale orange solution, indicating that the copper(I) complex had disassociated and copper(I) oxidised. After several weeks at room temperature red block shaped single crystals of **5** had formed. As the product was not a isolated a yield was not determined.

***N*-(3-Methyl-2-oxobutyl)pyridinium bromide:** Bromination of 3-methyl-2-butanone was accomplished following Marquet's procedure:[406] to a solution of 3-methyl-2-butanone (16.09 mL, 150 mmol) in MeOH(90 mL), cooled to 0 °C with an ice batch, bromine (7.73 mL, 150 mmol) was added in a steady stream. After 45 min, the reaction was allowed to warm up to room temperature, water (45 mL) was added to the yellow solution and the mixture was stirred over night. The next day, the mixture is poured into water (135 mL) and was extracted with Et_2O (4×75 mL). The organic phase was washed with

sat. $NaHCO_{3(aq)}$ (40 mL), brine (2×40 mL), dried with $CaCl_2$ and the solvent evaporated to give a yellow oil (21.86 g), containing a mixture (1:9) of 3-bromo-3-methyl-2-butanone and the target compound 1-bromo-3-methyl-2-butnanone (119 mmol, 79%) and is used in the next steep without further purification. The ^{1}H NMR is in good agreement with the one reported in the literature.
^{1}H NMR (400 MHz, $CDCl_3$, 3-bromo-3-methyl-2-butanone):δ/ppm 2.46 (s, 3H, C(O)CH_3, 1.88 (s, 6H, BrC(C$\mathbf{H}_3$)$_2$).
^{1}H NMR (400 MHz, $CDCl_3$, 1-bromo-3-methyl-2-butnanone):δ/ppm 4.00 (s, 2H, CH_2Br), 3.00 (sept, ^3J =6.9 Hz 1H, C$\mathbf{H}$(CH_3)$_2$), 1.19 (d, ^3J =6.9 Hz, 6H, CH_3).
Crude 1-bromo-3-methyl-2-butnanone (11.11g, 61 mmol) and pyridine (5.79 mL, 67 mmol) are each dissolved in Et_2O (50 mL), the solutions combined and stirred at room temperature resulting in a more intense yellow solution immediately and precipitation starting after a few minutes. After stirring for 65 h (note that over night is more than sufficient) the product was isolated by filtration, washed with Et_2O (50 mL) and dried at air, giving *N*-(3-Methyl-2-oxobutyl)pyridinium bromide as colourless solid (13.11 g, 54 mmol, 88%).
^{1}H NMR (400 MHz, $CDCl_3$):δ/ppm 9.39 (d, 2H, ^3J =7.1 Hz, 2H, H^{Py2}), 8.50 (t, 1H, ^3J =7.8 Hz, 2H, H^{Py4}), 8.06 (t, 2H, ^3J =7.1 Hz, 2H, H^{Py3}), 6.79 (s, 2H, CH_2), 3.04 (sept, ^3J =6.9 Hz, 1H, C$\mathbf{H}$(CH_3)$_2$), 1.29 (d, ^3J =6.9 Hz, 6H, CH_3).
^{13}C NMR (100 MHz, $CDCl_3$):δ/ppm 204.5 (CO), 146.5 (C^{Py4}), 145.2 (C^{Py2}), 127.4 (C^{Py3}), 67.3 (CH_2), 39.3 (**C**H(CH_3)$_2$), 17.9 (CH_3).
APCI-MS: m/z 164.1071 $[M]^+$ (calc. 164.1070).
Anal. Calcd. (Found) for $C_{10}H_{14}BrNO$: C 49.20 (47.91), H 5.78 (5.53), N 5.71 (5.51).
IR ($\tilde{\nu}$/cm^{-1}): 3027(m), 1731(s), 1635(s), 1490(s), 1465(m), 1384(m), 1366(m), 1331(s), 1316(m), 1218(m), 1200(m), 1105(s), 1098(m), 1049(s), 1021(m), 776(s), 689(s), 654(w), 579(m), 463(m).

4,4'-difuryl-6,6'-diisopropyl-2,2-bipyridine ($iPr_2BpyFur_2$):

(1*E*,5*E*)-1,6-Di(2-furyl)hexa-1,5-diene-3,4-dione (1.00 g, 4.13 mmol), *N*-(3-Methyl-2-oxobutyl)pyridinium bromide (2.20 g, 8.26 mmol) and NH_4OAc (4.14 g, 54 mmol) were heated to reflux in MeOH (40 mL) for 16 h. After cooling to room temperature, it was placed in a fridge (4 °C) to crystallise. After 1 d, the product was isolated as by filtration, washed with cold MeOH (10 mL) and dried in air, yielding a beig solid (613 mg, 1.65 mmol, 40%). ^{1}H NMR (400 MHz, $CDCl_3$, ring A = pyridine, ring B = furan): δ/ppm 8.55 (d, ^4J =1.4 Hz, 2H, H^{A3}), 7.60 (d, ^3J =1.3 Hz, 2H, H^{B5}), 7.47 (d,

^4J =1.4 Hz, 2H, H^{A5}), 7.00 (d, ^3J =3.4 Hz, 2H, H^{B3}), 6.57 (d, ^3J =3.4 1.8 Hz, 2H, H^{B4}), 3.23 (sept, ^3J =6.9 Hz, C**H**$(CH_3)_2$) 1.45 (d, 12H, ^3J =6.9 Hz, H^{Me}).
^{13}C NMR (100 MHz, $CDCl_3$): δ/ppm 167.3 (C^{A6}), 156.2 (C^{A2}), 152.5 (C^{B2}), 143.3 (C^{B5}), 138.6 (C^{A4}), 114.5 (C^{A5}), 113.1 (C^{A3}), 111.9 (C^{B4}), 108.3 (C^{B3}), 36.5 ($C^{\mathbf{C}H(CH3)2}$) 22.7 (C^{Me}).
APCI-MS: m/z 373.1916 $[M]^+$ (calc. 373.1911).
Anal. Calcd. (Found) for $C_{24}H_{24}N_2O_2$: C 77.39 (77.04), H 6.50 (6.45), N 7.52 (7.51).
IR ($\tilde{\nu}$/cm^{-1}): 2964(m), 1606(s), 1573(s), 1547(s), 1493(m), 1420(m), 1365(m), 1322(s), 1011(m), 988(m), 933(m), 884(s), 871(m), 807(s), 800(m), 757(s), 743(s), 700(w), 685(m), 593(m).

6,6'-Diisopropyl-2,2'-bipyridine-4,4'-dicarboxylic acid (H_2L3):
Oxidation of the furyl groups of $iPr_2BpyFur_2$ was accomplished by adapting a procedure by Zyryanov *et al.*[407] $iPr_2BpyFur_2$ (200 mg, 0.54 mmol) was suspended in a mixture of pyridine (3 mL) and NaOH (215 mg, 5.4 mmol) in water (1 mL). Then, $KMnO_4$ (849 mg, 5.4 mmol) were added portion wise over the course of two hours. The mixture was brought to a reflux for 15 min, after which it was diluted with water (10 mL), filtered through a celite plug and acidified with HCl (2M). The precipitate was filtered off, washed with water (10 mL) and dried under vacuum, giving H_2**L3** as a colourless powder (62 mg, 0.19 mmol, 35%).
^{1}H NMR (400 MHz, d_6-DMSO, ring A = pyridine): δ/ppm 13.74 (br, 1H, CO_2H), 8.69 (d, ^4J =1.2 Hz, 2H, H^{A3}), 7.79 (d, ^4J =1.2 Hz, 2H, H^{A5}), 3.24 (sept, ^3J =6.9 Hz, 2H, C**H**$(CH_3)_2$), 1.35 (d, ^3J =6.9 Hz, 12H, H^{Me}).
^{13}C NMR (100 MHz, d_6-DMSO): δ/ppm 168.1 (C^{A6}), 166.8 (CO_2H), 155.6 (C^{A2}), 140.4 (C^{A4}), 120.9 (C^{A5}), 117.7 (C^{A3}), 36.0 ($C^{\mathbf{C}HMe2}$), 22.8 (C^{Me}).
APCI-MS: m/z 327.1358 $[M-H]^-$ (calc. 327.1350).
Anal. Calcd. (Found) for $C_{18}H_{20}N_2O_4$: C 65.84 (63.92), H 6.14 (5.90), N 8.53 (8.24).

5,5'-((1,2-phenylenebis(azanediyl))bis(ethan-1-yl-1-ylidene))bis(2,2-dimethyl-1,3-dioxane-4,6-dione): The synthesis was accomplished following a procedure reported by Harwood *et al.*[69] A solution of trimethyl orthoacetate (200 mL, 1.57mol) and Meldrum's acid (8.00 g, 55.5 mmol) was heated to reflux at 120 °C for 20 min. The resulting yellow solution was cooled to 40 °C and *o*-phenylenediamine (2.76 g, 25.52 mmol) was added portion wise. The solution was then heated to reflux for 2 h and left to stir overnight at room temperature. The white precipitate was filtered and washed with

cold Et_2O (2× 100 mL) to give the desired flaky white solid (5.87 g, 13.2 mmol, 52%).
^{1}H NMR (400 MHz, $CDCl_3$): δ/ppm 12.82 (s, 2H, NH), 7.53 (dd, ^3J =5.9 Hz, ^4J =3.5 Hz, 2H, H^{Ph3}), 7.39 (dd, ^3J =5.8 Hz, ^4J =3.6 Hz, 2H, H^{Ph4}), 2.57 (s, 6H, $H^{NCC\mathbf{H}3}$), 2.57 (s, 12H, $H^{C(CH3)2}$).
^{13}C NMR (100 MHz, $CDCl_3$): δ/ppm 173.1 (C^{CO2}), 167.6 (C^{CO2}), 162.4 ($C^{N\mathbf{C}CH3}$), 132.4 (C_q^{Ph1}), 129.3 (C^{Ph2}), 128.0 (C^{Ph3}), 103.3 ($C^{\mathbf{C}(CH3)2}$), 87.4 ($C^{O2C\mathbf{C}CO2}$), 26.6 ($C^{C(\mathbf{C}H3)2}$), 19.6 ($C^{NC\mathbf{C}H3}$).
ESI-MS: m/z 911.2954 $[2\,M + Na]^+$ (calc. 444.1533).
IR ($\tilde{\nu}$/cm^{-1}): 3000(w), 2943(w), 1711(s), 1688(s), 1644(s), 1575(s), 1543(s), 1461(m), 1414(m), 1347(s), 1295(s), 1267(s), 1199(s), 1151(m), 1059(m), 1020(w), 952(m), 921(m), 847(m), 802(s), 774(m), 727(m).

Neocuproine-4,7-diol (Curp(OH)$_2$): The synthesis was accomplished following a procedure reported by Harwood *et al.*[69] Diphenyl ether (178 mL) at 235 °C was treated portion wise with 4 (5.87 g, 13.21 mmol). The resulting yellow/orange solution was heated to reflux for 45 min, cooled to 70 °C, filtered and the brown precipitate was washed with acetone (2× 40 mL), hexane (2× 40 mL) and Et_2O (2× 40 mL) to give a light brown powder (2.82 g, 11.74 mmol, 89%). The reported solubility of Curp(OH)$_2$ in D_2O with NaOD was not observed.
ESI-MS: m/z 241.0966 $[M^+H]^+$ (calc. 240.0899).
IR ($\tilde{\nu}$/cm^{-1}): 3330(m), 3239(w), 3058(w), 2983(w), 1681(m), 1597(s), 1500(s), 1429(m), 1303(m), 1216(s), 1169(m), 1033(m), 828(s), 709(s).

4,7-Dichloro-neocuproine (CuprCl$_2$, 7): The synthesis was based on a procedure reported by Harwood *et al.*[69] Curp(OH)$_2$ (2.73g 11.4 mmol) were dissolved in $POCl_3$ (21.25 mL, 227 mmol) and brough to reflux for 3.5 h. After cooling to room temperature, the mixture was carefully poured into ice (100 g) / water (50 mL) and stirred for 15 min. Then, $CHCl_3$ (50 mL) was added and the mixture was brought to pH=13 with aq. NaOH (40%). The aqueous phase was extracted two additional times with $CHCl_3$ (50 mL) and the combined organic phases were dried over $NaSO_4$, filtered and evaporated to dryness under reduced pressure. $CurpCl_2$ was obtained as a solid (3.03 g, 10.9 mmol, 96%) with colours ranging from off-white, light brown and even light violet, all showing identical spectroscopical data.
^{1}H NMR (400 MHz, $CDCl_3$): δ/ppm 8.28 (s, 2H, $H^{5,6}$), 7.67 (s, 2H, $H^{3,8}$), 2.98 (s, 6H, CH_3).

^{13}C NMR (100 MHz, $CDCl_3$): δ/ppm 159.98 ($C^{2,9}$), 143.03 ($C^{1a,10a}$), 125.13 ($C^{4a,7a}$), 124.28 ($C^{5,6}$), 122.22 ($C^{3,8}$), 25.76 (C^{CH3}), ($C^{4,7}$) not observed).
ESI-MS: m/z 277.0298 $[M + H]^+$, 299.0118 $[M^+Na]^+$ (calc. 276.0221).
IR ($\tilde{\nu}$/cm^{-1}): 3455(m), 2921(w), 2299(w), 1924(w), 1721(w), 1572(m), 1440(m), 1372(m), 1343(m), 1240(m), 1172(w), 1103(w), 1026(w), 901(m), 837(s), 809(s), 752(w), 710(s).

4,7-Di(4'-pyridyl)neocuproine ($CuprPy_2$): The synthesis was adapted from a procedure by Buchwald *et al.* and carried out under general Schlenk conditions.[357] A three-necked round bottom flask was charged with $CuprCl_2$ (1.00 g, 3.61 mmol), 4-pyridylboronic acid hydrate (1.53 g, 10.8 mmol), K_3PO_4 ()3.06 g, 14.4 mmol), $Pd(dba)_2$ (104 mg, 0.18 mmol) and SPhos (148 mg, 0.36 mmol). The round bottom flask was attached to a cooler and stopped with a glass stopper as well as a rubber septum. After evacuation and purging with nitrogen were carried out in triplicate, degassed 1-butanol (16 mL) was added and the septum replaced with a glass stopper. The mixture was heated to 120 °C for 19 h and after cooling to room temperature was added to water (90 mL). The grey suspension was filtered, washed with water (100 mL), Et_2O (100 mL), dried in air and the product dissolved in DCM (200 mL) and filtered over a celite plug to remove palladium black. After removal of the solvent under reduced pressure, $CuprPy_2$ was obtained as a colourless solid (771 mg, 2.13 mmol, 59%). ^{1}H NMR (400 MHz, $CDCl_3$): δ/ppm 8.82 (d, $^3J = 5.9$ Hz, 4H, H^{Py2}), 7.71 (s, 2H, $H^{Phen5,6}$), 7.49 (s+d, $^3J = 5.9$ Hz, 6H, $H^{Phen3,8+Py3}$) 3.06 (s, 6H, CH_3).
^{13}C NMR (100 MHz, $CDCl_3$): δ/ppm 159.4 ($C^{Phen2,9}$), 150.1 (C^{Py2}), 146.1 ($C^{Phen4,7}$), 145.9 ($C^{Phen4a,6a}$), 145.7 ($C^{Phen1a,10a}$), 124.4 (C^{Py3}), 123.9 (C^{Py4}), 123.8 ($C^{Phen3,8}$), 122.8 ($C^{Phen5,6}$), 26.1 (CH_3).
ESI-MS: m/z 363.1593 $[M + H]^+$, 385.1424 $[M + Na]^+$ (calc. 362.1531).
IR ($\tilde{\nu}$/cm^{-1}): 3018(w), 2919(w), 1970(w), 1801(w), 1576(m), 1539(m), 1482(m), 1410(s), 1378(m), 1271(w), 1226(w), 1171(w), 1102(w), 1062(w), 1032(w), 990(w), 892(m), 835(s), 738(m), 705(m), 674(m), 619(s).
Anal. Calcd. (Found) for $C_{24}H_{18}N_4$: C 79.54 (78.67), H 5.01 (5.00), N 15.46 (14.92).

Bis(4,7-di(4'-pyridyl)neocuproine)copper(I) hexafluorophosphate ($[Cu(CuprPy_2)_2]PF_6$, 28): A solution of $CuprPy_2$ (200 mg, 0.553 mmol) in CH_3Cl (5 mL) was added to a solution of $[Cu(MeCN)_4]PF_6$ (103 mg, 0.276 mmol) in MeCN (5 mL), resulting in

crimson solution, which was stirred for 30 min, after which solvents were removed under reduced pressure. The complex **28** was isolated as a red solid (153 mg, 0.164 mmol, 59%). Single crystals were grown by diffusion of Et_2O into a MeCN solution of the complex.
^{1}H NMR (600 MHz, d_3-MeCN): δ/ppm 8.87 (br, 8H, H^{Py2}), 8.03 (s, 4H, $H^{Phen5,6}$), 7.91 (s, 4H, $H^{Phen3,8}$), 7.65 (d, $^3J = 4.0$ Hz, 8H, H^{Py3}), 2.58 (s, 12H, CH_3).
^{13}C NMR (151 MHz, MeCN): δ/ppm 159.1 ($C^{Phen2,9}$), 151.3 (C^{Py2}), 147.6 ($C^{Phen4,7}$), 145.5 (C^{Py4}), 144.6 ($C^{Phen1a,10a}$), 127.0 ($C^{Phen3,8}$), 126.0 ($C^{Phen4a,6a}$), 125.2 (C^{Py3}), 124.5 ($C^{Phen5,6}$), 26.2 (CH_3).
^{19}F NMR (377 MHz, d_3-MeCN): δ/ppm -72.9 (d, $J_{PF} = 707$ Hz, PF_6^-).
^{31}P NMR (162 MHz, d_3-MeCN): δ/ppm -144.6 (sept, $J_{PF} = 707$ Hz, PF_6^-).
ESI-MS: m/z 787.2354 $[M]^+$ (calc. 787.2359) .
Anal. Calcd. (Found) for $C_{48}H_{36}Cu_1F_6N_8P$: C 79.54 (78.67), H 5.01 (5.00), N 15.46 (14.92).
IR ($\tilde{\nu}$/cm^{-1}): 3665(w), 3593(w), 1622(w), 1596(m), 1576(m), 1542(w), 1514(w), 1486(w), 1437(w), 1413(m), 1387(w), 1069(w), 990(w), 877(w), 829(s), 753(w), 732(m), 698(m), 629(s).

[Cu(CuprCobal$_2$)(Cl)$_2$(OH$_2$)][Co(CuprCobal$_2$)(Cl)$_2$] (9): A solution of $CoCl_2 \cdot 6\,H_2O$ (26.4 mg, 0.118 mmol) and dimethylgyloxime (28.8 mg, 0.258 mmol) in ethanol was heated to 55 °C for 15 min. After cooling to room temperature 3 mL of this solution was layered under MeOH (4mL), on top of which a solution of **28** (3 mL, 2mM) was layered. After four days dark reddish green single crystals had formed. Titanium oxo clusters were generally synthesised under autogenous pressure in a 20mL crimp vial fitted with butyl rubber seal, placed in an oven preheated at 80 celsius. Stirring bars were removed prior sealing.

Procedure A: Carboxylic acid (RCO_2H, 0.89 mmol, 2.66 eq.) and phenylphosphonic acid ($PhPO_3H_2$, 106 mg, 0.67 mmol, 2 eq.) were dissolved in *iso*-propanol (iPrOH, 5.5 mL). Then titanium(IV) ispropoxide ($Ti(OiPr)_4$, 910 µL, 3.0 mmol, 9 eq.) was added dropwise with stirring. The stirring bar was removed and the crimp vial sealed and place in an oven at 80 °C for 3d, after which it was cooled to room temperature (RT). The crystalline product was isolated by filtration and washed with iPrOH until the filtrate became colourless, and finally dried in air.

Procedure B: RCO_2H (0.445 mmol, 2.66 eq.) and $PhPO_3H_2$ (53 mg, 0.335 mmol, 2 eq.) were dissolved in *iso*-propanol (iPrOH, 5.5 mL). Then $Ti(OiPr)_4$ (445 µL, 1.5 mmol, 9 eq.) was added dropwise with stirring. The stirring bar was removed and the crimp vial sealed and place in an oven at 80 °C for 3 d, after which it was cooled to room temperature (RT). The crystalline product was isolated by filtration and washed with iPrOH until the filtrate became colourless, and finally dried in air.

$[Ti_5O_2(OiPr)_6(O_3PPh)_2(pAbz)_4]$ (10): *p*-Aminobenzoic acid (pAbzH, 122 mg, 0.89 mmol, 2.66 eq) and $PhPO_3H_2$ (106 mg, 0.67 mmol, 2 eq) were dissolved in iPrOH (5.5 mL). Then $Ti(OiPr)_4$ (610 µL, 2.0 mmol, 6 eq) was added dropwise resulting in an orange slurry, which turned into a yellow solution upon heating to 80 °C. After 3 d the solution was cooled to room temperature, filtered and washed with iPrOH and dried at air. **29a** was isolated as orange crystals (169 mg, 113 µmol, 34%).
Anal. Calcd. (Found) for $C_{58}H_{76}N_4O_{23}P_2Ti_5$: C 46.49 (46.24), H 5.11 (5.07), N 3.74 (3.54).
IR ($\tilde{\nu}/cm^{-1}$): 3484(m), 3396(s), 2970(s), 2926(s), 1624(m), 1603(m), 1584(m), 1531(s), 1516(m), 1370(m), 1321(m), 1179(s), 1137(m), 1079(s), 1065(m), 1035(s), 972(s), 850(m), 782(s), 718(s), 695(m), 640(s), 601(s), 546(m), 430(s).

$[Ti_6O_4(OiPr)_{10}(O_3PPh)_2(pAbz)_2]$ (11a): To pAbzH (122 mg, 0.89 mmol, 2.66 eq) and $PhPO_3H_2$ (106 mg, 0.67 mmol, 2 eq) dissolved in iPrOH (5.5 mL) was added HCl (37%, 87 µL). The dropwise addition of $Ti(OiPr)_4$ (910 µL, 3.0 mmol, 9 eq)) resulted in a dark orange solution. Upon heating to 80 °C, the mixture turned yellow and crystallisation was observed within a few hours. After 24h the mixture was cooled to room temperature, was filtered, washed with iPrOH and yielded **11a** as yellow crystals (440 mg, 113 µmol, 86%) and dried at air.
Anal. Calcd. (Found) for $C_{56}H_{92}N_2O_{24}P_2Ti_6$: C 44.06 (43.91), H 6.08 (6.08), N 1.39 (1.75).
IR ($\tilde{\nu}/cm^{-1}$): 3351(m), 2968(s), 2926(s), 1605(s), 1516(m), 1395(m), 1317(m), 1226(s), 1141(m), 1112(m), 1065(m), 1037(s), 1015(m), 995(s), 943(m), 850(s), 771(s), 723(m), 677(s), 628(s), 596(m), 563(s), 506(s), 471(m), 432(s).

$[Ti_6O_4(OiPr)_{10}(O_3PPh)_2(pAPhBz)_2]$ (12a): According to Procedure B with 4-(4'-Aminophenyl)benzoic acid (pAPhBzH, 95 mg). The yellow suspension became

thicker and orange upon the addition of $Ti(OiPr)_4$. **12a** was isolated as yellow crystals yielding 191 mg, but unfortunately a pure sample could not be obtained.
IR ($\tilde{\nu}/cm^{-1}$): 3375(m), 2970(s), 2927(s), 1622(s), 1600(m), 1583(m), 1568(m), 1526(s), 1498(m), 1463(m), 1401(m), 1378(s), 1362(m), 1331(s), 1299(m), 1243(s), 1140(s), 1120(m), 1073(s), 1063(s), 1037(s), 1012(m), 988(m), 945(m), 850(s), 780(m), 753(s), 725(s), 675(m), 592(m), 563(s), 512(s), 461(s), 436(m), 413(m).

$[Ti_6O_4(OiPr)_{10}(O_3PPh)_2(mAbz)_2]$ (13a): Procedure A with *m*-aminobenzoic acid (mAbzH, 122 mg). Addition of $Ti(OiPr)_4$ resulted in a pale yellow suspension. **13a** was isolated as beige crystals (265 mg, 0.174 mmol, 52%).
Anal. Calcd. (Found) $C_{56}H_{92}N_2O_{24}P_2Ti_6$: C 44.06 (43.75), H 6.08 (5.98), N 1.39 (1.76).
IR ($\tilde{\nu}/cm^{-1}$): 3345(m), 2968(s), 2929(s), 1625(s), 1542(m), 1459(m), 1405(m), 1376(s), 1362(m), 1325(m), 1279(m), 1162(s), 1141(m), 1078(s), 1063(m), 1035(s), 1012(s), 996(m), 940(s), 852(s), 835(m), 771(s), 723(s), 688(m), 677(s), 662(s), 602(s), 563(m), 520(m), 501(m), 447(s), 418(s).

$[Ti_6O_4(OiPr)_{10}(O_3PPh)_2(DmAbz)_2] \cdot 2\,iPrOH$ ($14a \cdot 2\,iPrOH$): Following Procedure B with 3,5-diaminobenzoic acid (DmAbzH, 68 mg). The addition of $Ti(OiPr)_4$ resulted in a grey suspension, which turned deep dark red upon heating to 80 °C. After 7d the mxiture was cooled to RT and washed with iPrOH until the filtrate was colourless and then dried at air. **14a** was isolated as dark red crystals (171 mg, 0.114 mmol, 68%).
Anal. Calcd. (Found) for $C_{62}H_{110}N_4O_{26}P_2Ti_6$: C 44.41 (41.99), H 6.61 (6.06), N 3.38 (3.48).
IR ($\tilde{\nu}/cm^{-1}$): 3376(m), 2970(s), 2930(s), 1617(s), 1539(m), 1410(m), 1377(m), 1362(s), 1333(m), 1242(m), 1190(m), 1140(s), 1118(m), 1072(s), 1037(m), 1012(s), 985(s), 947(m), 854(s), 782(s), 751(s), 722(m), 676(m), 595(m), 576(s), 558(m), 467(s), 433(s).

$[Ti_6O_4(OiPr)_{10}(O_3PPh)_2(oAbz)_2] \cdot 0.84\,iPrOH$ ($15a \cdot 0.84\,iPrOH$): Following Procedure B with *o*-aminobenzoic acid (oAbzH, 61 mg). The colourless solution turned into an orange slurry upon the addition of $Ti(OiPr)_4$ and into a yellow solution after it reached 80 °C. During reproducibility tests reaction times of 3-11d have been observed. **15a** was isoalted as pale yellow crystals (144 mg, 0.91 mmol, 54%).

Anal. Calcd. (Found) for $C_{58.6}H_{99}N_2O_{24.9}P_2Ti_6$: C 44.59 (43.62), H 6.32 (5.97), N 1.78 (1.75).
IR ($\tilde{\nu}$/cm^{-1}): 3381(m), 2968(s), 2925(s), 1618(s), 1574(m), 1547(m), 1524(m), 1404(s), 1378(m), 1360(m), 1328(m), 1304(s), 1259(m), 1140(s), 1075(m), 1038(s), 1014(s), 994(m), 947(s), 855(s), 838(s), 772(m), 745(m), 723(m), 678(s), 662(m), 604(s), 562(s), 453(m), 413(s).

$[Ti_6O_4(OiPr)_8(Cl)_2(O_3PPh)_2(oAbz)_2]$ (16a): To a solution of oAbzH (122 mg, 0.89 mmol, 2.66 eq) and $PhPO_3H_2$ (106 mg, 0.67 mmol, 2 eq) in iPrOH (5.5 mL) was added HCl (37%, 87 µL). The dropwise addition of $Ti(OiPr)_4$ (910 µL, 3.0 mmol, 9 eq)) resulted in a dark orange solution. Upon heating to 80 °C, the mixture turned yellow and crystallisation was observed within a few hours. After 24h the mixture filtered hot (cooling to RT leads to precipitation of an unidentified byproduct), washed with iPrOH and yielded **30a** as deep yellow crystals (148 mg, 100 µmol, 30%) and dried at air.
Anal. Calcd. (Found) for $C_{50}H_{78}Cl_2N_2O_{22}P_2Ti_6$: C 40.60 (40.28), H 5.32 (5.24), N 1.89 (1.69).
IR ($\tilde{\nu}$/cm^{-1}): 3480(m), 3367(s), 2971(s), 1620(s), 1570(m), 1516(m), 1456(m), 1399(s), 1346(m), 1300(m), 1265(m), 1139(s), 1058(m), 1037(s), 1006(m), 993(s), 937(s), 823(m), 747(s), 689(s), 667(m), 605(s), 558(s), 509(m), 451(s), 415(m).

$[Ti_6O_4(OiPr)_{10}(O_3PPh)_2(FcCHN{-}4{-}Bz)_2] \cdot 2\,iPrOH$ (11b · 2 iPrOH): According to Procedure B with pAbzH (61 mg) and ferrocenecarboxaldehyde (FcCHO, 95mg, 0.45 mmol, 2.66 eq). Addition of $Ti(OiPr)_4$ resulted in a red solution. **11b** was isolated as reddish brown crystals (292 mg, 0.143 mmol, 86%).
Anal. Calcd. (Found) for $C_{84}H_{124}Fe_2N_2O_{26}P_2Ti_6$: C 49.49 (45.30), H 6.13 (5.16), N 1.37 (1.31).
IR ($\tilde{\nu}$/cm^{-1}): 3267(m), 2969(s), 1593(s), 1534(s), 1397(m), 1217(m), 1139(m), 1066(s), 1037(m), 996(m), 947(m), 771(s), 721(m), 677(s), 601(m), 565(s), 447(s).

$[Ti_6O_4(OiPr)_{10}(O_3PPh)_2(FcCHN{-}3{-}Bz)_2]$ (13b): Procedure B with mAbzH (61 mg) and FcCHO (95mg, 0.45 mmol, 2.66 eq). Addition of $Ti(OiPr)_4$ resulted in a red solution. **11b** was isolated as reddish brown crystals.
Anal. Calcd. (Found) for $C_{84}H_{124}Fe_2N_2O_{26}P_2Ti_6$: C 48.83 (48.56), H 5.67 (5.77), N

1.46 (1.40).
IR ($\tilde{\nu}$/cm^{-1}): 2969(m), 1624(s), 1595(s), 1549(s), 1401(m), 1374(m), 1225(m), 1118(s), 1078(m), 1037(m), 1013(m), 944(s), 835(m), 818(s), 769(m), 723(s), 677(s), 660(m), 608(s), 566(s), 474(s), 433(m).

$[Ti_6O_4(OiPr)_{10}(O_3PPh)_2(PyrCHN{-}4{-}Bz)_2]$ (11c): Procedure B with pAbzH (61 mg) and 2-formylpyridine (PyrCHO, 42 µL, 0.45 mmol, 2.66 eq). **11c** was isolated as yellow crystals (218 mg, 0.128 mmol, 76%).
Anal. Calcd. (Found) for $C_{68}H_{98}N_4O_{24}P_2Ti_6$: C 47.91 (47.47), H 5.80 (5.84), N 3.29 (3.08).
IR ($\tilde{\nu}$/cm^{-1}): 3394(m), 2973(s), 2926(s), 1601(s), 1531(m), 1399(m), 1375(m), 1324(s), 1136(m), 1063(m), 1036(m), 991(s), 951(m), 854(s), 782(m), 756(s), 722(s), 698(m), 666(s), 598(s), 583(s), 563(m), 520(m), 446(s), 436(s).

$[Ti_6O_4(OiPr)_{10}(O_3PPh)_2(PyrCHN{-}3{-}Bz)_2]$ (13c): Procedure B with mAbzH (61 mg) and PyrCHO (48 µL, 0.50 mmol, 3 eq). **11c** was isolated as yellow crystals (248 mg, 0.166 mmol, 99%).
Anal. Calcd. (Found) for $C_{68}H_{98}N_4O_{24}P_2Ti_6$: C 47.91 (47.78), H 5.80 (5.842), N 3.29 (3.13).
IR ($\tilde{\nu}$/cm^{-1}): 2969(m), 2925(s), 1642(s), 1586(s), 1552(m), 1437(m), 1398(m), 1378(s), 1363(m), 1324(m), 1215(m), 1141(s), 1116(m), 1076(s), 1038(m), 1016(s), 984(s), 945(m), 854(s), 769(s), 723(m), 702(s), 676(s), 600(m), 562(s), 544(m), 527(s), 467(s), 437(s).

$[Ti_6O_4(OiPr)_{10}(O_3PPh)_2(MeImCHN{-}4{-}Bz)_2] \cdot 2\,iPrOH$ (11d): According to Procedure B with pAbz (61 mg) and *N*-methyl-imidazole-2-carbaldehyde (MeImCHO, 54mg, 0.49 mmol, 2.90 eq), heated for 7 d. **11d** was isolated as pale yellow crystals (276mg, 0.161 mmol, 96%).
Anal. Calcd. (Found) for $C_{72}H_{116}N_6O_{26}P_2Ti_6$: C 47.23 (45.98), H 6.38 (6.19), N 4.59 (4.36).
IR ($\tilde{\nu}$/cm^{-1}): 3399(m), 2970(s), 1624(s), 1603(s), 1516(m), 1372(m), 1320(m), 1224(s), 1137(m), 1065(m), 975(m), 851(s), 782(m), 724(s), 696(m), 544(s), 446(s).

$[Ti_6O_4(OiPr)_{10}(O_3PPh)_2(MeImCHN{-}4{-}PhBz)_2]$ (12d): Procedure B with pAPhbzH (95 mg) and MeImCHO (49mg, 0.45 mmol, 2.66 eq). **15c**) was isolated as yellow

crystals (294mg, 0.158 mmol, 94%).
Anal. Calcd. (Found) for $C_{78}H_{108}N_6O_{24}P_2Ti_6$: C 50.29 (49.28), H 5.84 (5.82), N 4.51 (4.22).
IR ($\tilde{\nu}$/cm^{-1}): 3373(m), 2971(s), 2927(s), 2331(s), 1624(m), 1584(m), 1533(m), 1463(s), 1403(m), 1377(m), 1331(m), 1289(s), 1243(m), 1139(s), 1064(m), 1037(s), 1011(s), 995(m), 946(s), 795(s), 781(s), 752(m), 723(m), 670(m), 592(s), 563(m), 508(s), 470(s), 433(m).

$[Ti_6O_4(OiPr)_{10}(O_3PPh)_2(MeImCHN{-}3{-}Bz)_2]$ (13d): Procedure B with mAbzh (61 mg) and MeImCHO (49mg, 0.45 mmol, 2.66 eq). **13d** was isolated as pale colourless crystals (285mg, 0.167 mmol, 99%).
Anal. Calcd. (Found) for $C_{66}H_{100}N_4O_{24}P_2Ti_6$: C 47.80 (45.96), H 6.02 (6.33), N 3.28 (4.29).
IR ($\tilde{\nu}$/cm^{-1}): 3328(m), 2968(s), 1628(s), 1547(s), 1400(m), 1376(m), 1362(m), 1325(s), 1139(m), 1064(m), 1036(m), 1009(s), 941(m), 854(s), 836(m), 763(s), 722(s), 677(m), 667(s), 600(s), 567(s), 511(m), 452(m).

$[Ti_6O_4(OiPr)_{10}(O_3PPh)_2(PyrCH_2NH{-}2{-}Bz)_2]$ (15b): Procedure A with oAbzH (122 mg) and PyrCHO(85 µL, 0.45 mmol, 2.66 eq). **15b** was isolated as yellow crystals (452 mg, 0.265 mmol, 79%).
Anal. Calcd. (Found) for $C_{68}H_{102}N_4O_{24}P_2Ti_6$: C 47.80 (47.78), H 6.02 (6.02), N 3.28 (3.10).
IR ($\tilde{\nu}$/cm^{-1}): 3335(m), 2968(s), 2929(s), 1614(s), 1584(m), 1543(m), 1511(m), 1439(s), 1400(m), 1377(m), 1362(m), 1324(s), 1296(m), 1139(s), 1064(m), 1037(s), 1011(s), 946(m), 854(s), 779(s), 747(s), 722(m), 678(m), 660(m), 599(s), 564(m), 523(s), 462(s), 452(m).

$[Ti_6O_4(OiPr)_{10}(O_3PPh)_2(MeImCH_2NH{-}2{-}Bz)_2]$ (15c): Procedure B with oAbzH (61 mg) and MeImCHO (49mg, 0.45 mmol, 2.66 eq). **15c** was isolated as pale yellow crystals (182mg, 0.122 mmol, 73%).
Anal. Calcd. (Found) for $C_{68}H_{102}N_4O_{24}P_2Ti_6$: C 47.80 (45.96), H 6.02 (6.33), N 3.28 (4.29).
IR ($\tilde{\nu}$/cm^{-1}): 3328(m), 2970(s), 1611(s), 1546(s), 1510(m), 1463(m), 1403(m), 1361(s),

1325(m), 1284(m), 1259(m), 1139(s), 1075(m), 1036(s), 1012(m), 947(s), 852(s), 771(m), 752(s), 720(s), 678(s), 667(m), 597(m), 558(m), 521(s), 447(s), 431(s).

$[Ti_6O_4(OiPr)_{10}(O_3PPh)_2(Me_2Quinox{-}6{-}CO_2)_2]$ (17): Following Procedure B with 3,4-diaminobenzoic acid (68 mg) and diacetyl (38 µL, 0.45 mmol, 2.66 eq). **17a** was isolated as beige crystals (193mg, 0.117 mmol, 70%).
Anal. Calcd. (Found) for $C_{64}H_{98}N_4O_{24}P_2Ti_6$: C 46.40 (45.95), H 5.96 (5.91), N 3.38 (3.33).

$[Ti_6O_4(OiPr)_{10}(O_3PPh)_2(Me_2Quinox{-}5{-}CO_2)_2]$ (18): Following Procedure B with 2,3-diaminobenzoic acid (68 mg) and diacetyl (38 µL, 0.45 mmol, 2.66 eq). **18a** was isolated as light brown crystals (78mg, 0.047 mmol, 28%).
Anal. Calcd. (Found) for $C_{64}H_{98}N_4O_{24}P_2Ti_6$: C 46.40 (42.13), H 5.96 (5.11), N 3.38 (3.52).

$[Ti_{14}O_6(OiPr)_{26}(O_3PPh)_8(\beta{-}Ala)_2] \cdot 2\,iPrOH$ ($19 \cdot 2\,iPrOH$): Procedure A with β-alanine (β−AlaH, 79 mg). $\mathbf{19} \cdot 2\,$iPrOH was isolated as colourless crystals (114mg, 0.030 mmol, 35% based on $PhPO_3H_2$). Microanalysis revealed severe impurity of the bulk material.
Anal. Calcd. (Found) for $C_{138}H_{249}N_2O_{62}P_8Ti_{14}$: C 43.09 (32.95), H 6.53 (4.64), N 0.73 (0.72).
IR ($\tilde{\nu}/cm^{-1}$): 2970(m), 1587(s), 1438(s), 1409(s), 1377(m), 1336(m), 1138(m), 1080(s), 1065(m), 1038(m), 982(m), 947(s), 751(m), 723(s), 693(m), 556(s), 428(s).

(*S*)-2-(1,8-Naphthalimido)propanoic Acid (NaphthAlaH): NaphthAlaH was prepared following Reger's procedure. It was obtained as a colourless solid (4.23 g, 15.7 mmol, 79%). The ^{1}H NMR spectrum is in good agreement with the reported one.
^{1}H NMR (d_6-DMSO, 400 MHz): δ/ppm 12.72 (s, 1H, CO_2H), 8.50 (dd, $^3J = 7.3$ Hz, $^4J = 0.9$ Hz, 2H, 2-Naphth), 8.46 (dd, $^3J = 8.3$ Hz, $^4J = 0.8$ Hz, 2H, 4-Naphth), 7.87(dd, $^3J = 7.5$ Hz, $^3J = 8.1$ Hz, 2H, 3-Naphth), 5.60(q, $^3J = 7.0$ Hz, 1H, α-CH), 1.55(d, $^3J = 7.0$ Hz, 3H, CH_3).
Anal. Calcd. (Found) for $C_{16}H_{11}NO_4$: C 66.91 (68.61), H 4.12 (3.66), N 5.20 (3.44).

$[Ti_6O_4(OiPr)_{10}(O_3PPh)_2(NaphthAla)_2]$ (20): Procedure A with NaphthAlaH (240 mg), for four to 14 d. **20** was obtained as colourless crystals (143 mg, 0.080 mmol, 24%).
Anal. Calcd. (Found) for $C_{72}H_{100}N_2O_{28}P_2Ti_6$: C 48.29 (48.07), H 5.63 (5.53), N 1.56 (1.46).
IR ($\tilde{\nu}$/cm^{-1}): 2969(m), 2928(s), 2863(s), 1705(s), 1662(m), 1625(m), 1569(m), 1532(s), 1464(m), 1439(m), 1415(m), 1377(s), 1361(m), 1341(s), 1301(m), 1241(s), 1162(s), 1139(m), 1063(s), 1037(s), 994(m), 946(s), 890(s), 837(m), 794(s), 778(s), 751(s), 723(m), 664(m), 594(m), 565(s), 534(m), 502(m), 464(m), 432(s).

$[Ti_6O_4(OiPr)_{10}(O_3PPh)_2(BzN_2Ph)_2]$ (11e): Procedure B with 4-(phenylazo)benzoic acid (101 mg, 0.446 mmol). **11e** was obtained as orange red crystals (185 mg, 0.124 mmol, 74%).
Anal. Calcd. (Found) for $C_{68}H_{98}N_4O_{24}P_2Ti_6$: C 47.91 (47.72), H 5.80 (5.79), N 3.29 (3.07).
IR ($\tilde{\nu}$/cm^{-1}): 3321(m), 2974(s), 2926(s), 2868(s), 1592(m), 1538(m), 1496(m), 1465(s), 1440(m), 1401(m), 1377(m), 1362(s), 1331(m), 1217(s), 1134(m), 1074(s), 1061(s), 1036(m), 995(s), 948(s), 850(s), 837(m), 803(m), 786(m), 775(s), 756(s), 723(s), 692(m), 660(s), 603(s), 585(s), 564(m), 516(m), 443(m).

$[Ti_6O_4(OiPr)_{10}(O_3PPh)_2(MR)_2]$ (15d): Procedure B with methyl red (HMR, 240 mg). **15d** was isolated as red crystals (160 mg, 0.089 mmol, 53%).
Anal. Calcd. (Found) for $C_{72}H_{108}N_6O_{24}$: C 48.29 (48.07), H 6.08 (6.00), N 4.69 (4.52).
IR ($\tilde{\nu}$/cm^{-1}): 2971(m), 2857(s), 1600(s), 1548(s), 1518(m), 1485(m), 1447(m), 1407(s), 1362(m), 1312(m), 1246(m), 1139(s), 1084(m), 1065(s), 1036(m), 1015(s), 996(s), 945(m), 809(s), 764(s), 751(s), 733(m), 723(m), 695(m), 674(s), 660(s), 604(s), 570(m), 551(s), 515(s), 469(s), 427(m).

$[Ti_6O_4(OiPr)_{10}(O_3PPh)_2(O_2CFluo)_2]$ (21): Procedure B with fluorene-9-carboxylic acid (FluoCO_2H, 94 mg). **21** was isolated as colourless crystals (205 mg, 0.123 mmol, 73%).
Anal. Calcd. (Found) for $C_{70}H_{98}O_{24}P_2Ti_6$: C 50.27 (50.25), H 5.92 (5.97).
IR ($\tilde{\nu}$/cm^{-1}): 2969(m), 2929(s), 1568(s), 1438(s), 1393(m), 1361(m), 1330(m), 1293(s), 1137(m), 1064(m), 1036(m), 995(s), 943(m), 851(s), 785(m), 736(s), 720(s), 692(m), 672(s), 585(s), 566(m), 437(s).

$[Ti_6O_4(OiPr)_{10}(O_3PPh)_2(O_2CPyr)_2]$ (22): 1-Pyrenecarboxylic acid (50 mg, 0.204 mmol) and $PhPO_3H_2$ (26 mg, 0.168 mmol) were dissolved in iPrOH (5.5 mL) and $Ti(OiPr)_4$ (0.228 mL) was added drop-wise resulting in a yellow slurry which was heated in a sealed crimp vial at 80 °C for four days. After cooling to room temperature, the product was isolated by filtration, washed with iPrOH and dried at air. **22** was obtained as yellow crystals (120 mg, 0.075 mmol, 89%).
Anal. Calcd. (Found) for $C_{76}H_{98}O_{24}P_2Ti_6$: C 52.32 (52.27), H 5.66 (5.61).
IR ($\tilde{\nu}/cm^{-1}$): 2971(m), 2924(s), 1558(s), 1529(s), 1438(m), 1395(m), 1361(m), 1138(s), 1079(m), 1063(m), 1036(m), 995(s), 947(m), 841(s), 789(m), 750(s), 713(s), 693(m), 673(s), 643(s), 585(s), 564(m), 512(m), 471(m), 431(s).

$[Ti_6O_4(OiPr)_{10}(O_3PPh)_2(O_2CAcr)_2]$ (23): Procedure B with acridine-9-carboxylic acid hydrate (107 mg) heated for seven days. **23** was obtained as golden yellow crystals (241 mg, 0.142 mmol, 85%).
Anal. Calcd. (Found) for $C_{70}H_{96}N_2O_{24}P_2Ti_6$: C 49.50 (49.11), H 5.70 (5.66), N 1.65 (1.54).
IR ($\tilde{\nu}/cm^{-1}$): 3275(m), 2971(s), 2917(s), 1683(s), 1636(m), 1613(m), 1561(m), 1547(s), 1519(m), 1489(m), 1432(m), 1388(s), 1362(m), 1321(s), 1281(m), 1124(s), 1078(s), 1064(m), 1037(s), 993(s), 939(s), 856(m), 838(m), 788(s), 771(s), 757(s), 742(m), 722(m), 698(m), 659(s), 641(m), 583(m), 561(m), 513(s), 419(m).

$[Ti_6O_4(OiPr)_{10}(O_3PPh)_2(O_2CCoum)_2]$ (24a): Procedure A with coumarin-3-carboxylic acid (169 mg). **24a** was obtained as colourless crystals (145 mg, 0.089 mmol, 27%).
Anal. Calcd. (Found) for $C_{62}H_{90}O_{28}P_2Ti_6$: C 45.62 (45.18), H 5.56 (5.61).
IR ($\tilde{\nu}/cm^{-1}$): 2969(m), 2925(s), 1754(s), 1624(s), 1576(m), 1562(m), 1530(m), 1456(s), 1397(m), 1376(m), 1360(m), 1334(s), 1281(m), 1254(s), 1142(m), 1115(s), 1066(s), 1037(w), 1012(m), 982(m), 946(m), 853(s), 811(s), 749(s), 692(m), 668(m), 647(m), 594(s), 521(m), 464(m), 452(m), 435(s), 413(m).

$[Ti_6O_4(OiPr)_{10}(O_3PPh)_2(O_2CCoumNEt_2)_2]$ (24b):
Procedure B with 7-(diethylamino)coumarin-3-carboxylic acid ($CoumNEt_2H$, 116 mg). **24b** was obtained as yellow crystals (95 mg, 0.054 mmol, 32%).
Anal. Calcd. (Found) for $C_{70}H_{108}N_2O_{28}P_2Ti_6$: C 47.37 (47.00), H 6.13 (6.09), N 1.58

(1.51).
IR ($\tilde{\nu}$/cm^{-1}): 2961(m), 1746(s), 1619(s), 1595(s), 1560(m), 1513(m), 1443(m), 1396(s), 1377(m), 1346(m), 1300(m), 1248(s), 1205(m), 1189(s), 1118(m), 1067(s), 1039(s), 997(m), 953(s), 847(s), 823(m), 788(s), 765(m), 756(s), 715(s), 690(s), 668(m), 646(m), 597(m), 547(s), 527(m), 467(m), 439(m).

$[Ti_6O_4(OiPr)_{10}(O_3PPh)_2(C343)2]$ (24c): Coumarin 343 (C343H, 57 mg, 0.200 mmol) and $PhPO_3H_2$ (24 mg, 0.150 mmol) were mixed with iPrOH in a crimp vial. After the drop-wise addition of $Ti(OiPr)_4$ (0.204 mL, 0.672 mmol) the vial was sealed and put into an oven pre-heated at 80 °C. After three days, the mixture was cooled to room temperature and the product isolated by filtration, washed with iPrOH until the filtrate was colourless and dried in air. **24c** was obtained as yellow crystals.
Anal. Calcd. (Found) for $C_{74}H_{108}N_2O_{28}P_2Ti_6$: C 48.76 (47.84), H 5.97 (5.83), N 1.54 (1.31).
IR ($\tilde{\nu}$/cm^{-1}): 2839(m), 1736(s), 1618(s), 1594(s), 1560(m), 1517(m), 1443(m), 1392(s), 1358(m), 1308(m), 1271(m), 1213(s), 1176(m), 1140(s), 1121(m), 1075(s), 1038(s), 1011(m), 952(s), 886(s), 863(s), 795(m), 754(m), 733(m), 721(s), 698(s), 667(s), 623(m), 598(s), 553(s), 529(s), 473(m), 447(m), 409(s).

$[Ti_6O_4(OiPr)_{10}(O_3PPh)_2(O_2AQ)_2]$ (25): For a mixture **25**α and **25**β: Procecure B with anthraquinone-2-carboxylic acid ($AQCO_2$, 112 mg) for 1 d. The reaction mixture was filtered hot, washed with iPrOH and dried in air. **25** was initially obtained as yellow crystals (170 mg, 0.07 mmol, 58%). After a few days under ambient conditions **25**α (yellow) and **25**β (reddish magenta) can be discerned by colour.
Anal. Calcd. (Found) for $C_{72}H_{94}O_{28}P_2Ti_6$: C 40.23 (48.65), H 5.39 (5.18).
IR ($\tilde{\nu}$/cm^{-1}): 2971(m), 1678(s), 1592(s), 1554(s), 1423(m), 1401(m), 1323(m), 1287(s), 1141(m), 1065(m), 1037(m), 994(s), 930(m), 855(s), 772(m), 754(s), 705(s), 694(m), 673(s), 598(s), 432(m), 413(s). For **25**α: $AQCO_2$ (125 mg, 0.891) and $PhPO_3H_2$ were suspended in iPrOH (22ṁL) in a single neck round bottom flask and Ti(OiPr) (0.910 mL, 3.00 mmol) was added dropwise. The flask was attached to a cooler (top open to air) and the mixture was heated to 80 °C with mild stirring (200 rpm) for 3 d. The mixture was filtered hot, washed with iPrOH and dried at air. **25**α was isolated as a beige powder (261 mg, 0.174 mmol, 52%).
For **25**α^*: $AQCO_2$ (112 mg) and $PhPO_3H_2$ (0.53 mg, 0.335 mmol) were suspended in iPrOH (11ṁL) and the mixture bubbled with nitrogen for 20 min, after which $Ti(OiPr)_4$

(0.455 mL, 1.50 mmol) were added drop wise. The yellow suspension was bubbled with nitrogen for an additional 15 min, during which the mixture turned to grey and then faint violet. After replacing the seal, the mixture was heated to 80 °C and within hours gave an intense violet solution. The mixture was kept in the oven for one week, after which it was filtered hot, washed with iPrOH and dried in air. The filtrate turned colourless within seconds of exposure to air, whereas the isolated crystals (285 mg, 0.162 mmol, 97%) were initially violet and turned off-white within minutes and yellow to orange over days.
For **25**α^* and **25**γ^*: Same procedure as for **25**α^*, except that MeCN was used as solvent. The product is mostly amorphous material, accompanied by few single crystals.

Methyl 4-carboxy-2'-azachalcone: The synthesis was based on a procedure by Araki *et al.* for 4-bromo-2'-azachalcone. Methyl 4-formylbenzoate (8.21 g, 50 mmol) was dissolved in MeOH (200 mL) and aq. NaOH (37,5 mL, 1M, 37.5 mmol) and 2-acetylpyridine (5.89 mL, 52.5 mmol) was added. After 5 min the solution had turned into a solid slurry, which was filtered after 30 min, washed with water (200 mL), dried in air and then recrystallised from EtOH. The product was isolated by filtration and dried in air, yielding methyl 4-carboxy-2'-azachalcone as yellow needles (8.22 g, 30.8 mmol, 62%).
^{1}H NMR (400 MHz, $CDCl_3$, ring A = Py, ring C = Ph): δ/ppm 8.74 (d, ^3J = 4.3 Hz, 1H, H^{A6}), 8.36 (d, ^3J = 16.1 Hz, 1H, PhC**H**CH), 8.18 (d, ^3J = 7.8 Hz, 1H, H^{A3}), 8.06 (d, ^3J = 8.3 Hz, 2H, H^{C2}), 7.91 (d, ^3J = 15.9 Hz, 1H, PhCHC**H**), 7.86 (ddd, ^3J = 7.7 Hz, ^3J = 7.7 Hz, ^4J = 1.0 Hz, 1H, H^{A5}), 7.76 (d, ^3J = 8.3 Hz, 2H, H^{C3}), 7.49 (ddd, ^3J = 4.8 Hz, ^3J = 7.5 Hz, ^4J = 1.0 Hz, 1H, H^{A4}), 3.92 (s, 3H, CH_3).
^{13}C NMR (100 MHz, $CDCl_3$): δ/ppm 189.2 (C(O)), 166.5 (CO_2), 153.9 (C^{A1}), 148.9 (C^{A6}), 143.0 (PhCH**C**H), 139.4 (C^{C4}), 137.1 (C^{A5}), 131.5 (C^{C1}), 130.0 (C^{C2}), 128.6 (C^{C3}), 127.1 (C^{A4}), 123.0 (Ph**C**HCH), 122.9 (C^{A3}), 52.3 (OCH_3).
Anal. Calcd. (Found) for $C_{19}H_{16}N_2O_2$: C 74.98 (74.86), H 5.30 (5.14), N 9.20 (9.15).
IR ($\tilde{\nu}$/cm^{-1}): 1721(m), 1672(s), 1607(s), 1582(s), 1436(m), 1327(m), 1280(m), 1217(s), 1185(m), 1103(m), 1023(m), 996(s), 984(m), 799(s), 757(m), 696(s), 666(s), 615(m), 492(s), 482(s).

Methyl 4-carboxyphenyl-6-methyl-2,2'-bipyridine (MeBpyBzMe): Methyl 4-carboxy-2'-azachalcone (2.10 g, 7.86 mmol), *N*-acetonyl-pyridinium chloride (1.35 g, 7.86 mmol) and NH_4OAc (18.17 g, 236 mmol) were brought to reflux in MeOH for 24 h. After

cooling down, the yellow suspension was filtered, washed with minimal amounts of cold MeOH and dried at air. MeBpyBzMe was obtained as an off-white solid (1.37 g, 4.5 mmol, 57%).
^{1}H NMR (400 MHz, $CDCl_3$, ring A = Py, ring B = MePy, ring C = Ph): δ/ppm 8.73 (dd, $^3J = 4.8$ Hz, $^4J = 0.8$ Hz, 1H, H^{A6}), 8.49 (d, $^3J = 6.7$ Hz, H^{A5}), 8.48 (s, 1H, H^{B5}), 8.16 (d, $^3J = 8.5$ Hz, 1H, H^{C3}), 7.86 (ddd, $^3J = 7.7$ Hz, $^3J = 7.7$ Hz, $^4J = 1.7$ Hz, 1H, H^{A5}), 7.84 (d, $^3J = 8.4$ Hz, 2H, H^{C2}) 7.44 (d, $^4J = 1.3$ Hz, H^{B3}), 7.35 (ddd, $^3J = 4.8$ Hz, $^3J = 7.5$ Hz, $^4J = 1.1$ Hz, 1H, H^{A4}), 3.98 (s, 3H, CO_2Me), 2.73 (s, 3H, Me).
^{13}C NMR (100 MHz, $CDCl_3$): δ/ppm 166.8 (CO_2), 158.8 (C^{B6}), 156.3 (C^{A2}), 156.2 (C^{B2}), 149.2 (C^{A6}), 148.4 (C^{B4}), 143.0 (C^{C4}), 137.0 (C^{A5}), 130.4 (C^{C1}), 130.2 (C^{C3}), 127.2 (C^{C2}), 123.8 (C^{A4}), 121.5 (C^{A5}), 121.3 (C^{B3}), 116.4 (C^{B5}), 52.3 (OCH_3), 24.8 (CH_3).
APCI-MS: m/z 305.1290 $[M]^+$ (calc. 305.1285).
Anal. Calcd. (Found) for $C_{18}H_{14}N_2O_2$: C 74.47 (62.91), H 4.86 (4.20), N 9.65 (8.03).
IR ($\tilde{\nu}/cm^{-1}$): 1714(m), 1606(s), 1586(s), 1567(s), 1552(m), 1429(m), 1393(m), 1375(s), 1288(m), 1181(m), 1114(m), 1104(s), 851(m), 789(s), 769(m), 731(s), 703(s), 658(m), 622(s), 493(s).

4-Carboxyphenyl-6-methyl-2,2'-bipyridine (MeBpyBzH): To a solution of MeBpyBzMe (1.00 g, 3.29 mmol) in THF (25 mL) was added an aqueous solution of $LiOH \cdot H_2O$ (689 mg, 16.3 mmol, 10 mL) was added, resulting in an orange solution which was heated at reflux over night. After cooling to room temperature, the mixture was acidified with HCl (1M) resulting in a colourless precipitate, which was filtered off, washed with water and dried at 80 °C. MeBpyBzH was obtained as a colourless solid (832 mg, 2.87 mmol, 87%).
^{1}H NMR (600 MHz, d_6-DMSO, ring A = Py, ring B = MePy,ring C = Bz): δ/ppm 13.13 (br, 1H, CO_2H), 8.72 (d, $^4J = 3.8$ Hz, 1H, H^{A6}), 8.52 (s, 1H, H^{B3}), 8.44 (d, $^3J = 7.9$ Hz, 1H, H^{A3}), 8.09 (d, $^3J = 8.0$ Hz, 2H, H^{C2}), 7.97 (m, 3H, H^{A4+C3}), 7.72 (s, 1H, H^{B5}), 7.49 (t, 1H, H^{A5}), 2.65 (s, 3H, CH_3) ^{13}C NMR (151 MHz, d_6-DMSO): δ/ppm 167.4 (CO_2H), 159.1 C^{B6}), 155.7 (C^{B2}), 155.3 (C^{A2}), 149.7 (C^{A6}), 148.0 (C^{B4}), 142.0 (C^{C4}), 137.9 (C^{A4}), 131.8 (C^{C1}), 130.6 (C^{C2}), 127.6 (C^{C3}), 124.8 (H^{A5}), 121.8 (H^{A5}), 121.2 (C^{A3}), 115.7 (C^{B3}), 24.7 (CH_3).
Anal. Calcd. (Found) for $C_{18}H_{14}N_2O_2$: C 74.47 (62.91), H 4.86 (4.20), N 9.65 (8.03). IR ($\tilde{\nu}/cm^{-1}$): 3386(m), 1695(s), 1592(s), 1271(s), 1253(m), 1236(m), 852(m), 784(s), 769(m), 742(m), 729(m), 702(s), 685(m), 633(s), 621(m), 579(s), 548(s), 512(w),

490(m), 470(m), 455(m), 404(s).

[Cu(Xantphos)(MeBpyBzMe)]PF_6 (26a): $[Cu(MeCN)_4]PF_6$ (75 mg, 0.200 mmol) and xantphos (61 mg, 0.200 mmol) were dissolved in DCM (20 mL) and stirred at room temperature. After 30 min, MeBpyMe (116 mg, 0.200 mmol) was added, turning the solution deep yellow immediately. After another 45 min of stirring, hexanes (130 mL) were added resulting in the precipitation of the complex, which was then filtered and dried at air. **26a** was isolated as a yellow solid (110 mg, 0.096 mmol, 48%). Single crystals were grown from diffusion of iPrOH into a solution of the complex in MeCN.
^{1}H NMR (400 MHz, $CDCl_3$, ring A = Py, ring B = MePy,ring C = Ph): δ/ppm 8.37 (d, ^3J = 8.0,Hz, 1H, H^{A6}), 8.34 (s, 1H, H^{B3}), 8.27 (m, 3H, H^{A3+C2}), 8.03 (t, ^3J = 7.7 Hz, 2H, H^{A4}), 7.91 (d, ^3J = 8.2 Hz, 2H, H^{C3}), 7.74 (d, ^3J = 7.6 Hz, 2H, H^{D4}), 7.56 (s, 1H, H^{B5}) 7.38-7.33 (m, 5H, H^{A5+E2}), 7.22 (m, 6H, H^{D5+E2}), 7.14 (m, 8H, H^{E3}), 6.95 (m, 4H, H^{E4}), 6.69 (m, 2H, H^{D6}), 3.99 (s, 3H, $CH_3{}^{CO2Me}$), 2.12 (s, 3H, $CH_3{}^{MeBpy}$), 1.88 (s, 3H, $CH_3{}^{XP}$), 1.74 (s, 3H, $CH_3{}^{XP}$).
^{13}C NMR (100 MHz, $CDCl_3$): δ/ppm 166.2 ($\mathbf{C}O_2Me$), 158.9 (C^{B6}), 154.9 (tJ_{PC} = 6.2), 152.1 (C^{A2}), 151.9 (C^{B2}), 150.1 (C^{B4}), 148.7 (C^{A3}), 140.8 (C^{C4}), 138.7 (C^{A4}), 133.9 (C^{D3}), 133.0 (t, J_{PC} = 7.9 Hz, C^{D6}), 132.6 (t, J_{PC} = 7.8 Hz, C^{E3}), 131.8-131.2 (m, C^{E1}), 130.8 (C^{D6}), 130.5 (C^{C2}), 130.1 (C^{E2}), 130.0 (C^{E2}), 128.8 (m, C^{E2+E3}), 127.4 (C^{D4}), 127.3 (C^{C3}), 126.0 (C^{A5}), 125.2 (C^{D5}), 123.8 (C^{B5}), 122.7 (C^{A1}), 120.3 (t, J_{PC} = 13.6 Hz, C^{D1}) 117.9 (C^{B3}), 52.3 ($C^{CO2\mathbf{C}H3}$), 36.1 ($C^{XP-\mathbf{C}(Me2)}$), 29.5 ($CH_3{}^{MeBpy}$), 26.4 ($CH_3{}^{XP}$), 26.0 ($CH_3{}^{XP}$). C^{C1} was not observed.
^{31}P NMR (162 MHz, d_3−MeCN): δ/ppm -12.6 (br, xantphos), -144.64 (sept, J_{PF} = 711 Hz, $PF_6{}^-$).
ESI-MS: m/z 945.2427 $[M]^+$ (calc. 931.2231).
IR ($\tilde{\nu}$/cm^{-1}): 2976(m), 1720(s), 1609(s), 1551(s), 1480(m), 1436(m), 1405(m), 1279(s), 1226(m), 1192(m), 1109(m), 1065(s), 1018(m), 999(s), 876(m), 837(s), 792(s), 773(m), 743(s), 695(s), 663(m), 623(s), 609(s), 557(m), 534(s), 511(s), 504(s), 482(m), 462(m), 447(m), 412(s).

[Cu(Xantphos)(MeBpyBzH)]PF_6 (26b): The synthesis and isolation were respectively carried out under general Schlenk and ambient conditions $[Cu(MeCN)_4]PF_6$ (363 mg, 1.00 mmol) and xantphos (579 mg, 1.00 mmol) were dissolved in dry DCM (20 mL) and heated to reflux for 2 h, resulting in a colourless solution. After cooling to room temperature, solid MeBpyBzH (290 mg, 1.00 mmol) was added and the mixture turned

deep yellow immediately. After reflux over night, the solution was cooled to room temperature and the product precipitated by the addition of hexanes. After filtration, the solid was dried in air and **26b** was obtained as a yellow solid (876 mg, 0.81 mmol, 81%).

^{1}H NMR (400 MHz, d_3-MeCN, rings: A = Py, B = MePy, C = Bz, D= xanthene, E = Ph): δ/ppm 8.46 (d, ^{3}J = 8.2, 1H, H^{A3}), 8.43 (s, 1H, H^{B3}) 8.42 (s, 1H, H^{A6}), 8.22 (d, ^{3}J = 8.5 Hz, 2H, H^{C2}), 8.03 (ddd, ^{3}J = 7.9 Hz, ^{4}J = 1.6 Hz, H^{A4}), 7.98 (d, ^{3}J = 8.5 Hz, 2H, H^{C3}), 7.79 (d, ^{3}J = 7.5 Hz, 2H, H^{D4}), 7.68 (d, ^{4}J = 1.2 Hz, 1H, H^{B5}), 7.44 (dd, ^{3}J = 6.6 Hz, ^{3}J = 5.2 Hz, 1H H^{A5})), 7.38-7.25 (overlapping, m, 10H, $H^{D5+E2+E3'}$), 7.14 (m, 8H, H^{E3}), 6.91 (m, 4H, H^{E4}), 6.67 (m, 2H, H^{D6}), 2.00 (s, 3H, $CH_3{}^{MeBpy}$), 1.86 (s, 3H, $CH_3{}^{XP}$), 1.66 (s, 3H, $CH_3{}^{XP}$).

^{13}C NMR (100 MHz, d_3−MeCN): δ/ppm 166.3 (CO_2H), 158.8 (C^{B6}), 154.9 (C^{D2}), 152.3 (C^{A2}), 152.0 (C^{B2}), 149.7 (C^{B4}), 148.9 (C^{A6}), 141.2 (C^{C4}), 138.7 (C^{A4}), 134.1 (C^{D3}), 133.0 (t, J_{PC} = 6.9 Hz, $C^{E4'}$), 132.6 (t, J_{PC} = 6.9 Hz,C^{E4}), 131.8-131.4 (m, C^{E1}), 131.4 (C^{C1}), 130.6 (C^{D6}), 130.5 (C^{C3}), 130.2 (C^{E2}), 128.8 (m, C^{D5+E3}), 127.7 (C^{C3+D4}), 126.1 (C^{A5}), 125.3 (C^{D5}), 124.1 (C^{B5}), 123.1 (C^{A3}), 120.5 (C^{D1}), 118.4 (C^{B3}), 36.0 ($C^{XP-\mathbf{C}(Me2)}$), 29.3 ($CH_3{}^{MeBpy}$), 25.5 ($CH_3{}^{XP}$), 25.3 ($CH_3{}^{XP}$).

^{31}P NMR (162 MHz, d_3−MeCN): δ/ppm -13.1 (br, xantphos), -144.64 (sept, J_{PF} = 707 Hz, $PF_6{}^{-}$).

ESI-MS: m/z 931.2264 $[M]^+$ (calc. 931.2274).

Anal. Calcd. (Found) for $C_{64}H_{50}CuF_6N_2O_3P_2$: C 63.54 (60.62), H 4.30 (4.17), N 2.60 (2.43). IR ($\tilde{\nu}$/cm^{-1}): 3058(m), 2976(s), 1720(s), 1688(s), 1608(m), 1480(m), 1436(m), 1404(s), 1281(m), 1225(m), 1096(m), 1066(s), 1017(m), 999(s), 876(m), 834(s), 792(s), 774(m), 741(s), 694(s), 623(m), 556(s), 534(m), 505(s), 485(m), 463(s), 411(s).

$[Ti_6O_4(OiPr)_{10}(O_3PPh)_2(BzMeBpy)_2]$ (27a): MeBpyBzH (259 mg, 0.891 mmol) and $PhPO_3H_2$ (106 mg, 0.670 mmol) were suspended in iPrOH (6 mL) in a crimp vial and $Ti(OiPr)_4$ (0.910 mL, 3.00 mmol) was added drop-wise. After sealing, the mixture was heated in an oven at 80 °C for 14 d (at lower concentration 7 d is sufficient). After cooling to room temperature, the product was isolated by filtration, washed with iPrOH and dried in air. The product was isolated as colourless crystals (574 mg, 0.313 mmol, 93%). Anal. Calcd. (Found) for $C_{78}H_{106}N_4O_{24}P_2Ti_6$: C 51.12 (50.05), H 5.83 (5.77), N 3.06 (2.69).

IR ($\tilde{\nu}$/cm^{-1}): 2973(s), 2927(m), 2159(w), 1604(s), 1549(s), 1404(s), 1360(m), 1140(m), 1112(m), 1073(s), 1038(m), 1013(s), 994(m), 943(s), 856(m), 780(a), 747(m), 699(m),

671(m), 608(w).

$[Ti_6O_4(OiPr)_{10}(O_3PPh)_2\{Cu(Xantphos)(MeBpyBz)\}_2](PF_6)_2$ (27b):

From **27a**: Synthesis and work-up were respectively carried out under standard Schlenk and ambient conditions. A three-necked round bottom flask was charged with Xantphos (63 mg, 0.109 mmol) and $[Cu(MeCN)_4]PF_6$ (27 mg, 0.109 mmol), attached to a cooler and stoppered with a glass stopper and rubber septum. After evacuation and purging with nitrogen was carried out in triplicate, dry DCM (10 mL) were added and the mixture was heated at reflux over night. After cooling down to room temperature, solid **27a** (100 mg, 0.055 mmol) was added, upon which the mixture turned yellow immediately. The mixture was heated to reflux for an additional 4 h and after cooling down to room temperature the deep yellow suspension was poured into hexanes (90 mL) resulting in a yellow precipitate. The product was isolated by filtration and dried at air. **27b** was obtained as a yellow powder (121 mg, 0.036 mmol. 66%).

Anal. Calcd. (Found) for $C_{156}H_{170}Cu_2F_{12}N_4O_{26}P_8Ti_6$: C 54.99 (50.29), H 5.03 (4.12), N 1.64 (1.73).

IR ($\tilde{\nu}/cm^{-1}$): 3057(m), 2976(s), 1719(s), 1610(s), 1555(m), 1480(m), 1436(m), 1405(s), 1227(m), 1141(m), 1066(m), 1017(s), 992(m), 838(s), 780(m), 749(s), 694(s), 598(m), 557(s), 534(s), 502(m), 484(s), 460(s).

From **26b**: **26b** (286 mg, 0.266 mmol) and $PhPO_3H_2$ (32 mg, 0.200 mmol) were dissolved in iPrOH (11 mL) in a 20 mL crimp vial. Then, $Ti(OiPr)_4$ (0.272 mL, 0.896 mmol) were added drop-wise, the vial was sealed and placed sideways in an oven pre-heated at 80 °C. After 7 d, the mixture was filtered hot and washed with iPrOH until the filtrate was colourless and dried in air. **27b** · 4 iPrOH was obtained as yellow crystals (268 mg, 0.074 mmol, 74%). Single crystals for SCXRD analysis were removed before filtration, as crystallinity is mostly lost outside the mother liquor.

Anal. Calcd. (Found) for $C_{156}H_{170}Cu_2F_{12}N_4O_{26}P_8Ti_6$: C 54.99 (50.86), H 5.03 (4.45), N 1.64 (1.62).

IR ($\tilde{\nu}/cm^{-1}$): 3058(m), 2974(s), 1717(s), 1597(s), 1555(m), 1481(m), 1435(m), 1404(s), 1226(m), 1140(m), 1065(m), 1036(s), 991(m), 950(s), 836(m), 781(s), 742(s), 694(m), 600(s), 556(s), 533(m), 502(s), 482(m), 459(s).

9. Bibliography

[1] United Nations, *World Population Prospects 2019*, Department of Economic and Social Affairs, Population Division, 2019.

[2] M. Asif and T. Muneer, *Renew. Sustain. Energy Rev.*, 2007, **11**, 1388–1413.

[3] C. D. Keeling, S. C. Piper, R. B. Bacastow, M. Wahlen, T. P. Whorf, M. Heimann and H. A. Meijer, in *A Hist. Atmos. CO2 Its Eff. Plants, Anim. Ecosyst.*, Springer-Verlag, New York, 2005, pp. 83–113.

[4] C. C. Hay, E. Morrow, R. E. Kopp and J. X. Mitrovica, *Nature*, 2015, **517**, 481–484.

[5] REN21, *Renewables 2019 Global Status Report*, REN21 Secretariat, Paris, 2019.

[6] I. Staffell, D. Scamman, A. Velazquez Abad, P. Balcombe, P. E. Dodds, P. Ekins, N. Shah and K. R. Ward, *Energy Environ. Sci.*, 2019, **12**, 463–491.

[7] N. P. Brandon and Z. Kurban, *Philos. Trans. R. Soc. A*, 2017, **375**, 1–17.

[8] EEA, *Air quality in Europe—2016 report*, European Environment Agency, Luxembourg, 2016.

[9] H. Thomas, F. Armstrong, N. Brandon, B. David, A. Barron, J. Durrant, A. Guwy, A. Kucernak, M. Lewis, J. Maddy, I. Metcalfe and A. Porch, *R. Soc.*, 2018, 1–36.

[10] D. Archer, *Global Warming: Understanding the Forecast*, John Wiley & Sons, 2nd edn., 2011.

[11] *BP Statistical Review of World Energy Statistical Review of World 2019*, 2019.

[12] M. O. Reese, S. Glynn, M. D. Kempe, D. L. McGott, M. S. Dabney, T. M. Barnes, S. Booth, D. Feldman and N. M. Haegel, *Nat. Energy*, 2018, **3**, 1002–1012.

[13] J. H. Kim, D. Hansora, P. Sharma, J. W. Jang and J. S. Lee, *Chem. Soc. Rev.*, 2019, **48**, 1908–1971.

[14] A. Hagfeldt, G. Boschloo, L. Sun, L. Kloo and H. Pettersson, *Chem. Rev.*, 2010, **110**, 6595–6663.

[15] D. M. Bagnall and M. Boreland, *Energy Policy*, 2008, **36**, 4390–4396.

[16] E. K. Kalyanasundaram, M. Bertoz, J. Bisquert, F. De Angelis, H. Desilvestro, F. Fabregat-Santiago, S. Fantacci, A. Hagfeldt, S. Ito, K.-J. Jiang, K. Kalyanasundaram, P. V. Kamat, L. Kavan, J.-E. Moser, K. Nazeeruddin, L. Peter, H. J. Snaith, G. Tulloch, S. Tulloch, S. Uchida, S. Yanagida and J.-h. Yum, *Dye-Sensitizsed Solar Cells*, EPFL Press, Lausanne, 2010.

[17] M. A. Green, *Third Generation Photovoltaics*, Springer, 2003.

[18] N. R. E. Laboratory, *Best Research-Cell Efficiency Chart*, `https://www.nrel.gov/pv/cell-efficiency.html`, retrieved 10/12/2019.

[19] B. O'Regan and M. Grätzel, *Nature*, 1991, **353**, 737–740.

[20] C. E. Housecroft and E. C. Constable, *Chem. Soc. Rev.*, 2015, **44**, 8386–98.

[21] M. Grätzel, *Inorg. Chem.*, 2005, **44**, 6841–6851.

[22] M. Grätzel, *Acc. Chem. Res.*, 2009, **42**, 1788–1798.

[23] `https://www.rsc.org/periodic-table`, retrieved 03/12/2019.

[24] `http://www.infomine.com/investment/metal-prices/ruthenium/`, retrieved 03/12/2019.

[25] `http://www.infomine.com/investment/copper/`, retrieved 03/12/2019.

[26] N. Alonso-Vante, J. F. Nierengarten and J. P. Sauvage, *J. Chem. Soc. Dalt. Trans.*, 1994, **11**, 1649–1654.

[27] T. Bessho, E. C. Constable, M. Graetzel, A. Hernandez Redondo, C. E. Housecroft, W. Kylberg, M. K. Nazeeruddin, M. Neuburger and S. Schaffner, *Chem. Commun.*, 2008, 3717.

[28] E. C. Constable, A. H. Redondo, C. E. Housecroft, M. Neuburger and S. Schaffner, *Dalt. Trans.*, 2009, 6634.

[29] B. Bozic-Weber, V. Chaurin, E. C. Constable, C. E. Housecroft, M. Meuwly, M. Neuburger, J. a. Rudd, E. Schönhofer and L. Siegfried, *Dalt. Trans.*, 2012, **41**, 14157–14169.

[30] B. Bozic-Weber, E. C. Constable and C. E. Housecroft, *Coord. Chem. Rev.*, 2013, **257**, 3089–3106.

[31] B. Bozic-Weber, S. Y. Brauchli, E. C. Constable, S. O. Fürer, C. E. Housecroft, F. J. Malzner, I. A. Wright and J. A. Zampese, *Dalt. Trans.*, 2013, **42**, 12293.

[32] B. Bozic-Weber, S. Y. Brauchli, E. C. Constable, S. O. Fürer, C. E. Housecroft and I. A. Wright, *Phys. Chem. Chem. Phys.*, 2013, **15**, 4500.

[33] Y. Cao, Y. Saygili, A. Ummadisingu, J. Teuscher, J. Luo, N. Pellet, F. Giordano, S. M. Zakeeruddin, J. E. Moser, M. Freitag, A. Hagfeldt and M. Grätzel, *Nat. Commun.*, 2017, **8**, 1–8.

[34] M. Sandroni, M. Kayanuma, A. Planchat, N. Szuwarski, E. Blart, Y. Pellegrin, C. Daniel, M. Boujtita and F. Odobel, *Dalt. Trans.*, 2013, **42**, 10818–10827.

[35] M. Sandroni, L. Favereau, A. Planchat, H. Akdas-Kilig, N. Szuwarski, Y. Pellegrin, E. Blart, H. Le Bozec, M. Boujtita and F. Odobel, *J. Mater. Chem. A*, 2014, **2**, 9944–9947.

[36] F. J. Malzner, S. Y. Brauchli, E. C. Constable, C. E. Housecroft and M. Neuburger, *RSC Adv.*, 2014, **4**, 48712–48723.

[37] Y. Saygili, M. Söderberg, N. Pellet, F. Giordano, Y. Cao, A. B. Munoz-García, S. M. Zakeeruddin, N. Vlachopoulos, M. Pavone, G. Boschloo, L. Kavan, J. E. Moser, M. Grätzel, A. Hagfeldt and M. Freitag, *J. Am. Chem. Soc.*, 2016, **138**, 15087–15096.

[38] A. Colombo, C. Dragonetti, D. Roberto, A. Valore, P. Biagini and F. Melchiorre, *Inorganica Chim. Acta*, 2013, **407**, 204–209.

[39] S. Sakaki, T. Kuroki and T. Hamada, *J. Chem. Soc. Dalt. Trans.*, 2002, 840–842.

[40] E. Generalic, `https://www.periodni.com/rare_earth_elements.html`, retrieved 03/12/2019.

[41] D. R. McMillin, M. T. Buckner and B. T. Ahn, *Inorg. Chem.*, 1977, **16**, 943–945.

[42] N. Armaroli, *Chem. Soc. Rev.*, 2001, **30**, 113–124.

[43] K. Kalyanasundaram, *Coord. Chem. Rev.*, 1982, **46**, 159–244.

[44] T. J. Meyer, *Pure Appl. Chem.*, 1986, **58**, 1193–1206.

[45] A. Juris, V. Balzani, F. Barigelletti, S. Campagna, P. Belser and A. von Zelewsky, *Coord. Chem. Rev.*, 1988, **84**, 85–277.

[46] M. S. Lazorski and F. N. Castellano, *Polyhedron*, 2014, **82**, 57–70.

[47] M. Iwamura, S. Takeuchi and T. Tahara, *Acc. Chem. Res.*, 2015, **48**, 782–791.

[48] C. C. Phifer and D. R. McMillin, *Inorg. Chem.*, 1986, **25**, 1329–1333.

[49] A. K. Ichinaga, J. R. Kirchhoff, D. R. McMillin, P. A. Marnot, C. O. Dietrich-Buchecker and J. P. Sauvage, *Inorg. Chem.*, 1987, **26**, 4290–4292.

[50] R. M. Everly and D. R. McMillin, *J. Phys. Chem.*, 1991, **95**, 9071–9075.

[51] C. T. Cunningham, K. L. Cunningham, J. F. Michalec and D. R. McMillin, *Inorg. Chem.*, 1999, **38**, 4388–4392.

[52] M. T. Miller, P. K. Gantzel and T. B. Karpishin, *J. Am. Chem. Soc.*, 1999, **121**, 4292–4293.

[53] M. T. Miller, P. K. Gantzel and T. B. Karpishin, *Inorg. Chem.*, 1999, **38**, 3414–3422.

[54] M. T. Miller and T. B. Karpishin, *Inorg. Chem.*, 1999, **38**, 5246–5249.

[55] C. E. McCusker and F. N. Castellano, *Inorg. Chem.*, 2013, **52**, 8114–8120.

[56] N. A. Gothard, M. W. Mara, J. Huang, J. M. Szarko, B. Rolczynski, J. V. Lockard and L. X. Chen, *J. Phys. Chem. A*, 2012, **116**, 1984–1992.

[57] L. Y. Zou, M. S. Ma, Z. L. Zhang, H. Li, Y. X. Cheng and A. M. Ren, *Org. Electron.*, 2012, **13**, 2627–2638.

[58] R. S. Khnayzer, C. E. McCusker, B. S. Olaiya and F. N. Castellano, *J. Am. Chem. Soc.*, 2013, **135**, 14068–14070.

[59] B. M. Hockin, C. Li, N. Robertson and E. Zysman-Colman, *Catal. Sci. Technol.*, 2019, **9**, 889–915.

[60] J.-M. Kern and J.-P. Sauvage, *J. Chem. Soc., Chem. Commun.*, 1987, 546–548.

[61] M. Pirtsch, S. Paria, T. Matsuno, H. Isobe and O. Reiser, *Chem. Eur. J.*, 2012, **18**, 7336–7340.

[62] Z. Zhang, X. Tang, C. S. Thomoson and W. R. Dolbier, *Org. Lett.*, 2015, **17**, 3528–3531.

[63] S. P. Luo, Esteban Mejía, A. Friedrich, A. Pazidis, H. Junge, A. E. Surkus, R. Jackstell, S. Denurra, S. Gladiali, S. Lochbrunner and M. Beller, *Angew. Chem. Int. Ed.*, 2013, **52**, 419–423.

[64] E. Mejía, S.-P. Luo, M. Karnahl, A. Friedrich, S. Tschierlei, A.-E. Surkus, H. Junge, S. Gladiali, S. Lochbrunner and M. Beller, *Chem. Eur. J.*, 2013, **19**, 15972–15978.

[65] S. Fischer, D. Hollmann, S. Tschierlei, M. Karnahl, N. Rockstroh, E. Barsch, P. Schwarzbach, S. P. Luo, H. Junge, M. Beller, S. Lochbrunner, R. Ludwig and A. Brückner, *ACS Catal.*, 2014, **4**, 1845–1849.

[66] N.-Y. Chen, L.-M. Xia, A. J. J. Lennox, Y.-Y. Sun, H. Chen, H.-M. Jin, H. Junge, Q.-A. Wu, J.-H. Jia, M. Beller and S.-P. Luo, *Chem. Eur. J.*, 2017, **23**, 3631–3636.

[67] A. M. Dumas and E. Fillion, *Acc. Chem. Res.*, 2010, **43**, 440–454.

[68] A. F. Larsen and T. Ulven, *Org. Lett.*, 2011, **13**, 3546–3548.

[69] A. C. Edwards, C. Wagner, A. Geist, N. A. Burton, C. A. Sharrad, R. W. Adams, R. G. Pritchard, P. J. Panak, R. C. Whitehead and L. M. Harwood, *Dalt. Trans.*, 2016, **45**, 18102–18112.

[70] J. Kim, D. R. Whang and S. Y. Park, *ChemSusChem*, 2017, **10**, 1883–1886.

[71] S. O. Scottwell, A. B. Elliott, K. J. Shaffer, A. Nafady, C. J. McAdam, K. C. Gordon and J. D. Crowley, *Chem. Commun.*, 2015, **51**, 8161–8164.

[72] F. Kröhnke, *Synthesis (Stuttg).*, 1976, **1976**, 1–24.

[73] M. Schmittel and A. Ganz, *Chem. Commun.*, 1997, 999–1000.

[74] C. O. Dietrich-Buchecker, J. P. Sauvage and J. P. Kintzinger, *Tetrahedron Lett.*, 1983, **24**, 5095–5098.

[75] J. P. Sauvage and J. Weiss, *J. Am. Chem. Soc.*, 1985, **107**, 6108–6110.

[76] J. F. Nierengarten, C. O. Dietrich-Buchecker and J. P. Sauvage, *J. Am. Chem. Soc.*, 1994, **116**, 375–376.

[77] H. Sleiman, P. Baxter, J. M. Lehn and K. Rissanen, *J. Chem. Soc. Chem. Commun.*, 1995, 715–716.

[78] S. De, K. Mahata and M. Schmittel, *Chem. Soc. Rev.*, 2010, **39**, 1555–1575.

[79] L. Kohler, D. Hayes, J. Hong, T. J. Carter, M. L. Shelby, K. A. Fransted, L. X. Chen and K. L. Mulfort, *Dalt. Trans.*, 2016, **45**, 9871–9883.

[80] B. Bozic-Weber, S. Y. Brauchli, E. C. Constable, S. O. Fürer, C. E. Housecroft and I. A. Wright, *Phys. Chem. Chem. Phys.*, 2013, **15**, 4500–4504.

[81] S. Y. Brauchli, F. J. Malzner, E. C. Constable and C. E. Housecroft, *RSC Adv.*, 2015, **5**, 48516–48525.

[82] Y. Zhang, M. Schulz, M. Wächtler, M. Karnahl and B. Dietzek, *Coord. Chem. Rev.*, 2018, **356**, 127–146.

[83] C. E. Palmer and D. R. McMillin, *Inorg. Chem.*, 1987, **26**, 3837–3840.

[84] D. G. Cuttell, S.-M. Kuang, P. E. Fanwick, D. R. McMillin and R. A. Walton, *J. Am. Chem. Soc.*, 2002, **124**, 6–7.

[85] C. A. Tolman, *Chem. Rev.*, 1977, **77**, 313–348.

[86] P. C. Kamer, P. W. Van Leeuwen and J. N. Reek, *Acc. Chem. Res.*, 2001, **34**, 895–904.

[87] P. Dierkes and P. N. M. van Leeuwen, *J. Chem. Soc., Dalt. Trans.*, 1999, 1519–1529.

[88] K. Kubiček, S. Thekku Veedu, D. Storozhuk, R. Kia and S. Techert, *Polyhedron*, 2017, **124**, 166–176.

[89] M. Nishikawa, Y. Wakita, T. Nishi, T. Miura and T. Tsubomura, *Dalt. Trans.*, 2015, **44**, 9170–9181.

[90] A. J. J. Lennox, S. Fischer, M. Jurrat, S.-P. Luo, N. Rockstroh, H. Junge, R. Ludwig and M. Beller, *Chem. Eur. J.*, 2016, **22**, 1233–1238.

[91] S. Keller, A. Pertegás, G. Longo, L. Martínez, J. Cerdá, J. M. Junquera-Hernández, A. Prescimone, E. C. Constable, C. E. Housecroft, E. Ortí and H. J. Bolink, *J. Mater. Chem. C*, 2016, **4**, 3857–3871.

[92] R. D. Costa, D. Tordera, E. Ortí, H. J. Bolink, J. Schönle, S. Graber, C. E. Housecroft, E. C. Constable and J. A. Zampese, *J. Mater. Chem.*, 2011, **21**, 16108–16118.

[93] S. Keller, A. Prescimone, H. Bolink, M. Sessolo, G. Longo, L. Martínez-Sarti, J. M. Junquera-Hernández, E. C. Constable, E. Ortí and C. E. Housecroft, *Dalt. Trans.*, 2018, **47**, 14263–14276.

[94] T. J. Penfold, S. Karlsson, G. Capano, F. A. Lima, J. Rittmann, M. Reinhard, M. H. Rittmann-Frank, O. Braem, E. Baranoff, R. Abela, I. Tavernelli, U. Rothlisberger, C. J. Milne and M. Chergui, *J. Phys. Chem. A*, 2013, **117**, 4591–4601.

[95] F. Gärtner, A. Boddien, E. Barsch, K. Fumino, S. Losse, H. Junge, D. Hollmann, A. Brückner, R. Ludwig and M. Beller, *Chem. Eur. J.*, 2011, **17**, 6425–6436.

[96] S. Tschierlei, M. Karnahl, N. Rockstroh, H. Junge, M. Beller and S. Lochbrunner, *ChemPhysChem*, 2014, **15**, 3709–3713.

[97] X. Zhang, M. Cibian, A. Call, K. Yamauchi and K. Sakai, *ACS Catal.*, 2019, **9**, 11263–11273.

[98] N. Armaroli, G. Accorsi, M. Holler, O. Moudam, J. F. Nierengarten, Z. Zhou, R. T. Wegh and R. Welter, *Adv. Mater.*, 2006, **18**, 1313–1316.

[99] S. Igawa, M. Hashimoto, I. Kawata, M. Yashima, M. Hoshino and M. Osawa, *J. Mater. Chem. C*, 2013, **1**, 542–551.

[100] C. B. Larsen and O. S. Wenger, *Chem. Eur. J.*, 2018, **24**, 2039–2058.

[101] A. C. Hernandez-Perez and S. K. Collins, *Angew. Chem. Int. Ed.*, 2013, **52**, 12696–12700.

[102] A. C. Hernandez-Perez, A. Caron and S. K. Collins, *Chem. Eur. J.*, 2015, **21**, 16673–16678.

[103] A. C. Hernandez-Perez and S. K. Collins, *Acc. Chem. Res.*, 2016, **49**, 1557–1565.

[104] B. Michelet, C. Deldaele, S. Kajouj, C. Moucheron and G. Evano, *Org. Lett.*, 2017, **19**, 3576–3579.

[105] A. Call, C. Casadevall, F. Acuña-Parés, A. Casitas and J. Lloret-Fillol, *Chem. Sci.*, 2017, **4**, 1845–1849.

[106] S. R. Batten, N. R. Champness, X. M. Chen, J. Garcia-Martinez, S. Kitagawa, L. Öhrström, M. O'Keeffe, M. P. Suh and J. Reedijk, *Pure Appl. Chem.*, 2013, **85**, 1715–1724.

[107] G. M. J. Schmidt, *Pure Appl. Chem.*, 1971, **27**, 647–678.

[108] B. Hoskins and R. Robson, *J. Am. Chem. Soc.*, 1989, **111**, 5962–5964.

[109] R. W. Gable, B. F. Hoskins and R. Robson, *J. Chem. Soc. Chem. Commun.*, 1990, **96**, 762–763.

[110] R. W. Gable, B. F. Hoskins and R. Robson, *J. Chem. Soc., Chem. Commun.*, 1990, **53**, 1677–1678.

[111] B. F. Abrahams, B. F. Hoskins and R. Robson, *J. Am. Chem. Soc.*, 1991, **113**, 3606–3607.

[112] S. R. Batten, B. F. Hoskins and R. Robson, *J. Chem. Soc. Chem. Commun.*, 1991, 445–447.

[113] B. F. Abrahams, M. J. Hardie, B. F. Hoskins, R. Robson and E. E. Sutherland, *J. Chem. Soc. Chem. Commun.*, 1994, **2**, 1049–1050.

[114] B. F. Abrahams, B. F. Hoskins, D. M. Michail and R. Robson, *Nature*, 1994, **369**, 727–729.

[115] M. J. Zaworotko, *Chem. Soc. Rev.*, 1994, **23**, 283–288.

[116] S. Subramanian and M. J. Zaworotko, *Angew. Chem. Int. Ed.*, 1995, **34**, 2127–2129.

[117] L. R. MacGillivray, S. Subramanian and M. J. Zaworotko, *J. Chem. Soc. Chem. Commun.*, 1994, 1325–1326.

[118] L. Carlucci, G. Ciani, D. M. Proserpio and A. Sironi, *Angew. Chem. Int. Ed.*, 1995, **34**, 1895–1898.

[119] L. Carlucci, G. Ciani, D. M. Proserpio and A. Sironi, *J. Am. Chem. Soc.*, 1995, **117**, 4562–4569.

[120] O. M. Yaghi, D. A. Richardson, G. Li, C. E. Davis and T. L. Groy, *MRS Proc.*, 1994, **371**, 15.

[121] O. M. Yaghi and H. Li, *J. Am. Chem. Soc.*, 1995, **117**, 10401–10402.

[122] O. M. Yaghi, G. Li and H. Li, *Nature*, 1995, **378**, 703–706.

[123] H. Li, M. Eddaoudi, T. L. Groy and O. M. Yaghi, *J. Am. Chem. Soc.*, 1998, **120**, 8571–8572.

[124] M. Kondo, T. Yoshitomi, H. Matsuzaka, S. Kitagawa and K. Seki, *Angew. Chem. Int. Ed.*, 1997, **36**, 1725–1727.

[125] M. Kondo, T. Okubo, A. Asami, S. I. Noro, T. Yoshitomi, S. Kitagawa, T. Ishii, H. Matsuzaka and K. Seki, *Angew. Chem. Int. Ed.*, 1999, **38**, 140–143.

[126] M. O'Keeffe, M. Eddaoudi, H. Li, T. Reineke and O. M. Yaghi, *J. Solid State Chem.*, 2000, **152**, 3–20.

[127] G. Férey, *J. Solid State Chem.*, 2000, **152**, 37–48.

[128] A. Wells, *Three Dimensional Nets and Polyhedra*, Wiley, 1977.

[129] M. O'Keeffe, M. a. Peskov, S. J. Ramsden and O. M. Yaghi, *Acc. Chem. Res.*, 2008, **41**, 1782–1789.

[130] J. V. Smith, *Chem. Rev.*, 1988, **88**, 149–182.

[131] D. W. Breck, *Zeolite Molecular Sieves: Structure, Chemistry, and Use*, Wiley New York, 1973.

[132] O. M. Yaghi, M. O'Keeffe, N. W. Ockwig, H. K. Chae, M. Eddaoudi and J. Kim, *Nature*, 2003, **423**, 705–714.

[133] W. Lu, Z. Wei, Z.-Y. Gu, T.-F. Liu, J. Park, J. Park, J. Tian, M. Zhang, Q. Zhang, T. Gentle Iii, M. Bosch and H.-C. Zhou, *Chem. Soc. Rev.*, 2014, **43**, 5561.

[134] M. Eddaoudi, J. Kim, N. Rosi, D. Vodak, J. Wachter, M. O'Keeffe and O. M. Yaghi, *Science*, 2002, **295**, 469–472.

[135] V. A. Blatov, M. O'Keeffe and D. M. Proserpio, *CrystEngComm*, 2010, **12**, 44.

[136] H. Furukawa, K. E. Cordova, M. O'Keeffe and O. M. Yaghi, *Science*, 2013, **341**, 1230444–1230444.

[137] J. H. Cavka, S. Jakobsen, U. Olsbye, N. Guillou, C. Lamberti, S. Bordiga and K. P. Lillerud, *J. Am. Chem. Soc.*, 2008, **130**, 13850–13851.

[138] G. Férey, C. Serre, C. Mellot-Draznieks, F. Millange, S. Surblé, J. Dutour and I. Margiolaki, *Angew. Chem. Int. Ed.*, 2004, **43**, 6296–6301.

[139] G. Ferey, *Science*, 2005, **309**, 2040–2042.

[140] F. Paquin, J. Rivnay, A. Salleo, N. Stingelin and C. Silva, *J. Mater. Chem. C*, 2015, **3**, 10715 – 10722.

[141] A. Schoedel, M. Li, D. Li, M. O'Keeffe and O. M. Yaghi, *Chem. Rev.*, 2016, **116**, 12466–12535.

[142] T. Loiseau, C. Serre, C. Huguenard, G. Fink, F. Taulelle, M. Henry, T. Bataille and G. Férey, *Chem. Eur. J.*, 2004, **10**, 1373–1382.

[143] Stephen S.-Y. Chui, *Science*, 1999, **283**, 1148–1150.

[144] N. Stock and S. Biswas, *Chem. Rev.*, 2012, **112**, 933–969.

[145] A. Rabenau, *Angew. Chem. Int. Ed.*, 1985, **24**, 1026–1040.

[146] T. Ahnfeldt, N. Guillou, D. Gunzelmann, I. Margiolaki, T. Loiseau, G. Férey, J. Senker and N. Stock, *Angew. Chem. Int. Ed.*, 2009, **48**, 5163–5166.

[147] P. Long, H. Wu, Q. Zhao, Y. Wang, J. Dong and J. Li, *Microporous Mesoporous Mater.*, 2011, **142**, 489–493.

[148] E. R. Cooper, C. D. Andrews, P. S. Wheatley, P. B. Webb, P. Wormald and R. E. Morris, *Nature*, 2004, **430**, 1012–1016.

[149] E. R. Parnham and R. E. Morris, *Acc. Chem. Res.*, 2007, **40**, 1005–1013.

[150] L. Xu, E.-Y. Choi and Y.-U. Kwon, *Inorg. Chem.*, 2007, **46**, 10670–10680.

[151] S. Chen, J. Zhang and X. Bu, *Inorg. Chem.*, 2008, **47**, 5567–5569.

[152] J. Zhang, S. Chen and X. Bu, *Angew. Chem. Int. Ed.*, 2008, **47**, 5434–5437.

[153] A. D. Burrows, K. Cassar, R. M. W. Friend, M. F. Mahon, S. P. Rigby and J. E. Warren, *CrystEngComm*, 2005, **7**, 548.

[154] N. Zhu, G. Tobin and W. Schmitt, *Chem. Commun.*, 2012, **48**, 3638.

[155] S. Diring, S. Furukawa, Y. Takashima, T. Tsuruoka and S. Kitagawa, *Chem. Mater.*, 2010, **22**, 4531–4538.

[156] T. Tsuruoka, S. Furukawa, Y. Takashima, K. Yoshida, S. Isoda and S. Kitagawa, *Angew. Chem. Int. Ed.*, 2009, **48**, 4739–4743.

[157] P. Li, R. C. Klet, S. Y. Moon, T. C. Wang, P. Deria, A. W. Peters, B. M. Klahr, H. J. Park, S. S. Al-Juaid, J. T. Hupp and O. K. Farha, *Chem. Commun.*, 2015, **51**, 10925–10928.

[158] M. Li and M. Dincă, *J. Am. Chem. Soc.*, 2011, **133**, 12926–12929.

[159] N. Campagnol, T. R. Van Assche, M. Li, L. Stappers, M. Dinca, J. F. Denayer, K. Binnemans, D. E. De Vos and J. Fransaer, *J. Mater. Chem. A*, 2016, **4**, 3914–3925.

[160] A. Martinez Joaristi, J. Juan-Alcañiz, P. Serra-Crespo, F. Kapteijn and J. Gascon, *Cryst. Growth Des.*, 2012, **12**, 3489–3498.

[161] M. Li and M. Dincă, *Chem. Mater.*, 2015, **27**, 3203–3206.

[162] J. Klinowski, F. A. Almeida Paz, P. Silva and J. Rocha, *Dalt. Trans.*, 2011, **40**, 321–330.

[163] G. H. Albuquerque and G. S. Herman, *Cryst. Growth Des.*, 2017, **17**, 156–162.

[164] Z. Ni and R. I. Masel, *J. Am. Chem. Soc.*, 2006, **128**, 12394–12395.

[165] A. Pichon and S. L. James, *CrystEngComm*, 2008, **10**, 1839–1847.

[166] M. Klimakow, P. Klobes, A. F. Thünemann, K. Rademann and F. Emmerling, *Chem. Mater.*, 2010, **22**, 5216–5221.

[167] W. J. Son, J. Kim, J. Kim and W. S. Ahn, *Chem. Commun.*, 2008, 6336–6338.

[168] M. Bigdeli and A. Morsali, *Ultrason. Sonochem.*, 2015, **27**, 416–422.

[169] A. G. Slater and A. I. Cooper, *Science*, 2015, **348**, aaa8075.

[170] A. U. Czaja, N. Trukhan and U. Müller, *Chem. Soc. Rev.*, 2009, **38**, 1284–1293.

[171] S. S. Kaye, A. Dailly, O. M. Yaghi and J. R. Long, *J. Am. Chem. Soc.*, 2007, **129**, 14176–14177.

[172] H. Furukawa, M. A. Miller and O. M. Yaghi, *J. Mater. Chem.*, 2007, **17**, 3197–3204.

[173] A. G. Wong-Foy, A. J. Matzger and O. M. Yaghi, *J. Am. Chem. Soc.*, 2006, **128**, 3494–3495.

[174] O. K. Farha, A. Ö. Yazaydin, I. Eryazici, C. D. Malliakas, B. G. Hauser, M. G. Kanatzidis, S. T. Nguyen, R. Q. Snurr and J. T. Hupp, *Nat. Chem.*, 2010, **2**, 944–948.

[175] D. Yuan, D. Zhao, D. Sun and H. C. Zhou, *Angew. Chem. Int. Ed.*, 2010, **49**, 5357–5361.

[176] L. Wang and R. T. Yang, *Energy Environ. Sci.*, 2008, **1**, 268–279.

[177] R. Grünker, V. Bon, P. Müller, U. Stoeck, S. Krause, U. Mueller, I. Senkovska and S. Kaskel, *Chem. Commun.*, 2014, **50**, 3450–3452.

[178] H. Furukawa, N. Ko, Y. B. Go, N. Aratani, S. B. Choi, E. Choi, A. O. Yazaydin, R. Q. Snurr, M. O'Keeffe, J. Kim and O. M. Yaghi, *Science*, 2010, **329**, 424–428.

[179] J. S. Choi, W. J. Son, J. Kim and W. S. Ahn, *Microporous Mesoporous Mater.*, 2008, **116**, 727–731.

[180] A. R. Millward and O. M. Yaghi, *J. Am. Chem. Soc.*, 2005, **127**, 17998–17999.

[181] P. L. Llewellyn, S. Bourrelly, C. Serre, A. Vimont, M. Daturi, L. Hamon, G. De Weireld, J.-s. Chang, D.-y. Hong, Y. Kyu Hwang, S. Hwa Jhung and G. Férez, *Langmuir*, 2008, **24**, 7245–7250.

[182] J. R. Li, J. Yu, W. Lu, L. B. Sun, J. Sculley, P. B. Balbuena and H. C. Zhou, *Nat. Commun.*, 2013, **4**, 1–8.

[183] S. Xiang, Y. He, Z. Zhang, H. Wu, W. Zhou, R. Krishna and B. Chen, *Nat. Commun.*, 2012, **3**, 954.

[184] D. X. Xue, A. J. Cairns, Y. Belmabkhout, L. Wojtas, Y. Liu, M. H. Alkordi and M. Eddaoudi, *J. Am. Chem. Soc.*, 2013, **135**, 7660–7667.

[185] D. Lässig, J. Lincke, J. Moellmer, C. Reichenbach, A. Moeller, R. Gläser, G. Kalies, K. A. Cychosz, M. Thommes, R. Staudt and H. Krautscheid, *Angew. Chem. Int. Ed.*, 2011, **50**, 10344–10348.

[186] R. Vaidhyanathan, S. S. Iremonger, G. K. H. Shimizu, P. G. Boyd, S. Alavi and T. K. Woo, *Science*, 2010, **330**, 650–653.

[187] A. Banerjee, S. Nandi, P. Nasa and R. Vaidhyanathan, *Chem. Commun.*, 2016, **52**, 1851–1854.

[188] Z. R. Herm, J. A. Swisher, B. Smit, R. Krishna and J. R. Long, *J. Am. Chem. Soc.*, 2011, **133**, 5664–5667.

[189] P. Nugent, E. G. Giannopoulou, S. D. Burd, O. Elemento, E. G. Giannopoulou, K. Forrest, T. Pham, S. Ma, B. Space, L. Wojtas, M. Eddaoudi and M. J. Zaworotko, *Nature*, 2013, **495**, 80–84.

[190] S. Ma, D. Sun, J. M. Simmons, C. D. Collier, D. Yuan and H. C. Zhou, *J. Am. Chem. Soc.*, 2008, **130**, 1012–1016.

[191] F. Gándara, H. Furukawa, S. Lee and O. M. Yaghi, *J. Am. Chem. Soc.*, 2014, **136**, 5271–5274.

[192] Y. He, W. Zhou, G. Qian and B. Chen, *Chem. Soc. Rev.*, 2014, **43**, 5657–5678.

[193] J. a. Mason, J. Oktawiec, M. K. Taylor, M. R. Hudson, J. Rodriguez, J. E. Bachman, M. I. Gonzalez, A. Cervellino, A. Guagliardi, C. M. Brown, P. L. Llewellyn, N. Masciocchi and J. R. Long, *Nature*, 2015, **advance on**, 357–361.

[194] D. Alezi, Y. Belmabkhout, M. Suyetin, P. M. Bhatt, L. J. Weseliński, V. Solovyeva, K. Adil, I. Spanopoulos, P. N. Trikalitis, A. H. Emwas and M. Eddaoudi, *J. Am. Chem. Soc.*, 2015, **137**, 13308–13318.

[195] C. M. Simon, J. Kim, D. A. Gomez-Gualdron, J. S. Camp, Y. G. Chung, R. L. Martin, R. Mercado, M. W. Deem, D. Gunter, M. Haranczyk, D. S. Sholl, R. Q. Snurr and B. Smit, *Energy Environ. Sci.*, 2015, **8**, 1190–1199.

[196] L. Pan, D. H. Olson, L. R. Ciemnolonski, R. Heady and J. Li, *Angew. Chem. Int. Ed.*, 2006, **45**, 616–619.

[197] E. D. Bloch, W. L. Queen, R. Krishna, J. M. Zadrozny, C. M. Brown and J. R. Long, *Science*, 2012, **335**, 1606–1610.

[198] H. Wu, Q. Gong, D. H. Olson and J. Li, *Chem. Rev.*, 2012, **112**, 836–868.

[199] T. L. Hu, H. Wang, B. Li, R. Krishna, H. Wu, W. Zhou, Y. Zhao, Y. Han, X. Wang, W. Zhu, Z. Yao, S. Xiang and B. Chen, *Nat. Commun.*, 2015, **6**, 1–9.

[200] A. Cadiau, K. Adil, P. M. Bhatt, Y. Belmabkhout and M. Eddaoudi, *Science*, 2016, **353**, 137–140.

[201] Y. Cui, B. Li, H. He, W. Zhou, B. Chen and G. Qian, *Acc. Chem. Res.*, 2016, **49**, 483–493.

[202] M. D. Allendorf, R. J. Houk, L. Andruszkiewicz, A. A. Talin, J. Pikarsky, A. Choudhury, K. A. Gall and P. J. Hesketh, *J. Am. Chem. Soc.*, 2008, **130**, 14404–14405.

[203] S. Achmann, G. Hagen, J. Kita, I. M. Malkowsky, C. Kiener and R. Moos, *Sensors*, 2009, **9**, 1574–1589.

[204] A. Venkatasubramanian, M. Navaei, K. R. Bagnall, K. C. McCarley, S. Nair and P. J. Hesketh, *J. Phys. Chem. C*, 2012, **116**, 15313–15321.

[205] E. Barea, C. Montoro and J. A. Navarro, *Chem. Soc. Rev.*, 2014, **43**, 5419–5430.

[206] M. J. Katz, J. E. Mondloch, R. K. Totten, J. K. Park, S. T. Nguyen, O. K. Farha and J. T. Hupp, *Angew. Chem. Int. Ed.*, 2014, **53**, 497–501.

[207] N. S. Bobbitt, M. L. Mendonca, A. J. Howarth, T. Islamoglu, J. T. Hupp, O. K. Farha and R. Q. Snurr, *Chem. Soc. Rev.*, 2017, **46**, 3357–3385.

[208] Y. Inokuma, M. Kawano and M. Fujita, *Nat. Chem.*, 2011, **3**, 349–358.

[209] Y. Inokuma, S. Yoshioka, J. Ariyoshi, T. Arai, Y. Hitora, K. Takada, S. Matsunaga, K. Rissanen and M. Fujita, *Nature*, 2013, **495**, 461–466.

[210] K. Yan, R. Dubey, T. Arai, Y. Inokuma and M. Fujita, *J. Am. Chem. Soc.*, 2017, **139**, 11341–11344.

[211] K. Liang, R. Ricco, C. M. Doherty, M. J. Styles, S. Bell, N. Kirby, S. Mudie, D. Haylock, A. J. Hill, C. J. Doonan and P. Falcaro, *Nat. Commun.*, 2015, **6**, 4–11.

[212] X. Lian, Y. Fang, E. Joseph, Q. Wang, J. Li, S. Banerjee, C. Lollar, X. Wang and H. C. Zhou, *Chem. Soc. Rev.*, 2017, **46**, 3386–3401.

[213] L. Ma, C. Abney and W. Lin, *Chem. Soc. Rev.*, 2009, **38**, 1248–1256.

[214] L. Zhu, X. Q. Liu, H. L. Jiang and L. B. Sun, *Chem. Rev.*, 2017, **117**, 8129–8176.

[215] J. Liu, L. Chen, H. Cui, J. Zhang, L. Zhang and C.-Y. Su, *Chem. Soc. Rev.*, 2014, **43**, 6011–6061.

[216] D. Farrusseng, S. Aguado and C. Pinel, *Angew. Chem. Int. Ed.*, 2009, **48**, 7502–7513.

[217] Y. K. Hwang, D. Y. Hong, J. S. Chang, H. Seo, M. Yoon, J. Kim, S. H. Jhung, C. Serre and G. Férey, *Appl. Catal. A Gen.*, 2009, **358**, 249–253.

[218] P. Horcajada, S. Surblé, C. Serre, D. Y. Hong, Y. K. Seo, J. S. Chang, J. M. Grenèche, I. Margiolaki and G. Férey, *Chem. Commun.*, 2007, **100**, 2820–2822.

[219] L. Mitchell, B. Gonzalez-Santiago, J. P. Mowat, M. E. Gunn, P. Williamson, N. Acerbi, M. L. Clarke and P. A. Wright, *Catal. Sci. Technol.*, 2013, **3**, 606–617.

[220] K. Barthelet, J. Marrot, D. Riou and G. Férey, *Angew. Chem. Int. Ed.*, 2002, **41**, 281.

[221] S.-H. Cho, B. Ma, S. T. Nguyen, J. T. Hupp and T. E. Albrecht-Schmitt, *Chem. Commun.*, 2006, 2563–2565.

[222] P. Serra-Crespo, E. V. Ramos-Fernandez, J. Gascon and F. Kapteijn, *Chem. Mater.*, 2011, **23**, 2565–2572.

[223] M. G. Goesten, J. Juan-Alcañiz, E. V. Ramos-Fernandez, K. B. Sai Sankar Gupta, E. Stavitski, H. Van Bekkum, J. Gascon and F. Kapteijn, *J. Catal.*, 2011, **281**, 177–187.

[224] J. M. Roberts, B. M. Fini, A. A. Sarjeant, O. K. Farha, J. T. Hupp and K. A. Scheidt, *J. Am. Chem. Soc.*, 2012, **134**, 3334–3337.

[225] A. Henschel, K. Gedrich, R. Kraehnert and S. Kaskel, *Chem. Commun.*, 2008, 4192–4194.

[226] B. Yuan, Y. Pan, Y. Li, B. Yin and H. Jiang, *Angew. Chem. Int. Ed.*, 2010, **49**, 4054–4058.

[227] E. Collini, C. Y. Wong, K. E. Wilk, P. M. Curmi, P. Brumer and G. D. Scholes, *Nature*, 2010, **463**, 644–647.

[228] J.-L. Wang, C. Wang and W. Lin, *ACS Catal.*, 2012, **2**, 2630–2640.

[229] S. Pullen, H. Fei, A. Orthaber, S. M. Cohen and S. Ott, *J. Am. Chem. Soc.*, 2013, **135**, 16997–17003.

[230] Z. M. Zhang, T. Zhang, C. Wang, Z. Lin, L. S. Long and W. Lin, *J. Am. Chem. Soc.*, 2015, **137**, 3197–3200.

[231] M. Martin-Sabi, J. Soriano-López, R. S. Winter, J. J. Chen, L. Vilà-Nadal, D. L. Long, J. R. Galán-Mascarós and L. Cronin, *Nat. Catal.*, 2018, **1**, 208–213.

[232] W. A. Shah, A. Waseem, M. A. Nadeem and P. Kögerler, *Appl. Catal. A Gen.*, 2018, **567**, 132–138.

[233] W. A. Maza, A. J. Haring, S. R. Ahrenholtz, C. C. Epley, S. Y. Lin and A. J. Morris, *Chem. Sci.*, 2016, **7**, 719–727.

[234] J. Zhu, P. Z. Li, W. Guo, Y. Zhao and R. Zou, *Coord. Chem. Rev.*, 2018, **359**, 80–101.

[235] M. Dan-Hardi, C. Serre, T. Frot, L. Rozes, G. Maurin, C. Sanchez, G. Férey and G. Maurín, *J. Am. Chem. Soc.*, 2009, **131**, 10857–10859.

[236] M. Eshel, A. Bino, I. Felner, D. C. Johnston, M. Luban and L. L. Miller, *Inorg. Chem.*, 2000, **39**, 1376–1380.

[237] C. Zlotea, D. Phanon, M. Mazaj, D. Heurtaux, V. Guillerm, C. Serre, P. Horcajada, T. Devic, E. Magnier, F. Cuevas, G. Férey, P. L. Llewellyn and M. Latroche, *J. Chem. Soc. Dalt. Trans.*, 2011, **40**, 4879–4881.

[238] C. H. Hendon, D. Tiana, M. Fontecave, C. Sanchez, L. D'Arras, C. Sassoye, L. Rozes, C. Mellot-Draznieks and A. Walsh, *J. Am. Chem. Soc.*, 2013, **135**, 10942–10945.

[239] Y. Fu, D. Sun, Y. Chen, R. Huang, Z. Ding, X. Fu and Z. Li, *Angew. Chem. Int. Ed.*, 2012, **51**, 3364–3367.

[240] Y. Horiuchi, T. Toyao, M. Saito, K. Mochizuki, M. Iwata, H. Higashimura, M. Anpo and M. Matsuoka, *J. Phys. Chem. C*, 2012, **116**, 20848–20853.

[241] D. Sun, L. Ye and Z. Li, *Appl. Catal. B Environ.*, 2015, **164**, 428–432.

[242] C. T. Saouma, C. C. Tsou, S. Richard, R. Ameloot, F. Vermoortele, S. Smolders, B. Bueken, A. G. Dipasquale, W. Kaminsky, C. N. Valdez, D. E. De Vos and J. M. Mayer, *Chem. Sci.*, 2019, **10**, 1322–1331.

[243] T. Devic and C. Serre, *Chem. Soc. Rev.*, 2014, **43**, 6097–6115.

[244] H. L. Nguyen, F. Gándara, H. Furukawa, T. L. H. Doan, K. E. Cordova and O. M. Yaghi, *J. Am. Chem. Soc.*, 2016, **138**, 4330–4333.

[245] H. L. Nguyen, *New J. Chem.*, 2017, **41**, 14030–14043.

[246] K. Hong and H. Chun, *Inorg. Chem.*, 2013, **52**, 9705–9707.

[247] S. Yuan, T.-f. Liu, D. Feng, J. Tian, K. Wang, J. Qin, Q. Zhang, Y.-P. Chen, M. Bosch, L. Zou, S. J. Teat, S. J. Dalgarno and H.-C. Zhou, *Chem. Sci.*, 2015, **6**, 3926–3930.

[248] S. Wang, H. Reinsch, N. Heymans, M. Wahiduzzaman, C. Martineau-Corcos, G. De Weireld, G. Maurin and C. Serre, *Matter*, 2020, **2**, 1–11.

[249] U. Schubert, *Chem. Soc. Rev.*, 2011, **40**, 575–582.

[250] R. Sessoli, D. Gatteschi, A. Caneschi and M. A. Novak, *Nature*, 1993, **365**, 141–143.

[251] X. J. Kong, L. S. Long, Z. Zheng, R. B. Huang and L. S. Zheng, *Acc. Chem. Res.*, 2010, **43**, 201–209.

[252] J. R. Lombardi and B. Davis, *Chem. Rev.*, 2002, **102**, 2431–2460.

[253] Y. G. Huang, F. L. Jiang and M. C. Hong, *Coord. Chem. Rev.*, 2009, **253**, 2814–2834.

[254] L. Rozes and C. Sanchez, *Chem. Soc. Rev.*, 2011, **40**, 1006–1030.

[255] W. H. Fang, L. Zhang and J. Zhang, *Chem. Soc. Rev.*, 2018, **47**, 404–421.

[256] P. Coppens, Y. Chen and E. Trzop, *Chem. Rev.*, 2014, **114**, 9645–9661.

[257] D. L. Long, E. Burkholder and L. Cronin, *Chem. Soc. Rev.*, 2007, **36**, 105–121.

[258] S. T. Zheng and G. Y. Yang, *Chem. Soc. Rev.*, 2012, **41**, 7623–7646.

[259] L. Vilà-Nadal and L. Cronin, *Nat. Rev. Mater.*, 2017, **2**, 17054.

[260] X. Chen and S. S. Mao, *Chem. Rev.*, 2007, **107**, 2891–2959.

[261] A. Fujishima and K. Honda, *Nature*, 1972, **238**, 37–38.

[262] X. Chen, S. Shen, L. Guo and S. S. Mao, *Chem. Rev.*, 2010, **110**, 6503–6570.

[263] `https://agmetalminer.com/metal-prices/titanium/`, retrieved 12/12/2019.

[264] L. Vilà-Nadal, A. Rodríguez-Fortea, L.-K. Yan, E. F. Wilson, L. Cronin and J. M. Poblet, *Angew. Chem. Int. Ed.*, 2009, **48**, 5452–5456.

[265] R. Schmid, A. Mosset and J. Galy, *J. Chem. Soc. Dalt. Trans.*, 1991, **3**, 1999–2005.

[266] C. F. Negre, K. J. Young, M. B. Oviedo, L. J. Allen, C. G. Sánchez, K. N. Jarzembska, J. B. Benedict, R. H. Crabtree, P. Coppens, G. W. Brudvig and V. S. Batista, *J. Am. Chem. Soc.*, 2014, **136**, 16420–16429.

[267] Y. Chen, E. Trzop, A. Makal, Y. S. Chen and P. Coppens, *Dalt. Trans.*, 2014, **43**, 3839–3841.

[268] W. H. Casey, *Chem. Rev.*, 2006, **106**, 1–16.

[269] A. C. Skapski and P. G. H. Troughton, *Acta Crystallogr. B*, 1970, **26**, 716–722.

[270] K. Döppert and U. Thewalt, *J. Organomet. Chem.*, 1986, **301**, 41–48.

[271] I. Gautier-Luneau, A. Mosset and J. Galy, *Zeitschrift fur Krist. - New Cryst. Struct.*, 1987, **180**, 83–95.

[272] S. Doeuff, Y. Dromzee, F. Taulelle and C. Sanchez, *Inorg. Chem.*, 1989, **28**, 4439–4445.

[273] V. W. Day, T. A. Eberspacher, W. G. Klemperer and C. W. Park, *J. Am. Chem. Soc.*, 1993, **115**, 8469–8470.

[274] M. Czakler, C. Artner and U. Schubert, *Eur. J. Inorg. Chem.*, 2013, 5790–5796.

[275] S. Wang, T. Kitao, N. Guillou, M. Wahiduzzaman, C. Martineau-Corcos, F. Nouar, A. Tissot, L. Binet, N. Ramsahye, S. Devautour-Vinot, S. Kitagawa, S. Seki, Y. Tsutsui, V. Briois, N. Steunou, G. Maurin, T. Uemura and C. Serre, *Nat. Commun.*, 2018, **9**, 1–9.

[276] T. P. Vaid, E. B. Lobkovsky and P. T. Wolczanski, *J. Am. Chem. Soc.*, 1997, **119**, 8742–8743.

[277] J. Rocha, L. D. Carlos, F. A. Paz and D. Ananias, *Chem. Soc. Rev.*, 2011, **40**, 926–940.

[278] J. D. Sokolow, E. Trzop, Y. Chen, J. Tang, L. J. Allen, R. H. Crabtree, J. B. Benedict and P. Coppens, *J. Am. Chem. Soc.*, 2012, **134**, 11695–11700.

[279] M. Y. Gao, F. Wang, Z. G. Gu, D. X. Zhang, L. Zhang and J. Zhang, *J. Am. Chem. Soc.*, 2016, **138**, 2556–2559.

[280] S. Wang, H. C. Su, L. Yu, X. W. Zhao, L. W. Qian, Q. Y. Zhu and J. Dai, *Dalt. Trans.*, 2015, **44**, 1882–1888.

[281] L. Cui, P. Liu, L. Yang, X. Shu, Q. Zhu and J. Dai, *Chem. – An Asian J.*, 2019, **14**, 3198–3204.

[282] M. G. Reichmann, F. J. Hollander and A. T. Bell, *Acta Crystallogr. C*, 1987, **43**, 1681–1683.

[283] V. W. Day, T. A. Eberspacher, Y. Chen, J. Hao and W. G. Klemperer, *Inorganica Chim. Acta*, 1995, **229**, 391–405.

[284] G. Zhang, J. Hou, M. Li, C. H. Tung and Y. Wang, *Inorg. Chem.*, 2016, **55**, 4704–4709.

[285] Z. Zhang, H. Yoshikawa and K. Awaga, *Chem. Mater.*, 2016, **28**, 1298–1303.

[286] J. Hu, L. Zhan, G. Zhang, Q. Zhang, L. Du, C. H. Tung and Y. Wang, *Inorg. Chem.*, 2016, **55**, 8493–8501.

[287] G. Zhang, C. Liu, D. L. Long, L. Cronin, C. H. Tung and Y. Wang, *J. Am. Chem. Soc.*, 2016, **138**, 11097–11100.

[288] B. Tang and K. H. Row, *Monatsh. Chem.*, 2013, **144**, 1427–1454.

[289] N. Narayanam, W. H. Fang, K. Chintakrinda, L. Zhang and J. Zhang, *Chem. Commun.*, 2017, **53**, 8078–8080.

[290] N. Steunou, G. Kickelbick, K. Boubekeur and C. Sanchez, *J. Chem. Soc. Dalt. Trans.*, 1999, 3653–3655.

[291] C. Chaumont, E. Huen, C. Huguenard, P. Mobian and M. Henry, *Polyhedron*, 2013, **57**, 70–76.

[292] C. Chaumont, P. Mobian and M. Henry, *Dalt. Trans.*, 2014, **43**, 3416–3419.

[293] J. A. Fernández, X. López and J. M. Poblet, *J. Mol. Catal. A Chem.*, 2007, **262**, 236–242.

[294] R. J. Swope, J. R. Smyth and A. C. Larson, *Am. Mineral.*, 1995, **80**, 448–453.

[295] C. J. Howard, T. M. Sabine and F. Dickson, *Acta Crystallogr. B*, 1991, **47**, 462–468.

[296] J. A. Ibers, *Nature*, 1963, **197**, 686–687.

[297] V. W. Day, T. A. Eberspacher, W. G. Klemperer, C. W. Park and F. S. Rosenberg, *J. Am. Chem. Soc.*, 1991, **113**, 8190–8192.

[298] C. F. Campana, Y. Chen, V. W. Day, W. G. Klemperer and R. A. Sparks, *J. Chem. Soc. Dalt. Trans.*, 1996, **53**, 691.

[299] J. F. Keggin, *Nature*, 1933, **131**, 908–909.

[300] J.-X. Liu, M.-Y. Gao, W.-H. Fang, L. Zhang and J. Zhang, *Angew. Chem. Int. Ed.*, 2016, **55**, 5160–5165.

[301] T. J. Boyle, R. P. Tyner, T. M. Alam, B. L. Scott, J. W. Ziller and B. G. Potter, *J. Am. Chem. Soc.*, 1999, **121**, 12104–12112.

[302] W. H. Fang, L. Zhang and J. Zhang, *J. Am. Chem. Soc.*, 2016, **138**, 7480–7483.

[303] G. Guerrero, M. Mehring, P. H. Mutin, F. Dahan and A. Vioux, *J. Chem. Soc. Dalt. Trans.*, 1999, **61**, 1537–1538.

[304] T. Krämer, F. Tuna and S. D. Pike, *Chem. Sci.*, 2019, **10**, 6886–6898.

[305] Y. Chen, E. Trzop, J. D. Sokolow and P. Coppens, *Chem. Eur. J.*, 2013, **19**, 16651–16655.

[306] M. Czakler, C. Artner and U. Schubert, *Eur. J. Inorg. Chem.*, 2014, 2038–2045.

[307] W. H. Fang, L. Zhang and J. Zhang, *Dalt. Trans.*, 2017, **46**, 803–807.

[308] Q. R. Ding, G. L. Xu, L. Zhang and J. Zhang, *Dalt. Trans.*, 2019, **48**, 9916–9919.

[309] X. X. Liu, S. Chen, W. H. Fang, L. Zhang and J. Zhang, *Inorg. Chem.*, 2019, **58**, 7267–7273.

[310] Y.-z. Yu, Y.-R. Zhang, C.-h. Geng, L. Sun, Y. Guo, Y.-r. Feng, Y.-x. Wang and X.-m. Zhang, *Inorg. Chem.*, 2019, **58**, 16785–16791.

[311] Y. Fu, Z. Xu and F. Zhang, *J. Mol. Struct.*, 2008, **873**, 168–172.

[312] G. Zhang, J. Hou, C. H. Tung and Y. Wang, *Inorg. Chem.*, 2016, **55**, 3212–3214.

[313] U. Kortz, S. S. Hamzeh and N. A. Nasser, *Chem. Eur. J.*, 2003, **9**, 2945–2952.

[314] Y. Sakai, K. Yoza, C. N. Kato and K. Nomiya, *Chem. Eur. J.*, 2003, **9**, 4077–4083.

[315] G. A. Al-Kadamany, F. Hussain, S. S. Mal, M. H. Dickman, N. Leclerc-Laronze, J. Marrot, E. Cadot and U. Kortz, *Inorg. Chem.*, 2008, **47**, 8574–8576.

[316] T. McGlone, L. Vilà-Nadal, H. N. Miras, D. L. Long, J. M. Poblet and L. Cronin, *Dalt. Trans.*, 2010, **39**, 11599–11604.

[317] Y.-J. Liu, W.-H. Fang, L. Zhang and J. Zhang, *Coord. Chem. Rev.*, 2020, **404**, 213099.

[318] R. C. Snoeberger, K. J. Young, J. Tang, L. J. Allen, R. H. Crabtree, G. W. Brudvig, P. Coppens, S. Batista and J. B. Benedict, *J. Am. Chem. Soc.*, 2012, **24**, 1–28.

[319] H. C. Su, Y. Y. Wu, J. L. Hou, G. L. Zhang, Q. Y. Zhu and J. Dai, *Chem. Commun.*, 2016, **52**, 4072–4075.

[320] Y. Guo, J.-L. Hou, W. Luo, Z.-Q. Li, D.-H. Zou, Q.-Y. Zhu and J. Dai, *J. Mater. Chem. A*, 2017, **5**, 18270–18275.

[321] J. L. Hou, W. Luo, Y. Guo, P. Zhang, S. Yang, Q. Y. Zhu and J. Dai, *Inorg. Chem.*, 2017, **56**, 6451–6458.

[322] Y. Fan, H. M. Li, R. H. Duan, H. T. Lu, J. T. Cao, G. D. Zou and Q. S. Jing, *Inorg. Chem.*, 2017, **56**, 12775–12782.

[323] Y. Y. Wu, X. W. Lu, M. Qi, H. C. Su, X. W. Zhao, Q. Y. Zhu and J. Dai, *Inorg. Chem.*, 2014, **53**, 7233–7240.

[324] Y. Y. Wu, W. Luo, Y. H. Wang, Y. Y. Pu, X. Zhang, L. S. You, Q. Y. Zhu and J. Dai, *Inorg. Chem.*, 2012, **51**, 8982–8988.

[325] K. Su, M. Wu, Y. Tan, W. Wang, D. Yuan and M. Hong, *Chem. Commun.*, 2017, **53**, 9598–9601.

[326] S. Liu, W. Hu, J. K. Nath, J. Tong, X. Hou, W. Liu, J. Yang and B. Liu, *Dalt. Trans.*, 2017, **46**, 678–684.

[327] J. Zhang, W. Hu, J. Zhang, S. Liu, J. Tong, X. Hou, W. Liu, J. Yang and B. Liu, *J. Phys. Chem. C*, 2017, **121**, 18326–18332.

[328] D. F. Lu, X. J. Kong, T. B. Lu, L. S. Long and L. S. Zheng, *Inorg. Chem.*, 2017, **56**, 1057–1060.

[329] Y. Lv, Z. Cai, D. Yan, C. Su, W. Li, W. Chen, Z. Ren, Y. Wei, O. Mi, C. Zhang and D. S. Wright, *RSC Adv.*, 2016, **6**, 57–60.

[330] G. L. Zhang, S. Wang, J. L. Hou, C. J. Mo, C. J. Que, Q. Y. Zhu and J. Dai, *Dalt. Trans.*, 2016, **45**, 17681–17686.

[331] P. Y. Liu, L. N. Cui, L. Yang, X. P. Shu, Q. Y. Zhu and J. Dai, *Chem. Commun.*, 2019, **55**, 12360–12363.

[332] Y. Lv, W. Du, Y. Ren, Z. Cai, K. Yu, C. Zhang, Z. Chen and D. S. Wright, *Inorg. Chem. Front.*, 2016, **3**, 1119–1123.

[333] K. Hong, W. Bak and H. Chun, *Inorg. Chem.*, 2014, **53**, 7288–7293.

[334] A. Kobayashi, T. Ohba, E. Saitoh, Y. Suzuki, S.-i. Noro, H.-C. Chang and M. Kato, *Inorg. Chem.*, 2014, **53**, 2910–2921.

[335] S. Abednatanzi, P. G. Derakhshandeh, A. Abbasi, P. Van Der Voort and K. Leus, *ChemCatChem*, 2016, **8**, 3672–3679.

[336] C. A. Kent, B. P. Mehl, L. Ma, J. M. Papanikolas, T. J. Meyer and W. Lin, *J. Am. Chem. Soc.*, 2010, **132**, 12767–12769.

[337] A. Coskun, M. Hmadeh, G. Barin, F. Gándara, Q. Li, E. Choi, N. L. Strutt, D. B. Cordes, A. M. Z. Slawin, J. F. Stoddart, J.-P. Sauvage and O. M. Yaghi, *Angew. Chem. Int. Ed.*, 2012, **51**, 2160–2163.

[338] A. Kobayashi, A. Sugiyama, T. Ohba, Y. Suzuki, H.-C. Chang and M. Kato, *Chem. Lett.*, 2014, **43**, 1070–1072.

[339] V.-M. Mukkala and J. J. Kankare, *Helv. Chim. Acta*, 1992, **75**, 1578–1592.

[340] Z. Wang, X. Zhang, S. R. Batten, M. Kurmoo and S. Gao, *Inorg. Chem.*, 2007, **46**, 8439–8441.

[341] A. L. Spek, *J. Appl. Crystallogr.*, 2003, **36**, 7–13.

[342] H. Irving and R. J. P. Williams, *J. Chem. Soc.*, 1953, 3192–3210.

[343] R. D. Shannon, *Acta Crystallogr. A*, 1976, **32**, 751–767.

[344] S. Alvarez, P. Alemany, D. Casanova, J. Cirera, M. Llunell and D. Avnir, *Coord. Chem. Rev.*, 2005, **249**, 1693–1708.

[345] P. Van Der Sluis and A. L. Spek, *Acta Crystallogr. A*, 1990, **46**, 194–201.

[346] T. Steiner, *Angew. Chem. Int. Ed.*, 2002, **41**, 49–76.

[347] C. Janiak, *J. Chem. Soc. Dalt. Trans.*, 2000, 3885–3896.

[348] A. Le Bail, *Powder Diffr.*, 2005, **20**, 316–326.

[349] F. N. Castellano, T. A. Heimer, M. T. Tandhasetti and G. J. Meyer, *Chem. Mater.*, 1994, **6**, 1041–1048.

[350] G. Deacon and R. Phillips, *Coord. Chem. Rev.*, 1980, **33**, 227–250.

[351] O. Yaghi, M. Kalmutzki and C. Diercks, *Introduction to Reticular Chemistry: Metal-Organic Frameworks and Covalent Organic Frameworks*, Wiley, 2019.

[352] S. Garakyaraghi, E. O. Danilov, C. E. McCusker and F. N. Castellano, *J. Phys. Chem. A*, 2015, **119**, 3181–3193.

[353] A. Hernández Redondo, *Ph.D. thesis*, University of Basel, 2009.

[354] D. M. Proserpio, *Nat. Chem.*, 2010, **2**, 435–436.

[355] F. Kübel and J. Strähle, *Zeitschrift für Naturforsch. B*, 1982, **37**, 272–275.

[356] C. Li, M. Schwab, Y. Zhao, L. Chen, I. Bruder, I. Münster, P. Erk and K. Müllen, *Dye. Pigment.*, 2013, **97**, 258–261.

[357] T. E. Barder, S. D. Walker, J. R. Martinelli and S. L. Buchwald, *J. Am. Chem. Soc.*, 2005, **127**, 4685–4696.

[358] F. K. Klemens, P. E. Fanwick, J. K. Bibler and D. R. McMillin, *Inorg. Chem.*, 1989, **28**, 3076–3079.

[359] C. S. Smith and K. R. Mann, *Chem. Mater.*, 2009, **21**, 5042–5049.

[360] W. L. Parker and G. A. Crosby, *J. Phys. Chem.*, 1989, **93**, 5692–5696.

[361] C. E. McCusker and F. N. Castellano, *Inorg. Chem.*, 2015, **54**, 6035–6042.

[362] Y. Pellegrin and F. Odobel, *Comptes Rendus Chim.*, 2017, **20**, 283–295.

[363] M. Amutha Selvi, K. Arun Kumar and A. Dayalan, *Acta Cryst.*, 2011, **E67**, m851–m852.

[364] J. B. Benedict and P. Coppens, *J. Am. Chem. Soc.*, 2010, **132**, 2938–2944.

[365] J. B. Benedict, R. Freindorf, E. Trzop, J. Cogswell and P. Coppens, *J. Am. Chem. Soc.*, 2010, **132**, 13669–13671.

[366] Y. Lv, J. Cheng, A. Steiner, L. Gan and D. S. Wright, *Angew. Chem. Int. Ed.*, 2014, **53**, 1934–1938.

[367] P. D. Matthews, T. C. King and D. S. Wright, *Chem. Commun.*, 2014, **50**, 12815–12823.

[368] S. Hanf, P. D. Matthews, N. Li, H. K. Luo and D. S. Wright, *Dalt. Trans.*, 2017, **46**, 578–585.

[369] D. Chen, X. Zhang and A. F. Lee, *J. Mater. Chem. A*, 2015, **3**, 14487–14516.

[370] H. T. Lv, H. M. Li, G. D. Zou, Y. Cui, Y. Huang and Y. Fan, *Dalt. Trans.*, 2018, **47**, 8158–8163.

[371] J. L. Hou, Y. G. Weng, P. Y. Liu, L. N. Cui, Q. Y. Zhu and J. Dai, *Inorg. Chem.*, 2019, **58**, 2736–2743.

[372] D.-H. Zou, L.-N. Cui, P.-Y. Liu, S. Yang, Q.-Y. Zhu and J. Dai, *Inorg. Chem.*, 2019, **58**, 9246–9252.

[373] H. T. Lv, Y. Cui, Y. M. Zhang, H. M. Li, G. D. Zou, R. H. Duan, J. T. Cao, Q. S. Jing and Y. Fan, *Dalt. Trans.*, 2017, **46**, 12313–12319.

[374] S. Dai, L. Jiang, C. Zhao, F. Chen, R. Chen, R. Qin, W. Zhang, W. Zhang, B. Wu and N. Zheng, *ChemNanoMat*, 2019, **5**, 1110–1114.

[375] K. Matsumoto, Y. Sawada, B. Saito, K. Sakai and T. Katsuki, *Angew. Chem. Int. Ed.*, 2005, **44**, 4935–4939.

[376] W. Ding, C. T. Sanderson, R. C. Conover, M. K. Johnson, I. J. Amster and C. Kutal, *Inorg. Chem.*, 2003, **42**, 1532–1537.

[377] M. Y. Gao, W. H. Fang, T. Wen, L. Zhang and J. Zhang, *Cryst. Growth Des.*, 2017, **17**, 3592–3595.

[378] D. L. Reger, A. Debreczeni, J. J. Horger and M. D. Smith, *Cryst. Growth Des.*, 2011, **11**, 4068–4079.

[379] S. Coffey and V. Boyd, *J. Chem. Soc.*, 1954, 2468–2470.

[380] T. J. Boyle, F. Guerrero, T. M. Alam, K. A. Dunnigan, J. M. Sears and D. R. Wheeler, *Inorg. Chem.*, 2020, **59**, 880–890.

[381] M. Y. Gao, X. Fan, L. Zhang and J. Zhang, *Inorg. Chem.*, 2018, **57**, 5642–5647.

[382] J. F. Wang, W. H. Fang, D. S. Li, L. Zhang and J. Zhang, *Inorg. Chem.*, 2017, **56**, 2367–2370.

[383] L. P. Hammett, *J. Am. Chem. Soc.*, 1937, **59**, 96–103.

[384] D. D. Perrin, B. Dempsey and E. P. Serjeant, *pK a Prediction for Organic Acids and Bases*, Springer Netherlands, Dordrecht, 1981, vol. 152, p. 308.

[385] C. Hansch, A. Leo and R. W. Taft, *Chem. Rev.*, 1991, **91**, 165–195.

[386] M. J. Dewar and P. J. Grisdale, *J. Am. Chem. Soc.*, 1962, **84**, 3548–3553.

[387] M. J. Dewar and P. J. Grisdale, *J. Am. Chem. Soc.*, 1962, **84**, 3539–3541.

[388] F. Lakadamyali and E. Reisner, *Chem. Commun.*, 2011, **47**, 1695–1697.

[389] S. Tschierlei, A. Neubauer, N. Rockstroh, M. Karnahl, P. Schwarzbach, H. Junge, M. Beller and S. Lochbrunner, *Phys. Chem. Chem. Phys.*, 2016, **18**, 10682–10687.

[390] J. Huo, Y.-B. Zhang, W.-Y. Zou, X. Hu, Q. Deng and D. Chen, *Catal. Sci. Technol.*, 2019, **9**, 2716–2727.

[391] M. Karnahl, E. Mejía, N. Rockstroh, S. Tschierlei, S. P. Luo, K. Grabow, A. Kruth, V. Brüser, H. Junge, S. Lochbrunner and M. Beller, *ChemCatChem*, 2014, **6**, 82–86.

[392] N. Bloembergen, E. M. Purcell and R. V. Pound, *Phys. Rev.*, 1948, **73**, 679–712.

[393] N. Armaroli and H. J. Bolink, *Top. Curr. Chem.*, 2016, **374**, 44.

[394] Q. Zhang, Q. Zhou, Y. Cheng, L. Wang, D. Ma, X. Jing and F. Wang, *Adv. Mater.*, 2004, **16**, 432–436.

[395] G. M. Sheldrick, *CELL NOW*, Bruker-AXS Inc, Madison, Wisconsin, USA, 2008.

[396] Bruker, *SAINT+*, Bruker-AXS Inc, Madison, Wisconsin, USA, 2009.

[397] Bruker, *SADABS*, Bruker-AXS Inc, Madison, Wisconsin, USA, 2004.

[398] G. M. Sheldrick, *TWINABS*, University of Göttingen, Germany, 2008.

[399] G. M. Sheldrick, *Acta Crystallogr. A*, 2015, **71**, 3–8.

[400] G. M. Sheldrick, *Acta Crystallogr. A*, 2008, **64**, 112–122.

[401] O. V. Dolomanov, L. J. Bourhis, R. J. Gildea, J. A. K. Howard and H. Puschmann, *J. Appl. Crystallogr.*, 2009, **42**, 339–341.

[402] A. L. Spek, *Acta Crystallogr. C*, 2015, **71**, 9–18.

[403] A. Boultif and D. Louër, *J. Appl. Crystallogr.*, 2004, **37**, 724–731.

[404] A. Altomare, C. Cuocci, C. Giacovazzo, A. Moliterni, R. Rizzi, N. Corriero and A. Falcicchio, *J. Appl. Crystallogr.*, 2013, **46**, 1231–1235.

[405] T. Renouard and M. Grätzel, *Tetrahedron*, 2001, **57**, 8145–8150.

[406] M. Gaudry and A. Marquet, *Org. Synth.*, 1976, **55**, 24.

[407] D. S. Kopchuk, N. V. Chepchugov, G. A. Kim, G. V. Zyryanov, I. S. Kovalev, V. L. Rusinov and O. N. Chupakhin, *Tetrahedron Lett.*, 2016, **57**, 296–299.

A. Appendix

Table A.1: Additional hydrogen bonds in **2(Mn)**.

Donor—H$\cdots$Acceptor	D—H [Å]	H$\cdots A$ [Å]	$D\cdots A$ [Å]	D—H$\cdots A$ [°]
O11—H11A$\cdots$O4^a	0.98	1.95	2.891(6)	159
O11—H11B$\cdots$O5^b	0.98	1.73	2.691(5)	165
O12—H12A$\cdots$O16	0.98	1.80	2.617(8)	138
O12—H12A$\cdots$O15	0.98	2.09	3.06(2)	167
O12—H12B$\cdots$O1^c	0.98	1.71	2.626(5)	154

Symmetry key: $^a\frac{1}{2}+x, \frac{1}{2}+y, z$; $^b x, 1-y, -\frac{1}{2}+z$; $^c x, 2-y, -\frac{1}{2}+z$.

Table A.2: Additional hydrogen bonds in **2(Co)**.

Donor—H$\cdots$Acceptor	D—H [Å]	H$\cdots A$ [Å]	$D\cdots A$ [Å]	D—H$\cdots A$ [°]
O9—H9C$\cdots$O1	0.98	2.13	2.717(8)	117
O9—H9D$\cdots$O8	0.98	2.00	2.897(8)	151
O10—H10A$\cdots$O4B	0.98	1.75	2.48(2)	128
O10—H10B$\cdots$O5	0.98	1.64	2.572(9)	156

Symmetry key: $^a-\frac{1}{2}+x, \frac{3}{2}-y, -\frac{1}{2}+z$; $^b-\frac{1}{2}+x, -\frac{1}{2}+y, z$; $^c-\frac{1}{2}+x, \frac{1}{2}-y, -\frac{1}{2}+z$.

Table A.3: Additional hydrogen bonds in **2(Cu)**.

Donor—H$\cdots$Acceptor	D—H [Å]	H$\cdots A$ [Å]	$D\cdots A$ [Å]	D—H$\cdots A$ [°]
O9—H9B$\cdots$O8A	0.98	2.21	3.0896(2)	148
O9—H9B$\cdots$O8B	0.98	2.36	3.2106(2)	145
O9—H9B$\cdots$O8B^a	0.98	2.21	2.9772(2)	134
O10—H10A$\cdots$O4B	0.98	1.93	2.5005(2)	114
O10—H10B$\cdots$O5^b	0.98	1.58	2.5194(2)	157
O11—H11B$\cdots$O4A	0.98	2.31	3.2003(2)	150
O11—H11B$\cdots$O4B	0.98	2.15	3.0665(2)	154
O11—H11B$\cdots$O4A^c	0.98	2.25	2.9535(2)	127
O12—H12A$\cdots$O8A^d	0.98	1.95	2.5078(2)	114
O12—H12B$\cdots$O1^e	0.98	1.59	2.5055(2)	153

Symmetry key: $^a x, -1+y, z$; $^b\frac{1}{2}+x, \frac{3}{2}-y, 1/2+z$; $^c 1-x, y, \frac{1}{2}-z$; $^d\frac{1}{2}+x, \frac{1}{2}+y, z$; $^e\frac{1}{2}+x, \frac{3}{2}-y, \frac{1}{2}+z$.

Table A.4: Additional hydrogen bonds in **2(Zn)**.

Donor—H$\cdots$Acceptor	D—H [Å]	H$\cdots A$ [Å]	$D\cdots A$ [Å]	D—H$\cdots A$ [°]
O9—H9A$\cdots$O8A^{a}	0.98	2.21	3.0436(1)	142
O9—H9A$\cdots$O8B^{a}	0.98	2.04	3.0038(1)	167
O9—H9A$\cdots$O8Ab	0.98	2.11	2.4934(1)	101
O9—H9B$\cdots$O1^{c}	0.98	1.93	2.6891(1)	132
O10—H10A$\cdots$O4B	0.98	1.83	2.3589(1)	110
O10—H10B$\cdots$O12^{d}	0.98	2.38	2.8641(1)	110
O11—H11A$\cdots$O4A	0.98	2.19	3.0549(1)	147
O11—H11A$\cdots$O4B	0.98	2.01	2.9701(1)	165
O11—H11B$\cdots$O5^{e}	0.98	1.90	2.7080(1)	138
O12—H12A$\cdots$O1^{c}	0.98	1.56	2.5253(1)	166
O12—H12B$\cdots$O8B^{a}	0.98	1.78	2.4308(1)	120

Symmetry key: $^{a}x, 1+y, z$; $^{b}1-x, 1+y, \frac{1}{2}-z$; $^{c}\frac{1}{2}+x, \frac{1}{2}-y, \frac{1}{2}+z$.

Table A.5: Additional hydrogen bonds in **2(Cd)**.

Donor—H$\cdots$Acceptor	D—H [Å]	H$\cdots A$ [Å]	$D\cdots A$ [Å]	D—H$\cdots A$ [°]
O9—H9A$\cdots$O8A^{a}	0.99	2.34	3.1703(2)	140
O9—H9A$\cdots$O8B^{a}	0.99	2.13	2.9079(2)	134
O9—H9A$\cdots$O8A^{b}	0.99	1.98	2.6831(2)	125
O10—H10A$\cdots$O5^{c}	0.98	1.64	2.5829(2)	159
O10—H10B$\cdots$O4B	0.99	1.78	2.3589(1)	114
O11—H11A$\cdots$O5^{d}	0.87	2.11	2.7763(2)	132
O11—H11B$\cdots$O4A	0.87	2.31	3.1446(2)	160
O11—H11B$\cdots$O4B	0.87	2.13	2.9796(2)	166
O12—H12B$\cdots$O1^{d}	0.98	1.67	2.6333(2)	165

Symmetry key: $^{a}x, 1+y, z$; $^{b}1-x, 1+y, \frac{1}{2}-z$; $^{c}x, 1-y, \frac{1}{2}+z$; $^{d}\frac{1}{2}+x, \frac{1}{2}-y, \frac{1}{2}+z$.

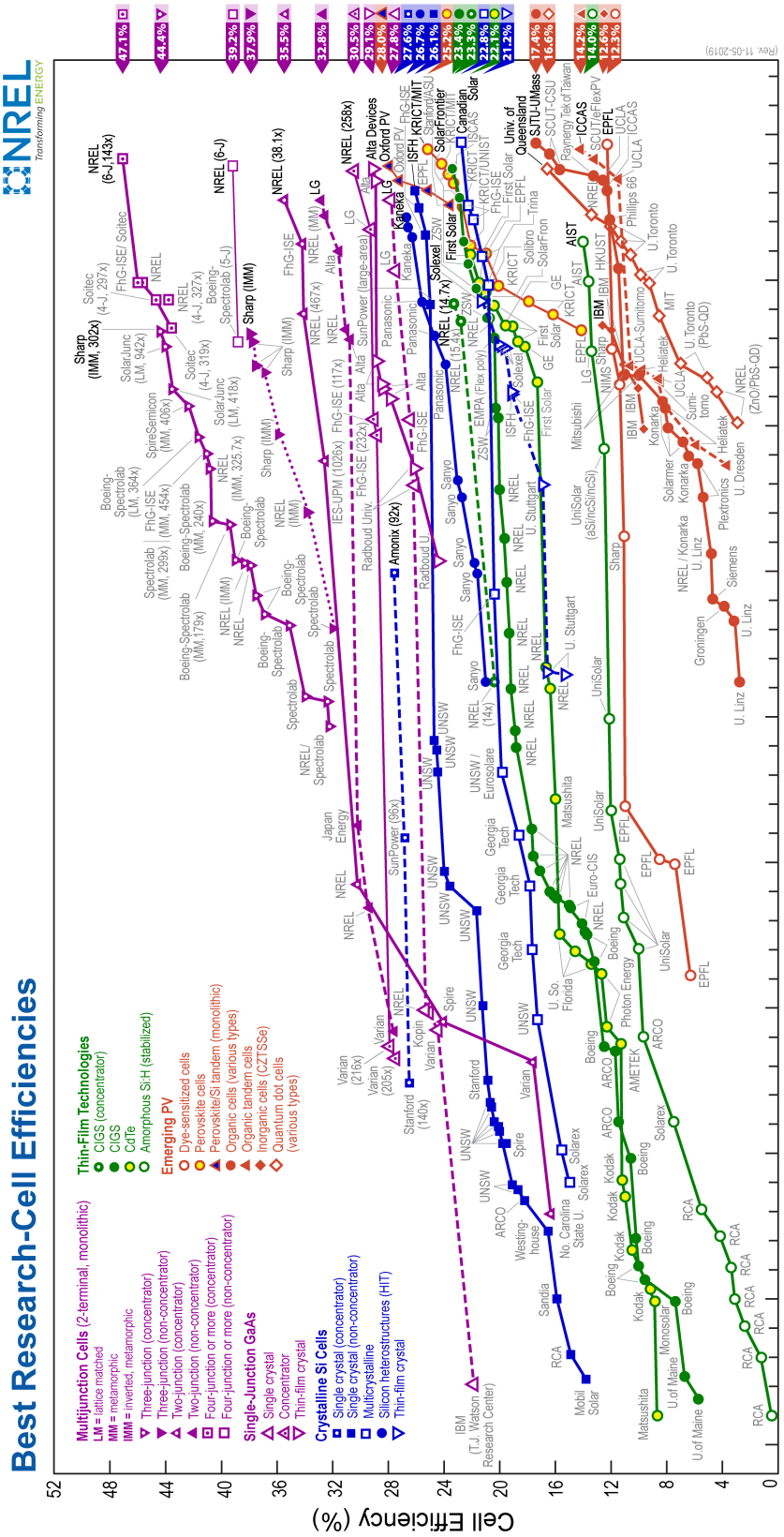


Figure A.1: Best efficiencies of research-photovoltaic cells.[18]

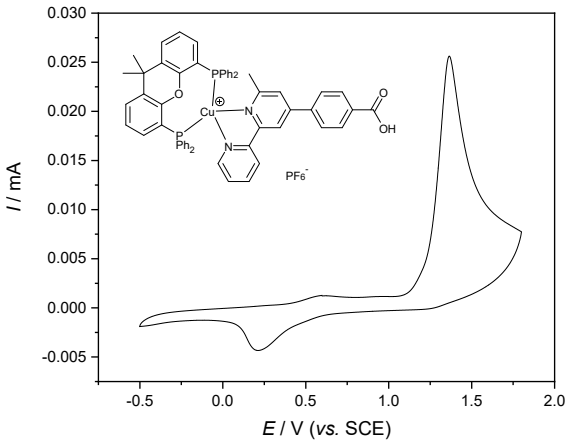


Figure A.2: Cyclic voltammograms of **26b** (10 mM). Experiment was carried using 0.1 M nBu_4PF_6 in DCM as electrolyte, at a scan rate of 50 mV s^{-1}